NanoScience and Technology

Roman Krahne · Liberato Manna
Giovanni Morello · Albert Figuerola
Chandramohan George
Sasanka Deka

Physical Properties of Nanorods

Springer

NanoScience and Technology

For further volumes:
http://www.springer.com/series/3705

The series NanoScience and Technology is focused on the fascinating nano-world, mesoscopic physics, analysis with atomic resolution, nano and quantum-effect devices, nanomechanics and atomic-scale processes. All the basic aspects and technology-oriented developments in this emerging discipline are covered by comprehensive and timely books. The series constitutes a survey of the relevant special topics, which are presented by leading experts in the field. These books will appeal to researchers, engineers, and advanced students.

Roman Krahne · Liberato Manna
Giovanni Morello · Albert Figuerola
Chandramohan George
Sasanka Deka

Physical Properties of Nanorods

Springer

Roman Krahne
Chandramohan George
Nanostructures
Istituto Italiano di Tecnologia
Genoa
Italy

Liberato Manna
Nanochemistry
Istituto Italiano di Tecnologia
Genoa
Italy

Giovanni Morello
Nanoscience Institute of CNR
Lecce
Italy

Albert Figuerola
Departament de Química Inorgànica—
Institut de Nanociència i Nanotecnologia
(IN2UB)
Universitat de Barcelona
Barcelona
Spain

Sasanka Deka
Department of Chemistry
University of Delhi
Delhi
India

ISSN 1434-4904
ISBN 978-3-642-36429-7 ISBN 978-3-642-36430-3 (eBook)
DOI 10.1007/978-3-642-36430-3
Springer Heidelberg New York Dordrecht London

Library of Congress Control Number: 2013937190

Preface

Understanding the size and shape dependence of physical properties in nanoscale particles is a fundamental step towards the design, the fabrication, and the assembly of materials and devices with predictable behavior. In recent years, there has been a remarkable advancement in the ability to fabricate shape-controlled nanoparticles, for example rods, wires, and nanoparticles with branched shapes, especially via synthetic approaches in solution. Shape-controlled inorganic nanoparticles are among the most promising candidates as building blocks in nanoscale materials and devices, both because their physical properties are modified considerably compared to those of spherical nanoparticles and because their intrinsic geometry opens many new opportunities for their assembly into organized super-structures. In this book, we have decided to review the physical properties of elongated inorganic nanoparticles, with particular emphasis on the transition in these properties when the shape of the nanoparticles evolves from a sphere to a rod, but we will consider in many cases also nanowires. From the point of view of specific properties and materials, we have decided to cover the optical properties of semiconductors and noble metals, the electrical properties of semiconductors, the magnetic properties of various metals and metal oxides, the catalytic properties of various classes of materials, and the mechanical properties of metals and metal alloys.

Chapter 1 will give an introduction into some basic quantum physics concepts, specifically tailored to the following Chaps. 2 and 3 that are devoted to the optical and electrical properties of semiconductor nanorods. Semiconductor nanocrystals are among the most studied materials in nanoscience nowadays, due to the large number of potential applications employing these materials, for example, in optical devices (lasers [1–3], light emitting diodes [4, 5], photo-detectors [6], solar cells [7–9]), or biological labeling [10, 11], to cite a few. Elongated, rod-shaped semiconductor nanocrystals possess interesting physical properties which depend on their size, aspect ratio, and chemical composition, and these nanoparticles have been proposed as active materials in light emitting devices [12], photocatalysis [13], optically induced light modulation [14], photovoltaics, [7–9, 15] wave-function engineering [16–18], and optical memory elements exploiting the exciton

storage process [19]. More in general, these nanoparticles have been considered as replacement for spherical nanocrystals (the so-called "quantum dots") in all those studies in which the elongated shape could in principle add new or improved properties.

Chapter 4 will deal with optical properties of elongated metal nanocrystals. Metallic nanocrystals have been proposed in a wide range of applications in various fields, among them sensing, biosensing, photodynamic therapy, photovoltaics, optics (light emitting diodes, photo detectors, lasers, imaging techniques beyond the diffraction limit), nano-optics, and nano-electronics (for example plasmonic waveguides) [20–32]. Metal nanostructures can interact strongly with light in the visible and near infrared region of the spectrum, due to the presence of free electrons, which can be promoted both to empty energy levels in the same band or to levels of an empty overlapping band. An incident electromagnetic field can elicit collective oscillations of these free electrons [20–23], which cause a displacement of the electrons from the nuclei, leading to the formation of various possible distributions in the surface charges. This creates Coulomb interactions between positive and negative charges, which induce restoring oscillating forces acting on free electrons. Each type of surface charge distribution is characterized by a collective oscillation mode, also termed as localized surface plasmon resonance. Various factors influence the possible types of SPRs in nanostructures and the frequencies at which they are observed and the shape of metal nanoparticles is certainly one of them. As an example, in rod-shaped nanoparticles the plasmon mode is split into two modes, a longitudinal one and a transverse one. There are many other physical effects connected with an elongated shape which differ from the spherical case, and these will be covered in detail in Chap. 4.

In Chap. 5 we will review the magnetic properties of elongated nanoparticles. Many of the applications of magnetic nanoparticles are in life sciences and biomedicine [33–35]. Superparamagnetism is the term used for describing the absence of coercivity and remanent magnetization in particles that still maintain a considerable amount of polarizable spins under the effect of an external magnetic field [36, 37]. These magnetic nanocrystals, also known as superparamagnets, combine their reduced sizes with their magnetic field responsive character even if no residual magnetization is observed in the absence of an external magnetic field. For this reason they have been proposed as vectors for both in vitro and in vivo transport of different drugs or biomolecules attached to their surfaces, thereby providing selective access to cellular or molecular levels which are inaccessible to conventional therapeutic approaches. In the same way, they can also be used in biodetection and bioseparation techniques since once the target molecule has been attached to the nanocrystals, the application of an external magnetic field will allow their recovery [38, 39]. Iron oxide is clearly the most suitable material for such purposes due to its high chemical stability, biocompatibility, and superparamagnetic properties and iron oxide nanoparticles are being already used in several diagnostic and therapeutic techniques [40].

The achievement of higher coercivity values in particles with reduced size for information storage devices, or faster magnetic responses for smaller biomedical vectors, could be possible if one considers not only the finite size effects of spherical nanocrystals but also the additional phenomena arising from the shape anisotropy of particles such as nanorods. Nanorods or other one-dimensional nanosystems could also be capable of widening the temperature range of applications of a certain magnetic material compared to its bulk form (as will be shown later). The uniaxial shape anisotropy of metallic and oxide nano-objects will probably become a key factor for the development of improved devices. This chapter will also present an overview of various classes of magnetic materials that have been synthesized in nanorod shapes.

Chapter 6 will deal with the catalytic properties of elongated nanoparticles. Today, there is an increasing demand for catalytic materials, in terms of catalytic efficiency, cost of production, specificity, durability, and environmental sustainability [41–44]. This demand is driving research towards the exploitation of new nanoscale catalyst particles, in which the individual components have specific size, shape, exposure of specific reactive surfaces, and suitable combination of materials [45, 46]. Micro- and nanoparticles of various materials have been used as catalysts for many years [47–50], and experimental evidence has been collected so far demonstrating that the catalytic activity of particles is strongly related to their size, and in particular that nanosized particles exhibit increased catalytic activity with respect to larger particles, due to their higher surface to volume ratio [51, 52]. With recent advances in the synthesis of inorganic nanoparticles with controlled size and morphology [53–56], interest has grown towards the understanding of how the catalytic performance of these materials is dependent on shape. In terms of catalytic properties, there are several reasons why an elongated morphology is often preferable over a spherical morphology, and these will be described in Chap. 6, along with several case studies of nanorod-shaped catalysts.

Chapter 7 deals mainly with the mechanical properties of elongated nanoparticles. The miniaturization of micro electromechanical devices and the fabrication of thin films in the electronic industry have started to raise questions already decades ago about the mechanical behavior of confined systems. Early experiments on tensile testing of metal whiskers with micrometer transverse sides have evidenced strengths much higher than the bulk value [57], and recently pure metals and alloys with at least one dimension in the micro- and nanoscale range have been investigated, thanks to advances in the fabrication of new generations of samples suitable for mechanical testing (for example micro pillars prepared by focused ion beam) and in various techniques for studying their stress and deformation properties. Those studies have revealed a marked deviation in the mechanical properties of samples from bulk-like behavior already when their size is of the order of a few micrometers, which is comparable to the length scale of many plasticity mechanisms based on dislocation nucleation and propagation. The increased

strength of single nanocrystals could be useful for applications of these materials as active probes in nano-indentation, scanning probe microscopy, and field emission [58–60], to cite a few. Chapter 7 ends with a paragraph on melting studies on nanorods.

Finally, we conclude this book with some remarks and an outlook on the future directions in this field.

Genoa — Roman Krahne, Liberato Manna, Chandramohan George
Lecce — Giovanni Morello
Barcelona — Albert Figuerola
Delhi — Sasanka Deka

References

1. Chan Y, Caruge JM, Snee PT, Bawendi MG (2004) Multiexcitonic two-state lasing in a CdSe nanocrystal laser. Appl Phys Lett 85(13):2460–2462
2. Klimov VI, Ivanov SA, Nanda J, Achermann M, Bezel I, McGuire JA, Piryatinski A (2007) Single-exciton optical gain in semiconductor nanocrystals. Nature 447(7143):441–446
3. Klimov VI, Mikhailovsky AA, Xu S, Malko A, Hollingsworth JA, Leatherdale CA, Eisler HJ, Bawendi MG (2000) Optical gain and stimulated emission in nanocrystal quantum dots. Science 290(5490):314–317
4. Caruge JM, Halpert JE, Wood V, Bulovic V, Bawendi MG (2008) Colloidal quantum-dot light-emitting diodes with metal-oxide charge transport layers. Nat Phot 2(4):247–250
5. Anikeeva PO, Halpert JE, Bawendi MG, Bulovic V (2009) Quantum dot light-emitting devices with electroluminescence tunable over the entire visible spectrum. Nano Lett 9(7):2532–2536
6. Oertel DC, Bawendi MG, Arango AC, Bulovic V (2005) Photodetectors based on treated CdSe quantum-dot films. Appl Phys Lett 87(21):art. no. 213505
7. Huynh WU, Dittmer JJ, Alivisatos AP (2002) Hybrid nanorod-polymer solar cells. Science 295(5564):2425–2427
8. Kim S, Fisher B, Eisler HJ, Bawendi M (2003) Type-II quantum dots: CdTe/CdSe(core/shell) and CdSe/ZinTe(core/shell) heterostructures. J Am Chem Soc 125(38):11466–11467
9. Gur I, Fromer NA, Geier ML, Alivisatos AP (2005) Air-stable all-inorganic nanocrystal solar cells processed from solution. Science 310(5747):462–465
10. Deka S, Quarta A, Lupo MG, Falqui A, Boninelli S, Giannini C, Morello G, De Giorgi M, Lanzani G, Spinella C, Cingolani R, Pellegrino T, Manna L (2009) CdSe/CdS/ZnS Double shell nanorods with high photoluminescence efficiency and their exploitation as biolabeling probes. J Am Chem Soc 131(8):2948–2958
11. Michalet X, Pinaud F, Lacoste TD, Dahan M, Bruchez MP, Alivisatos AP, Weiss S (2001) Properties of fluorescent semiconductor nanocrystals and their application to biological labeling. Single Mol 2(4):261–276
12. Zhou RH, Chang HC, Protasenko V, Kuno M, Singh AK, Jena D, Xing H (2007) CdSe Nanowires with illumination-enhanced conductivity: Induced dipoles, dielectrophoretic assembly, and field-sensitive emission. J Appl Phys 101(7):art. no. 073704
13. Hewa-Kasakarage NN, El-Khoury PZ, Tarnovsky AN, Kirsanova M, Nemitz I, Nemchinov A, Zamkov M (2010) Ultrafast carrier dynamics in Type II ZnSe/CdS/ZnSe nanobarbells. ACS Nano 4(4):1837–1844

14. Petti L, Rippa M, Fiore A, Manna L, Mormile P (2010) Optically induced light modulation in an hybrid nanocomposite system of inorganic CdSe/CdS nanorods and nematic liquid crystals. Opt Mater 32(9):1011–1016
15. Farva U, Park C (2010) Colloidal synthesis and air-annealing of CdSe nanorods for the applications in hybrid bulk hetero-junction solar cells. Mater Lett 64(13):1415–1417
16. Muller J, Lupton JM, Rogach AL, Feldmann J, Talapin DV, Weller H (2004) Monitoring surface charge movement in single elongated semiconductor nanocrystals. Phys Rev Lett 93(16):art. no. 167402
17. Muller J, Lupton JM, Lagoudakis PG, Schindler F, Koeppe R, Rogach AL, Feldmann J, Talapin DV, Weller H (2005) Wave function engineering in elongated semiconductor nanocrystals with heterogeneous carrier confinement. Nano Lett 5(10):2044–2049
18. Muller J, Lupton JM, Rogach AL, Feldmann J, Talapin DV, Weller H (2005) Monitoring surface charge migration in the spectral dynamics of single CdSe/CdS nanodot/nanorod heterostructures. Phys Rev B 72(20):art. no. 205339
19. Kraus RM, Lagoudakis PG, Rogach AL, Talapin DV, Weller H, Lupton JM, Feldmann J (2007) Room-temperature exciton storage in elongated semiconductor nanocrystals. Phys Rev Lett 98(1):art. no. 017401
20. Klimov V (2004) Semiconductor and metal nanocrystals. Marcel Dekker, New York
21. Noguez C (2005) Optical properties of isolated and supported metal nanoparticles. Opt Mater 27(7):1204–1211
22. Link S, El-Sayed MA (2000) Shape and size dependence of radiative, non-radiative and photothermal properties of gold nanocrystals. Intern Rev Phys Chem 19(3):409–453
23. Perez-Juste J, Pastoriza-Santos I, Liz-Marzan LM, Mulvaney P (2005) Gold nanorods: Synthesis, characterization and applications. Coord Chem Rev 249(17–18):1870–1901
24. Gonzalez AL, Reyes-Esqueda JA, Noguez C (2008) Optical properties of elongated noble metal nanoparticles. J Phys Chem C 112(19):7356–7362
25. Myroshnychenko V, Rodriguez-Fernandez J, Pastoriza-Santos I, Funston AM, Novo C, Mulvaney P, Liz-Marzan LM, de Abajo FJG (2008) Modelling the optical response of gold nanoparticles. Chem Soc Rev 37(9):1792–1805
26. Zhang JZ, Noguez C (2008) Plasmonic optical properties and applications of metal nanostructures. Plasmonics 3(4):127–150
27. Kelly KL, Coronado E, Zhao LL, Schatz GC (2003) The optical properties of metal nanoparticles: The influence of size, shape, and dielectric environment. J Phys Chem B 107(3):668–677
28. Meier M (2007) Plasmonics: Fundamentals and applications. Springer, New York
29. Link S, El-Sayed MA (2003) Optical properties and ultrafast dynamics of metallic nanocrystals. Ann Rev Phys Chem 54:331–366
30. Huang X, Neretina S, El-Sayed MA (2009) Gold nanorods: From synthesis and properties to biological and biomedical applications. Adv Mater 21:4880–4910. doi:10.1002/adma.200802789
31. Liz-Marzan LM (2006) Tailoring surface plasmons through the morphology and assembly of metal nanoparticles. Langmuir 22:32–41. doi:10.1021/la0513353
32. Schwartzberg AM, Olson TY, Talley CE, Zhang JZ (2006) Synthesis, characterization, and tunable optical properties of hollow gold nanospheres. J Phys Chem B 110(40):19935–19944
33. Dobson J (2006) Magnetic nanoparticles for drug delivery. Drug Dev Res 67(1):55–60
34. Park K, Lee S, Kang E, Kim K, Choi K, Kwon IC (2009) New generation of multifunctional nanoparticles for cancer imaging and therapy. Adv Funct Mater 19(10):1553–1566
35. Wilhelm C, Lavialle F, Péchoux C, Tatischeff I, Gazeau F (2008) Intracellular trafficking of magnetic nanoparticles to design multifunctional biovesicles. Small 4(5):577–582
36. Jeong U, Teng X, Wang Y, Yang H, Xia Y (2007) Superparamagnetic colloids: Controlled synthesis and niche applications. Adv Mater 19(1):33–60
37. Lin X-M, Samia ACS (2006) Synthesis, assembly and physical properties of magnetic nanoparticles. J Magn Magn Mater 305(1):100–109

38. Lu A-H, Salabas EL, Schüth F (2007) Magnetic nanoparticles: Synthesis, protection, functionalization, and application. Angew Chem Int Edit 46(8):1222–1244
39. Dave SR, Gao X (2009) Monodisperse magnetic nanoparticles for biodetection, imaging, and drug delivery: A versatile and evolving technology. Wiley Interdisc Rev Nanomed Nanobiotechnol 1(6):583–609
40. Figuerola A, Di Corato R, Manna L, Pellegrino T (2010) From iron oxide nanoparticles towards advanced iron-based inorganic materials designed for biomedical applications. Pharm Res 62(2):126–143
41. Somorjai GA, Park JY (2008) Molecular factors of catalytic selectivity. Angew ChemInt Edit 47(48):9212–9228. doi:10.1002/anie.200803181
42. Min BK, Friend CM (2007) Heterogeneous gold-based catalysis for green chemistry: Low-temperature CO oxidation and propene oxidation. Chem Rev 107(6):2709–2724. doi:10.1021/cr050954d
43. Heitbaum M, Glorius F, Escher I (2006) Asymmetric heterogeneous catalysis. Angew Chem Int Edit 45(29):4732–4762. doi:10.1002/anie.200504212
44. Roucoux A, Schulz J, Patin H (2002) Reduced transition metal colloids: A novel family of reusable catalysts? Chem Rev 102(10):3757–3778. doi:10.1021/cr010350j
45. Norskov JK, Bligaard T, Rossmeisl J, Christensen CH (2009) Towards the computational design of solid catalysts. Nat Chem 1(1):37–46
46. Cuenya BR (2010) Synthesis and catalytic properties of metal nanoparticles: Size, shape, support, composition, and oxidation state effects. Thin Solid Films 518(12):3127–3150. doi:10.1016/j.tsf.2010.01.018
47. Lewis LN (1993) Chemical catalysis by colloids and clusters. Chem Rev 93(8):2693–2730
48. Schmid G (1992) Large clusters and colloids—metals in the embryonic state. Chem Rev 92(8):1709–1727
49. Astruc D, Lu F, Aranzaes JR (2005) Nanoparticles as recyclable catalysts: The frontier between homogeneous and heterogeneous catalysis. Angew Chem Int Edit 44(48):7852–7872. doi:10.1002/anie.200500766
50. Gates BC (1995) Supported metal clusters: Synthesis, structure, and catalysis. Chem Rev 95(3):511–522
51. Wilson OM, Knecht MR, Garcia-Martinez JC, Crooks RM (2006) Effect of Pd nanoparticle size on the catalytic hydrogenation of allyl alcohol. J Am Chem Soc 128(14):4510–4511. doi:10.1021/ja058217m
52. Herzing AA, Kiely CJ, Carley AF, Landon P, Hutchings GJ (2008) Identification of active gold nanoclusters on iron oxide supports for CO oxidation. Science 321(5894):1331–1335. doi:10.1126/science.1159639
53. El-Sayed MA (2004) Small is different: Shape-, size-, and composition-dependent properties of some colloidal semiconductor nanocrystals. Acc Chem Res 37(5):326–333
54. Yin Y, Alivisatos AP (2005) Colloidal nanocrystal synthesis and the organic–inorganic interface. Nature 437(7059):664–670
55. Cozzoli PD, Pellegrino T, Manna L (2006) Synthesis, properties and perspectives of hybrid nanocrystal structures. Chem Soc Rev 35(11):1195–1208
56. Tao AR, Habas S, Yang PD (2008) Shape control of colloidal metal nanocrystals. Small 4(3):310–325
57. Brenner SS (1959) In: Doremus RH, Roberts BW, Turnbull D (eds) Growth and perfection of crystals. Wiley, New York
58. Greer JR, Nix WD (2005) Size dependence of mechanical properties of gold at the sub-micron scale. Appl Phys A Mater Sci Process 80(8):1625–1629
59. Chattopadhyay S, Chen LC, Chen KH (2006) Nanotips: Growth, model, and applications. Crit Rev Solid State Mater Sci 31(1–2):15–53
60. Mazilova TI, Mikhailovskij IM, Ksenofontov VA, Sadanov EV (2009) Field-Ion microscopy of quantum oscillations of linear carbon atomic chains. Nano Lett 9(2):774–778

Acknowledgment

The entire book was derived from an article that we have published in Physics Reports (Roman Krahne, Giovanni Morello, Albert Figuerola, George Chandramohan, Sasanka Deka and Liberato Manna, Physical Properties of Inorganic Elongated Nanoparticles. Physics Reports Volume 501, Issues 3–5, April 2011, Pages 75–221 (2011) doi:10.1016/j.physrep.2011.01.001).

Contents

Chapter 1
Quantum Effects in Confined Systems

In this chapter we give a short introduction to the basic concept of a particle in a box for the discussion of quantum effects in one dimension. This concept will then be expanded to three dimensions in cylindrical coordinates, which are the most adequate to describe rod shaped nanostructures.

A system in which the motion of electrons or other particles (holes, excitons, etc.) is restricted in one or more dimensions, due to some potential profile, is usually referred to as a "low-dimensional" system and shows quantum confinement effects. Due to their dual wave-particle nature, electrons in a solid are treated as particles having an effective mass m^* (accounting for the periodicity of the crystal potential) and a linear momentum arising from their wave-like nature $\vec{p} = \hbar\vec{k}$. Here, $\hbar$ is the Planck's constant divided by 2π, and $\vec{k}$ represents the wavenumber of the associated wave of wavelength $\lambda = 2\pi/k$. The behavior of the electrons is strongly sensitive to the dimensions of the solid in which they move. In the bulk, the infinite extension of the solid is imposed by assigning the so-called periodic boundary conditions, such that the electrons are not affected by the borders of solid in terms of wave function and energy. If however the dimensions of the solid are reduced, the electrons start to "feel" the borders and the assumption of infinite extension of the solid in all the three spatial coordinates does not hold any more. In such a case the system is considered as "quantized".

1.1 One-Dimensional Quantum Box

The simplest way to understand what happens to electrons in the case of a quantized system (in terms of wavefunctions and energies) is to consider the classical textbook case of an electron in a box, which is approached by solving the Schrödinger equation in one dimension (Fig. 1.1) [1]:

$$\frac{d^2\psi}{dx^2} + \frac{2mE}{b^2} = V \quad \text{with} \quad V = \left\{ \begin{array}{ll} 0, & -a/2 < x < a/2 \\ \infty, & x \leq -a/2, x \geq a/2 \end{array} \right\} \tag{1.1}$$

R. Krahne et al., *Physical Properties of Nanorods*,
NanoScience and Technology, DOI: 10.1007/978-3-642-36430-3_1,

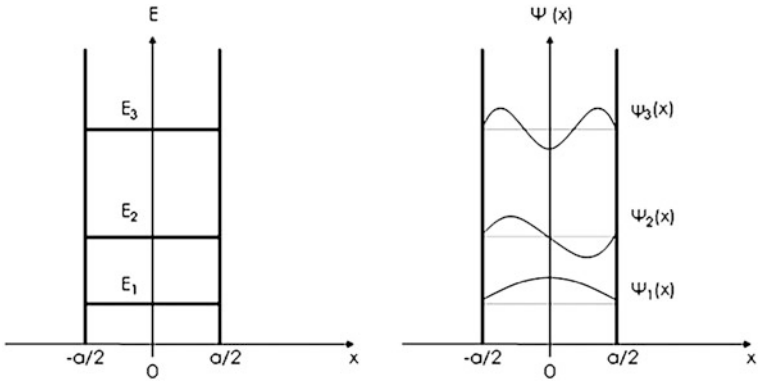

Fig. 1.1 Electrons in a one dimensional quantum box: energy levels and wave functions

We seek for a solution of the form:

$$\psi(x) = Ae^{ikx} + Be^{-ikx} \tag{1.2}$$

Since the potential is infinitely high at the border regions, we need to impose the conditions that the wave functions have to vanish at the borders (i.e. $\psi(-a/2) = 0$ and $\psi(a/2) = 0$, see Fig. 1.1). Upon imposing $\psi(-a/2) = 0$ we obtain:

$$\psi(x) = A\left(e^{ikx} - e^{-ikx}\right) = 2iA\sin(kx) \tag{1.3}$$

and, after substitution in the Schrödinger equation we obtain the following expression for the energy:

$$E = \frac{\hbar^2 k^2}{2m} \tag{1.4}$$

Since $\psi(a/2) = 0$, the following identity must hold:

$$\psi(a/2) = 2iA\sin(ka) = 0 \tag{1.5}$$

The identity is verified only when $ka = n\pi$, with n = 1, 2, 3. Therefore the parameter k is quantized, and the separation between two consecutive values of k is $\Delta k = \Delta n\pi/a$. The quantization energy is expressed as:

$$E_n = \frac{\hbar^2 \pi^2}{2ma^2} n \tag{1.6}$$

In the expression above, the confinement energy is inversely proportional to the square of the size a of the box. As a result, a large value of a corresponds to small spacing of the values in k-space. In the bulk, for example, in which a is practically infinite, there will be a continuous distribution of states in the k-space, in all spatial directions. In a quantum well only one spatial dimension is reduced (down to a few nm), and the electrons can freely move only in a plane, i.e. they behave as a

two-dimensional electron gas (2DEG). The wave numbers have a quasi-continuous distribution along that plane, whereas they are "quantized" along the reduced dimension, following the relation $\Delta k = \Delta n\pi/a$. Several quantum well systems have been fabricated and studied to date (for an overview of some of the pioneering works see for example Refs. [2–6]). If the movement is restricted in two directions, the system is referred to as a "quantum wire", and the electrons can move freely only along the non-reduced dimension. Examples of 1D systems are inorganic semiconductor and metallic nanowires, some organic molecules and carbon nanotubes [7–19]. In the case of quantization in all directions, the electrons possess discrete wavenumbers in the *k*-space and the system is called a "quantum dot". One way to discriminate among the different quantized systems in terms of electronic states is via the density of states function D(E), which represents the number of electronic states in a unitary interval of energy (Fig. 1.2).

In a bulk material (a three-dimensional solid) the density of states follows the well known dependence on the square root of the energy (3D case in Fig. 1.2). This situation corresponds to a quasi-continuous distribution of states for a free-electron gas. In the 2D case (i.e. a two-dimensional solid, 2D case in Fig. 1.2), the global density of states function preserves the quasi-continuous character but becomes a step function framed by the initial square root function. As a consequence, a zero-point energy is introduced and the step spacing is dictated by the energy spacing along the quantized direction. In the 1D case (the "quantum wire") the wave numbers are quantized in two directions and the density of states follows a saw-tooth function (1D case in Fig. 1.2). The latter still describes a quasi-continuous distribution of states, but is now characterized by series of singularities corresponding to the quantization introduced in two dimensions, while the hyperbolas in between two singularities are well described by the reverse of square root of the energy. The 0D sketch of Fig. 1.2 shows what happens in the case of quantization in all three dimensions. The quasi-continuous distribution of states has now collapsed into a series of discrete levels, represented by several Dirac delta functions. In the case of a flat potential with infinite boundaries, the level spacing increases with energy, as described by Eq. (1.6). Such atomic-like structure in the density of states makes these 0D systems fascinating objects, for what concerns both fundamental physics and technological applications [20–25].

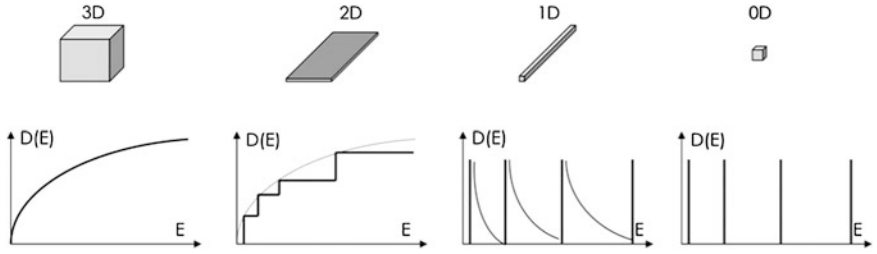

Fig. 1.2 Evolution of the "density of states" function from a bulk (3D solid) to a 2D, 1D and 0D system

1.2 Quantum Confinement in Nanorods

The finite size of the nanorods leads to quantum confinement effects and consequently affects their energy level structure. The optical, electrical, and mechanical properties of the nanorods can be discussed in terms of the related quasi-particles like excitons, electrons, holes, and phonons confined to a cylinder with length L and diameter D. Quantum size effects will have significant impact if the length L, or the diameter D, or both, are of the order or smaller than the Bohr radius associated with the respective quasi-particle. This effective Bohr radius is defined as $a_b = \varepsilon(m/m^*)a_0$, where m and a_0 are the electron mass and Bohr radius, respectively, m^* is the effective mass of the quasi-particle in the bulk material of which the nanocrystal is composed and ε is the dielectric constant of the nanocrystal material in the bulk. The energy spectrum of a quasi-particle confined to a cylinder can be derived from the three-dimensional Schroedinger equation in cylindrical coordinates r, ϕ, and z, and towards that scope we will briefly sketch the solutions in these coordinates. In the simplest case, we can discuss a free particle with effective mass m^* that is confined by infinitely high potential barriers within the cylinder with radius R = D/2 and length L, i.e. the potential V(r) = 0 for r < R and infinite otherwise. In this case independent solutions for the three coordinates can be found of the form [26]:

$$\psi(r,\phi,z) = \rho(r)\Phi(\phi)Z(z) \tag{1.7}$$

Where:

$$\frac{d^2Z}{dz^2} = k_{zk}^2 Z \tag{1.8}$$

$$\frac{d^2\Phi(\phi)}{d\phi^2} = -l^2\Phi \tag{1.9}$$

$$r^2\frac{d^2\rho}{dr^2} + r\frac{d\rho}{dr} + \left(k_{\mathrm{In}}^2 r^2 - l^2\right)\rho = 0 \tag{1.10}$$

With the relation $\kappa^2 = k_{zk}^2 + k_{\mathrm{In}}^2$ for the momentum vector. The solution in z, along the c axis of the rod, is of the form

$$Z(z) = \sin(k_{zk}) = \sin\left(\frac{k\pi}{L}z\right),\ k = 1,2,3,\ldots, \tag{1.11}$$

and has a similar form as the result obtained for a box potential in Eq. (2.5).

In the radial direction we obtain solutions to the Bessel equation:

$$\rho(r) = AJ_l(k_{\mathrm{In}}r) + BY_l(k_{\mathrm{In}}e) \tag{1.12}$$

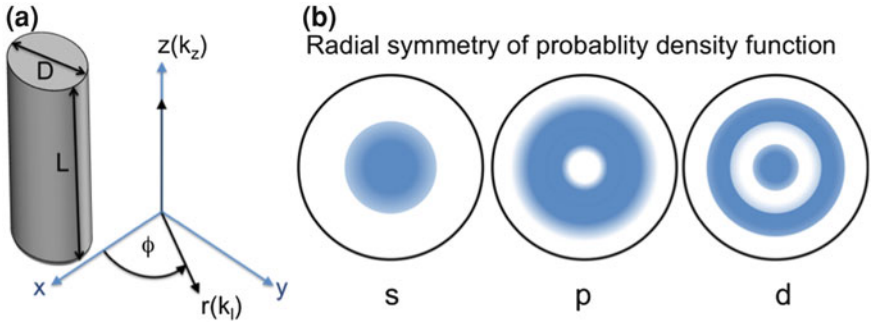

Fig. 1.3 **a** Illustration of the cylindrical coordinates r(kl), z(kz), and f with respect to the rod shape. **b** Schematic illustration of the radial symmetry of the probability density function corresponding to the wave functions in Fig. 1.1

With A and B numbers and J_l and Y_l Bessel functions of the order l of the first and second kind. Due to the radial symmetry this leads to ring like distribution of the wave functions around the z axis of the nanorod as illustrated in Fig. 1.3.

References

1. Yoffe AD (2001) Adv Phys 50(1):1–208
2. Yuan YR, Pudensi MAA, Vawter GA, Merz JL (1985) J Appl Phys 58:397–403
3. Bergman JP, Zhao QX, Holtz PO, Monemar B, Sundaram M, Merz JL, Gossard AC (1991) Time-resolved measurements of the radiative recombination in Gaas/Alxga1-Xas heterostructures. Phys Rev B 43(6):4771–4776
4. Knap W, Borovitskaya E, Shur MS, Hsu L, Walukiewicz W, Frayssinet E, Lorenzini P, Grandjean N, Skierbiszewski C, Prystawko P, Leszczynski M, Grzegory I (2002) Acoustic phonon scattering of two-dimensional electrons in GaN/AlGaN heterostructures. Appl Phys Lett 80(7):1228–1230
5. Katz O, Horn A, Bahir G, Salzman J (2003) Electron mobility in an AlGaN/GaN two-dimensional electron gas I–carrier concentration dependent mobility. IEEE Trans Elec Dev 50(10):2002–2008
6. Mora-Ramos ME, Tutor J, Velasco VR (2006) Interface-phonon-limited two-dimensional mobility in AlGaN/GaN heterostructures. J Appl Phys 100 (12): Article no 123708
7. Hu JT, Odom TW, Lieber CM (1999) Chemistry and physics in one dimension: Synthesis and properties of nanowires and nanotubes. Acc Chem Res 32(5):435–445
8. Cui Y, Lieber CM (2001) Functional nanoscale electronic devices assembled using silicon nanowire building blocks. Science 291(5505):851–853
9. Hakkinen H, Barnett RN, Scherbakov AG, Landman U (2000) Nanowire gold chains: formation mechanisms and conductance. J Phys Chem B 104(39):9063–9066
10. Cobden DH (2001) Molecular electronics–nanowires begin to shine. Nature 409(6816):32–33
11. Cui XD, Primak A, Zarate X, Tomfohr J, Sankey OF, Moore AL, Moore TA, Gust D, Harris G, Lindsay SM (2001) Reproducible measurement of single-molecule conductivity. Science 294(5542):571–574
12. Tans SJ, Devoret MH, Dai HJ, Thess A, Smalley RE, Geerligs LJ, Dekker C (1997) Individual single-wall carbon nanotubes as quantum wires. Nature 386(6624):474–477

13. Saito S (1997) Carbon nanotubes for next-generation electronics devices. Science 278(5335):77–78
14. Yao Z, Postma HWC, Balents L, Dekker C (1999) Carbon nanotube intramolecular junctions. Nature 402(6759):273–276
15. de Heer WA, Chatelain A, Ugarte D (1995) A carbon nanotube field-emission electron source. Science 270(5239):1179–1180
16. Srivastava S, Santos A, Critchley K, Kim KS, Podsiadlo P, Sun K, Lee J, Xu CL, Lilly GD, Glotzer SC, Kotov NA (2010) Light-controlled self-assembly of semiconductor nanoparticles into twisted ribbons. Science 327(5971):1355–1359
17. Duan XF, Huang Y, Agarwal R, Lieber CM (2003) Single-nanowire electrically driven lasers. Nature 421(6920):241–245
18. Oulton RF, Sorger VJ, Zentgraf T, Ma RM, Gladden C, Dai L, Bartal G, Zhang X (2009) Plasmon lasers at deep sub wavelength scale. Nature 461(7264):629–632
19. Baughman RH, Zakhidov AA, de Heer WA (2002) Carbon nanotubes–the route toward applications. Science 297(5582):787–792
20. Bawendi MG, Steigerwald ML, Brus LE (1990) The quantum mechanics of larger semiconductor clusters (quantum dots). Ann Rev Phys Chem 41(V41):477–496
21. Alivisatos AP (1996) Semiconductor clusters, nanocrystals, and quantum dots. Science 271:933–937
22. Alivisatos AP (1998) Electrical studies of semiconductor-nanocrystal colloids. MRS Bull 23(2):18–23
23. Nirmal M, Dabbousi BO, Bawendi MG, Macklin JJ, Trautman JK, Harris TD, Brus LE (1996) Fluorescence intermittency in single cadmium selenide nanocrystals. Nature 383(6603):802–804
24. Konstantatos G, Howard I, Fischer A, Hoogland S, Clifford J, Klem E, Levina L, Sargent EH (2006) Ultrasensitive solution-cast quantum dot photo detectors. Nature 442(7099):180–183
25. Beaulac R, Schneider L, Archer PI, Bacher G, Gamelin DR (2009) Light-induced spontaneous magnetization in doped colloidal quantum dots. Science 325(5943):973–976
26. Eisberg R, Resnick R (1985) Quantum Physics of Atoms, Molecules, Solids, Nuclei, and Particles, 2nd edn. Wiley, New York

Chapter 2
Optical Properties of Semiconductor Nanorods

2.1 Introduction

The optical properties of nanocrystals are dictated by their electronic structure, and we start this section with discussing the behavior of electron–hole pairs, the so called excitons, in confined systems. We then describe the optical peculiarities of semiconductor nanorods by highlighting the main characteristics that distinguish them from the more traditional quantum dots. The first part of this section will focus on the comprehension of the general properties of nanorods made of a single material (henceforth referred to as "homo-structures"), while in the second part of the section we will highlight the properties of nanorods made of sections of different materials (henceforth referred to as "heterostructures"), which have been synthesized by various groups thanks to the latest developments in colloidal nanocrystal synthesis.

2.2 Excitons and Quantum Confinement Regimes

The energy gap of a semiconductor is the energetic separation between the lowest unoccupied electronic state and the highest occupied state at 0 K. The exciton band gap is written as:

$$E_g = E_{g0} + E_q + E_C \tag{2.1}$$

where E_{g0} is the energy gap of the corresponding bulk solid, E_q is the contribution introduced by the quantization and corresponds to the zero-point energy for each system, and E_C is the contribution of the Coulomb attraction between electrons and holes. Their relative contribution is basically related to the degree of confinement to which a system is subjected. In order to better define the role of the quantum confinement on each term of the above expression, we need to introduce the concept of "exciton", which is a "quasi-particle". An exciton is a bound system, composed of an electron (e) and a hole (h) that experience a mutual Coulomb

R. Krahne et al., *Physical Properties of Nanorods*,
NanoScience and Technology, DOI: 10.1007/978-3-642-36430-3_2,

interaction. Here, we will be dealing with a particular type of exciton, in which the e–h distance is much larger than the lattice constant of the crystal in which it is formed, and is usually referred to as a "Wannier-Mott exciton" [1]. One key parameter associated with the exciton is its binding energy, which is defined as:

$$E_b = \frac{\hbar^2}{2\mu r_B^2} \tag{2.2}$$

In the expression above, μ is the reduced mass of the exciton, defined as $1/\mu = (1/m_e + 1/m_h)$, m_e and m_h being the effective masses of electrons and holes, respectively. r_B represents instead the Bohr radius of the exciton, defined as:

$$r_B = \frac{\hbar^2 \varepsilon^2}{\mu e^2} \tag{2.3}$$

with ε being the dielectric constant of the semiconductor. The Bohr radius of the exciton represents its natural spatial extension after its creation (i.e. upon electron–hole pair generation) until its annihilation (upon electron–hole recombination). In bulk semiconductors such radius ranges from a few nm to some tens of nm, depending on the material. The quantization energy is related to the zero-point energy of electrons and holes in the system, and it has always a positive value. In a spherical nanocrystal, for instance, it is defined as [2]:

$$E_q^{e,h} = \frac{\hbar^2 \pi^2}{2m_{e,h} a^2} \tag{2.4}$$

The Coulomb contribution is in general negative, but in some cases it can also be positive (see later in this section). It is proportional to $e^2/\varepsilon^2 a$ and in a spherical quantum dot it can be estimated (as a first approximation) as being equal to [2]:

$$E_C = -1.8 \frac{e^2}{\varepsilon^2 a} \tag{2.5}$$

Therefore, by considering all contributions, the energy gap can be derived from the following expression:

$$E_g = E_{g0} + \frac{\hbar^2 \pi^2}{2m_e a^2} + \frac{\hbar^2 \pi^2}{2m_h a^2} - 1.8 \frac{\hbar^2}{\mu r_B a} \tag{2.6}$$

The optical properties of a semiconductor nanocrystal are dictated by the ratio between the spatial confinement, i.e. the size of the nanocrystal (a), and the Bohr radius r_B of the exciton. Depending on this ratio, three different regimes of quantization can be defined: weak ($a \gg r_B$), intermediate ($a \approx r_B$) and strong ($a < r_B$). In the weak confinement regime, the Coulomb term dominates. Electrons and holes can form the exciton and do not actually "feel" the "restricted" size of the semiconductor. In the intermediate regime, the system can behave in different ways, depending on the ratios between a and the Bohr radii of electrons (r_e) and of the holes (r_h), respectively. In the case that r_h is smaller than r_e the hole will stay

confined at the center of the nanocrystal with the electron orbiting around it, similarly to the case of a donor impurity [3, 4], if a falls in between r_h and r_e. In the strong confinement regime the quantization term dominates over the binding energy of exciton.

2.3 Optical Properties of Nanorods: Overview

The dependence of the energy gap on the size of the nanocrystals is used as a powerful tool for designing materials with well-controlled optical properties. The continuous progress in the development of novel and sophisticated synthesis techniques has opened the possibility to exploit other key parameters for engineering the electronic structure of nanocrystals, such as the shape and the chemical composition. In this respect chemical approaches employing the so-called "high-temperature" thermal reaction of precursors in surfactants have become a popular route to colloidal nanoparticles. This method is so powerful and versatile that a large fraction of nanocrystals discussed in this review have been fabricated in this way. It is also important to note that this method, as many others, yields nanocrystals that are stabilized in the liquid phase by means of a monolayer of organic molecules (i.e. the surfactants) bound to their surface. These molecules need to be considered as a fundamental component of the nanocrystal as they play an important roles in the various physical properties of the nanocrystal, as will be discussed extensively in this review.

Elongated (i.e. rod-shaped) nanocrystals, also known as nanorods, are probably the most studied nanocrystal systems after the spherical ones. Other more complex shapes have been investigated too, but they will not be discussed here [5]. The typical lengths of the nanorods span from tens to some hundreds of nm, while their diameters are generally in the range of a few nm. These nanorods can be considered as intermediate systems between quantum dots and nanowires, since the nanorod length is typically larger than the Bohr radius. Therefore the carriers experience strong confinement only along two dimensions, whereas they can delocalize along the long axis of the rod, giving rise to the so called 1D exciton [6]. This confinement leads to a variety of new properties with respect to spherical nanocrystals, in terms of electronic structure, symmetry, polarization and carrier dynamics.

2.4 Electronic Structure of CdSe Nanorods: A Case Study

Among rod-shaped semiconductor nanocrystals, CdSe nanorods represent probably the most investigated samples, for what concerns both their optical and their electronic properties. Here, we will give an overview of their electronic structure, by highlighting some of the pioneering works in the field (for example those by

Efros et al. [7–9] and by Woggon et al. [10–13]). The concepts discussed here can be considered as of general validity for nanocrystals having hexagonal crystallographic structure and are applicable to nanorods of a wide range diameters and lengths. The starting point is to consider a nanocrystal with dimensions that are much greater than its lattice constant, such that the effective mass approximation [7] is applicable. This condition is practically fulfilled in all cases, since the nanocrystal diameter is hardly smaller than 2–3 nm. In the case of quantum dots, the notation used to name the quantum states follows closely that of an atomic system. We define the total angular momentum J = (L + S) as the sum of the total orbital angular momentum L and the multiplicity term S, the latter accounting for the electron spin. The relative momentum projections are j, l, and s. The electron ground state has s-symmetry and presents a double degeneracy, which is due exclusively to the spin momentum. Thus J = 0 + 1/2, its projections are j = ±1/2, and the state is conventionally indicated as $1S_e$. On the other hand, the first hole level, having a p-symmetry, is fourfold degenerate, having J = 1 + 1/2 = 3/2 (j = 3/2, 1/2, −1/2, −3/2), and is named $1S_{3/2}$. The composition of the two ground states yields the eightfold degenerate exciton ground state $1S_{3/2}1S_e$.

Various effects intervene to lift the degeneracy of the states, namely the internal crystal field, shape effects and the electron–hole exchange interaction. The first effect arises from an intrinsic property of semiconductors that have hexagonal lattice structure and therefore manifests itself in both bulk and nanoscale materials. The second effect results from the deviation from the ideal spherical shape of nanocrystals, while the third accounts for mixing of electron and hole spins. The first two effects can be grouped together, as they arise from the intrinsic asymmetry of the material/nanocrystal (see Fig. 2.1). The intrinsic crystal field produces a first splitting of the valence band, i.e. the lowest hole state, in the so called Kramers doublet, which consists of two doubly degenerate states with j = ±1/2 and j = ±3/2 [7]. Let us define a parameter β as the ratio between the mass of the light hole m_{lh} and the mass of the heavy hole m_{hh} (hence $\beta = m_{lh}/m_{hh}$). The energetic splitting due to the intrinsic crystal field is then expressed as [7]:

$$\Delta_1 = \Delta_{CF} f(\beta) \tag{2.7}$$

where Δ_{CF} is a parameter related to the crystal field (CF) splitting in a crystal with hexagonal structure, contributing to determine the hole ground state as that having |j| = 3/2, while $f(\beta)$ is a function which is unique for each material (see Ref. [7] for details). It is worth to stress that Δ_1 does not depend on the size of nanocrystal. Since $f(\beta)$ is always positive, the lowest hole level is fixed with the heavy-hole state with |j| = 3/2.

In order to take the shape anisotropy into account, let us model an elongated nanocrystal as an axially symmetric ellipsoidal particle (i.e. an ellipsoid with principal axes $a = b < c$), and let us define the ratio of the major to minor axes as $c/b = 1 + \varepsilon$, ε being the ellipticity. The induced splitting in this case is:

$$\Delta_2 = 2u(\beta)E_1(\beta)\varepsilon \tag{2.8}$$

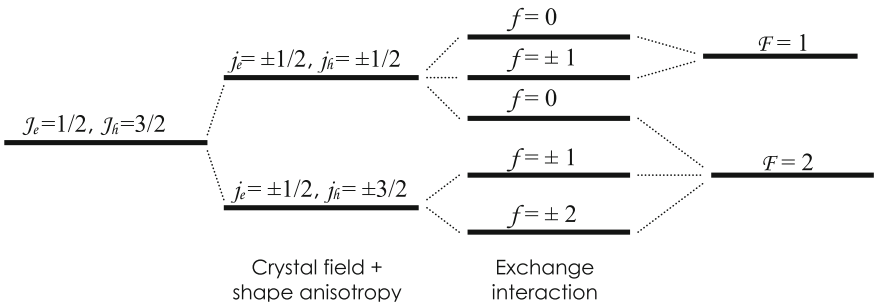

Fig. 2.1 Fine structure splitting of the lowest excitonic states $F = 1$ and $F = 2$ in CdSe nanocrystals due to crystal field, shape anisotropy and exchange interactions

Here, $u(\beta)$ is a dimensionless function associated with the hole-level splitting due to the crystal shape (see Fig. 2.2), for details see Ref. [7]) and $E_1(\beta)$ is the hole ground state energy which can be written as:

$$E_1(\beta) = \frac{\hbar^2 \varphi^2(\beta)}{2m_{hh}a^2} \tag{2.9}$$

where $\varphi^2(\beta)$ is a term related to the spherical Bessel functions and a is related to the nanocrystal size. For quasi spherical nanocrystals $a = (b^2c)^{1/3}$.

Another important point is the trend in the function $u(\beta)$, in particular for what concerns its sign [7]. As shown in Fig. 2.2c $u(\beta)$, reverses its sign past a certain value of β, meaning that for some materials the shape anisotropy induces a negative splitting. Since the global energy splitting is the sum of the single asymmetry contributions $(\Delta_t = \Delta_1 + \Delta_2)$, the final result can reverse the hole ground state between |j| = 3/2 and |j| = 1/2. A negative Δ_2 is found for example in CdSe nanorods, for which $\beta = 0.28$, and where a possible inversion would depend on the hole ground state energy and on the radius of rods.

We now discuss the excitons, formed by composition of these electron–hole states, which result in two-excitonic fourfold degenerate states, having total angular momentum F = 1 and F = 2 (see right side of Fig. 2.1). The exchange interaction contributes to an increase of the splitting of the remaining states, defining a fine structure for nanocrystals for a series of possible shapes, as depicted in Fig. 2.3 [7].

The relevant quantum number, in this case, is the projection f of the total angular momentum F. The fine structure of the lowest excitonic level is composed by a distribution of states having different values of f: one state with f = ±2, two states with f = ±1 (named Upper and Lower, depending on the branch they originate) and two others with f = 0 (Upper and Lower). Only three of them are optically active, namely the states 0^U, $\pm 1^U$ and $\pm 1^L$, whereas the remaining ±2 and 0^L states are passive [7]. The ±2 state is optically forbidden because photons cannot have an angular momentum ±2. The 0^L has zero optical transition probability because of an interference phenomenon between the two indistinguishable states

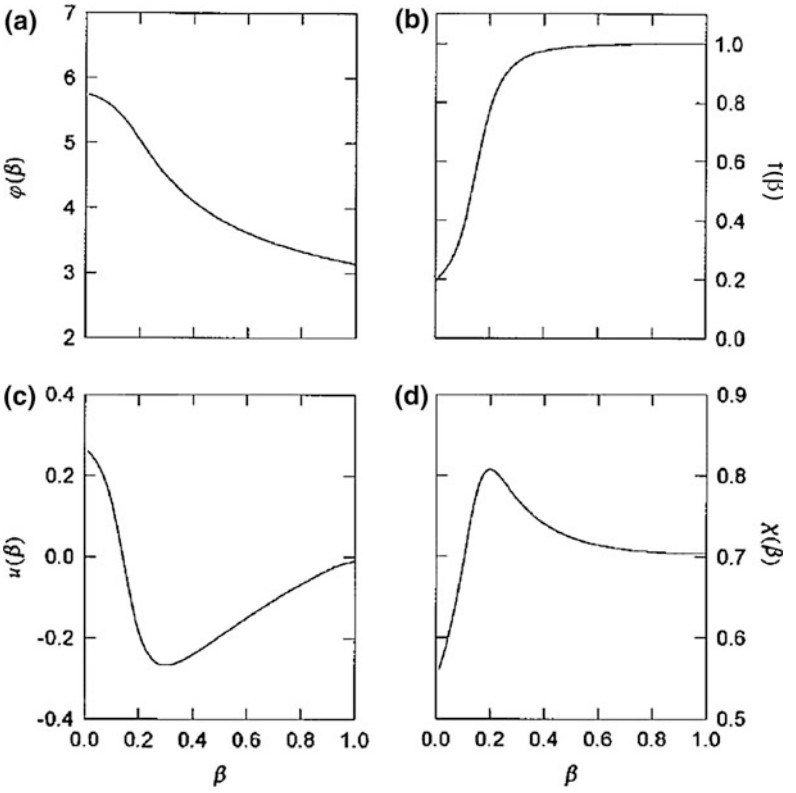

Fig. 2.2 **a** Dependence of the hole ground state function on the light-to-heavy hole ratio mass β. **b–d** Dimensionless functions associated with: **b** hole level splitting due to hexagonal lattice structure, **c** the hole splitting due to the crystal shape asymmetry, **d** the exciton splitting due to the electron–hole-interaction. Taken with permission from Ref. [7]

with zero angular momentum [2], due to the influence of the electron–hole exchange interaction.

The shape of the nanocrystal can have significant influence on which of the above states represents the exciton ground state. For perfectly spherical nanocrystals the ± 2 is the ground state, whereas in prolate nanocrystals an inversion of the ± 2 with the 0^L state can occur, because the state ± 2 originates from the hole state with $|j| = 3/2$, whilst 0^L arises from the state $|j| = 1/2$. When the conditions for the sign change of Δ_t are met, the ground state is inverted. Nanorods can be approximated by axially symmetric prolate ellipsoids with ellipticity ε defined as $\varepsilon = (2r_B/b) - 1$, with b being the ellipsoid diameter and r_B the Bohr radius. In the case of strong lateral confinement $(b < 2r_B)$, the ellipsoids are subject to a possible inversion of the ground state between $\pm$ 2 and 0^L. Following Eq. (2.8), the shape asymmetry can lead to a negative splitting value Δ_2 and then to a negative net splitting $\Delta_t = \Delta_1 + \Delta_2 < 0$, if the ellipsoid radius is smaller than a critical value.

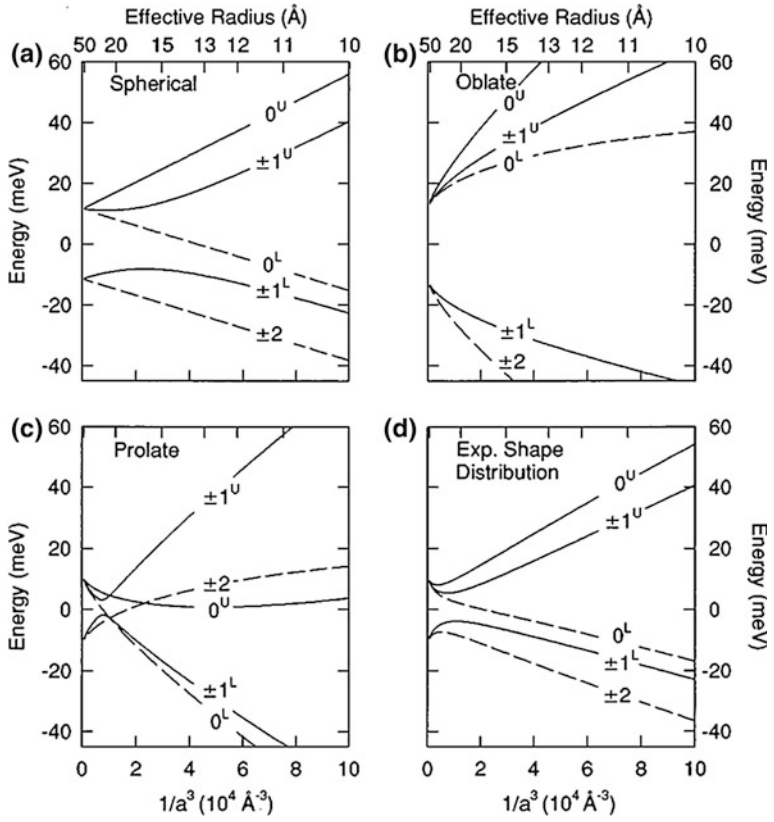

Fig. 2.3 Evolution of the band-edge exciton as a function of the nanocrystal size calculated for four different shapes. Reprinted with permission from Ref. [7]

This can happen because Δ_2 becomes increasingly important in the strong confinement regime, and at some point it would cause the light-hole state with $j = \pm 1/2$ to become the hole ground state. The coupling with the electron state $1S_e$ yields a fourfold degenerate state, with angular momentum 0 (two states) and ± 1. The hole state with $j = \pm 3/2$ yields the second doubly degenerate state with momentum ± 1 and ± 2. In practice, the new lowest exciton level would be the state 0^L and the exciton fine structure resembles that of Fig. 2.3c.

Woggon and co-workers [10] calculated the electronic fine structure of a single CdSe nanorod, taking into account the typical electron–hole exchange interaction for their system (see Fig. 2.4). As expected, by varying the rod radius, two regimes could be identified: for a radius smaller than about 3.7 nm the arrangement of states reflects the well-known fine structure of a spherical nanocrystal, i.e. the lowest energy exciton has angular momentum ± 2. For larger radii on the other hand the exciton ground state has zero angular momentum projection along the major rod axis. This would induce a strongly polarized emission of light, as

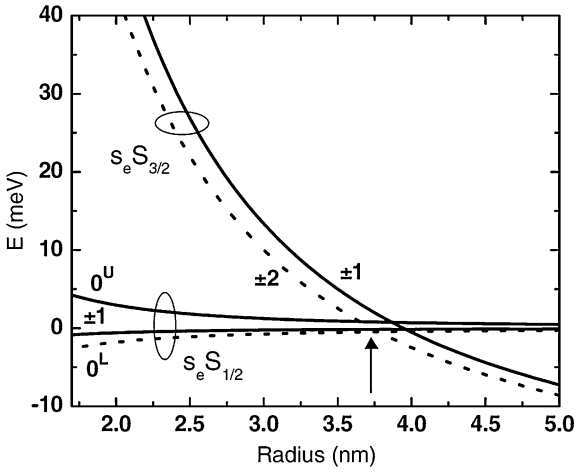

Fig. 2.4 Calculated exciton fine structure of CdSe nanorods. Taken with permission from Ref. [10]

opposed to the quasi-circularly polarized emission predicted for the ±1 excitons. Due to the small energetic separation among these states, thermal population processes give rise to novel phenomena in terms of polarization and carrier relaxation (as discussed later on).

2.5 Relaxation Mechanisms in Nanorods

The carrier mobility in nanorods has a 1D character [6], and this leads to optical properties in nanorods that are remarkably different from those of spherical nanocrystals, among them photoluminescence (PL) lineshape and polarization, radiative and nonradiative transitions, and their dependence on nanocrystal size and temperature. Their understanding represents a first step towards the exploitation of such nanostructures in optical devices. In this section we will discuss the basic optical properties of nanorods in terms of relaxation processes and spectral features, by stressing the differences between nanorods that are entirely made of one material (homo-structures) and those made by sections of different materials (heterostructures). We will distinguish the case of electron–hole relaxation inside the same material from that of relaxation concerning carriers localized in two different materials. In the first case, the possible optical transition is named of type-I, whereas in the second case is of type-II.

2.5.1 One-Dimensional Excitons in Homostructures

In the previous section we have described the fine structure of the ground state exciton in nanorods having a wurtzite structure. Here we will summarize the

experimental evidences collected by optical spectroscopy measurements, carried out on single nanorods and on ensembles of nanorods, and we will highlight the differences of nanocrystals with respect to the more traditional spherical nanocrystals. In nanorods, two confinement regimes can coexist, causing the transition energy to vary mainly as a function of the lateral confinement instead of the rod length. In Fig. 2.5 the effect is clearly visible from the absorption spectra of a series of CdSe nanorods of different diameters and lengths [14]. Two sets of five samples were analyzed in the study (Fig. 2.5). In one set (Fig. 2.5a), the nanorods had different lengths (12.5, 17.5, 25, 30 and 35 nm, from a to e) and comparable diameters (around 5 nm), while in the other set (Fig. 2.5a), the nanorods had different diameters (3.5, 4, 4.25, 4.5 and 5 nm from a to e) and comparable lengths (around 20 nm). By changing the nanorod length there was no appreciable shift of the optical transitions, whereas by increasing the radius an evident red-shift of the absorption peaks was observable.

Optical spectroscopy combined with scanning tunneling spectroscopy (STS) measurements, performed by Banin, Millo and co-workers [15, 16] and by El-Sayed and co-workers [14] have revealed a manifold of degenerate states which are split by crystal and shape anisotropy and by the electron-hole exchange interaction (see Fig. 2.6). These works anticipated the subsequent theoretical and experimental results on the exciton fine structure reported by Woggon and co-workers [10] (the reader can refer to chapter 3 for a more detailed discussion on the STS experiments).

Nanorod homostructures often show only one emission peak [17], corresponding to carrier relaxation from the lowest exciton state, similar to spherical nanocrystals. At room temperature, the PL broadening is around 70–100 meV for a sample of rods with narrow distributions of lengths and diameters. Such broadening [7], as in spherical quantum dots, is the result of two contributions,

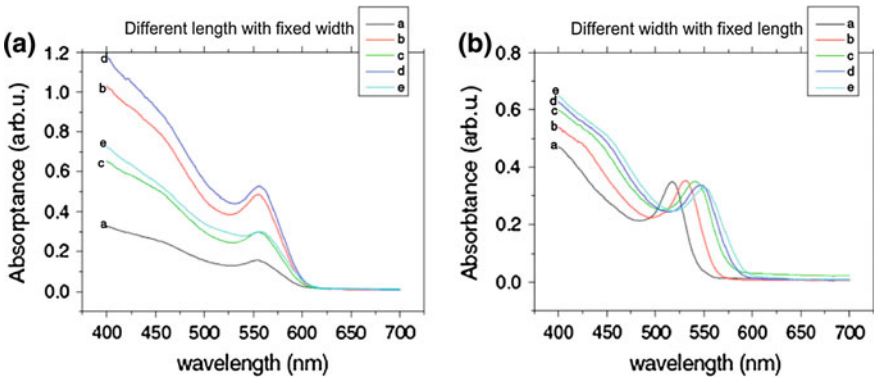

Fig. 2.5 **a** Optical absorption spectra of a series of CdSe nanorods with 5 nm width having different lengths of 12.5, 17.5, 25, 30, 35 nm. **b** Optical absorption of a series of CdSe nanorods with 20 nm length having different diameters of 2.5, 4, 4.25, 4.5, 5 nm. Reprinted with permission from Ref. [14]

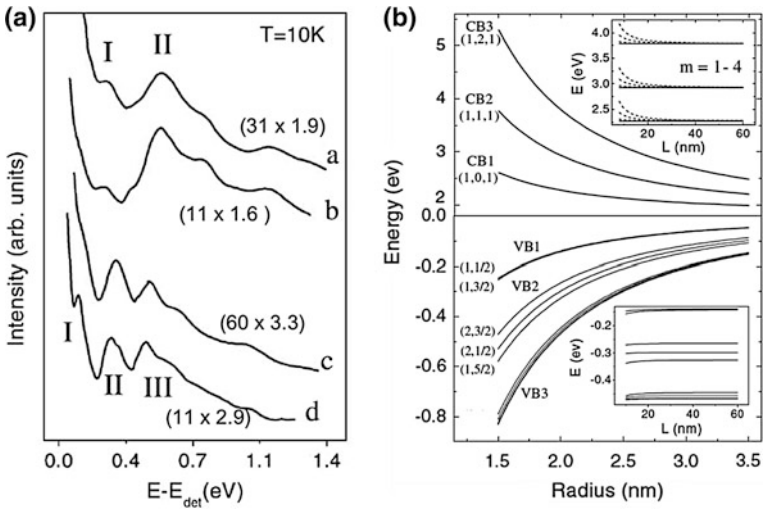

Fig. 2.6 **a** Photoluminescence excitation (PLE) spectra of CdSe nanorods of different sizes (corresponding length x diameter is indicated in brackets), showing peaks related to the first exciton transitions. It is evident that the diameter has a strong influence on the exciton level structure, whereas nanorods with different lengths but comparable diameter show similar spectra. The detection energy E_{det} was 2.25 eV for spectra *a* and *b*, and 2.03 eV for spectra *c* and *d*. **b** Conduction and valence band states distribution as function of the rod radius. Taken with permission from Ref. [15]

namely inhomogeneous and homogeneous broadening. Inhomogeneous broadening is mainly affected by the general quality of the sample and is related to the size dispersion, thickness fluctuations in single rods, quality of the rod surface, and it can be controlled (in principle) by improving these parameters. This type of broadening represents often an obstacle for the study of the intrinsic physical properties of semiconductor nanorods, and it can be bypassed only by performing experiments on single rods. Homogeneous broadening refers instead to coupling of charge carriers to phonons, is an intrinsic process and cannot be overcome by any improvement in synthesis. It will be discussed in detail in the following.

2.5.2 Temperature and Size-Dependence of the Exciton Relaxation Processes

After excitation, charge carriers inside a crystal tend to restore the initial state of equilibrium by losing their excess energy. As in all semiconductor systems, semiconductor nanorods undergo several possible relaxation pathways. In the present discussion, we separate such processes in two main categories, namely radiative processes (i.e. loss of energy by means of the emission of photons) and non-radiative processes (i.e. loss of energy via any other mechanism). The most

common non-radiative relaxation process is the creation of phonons (i.e. lattice vibrations) via carrier-phonon interaction, which leads to heating of the material. This coupling does not influence exclusively the decay of the carries towards lower energetic states, since in some particular cases it can promote the carriers into higher energy states, allowing them to escape from the material, by means of a process known as "thermal escape" [18–20]. Multi-carrier scattering processes are additional non-radiative relaxation processes, and they are all generally grouped in a class, the so-called "Auger-type" mechanisms [21–30]. They manifest when two or more electron-hole (e–h) pairs are present in the semiconductor, and consist in the transfer of the energy of an e–h pair to a third particle (electron, hole or exciton).

2.5.3 *Exciton–Phonon Interaction: Homogeneous Broadening*

The main features that distinguish nanostructures from bulk materials originate from the localized character of the electron and hole wavefunction and the discrete nature of their optical transitions. In the bulk, the broadening of the exciton line is mainly determined by the polar coupling of both electrons and holes to optical phonons [31]. The piezoelectric and deformation potential coupling of the carriers to acoustic phonons is usually not very important [32]. This situation is different in nanostructures, where the local charge neutrality character of the exciton becomes predominant, producing an ideal null polar coupling of the exciton to optical phonons [33]. This holds true for infinite barriers, for which the electron and hole wavefunctions are practically identical. In general, in real systems with a finite barrier a decrease of the polar coupling with increasing barrier is expected [33–35]. On the other hand, since the deformation potential coupling is proportional to $1/R^2$ (R being the radius of a spherical dot), the coupling strength to acoustic phonons is increased as the dimensions are reduced below the Bohr radius [32, 36]. Also the temperature affects each of these contributions. The temperature dependence of the spectral line width can be expressed as [37]:

$$\Gamma(T) = \Gamma_0 + \sigma T + \gamma N_{LO}(T) \tag{2.10}$$

where Γ_0 is the inhomogeneous broadening, σ is the exciton-acoustic phonons coupling coefficient, γ is the coefficient accounting for the exciton-optical (LO) phonon coupling and N_{LO} represents the Bose function for LO phonon occupation:

$$N_{LO} = \frac{1}{e^{E_{LO}/k_B T} - 1}. \tag{2.11}$$

In the expression above E_{LO} is the energy of the longitudinal optical phonon with momentum $k = 0$ (i.e. the phonon that preferably couples to the lowest exciton state) and k_B is the Boltzmann's constant. Due to the different energetic

dispersion curves of acoustic and optical phonons, the two couplings dominate at different temperature ranges. The acoustic phonons, having smaller energies (a few meV), contribute heavily to the broadening at low temperature (until 50–70 K [19]), whereas the optical phonons (with energies of a few tens of meV) dominate at higher temperature [19]. Nanorods having wurtzite structure, like CdS and CdSe, present a pronounced polar character, where the Frch interaction (with optical phonons) is the predominant coupling mechanism between charge carriers and optical phonons [38]. In the study of the exciton-LO phonon interaction, the fundamental quantity considered is the so called Huang-Rhys factor [34]. Experimentally, an estimation of the Huang-Rhys factor is possible by Raman spectroscopy, by simply considering the ratio of the signal intensity of the first to the zero order phonon replica [38]. Lange and co-workers [38] have performed Raman studies on CdSe nanorods and demonstrated an increase of the exciton-phonon coupling with decreasing rod radius, and the effect could be enhanced by growing a ZnS shell on the surface of nanocrystals acting as passivating layer (see Fig. 2.7). The Huang-Rhys factor remained below the bulk value, according to the model of Nomura et al. [34].

Quantum confinement affects not only the coupling strength of charge carriers with phonons, but also the energy of the LO phonons. This happens in quantum dots as well as in nanorods. Cardona and co-workers [39] have determined the dispersion of the LO phonons as function of the spherical nanocrystals size on the basis of the asymmetric lineshape of Raman spectra (Fig. 2.8). They found a decrease of the energy of the optical modes with decreasing size, and explained the low energy asymmetry of Raman spectra as due to the contribution of off-resonance vibronic modes.

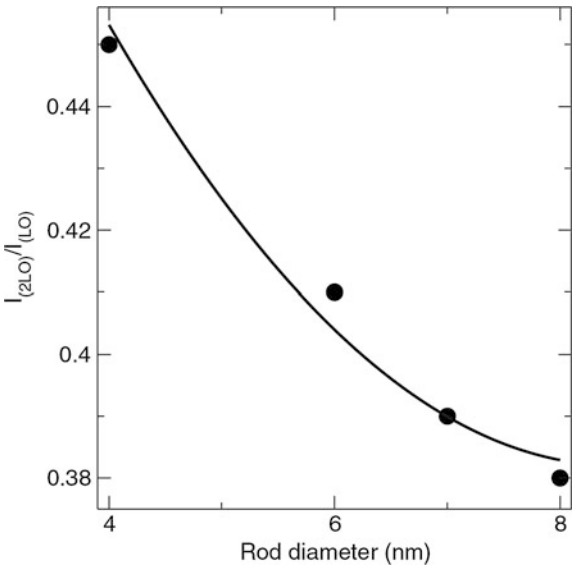

Fig. 2.7 Size dependence of the ratio between the second and the first order phonon replica of CdSe/ZnS nanorods. The solid line is a guide to the eye. Taken with permission from Ref. [38]

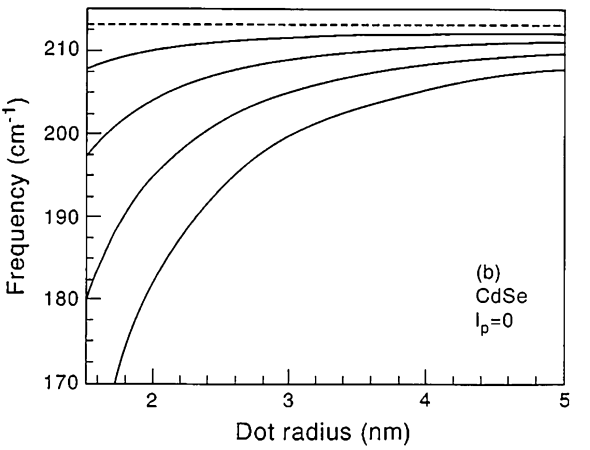

Fig. 2.8 Dependence of the first four optical-vibronic $l_p = 0$ modes on the CdSe dot radius. Taken with permission from Ref. [39]

In nanorods, the red-shift of the phonon modes becomes more pronounced, for example due to the loss of spherical symmetry which leads to the detection of vibrational modes with non-zero angular momentum. Lange et al. [38, 40] and Nobile et al. [41] have conducted independent studies (summarized in Fig. 2.9) on the role of quantum confinement on the optical phonon energies. They found a red-shift of the LO phonon energy with decreasing rod diameter, accompanied by a substantial independence on the aspect ratio. This red-shift can be understood in a simple picture by considering the negative dispersion of the optical phonon branches with respect to the transferred wave vector k, where $k = 2\pi/d$, d being the diameter of the nanorod. Detailed theoretical calculations of the confined phonon modes in high aspect ratio ellipsoids, supported by Raman experiments on CdSe nanorods, have resolved a fine structure of the phonon modes perpendicular and parallel to the long axis of the nanocrystals (Fig. 2.9). The energy of surface optical (SO) phonon modes can be approximated following the approach by Gupta et al. [42]:

$$\omega_{SO}^2 = \omega_{TO}^2 + \frac{\varpi_p^2}{\varepsilon + \varepsilon_m f(x)}; \;\; x = q \cdot d/2 \tag{2.12}$$

with:

$$\varpi_p^2 = \varepsilon_\infty (\omega_{LO}^2 - \omega_{TO}^2), \; q = 2\pi/L, \; f(x) = (I_0(x) \cdot K_1(x))/(I_1(x) \cdot K_0(x)) \tag{2.13}$$

where I and K are Bessel functions. Therefore the SO phonon energy depends on both the length L and the diameter d of the nanorods [41–43].

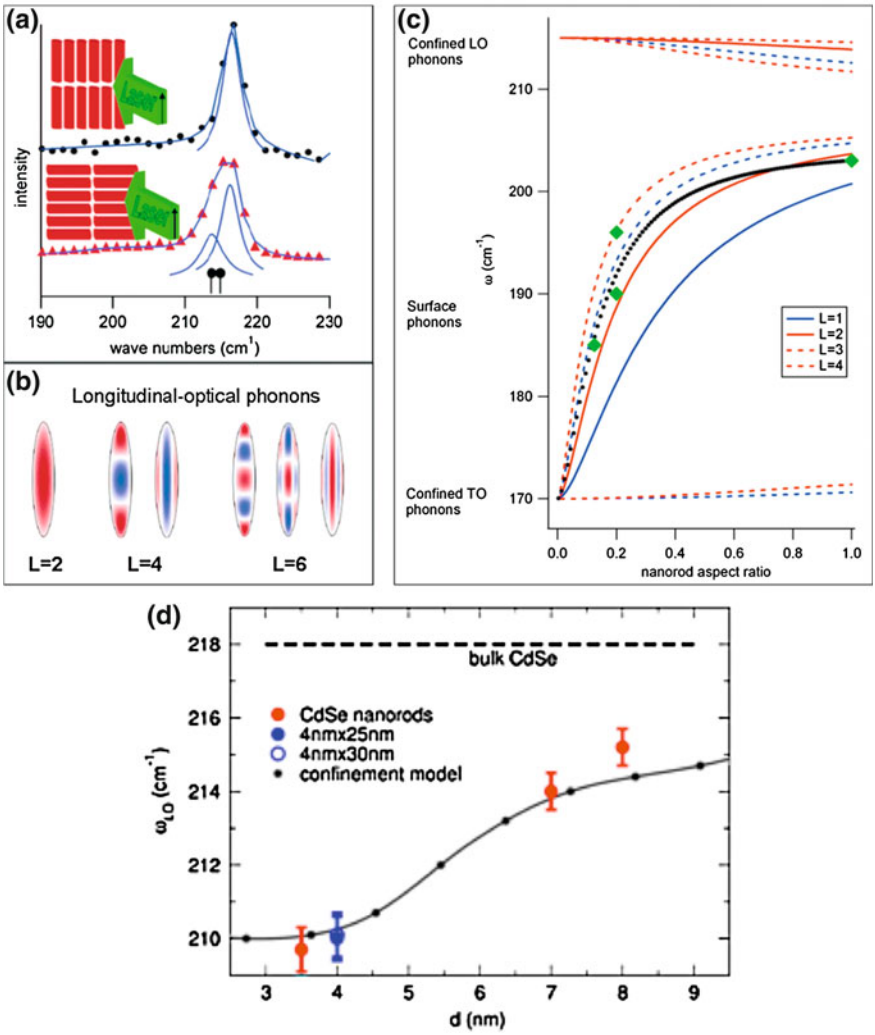

Fig. 2.9 **a** Raman spectra showing the LO phonon mode excited with light polarized parallel and perpendicularly with respect to the long axis of the nanorods. **b** Cross sections of the calculated phonon potential for the LO Raman-active odes with $M = 0$ and different angular momentum L. (a) and (b) are taken for Ref. [119] **c** Calculated energy of the different phonon modes versus the rod aspect ratio. The red and blue lines are calculated from the model in Ref. [119], the black line shows the dispersion of the SO modes according to the model of Gupta et al., and the green dot are data points from Ref. [120]. **d** Frequency of the LO-phonons as a function of rod diameter Taken with permission from Ref. [40]

2.5.4 Auger Effects in Nanorods

Multicarrier Auger effects play a fundamental role in the relaxation processes of nanostructures. Auger recombination represents a limitation for the use of nanostructures in optical devices requiring optical gain, since non-radiative multiparticle scattering hinders the desired population inversion. However, the Auger efficiency can be significantly reduced by a wise choice of materials and via engineering of the band alignment and wavefunction localization [44–46]. The physical interest on the Auger processes resides in the role played by the quantum confinement on the assignment of the new selection rules and the Auger efficiency in nanoparticles with respect to the bulk. Quantum confinement increases the Coulomb interaction between the charge carriers inside the nanomaterial with respect to the bulk counterpart. Moreover, the translation momentum conservation acting in bulk materials is broken in nanoparticles, allowing for more efficient Auger processes [21, 47, 48]. On the other hand, the discreteness of electronic states in nanocrystals should imply a reduced availability of states that can satisfy the energy conservation condition, whereas in the bulk a continuum of states is always guaranteed (in this sense, Auger recombination would be more efficient in the bulk). The interplay of both contributions determines the net effect in each system. In this regard, several differences arise when considering nanorods instead of spherical nanoparticles.

Since the Auger recombination rate is strongly sensitive to the carrier density and consists in e–h pair annihilation, such a mechanism affects the temporal trend of the relaxation processes. Therefore, the general procedure for studying Auger mechanisms occurring in nanoparticles consists in time resolved (TR) measurements of both the PL (TRPL) and the transient absorption (TA) as function of the photogenerated carrier density. The simplest way to analytically describe an Auger process is to consider the following equation [30]:

$$\frac{dn}{dt} = -C_A(M)n^M \tag{2.14}$$

This equation expresses the decay rate of the average population density n in the presence of M interacting particles (intended as electrons, holes or excitons). The key parameter is the Auger constant $C_A(M)$ which corresponds to the actual probability for the Auger process to occur. It is dependent on the average number of interacting carriers in the system considered. The general solution of Eq. (2.14) is:

$$n(t) = \frac{n(0)}{\left(1 + \frac{1}{M-1} C_A(M) n(0)^{M-1} t\right)^{M-1}} \tag{2.15}$$

This expression is employed to extract the Auger constant by means of a fitting procedure of $n(t)$, which is given by the measured temporal decay; the quantity $n(0)$ is usually known, while M is often kept as parameter. M becomes a key

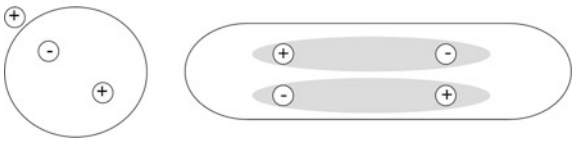

Fig. 2.10 Sketch of the exciton extension in spherical (*left image*) and rod-shaped (*right image*) nanocrystals and relative implications in Auger processes. In spherical nanocrystals the interacting charge carriers can be considered independent, giving M = 3, whereas in nanorods four carriers (two e–h pairs) can be considered as two interacting particles (two excitons), giving M = 2

parameter if one wants to determine in which regime Auger mechanisms take place. In quantum confined systems, there are two main types of mechanisms: three-carrier relaxation and biexcitonic Auger relaxation. The first occurs in the strong 0D confinement regime and provides $M = 3$, whereas the second gives $M = 2$ and occurs in the case of a 1D system. In strongly confined 0D nanocrystals the Coulomb contribution to the exciton energy is negligible with respect to the confinement term (see discussion at the beginning of this section). This makes it possible to consider the charge carriers in the dot as independent particles, thus producing a cubic behavior in Eq. (2.14) [21]. The minimum number of carriers allowing Auger relaxation is then $M = 3$, i.e. the energy possessed by an e–h pair is transferred to a third carrier. In the case of nanorods, e–h pairs give rise to 1D excitons, since the exciton extends along the long axis of the nanorods (see Fig. 2.10). Along that direction, the confinement energy can have a smaller contribution with respect to the Coulomb interaction, allowing for the formation of a 1D exciton. Therefore, in terms of Auger mechanism, one must consider two excitons as the minimum number of interacting particles, thus $M = 2$, as one exciton can transfer its energy only to a second exciton.

Comparative studies carried out on spherical nanocrystals and on nanorods with various aspect ratios have provided an estimate of the size ranges of the two regimes and of the relevant Auger constants. Klimov and co-workers have demonstrated that below an aspect ratio AR = 8 charge carriers in nanorods behave as uncorrelated particles, whereas above this value e-h pairs organize themselves in 1D excitons and recombine via a biexcitonic Auger process [29]. The Auger constant that gives a measure of the Auger efficiency in systems with the same volume was found to be larger in nanorods than in spherical nanocrystals of equal volume. In Fig. 2.11 we show this result in terms of Auger lifetime (which is inversely proportional to the Auger constant), as derived from Ref. [29]. This behavior has been ascribed to the major surface contribution to the matrix element of the Auger transition: nanorods have a larger surface area when compared to spherical nanocrystals of equal volume, and this should lead to a larger Auger constant [29].

The surface plays also a non-trivial role in defining the optical properties of nanorods, especially for what concerns the existence of surface states and their influence on the carrier dynamics. The efficiency of the Auger processes may be

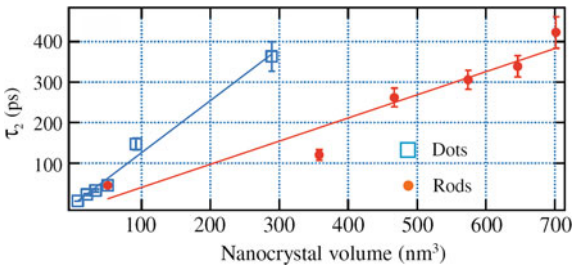

Fig. 2.11 Auger time constant of two e–h pairs recombining in dots (*blue symbols*) and rods (*red symbols*), as a function of the nanocrystal volume. Taken with permission from Ref. [29]

affected by means of trapping at such states [48]. This has important implications on the carrier cooling from higher excited states to the band-edge, which depends on the Auger efficiency, as demonstrated by Klimov and co-workers [28]. In their study, they showed that in nanorods multicarrier generation can cause an Auger heating, consisting in the increase of the energy of an exciton, as a consequence of an energy transfer event deriving from a second exciton recombination. The consequent increase in carrier temperature competes with the more classic phonon emission as a relaxation channel, and decreases the carrier cooling in the high excitation density regime.

2.6 Single Nanorod Properties

As said before, CdSe represents perhaps the most studied system among the spherical and elongated semiconductor nanoparticles. They are commonly considered as prototype materials in the study of the optical properties of single nanoparticles with wurtzite structure. Lorentzian lineshape, spectral diffusion, and intermittent emission (called "blinking") are some of the properties shared by single spherical and elongated nanocrystals [11, 49, 50]. Defect states can induce charge accumulation by classical carrier trapping at defects lying at energies lower than the band gap, which occurs following an excitation. Irregularities in the nanocrystal shape can lead to charge storage in absence of an excitation, if a distribution of a permanent surface charge can be created. This happens when the rod does not extend perfectly along the wurtzite c-axis, but is twisted with respect to such axis, which can be realized if some stacks of unit cells along the c axis do not span the whole length of the rods, thus creating tiny polar facets along the lateral sides of the rod (see Fig. 2.12). In such a situation, as observed by Krishnan et al. [50], a net surface-charge density is found at the surface of the rod.

The exposed cells are characterized by uncompensated charges, giving rise to an accumulation of a density of charge. The propensity of charges to distribute easily on the rod surface influences strongly the optical properties of single nanorods, especially for what concerns the emission energy and its intensity. For single nanorod experiments, major efforts have been made towards the comprehension of both the role of the surface on the localization and recombination of

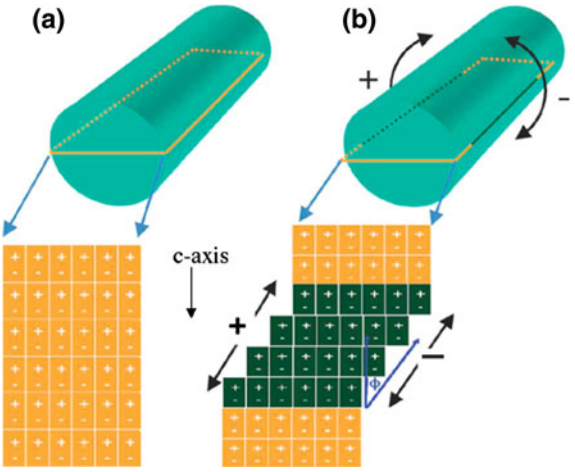

Fig. 2.12 Representation of two different rods grown along a parallel **a** and a tilted **b** direction with respect to the c-axis of the wurtzite structure. In the first case, the rod is a perfect cylinder, and no polar facets are created at the lateral sides of the rod. In the second case, the rod has a more irregular shape, which can lead to exposure of tiny polar facets at the lateral sides of the rod

carriers, and on its impact on the polarization of emission and on the exciton fine structure.

Single nanorod spectra present more complicated dynamics in the temporal evolution of the emission energy, line shape, and intensity, when compared to spherical nanocrystals. Under continuous wave excitation, nanorods show the typical intermittent behavior, as observed in other well-studied systems. At low temperature, single rod spectra are characterized by a broadening of the order of a few meV, and have in general an asymmetric line shape [10, 11, 51]. This asymmetry, which is observable only at temperatures below 15 K, can be ascribed to several reasons. These include charged excitons, fine structure of the lowest excitonic state, acoustic phonon contributions and influence of internal electric fields. In the following, we will discuss the single contributions of phonons, charged excitons, as well as internal and external electric fields, on the spectral features of single rods.

2.6.1 Charged/Neutral Excitons and Phonon Contributions

The role of charged excitons on the spectral features has been studied extensively by means of PL measurements at low temperature, which were performed as a function of the excitation density [11]. The fundamental difference between charged and neutral exciton spectra lies on the effect of the excess of charge on the fine structure of the lowest excitonic state. For neutral excitons a double peak emission usually arises from single nanorods at low temperature ($\sim$5 K), and is assigned to intrinsic bright states. This feature vanishes at higher temperature, as thermal population contributes to a state mixing. The spectral line shape of Fig. 2.13, can be explained by the theoretical fine structure, as discussed by Woggon et al. in Ref. [10]. As shown in Sect. 2.4 (Fig. 2.4) nanorods experience

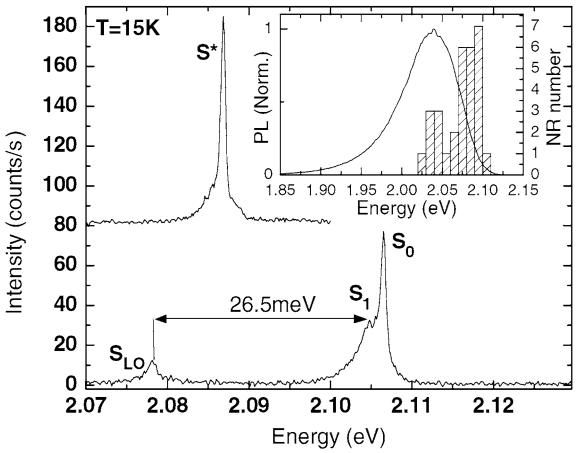

Fig. 2.13 Two single CdSe rod spectra detected at 15 K. The upper part corresponds to a charged exciton spectrum, showing fine structure due to excess charge, whereas the bottom spectrum refers to a neutral exciton, showing peaks (labeled as S_0 and S_1) belonging to the rod fine structure. Inset: statistics on 30 single nanorods. Taken with permission from Ref. [10]

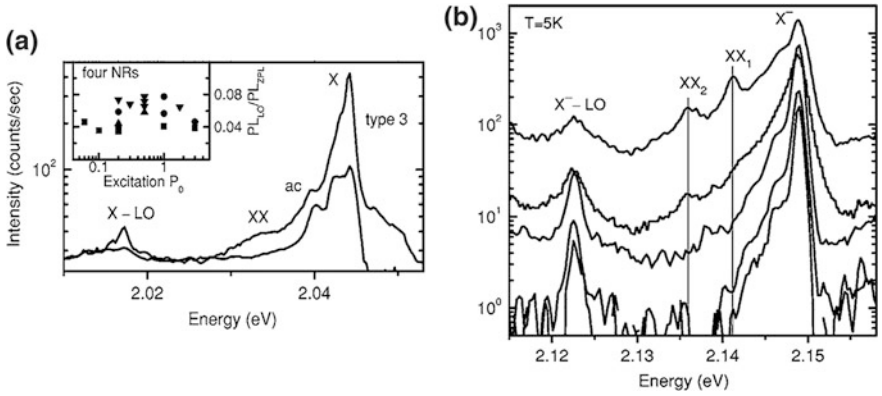

Fig. 2.14 Power dependence of a single rod emission for a neutral exciton **a** and a charged exciton **b**. Taken with permission from Ref. [11]

an inversion of the ground state fine structure below a critical rod radius of $\sim$3.7 nm, which induces a change in the effective ground state of the rod.

Nanocrystals with spherical symmetry have a fixed dark ground state that is characterized by a momentum projection of ± 2. Nanorods with radius smaller than 3.7 nm have instead a ground state with projection 0 (dark, labeled 0^L, contrary to the higher energy, bright 0^U state). Despite the dark nature of the state 0^L, its proximity to the nearest bright state (labeled ± 1) is of the order of some μeV, which allows the thermal population of the bright one at very low temperature. In this sense, it is common to assign the dual nature of the single rod spectra (the

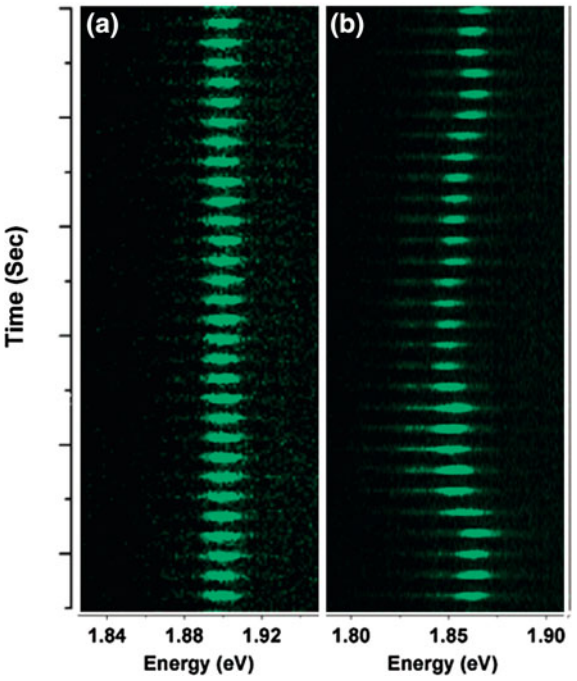

Fig. 2.15 Temporal evolution of the PL spectra of two representative CdSe nanorods. The rod in (**a**) shows very stable emission, while the emission features of the rod in (**b**) are fluctuating due to local electric fields induced by unstable charge localization along the rod. Taken with permission from Ref. [52]

peaks S1 and S0 of Fig. 2.13) to the emission of the lowest bright states ± 1 and 0^U. PL spectra showing the fine structured exciton ground state are considered a fingerprint of neutral exciton emission. For a charged exciton (trion) the fine structure is expected to vanish due to the excess charge present in the rod [11]. The charged exciton peak is shifted with respect to the neutral exciton due to Coulomb interaction in the trion system. In addition, at high excitation density also the recombination from biexcitons (XX) can be observed (see Fig. 2.14).

2.6.2 *Influence of Electric Fields on the Optical Properties of Single Nanorods*

Stark effect experiments, i.e. the study of the impact of an external electric field on the electronic structure, represent the most common approach to study and control the carrier localization along the rod. Fluctuations in the emission energy, PL intensity and broadening are the main distinguishing quantities in nanorods [52]. Figure 2.15 shows typical time traces from two different nanorods belonging to the same sample of CdSe nanorods, measured at 10 K, under CW excitation and without external electric field [52].

At first glance, the two rods have dissimilar emission energies, broadening and relative temporal evolutions. In particular, rod A shows a very stable behavior,

consisting of an unmodified PL spectrum over time, whereas rod B shows considerable instability, as if it underwent mutating conditions during its emission process. Systematic studies carried out on large sets of nanorods [53] and by continuous monitoring of the same nanorod, have indicated a close correlation between the emission energy, the broadening and the intensity of the PL signal. As a general trend, a red-shift of the emission energy corresponds to an increase of the full width at half maximum (FWHM) and a decrease of the emission intensity (Fig. 2.16) [52].

Interestingly, such a behavior can also be induced by applying an external electric field, as shown in Fig. 2.17. Here, a bimodal switching effect is seen when an electric field is applied to the nanorods, which either turns the PL of some rods off or turns the PL of some others on. This behavior can be understood considering the effect of the surface and the elongated shape of the rods, which can

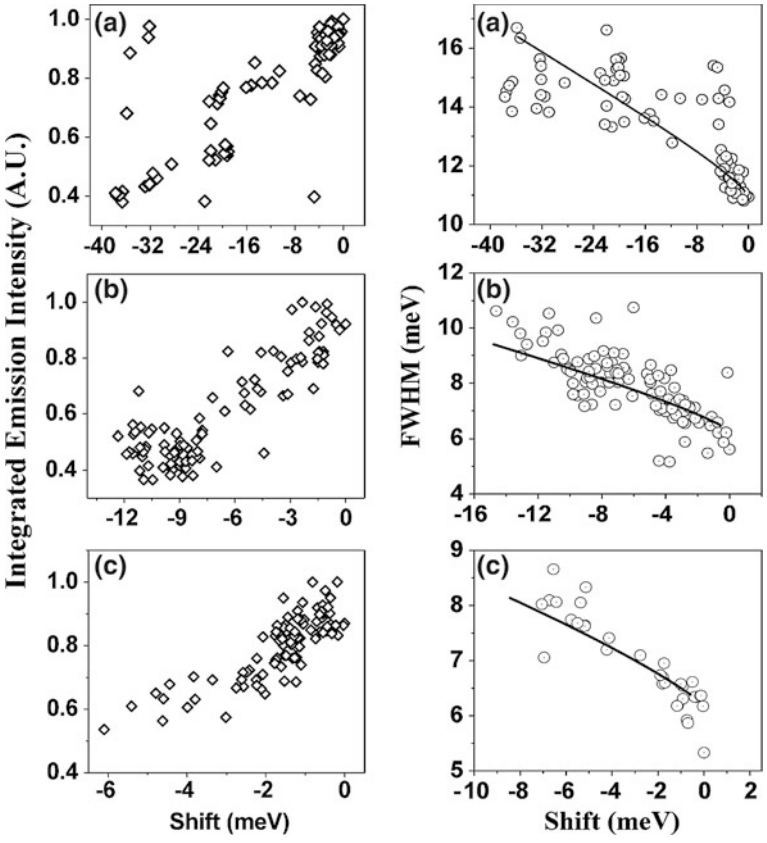

Fig. 2.16 Statistical analysis of the emission properties of three single nanorods subject only to local field effects. *Left panels* show the integrated PL intensity reduction with increasing red shift. *Right panels* correlate the spectral broadening to the energetic shift: a red shift corresponds to an increased FWHM. Taken with permission from Ref. [52]

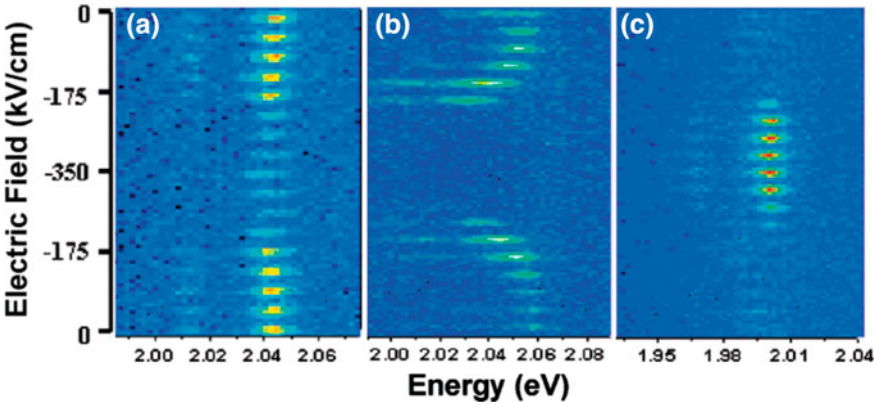

Fig. 2.17 Switching single nanorods due to external electric fields. The three panels show the emission behavior of three rods located in between interdigitated electrodes under applied bias. The emission of the rods in **a**, **b** is switched off due to electric field, where rod **b** also exhibits **a** red shift, while rod **c** is switched on. Taken with permission from Ref. [52]

lead to a varying overlap of the electron–hole wave functions. Such variations can have either extrinsic or intrinsic sources. Extrinsic sources are for example external electric fields, whereas intrinsic sources could be related to the dynamics of carriers from/to surface trap states, which induce the formation of varying local fields. If on one hand the elongated shape offers the possibility to localize the e–h wave functions in several configurations, the extended surface of the nanorods contributes heavily to the creation of numerous trap sites, at which carriers can be localized.

When nanocrystals are subject to an external electric field, they experience the so-called quantum confined Stark effect (QCSE), which induces a red shift of the optical transitions (both in absorption and emission), a decrease of the transition probabilities [52] and an increase of the spectral broadening. As an example, Fig. 2.18 provides a qualitative description of the exciton distortion induced by the application of an electric field. For nanorods aligned along the electric field direction, electrons and holes are pulled in opposite directions, towards the ends of the rods. The result is that their wave function overlap is reduced, and the optical transition red-shifts and decreases in intensity (due to a decrease in the oscillator strength). The process depends strongly on the mutual orientations of the electric field and the long axis of the rod: if they are parallel, the effect is maximized, whereas if they are perpendicular the influence of the electric field is negligible (Fig 2.18).

Concerning the correlation of the broadening of the emission peak with the PL intensity and the emission energy we refer to the treatment of Ref. [52]. The starting point is to consider the energetic shift caused by an electric field up to the second order:

$$\Delta E = \mu\varepsilon + \frac{1}{2}\alpha\varepsilon^2 \tag{2.16}$$

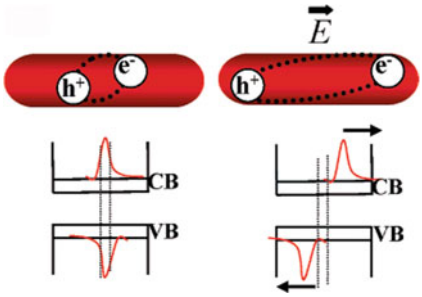

Fig. 2.18 Effects of local electric field on the exciton extension along the rod, leading to a reduction of e–h overlap. Taken with permission from Ref. [52]

Here, ΔE is the energy shift, ε is the electric field (due to external or local fields), μ the dipole moment and α the polarizability. By differentiating Eq. (2.16) one can obtain the expression for the predicted change in the spectral width:

$$\delta(\Delta E) = (\mu + \alpha\varepsilon)\delta\varepsilon \tag{2.17}$$

μ and α can be found experimentally by Stark effect measurements. $\delta\varepsilon$, if referred to fluctuations of local charges, is related to the distance of such charges from the exciton and then to the spatial fluctuation [52].

2.6.3 Polarization Properties

The polarization properties of nanorods represent one of their distinctive characteristics with respect to other colloidal nanocrystals, like for example spherical quantum dots, and have received much attention recently (both from the theoretical and experimental point of view). As previously discussed, the electronic structure of rods is strongly affected by their size and shape, in particular by their aspect ratio (AR). The fine structure of the lowest exciton state is the dominating factor in defining not only the character of the emitting state (whether dark or bright) but also the polarization properties. Since we deal with nanostructures with AR > 1, only the component of the angular momentum having projections along the z long axis of the rod should be considered. In particular, in nanorods a symmetry change of the 1D exciton ground state occurs at a certain radius [10] or AR [54], as was already discussed in Sect. 2.4.

Here, the optical transition should be strongly polarized along the wurtzite c-axis (axis z in Fig. 2.19), with an increasing polarization degree with increasing AR. Polarization spectroscopy on single nanorods provides experimental proof of the theoretical predictions. Polarized emission up to 80 % has been demonstrated for CdSe nanorods with AR > 2 [17] whereas for spherical nanocrystals only values up to 10 % were obtained, see Fig. 2.20b.

Excitation polarization measurements demonstrated the optical transition polarization of nanorods both in one- [55] and two- [56] photon-excitation experiments, as displayed in Fig. 2.21. In the one-photon experiment, the

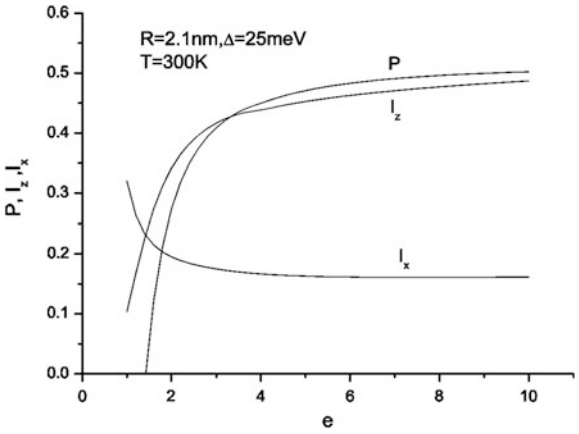

Fig. 2.19 Example of theoretical polarization variation of rods having a fixed radius and varying aspect ratio (*e*). Taken with permission from Ref. [54]

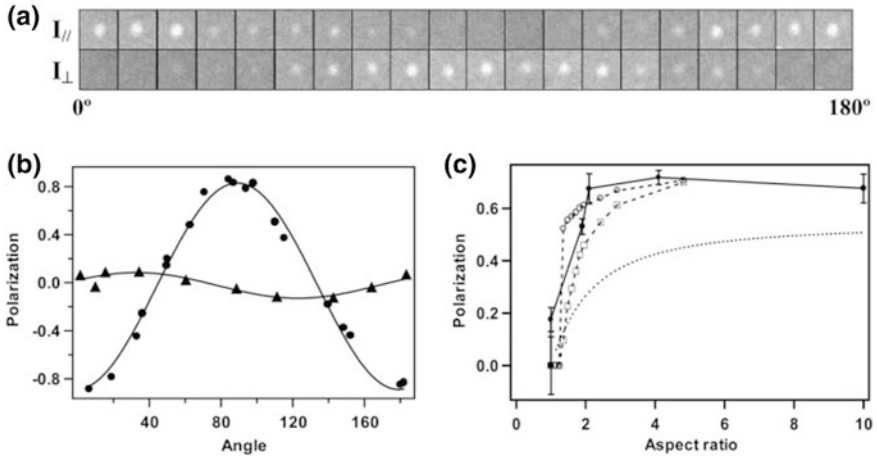

Fig. 2.20 **a** Imaging of the emission of a single rod recorded in mutually perpendicular polarization directions simultaneously. **b** Plot of the polarization degree as a function of the rotation angle of the nanorods in **a** (*solid circles*) and the polarization for a single spherical nanocrystal (*triangles*). **c** Experimental polarization factor as a function of the aspect ratio of the rods. Taken with permission from Ref. [17]

polarization curve followed the typical $\cos^2(\Theta)$ function, whereas a dependence on $\cos^4(\Theta)$ was found in two-photon excitation, according to the nonlinear character of the two-photon absorption process. The level crossover occurring in nanorods and proposed by diverse theoretical approaches [10, 17] allows to understand the polarization dependence of the nanorods excitation. Indeed, the ground state becomes bright in rods, allowing for the absorption of polarized light along the major *c*-axis.

Experimental [57] and theoretical [58] studies on free standing InP nanowires showed that the polarization properties of the band edge transition in one-dimensional semiconductor nanostructures depend both on the intrinsic level structure, which shows p-type wave function characteristics, and on the geometry of the dielectric environment of a cylindrical structure where the diameter is much smaller than the wavelength of the light (Fig. 2.21c–d). In this case, the light wave component along the wire is not reduced, while the component perpendicular to the wire is strongly attenuated. The combination of these two effects can explain the giant polarization of the band edge transition, of up to 96 %, that was observed in InP nanowires. Temperature dependent polarization measurements can help to distinguish between the band structure and the geometrical contributions, as the first should depend on the temperature, while the second should not.

2.7 Nanorod Heterostructures

We will now discuss different types of nanorod heterostructures and their respective optical properties, as well as their potential for device applications. Our main focus will be on semiconductor heterostructures consisting of materials with different band gaps, and we will briefly mention also semiconductor–metal heterostructures. Many excellent reviews have appeared recently on this topic [59–62], and the reader is directed to those reviews for more in-depth coverage. Figure 2.22a shows some of the nanorod heterostructures that have been reported so far by various groups, while Fig. 2.22b shows two possibilities of band alignment for semiconductor heterostructures, namely type-I and type-II. In type-I heterostructures, the optically excited carriers are confined in the lower band gap material, whereas in type-II heterostructures the electrons are localized in one material, and the holes in the other material. As we will see shortly, for some materials the band alignment can be tuned from a type-I to quasi type-II, where the holes are localized in one material and the electrons are delocalized over the whole nanostructure, via quantum confinement effects. In many cases, the appropriate choice of materials and the geometry allows to obtain suitable energy gaps for the targeted application. Among the rod-like heterostructures that have been fabricated so far, we find dot-in-a-rod structures [53, 63, 64], collinear nanorods [65–71], nanobarbells [72, 73] and magnetic-semiconductor nanorods [74, 75].

2.7.1 Semiconductor Dot/Rod Heterostructures

This particular type of nanorod heterostructure is characterized by a spherical core of material A and a rod-shaped shell of material B, as illustrated in Fig. 2.23 for two different material combinations that result in type-I and type-II band alignment, respectively. In the type-I structure, electrons and holes are localized in the

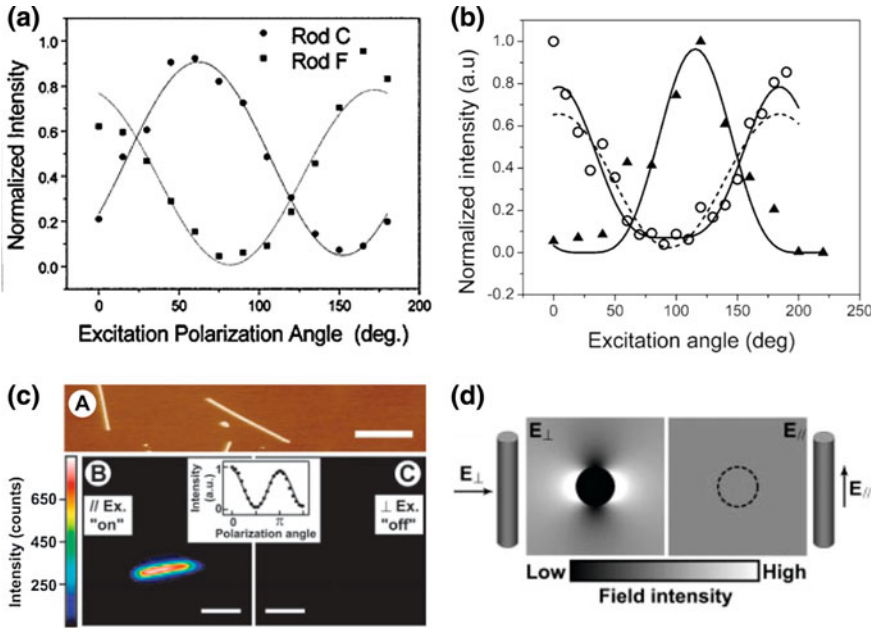

Fig.2.21 **a** Polarized excitation measurements performed on two single nanorods (*symbols*) and relative best fit curves (*continuous lines*) to the $\cos^2(\Theta)$ function of the excitation angle. Taken with permission from Ref. [55]. **b** Polarized excitation experiment carried out by two-photon excitation. Symbols represent the experimental data, whereas continuous lines are the best fit curves to the $\cos^4(\Theta)$ function. Taken with permission from Ref. [56]. **c** AFM image of InP nanowires (scale bar = 5 micrometer) (*A*), and the PL emission intensity of a single InP nanowire recorded with exciting light polarization parallel (*B*) and perpendicular (*C*) to the nanowire. The scale is 3 micrometer. **d** Dielectric constant model for light polarization parallel and perpendicular to a cylinder. **c** and **d** are taken with permission from Ref. [57]

same spatial region, namely the core region, before recombination, because both the lowest electron state and the highest hole state reside in the same material. In several reported cases, however, the electrons are delocalized over the whole rod volume due to the small conduction band offset [53, 76, 77]. The situation is different for type-II structures, where the minimum of the conduction band and the maximum of valence band are located in different materials regions of the system. This makes a type-II transition from the minimum of the conduction band in material A (rod-shell) to the maximum of the valence band in material B (core) possible.

In the following, we will focus on the case of the CdSe/CdS dot/rod system sketched in Fig. 2.23 (left panel), where a spherical CdSe core is embedded in an outer CdS rod. Typical absorption and emission spectra of such nanorods are displayed in Fig. 2.24 [78, 79]. We find that the absorption is dominated by the CdS shell, whereas the emission originates from states related to the CdSe core. This behavior is clearly advantageous for the optical emission properties, because a large 1D system (i.e. the entire rod) is capable is harvesting the excitation light, whereas

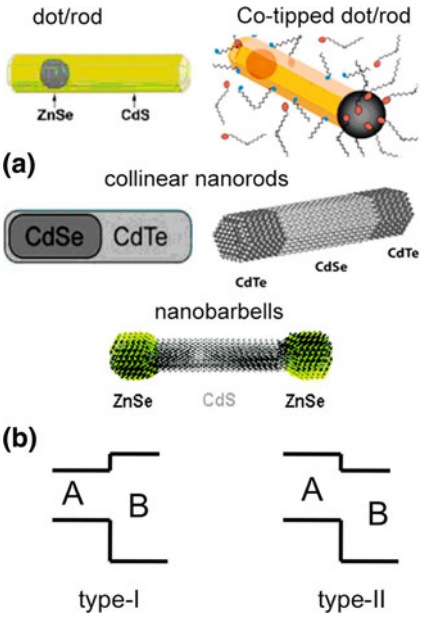

Fig. 2.22 **a** Examples of heterostructured nanorods: dot/rod, Co-tipped, collinear nanorods and nanobarbells. **b** Band alignment of type-I and type-II heterostructures

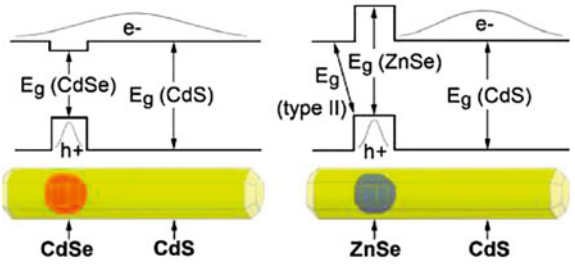

Fig. 2.23 Sketches of two possible nanorod heterostructures that have been synthesized by wet-chemical approaches, and relative band-alignment and e–h wavefunction localization Taken with permission from Ref. [63]

the emission comes from a small 0D system with well-defined level structure, i.e. the CdSe core.

In order to better interpret the experimental data, theoretical absorption spectra were calculated using the envelope function approximation [64], which allowed to assign the strong onset in absorption at higher energy to the lowest excitonic transition of CdS, while the much smaller peak at lower energy could be assigned to the transition occurring in the CdSe core. The emission peak was slightly red-shifted with respect to the lowest CdSe absorption, suggesting a direct origin from the core. The photoluminescence excitation (PLE) measurements on two representative samples of nanorods having different ARs 6 and 19, respectively, (see Fig. 2.25) confirmed this result [64]. The narrow line width of the peaks in PLE at low temperature made it possible to resolve the phonon replica of the PL emission. Here, the energy shift of the phonon replica was 26 meV, which corresponds to the LO phonon energy in CdSe and therefore provided a clear proof that the emission originated from the core material (Fig. 2.25).

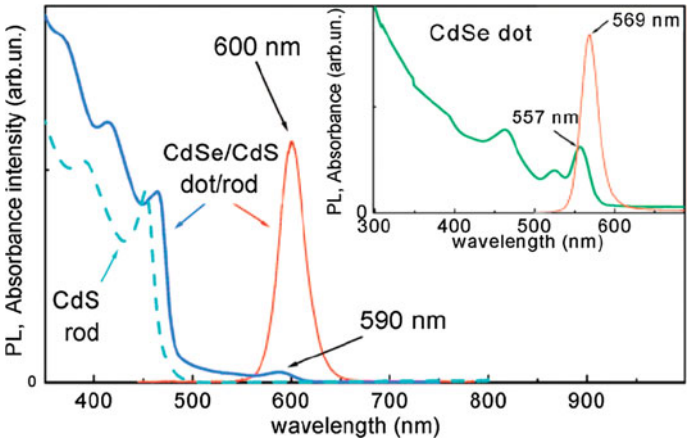

Fig. 2.24 Absorption (*blue*) and photoluminescence (*red*) of core–shell nanorods. The absorption is dominated by the nanorod shell due to its much larger volume with respect to the core. The emission peak is slightly red-shifted with respect to the first absorption peak related to transitions of the core. The *dashed line* shows the absorption of CdS only nanorods, and the inset displays the absorption and emission of spherical CdSe nanocrystals that were used as seeds for the core–shell rod synthesis. Taken with permission from Ref. [78]

2.7.2 Electron–Hole Dynamics in Core–Shell Nanorods

Pump-probe transient absorption measurements have been performed to study the carrier dynamics in core–shell nanorods [80]. In such experiments the sample is excited by a short pulse at a specific wavelength, and then the relative change in transmission $\Delta T/T$ is measured at defined delay intervals (normalized by the transmission without prior excitation). The normalized relative transmission reflects the population of the electronic levels caused by the excitation pulse. Such pump-probe experiments have revealed the role of surface and interface states in core–shell nanorods [80]. As an example, a recent work studied the ultrafast electron–hole dynamics of CdSe (spherical core)/CdS (rod shell) nanocrystals and pointed at electron delocalization even for the low energy transitions in these systems [78]. Figure 2.26 shows $\Delta T/T$ spectra at different time delays for two excitation energies: high energy at 390 nm exciting carrier in the CdS shell, and low energy at 590 nm exciting carriers in the CdSe core. At high excitation energy, a strong instantaneous photobleaching for the levels associated with the shell is observed (at around 460 nm), followed by a much slower build up of a peak at 590 nm due to carrier relaxation into the core. However, in the case of excitation of carriers in the core levels, also an instantaneous photo-bleaching at 460 nm is observed. This indicates bleaching of the electronic states of the shell, due to the delocalization of the electrons in the conduction band. As we will see later on, many optical experiments can be explained assuming electron delocalization in such nanostructures.

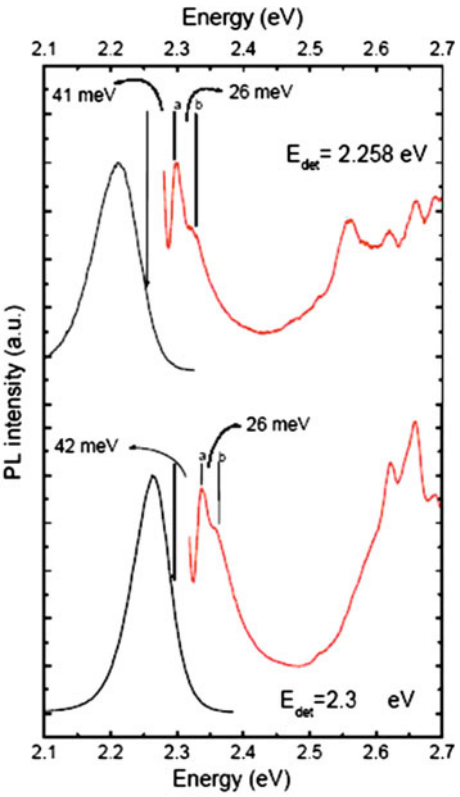

Fig. 2.25 PL (*black lines*) and PLE (*red lines*) spectra of two representative samples of CdSe/CdS nanorods having aspect ratios equal to 19 (*top*) and 9 (*bottom*), as recorded at 10 K. The detection energies are indicated by the *arrows* on the *blue* side of the PL. The lowest resonances in the PLE signal correspond to the ground state resonance **a** and its phonon replica **b**. Reprinted with permission from Ref. [64]

2.7.3 Photoluminescence Studies on Single Core–Shell Nanorods

Mueller et al. studied the optical properties of single nanorods developed by the classical wet-synthesis method and determined the role of surface charges on the spectral position, intensity and broadening [76]. Figure 2.27a shows two PL spectra recorded from the same core–shell nanorod at different times, manifesting fluctuations of the PL peak over time. They could correlate this spectral jitter to fluctuations of the charges on the surface of the nanorods [76]. In nanorods, in contrast to spherically symmetric nanostructures, these fluctuations can strongly influence the electronic level structure via the quantum confined Stark effect (QCSE). In detail, when the surface charges are close to the core, where the

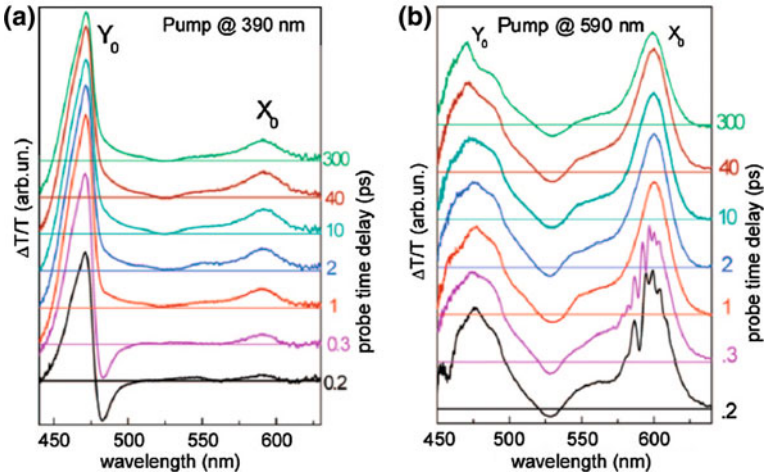

Fig. 2.26 Normalized transient absorption spectra recorded from core-shell nanorods fabricated by the seeded growth method. **a** Excitation energy corresponding to transitions in the CdS shell, **b** and corresponding to transitions in the CdSe core. Taken with permission from Ref. [78]

emission occurs, the PL peak is red-shifted and broadened due to the Stark effect, and when the surface charges are localized at the far end with respect to the core, the PL occurs at higher energy and with a sharper line width (Fig. 2.27b, c).

These findings point directly to the possibility to tailor the wave function distribution by the aspect ratio of the nanorods, which was further discussed by Mueller et al. [53]. In addition to the aspect ratio, Muller et al. demonstrated that also external electric fields can be used to tune the nanorod emission intensity and wavelength [53, 81]. Also the Fer energy transfer between nanorods and organic dye molecules (Fig. 2.27d, e) could be tuned by external electric fields in a way that the emission originated from the nanorod at zero electric field, and from the organic dye when an electric field was applied. Controlled switching in between these two states is shown in Fig. 2.27f, g, h. In these core–shell nanorods, the wavefunction distributions of the electrons and holes could be modified strongly by an external electric field, from a configuration with large overlap of electrons and holes in the core region, to a spatial separation where the holes were localized in the core and the electrons forced to the opposite tip by the electric field. In the latter case, the emission intensity was largely reduced due to the small spatial overlap of the electron and hole wave functions, and the emission was red-shifted due to the band bending, as shown in Fig. 2.28a. Indeed, Kraus et al. [81] showed that exciton emission could be quenched by the electric field and that it could be recovered after microsecond time scales by switching the electric field off, as shown in Fig. 2.28c, e.

The screening of the Stark effect by high intensity excitation was studied by Morello et. al. [82]. Consecutive PL acquisitions on single core–shell nanorods fabricated by the seeded growth method showed only small fluctuations of the

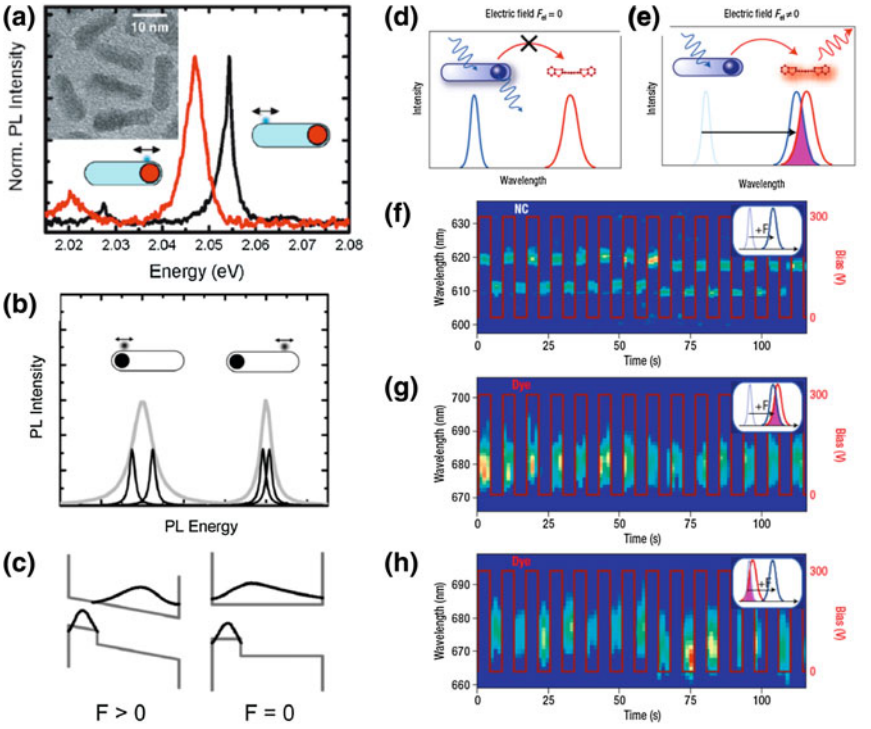

Fig. 2.27 **a** Fluctuations in the emission energy recorded from single CdSe/CdS nanorods. Taken with permission from Ref. [76]. **b** Illustration of the origin of these fluctuations due to surface charges from Ref. [77]. **c** band bending induced by electric field. **d**, **e** Mechanism of Foerster energy transfer from nanorods to organic dyes, which is controlled by an external electric field. **f** Switching of the PL of single nanorods by an external electric field. **g**, **h** Switching the emission of nanocrystal-dye couples on and off by an external electric field for two different nanocrystal-dye combinations. Taken with permission from Ref. [121]

energetic position (of the order of a few meV) due to the spectral diffusion, which was indicative of a low level of surface charge fluctuations. However, an increase in the excitation density resulted in a systematic blue-shift of the emission peak, which varied in the range from 15 to 35 meV for different rods (see Fig. 2.29c). The reversibility of the experiment implied that this shift could be considered as an intrinsic property, rather than due to some photo-degradation process. Figure 2.29d shows power-dependent PL positions taken at different temporal delays. Here, 2 $\mu J/cm^2$ refers to an excitation density corresponding to a low excitation regime (less than one photogenerated e–h pair per rod), whereas at higher densities the system is in the multiexciton generation regime. A noticeable dynamical red-shift occurred in the multiexcitonic regime (with a maximum shift of 25 meV measured at excitation density of 107 $\mu J/cm^2$), in contrast to the almost constant temporal PL position featuring the low density excitation measurement.

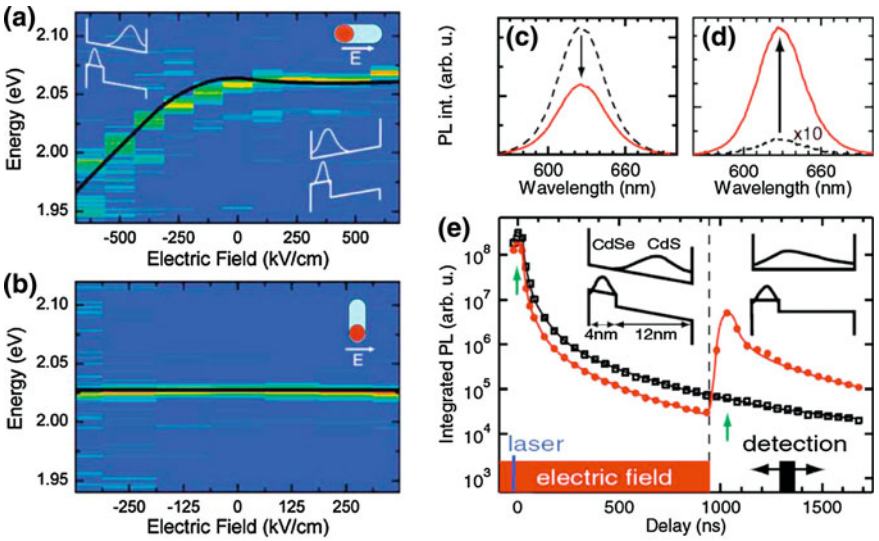

Fig. 2.28 **a**, **b** Energy shift of the emission peak of a single CdSe/CdS nanorod induced via the Stark effect by an external electric field. In **a** the e-field is oriented parallel to the long axis of the rod, and in **b** is perpendicular. **a**, **b** are taken with permission from Ref. [53]. **c**, **d** Electrical exciton storage in semiconductor nanocrystals at room temperature. **c** Prompt emission spectrum recorded in a 50 ns window overlaying excitation with (*solid line*) and without (*dashed line*) an electric field pulse. **d** As in **c** but with the detection placed 1.03 μs after excitation following the 1 μs field pulse. In this case the stored excitons result in a luminescence flash. **e** Time resolved PL decay with (*full circles*) and without (hollow squares) an electric field pulse of 1 μs duration. The arrows show the times of recording the spectra in **c** and **d**. The sketches indicate the separation of electron and hole wave functions during and after application of the field. **c**–**e** are taken with permission from Ref. [81]

A transient red-shift resulting from the photo-induced dynamical de-screening of an internal electric field is a commonly observed process in a number of systems exhibiting internal electric fields. For example, in GaN-based systems [83, 84] the piezoelectric nature of the material gives rise to a polarization that originates from the lattice strain at the GaN/AlN interface. We note that the lattice mismatch at the GaN/AlN interface is comparable to that of CdSe/CdS heterostructures (of the order of 4.1 % [66, 78, 82]). In addition to the screening of an internal field, another possible reason for the blue-shifted high power spectra could be of bi-excitonic origin. However, theoretical calculations allowed to rule out the biexciton emission as cause of the observed nonlinearity [82].

Another appealing property of CdSe/CdS core–shell nanorods is that they can act as single photon sources. An experimental proof for single photon emission is to measure the coincidence of the emitted photons in a high sensitivity Hanbury Brown and Twiss setup based on two avalanche photodetectors [85]. For single photon emitters the coincidence histogram shows negligible counts at zero delay time, an effect that is called photon anti-bunching [86, 87], in contrast to the

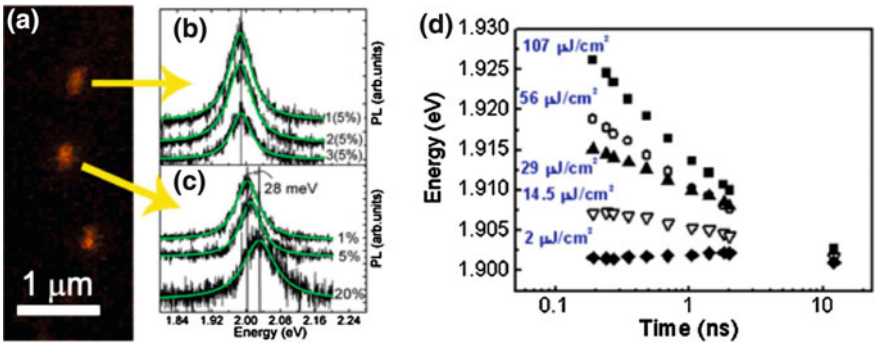

Fig. 2.29 **a** Image of a random field of single nanorods acquired by scanning the sample across a diffraction-limited laser spot of a confocal microscope. The sample was prepared by drop casting a nanomolar nanorod solution onto a cover glass and by rapidly blowing off the solution by means of a strong nitrogen flow. **b** Spectra collected consecutively from a single rod (*black lines*) (identified by the arrow in panel **a**) obtained at the same laser power, and relative Lorentzian best fit curves (*green lines*). **c** PL spectra from a single rod (*black lines*) (indicated by arrow in panel **a**) obtained by varying the excitation power, from 1 to 20 % of the maximum available power (1 mW), and relative Lorentzian best fit curves (*green lines*) Taken with permission from Ref. [82]. **d** Transient emission energies measured at different delays after the excitation, recorded at excitation densities ranging from 2 $\mu J/cm^2$, at which no shift was observed, to the maximum value (107 $\mu J/cm^2$) allowed by the experimental set-up. Taken with permission from Ref. [82]

photon bunching that occurs in the emission of thermal light sources due to the boson nature of photons. Pisanello et al. [88] investigated the potential of single core–shell nanorods as fully polarized single photon sources operating at room temperature, and confirmed also the spatial directionality of the nanorod emission, which resembles the emission geometry of a dipole antenna (Fig. 2.30).

2.7.4 Type-I and Type-II Transitions in CdSe/CdS Nanorods

For bulk and superlattice structures the band alignment at the CdSe/CdS interface is of type-I [89, 90]. However, for nanostructures this might be different due to quantum confinement effects. For holes the bulk valence band-offset is of about 0.8 eV, which is too large to be inverted by quantization effects, especially if we consider the higher effective mass of the holes with respect to the electrons. In the conduction band, on the other hand, it is possible to have a positive or negative band-offset, depending on the quantization energy in the core. Indeed, the reported values span the large range from −0.25 to +0.27 eV [63]. So far the most practical way to describe CdSe/CdS dot/rod heterostructures has been to assume a zero conduction band-offset [53, 77], thus implying a quasi-type-II structure, provided that the experimental results could be well explained. The possibility of tuning the core size in these nanostructures, using the so-called “seeded growth” approach

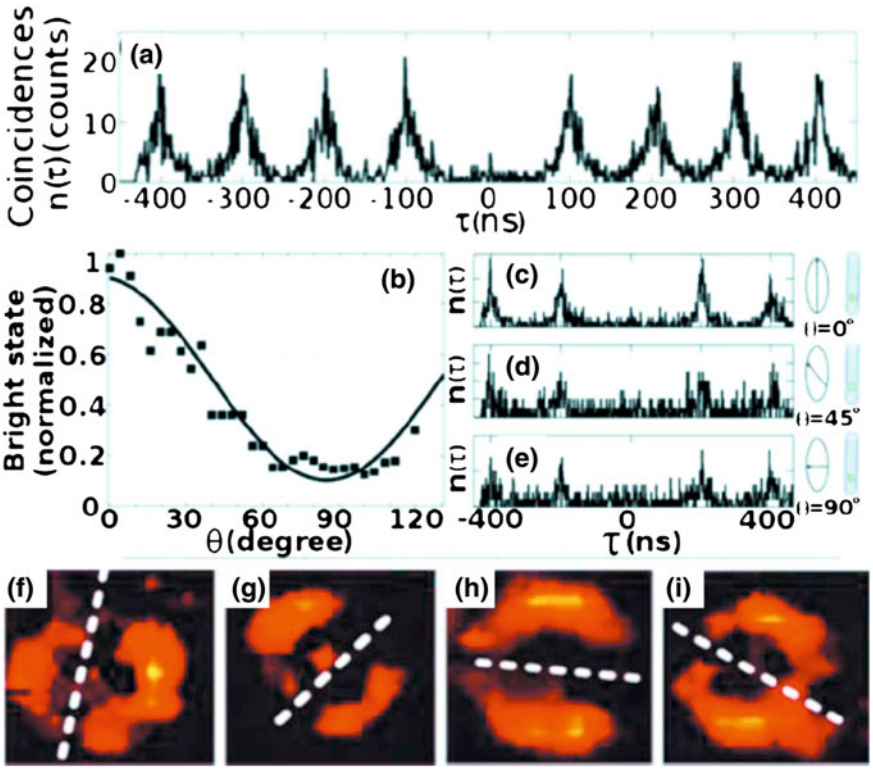

Fig. 2.30 **a** Antibunching of the single nanorod emission. **b** Normalized PL amplitude versus polarization angle of a single nanorod. **c–e** Antibunching traces relative to three different emission polarizations. **f–i** Spatially resolved emission of single nanorods by defocalized emission measurements in a confocal microscope. Taken with permission from Ref. [88]

[64] has allowed to study the conduction band offsets in these core/shell nanorods in more detail.

As was discussed earlier in this section, many optical experiments can be well explained by a flat conduction band profile, whereas electrical studies by scanning probe spectroscopy have revealed a pronounced confinement of the electrons in the core region (see also Chap. 3 on electrical properties). This contradiction has been resolved recently by a work of Banin et al. [91], in which a systematic PL and absorption study on nanorods with different core and shell sizes has shown that the electron delocalization is strongly sensitive to the core size. In detail, the lowest level in the conduction band is localized in the core for large core sizes (in that work this meant diameters above 2.8 nm) and the system behaves like a type-I structure, whereas for smaller cores the quantum confinement raises the energy of this level above the conduction band minimum of the shell. The experimental evidence of such behavior was obtained by varying the excitation density of an ensemble of rods. In general, at low excitation density (corresponding to a

generation of less than one e–h pair per rod) only one PL peak was observed and was associated to single exciton emission. With increasing excitation power density (up to three orders of magnitude) additional peaks gradually appeared, which were ascribed to biexciton and triexciton emission (in order of apparition). Banin et al. found that depending on the core size the biexciton PL may be red- or blue-shifted with respect to the single exciton energy. This shift provides a measure of the biexciton binding energy, which is different in type-I and type-II systems. The biexciton is composed of four carriers (two electrons and two holes), which in a type-I structure are distributed in the same spatial region, whereas in type-II structure electrons and holes are spatially separated into different regions. The result is depicted in Fig. 2.31. When the four carriers reside in the same material, they can distribute in order to minimize the Coulomb interaction among them, resulting in an energetically favorable bound biexcitonic system. The binding energy is thus negative and the consequent emission is red-shifted with respect to the single exciton PL (Fig. 2.31, left panel).

On the contrary, in a type-II configuration only carriers having the same charge reside in the same spatial region, as they are obliged to do so by the particular conduction and valence band-offset (Fig. 2.31, right panel). The result is that the Coulomb interaction between the charge carriers is not minimized, thus a blue-shift with respect to the exciton energy is predicted and is actually measured in several nanostructures [44, 45].

Figure 2.32 shows the optical spectra for nanorods with a large (a) and small (b) core size, and summarizes the results obtained by Banin and co-workers on CdSe/CdS nanorods having different core diameters [91]. For core diameters larger than 2.8 nm the biexcitonic peak was red-shifted with respect to the single exciton peak and for diameters smaller than 2.8 nm the relative positions of the exciton and biexciton were inverted, indicating the shift from a type-I to a type-II system (see Fig. 2.32c).

Recent photoluminescence studies have revealed a partial temperature-dependent delocalization of the electron wavefunction into the CdS shell, independently from the core size. In particular, Rain al. [92] have found evidence for an increase

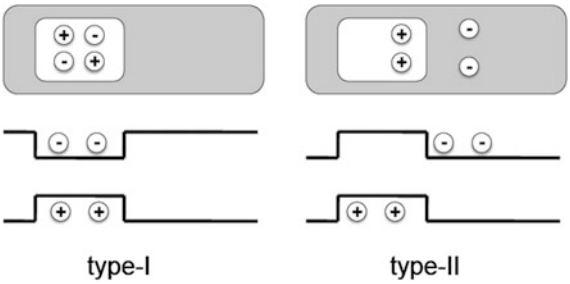

Fig. 2.31 Sketch of the biexciton system in type-I and type-II heterostructures. In type-I structures the four photogenerated charges reside in the same material in a quadrupole configuration. The type-II materials constrain just the charges having the same sign to stay in the same materials, giving rise to an unfavorable energetic configuration for the biexciton

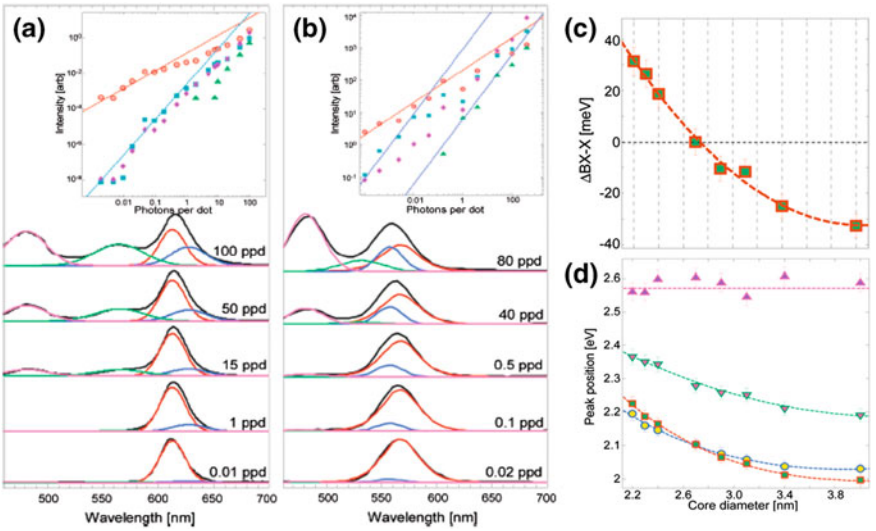

Fig. 2.32 **a** Transient emission spectra (*solid black line*) measured at the peak of the excitation pulse at increasing pulse energies ranging from 0.01 to 150 photon per dot (ppd) **a** for 4 nm diameter CdSe cores embedded in 45 × 6 nm CdS rods, **b** for 2.2 nm diameter CdSe cores embedded in 114 × 4.7 nm CdS rods. **c** Plot of the difference between the biexciton and exciton energetic positions for CdSe/CdS nanorods as function of the seed diameter. The crossover from negative values (attractive biexciton binding energy) to positive energies (repulsive biexciton binding energy) constitutes a fingerprint of the transformation of the system from type-I to type-II. **d** multiexciton peaks as function of the core dimensions: exciton (*circles*), biexciton (*squares*), triexciton (*downward-pointing triangles*) and CdS exciton (*triangles*). The crossover involving exciton and biexciton is noticeable. Taken with permission from Ref. [91]

in lifetime that was ascribed to thermal electron delocalization, corroborating the previously discussed findings of pump-probe experiments and recent femtosecond cross-polarized transient grating studies [93]. At the same time the PL energy and broadening followed a classical thermal behavior referable to type-I semiconductors, and the extracted physical parameters of the emitting species like Debye temperature and optical phonons energies were ascribable to the CdSe core material [92], pointing toward a major role of the electron delocalization only on what concerns the radiative rate of CdSe/CdS nanorods.

2.7.5 Optical Properties of Ordered Nanorod Assemblies

As discussed earlier in this section, the advent of the seeded growth approach for the fabrication of core–shell nanorods has significantly improved the quality of the nanorod samples in terms of monodispersity, line width of the emission, and quantum yield [64]. This new synthesis technique, where the seed is fabricated and size selected in a prior step, has boosted the progress on assembly of anisotropic

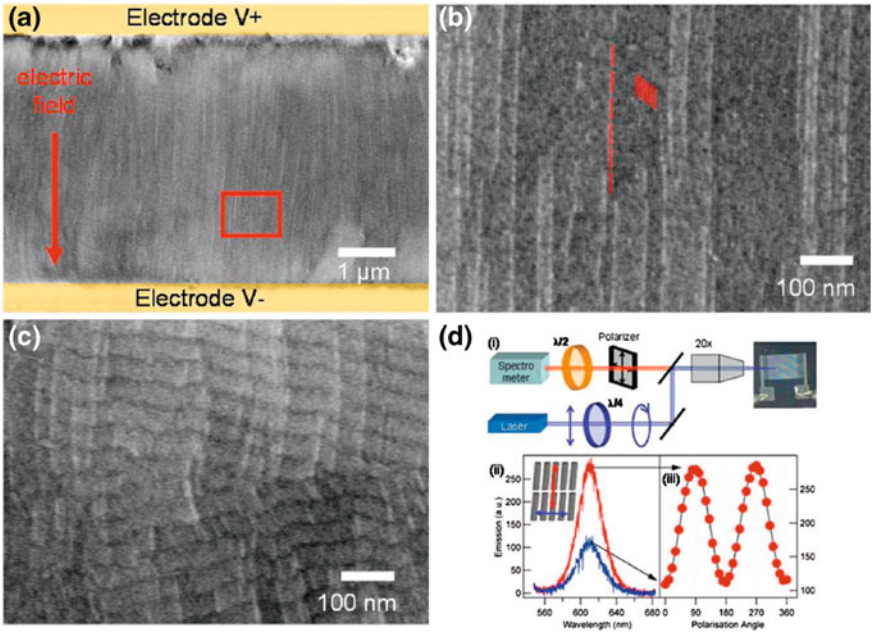

Fig. 2.33 **a–c** SEM images of nanorods aligned by means of electric fields. **d** Schematic illustration of the setup (*i*) employed for the polarization measurements and relative results (*ii*, *iii*). Spectra in (*ii*) show the emission polarized parallel (*red signal*) and perpendicularly (*blue signal*) to the alignment direction. Panel (*iii*) show the PL versus the polarization angle (*red symbols*) fitted to a $\cos^2$ function (*black line*). Taken with permission from Ref. [64]

nanocrystals, on the study of optical properties of such assemblies, and additionally on the fabrication of branched nanocrystals [91, 94, 95]. An interesting feature of nanorods with uniform lengths and diameters consists in the possibility to align them over large areas [64, 96, 97]), as shown in Fig. 2.33. Confocal spectroscopy made it possible to optically characterize regions of nanorods aligned according to various geometries with respect to a substrate, namely lateral, vertical and random. As one example, arrays of laterally aligned CdSe/CdS nanorods exhibited linearly polarized emission approaching a degree of polarization of 80 % [63, 88]. Figure 2.33 shows scanning electron microscopy (SEM) images of laterally aligned nanorods, and the polarized signal originating from those areas.

Figure 2.34 reports the spatially resolved PL spectra collected from regions showing different types of nanorod alignment [64]. Measurements on regions of rods vertically oriented with respect to the substrate were almost non emissive in the vertical direction and the weak PL was slightly blue-shifted (a few meV) with respect to the more intense signal originating from disordered nanorods. A more pronounced blue-shift (up to 30 meV) and much higher intensity of the PL were noticeable on lateral assemblies. The difference in PL intensity between laterally- and vertically-aligned nanorods could be ascribed to the spatial anisotropy of the optical dipole emission

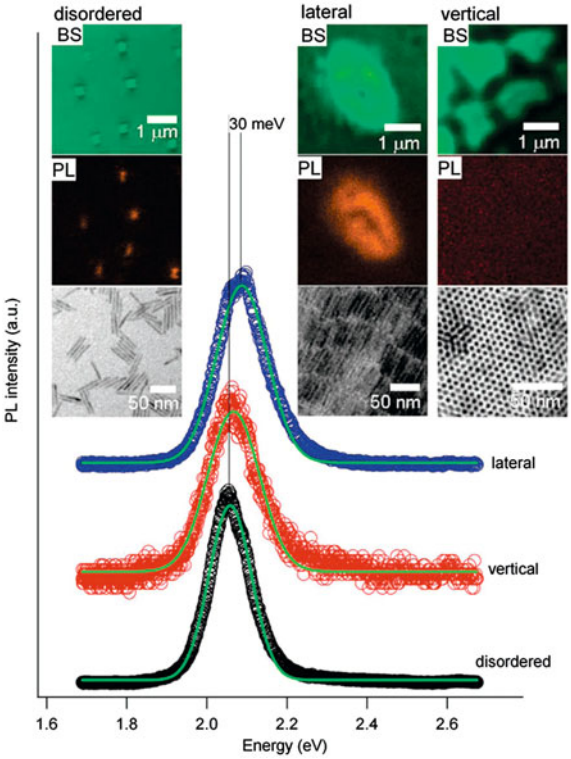

Fig. 2.34 (Main panel): PL from region of laterally-, vertically-aligned and disordered nanorods with relative Gaussian best fit curves (*green lines*). Upper panels show TEM, PL and backscattering images from the same regions. Taken with permission from Ref. [64]

in nanorods. The transition dipole in such nanorods is parallel to the rod long axis, thus the PL intensity is expected to be maximal in the plane perpendicular to the dipole and minimal in the direction of the long axis. The unexpected behavior consists in the energy shift, and a possible explanation of this effect is the screening of an internal (piezo) electric field present in the individual nanorods due to the photogenerated charge distributions in neighboring rods (as discussed in detail earlier).

The possibility to organize nanorods into ordered arrays on micrometer and millimeter length scales makes them an interesting material for macroscopic optical applications. As an example, Rizzo et al. fabricated a polarized light emitting diode based on an array of laterally oriented nanorods [98]. Also, nanorods can be employed as active material for lasing devices. Here, typically, the emitting medium is embedded in an external resonator for optical feedback [99–101]. A novel approach for self assembled micro-lasers was proposed recently by Zavelani et al. [102, 103]. Here the coffee stain effect that governs the microfluidic dynamics in an evaporating droplet [104, 105] led to the formation of well-defined stripes that consisted of densely packed, laterally aligned nanorods. The borders of these stripes were sharp and smooth enough to form a resonant cavity that was able to sustain laser emission both from core- and shell transitions of the nanorods [103], as can be seen in Fig. 2.35.

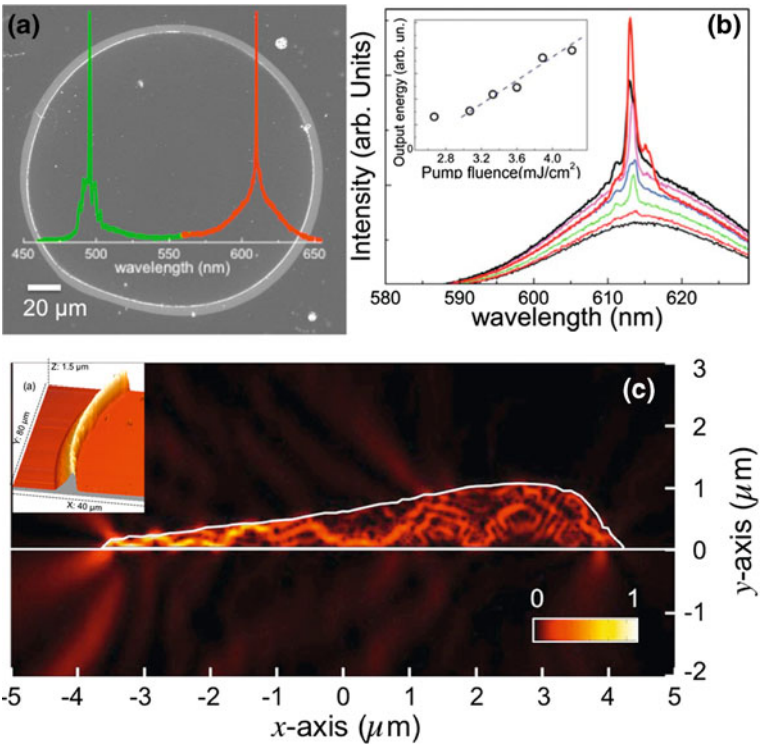

Fig. 2.35 Lasing from self-assembled nanorod cavities. **a** Scanning electron microscope (SEM) image of the coffee stain deposit formed by jet deposition of a solution of nanorods dissolved in toluene, overlaid with laser emission spectra in the red and green. The borders of the coffee stain ring are well defined and function as a resonant cavity able to sustain lasing. **b** Emission from a coffee stain nanorod deposit for different pump excitation intensities, the inset shows the linear input-out typical for laser action. Taken with permission from Ref. [102]. **c** Finite elements modeling of the resonant modes sustained by a cavity with a cross section corresponding to the shape that was obtained by atomic-force microscopy measurements (*see inset*) on the coffee stain rings. Taken with permission from Ref. [122]

2.7.6 Collinear Nanorods and Nanobarbells

Collinear heterostructures exhibit a direct exposure of both materials of their surface and are interesting candidates for photovoltaic [65–70] and photocatalytic [71–73] applications (see also Chapter 6). Among the type-II rod-like systems, CdSe/CdTe has the advantages of a well controlled synthesis and small lattice mismatch between the two materials. Therefore it is the most studied heterostructure with type-II band-alignment [68–70, 72, 106, 107]. Optical investigation techniques including steady-state (absorption and PL measurements) and time-resolved spectroscopy allow to monitor effectively the carrier dynamics and localization in these nanostructures. Figure 2.36 shows typical absorption and PL

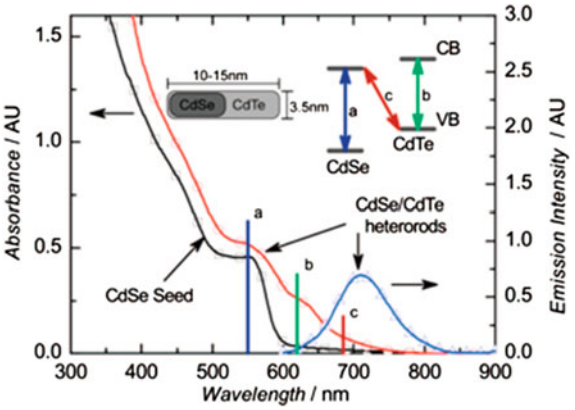

Fig. 2.36 Absorption and PL spectra of a representative coaxial CdSe/CdTe heterostructure. *Inset* sketch of the band-alignment and labeling of the transitions indicated on the rod absorption (*red line*). Taken with permission from Ref. [70]

spectra of collinear CdSe/CdTe nanorods. The absorption spectra show features arising from a superposition of the single sections that constitute the heterostructure, whereas the PL signal occurs at an energy that is well below the band gap of the single material sections, if these are considered separately.

In collinear nanorods the emission from the CdSe material is often observed as well, but with a strongly reduced intensity with respect to the core–shell or tetrapod systems [68, 94, 107]. The presence of such visible emission has been ascribed to ultrafast hole transfer from the core to the outer material and/or to resonant energy transfer from seeds having band gap larger than the shell [107]. Further evidence of the real nature of the detected PL signal is usually obtained by analyzing the lifetime of both emission peaks. Due to the spatial separation of e–h wavefunctions, the radiative rate (proportional to the e–h wavefunctions overlap) is strongly reduced with respect to a type-I optical transition. This is reflected in time-resolved measurements showing type-II PL lifetime ranging from few hundreds of nanoseconds to some microseconds against the more classical PL decay on the nanosecond timescale observed in type-I transitions [106–108].

Collinear nanorods are preferred in the study of the fundamental physical properties, since it is possible to discern the role of core and shell in the absorption process. This allowed to precisely determine the dynamics of charge carriers after generation by means of pump-probe technique. Transient absorption measurements performed by Dooley and co-workers have disclosed the real carrier pathways finding an ultrafast charge separation on the 500 fs timescale [70]. The noteworthy characteristic of these systems, apart from the type-II transition, is the presence of a PL peak falling in the visible range and referable to radiative emission of the outer material (see for instance Fig. 2.36) [68, 69, 107].

Differently from some collinear and dot/rod systems, where an internal seed material is always buried in an outer material having the role of both charge separator and passivating agent, nanobarbells are characterized by having a second component deposited only on the tips of the rod (see Fig. 2.22) [72, 73]. Apart from the geometry, a fundamental difference with respect to the structures previously described lies in the role of the second material. Nanobarbells are of

potential interest for photocatalysis, where both the separated charges have to be readily available for chemical reactions, since both material components are directly exposed to the ambient conditions.

This specific geometry has also strong implications on the optical properties of the overall nanocrystal, since the second material does not grow as a passivating uniform layer on top of the starting rod. Indeed, the most common behavior in these structures consists in a drastic change of the luminescence performances, mainly due to trapping processes occurring on the surface of both exposed components. Depending on the material, the effect may correspond to an increase or decrease of the performances. Figure 2.37 shows an example of what happens for two different systems, CdSe/CdTe and ZnSe/CdS [72, 73]. In the CdSe/CdTe nanobarbells the PL is quenched after deposition of CdTe on the CdSe rod, which makes them ideal structures in photocatalytic applications (see Fig. 2.37a). On the contrary, the PL signal coming from ZnSe/CdS system transforms from a broad, trap related emission of CdS rods to a sharper, more intense signal falling in the same spectral range (Fig. 2.37b).

2.7.7 *Multifunctional Nanorods*

The advent of synthesis approaches allowing for narrow distributions of the geometric parameters of colloidal nanocrystals has directed the research towards the fabrication of more elaborate multi-component nanostructures, which in principle would be able to fulfill multiple tasks simultaneously. In particular, the combination of magnetic and optical properties is attractive for application of such nanocrystals as bio-labeling and analytical separation, drug delivery or multimodal diagnostics and therapeutics. Among the several colloidal nanostructures that have

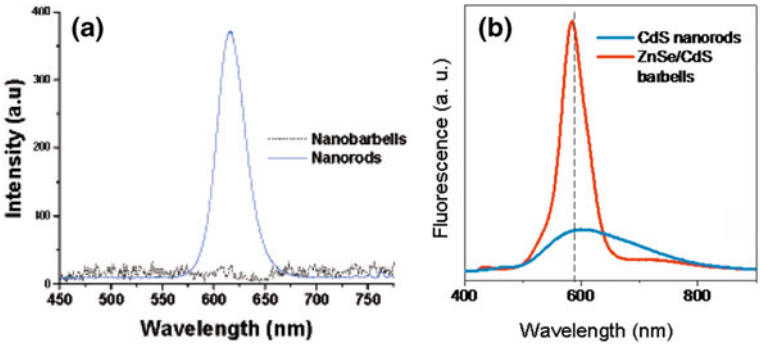

Fig. 2.37 **a** Collapse of the CdSe/CdTe nanobarbells PL respect to the starting CdSe nanorods. Taken with permission from Ref. [72]. **b** Comparison between PL coming from CdS nanorods (*blue line*) and ZnSe/CdS nanobarbells (*red line*) showing increased efficiency. Taken with permission from Ref. [73]

been reported in the last years (and not limited to nanorods), we mention Co/CdSe core–shell nanocrystals [109], FePt-CdX (X = S, Se) heterodimers [110–113], γ-Fe_2O_3-MeX (Me = Cd, Zn, Hg and X = S, Se) heterodimers [114–116], CdSe/CdS, and CdSe nanorods decorated with PtNi/PtCo or Co domains [75, 117]. All these structures have been fabricated with the initial goal to "pack" into a single nanostructure magnetic and optical properties, although the final outcome has not always been very successful.

For what concerns nanorods for example, the basic idea in this direction is to grow other materials with optical/magnetic properties selectively at their tip regions. Unfortunately a common fate of metal-tipped nanorods is the drastic drop of their PL quantum yield (PL QY), due to fast semiconductor–metal charge transfer. However, the last generation of seeded grown CdSe/CdS nanorods (having a starting QY approaching 70 % at room temperature) offers the opportunity to preserve larger efficiency after semiconductor–metal coupling. Recently, fluorescent Co-tipped CdSe/CdS dot/rod heterostructures exhibiting ferromagnetic behavior at room temperature have been successfully reported [74]. In Fig. 2.38 we show an image of these Co-tipped nanorods, obtained by energy-filtered TEM (EFTEM). In the sample, which has been imaged before separation of the metal-tipped nanorods from unreacted rods, one can see clearly the selective growth of Co domains only on one tip region of individual rods, and in few cases the analysis allowed to identify this tip region as being far from the region of the CdS rod in which the initial CdSe was buried (for more details, see Ref. [74]). Figure 2.39a shows the optical absorption and emission spectra of the initial CdSe cores (i.e. the "seeds") of the CdSe/CdS nanorods, of physical mixtures of Co nanocrystals and CdSe/CdS nanorods, and finally of Co-tipped nanorods (the latter obtained after magnetic separation, hence containing a negligible amount of non-reacted nanorods). As discussed previously, the absorption from CdSe/CdS

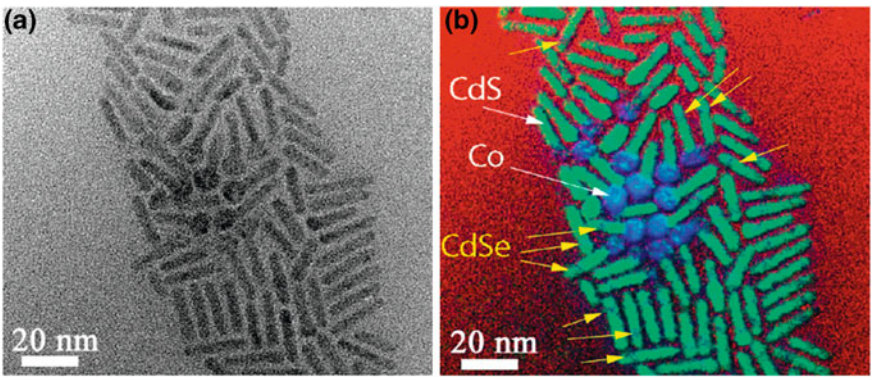

Fig. 2.38 **a** Elastic zero-loss EFTEM image of a sample of Co-tipped nanorods. **b** Composite false-color image obtained from **a** showing the different domains of the sample. CdS rod (*green*), cobalt domains (*blue spheres* on the tips of the rods), CdSe cores (*blue* zones inside the CdS rods). Taken with permission from Ref. [74]

nanorods presents a sharp profile in correspondence of the CdS excitonic absorption (about 495 nm) and a smooth behavior at longer wavelengths, where a weak CdSe absorption can be detected.

The relative PL emission clearly falls in the CdSe spectral domain, indicating a type-I recombination in the cores, and is slightly red-shifted (together with the lowest absorption peak) with respect to the starting seeds counterpart. This behavior, largely observed in heterostructures, is ascribed in this case to the electron wavefunction spreading, which leads to the observed red-shifts. The physical mixture of rods and Co particles has an absorption spectrum that reproduces a linear combination of the two systems considered, and a PL typical of the nanorods, with a PL quantum yield of about 25 %.

On the contrary, Co-tipped nanorods present an almost flat absorption as a consequence of the effective electronic coupling between the two components. Their PL QY, despite being only around 3 %, is nevertheless the highest efficiency reported so far for semiconductor-magnetic nanocrystals in which the two domains are directly bound to each other (i.e. without any molecule/polymer acting as a spacer between them). The reduction of the PL QY is explained in terms of fast charge transfer from the semiconductor to the metal particles and has been investigated by time resolved spectroscopy (see Fig. 2.39b). The PL from the CdSe/CdS nanorods decays in about 12 ns, whereas in a physical mixture of CdSe/CdS nanorods and Co nanoparticles the lifetime is about 7 ns. On the other hand, the Co-tipped rods exhibits a time constant of only 350 ps. Considering that these

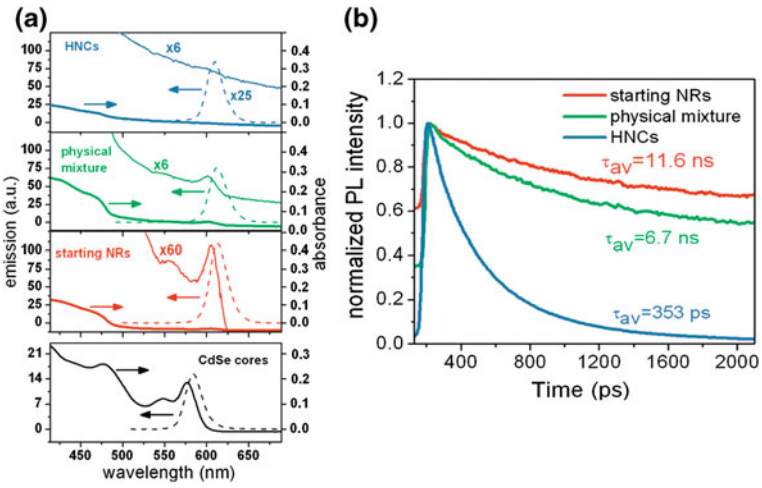

Fig. 2.39 **a** Series of absorption (*continuous lines*) and PL spectra (*dashed lines*) of starting CdSe cores (*black lines*), CdSe/CdS nanorods (*red lines*), a physical mixture of Co nanoparticles and CdSe/CdS nanorods (*green lines*), Co-tipped nanorods (*blue lines*). **b** Time traces of the PL recorded at room temperature on starting CdSe/CdS nanorods (*red line*), physical mixture of Co nanoparticles and CdSe/CdS nanorods (*green line*), Co-tipped nanorods (*blue line*). Taken with permission from Ref. [74]

three systems undergo a progressive decrease of their PL QY, the reduction of the lifetime cannot be ascribed to an increased radiative recombination rate (which would lead to a progressive increase of the PL efficiency). Instead, the reduction in lifetime in Co-tipped nanorods can be attributed to an increase of the non-radiative rate, due to the rapid charge transfer induced by the electronic communication between the semiconductor material and the cobalt domain attached to it. For the mixture of CdSe/CdS nanorods and Co nanoparticles, in which no direct Co-nanorod interface is present, the moderate decrease in the decay time can be ascribed to the activation of non-radiative channels different from charge transfer. Most likely, these are due to energy transfer from semiconductor to metal, as already observed in similar systems [118]. Despite the large reduction of the emission efficiency in Co-tipped nanorods, some detectable PL signal remains, which makes such heterostructures promising candidates as active media in optical/magnetic applications.

References

1. Schmelcher P (1993) Delocalization of excitons in a magnetic-field. Phys Rev B 48(19):14642–14645
2. Efros AL, Rosen M (2000) The electronic structure of semiconductor nanocrystals. Annu Rev Mater Sci 30:475–521
3. Ekimov AI, Onushchenko AA, Efros AL (1986) JETP Lett 43:376
4. Ekimov AI, Efros AL, Ivanov MG, Onushchenko AA, Shumilov SK (1989) Donor-like exciton in zero-dimension semiconductor structures. Solid State Commun 69(5):565–568
5. Li JB, Wang LW (2003) Shape effects on electronic states of nanocrystals. Nano Lett 3(10):1357–1363
6. Shabaev A, Efros AL (2004) 1D exciton spectroscopy of semiconductor nanorods. Nano Lett 4(10):1821–1825
7. Efros AL, Rosen M, Kuno M, Nirmal M, Norris DJ, Bawendi M (1996) Band-edge exciton in quantum dots of semiconductors with a degenerate valence band: dark and bright exciton states. Phys Rev B 54(7):4843–4856
8. Norris DJ, Efros AL, Rosen M, Bawendi MG (1996) Size dependence of exciton fine structure in CdSe quantum dots. Phys Rev B 53(24):16347–16354
9. Nirmal M, Norris DJ, Kuno M, Bawendi MG, Efros AL, Rosen M (1995) Observation of the dark exciton in CdSe quantum dots. Phys Rev Lett 75(20):3728–3731
10. Le Thomas N, Herz E, Schops O, Woggon U, Artemyev MV (2005) Exciton fine structure in single CdSe nanorods. Phys Rev Lett 94(1):016803
11. Le Thomas N, Allione M, Fedutik Y, Woggon U, Artemyev MV, Ustinovich EA (2006) Multiline spectra of single CdSe/ZnS core-shell nanorods. Appl Phys Lett 89(26):263115
12. Lange H, Machon M, Artemyev M, Woggon U, Thomsen C (2007) Effect of ZnS shell on the Raman spectra from CdSe nanorods. Phys Stat Sol Rap Res Lett 1(6):274–276
13. Artemyev M, Moller B, Woggon U (2003) Unidirectional alignment of CdSe nanorods. Nano Lett 3(4):509–512
14. Talaat H, Abdallah T, Mohamed MB, Negm S, El-Sayed MA (2009) The sensitivity of the energy band gap to changes in the dimensions of the CdSe quantum rods at room temperature: STM and theoretical studies. Chem Phys Lett 473(4–6):288–292
15. Katz D, Wizansky T, Millo O, Rothenberg E, Mokari T, Banin U (2002) Size-dependent tunneling and optical spectroscopy of CdSe quantum rods. Phys Rev Lett 89(8):086801

16. Millo O, Katz D, Steiner D, Rothenberg E, Mokari T, Kazes M, Banin U (2004) Charging and quantum size effects in tunnelling and optical spectroscopy of CdSe nanorods. Nanotechnology 15(1):R1–R6
17. Hu JT, Li LS, Yang WD, Manna L, Wang LW, Alivisatos AP (2001) Linearly polarized emission from colloidal semiconductor quantum rods. Science 292(5524):2060–2063
18. De Giorgi M, Lingk C, von Plessen G, Feldmann J, De Rinaldis S, Passaseo A, De Vittorio M, Cingolani R, Lomascolo M (2001) Capture and thermal re-emission of carriers in long-wavelength InGaAs/GaAs quantum dots. Appl Phys Lett 79(24):3968–3970
19. Morello G, De Giorgi M, Kudera S, Manna L, Cingolani R, Anni M (2007) Temperature and size dependence of nonradiative relaxation and exciton-phonon coupling in colloidal CdTe quantum dots. J Phys Chem C 111(16):5846–5849
20. Valerini D, Creti A, Lomascolo M, Manna L, Cingolani R, Anni M (2005) Temperature dependence of the photoluminescence properties of colloidal CdSe/ZnS core/shell quantum dots embedded in a polystyrene matrix. Phys Rev B 71(23):235409
21. Klimov VI, Mikhailovsky AA, McBranch DW, Leatherdale CA, Bawendi MG (2000) Quantization of multiparticle Auger rates in semiconductor quantum dots. Science 287(5455):1011–1013
22. Fisher B, Caruge JM, Zehnder D, Bawendi M (2005) Room-temperature ordered photon emission from multiexciton states in single CdSe core-shell nanocrystals. Phys Rev Lett 94(8):087403
23. Pandey A, Guyot-Sionnest P (2007) Multicarrier recombination in colloidal quantum dots. J Chem Phys 127(11):111104
24. Achermann M, Hollingsworth JA, Klimov VI (2003) Multiexcitons confined within a subexcitonic volume: spectroscopic and dynamical signatures of neutral and charged biexcitons in ultrasmall semiconductor nanocrystals. Phys Rev B 68(24):245302
25. Wang LW, Califano M, Zunger A, Franceschetti A (2003) Pseudopotential theory of Auger processes in CdSe quantum dots. Phys Rev Lett 91(5):056404
26. Kraus RM, Lagoudakis PG, Muller J, Rogach AL, Lupton JM, Feldmann J, Talapin DV, Weller H (2005) Interplay between auger and ionization processes in nanocrystal quantum dots. J Phys Chem B 109(39):18214–18217
27. Klimov VI (2000) Optical nonlinearities and ultrafast carrier dynamics in semiconductor nanocrystals. J Phys Chem B 104(26):6112–6123
28. Achermann M, Bartko AP, Hollingsworth JA, Klimov VI (2006) The effect of Auger heating on intraband carrier relaxation in semiconductor quantum rods. Nat Phys 2(8):557–561
29. Htoon H, Hollingsworth JA, Dickerson R, Klimov VI (2003) Effect of zero- to one-dimensional transformation on multiparticle Auger recombination in semiconductor quantum rods. Phys Rev Lett 91(22):227401
30. Robel I, Bunker BA, Kamat PV, Kuno M (2006) Exciton recombination dynamics in CdSe nanowires: bimolecular to three-carrier Auger kinetics. Nano Lett 6(7):1344–1349
31. Liebler JG, Schmitt-Rink S, Haug H (1985) Theory of the absorption tail of wannier excitons in polar semiconductors. J Lumin 34:1–7
32. Takagahara T (1996) Electron-phonon interactions in semiconductor nanocrystals. J Lumin 70:129–143
33. Schmitt-Rink S, Miller DAB, Chemla DS (1987) Theory of the linear and nonlinear optical properties of semiconductor nanocrystallites. Phys Rev B 35:8113–8125
34. Nomura S, Kobayashi T (1992) Exciton-LO-phonon couplings in spherical semiconductor microcrystallites. Phys Rev B 45:1305–1316
35. Muljarov EA, Zimmermann R (2007) Exciton dephasing in quantum dots due to LO-phonon coupling: An exactly solvable model. Phys Rev Lett 98(18):187401
36. Gindele F, Hild K, Langbein W, Woggon U (2000) Temperature-dependent line widths of single excitons and biexcitons. J Lumin 87–89:381–383
37. Rudin S, Reinecke TL, Segall B (1990) Temperature-dependent exciton linewidths in semiconductors. Phys Rev B 42(17):11218–11231

38. Lange H, Artemyev M, Woggon U, Niermann T, Thomsen C (2008) Experimental investigation of exciton-LO-phonon couplings in CdSe/ZnS core/shell nanorods. Phys Rev B 77(19):193303
39. Trallero-Giner C, Debernardi A, Cardona M, Menendez-Proupin E, Ekimov AI (1998) Optical vibrons in CdSe dots and dispersion relation of the bulk material. Phys Rev B 57(8):4664–4669
40. Lange H, Artemyev M, Woggon U, Thomsen C (2009) Geometry dependence of the phonon modes in CdSe nanorods. Nanotechnology 20(4):045705
41. Nobile C, Kudera S, Fiore A, Carbone L, Chilla G, Kipp T, Heitmann D, Cingolani R, Manna L, Krahne R (2007) Confinement effects on optical phonons in spherical, rod-, and tetrapod-shaped nanocrystals detected by Raman spectroscopy. Phys Status Solidi A-Appl Mat 204(2):483–486
42. Gupta R, Xiong Q, Mahan GD, Eklund PC (2003) Surface optical phonons in gallium phosphide nanowires. Nano Lett 3(12):1745–1750
43. Krahne R, Chilla G, Schuller C, Carbone L, Kudera S, Mannarini G, Manna L, Heitmann D, Cingolani R (2006) Confinement effects on optical phonons in polar tetrapod nanocrystals detected by resonant inelastic light scattering. Nano Lett 6(3):478–482
44. Klimov VI, Ivanov SA, Nanda J, Achermann M, Bezel I, McGuire JA, Piryatinski A (2007) Single-exciton optical gain in semiconductor nanocrystals. Nature 447(7143):441–446
45. Nanda J, Ivanov SA, Achermann M, Bezel I, Piryatinski A, Klimov VI (2007) Light amplification in the single-exciton regime using exciton–exciton repulsion in type-II nanocrystal quantum dots. J Phys Chem C 111(42):15382–15390
46. Efros AL, Kharchenko VA, Rosen M (1995) Breaking the phonon bottleneck in nanometer quantum dots—role of Auger-like processes. Solid State Commun 93(4):281–284
47. Creti A, Anni M, Rossi MZ, Lanzani G, Manna L, Lomascolo M (2007) Role of defect states on Auger processes in resonantly pumped CdSe nanorods. Appl Phys Lett 91(9):093106
48. Wang S, Querner C, Fischbein MD, Willis L, Novikov DS, Crouch CH, Drndic M (2008) Blinking statistics correlated with nanoparticle number. Nano Lett 8(11):4020–4026
49. Wang S, Querner C, Emmons T, Drndic M, Crouch CH (2006) Fluorescence blinking statistics from CdSe core and core/shell nanorods. J Phys Chem B 110(46):23221–23227
50. Krishnan R, Hahn MA, Yu ZH, Silcox J, Fauchet PM, Krauss TD (2004) Polarization surface-charge density of single semiconductor quantum rods. Phys Rev Lett 92(21):216803
51. Li XZ, Xia JB (2003) Effects of electric field on the electronic structure and optical properties of quantum rods with wurtzite structure. Phys Rev B 68(16):165316
52. Rothenberg E, Kazes M, Shaviv E, Banin U (2005) Electric field induced switching of the fluorescence of single semiconductor quantum rods. Nano Lett 5(8):1581–1586
53. Muller J, Lupton JM, Lagoudakis PG, Schindler F, Koeppe R, Rogach AL, Feldmann J, Talapin DV, Weller H (2005) Wave function engineering in elongated semiconductor nanocrystals with heterogeneous carrier confinement. Nano Lett 5(10):2044–2049
54. Li XZ, Xia JB (2002) Electronic structure and optical properties of quantum rods with wurtzite structure. Phys Rev B 66(11):115316
55. Chen X, Nazzal A, Goorskey D, Xiao M, Peng ZA, Peng XG (2001) Polarization spectroscopy of single CdSe quantum rods. Phys Rev B 64(24):245304
56. Rothenberg E, Ebenstein Y, Kazes M, Banin U (2004) Two-photon fluorescence microscopy of single semiconductor quantum rods: direct observation of highly polarized nonlinear absorption dipole. J Phys Chem B 108(9):2797–2800
57. Wang J, Gudiksen MS, Duan X, Cui Y, Lieber CM (2001) Highly polarized photoluminescence and photodetection from single indium phosphide nanowires. Science 293(5534):1455–1457
58. Persson MP, Xu HQ (2004) Giant polarization anisotropy in optical transitions of free-standing InP nanowires. Phys Rev B 70:161310
59. Costi R, Saunders AE, Banin U (2010) Colloidal hybrid nanostructures: a new type of functional materials. Angew ChemInt Edit 49(29):4878–4897

60. Carbone L, Cozzoli PD (2010) Colloidal heterostructured nanocrystals: synthesis and growth mechanisms. Nano Today 5(5):449–493
61. Donega CDM (2011) Synthesis and properties of colloidal heteronanocrystals. Chem Soc Rev 40(3):1512–1546. doi:10.1039/C0CS00055H
62. Lo SS, Mirkovic T, Chuang CH, Burda C, Scholes GD (2011) Emergent Properties Resulting from Type-II Band Alignment in Semiconductor Nanoheterostructures. Adv Mater 23(2):180–197. doi:10.1002/adma.201002290
63. Steiner D, Dorfs D, Banin U, Della Sala F, Manna L, Millo O (2008) Determination of band offsets in heterostructured colloidal nanorods using scanning tunneling spectroscopy. Nano Lett 8(9):2954–2958. doi:10.1021/nl801848x
64. Carbone L, Nobile C, De Giorgi M, Sala FD, Morello G, Pompa P, Hytch M, Snoeck E, Fiore A, Franchini IR, Nadasan M, Silvestre AF, Chiodo L, Kudera S, Cingolani R, Krahne R, Manna L (2007) Synthesis and micrometer-scale assembly of colloidal CdSe/CdS nanorods prepared by a seeded growth approach. Nano Lett 7(10):2942–2950
65. Koo B, Korgel BA (2008) Coalescence and interface diffusion in linear CdTe/CdSe/CdTe heterojunction nanorods. Nano Lett 8(8):2490–2496
66. He J, Lo SS, Kim JH, Scholes GD (2008) Control of exciton spin relaxation by electron-hole decoupling in type-II nanocrystal heterostructures. Nano Lett 8(11):4007–4013
67. Shieh F, Saunders AE, Korgel BA (2005) General shape control of colloidal CdS, CdSe, CdTe quantum rods and quantum rod heterostructures. J Phys Chem B 109(18):8538–8542
68. Kumar S, Jones M, Lo SS, Scholes GD (2007) Nanorod heterostructures showing photoinduced charge separation. Small 3(9):1633–1639
69. Saunders AE, Koo B, Wang XY, Shih CK, Korgel BA (2008) Structural characterization and temperature-dependent photoluminescence of linear CdTe/CdSe/CdTe heterostructure nanorods. ChemPhysChem 9(8):1158–1163
70. Dooley CJ, Dimitrov SD, Fiebig T (2008) Ultrafast electron transfer dynamics in CdSe/CdTe donor-acceptor nanorods. J Phys Chem C 112(32):12074–12076
71. Hewa-Kasakarage NN, Kirsanova M, Nemchinov A, Schmall N, El-Khoury PZ, Tarnovsky AN, Zamkov M (2009) Radiative recombination of spatially extended excitons in (ZnSe/CdS)/CdS heterostructured nanorods. J Am Chem Soc 131(3):1328–1334
72. Halpert JE, Porter VJ, Zimmer JP, Bawendi MG (2006) Synthesis of CdSe/CdTe nanobarbells. J Am Chem Soc 128(39):12590–12591
73. Kirsanova M, Nemchinov A, Hewa-Kasakarage NN, Schmall N, Zamkov M (2009) Synthesis of ZnSe/CdS/ZnSe nanobarbells showing photoinduced charge separation. Chem Mater 21(18):4305–4309
74. Deka S, Falqui A, Bertoni G, Sangregorio C, Poneti G, Morello G, De Giorgi M, Giannini C, Cingolani R, Manna L, Cozzoli PD (2009) Fluorescent asymmetrically cobalt-tipped CdSe@CdS Core@Shell nanorod heterostructures exhibiting room-temperature ferromagnetic behavior. J Am Chem Soc 131(35):12817–12828
75. Maynadie J, Salant A, Falqui A, Respaud M, Shaviv E, Banin U, Soulantica K, Chaudret B (2009) Cobalt growth on the tips of CdSe nanorods. Angew ChemInt Edit 48(10):1814–1817
76. Muller J, Lupton JM, Rogach AL, Feldmann J, Talapin DV, Weller H (2004) Monitoring surface charge movement in single elongated semiconductor nanocrystals. Phys Rev Lett 93(16):167402
77. Muller J, Lupton JM, Rogach AL, Feldmann J, Talapin DV, Weller H (2005) Monitoring surface charge migration in the spectral dynamics of single CdSe/CdS nanodot/nanorod heterostructures. Phys Rev B 72(20):205339
78. Lupo MG, Della Sala F, Carbone L, Zavelani-Rossi M, Fiore A, Luer L, Polli D, Cingolani R, Manna L, Lanzani G (2008) Ultrafast electron-hole dynamics in core/shell CdSe/CdS dot/rod nanocrystals. Nano Lett 8(12):4582–4587
79. Talapin DV, Nelson JH, Shevchenko EV, Aloni S, Sadtler B, Alivisatos AP (2007) Seeded growth of highly luminescent CdSe/CdS nanoheterostructures with rod and tetrapod morphologies. Nano Lett 7(10):2951–2959

80. Creti A, Anni M, Zavelani-Rossi M, Lanzani G, Leo G, Della Sala F, Manna L, Lomascolo M (2005) Ultrafast carrier dynamics in core and core/shell CdSe quantum rods: role of the surface and interface defects. Phys Rev B 72(12):125346
81. Kraus RM, Lagoudakis PG, Rogach AL, Talapin DV, Weller H, Lupton JM, Feldmann J (2007) Room-temperature exciton storage in elongated semiconductor nanocrystals. Phys Rev Lett 98(1):017401
82. Morello G, Della Sala F, Carbone L, Manna L, Maruccio G, Cingolani R, De Giorgi M (2008) Intrinsic optical nonlinearity in colloidal seeded grown CdSe/CdS nanostructures: photoinduced screening of the internal electric field. Phys Rev B 78(19):195313
83. Ranjan V, Allan G, Priester C, Delerue C (2003) Self-consistent calculations of the optical properties of GaN quantum dots. Phys Rev B 68(11):115305
84. Salviati G, Rossi F, Armani N, Grillo V, Martinez O, Vinattieri A, Damilano B, Matsuse A, Grandjean N (2004) Optical and structural characterization of self-organized stacked GaN/AlN quantum dots. J Phys: Condens Matter 16(2):S115–S126
85. Brown RH, Twiss RQ (1956) A test of a new type of stellar interferometer on Sirius. Nature 178:1046–1048
86. Kimble HJ, Dagenais M, Mandel L (1977) Photon antibunching in resonance fluorescence. Phys Rev Lett 39:691–695
87. Purcell EM (1976) The question of correlation between photons in coherent light rays. Nature 178:1449–1450
88. Pisanello F, Martiradonna L, Lemenager G, Spinicelli P, Fiore A, Manna L, Hermier JP, Cingolani R, Giacobino E, De Vittorio M, Bramati A (2010) Room temperature-dipolelike single photon source with a colloidal dot-in-rod. Appl Phys Lett 96(3):033101
89. Langbein W, Hetterich M, Klingshirn C (1995) Many-body effects and carrier dynamics in CdSe/CdS stark superlattices. Phys Rev B 51(15):9922–9929
90. Halsall MP, Nicholls JE, Davies JJ, Cockayne B, Wright PJ (1992) CdS/CdSe intrinsic stark superlattices. J Appl Phys 71(2):907–915
91. Sitt A, Della Sala F, Menagen G, Banin U (2009) Multiexciton engineering in seeded core/shell nanorods: transfer from type-I to quasi-type-II regimes. Nano Lett 9(10):3470–3476
92. Ashroft NW, Mermin ND (1976) Solid state physics. Brooks Cole, New York
93. Kreibig U (1974) Electronic properties of small silver particles: the optical constants and their temperature dependence. J Phys F 4:999–1014
94. Fiore A, Mastria R, Lupo MG, Lanzani G, Giannini C, Carlino E, Morello G, De Giorgi M, Li Y, Cingolani R, Manna L (2009) Tetrapod-shaped colloidal nanocrystals of II-VI semiconductors prepared by seeded growth. J Am Chem Soc 131(6):2274–2282
95. Martiradonna L, Carbone L, Tandaechanurat A, Kitamura M, Iwamoto S, Manna L, De Vittorio M, Cingolani R, Arakawa Y (2008) Two-dimensional photonic crystal resist membrane nanocavity embedding colloidal dot-in-a-rod nanocrystals. Nano Lett 8(1):260–264
96. Ahmed S, Ryan KM (2009) Centimetre scale assembly of vertically aligned and close packed semiconductor nanorods from solution . Chem Commun 42:6421–6423
97. Baranov D, Fiore A, van Huis M, Giannini C, Falqui A, Lafont U, Zandbergen H, Zanella M, Cingolani R, Manna L (2010) Assembly of colloidal semiconductor nanorods in solution by depletion attraction. Nano Lett 10(2):743–749
98. Rizzo A, Nobile C, Mazzeo M, De Giorgi M, Fiore A, Carbone L, Cingolani R, Manna L, Gigli G (2009) Polarized light emitting diode by long-range nanorod self-assembling on a water surface. ACS Nano 3(6):1506–1512
99. Htoon H, Hollingworth JA, Malko AV, Dickerson R, Klimov VI (2003) Light amplification in semiconductor nanocrystals: quantum rods versus quantum dots. Appl Phys Lett 82(26):4776–4778
100. Kazes M, Lewis DY, Ebenstein Y, Mokari T, Banin U (2002) Lasing from semiconductor quantum rods in a cylindrical microcavity. Adv Mater 14(4):317–321
101. Kazes M, Lewis DY, Banin U (2004) Method for preparation of semiconductor quantum-rod lasers in a cylindrical microcavity. Adv Funct Mater 14(10):957–962

102. Zavelani-Rossi M, Lupo MG, Krahne R, Manna L, Lanzani G (2010) Lasing in self-assembled microcavities of CdSe/CdS core/shell colloidal quantum rods. Nanoscale 2(6):931–935
103. Mie G (1908) Ann Physik 25:377–445
104. Deegan RD, Bakajin O, Dupont TF, Huber G, Nagel SR, Witten TA (1997) Capillary flow as the cause of ring stains from dried liquid drops. Nature 389(6653):827–829
105. Nobile C, Carbone L, Fiore A, Cingolani R, Manna L, Krahne R (2009) Self-assembly of highly fluorescent semiconductor nanorods into large scale smectic liquid crystal structures by coffee stain evaporation dynamics. J Phys Condens Matter 21(26):264013
106. Chin PTK, Donega CDM, Bavel SS, Meskers SCJ, Sommerdijk N, Janssen RAJ (2007) Highly luminescent CdTe/CdSe colloidal heteronanocrystals with temperature-dependent emission color. J Am Chem Soc 129(48):14880–14886
107. Jones M, Kumar S, Lo SS, Scholes GD (2008) Exciton trapping and recombination in type IICdSe/CdTe nanorod heterostructures. J Phys Chem C 112(14):5423–5431
108. Donega CDM (2010) Formation of nanoscale spatially indirect excitons: evolution of the type-II optical character of CdTe/CdSe heteronanocrystals. Phys Rev B 81(16):165303
109. Kim H, Achermann M, Balet LP, Hollingsworth JA, Klimov VI (2005) Synthesis and characterization of Co/CdSe core/shell nanocomposites: bifunctional magnetic-optical nanocrystals. J Am Chem Soc 127(2):544–546
110. Zanella M, Falqui A, Kudera S, Manna L, Casula MF, Parak WJ (2008) Growth of colloidal nanoparticles of group II-VI and IV-VI semiconductors on top of magnetic iron-platinum nanocrystals. J Mater Chem 18(36):4311–4317
111. He SL, Zhang HW, Delikanli S, Qin YL, Swihart MT, Zeng H (2009) Bifunctional magneto-optical FePt-CdS hybrid nanoparticles. J Phys Chem C 113(1):87–90
112. Gao JH, Zhang B, Gao Y, Pan Y, Zhang XX, Xu B (2007) Fluorescent magnetic nanocrystals by sequential addition of reagents in a one-pot reaction: a simple preparation for multifunctional nanostructures. J Am Chem Soc 129(39):11928–11935
113. Gu HW, Zheng RK, Zhang XX, Xu B (2004) Facile one-pot synthesis of bifunctional heterodimers of nanoparticles: a conjugate of quantum dot and magnetic nanoparticles. J Am Chem Soc 126(18):5664–5665
114. Kwon KW, Shim M (2005) Gamma-Fe2O3/II-VI sulfide nanocrystal heterojunctions. J Am Chem Soc 127(29):10269–10275
115. McDaniel H, Shim M (2009) Size and growth rate dependent structural diversification of Fe3O4/CdS anisotropic nanocrystal heterostructures. ACS Nano 3(2):434–440
116. Selvan ST, Patra PK, Ang CY, Ying JY (2007) Synthesis of silica-coated semiconductor and magnetic quantum dots and their use in the imaging of live cells. Angew ChemInt Edit 46(14):2448–2452
117. Habas SE, Yang PD, Mokari T (2008) Selective growth of metal and binary metal tips on CdS nanorods. J Am Chem Soc 130(11):3294–3295
118. Hosoki K, Tayagaki T, Yamamoto S, Matsuda K, Kanemitsu Y (2008) Direct and stepwise energy transfer from excitons to plasmons in close-packed metal and semiconductor nanoparticle monolayer films. Phys Rev Lett 100(20):207404
119. Nobile C, Fonoberov VA, Kudera S, Della Torre A, Ruffino A, Chilla G, Kipp T, Heitmann D, Manna L, Cingolani R, Balandin AA, Krahne R (2007) Confined optical phonon modes in aligned nanorod arrays detected by resonant inelastic light scattering. Nano Lett 7(2):476–479
120. Krahne R, Chilla G, Schuller C, Kudera S, Tari D, De Giorgi M, Heitmann D, Cingolani R, Manna L (2006) Shape dependence of the scattering processes of optical phonons in colloidal nanocrystals detected by Raman Spectroscopy. J Nanoelectr Optoelect 1(1):104–107
121. Becker K, Lupton JM, Muller J, Rogach AL, Talapin DV, Weller H, Feldmann J (2006) Electrical control of Forster energy transfer. Nat Mater 5(10):777–781
122. Zavelani-Rossi M, Krahne R, Della Valle G, Longhi S, Franchini IR, Girardo S, Scotognella F, Pisignano D, Manna L, Lanzani G, Tassone F (2012) Self-assembled CdSe/CdS nanorod micro-lasers fabricated from solution by capillary jet deposition. Laser Photonics Rev 6(5):678–683

Chapter 3
Electrical Properties of Nanorods

3.1 Introduction

The electrical characterization of single nanorods can provide detailed information on the electronic level structure of the electrons and the holes. The most common contact configuration for electrical experiments on single nanorods (and single nanoparticles in general) is represented by a Double Barrier Tunnel Junction (DBTJ) [1], which is sketched in Fig. 3.1a. In this geometry the nanorod is connected to two electrodes (source and drain) via tunnel barriers that can be characterized by a capacitance and resistance. The tunnel barriers originate in most cases from the organic molecules that are needed to stabilize the surface of the nanorods, and/or from the specific contact scheme of the experiment, for example from the gap between the tip and nanorod in scanning probe experiments. Electrical experiments on thin films of nanorods are interesting with respect to possible device applications of this class of nanomaterials, for example in photovoltaics [2–5] or in light emitting devices [6]. The thin film can either be deposited on top of the electrodes that were previously fabricated on a planar, isolating substrate (usually in a stripe geometry with some microns in electrode distance), or vice versa the electrodes can be deposited on top of the nanorod film, for example by metal evaporation, or the nanorod film can be deposited on a conducting substrate and contacted in a vertical configuration with the second electrode on top of the film, for example by a metallic layer or a conductive scanning probe tip [7, 8].

In general, current transport measurements provide complementary information with respect to optical experiments, where the exciton level structure is probed. A comparison of the results of optical experiments and current transport is interesting in order to gain more insight into the intrinsic properties of the nanorods. Here we have to consider on one hand the Coulomb interaction in between the electron and the hole, which decreases the exciton energy with respect to the electron and hole level structure. And on the other hand possible Coulomb charging effects of the nanoparticle, and the applied bias leverage originating from the ratio of the contact resistances, which affects the observed energy gap in current-transport measurements [7, 8]. As a matter of fact, the way in which the nanorod is connected to the

R. Krahne et al., *Physical Properties of Nanorods*,
NanoScience and Technology, DOI: 10.1007/978-3-642-36430-3_3,

electrical contacts has a significant influence on its electrical response, and therefore we have to consider always the combined system of electrodes and nanocrystals.

3.2 Electrical Experiments on Single Nanorods

Here, we will discuss the specific case of nanorods that are weakly coupled to the external electrodes via contacts that exceed the quantum resistance $h/e^2 = 25.8$ k. This condition is fulfilled for scanning tunneling spectroscopy (STS) experiments and for most of the planar contact configurations. In this case the nanorod is connected to two electrodes in a DBTJ configuration, and we assign to each of the tunnel junctions a capacitance C and a resistance R. We can expect that the electric response is governed by a superposition of the electronic level structure of the nanorod and the Coulomb charging effects, if these energies exceed the thermal energy. In order to charge the nanorod with a single electron we require (1) that the tunneling rate of the charges onto the nanorod is larger than the one from the rod to the electrode, and (2) a finite charging energy ΔE that can be evaluated by the circuit diagram displayed in Fig. 3.1b to be $e^2/[2(C1 + C2)]$. The capacitance values determine also the voltage division between the junctions, $V1/V2 = C2/C1$. This voltage division leads to the leverage in the electrical circuit that was mentioned before:

$$\frac{V_{bias}}{V_1} = 1 + \frac{C_1}{C_2} \tag{3.1}$$

This leverage must be considered in order to obtain correct values for the electronic level structure of the nanorods. In STS the tip-nanorod distance is usually chosen in such a way that the nanorod-substrate capacitance is much larger than the nanorod-tip capacitance and therefore the applied bias drops almost entirely on the tip-nanorod junction. In planar devices, however, the leverage depends on the fixed contacts of source and drain electrodes to the nanorod, which in this case is an intrinsic property of the device. In most cases both electrodes are fabricated by the same process step (for example by EBL and thermal metal evaporation), which leads to an approximately even voltage division between the contacts. In such a symmetric configuration it is, for example, much harder to assign if the conductivity arises from the electrons or from the holes, since the bias window extends over both positive and negative polarity. We remark that on planar devices three-terminal measurements are possible, in which the charge tunneling can be controlled, for example via a planar backgate electrode. So far, however, only Coulomb charging of the nanocrystals has been observed in this way, and no signature of the semiconductor level structure was detected. The precise control over the contact properties in a fixed, device configuration remains still a challenge. For the electronic level structure of a nanorod in a DBTJ one should expect a superposition of the Coulomb charging

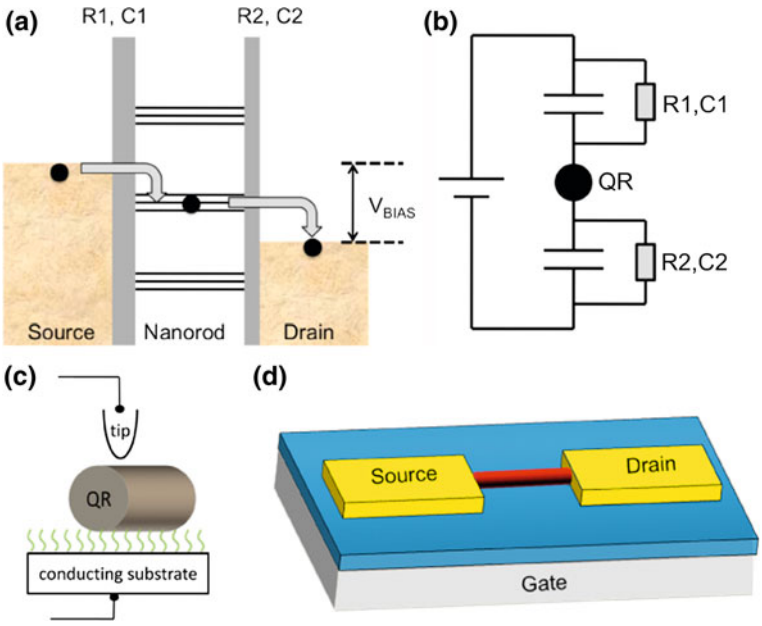

Fig. 3.1 **a** Schematic illustration of the charge tunneling process related to a single nanorod in between two electrodes, in the weak coupling regime. The electronic levels of the nanorod that are within the window of the bias voltage contribute to the conductance; **b** Circuit diagram describing such a junction. Schematics illustrating the contact geometry in scanning tunneling spectroscopy (**c**) and for planar electrode junctions (**d**). In the case of the planar device geometry a highly doped Si substrate coated with a thin oxide layer can be used as a back gate electrode

levels with the quantized energy levels of the nanorod if charging occurs. Based on the approach of Hanna and Tinkham [9] for the conductivity of spherical metallic particles, Porath et al. [1] calculated the tunneling rate from the electrode i = 1, 2 onto a nanoparticle with a discrete level spectrum in a DBTJ using the following expression:

$$\Gamma_i^+(n) = \frac{2\pi}{\mathrm{h}} \int |T_i(E)|^2 D_i(E - E_i) f(E - E_i) D_d(E - E_d)[1 - f(E - E_d)] dE \quad (3.2)$$

Here n is the number of excess electrons on the nanoparticle, $T_i(E)$ is the tunneling matrix element across the junction i, D_i and D_d are the density of states on the electrode i and the nanoparticle, E_i and E_d are the corresponding Fermi levels whose relative positions after tunneling $[E_d(n \pm 1) - E_i(n)]$ depend on n, and f(E) is the Fermi function. For practical purposes, $T_i(E)$ can be replaced by a phenomenological tunneling resistance parameter $R_i \propto T_i(E)^{-1}$. In order to gain some insight into the charging dynamics of a single nanoparticle, we will look at some limiting cases that are of practical interest. Let us first assume an asymmetric DBTJ with C1 $\ll$ C2, therefore the onset in tunneling occurs at junction 1. In this configuration, we will observe charge transport at positive bias due to the

electrons, while at negative bias the charge transport will be due to the holes. If R1 ≫ R2, then the tunneling rate off the nanoparticle is much larger than the tunneling rate onto the particle, i.e. the statistically the charges will tunnel into an "empty" nanoparticle, and therefore no Coulomb charging effects can be observed. In the opposite case, with R1 ≪ R2, the charges tunneling onto the nanoparticle remain there long enough such that the following charge has to overcome the Coulomb energy in order to tunnel onto the nanoparticle, and the Coulomb charging staircase can be observed in the I–V curve.

In the case of a more symmetric DBTJ, on one hand the leverage factor increases, and on the other hand simultaneous tunneling of electrons and holes can occur, which leads to much more complicated dynamics. Plots simulating tunneling spectra of this model for different limiting cases, and a detailed discussion on the charging dynamics can be found in Ref. [10]. For completeness, we will describe now the condition under which a tunneling current through a DBTJ can be observed. The condition for resonant tunneling is the line-up of the Fermi level of the nanorod with the Fermi level of one of the electrodes. Following Ref. [1], the probability distribution of n, P(n), can be determined from the steady state condition:

$$P(n)\left[\Gamma_i^+(n) + \Gamma_2^+(n)\right] = P(n+1)\left[\Gamma_i^-(n+1) + \Gamma_2^-(n+1)\right] \tag{3.3}$$

The tunneling current can then be calculated self-consistently from:

$$I(V) = e\sum P(n)\left[\Gamma_2^+(n) - \Gamma_2^-(n)\right] = e\sum P(n)\left[\Gamma_1^-(n) - \Gamma_1^+(n)\right] \tag{3.4}$$

3.2.1 Single Nanorod Conductance Probed by STS

STS is a powerful tool to probe the electronic level structure of single nanocrystals and their ensembles. For STS experiments, the nanorods are typically deposited from a highly diluted solution onto a conductive substrate, for example highly oriented pyrolytic graphite (HOPG), or onto a planar substrate covered with a gold film. The nanocrystal–substrate interface provides one electrical contact. The second contact is realized by the scanning tunneling tip, where the contact properties like resistance and capacitance can be tuned by the nanorod–tip distance. Figure 3.1c illustrates the experimental configuration and the related circuit diagram is shown in Fig. 3.1b. In particular, the distance in between the tip and the nanorod can be tuned such that almost all of the applied voltage drops on the tip-nanorod contact. This asymmetry allows to probe the conduction and valence band levels separately by applying positive and negative bias voltage, respectively. The contact resistance in between the nanorod and the conductive surface can be tuned to a certain extent, for example by surface functionalization with specific linker molecules, such as dithiols.

The experiments shown in Fig. 3.2a on single CdSe nanorods revealed that for CdSe, where the effective Bohr radius (5 nm) is about one order of magnitude smaller than the nanorod length, the confinement depends almost entirely on the nanorod diameter. This observation is supported by calculations based on a multi-band envelope function approximation that takes the coupling in between the light hole and heavy hole valence bands into account. Here the electrons and holes are treated as free particles with an effective mass confined by a cylindrical potential, with barrier height of 5 eV. If the CdSe nanorods are sufficiently decoupled from the conductive substrate, for example by organic molecules like dithiols, also Coulomb charging signatures can be observed in the STS spectra. The Coulomb charging

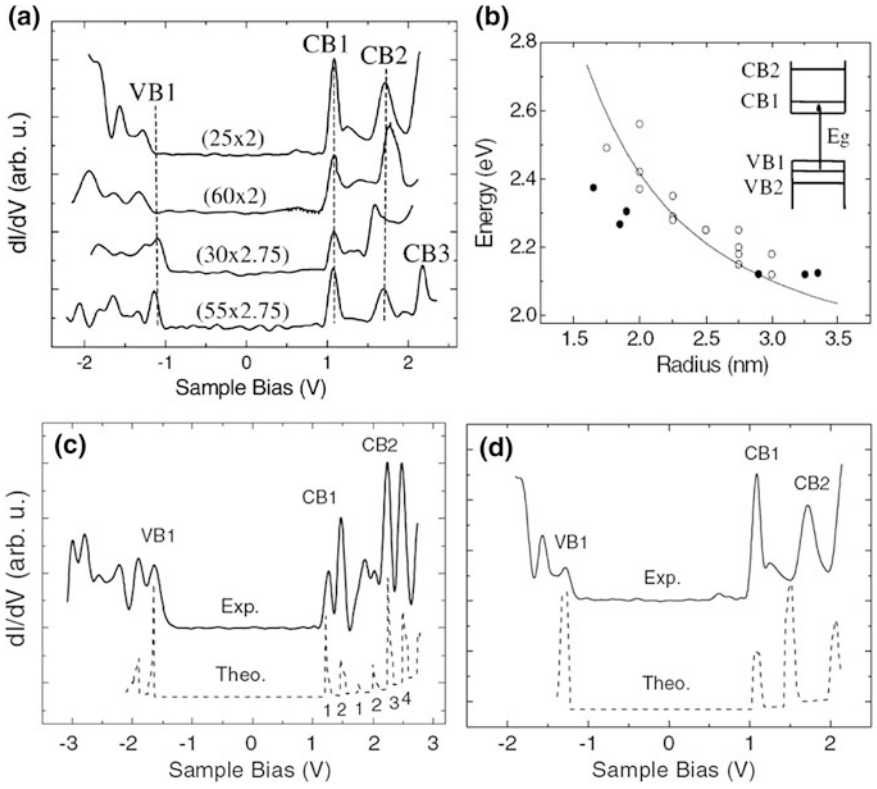

Fig. 3.2 **a** Scanning tunneling spectroscopy spectra of CdSe nanorods of various lengths and diameters; **b** Energy gap versus nanorod radius derived from optical (*full circles*) and tunneling (*open circles*) data. The optical data was corrected by the Coulomb interaction term. The *solid line* shows the result of a calculation based on a multiband envelope function approximation. The inset illustrates the energy level structure and the first optical transition. The derivative dI/dV of the current voltage spectrum is often plotted versus the voltage because peaks in the dI/dV versus V correlate to the electronic level structure of the system. Taken with permission from Ref. [12]. **c** STS spectra of CdSe nanorods coupled via dithiol molecules to a Au substrate that show Coulomb charging, while CdSe nanorods on HOPG exhibit only resonant tunneling (**d**). Taken with permission from Ref. [7]

energy can be expressed as $E = e^2/2C_{SUM}$, where e is the electron charge, and C_{SUM} accounts for the capacitive coupling of the nanorod to the leads. For a single nanorod in the experiment described above the contact capacitances were of the order of 10^{-19} F, which lead to a charging energy of around 0.4 eV [7]. Electron–phonon coupling has been observed in STS experiments at low temperature on CdSe dots and rods by Sun et al. [11], which manifested in phonon replicas in the differential tunneling current spectrum.

Figure 3.3 shows STS spectra recorded on InAs nanorods, where the Bohr radius (34 nm) is larger than the length of the nanorods. In this case also the nanorod length did influence the confinement energy, as the increase in the energy gap with decreasing rod length demonstrates. Furthermore, the optical spectroscopy and STS data recorded on InAs dots revealed a very strong discrepancy between the values for the band gap derived by the two techniques (the band gap obtained by STS is much larger than that observed in optical spectroscopy). This difference cannot be accounted for by simply correcting the optical data, which reflects the band gap of the exciton, i.e. of a bound electron–hole pair, with the Coulomb interaction term. Although this difference can be partly accounted for by voltage division effects that enlarge the tunneling gap, it seems that contributions arise from an intrinsic enlargement of the band gap observed in tunneling experiments. The latter could also be affected by dielectric confinement [13], which is a signature of 1D confinement.

The band structure of "dot-in-a-rod" CdSe/CdS core shell nanorods has been discussed in detail in Chap. 2. Complementary results with respect to the optical data reported so far were obtained by Steiner et al. [14] who were able to spatially resolve the electronic level structure of the electrons and holes by STS over the nanorod volume. The results are displayed in Fig. 3.4a, which reports the dI/dV spectra of different positions of the scanning probe tip with respect to the nanorod. Here positions 1 and 2 are over the CdS shell section of the nanorod, whereas at

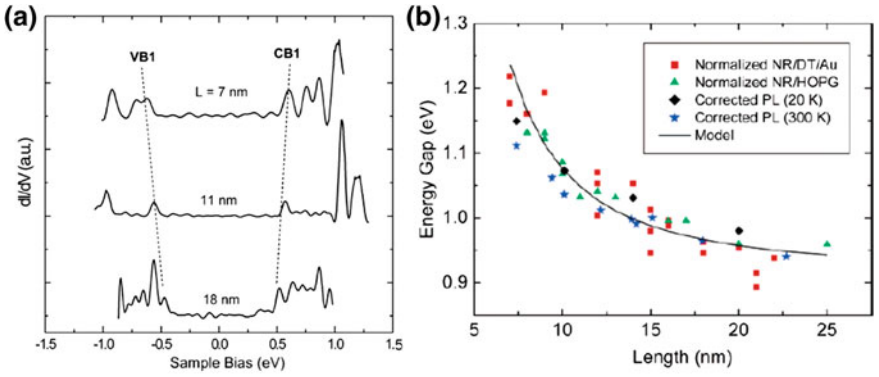

Fig. 3.3 **a** Tunneling spectra recorded on InAs nanorods on graphite. **b** Energy gap versus nanorod radius derived from optical and tunneling experiments. The optical data was corrected by the Coulomb interaction term. Taken with permission from Ref. [8]

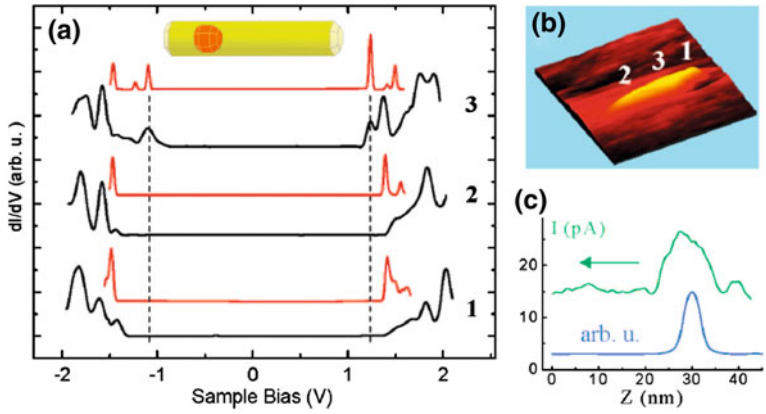

Fig. 3.4 **a** STS spectra of a single CdSe/CdS NR acquired at 4.2 K and on three different regions along the rod (*black lines*) compared with the corresponding theoretically predicted curves (*red lines*); **b** 3D STM image of an individual NR; **c** Cross-sections of the tunneling current at a sample bias of 1.2 V (*upper green curve*) that shows the larger tunneling current over the core region, and the calculated electron ground-state probability density assuming a band offset of 0.3 V (*blue curve*), that shows the localization of the electron ground state in the CdSe core. From Ref. [14]

position 3 the tip was on top of the nanorod CdSe core (Fig. 3.4b). We observe clearly the onset of tunneling current at lower bias on position 3, both for the valence band states (at negative bias), and for the conduction band states (at positive bias). Since the tunneling current gives a direct measure of the density of states below the probe tip, we can conclude that the lowest energetic levels of both electrons and holes are localized in the core for this nanorod sample. A scan along the long axis of the nanorod at constant positive bias voltage of 1.2 V, thus at the onset of conduction, clearly reveals the smaller band gap over the core region, and the data could be well fitted assuming a band offset at the core–shell interface of 0.3 V in the conduction band. This offset is much larger than the values deducted from optical pump-probe experiments, where the data could be well explained by assuming no band offset in the conduction band. A recent work of Banin et al. [15] unveiled this contradiction by that showing the conduction band offset depends very sensitively on the core size (see Chap. 2).

3.2.2 *Single Nanorod Conductance Probed in Planar Nano-Junctions*

A different strategy to contact single nanorods is to fabricate fixed electrical contacts by lithography or metal deposition techniques, which leads to structures that can be of interest for practical device applications. Here the challenge is to achieve the nanoscale resolution needed to address single nanorods that have a

length of around 50 nm or less, and to obtain control over the properties of the nanoscale contact. The tools of choice are in this respect electron-beam lithography (EBL) and electron-beam or focused-ion-beam induced deposition techniques. In general two strategies can be followed: (1) the electrodes are prepared prior to the deposition of the nanocrystals [16], and in this case the difficulty is the precise positioning of single nanorods into the electrode gap, or (2) the nanorods are deposited from a highly diluted solution on a planar substrate, mostly a silicon wafer covered with a thin insulating layer, and their position is mapped with respect to previously fabricated markers. This second case is so far the more successful approach and will be discussed in the following. In this EBL approach the sample is spin coated with PMMA, then the electrode pattern is aligned with respect to the nanorod that shall be contacted, and the PMMA is exposed with the electron beam [17–19]. In the case of electron or focused-ion beam induced metal deposition no PMMA deposition is needed since the metal is directly deposited by the beam. Hence mapping and deposition can be done in a single run [20].

We will now discuss nanorods contacted by EBL and subsequent metal deposition in more detail. Alivisatos et al. [17, 19] used the above described EBL overlayer approach to contact single CdSe and CdTe nanorods in planar electrode devices where the Si substrate was used as a back gate. One interesting question with respect to metal contacts to nanorods is if a Schottky barrier is formed in between the metal and the semiconductor material. For bulk materials the alignment of the Fermi level and the continuity of the vacuum level leads to a band bending in the metal–semiconductor interface region, as depicted in Fig. 3.5. The band alignment is made possible by charge transfer between the semiconductor

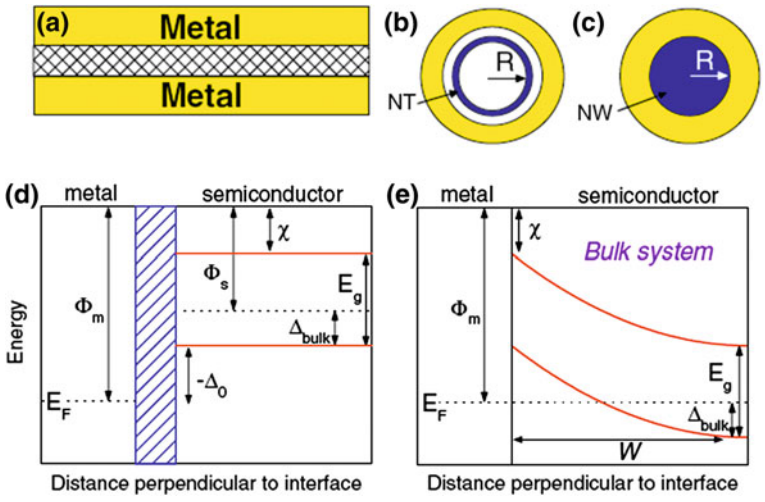

Fig. 3.5 Energy levels of bulk metal and semiconductor structures before (**a**) and after (**b**) being in contact. Φ_m and Φ_s are the work functions of the metal and semiconductor, respectively, χ is the electron affinity and E_g is the band gap of the semiconductor. Taken with permission from Ref. [21]

and the metal and leads to a depletion region of typically tens to hundreds of nanometers in width. This depletion region is referred to as the Schottky barrier. If we consider laterally fabricated metal contacts to nanorods that typically have diameters smaller than 10 nm, the interesting question is if such charge transfer, and consequently the band alignment is possible and a Schottky barrier can be formed.

Leonard and Talin [21] studied the properties of metal contacts fabricated laterally on semiconductor nanowires. They performed a self-consistent calculation of the charge and potential, by which they obtained the charge from the one-dimensional density of states:

$$D_{NR}(E) = \frac{\sqrt{2m^*}}{\pi \mathrm{h}}(E - E_G/2)^{-\frac{1}{2}} \tag{3.5}$$

In the expression above m^* is the effective mass and E_G is the energy gap of the semiconductor nanowire. The potential was derived by solving the Poisson equation in the nanowire numerically. The result of this calculation is that for silicon nanowires with diameters smaller than 10 nm the band bending is weak due to the limited available depletion width (see Fig. 3.6). However, for larger diameters, where according to the work function difference between the metal and the semiconductor an ohmic contact would be expected, the band bending leads to a Schottky barrier, for example in silicon nanowires with 10 nm diameter (Fig. 3.6b).

Demchenko and Wang [22] calculated the effect of lateral electrodes fabricated on CdSe rods on the energy gap and the wave function distribution of the carriers by an atomistic pseudopotential method. Since the nanorod diameter is of the range of a few nanometers, charge transfer between the rod and the metal electrode is limited due to the limited available depletion length, as discussed above. Therefore, a Schottky contact between the metal and the nanorod is assumed. Demchenko and Wang [22] showed that the surface polarization potential is surprisingly large, especially for small nanostructures, where it alters the familiar electronic structure and gives rise to a nanocontact phenomenon: electrode-induced wave function localization. In particular, the surface polarization potential is around 0.5 V lower in the region of the metallic contact (see Fig. 3.7a), and the nanorod band gap is significantly reduced. Also, the shape of the wave function in the conduction and valence band is considerably altered. While for the conduction band states the wave functions are just shrunk in the z-direction, the valence band states show a different nodal structure in comparison with their free rod counterparts. The continuity of the valence band states in Fig. 3.7c could favor charge transport. Therefore, the assumption that for laterally contacted nanorods the conduction is mediated by the valence band states could be reasonable. For charge transport, the wave function localization has to be overcome by an external electric field, which can be estimated to be around 0.5 V (for CdSe nanorods with 23 nm length that are covered for ¼ of their length by each contact).

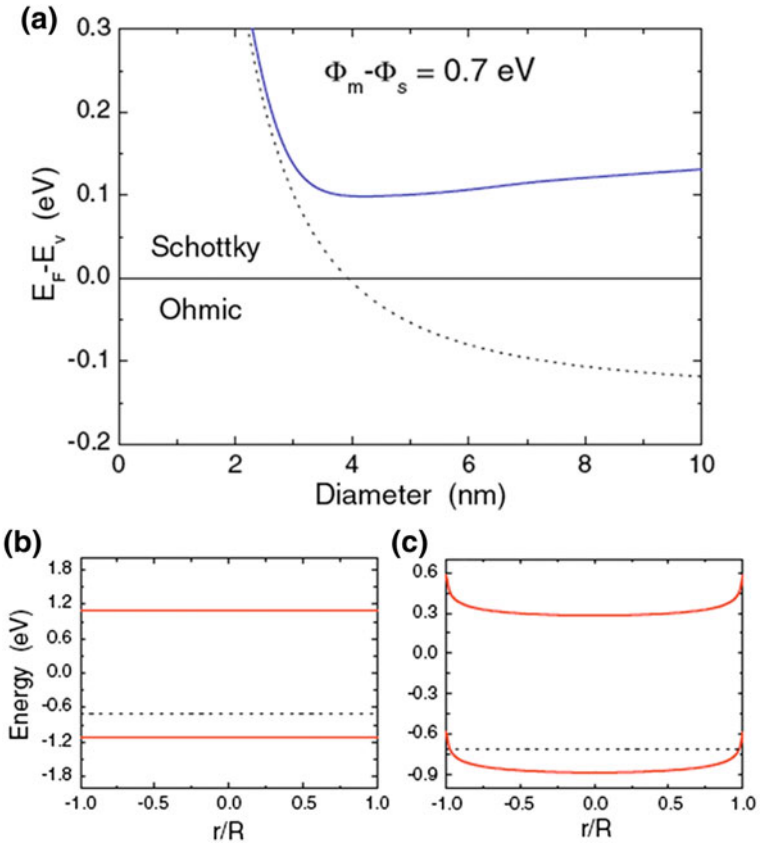

Fig. 3.6 Band bending across nanowires with diameters of 2 nm (**a**) and 10 nm (**b**). The dotted line shows the Fermi level. Taken with permission from Ref. [21]

The above described scheme of laterally fabricated Pd metal electrodes (see Fig. 3.8a, b) was realized experimentally by Cui et al. [19], in order to contact CdSe nanorods and by Trudeau et al. [17] to contact CdTe nanorods. In contrast to the STS experiments, the spectra obtained from the planar junctions did not reveal the semiconductor band gap, but showed a Coulomb charging gap (see Fig. 3.8c) of the order of some tens of meV. This finding could be the signature of the above described wave function localization that is induced by the metallic contacts. In a symmetric junction, the applied voltage bias will drop equally at the two barriers and therefore will result in a zero current plateau which spans a voltage range $V = 2E_{CB}/q$. The Coulomb charging energy in such a planar junction is about one order of magnitude smaller than in the STS experiments, due to the much larger contact capacitances. The deposition of electrodes by metal evaporation on the nanorod surface can lead to the migration of Au atoms towards the central region of the rod that was intended to be left uncoated by the metal. Trudeau et al. [17] have investigated this effect for CdTe nanorods that were partly overcoated with

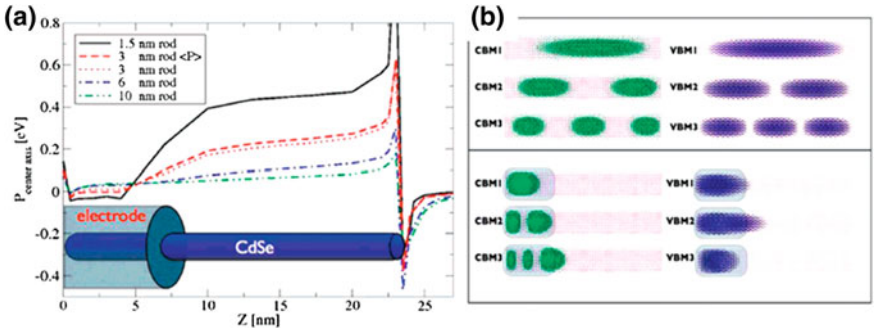

Fig. 3.7 **a** Polarization potential versus the z axis of a nanorod with different diameters. The sketch illustrates the metal-nanorod contact geometry; **b** Contour plots of the conduction-band minimum (CBM) and Valence-Band-Maximum (VBM) wave functions of nanorods with 3 nm diameter. The upper panel shows the case of a free standing rod, the lower panel the case of a nanorod with a metal electrode covering one quarter of its length. Taken with permission from Ref. [22]

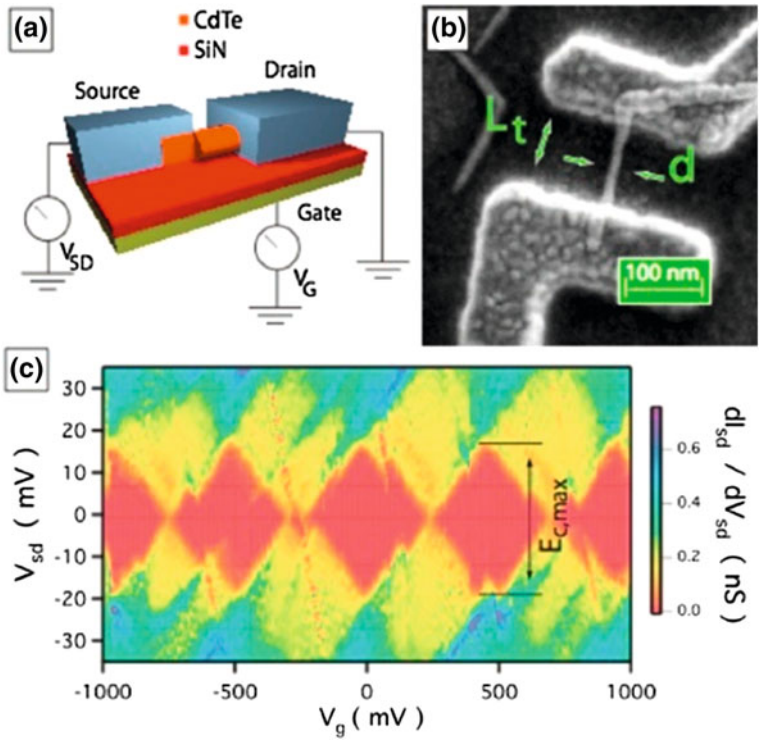

Fig. 3.8 **a** Schematic illustration of the lateral contact scheme; **b** SEM image of a CdTe nanorod contacted by Pd electrodes; **c** Color map of the conductance of a single nanorod versus source-drain and gate voltage. The color map shows the Coulomb blockade diamonds, which are a fingerprint of single electron tunneling (SET). Taken with permission from Ref. [17]

Pd. They observed the presence of Au atoms on the nanorod surface at a distance of tens of nanometers from the intended contact region. Short nanorods, with a length that did not exceed by much the migration distance of the Au atoms, showed a significantly reduced charging energy, compared to the charging energy of nanorods that were slightly longer.

Electron-beam induced deposition provides a single step approach to fabricate electrical contacts to single nanorods, with no need of a lithography process to define the electrode pattern. In this method the material for the electrodes is deposited from organometallic precursors injected from the gas phase into the electron beam, and the pattern of the scanning electron beam defines the electrode shape, allowing for nanoscale resolution. Moreover, the conductive behavior of single nanorods contacted by this method is different from the characteristics of the DBTJ, which suggests that the nanorod is in the strong coupling regime to the electrodes. Steinberg et al. [20] used EBID to contact single CdSe and CdS nanorods. In their measurements they observed smooth current voltage curves that could be fitted using the WKB approximation [23], which results in the Fowler–Nordheim formula [24] for current density. This finding suggests that the tunneling barrier typically formed at the contacts (which results from surface contamination or surfactants on the nanorod surface) is absent if EIBD was used for the fabrication of the electrode contacts. Instead, it seems that the electrons are injected through a triangular barrier, which is formed by the offset of the work functions at the interface ($\Phi_{metal} = 4.5$ V for tungsten and $\Phi_{nanorod}$ around 4.3–4.5 eV) and the tilted band structure resulting from the bias voltage. The electron affinity of the nanorods depends on the quantum confinement (which leads to a significant deviation from the electron affinity of the bulk material) and on the temperature. The first term can be estimated from the band gap values obtained by optical experiments, and the temperature dependence can be described by the Varshni equation [25]. Single nanorods contacted by EBID showed bi-and multi-stable conductive behavior [20], and this could be correlated to the charging and discharging dynamics of surface traps in the vicinity of the contacts and the nanorod surface. The bi-stable conductivity could be modeled by considering only a single surface trap, which makes this behavior interesting for charge sensor applications. The electrical injection of charge carriers into valence or conduction band levels is possible for a single nanorod connected in an electrode junction, if the applied bias potential exceeds the band gap of the nanorod. Radiative recombination of the injected charges would result in the emission of photons and consequently to electrically driven luminescence of the nanorods. Gudiksen et al. [18] also used the EBL overlay approach to contact single CdSe nanorods and employed the doped silicon substrate as a gate electrode (Fig. 3.9a). At low bias voltage the Coulomb charging behavior described above was observed. However, the nanorods started to emit light when the bias voltage exceeded a certain threshold value that was comparable to the band gap, as can be seen in Fig. 3.9b. The interesting question is if this electroluminescence originated indeed from the radiative recombination of carriers that were injected into the semiconductor nanorod. For this to occur, the Fermi levels of the source and drain electrodes would need to align with

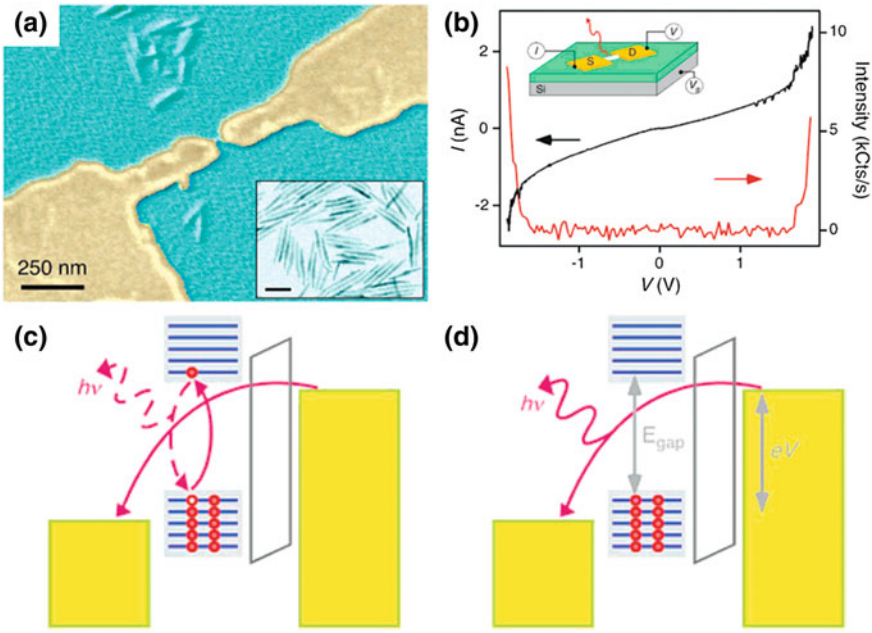

Fig. 3.9 **a** Scanning electron microscopy image in false color of a single nanorod trapped between source and drain electrodes. The inset shows a TEM image of the nanorods; **b** Electroluminescence intensity plotted together with a current voltage spectrum. The single nanorod transistor design is illustrated in the inset; **c**, **d** Illustrations of the processes that can lead to electroluminescence. In (**c**) a tunneling charge inelastically scatters and creates an exciton that recombines under the emission of a photon. In (**d**) the photon is created directly via the inelastic scattering of the tunneling charge. Taken with permission from Ref. [18]

conduction and valence band levels of the nanorod, respectively, which would be possible only for highly symmetric devices. Fits to the Coulomb charging of the nanorods at low bias voltage showed that electroluminescence was observed from devices with asymmetric tunnel resistances for the two contacts. Also the magnitude of the gap around zero bias varied considerably for the light emitting devices. These observations make resonant electron/hole injection very unlikely. The authors therefore suggest that the nanorod emission results from inelastic scattering of the injected carriers with excitons (Fig. 3.9c) or directly from inelastic tunneling which is resonantly enhanced by the exciton level structure of the nanorod (see Fig. 3.9d). Gudiksen et al. estimated the efficiency of the electroluminescence as 10^{-5} photons per electron passage, which is about a factor of 100 smaller than the best efficiency reported from a nanocrystal-organic hybrid light emitting device [26]. In a different work on electroluminescence of CdSe nanowires (which were considerably longer than the nanorods discussed so far) it was shown that the emission occurs in the vicinity of the metal electrode-semiconductor nanorod contacts, which confirmed that inelastic scattering of the tunneling electrons is at the origin of the electroluminescence [27].

3.2.3 Gold Tipped Nanorods (Nanodumbbells)

Metal–semiconductor hybrid nanocrystal structures provide a different approach towards electrical contacts to semiconductor nanorods. Recent advances in chemical synthesis enabled the controlled growth of small gold domains at the tips of CdS, CdSe or PbTe nanorods [28, 29]. In these nano-dumbbells the nanoscale metal–semiconductor interface is realized as an intrinsic property of the nanocrystal. Spatially resolved investigations by STS of Au-CdSe nano-dumbbells revealed a Coulomb blockade gap in the vicinity of the metal domain, and the electronic structure of the semiconductor nanorod at the center of the dumbbell, as shown in Fig. 3.10b. At position 1, above the metal domain, the series of peaks can be associated to the Coulomb charging of the Au cluster at the tip. Here the Coulomb charging energy can be approximated by the charging energy of a sphere, namely $E = e^2/2(4\pi\varepsilon_0 r)$, which yields a value of 700 meV for a sphere with radius of 1 nm. The I–V response can be modeled more accurately by a single electron tunneling (SET) process in a DTBJ as Steiner et al. described in their work [30]. The response at the center of the nanorod was very similar to the previously discussed spectra on bare CdSe nanorods (see Fig. 3.2). Interestingly, additional peaks appeared in the spectra taken above the metal semiconductor interface region, at the positions 2 and 3. These additional structures could be associated to localized metal–semiconductor interface states. Furthermore, an overall shift of the spectrum 3 with respect to spectrum 4 was observed which could be due to a voltage offset from a Schottky contact. Particularly interesting were the spectra recorded in the vicinity of the metal–semiconductor interface, which revealed localized metal induced gap states. In this region (with the tip in the vicinity of the metal semiconductor interface) negative differential conductance was observed, which could be ascribed to resonant alignment of the Coulomb blockade levels with the states that originate from the semiconductor level structure. One advantage of Au-nanorod dumbbells compared to bare nanorods towards applications in electric circuits could be their improved conductivity due to good contact formation of the Au domains with the metal electrodes. Indeed, Sheldon and coworkers showed a significantly increased conductivity of Au-CdSe dumbbells that were positioned into planar electrode junction by electrophoresis [16]. Nanodumbbells can also be interesting for visible light induced photocatalysis. Banin and coworkers introduced a novel synthesis method to obtain CdSe-Au dumbbells dissolved in water and showed that irradiation of the solution leads to charge transfer of the photo excited electrons from the CdSe rods to Au domains (as illustrated in the scheme in Fig. 3.10d), whereas the holes can be scavenged by ethanol present in the solution [31]. More recently, detailed EFM studies of the light induced charge separation that occurs in such nanodumbbells confirmed the above described charge transfer mechanism. Figure 3.10f, g shows the charge images of nanodumbbells on HOPG recorded in interleaved mode before (f) and after irradiation (g). In contrast to what was observed from the individual components,

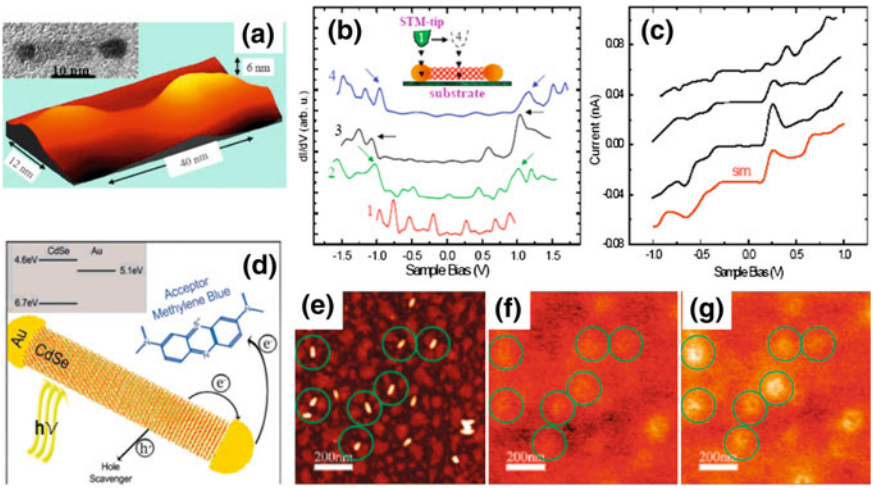

Fig. 3.10 **a** Scanning tunneling microscopy image of a CdSe nanorod with Au domains at the tips (a so-called dumbbell structure); **b** Scanning tunneling spectroscopy spectra recorded at different positions of the tip with respect to the dumbbell, as illustrated in the inset; **c** Current voltage characteristics that show negative differential conductance recorded with the tip in the vicinity of the metal–semiconductor interface. (**a**–**c**) are taken with permission from Ref. [30]; **d** Illustration of the charge transfer dynamics after photo excitation of nanodumbbells in aqueous solution. from [31]; **e**–**g** scanning probe images of CdSe-Au nanodumbbells on HOPG; **e** topography recorded in tapping mode; **f**, **g** are taken with permission from electric force signal derived from the AC signal in interleaved mode. The circles are guides to the eye that indicate the positions of individual nanodumbbells. Taken with permission from Ref. [32]

i.e. the CdSe nanorods and Au spheres which show positive charging, the nanodumbbells showed negative charging after illumination. Experiments on insulating substrates showed no charging effects, therefore the charging of the dumbbells depended critically on the escape pathways of the photo-generated hole from the CdSe nanorod to the substrate [32].

The above described nanodumbbells can be used as building blocks in order to obtain nanorod networks, in which the rods are linked by the metal nanoparticles [33], as illustrated in Fig. 3.11a. Such networks can be fabricated by adding molecular iodine to the nanodumbbell solution that acts as an etchant for the Au domains and results in fusion of the Au nanoparticles located at the tips of the CdSe nanorods or tetrapods. Therefore, the networks manifest semiconductor nanorods linked by all-inorganic metal–semiconductor interfaces (see Fig. 3.11c), which are much better defined than the tunnel barriers that typically form due to the presence of organic surfactants on the nanocrystal surface. Furthermore, the quality of the junctions can be significantly improved by thermal annealing at temperatures in the range of 200–300 °C, which leads to atomically flat interfaces, and even to epitaxial relationships in between the metal and semiconductor crystal structures (see Fig. 3.11b). The conductive properties of such all-inorganic networks should manifest the physics of Schottky junctions. Indeed, charge

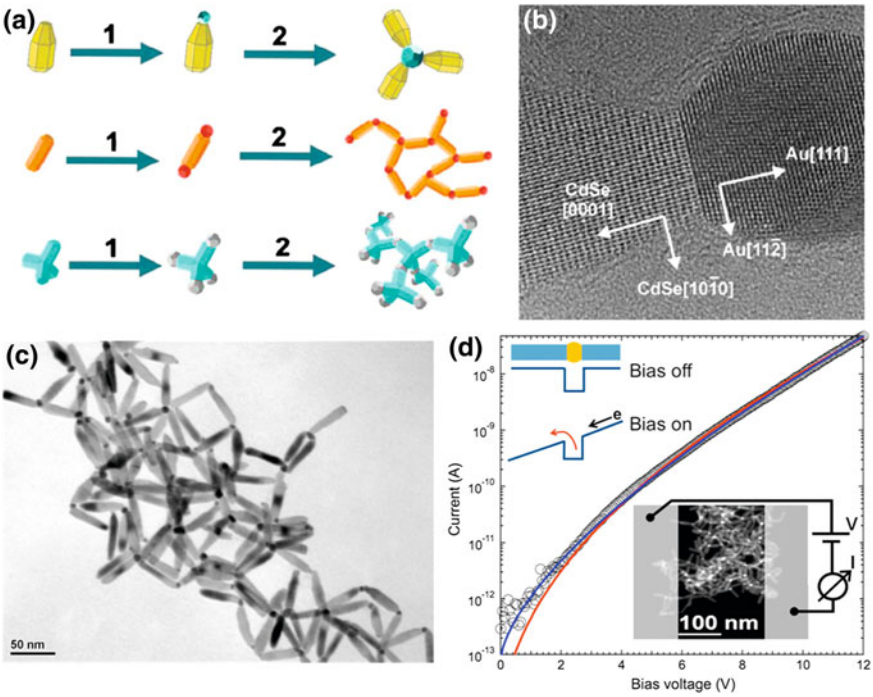

Fig. 3.11 **a** Schematic illustration of the network fabrication. In step 1 $AuCl_3$ is added to the nanocrystal solution to obtain the metal domains at the tips, and in step 2 molecular iodine is used to fuse metal domains located at the tips of different nanocrystals, thereby forming the networks. **b** High resolution transmission electron microscopy image revealing the epitaxial relationship between the CdSe semiconductor and the Au lattice (with permission from Ref [35]). **c** Transmission electron microscope image of a network composed of CdSE nanorods linked by Au domains. **d** Current–voltage curve recorded from nanorod network devices at room temperature (as illustrated in the inset) that can deviated from the 2D interface behavior (*red line*) and can be accurately modeled by considering nanosize spherical Au domains for the image charges (*blue line*). With permission from Ref [34]

transport measurements on such networks have revealed nanoscale effects on the Schottky contact formed between the semiconductor and metal portions due to their small size. Here the image charges in the metal that lead to a lowering of the Schottky barrier had to be calculated by considering the finite size of the Au nanoparticles in the junctions, in order to model accurately the current–voltage characteristics measured on the networks [34].

3.3 Electrical and Photoconduction Properties of Nanorod Assemblies

The electrical properties of assemblies of nanorods are of great interest for applications in photovoltaics and in light emitting devices. The more complex shape of nanorods with respect to spherical nanoparticles can lead to improved properties and performance. Defined geometrical arrangements that are coupled to distinctive physical properties of individual nanorods (for example, linearly polarized absorption and emission) could be translated into unique and predictable macroscopic properties of the ensembles. Close packed arrays of nanorods could lead to collective effects that would result, for example, from the structure of the superlattice that is formed.

3.3.1 Dark Current

The conductive properties of an oriented ensemble of nanorods could be expected to show signatures of mini-band formation and charge delocalization. Steiner et al. [36, 37] investigated ensembles of CdSe and InAs nanorods and found a significant reduction of the band gap measured on close packed ensembles of rods with respect to isolated nanorods. This reduction was more pronounced in InAs nanorods than in CdSe nanorods due to the larger Bohr radius and consequently stronger coupling in InAs. Also the geometry and orientation of the nanorod ensemble on the band gap have been measured by STS. A vertically packed cluster of CdSe nanorods demonstrated a stronger reduction of the band gap than an ensemble of laterally aligned nanorods [36].

One major factor for devices based on layers of nanorods is the electrical coupling in between the individual nanorods. Typically, the rod-to-rod charge transfer is very poor due to the isolating nature of the surfactants that cover the nanorod surface. One successful strategy to overcome this problem is to exchange the long chain surfactants that were used to stabilize the nanocrystals during the nanocrystal growth by shorter chain molecules, which might even supply charge carriers to the nanocrystals. In this respect surfactant exchanges with hydrazine and pyridine have lead to a significant increase in film conductivity, and hydrazine treatment resulted in n-type conductivity of PbSe nanocrystal films [38]. Recently, Talapin and coworkers demonstrated surfactant exchange with metal-chalcogenide complexes that enabled conductivities up to 200 Scm^{-1} in nanocrystal solids [23, 30]. Another strategy to increase the conductivity of the nanorod layer is to anneal the device under vacuum or under inert atmosphere, which leads to a removal of the volatile organics at lower temperatures (<220 °C), and to carbonization of the surfactants (at sufficiently high temperature, around 300–350 °C) [39].

Planar devices with micrometer spaced electrodes represent a useful tool to probe the photoelectrical properties of nanorod arrays, where the nanorods

can be deposited onto the electrode structures from solution either by spin coating, slow solvent evaporation under controlled atmosphere or by coffee stain evaporation processes [4, 5, 40]. Randomly oriented nanorod arrays were fabricated for example by Romero et al. [41] by drop casting the nanorod solution on interdigitated electrode structures. However, even by simple drop casting the nanorods tended to self assemble side-by-side into track like structures. These nanorod films demonstrated hysteresis and switching between high and low conductive states and also showed peculiar current oscillations. Considering that the conductive path between the electrodes is formed by nanorod tracks, which should provide the best electrical coupling, the origin of the film properties could be assigned to superlattice effects and tunneling through interface states related to the surfactant molecules. In the low conductive regime the current is dominated by charge tunneling through the insulating barriers between the rods. When the voltage bias exceeds a certain threshold value (that differs for each sample) the energy levels of a the nanorods and the interface state can align and charges can resonantly tunnel through barrier, as illustrated in Fig. 3.12, which leads to the switching into the higher conductive state. Following this model, the current oscillations that are observed in the higher

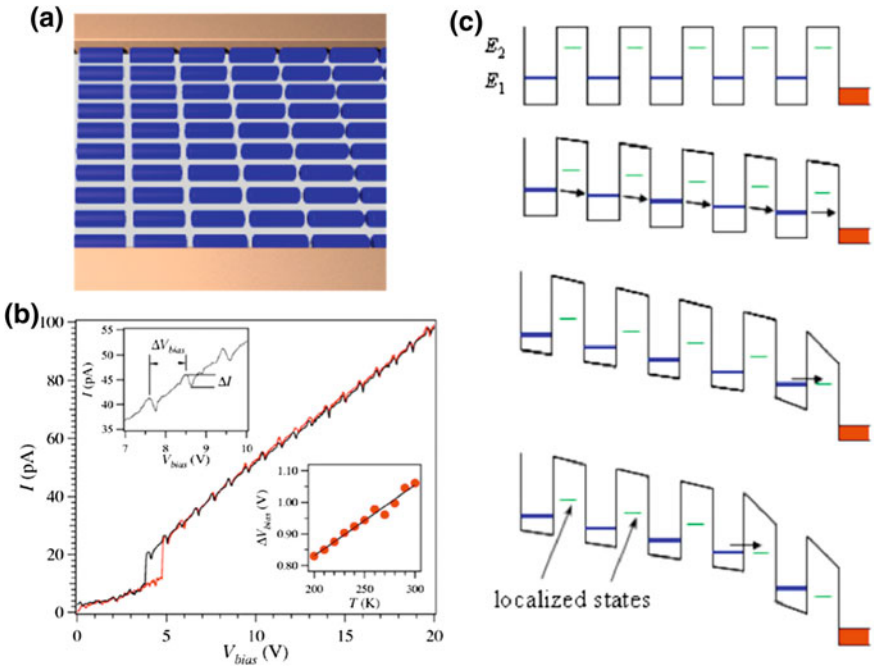

Fig. 3.12 Charge transport in rod arrays in which the long axis of the rods is oriented perpendicular to the external electric field. **a** Illustration of the nanorod array orientation with respect to the electrodes; **b** Current voltage characteristics of parallel tracks of nanorods showing hysteresis and periodic oscillations. The *upper* inset shows the oscillation on a magnified scale, the *lower* inset depicts the temperature dependence. Taken with permission from Ref. [41]

conductive state result from subsequent alignment of the nanorod and of the interface state levels with respect to the bias voltage. The sheet resistance of such randomly oriented nanorods is of the order of 10^{15} Ohm/cm, which is a considerably high value and is most likely due to the poor electrical coupling between the nanorods.

3.3.2 Photoconductivity in Nanorod Assemblies

Millo and coworkers studied the photoconductive properties of ordered nanorod arrays in which the long axis of the rods is oriented parallel to the electric field, as shown in Fig. 3.13 [4]. Hydrazine treatment was employed to reduce the inter-rod

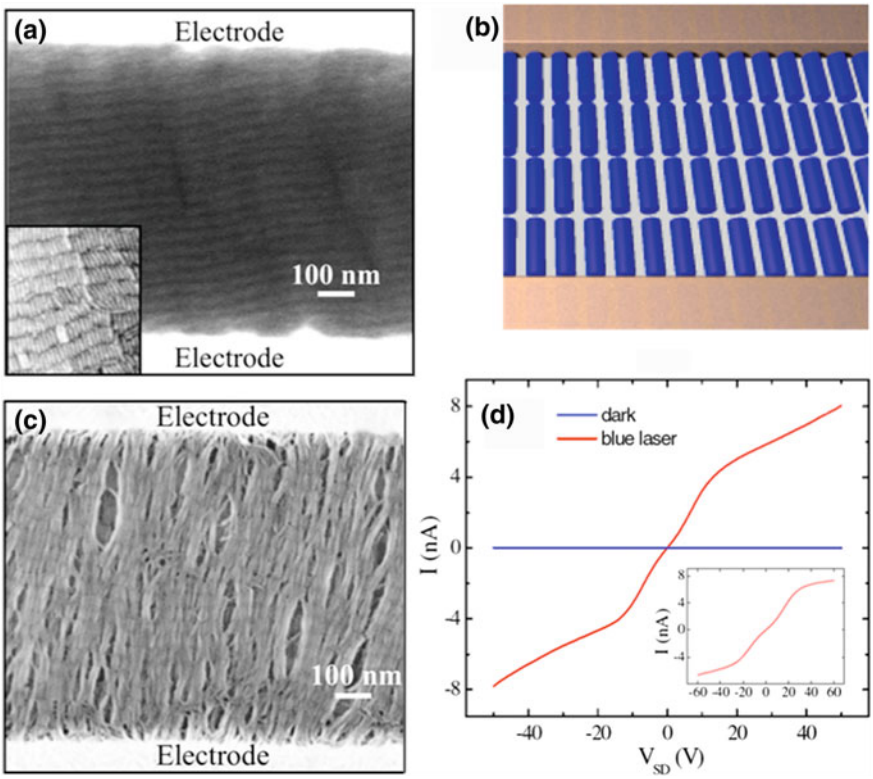

Fig. 3.13 Charge transport in rod arrays with rod orientation parallel to the external electric field. **a**, **b** Scanning electron microscopy image of aligned nanorod arrays in between planar electrodes. Treatment of the nanorod layer with hydrazine reduces the inter-rod distance and leads to cracks in the film; **c** Illustration of the nanorod alignment; **d** Non-linear current voltage response of nanorod arrays under blue laser illumination and in the dark. Taken with permission from Ref. [4]

distance and improve the photo conductivity. The non-linear current voltage response could be modeled by an field-ionization process [42], according to which the current in dependence of the site-to-site potential v can be expressed as:

$$I(V) \propto \frac{\exp\left(\frac{-4\sqrt{2}\hbar^2 d}{3m(ev-\gamma)}\left[\left(\frac{m\Phi}{\hbar^2}\right)^{3/2} - \left(\frac{m(\Phi+\gamma-ev)}{\hbar^2}\right)^{3/2}\right]\right)}{1+\exp\left(-\frac{ev-\gamma}{a}\right)} \tag{3.6}$$

Here m is the rest mass of the electron, e is the elementary charge, γ is the energy cost between the initial and final states that arises from the energy required to overcome the Coulomb interaction of the photoexcited electron–hole pair and the interaction of each charge with its respective image charges. A phenomenological parameter a describes the effective broadening of γ due to variations in the nanocrystal size and inter-nanocrystal separation. Φ and d are the height and the width of the tunnel barrier, respectively. The site-to-site potential can be evaluated by dividing the applied bias voltage by the number of rods that are needed to form a conductive path between the electrodes for the parallel and perpendicular configuration. Steiner et al. [4] observed a non-linearity in the photoconductivity of the nanorod arrays at the transition when the site-to-site potential exceeds the energy threshold that is needed to separate the photo-excited charges. Below this threshold the photoconductivity is dominated by the increasing effectiveness of the electric field in exciton ionization, whereas when the external field is larger than γ the photoconductivity is dominated by the tunneling through the inter-nanocrystal barrier characterized by Φ and d. Photoconductivity and photoluminescence should be complementary processes and indeed the quenching of the PL with increasing voltage bias and thus increasing photocurrent has been demonstrated [4, 5]. Persano et al. [5] compared the photoconductivity and PL quenching of core–shell CdSe/CdS nanorods arrays oriented parallel and perpendicular to the external electric field direction. They found that PL quenching is more effective for nanorod arrays where the long axis of the rods is oriented parallel to the electric field direction, as depicted in Fig. 3.14a.

This behavior can be explained by the more effective ionization along the long axis of the nanorods where the confinement length is much larger than the exciton Bohr radius. For type-I core–shell nanorods (see Chap. 2) the PL quenching depends also on the energy of the light excitation. For a fixed external electric field, the exciton ionization is more efficient when the charges are created in the shell (see Fig. 3.14b). If the exciting light energy is smaller than the band gap of the shell, then the photo excited charges are localized at the core and an additional energy barrier has to be overcome for exciton ionization. The spectral response of the photocurrent of the nanorods corresponds very well to their absorption spectra. Only at high energies above the band gap the photocurrent is reduced, due to more effective trapping of the photo-generated carriers at surface states [42, 43].

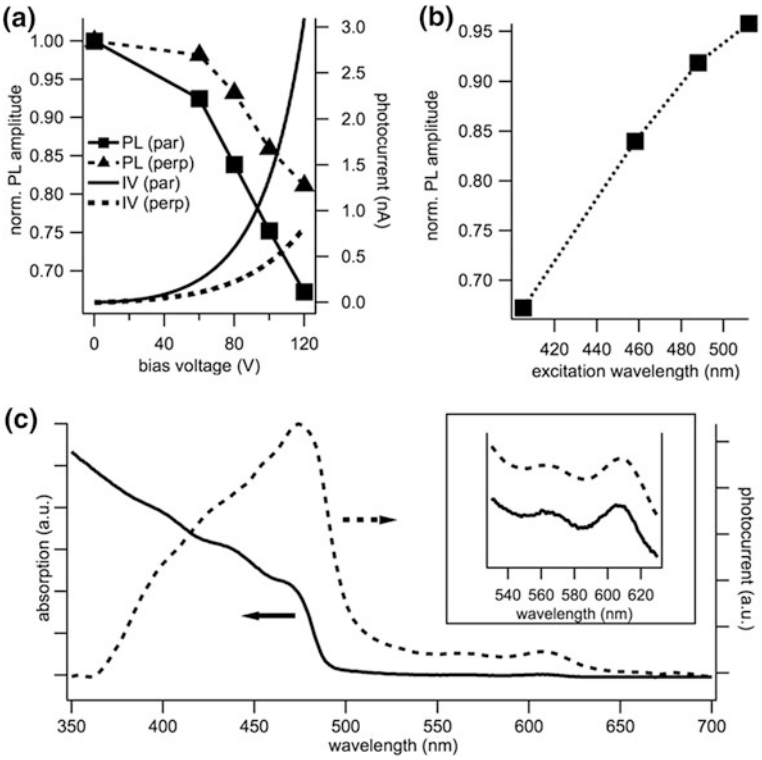

Fig. 3.14 **a** Normalized PL amplitude, PL_{BIAS}/PL_0, and photocurrent versus bias voltage for rod arrays oriented parallel and perpendicular to the external electric field; **b** Normalized PL amplitude versus laser excitation energy recorded at a bias voltage of 120 V for nanorod arrays oriented parallel to the external electric field; **c** Absorption and photocurrent spectra of CdSe/CdS core–shell nanorods recorded at a voltage bias of 64 V under ambient conditions. The inset shows absorption and photocurrent of the core on a magnified scale. Taken with permission from Ref. [5]

Another successful approach to describe the photoconductivity of nanocrystal solids is based on phenomenological models that use macroscopic quantities such as sheet resistance and voltage barrier [39, 44].

Kudera and coworkers [45] used scanning photocurrent microscopy to investigate the local photoresponse of thin films of close-packed core–shell CdSe/CdS nanorods that were deposited onto planar interdigitated electrodes. With the help of the local generation of excitons, they were able to analyze the influence of the charge transport pathway and to separate it from the contribution of the exciton dissociation. The measurements showed that even for highly homogeneous films, the spatial distribution of photocurrent generation developed distinct maxima, whose positions depended on the bias voltage and polarity. In their work the spatial photocurrent distribution was modeled by assuming exciton ionization according to the model of Leatherdale et al. [42] followed by a random walk of the photogenerated electrons and holes to their respective electrodes, similar to Mott's

theory of transport in amorphous materials. This framework allowed us to reconcile the microscopic model discussed in Eq. (3.6) with the phenomenological approach based on sheet resistance and voltage barrier.

3.4 Nanorod Assemblies for Photovoltaic Applications

Colloidal nanocrystals are an interesting material as active layers in photovoltaics, and nanorods should have advantageous properties regarding the absorption cross section, due to their higher surface area compared to spherical nanocrystals, and because their elongated shape should favor the extraction pathways for the photo generated charges. Such an idealized all-inorganic solar cell based on nanorods is sketched in Fig. 3.15a. All-inorganic nanocrystal solar cells of this type have been fabricated with spherical nanocrystals [46], but in the case of nanorods it was not possible, so far, to achieve homogeneous, ordered layers of nanorods on areas large enough to be interesting for solar cells. For example, the elongated rod-shape makes it more difficult to obtain films without any voids and electrical shortcuts.

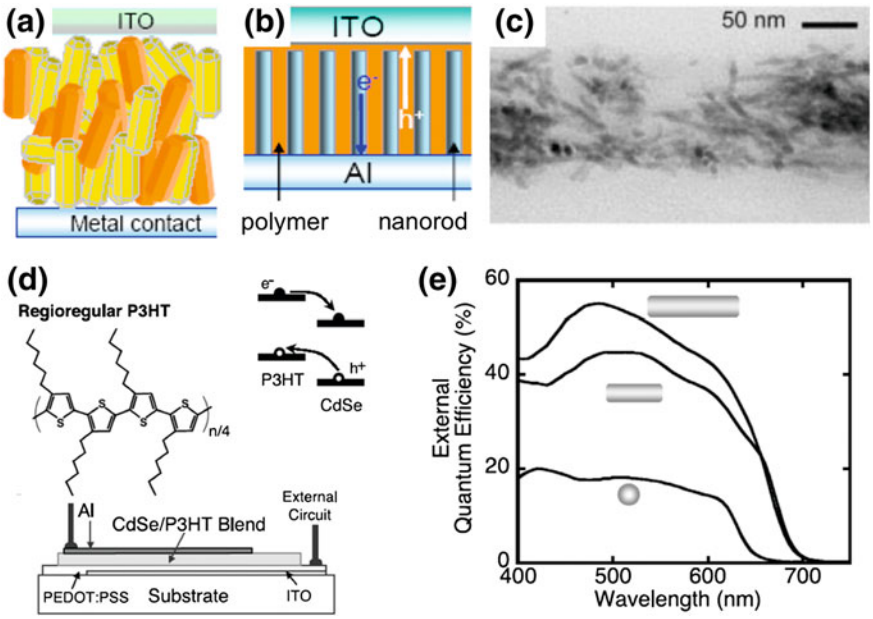

Fig. 3.15 **a** Idealized scheme of an all-inorganic solar cell based on a layer of nanorods. **b** Optimal design of a hybrid nanorod-polymer solar cell. **c** Cross section TEM image from a solar cell based on a blend of CdSe nanorods and conjugated polymer Poly(3-hexylthiophene) (P3HT). **d** Structure of P3HT, illustration of the charge transfer and the design of the solar cell. **e** Quantum efficiency of solar cells based on CdSe nanorods with 7, 30 and 60 nm length. (**c**–**e**) from Ref. [2]

Another option is to fabricate hybrid solar cell devices consisting of semiconductor nanorods and conjugated polymers (see Fig. 3.15b for an idealized design), which were investigated, for example by the group of Alivisatos [2, 3]. Here, nanorods and the polymer poly (3-hexylthiophene) (P3HT) were dissolved in pyridine and chloroform to form an organic/inorganic blend that could be spin-coated onto the anode, in which the P3HT promoted the hole conduction pathway and the rods the harvesting of the electrons. However, in such a blend the nanorods were mostly disordered (Fig. 3.15c). These works confirmed the higher external quantum efficiency of nanorods as compared to spherical nanoparticles, which lead a power conversion efficiency of 1.7 % under air mass 1.5 global solar conditions.

Solar cells based on vertically oriented nanorods have been realized recently by several groups [47–49]. For, example, porous aluminium templates enabled the fabrication of regular arrays of CdSe nanorods by electrochemical deposition as illustrated in Fig. 3.16Ia and demonstrated by the SEM images in Fig. 3.16II. In such ordered nanorod solar cells the harvesting of the electrons is facilitated by the CdSe nanorods (see energy diagram in Fig. 3.16Ib, while the holes are collected

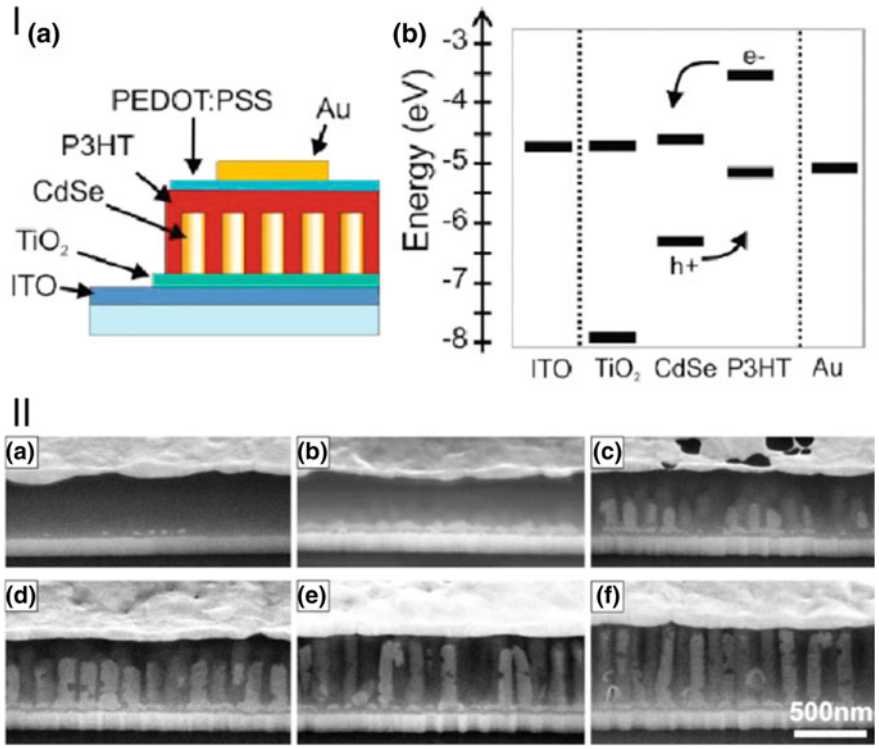

Fig. 3.16 I(*a*) Scheme of an idealized solar cell architecture based on an array of vertically aligned nanorods. (*b*) Corresponding energy diagram to the layered structure sketched in (*a*). II (*a–f*) Cross section scanning electron microscopy images of a series of devices with different nanorod lengths. With permission from Ref. [50]

by the organic polymer. The direct collection pathway provided for the electrons makes this architecture much more efficient than the irregular blends, and power conversion efficiencies of 1.38 % have been achieved [50]. A popular material for nanorods in solar cell devices is ZnO, which is discussed in the review in Ref. [51]. ZnO and TiO_2 nanorods and nanowires find also application in dye-sensitized solar cells [52–56].

3.5 Thermoelectric Properties of Nanorods

Thermoelectric materials allow for the direct conversion of temperature differences into electric voltage and vice versa, which makes them suitable for energy generation, as temperature sensors and as controllers and cooling elements. In principle, the thermoelectric properties originate from the difference in Fermi levels of two materials, combined with a low thermal conductivity that helps to maintain the temperature difference. If these materials are put into contact, the Fermi level alignment leads to charge diffusion over the interface and to an electric field that compensates the Fermi level difference. Assuming Boltzmann distributions for the charge carriers in both materials (n_1, n_2), the contact voltage can be expressed as:

$$\Delta U = \frac{kT}{e} \ln \frac{n_2}{n_1} \tag{3.7}$$

We see that this contact voltage at the material interface is temperature dependent, and therefore a difference in temperature at the two contact interfaces leads to a thermo-voltage, defined as:

$$U_{th} = \frac{k}{e} \ln \frac{n_2}{n_1} \Delta T \tag{3.8}$$

The thermoelectric power, also called Seebeck coefficient, S is defined from the open circuit electric field that is created by the temperature gradient:

$$\frac{\Delta V}{\Delta T} = S, \text{ or } E = S \, grad \, T \tag{3.9}$$

The sign of the thermo-voltage allows to identify the type of majority carriers (positive is p-type), as can be seen from Eq. (3.7). From the ratio of k/e in Eq. (3.7) we expect the thermoelectric power to be in the μV/K range. Another characteristic parameter is the Peltier coefficient Π that is defined by the heat absorbed by the lower junction per unit time P and the current I on the junction:

$$P = \Pi I, \tag{3.10}$$

which leads to $\Pi = ST$. Figure 3.17 lists the thermoelectric power of some materials at T = 0 °C with reference to Pb which is set to zero. The thermoelectric figure of merit is defined as

$$ZT \equiv S^2 \sigma T / \kappa, \tag{3.11}$$

where σ and κ are the electrical and thermal conductivity, respectively.

For bulk materials it is difficult to improve the ZT, because electrical and thermal conductivity are related via the Wiedemann–Franz-law, $\kappa/\sigma = LT$ (where L is the Lorenz number), and thus an increase in electrical conductivity results also in an increase in thermal conductivity. In this respect, nanostructured materials promise novel alternatives to increase the thermoelectric figure of merit, since size and quantum effects have different impact on the thermal and electrical conductivity. Nanowires are an especially appealing structure because the electrical conductivity is enhanced due to a reduced number of channels for electron scattering. At the same time, the electronic contribution to the thermal conductivity (electron scattering on phonons) is reduced, and for very small diameters surface scattering will further reduce the thermal conductivity. As an example, Dresselhaus and coworkers calculated the thermoelectric figure of merit (ZT) for Bi and Bi_2Te_3 nanowires in dependence of the nanowire diameter (see Fig. 3.18), and found a strong increase of ZT when the wire diameter was decreased below the mean free path of the electrons [58, 59].

Materials for thermoelectric applications should have a small electron effective mass and a highly anisotropic Fermi surface. A promising material system for thermoelectric experiments can be described by Pn_2X_3, where Pn stands for Bi, Sb, Pb, and X for S, Se, Te. We will now discuss briefly some thermoelectric experiments on nanorods from the above mentioned materials. Doped Bi_2Te_3 nanorods with 30–130 nm diameter were fabricated in a one-step, aqueous phase synthesis approach, and films obtained by drop casting of nanorod solution were annealed at 350 °C under vacuum. The Seebeck coefficient of these films was -100 μV/K, revealing the n-type doping, but was significantly lower than the Seebeck coefficient of undoped bulk Bi_2Te_3, which behaves as a p-type semiconductor [61]. Films of

Fig. 3.17 Thermoelectric power of some bulk metals at T = 0 °C, with reference to Pb which is set to zero. From Ref. [57]

Material	Thermopower (μV/K)
Sb	+35
Fe	+16
Zn	+3
Cu	+2.8
Ag	+2.7
Pb	0
Al	-0.5
Pt	-3.1
Ni	-19
Bi	-70

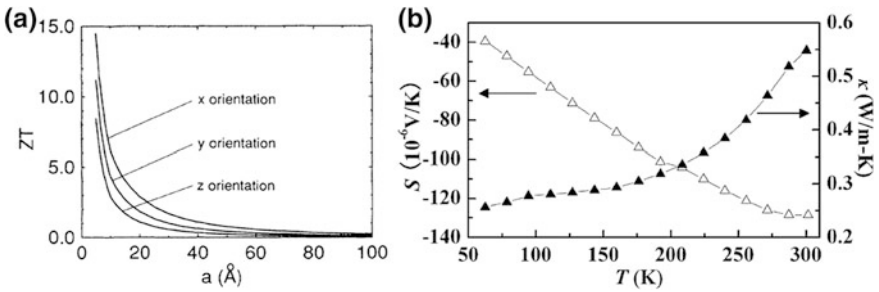

Fig. 3.18 **a** Thermoelectric figure of merit in dependence of wire width calculated for Bi_2Te_3 nanowires. Taken with permission from Ref. [58]; **b** Seebeck coefficient and thermal conductivity of Bi/Te core–shell nanowires. Taken with permission from Ref. [60]

cross-linked Bi_2S_3 nanorods have been fabricated on Si substrates and showed a high Seebeck coefficient of -755 μV/K [62]. High-aspect ratio PbTe nanorods were assembled into thin films onto glass substrates prepatterned with Au electrodes by dipcoating, and a subsequent hydrazine treatment was applied in order to enhance the film conductivity [63]. Such films showed a band gap of 0.27 eV, and a Seebeck coefficient of 263 μV/K, which is comparable to bulk PbTe. Te/Bi core–shell nanowires were fabricated by a two-step solution phase method, and the characterization of thin films of this 1D nanocomposite material yielded a high Seebeck coefficient of -128 μV/K at $T = 300$ K, but due to the comparatively low electrical conductivity the obtained ZT was only 0.05 [60].

An enhancement of the thermopower has also been observed by Zuev et al. in single nanowires of Sb_2Te_3 when the diameter became smaller than 40 nm [64]. This work showed also a linear increase in thermopower with increasing temperature according to the classical Mott relation for diffusive thermopower S, which is defined as [65]:

$$S = -\frac{\pi^2 k_B^2 T}{3e} \frac{d \ln \sigma(E)}{dE} \tag{3.12}$$

Furthermore a strong decrease in the conductivity of the nanowire with small diameter at low temperature was observed that could result from grain boundaries that hinder conduction and have more impact in structures with small diameter.

References

1. Porath D, Levi Y, Tarabiah M, Millo O (1997) Tunneling spectroscopy of isolated C-60 molecules in the presence of charging effects. Phys Rev B 56(15):9829–9833
2. Huynh WU, Dittmer JJ, Alivisatos AP (2002) Hybrid nanorod-polymer solar cells. Science 295(5564):2425–2427
3. Huynh WU, Dittmer JJ, Teclemariam N, Milliron DJ, Alivisatos AP, Barnham KWJ (2003) Charge transport in hybrid nanorod-polymer composite photovoltaic cells. Phys Rev B67(11):art. n. 115326

4. Steiner D, Azulay D, Aharoni A, Salant A, Banin U, Millo O (2009) Photoconductivity in aligned CdSe nanorod arrays. Phys Rev B 80(19):art. n. 195308
5. Persano A, De Giorgi M, Fiore A, Cingolani R, Manna L, Cola A, Krahne R (2010) Photoconduction properties in aligned assemblies of colloidal CdSe/CdS nanorods. ACS Nano 4(3):1646–1652
6. Rizzo A, Nobile C, Mazzeo M, De Giorgi M, Fiore A, Carbone L, Cingolani R, Manna L, Gigli G (2009) Polarized light emitting diode by long-range nanorod self-assembling on a water surface. ACS Nano 3(6):1506–1512
7. Millo O, Katz D, Steiner D, Rothenberg E, Mokari T, Kazes M, Banin U (2004) Charging and quantum size effects in tunnelling and optical spectroscopy of CdSe nanorods. Nanotechnology 15(1):R1–R6
8. Steiner D, Katz D, Millo O, Aharoni A, Kan S, Mokari T, Banin U (2004) Zero-dimensional and quasi one-dimensional effects in semiconductor nanorods. Nano Lett 4(6):1073–1077
9. Hanna AE, Tinkham M (1991) Variation of the Coulomb staircase in a two-junction system by fractional electron charge. Phys Rev B 44:5919–5922
10. Banin U, Millo O (2003) Tunneling and optical spectroscopy of semiconductor nanocrystals. Ann Rev Phys Chem 54:465–492
11. Sun ZX, Swart I, Delerue C, Vanmaekelbergh D, Liljeroth P (2009) Orbital and Charge-Resolved Polaron States in CdSe Dots and Rods Probed by Scanning Tunneling Spectroscopy. Phys Rev Lett 102(19):196401
12. Katz D, Wizansky T, Millo O, Rothenberg E, Mokari T, Banin U (2002) Size-dependent tunneling and optical spectroscopy of CdSe quantum rods. Phys Rev Lett 89(8):art. n. 086801
13. Shabaev A, Efros AL, Nozik AJ (2006) Multiexciton generation by a single photon in nanocrystals. Nano Lett 6(12):2856–2863
14. Steiner D, Dorfs D, Banin U, Della Sala F, Manna L, Millo O (2008) Determination of band offsets in heterostructured colloidal nanorods using scanning tunneling spectroscopy. Nano Lett 8(9):2954–2958. doi:10.1021/nl801848x
15. Sitt A, Della Sala F, Menagen G, Banin U (2009) Multiexciton engineering in seeded core/shell nanorods: transfer from type-I to quasi-type-II regimes. Nano Lett 9(10):3470–3476
16. Sheldon MT, Trudeau P-E, Mokari T, Wang L-W, Alivisatos AP (2009) Enhanced semiconductor nanocrystal conductance via solution grown contacts. Nano Lett 9(11):3676–3682
17. Trudeau PE, Sheldon M, Altoe V, Alivisatos AP (2008) Electrical contacts to individual colloidal semiconductor nanorods. Nano Lett 8(7):1936–1939. doi:10.1021/nl080678t
18. Gudiksen MS, Maher KN, Ouyang L, Park H (2005) Electroluminescence from a single-nanocrystal transistor. Nano Lett 5(11):2257–2261
19. Cui Y, Banin U, Bjork MT, Alivisatos AP (2005) Electrical transport through a single nanoscale semiconductor branch point. Nano Lett 5(7):1519–1523
20. Steinberg H, Lilach Y, Salant A, Wolf O, Faust A, Millo O, Banin U (2009) Anomalous temperature dependent transport through single colloidal nanorods strongly coupled to metallic leads. Nano Lett 9(11):3671–3675
21. Leonard F, Talin AA (2006) Size-dependent effects on electrical contacts to nanotubes and nanowires. Phys Rev Lett 97(2):art. n. 026804
22. Demchenko DO, Wang LW (2007) Localized electron states near a metal/semiconductor nanocontact. Nano Lett 7(10):3219–3222. doi:10.1021/nl072027n
23. Wolf E (1989) Principles of electron tunneling spectroscopy. Oxford University Press, Oxford
24. Fowler RH, Nordheim DL (1928) Electron emission in intense electric fields. Proc Roy Soc London Ser A Math Phys Eng Sci 119(781):173–181
25. Varshni YP (1967) Physica 34:149–154
26. Coe S, Woo WK, Bawendi M, Bulovic V (2002) Electroluminescence from single monolayers of nanocrystals in molecular organic devices. Nature 420(6917):800–803
27. Doh YJ, Maher KN, Ouyang L, Yu CL, Park H, Park J (2008) Electrically driven light emission from individual CdSe nanowires. Nano Lett 8(12):4552–4556

28. Carbone L, Kudera S, Giannini C, Ciccarella G, Cingolani R, Cozzoli PD, Manna L (2006) Selective reactions on the tips of colloidal semiconductor nanorods. J Mater Chem 16(40):3952–3956
29. Costi R, Saunders AE, Banin U (2010) Colloidal hybrid nanostructures: a new type of functional materials. Angew ChemInt Edit 49(29):4878–4897
30. Steiner D, Mokari T, Banin U, Millo O (2005) Electronic structure of metal-semiconductor nanojunctions in gold CdSe nanodumbbells. Phys Rev Lett 95(5):art. n. 056805
31. Costi R, Saunders AE, Elmalem E, Salant A, Banin U (2008) Visible light-induced charge retention and photocatalysis with hybrid CdSe-Au nanodumbbells. Nano Lett 8(2):637–641
32. Costi R, Cohen G, Salant A, Rabani E, Banin U (2009) Electrostatic force microscopy study of single Au-CdSe hybrid nanodumbbells: evidence for light-induced charge separation. Nano Lett 9(5):2031–2039
33. Figuerola A, Di Corato R, Manna L, Pellegrino T (2010) From iron oxide nanoparticles towards advanced iron-based inorganic materials designed for biomedical applications. Pharm Res 62(2):126–143
34. Lavieville R, Zhang Y, Casu A, Genovese A, Manna L, Di Fabrizio E, Krahne R (2012) Charge transport in nanoscale all-inorganic networks of semiconductor nanorods linked by metal domains. ACS Nano 6(4):2940–2947. doi:10.1021/nn3006625
35. Figuerola A, Huis MV, Zanella M, Genovese A, Marras S, Falqui A, Zandbergen H, Cingolani R, Manna L (2010) Epitaxial CdSe-Au nanocrystal heterostructures by thermal annealing. Nano Lett 10(8):3028–3036
36. Steiner D, Azulay D, Aharoni A, Salant A, Banin U, Millo O (2008) Electronic structure and self-assembly of cross-linked semiconductor nanocrystal arrays. Nanotechnology 19(6):art. n. 065201. doi:10.1088/0957-4484/19/6/065201
37. Steiner D, Aharoni A, Banin U, Millo O (2006) Level structure of InAs quantum dots in two-dimensional assemblies. Nano Lett 6(10):2201–2205
38. Talapin DV, Murray CB (2005) PbSe nanocrystal solids for n- and p-channel thin film field-effect transistors. Science 310(5745):86–89
39. Drndic M, Jarosz MV, Morgan NY, Kastner MA, Bawendi MG (2002) Transport properties of annealed CdSe colloidal nanocrystal solids. J Appl Phys 92(12):7498–7503
40. Persano A, Leo G, Manna L, Cola A (2008) Charge carrier transport in thin films of colloidal CdSe quantum rods. J Appl Phys 104(7):art. n. 074306
41. Romero HE, Calusine G, Drndic M (2005) Current oscillations, switching, and hysteresis in CdSe nanorod superlattices. Phys Rev B 72(23):art. n. 235401
42. Leatherdale CA, Kagan CR, Morgan NY, Empedocles SA, Kastner MA, Bawendi MG (2000) Photoconductivity in CdSe quantum dot solids. Phys Rev B 62(4):2669–2680
43. Creti A, Anni M, Zavelani-Rossi M, Lanzani G, Leo G, Della Sala F, Manna L, Lomascolo M (2005) Ultrafast carrier dynamics in core and core/shell CdSe quantum rods: role of the surface and interface defects. Phys Rev B 72(12):art. n. 125346
44. Franchini IR, Cola A, Rizzo A, Mastria R, Persano A, Krahne R, Genovese A, Falqui A, Baranov D, Gigli G, Manna L (2010) Phototransport in networks of tetrapod-shaped colloidal semiconductor nanocrystals. Nanoscale 2(10):2171–2179. doi:10.1039/C0nr00308e
45. Kudera S, Zhang Y, Di Fabrizio E, Manna L, Krahne R (2012) Spatial analysis of the photocurrent generation and transport in semiconductor nanocrystal films. Phys Rev B 86(7):075307
46. Ginger DS, Greenham NC (2000) Charge injection and transport in films of CdSe nanocrystals. J Appl Phys 87(3):1361–1368
47. Heitbaum M, Glorius F, Escher I (2006) Asymmetric heterogeneous catalysis. Angew ChemInt Edit 45(29):4732–4762. doi:10.1002/anie.200504212
48. Cuenya BR (2010) Synthesis and catalytic properties of metal nanoparticles: size, shape, support, composition, and oxidation state effects. Thin Solid Films 518(12):3127–3150. doi:10.1016/j.tsf.2010.01.018
49. Somorjai GA, Park JY (2008) Molecular factors of catalytic selectivity. Angew ChemInt Edit 47(48):9212–9228. doi:10.1002/anie.200803181

50. Schierhorn M, Boettcher SW, Peet JH, Matioli E, Bazan GC, Stucky GD, Moskovits M (2010) CdSe nanorods dominate photocurrent of hybrid CdSe, àíP3HT photovoltaic cell. ACS Nano 4(10):6132–6136. doi:10.1021/nn101742c
51. Gonzalez-Valls I, Lira-Cantu M (2009) Vertically-aligned nanostructures of ZnO for excitonic solar cells: a review. Energy Environ Sci 2(1):19–34. doi:10.1039/b811536b
52. Astruc D, Lu F, Aranzaes JR (2005) Nanoparticles as recyclable catalysts: the frontier between homogeneous and heterogeneous catalysis. Angew ChemInt Edit 44(48):7852–7872. doi:10.1002/anie.200500766
53. Schmid G (1998) Large metal clusters and colloids—metals in the embryonic state. Struct Dyn Prop Disperse Colloidal Syst 111:52–57
54. Wilson OM, Knecht MR, Garcia-Martinez JC, Crooks RM (2006) Effect of Pd nanoparticle size on the catalytic hydrogenation of allyl alcohol. J Am Chem Soc 128(14):4510–4511. doi:10.1021/ja058217m
55. Gates BC (1995) Supported metal clusters: synthesis, structure, and catalysis. Chem Rev 95(3):511–522
56. Stamenkovic VR, Fowler B, Mun BS, Wang GF, Ross PN, Lucas CA, Markovic NM (2007) Improved oxygen reduction activity on Pt3Ni(111) via increased surface site availability. Science 315:493–497. doi:10.1126/science.1135941
57. Vogel H (1997) Gerthsen Physik, 19th edn. Springer, Berlin
58. Hicks LD, Dresselhaus MS (1993) Thermoelectric figure of merit of a one-dimensional conductor. Phys Rev B 47(24):16631–16634
59. Lin YM, Sun XZ, Dresselhaus MS (2000) Theoretical investigation of thermoelectric transport properties of cylindrical Bi nanowires. Phys Rev B 62(7):4610–4623
60. Zhang GQ, Wang W, Li XG (2008) Enhanced thermoelectric properties of core/shell heterostructure nanowire composites. Adv Mater 20(19):3654–3656
61. Purkayastha A, Lupo F, Kim S, Borca-Tasciuc T, Ramanath G (2006) Low-temperature, template-free synthesis of single-crystal bismuth telluride nanorods. Adv Mater 18(4):496–500
62. Liufu SC, Chen LD, Yao Q, Wang CF (2007) Assembly of one-dimensional nanorods into Bi2S3 films with enhanced thermoelectric transport properties. Appl Phys Lett 90(11):art. n. 112106
63. Purkayastha A, Yan QY, Gandhi DD, Li HF, Pattanaik G, Borca-Tasciuc T, Ravishankar N, Ramanath G (2008) Sequential organic-inorganic templating and thermoelectric properties of high-aspect-ratio single-crystal lead telluride nanorods. Chem Mater 20(15):4791–4793
64. Zuev YM, Lee JS, Galloy C, Park H, Kim P (2010) Diameter Dependence of the Transport Properties of Antimony Telluride Nanowires. Nano Lett 10(8):3037–3040
65. Ashroft NW, Mermin ND (1976) Solid state physics. Brooks Cole, Orlando, FL (ISBN 0-03-049346-3)

Chapter 4
Optical Properties of Metal Nanorods

4.1 Overview

Metal nanostructures are well known to produce colors, due to their strong light absorption and scattering in the visible region of the spectrum (see Fig. 4.1). This property has been exploited in glass artworks like, for example, the rose window of the Notre Dame cathedral in Paris where silver and gold nanoparticles make the coloring of the glass. This effect is caused by one of the most important types of interactions of metal nanoparticles with the electromagnetic field. Metals are characterized by the presence of free electrons, which can be promoted via intra-band transitions to empty energy levels in the same band or to empty levels of an empty overlapping band, via absorption of low energy photons. An incident electromagnetic field can elicit collective oscillations of these free electrons [1–4]. Such oscillations become quickly resonant with the electromagnetic field, and the energy from the incoming radiation is absorbed and transformed into heat (absorption) and back into light (scattering). These collective and coherent oscillations of electrons cause a displacement of the electrons from the nuclei, leading to the formation of various possible distributions in the surface charges (Fig. 4.1). This in turn creates Coulomb interactions between positive and negative charges, which induce restoring oscillating forces acting on these free electrons. Each type of surface charge distribution is characterized by a collective oscillation mode, also termed as localized surface plasmon resonance (SPR). There are various factors that influence the possible types of SPRs in nanostructures and the frequencies at which they are observed. Other types of interactions of metal nanoparticles with the electromagnetic radiation are:

1. Absorption processes due to electronic transitions of bound electrons from occupied to empty bands (inter-band transitions);
2. Scattering processes due to accelerations of electrons in the nanostructures caused by the electromagnetic radiation, which leads to isotropic radiation.

Interband electronic transitions in metal nanoparticles are rather insensitive to particle size (except in the case of sub-2 nm metal clusters, which are made of a

R. Krahne et al., *Physical Properties of Nanorods*,
NanoScience and Technology, DOI: 10.1007/978-3-642-36430-3_4,

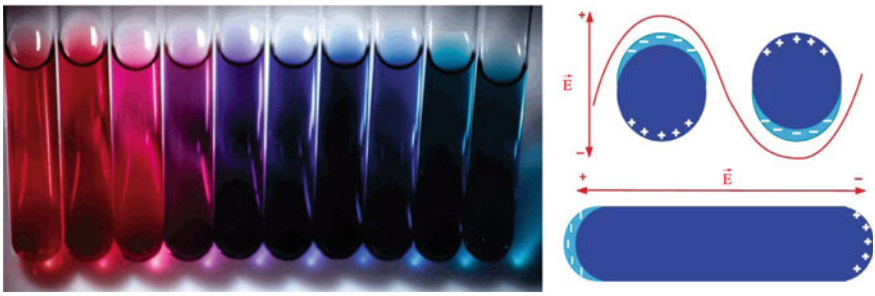

Fig. 4.1 *Left* vials containing gold nanoparticles (vial on the *far left*) and hollow nanoparticles (all the other vials) of various diameters and wall thicknesses. Taken with permission from Ref. [5]. *Right* sketches showing surface plasmon resonance in spherical nanoparticles and nanorods inside a polarized light field. Taken with permission from Ref. [6]

few atoms), and are located at high energy (for example above 3.8 eV in silver nanoparticles). For nanoparticles with diameters between 10 and 30 nm, the dominant effect in the visible region is the excitation of plasmon modes. In this size regime, and in the simple case of spherical nanoparticles, basically a single plasmon mode of dipolar character is excited and its wavelength is independent of particle size, but is strongly dependent on the dielectric function of the surrounding medium, and also the width of the plasmon resonance band remains poorly correlated with size. For particles smaller than 10 nm, a size that is significantly smaller than the mean free path of electrons, free electrons collide frequently with the surface of the nanoparticles, and this leads to broadening of the plasmon resonance band due to dephasing effects. At sizes above 30 nm other effects become non-negligible, like retardation, which lead to broadening and loss in intensity of the plasmon band, as well as to a spectral shift in the red. At sizes above 100 nm, the optical properties are dominated by scattering of light. In addition, higher order modes (i.e. quadrupolar, octupolar) start contributing to absorption.

The shape of metal nanoparticles has perhaps the most striking influence on their optical properties. As an example, in rod shaped nanoparticles the plasmon mode is split into two modes, a longitudinal one and a transverse one. In the following, our discussion will be as much as possible general and will cover all metal nanoparticles, but in some occasions we will focus our attention on gold nanoparticles, for several reasons: first of all gold nanoparticles do not undergo oxidations processes, hence their theoretical description does not need to take into account the presence of a surface oxide layer (which complicates considerably the theoretical treatment); secondly, gold nanoparticles are now fabricated in a variety of sizes and shapes, hence the testing of the various computational approaches on real samples is directly feasible; lastly, gold nanoparticles have been employed and/or proposed in a variety of applications. In this section, we will give a brief overview of the optical properties of metal nanoparticles in various size regimes, and we will focus then the attention on the effect of shape, with particular

emphasis on elongated nanoparticles. Many excellent research articles, reviews and books on this topic have been published in the last years, covering many aspects of localized surface plasmons in metal nanostructures [1–13].

In the following, we will be concerned mainly with the far-field behavior of metal nanoparticles, that is, their interaction with the electromagnetic field via absorption and scattering processes (each characterized by a specific single particle cross section, σ_{abs} and σ_{sc}). We will not deal here with the near-field properties, which govern the behavior of nanoparticles in close proximity with other particles/molecules. These will be discussed at that end of this section. Let us assume that we are dealing with a dilute sample of nanoparticles, hence each particle behaves independently from the others with respect to the incident radiation. Under these circumstances, the intensity of light that is transmitted through this sample is given by the expression:

$$I = I_0 e^{[-(\sigma_{abs}+\sigma_{sc})NL]} \tag{4.1}$$

In the above expression I_0 is the intensity of the incoming light, N is the number of particles per unit volume, and L is the length of the path travelled by the light in the sample. The quantity $\sigma_{abs} + \sigma_{sc}$ is also known as the extinction cross section.

4.2 Dielectric Function of Metal Nanoparticles

We follow here the approach described by Noguez [14]. Let us suppose, as a first approximation, that we can treat nanoparticles as objects with the same dielectric function ε as the bulk metal. In a metal, the dielectric function can be considered as formed by a contribution from the electrons at the Fermi level, which are essentially "free", and a contribution from bound electrons. We call the contribution of free electrons to ε as ε_{intra}. The bound electrons, populating fully occupied bands, interact only with higher energy photons and can be promoted to empty bands separated from the occupied band by an energy gap (therefore via inter-band transitions). We call the contribution of these electrons to ε as ε_{inter}. If ε_{exp} is the measured bulk dielectric constant, then we can write $\varepsilon_{exp} = \varepsilon_{inter} + \varepsilon_{intra}$.

The dependence of $\in_{intra}$ on the frequency ω can be described satisfactorily by the Drude model [15, 16]. This model approximates the metal as a plasma, i.e. a medium composed of an equal number of conduction band electrons and of positively charged ion cores, in which the conduction electrons are not bound to atoms. The contribution of these free electrons to the dielectric function is approximated to:

$$\varepsilon_{intra}(\omega) = 1 - \frac{\omega_p^2}{\omega(\omega + i/\tau)} \tag{4.2}$$

In the expression above, ω_p is the plasma frequency, defined by $\omega_p^2 = 4\pi n e^2/m$, with n the density of conduction electrons, while m and e are the mass and the

charge of the electron, respectively. The physical meaning of the plasma frequency can be easily understood in the following way. In the free electron plasma, if all the free electrons are slightly displaced in one direction with respect to the ions by application of an external electric field, a Coulomb force is created due to macroscopic displacement of the electrons with the respect to the positive ions lattice. This force tries to "pull" the electrons back, and, if the field is suddenly turned off (hence no other forces are acting on the system), the force causes the whole plasma to oscillate at a frequency equal to ω_p [16]. The "damping factor" $1/\tau$ in the Drude model arises instead from various scattering processes of electrons (mainly electron–electron and electron–phonon scattering) and is the inverse of its relaxation time τ.

In small particles (i.e. radii smaller than 10 nm), there is an additional size-dependent damping term which is related to electron scattering from the boundary of the particle. In this size regime the free electron contribution to dielectric function, which takes into account the surface damping term, is [17]:

$$\varepsilon_{intra}(\omega, R) = 1 - \frac{\omega_p^2}{\omega(\omega + i/\tau + i\omega_D)} \tag{4.3}$$

In the expression above $\omega_D = A \cdot v_F/R$ is a frequency damping term that is directly proportional to the Fermi velocity v_F (i.e. the Fermi velocity associated to the Fermi energy E_F via $E_F = \frac{1}{2}mv_F^2$) and is inversely proportional to the particle radius R through the constant A.

Since the dielectric function ε_{exp} can be measured, and the ε_{intra} part can be modelled using the Drude model, one can extract the behavior of ε_{inter} at varying wavelength for metal nanoparticles. Figure 4.2 shows the real part (ε_{real}) and the imaginary part (ε_{im}) of the dielectric function for Ag, Au, and Cu [7]. In the panels, both the real and the imaginary components are decomposed in their interband and intraband contribution. One can see for example that for silver the major contribution of interband transitions to the imaginary part is below 325 nm, while in gold is below 550 nm, and for copper is below 600 nm. On the other hand, the contribution of interband transitions to the real part is only a positive, slowly varying background in all cases. Interband transitions contribute to absorption, but do not contribute to plasmon modes. Therefore, as we shall see in the next section, in metal nanoparticles the optical absorption spectra are complicated by these interband transitions effects.

4.3 Plasmonic Properties of Small Spherical Metal Nanoparticles

In principle, one can model the behavior of metal nanoparticles by solving the Maxwell's equations for various sizes and shapes of the nanoparticle, and assuming for the metal nanoparticle the dielectric function of the bulk metal, based

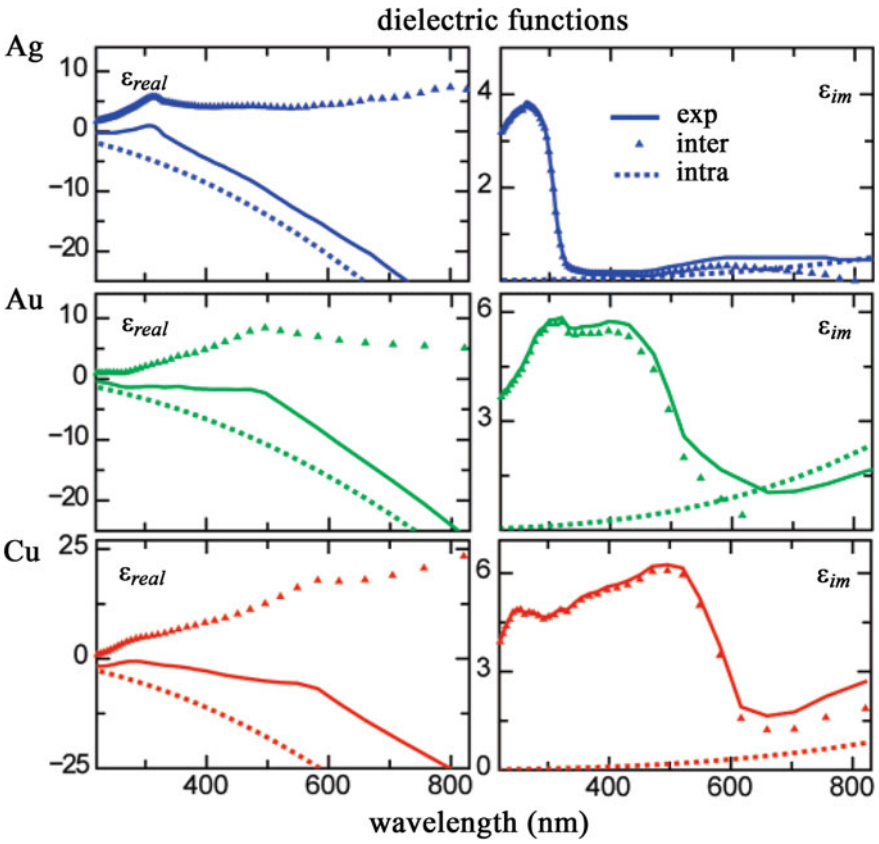

Fig. 4.2 Real part of the dielectric function (*left*) and imaginary part of the dielectric function (*right*) for silver, gold and copper. In each panel, the interband and intraband contributions are shown. Worth of notice is that ε_{im} is in general small compared to ε_{real} and that, above the short wavelength range that is dominated by interband transitions (325 nm for silver, 550 nm for gold and 600 nm for copper), ε_{im} does not vary much with wavelength. Taken with permission from Ref. [7]

only on the Drude model, as done by Mie [18], or considering also the contribution from interband transitions. The simplest case to treat is that of a spherical particle, in a uniform medium of dielectric function ε_{medium}, and immersed in a monochromatic radiation field having a plane wave form. The analytical solution of this problem exists, and yields an extinction cross section that is a series whose terms contain the various multipolar contributions for both extinction and scattering:

$$\sigma_{ext} = \frac{2\pi}{\eta|k|^2}\sum_{l=1}^{\infty}(2l+1)\mathrm{Re}\{A_l + B_l\} \tag{4.4}$$

$$\sigma_{sc} = \frac{2\pi}{\eta|k|^2}\sum_{l=1}^{\infty}(2l+1)\left(|A_l|^2 + |B_l|^2\right) \tag{4.5}$$

In the expression above $k = \frac{2\pi\sqrt{\varepsilon_{medium}}}{\lambda}$ is the magnitude of the wave vector of the incoming radiation, and A_l and B_l are the electric and magnetic scattering coefficients for the multipolar mode defined by l ($l = 1$ for dipole, $l = 2$ for quadrupole, $l = 3$ for octupole, and so on). They are expressed in terms of Riccati-Bessel functions that depend both on the particle radius R and on λ. The analytical solutions above give a satisfactory description of the optical behavior of metal nanoparticles in a broad range of sizes. There are also many approximate solutions to the problem, since one can distinguish various limiting cases. In one limiting case for example the size of the particle is much smaller than the wavelength λ of the radiation (by much smaller here we mean smaller than one tenth of λ). Then the field felt by the particle can be assumed to be constant throughout the particle (albeit it is still time dependent). This is called the "quasi-static" or "electrostatic", or also "non-retarded" regime. This is equivalent to assume that the speed of light can be considered infinite, so that the Maxwell equation correlating electric field $\boldsymbol{E}$ and magnetic inductance $\boldsymbol{B}$:

$$\nabla \times \boldsymbol{E} = -\frac{1}{c}\frac{\partial \boldsymbol{B}}{\partial t} \tag{4.6}$$

and the equation correlating magnetic field $\boldsymbol{H}$, electric displacement field $\boldsymbol{D}$ and the current density J_j:

$$\nabla \times \boldsymbol{H} = \frac{1}{c}\frac{\partial \boldsymbol{D}}{\partial t} + \frac{4\pi}{c}\boldsymbol{J}_f \tag{4.7}$$

are effectively reduced to $\nabla \times \boldsymbol{E} = 0$ and $\nabla \times \boldsymbol{H} = 0$. Under these approximations, there is no coupling between electric and magnetic fields, and the optical response of the nanoparticle is basically dictated by the electric field. From the terms in the expressions above, one can derive a simple expression for the multipolar polarizability, which is the following:

$$\alpha_l = \frac{3\lambda^2}{4\pi^2}A_l = 4\pi R^3 \varepsilon_{medium}\frac{l(\varepsilon - \varepsilon_{medium})}{l\varepsilon + (l+1)\varepsilon_{medium}} \tag{4.8}$$

Hence the resonance conditions occur for $\varepsilon = -\varepsilon_{medium}(l+1)/l$. Let us consider for now only the case of a dipole mode. Then the polarizability is given by the formula:

$$\alpha_1 = 4\pi R^3 \varepsilon_{medium}\frac{\varepsilon - \varepsilon_{medium}}{\varepsilon + 2\varepsilon_{medium}} \tag{4.9}$$

and the resonance is reached for $\varepsilon = -2\varepsilon_{medium}$. It turns out that for particle radii smaller than 30 nm the charges are essentially displaced homogeneously inside the particle (i.e. all free electrons are moving in phase), such that mainly an electrical

dipolar distribution of charges is generated on the surface of the particle. This is equivalent to say that the incident light polarizes uniformly the nanoparticles, hence the only significant contribution in the interaction of the small particle with the radiation is of electrical dipolar type, i.e. electric mutipoles are negligible. Furthermore, for small particles, say around 10 nm or smaller, their interaction with the incoming light is dominated by non-radiative processes (i.e. light is absorbed but is not emitted again). We can then assume that, at these small sizes, scattering, which is instead a radiative process and which indeed requires coupling between electric and magnetic field, is negligible (i.e. σ_{sc} is close to zero). Then the extinction cross section of a single particle is the same as the absorption cross section and can be approximated by [15]:

$$\sigma_{ext} \approx \sigma_{abs} = \frac{24\pi^2 R^3 \varepsilon_{medium}^{3/2}}{\lambda} \frac{\varepsilon_{im}}{(2\varepsilon_{medium} + \varepsilon_{real})^2 + \varepsilon_{im}^2} \tag{4.10}$$

Here R is the radius of the particle, and ε_{real} and ε_{im} and the real and imaginary parts of the dielectric function of the metal, respectively. An important aspect to notice is that ε_{im} is in general small compared to ε_{real} and does not vary much with the frequency ω (or with the wavelength), as shown in Fig. 4.2. Therefore, if we plot σ_{abs} versus ω, the maximum in absorption is reached for $\varepsilon_{real} = Re(\varepsilon(\omega)) = -2\varepsilon_{medium}$, (this is also known as the Froelich condition) while the peak width is dependent on ε_{im} and $\in_{medium}$. So, as a first approximation, the size of the particle has little influence on the peak position and on the width of the plasmon band. For gold nanoparticles in water, for example, the resonance peak is around 520 nm.

In the case of particle radii smaller than about 10 nm, however, the dielectric function of the particles becomes size dependent, as described above. It turns out that this so-called "non-local" or "surface dispersion", or "surface damping" effect does not influence the peak position of the resonance band. Instead, it leads to a broadening of the plasmon band, because the electrons lose coherence in their motion at each scattering event with the surface of the nanoparticle. Since the plasmon bandwidth Γ can be correlated to the dephasing time T_2 of the plasmon oscillation via the relation $\Gamma = 2\hbar/T_2$ (see also Sect. 4.7), a larger bandwidth means a faster dephasing of the oscillation. In small particles then the collision of the electrons with the surface introduces an additional term that contributes to the loss of coherence of the electron oscillation, therefore to a shortening of the overall dephasing time (and equivalently, a broadening of the band). The broadening of the plasmon band in small particles is so relevant that the band practically disappears for particle sizes smaller than 2 nm. Figure 4.3a, b reports the calculated extinction efficiency for two spherical silver particles, of radii equal to 5 and 50 nm, respectively, with and without contribution from surface damping. For the 5 nm particles the surface damping contribution is significant.

In a recent study Baida et al. [19] were able to record the optical extinction coefficient of individual silver nanoparticles in the size range between 10 and 50 nm, coated with a silica shell. The authors found that already for particles smaller than 25 nm the plasmon band started broadening, an effect that could be

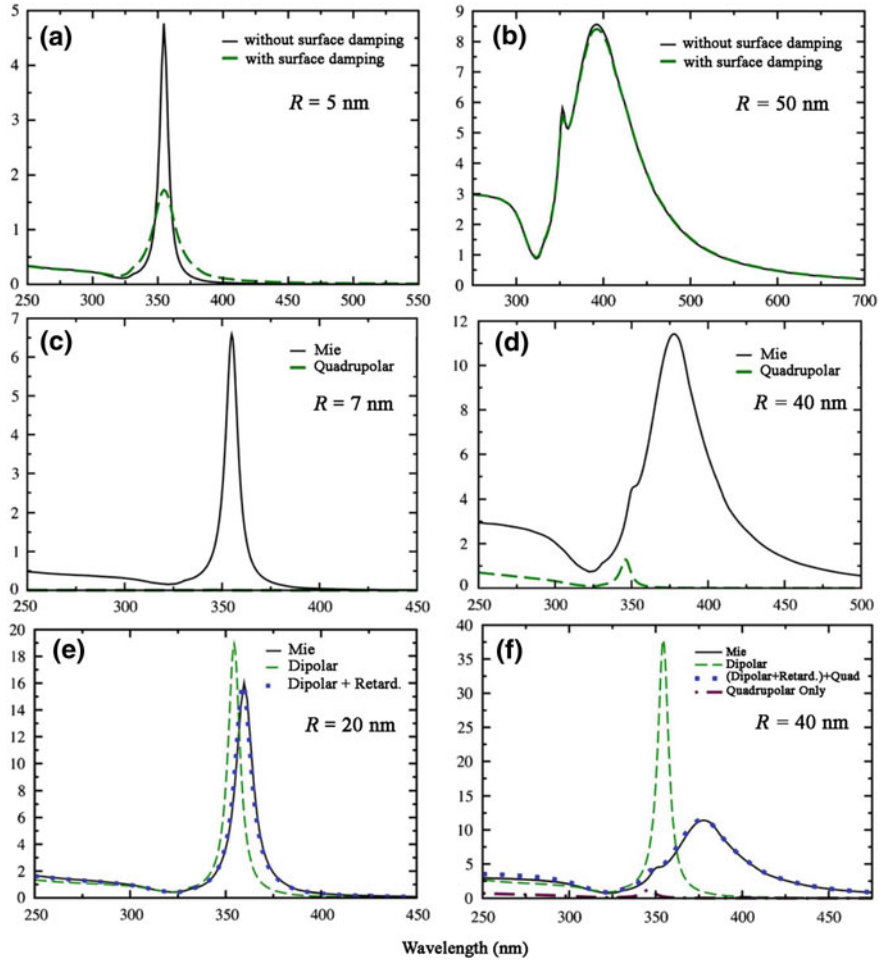

Fig. 4.3 **a**, **b** Extinction efficiency for Ag spherical nanoparticles with radius equal to 5 and 50 nm, respectively, calculated using the analytical solution of the Mie theory, excluding surface damping effects (*black line*) or including them (*green dashed line*). One can see that surface damping is relevant for the 5 nm particles, while it is negligible for the 50 nm ones. In (**b**), the additional peak at shorter wavelengths is due to the quadrupolar mode. The extinction at wavelengths shorter than 325 nm is due to absorption caused by interband transitions. The shape of the curve in this region is insensitive to size. **c**, **d** Absorption efficiency for spherical silver nanoparticles with radius equal to 7 and 40 nm, respectively, using the analytical solution of the Mie theory (*black curves*). The green *dashed curve* represents instead the contribution of the quadrupolar plasmon mode to extinction. This is negligible for the 7 nm particle, but can be already appreciated for the 40 nm particle (see also panel **b**); **e**, **f** Extinction efficiencies for spherical silver nanoparticles with radius equal to 20 and 40 nm, respectively, using the analytical solution of the Mie theory (*black lines*), considering only the dipolar approximation (*green dashed lines*), dipolar + retardation effects (*blue dotted lines*) for the 20 nm particle, dipolar + retardation effects + quadrupolar (*blue dotted lines*) for the 40 nm particle, and only the quadrupolar contribution for the 40 nm particle. Taken with permission from Ref. [2]

indeed interpreted classically due to surface damping. More in general, the authors found that the full width at half maximum of the plasmon resonance was inversely proportional to the size of the particles [19]. In the study, the authors pointed out that the surface contribution can be also interpreted quantum mechanically as due to a breakdown of the translational invariance, which reflects an increasing probability of dipolar transitions between electron eigenstates when the size of the particle is reduced, as the momentum is not a good quantum number any more. This study evidences that, especially for small metal clusters, one often needs to go beyond the simple and generic "classical" models that we have been describing above, and has to study more in detail the electronic structure of the specific metal. Various models have been developed in this respect. Two important reviews covering the physics of simple metal clusters (alkali metals and noble metals) are the work of de Heer [20], which compares the predictions of various theoretical models with experiments for spherical clusters, also covering non-spherical clusters (behavior of the mass-abundance spectra, polarizabilities, ionization potentials, photoelectron spectra, optical spectra, and fragmentation phenomena) and the work of Brack [21], which treats in detail the jellium model of simple metal clusters. From the bulk side (i.e. bulk metal surfaces) on the other hand, a broad overview of the various methods for calculating the electronic structure of metals surfaces (above all density functional theory) and electronic excitations at metal surfaces is the work of Liebsch [22]. In the Sect. 4.10.1, which describes the near field optical properties of metal nanoparticles, we will consider the case in which "classical" calculations and quantum mechanical calculations yield substantially different results.

4.4 Plasmonic Properties of Large Spherical Metal Nanoparticles

Many effects need to be taken into account for large nanoparticles. Let us consider first multipolar modes. In spherical nanoparticles, multipolar modes become non-negligible at particle radii around 30 nm and higher, where quadrupole modes start appearing. According to the Eq. (4.8), the resonance condition for a quadrupolar mode is $\varepsilon = -(2/3)\varepsilon_{medium}$, so it is shifted at lower energies with respect to the dipolar mode. The quadrupolar mode is first manifested as a small shoulder at the shorter wavelength side in the optical absorption spectrum that is still dominated by the dipolar plasmon mode, but as nanoparticle size increases the contribution from the quadrupolar mode increases (see Fig. 4.3b, d). In some cases, for example in Au nanoparticles, the quadrupolar mode, for small particle sizes, being weak in intensity, is hidden by the interband transitions [7]. In Ag nanoparticles instead, such overlap does not occur and therefore the quadrupolar mode is already evident at smaller sizes compared to gold [7]. Octupolar modes are relevant only for much bigger particles, and for even higher order modes, the resonance conditions

approach $\varepsilon = -\varepsilon_{medium}$, which is indeed the resonance condition of the planar surface plasmon (i.e. plasmon resonance for a flat metal surface in contact with a dielectric medium of dielectric function ε_{medium}). This is because in multipolar modes fast charge oscillations practically cancel out the interaction between distant charges, therefore each small region on the surface of the metal behaves as in a planar bulk metal. These considerations however, need to be taken with care, since at the large sizes at which multipolar modes are active, the optical behavior is additionally influenced by retardation effects. Indeed, in addition to multipolar modes, when the nanoparticles radius is about 30 nm or larger, retardation effects influence the optical response (see Fig. 4.3e, f). One of this retardation effects (the so-called "energy-shifting" effect) arises because the particle size is not any more negligible with respect to the wavelength of the radiation, or equivalently stated, the wavelength of the incoming radiation cannot be considered as infinite, hence the field is not homogeneous everywhere inside the particle. More precisely, these effects appear already when the diameter $2R$ of the particle is around 1/10 of the mode wavelength of the radiation in the medium surrounding the particle $\left(\lambda_m = \lambda/\sqrt{\varepsilon_{medium}}\right)$.

An elementary explanation of this effect can be sought by considering that when a dipole mode is excited in a spherical particle, the distance between opposite charges can be approximated to the nanoparticle diameter. Hence one side of the particle will "feel" any change occurring at the opposite side at the particle with a phase retardation equal to $2\pi \cdot 2R/\lambda_m$. The oscillation period of the dipole mode increases in order to take such retardation into account, which is equivalent to say that energy of the plasmon peak associated to a dipole mode shifts to the red as the particle size increases. When multipolar modes are involved, the distance between opposite charges on the surface of the particle is smaller than the particle diameter, and the phase retardation is smaller than in the dipolar mode. Indeed, the phase retardation in a spherical metal particle scales roughly as $2\pi \cdot 2R/(l \cdot \lambda_m)$ with $l = 1, 2, 3, \ldots$ for dipole, quadrupole, octupole mode, and so on. Dipole modes therefore are influenced more by the particle size, due to retardation effects, than higher order modes.

Another retardation effect is due to radiation scattering, which becomes already important for particles radii bigger than 20 nm, and is the dominant effect for particles radii above 100 nm. In these larger particles the electrons are accelerated as a consequence of the electromagnetic field generated by the incident radiation. Therefore, they also start radiating in all directions, which causes them to lose energy, i.e. part of the energy of the plasmonic oscillations is converted into photons. This leads to a broadening in the surface plasmon resonance and to a decrease in its intensity. Hence, as opposed to small particles, in large particles their interaction with the incoming light is dominated by radiative processes (i.e. energy is absorbed by the incoming light but is transformed again into photons).

In order to understand more quantitatively how the dipolar resonance is affected by retardation effects for large particle sizes, hence beyond the purely

electrostatic regime, a modified approach is required, which takes into account the finiteness of the wavelength of the incoming radiation. Let us consider the approach of Meier and Wokaun [23]. If we still stick to the approximation that the external field $\boldsymbol{E}_0$ is spatially uniform around the particle, then also the field that is generated inside the particle is uniform and equal to $\boldsymbol{E}_0 + \boldsymbol{E}_{dep}$, with $\boldsymbol{E}_{dep}$ being the so-called depolarization field [24]. Let us call $\boldsymbol{P}$ the polarization of a sphere of radius immersed in the external field $\boldsymbol{E}_0$. Then also $\boldsymbol{P}$ can be considered at a first approximation as homogeneous over the volume of the sphere and given by the expression:

$$4\pi\boldsymbol{P} = (\varepsilon - \varepsilon_{medium})\left(\boldsymbol{E}_0 - \boldsymbol{E}_{dep}\right) \tag{4.11}$$

Meier and Wokau [23] determined the depolarization field at the center of a spherical dielectric nanoparticle by assigning a dipole moment $dp = \boldsymbol{P}dV$ to each volume element dV of the particle, by calculating the dipolar field generated by each of these dipoles at the center of the particle, and by integrating over the whole volume of the sphere (i.e. over all the dipoles). This approach is known as the "Modified Long Wavelength Approximation". The depolarization field they found was related to the polarization through the following expression:

$$\boldsymbol{E}_{dep} = \left(-\frac{4\pi}{3} + k^2\frac{4\pi}{3}R^2 + ik^3\frac{2}{3}\frac{4\pi}{3}R^2\right)\boldsymbol{P} \tag{4.12}$$

where $k = 2\pi/\lambda$. The first factor in the parenthesis is the contribution to the depolarization in the quasi-static regime. The second term contributes to what is called "dynamic depolarization" [23, 25] and is interpreted as "dephasing" between radiation emitted by different regions of the particle [25]. It has also been interpreted as the depolarization field created by the oscillating dipole [14]. The third term is instead a purely imaginary term and is related to radiation emitted from the dipole. If we keep only the first term of Eq. (4.12) for determining the polarization in the expression (4.11), then we use this value of the polarization in the expression linking the dipolar polarizability α to the polarization $\boldsymbol{P}$ and to the external field $\boldsymbol{E}_0$:

$$\frac{4}{3}\pi R^3\boldsymbol{P} = \varepsilon_{medium}\alpha\boldsymbol{E}_0 \tag{4.13}$$

then we get the same expression for the dipolar polarizability as described by Eq. (4.9). A more complicated expression for the polarizability is obtained instead if we include also the second and the third term of expression (4.12) in the calculation. In addition, Meier and Wokaun considered the more elaborate case in which the polarization inside the particle is not uniform. In this case the exciting field felt by different regions of the particles is not the same, as discussed above. An expression for the dipolar polarizability of a sphere of radius R and volume V, which embeds all the effects described so far, is the following [23, 26]:

$$\alpha = \frac{1 - \left(\frac{1}{10}\right)(\varepsilon + \varepsilon_{medium})x^2 + O(x^4)}{\left(\frac{1}{3} + \frac{\varepsilon_{medium}}{\varepsilon - \varepsilon_{medium}}\right) - \frac{1}{30}(\varepsilon + 10\varepsilon_{medium})x^2 - i\frac{4\pi^2\varepsilon_{medium}}{3}\frac{V}{\lambda^3} + O(x^4)}\frac{3/2}{V} \tag{4.14}$$

In the expression above x is the so-called "size parameter" ($x = \pi R/\lambda$). In the denominator, the quadratic term is actually the "energy-shifting" effect of the depolarization field inside the nanoparticle, which causes a shift of the resonance peak, and is related to the second term of expression (4.12). Meier [10] gave an intuitive explanation of this term: simply stated, the bigger is the particle, the farther apart are the charges in the oscillating dipole and the smaller is the restoring force. Therefore, the resonance condition shifts to lower energies. The imaginary term in the denominator is related to radiation damping. The quadratic term in the numerator accounts instead for the "non-uniform" exciting field inside the particle, hence for the fact that the polarization throughout the particle has a varying phase, and it also causes a shift in the red of the resonance. The $O(x^4)$ terms can be safely ignored. One can easily see that if all the former terms are neglected, we get back the expression of the dipolar polarizability as described by Eq. (4.9). The retardation effects on the extinction efficiency of nanoparticles can be seen clearly in Fig. 4.3e, f. The theoretical work of Moroz [25] provides actually an ab initio first principle derivation of the expression (4.14) discussed above.

4.5 Plasmonic Properties of Ellipsoidal-Shaped Metal Nanoparticles

In metal nanoparticles whose shape deviates from that of a sphere, analytical solutions of the extinction cross section based on the Mie theory have not been found, and only approximations are available. A particularly fortunate case is that of ellipsoidal particles, for which analytical solutions are found in the quasi-static limit. For an ellipsoid with three principal axes of radii R_1, R_2, R_3 the dipolar polarizability along its ith axis in the quasi-static approximation is given by the expression [27]:

$$\alpha_i = V\varepsilon_{medium}\frac{\varepsilon - \varepsilon_{medium}}{\varepsilon_{medium} + N_i(\varepsilon - \varepsilon_{medium})} \tag{4.15}$$

In the expression above, V is the volume of the ellipsoid ($V = 4\pi R_1 R_2 R_3/3$) and the term N_i is the "geometrical factor" along the ith axis, which is given by the formula:

$$N_i = \frac{R_1 R_2 R_3}{2}\int_0^\infty \frac{ds}{(s + R_i^2)\sqrt{(s + R_1^2)(s + R_2^2)(s + R_3^2)}} \tag{4.16}$$

The three geometrical factors obey the relation $N_1 + N_2 + N_3 = 1$, hence in the case of a sphere $N_1 = N_2 = N_3 = 1/3$. From the equation above it can be seen that in ellipsoidal particles the resonance conditions are set by:

$$\varepsilon = \varepsilon_{medium}\left(1 - \frac{1}{N_i}\right) \tag{4.17}$$

In the simple case of $R_1 = R_2 \neq R_3$, one can define the aspect ratio of the ellipsoid as R_3/R_1. As soon as the aspect ratio increases (so we have a prolate ellipsoid), the N_3 polarizability along the 3rd axis decreases, and, according to the expression above, the resonance conditions for the polarizability along the 3rd axis (the longer axis) require larger negative values of ε. This is usually referred to as the "longitudinal plasmon resonance" and occurs at longer wavelength than in spherical nanoparticles. As an example, for gold ellipsoids with an aspect ratio equal to 6, N_3 is roughly equal to 0.05, so that the resonance condition requires $\in \approx -20\varepsilon_{medium}$. This is achieved at a wavelength of around 760 nm for nanoparticles in air (if one assumes for the dielectric function of gold that measured for bulk gold films [28]). On the other hand, the resonance condition for the polarizability along the short axes occurs at shorter wavelengths than in spheres. Again, in the previous case of an ellipsoid with aspect ratio equal to 6, $N_1 = N_2 \approx 0.5$, hence the resonance conditions for the transverse polarizability require $\varepsilon \approx -\varepsilon_{medium}$, which is achieved at a wavelengths shorter than that of a sphere (for which $\varepsilon = -2\varepsilon_{medium}$). Summarizing, in axially symmetric ellipsoidal particles ($R_1 = R_2 \neq R_3$) the dipolar resonance mode is split into one mode at longer wavelength (the longitudinal mode) and one mode at shorter wavelength (the transverse mode). This can be seen clearly in Fig. 4.4l.

Individual plasmon modes can be excited using light that is polarized such that its electric field is oscillating along one of the axes of the rods. This has been demonstrated for example by embedding gold nanorods in a polymer film, and then by stretching the film, which induced a preferential alignment of the rods along the stretching direction [4, 29]. Absorption by this film of light polarized either along the stretching direction or perpendicular to it caused selective excitation of the longitudinal and of the transverse plasmon modes, respectively. Individual plasmon modes were also excited on single nanorods, in a confocal microscope setup (see Sect. 4.7) [30].

In analogy with the case of spherical nanoparticles, if the overall aspect ratio of the ellipsoid is kept constant, but its overall size is increased, retardation effects start becoming relevant, so that in bigger rods the longitudinal plasmon resonances shifts to even longer wavelengths. An expression for the dipolar polarizability of the longitudinal mode in ellipsoids (i.e. along the principal axis with geometrical factor N) which takes into account these effects, and that is similar to that discussed above for spherical nanoparticles, was found recently by Kuwata et al. [26]:

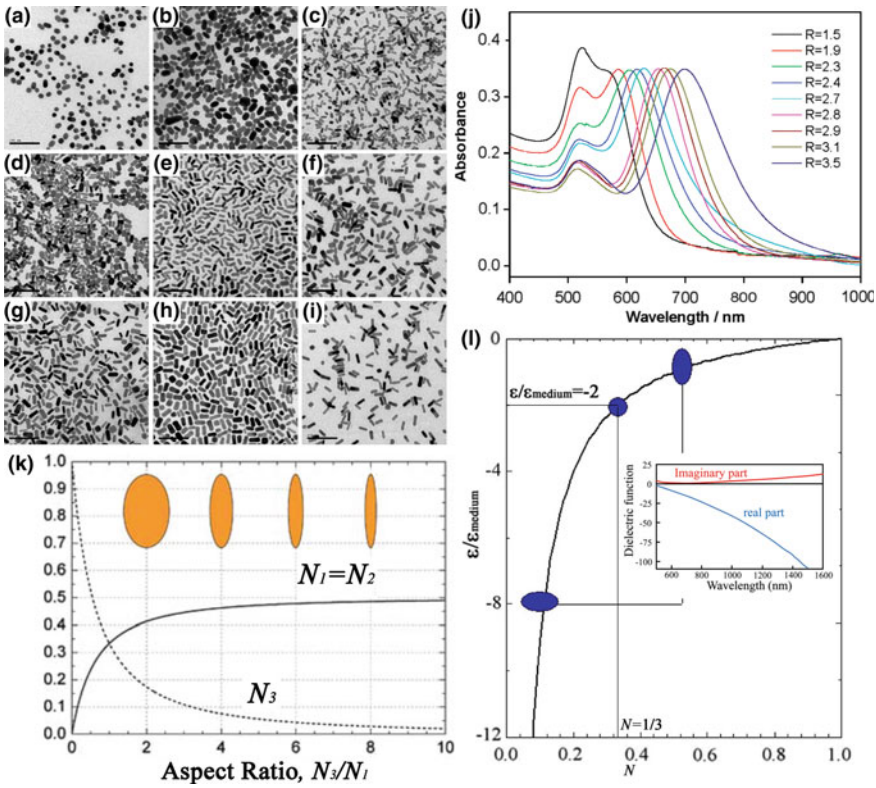

Fig. 4.4 **a-i** Transmission electron microscopy (*TEM*) images of gold nanorods of various aspect ratios synthesized by colloidal wet-chemical approaches. The black scale bar is the same in all the images and is equal to 100 nm. In going from (**a**) to (**i**) the aspect ratio of the particles increases from 1.5 to 3.5. Taken with permission from Ref. [45]. **j** UV-visible spectra of the samples displayed in (**a**–**i**). Taken with permission from Ref. [45]. **k** Geometrical factors for axially symmetric ellipsoids as a function of the aspect ratio. Taken with permission from Ref. [45]. **l** Curve correlating the plasmon resonance conditions as a function of the geometrical factor in a spheroidal particle. Taken with permission from Ref. [4]. The inset displays the dielectric function of gold [28] versus the wavelength, which indicates that the imaginary part of the dielectric function does not vary much with the wavelength. Therefore most of the variation in ε, at least above 550 nm, is due to variation in the real part. In a sphere, for which there is only one geometrical factor ($N = 1/3$), the resonance condition is met for $\varepsilon/\varepsilon_{medium} = -2$. In an axially symmetric ellipsoid, for which there are two geometrical factors, there are two resonance conditions, one is met for $\varepsilon/\varepsilon_{medium} > -2$, and corresponds to the transverse plasmon resonance, and the other is met for $\varepsilon/\varepsilon_{medium} < -2$, and corresponds to the longitudinal plasmon resonance. As can be seen from the inset, this condition is met at shorter wavelength for the transverse resonance mode (i.e. smaller negative values of ε) and at longer wavelength for the longitudinal resonance mode (i.e. larger negative values of ε)

$$\alpha \approx \frac{V}{\left(N + \frac{\varepsilon_{medium}}{\varepsilon - \varepsilon_{medium}}\right) + A\varepsilon_{medium}x^2 + B\varepsilon_{medium}x^4 - i\frac{4\pi^2\varepsilon_{medium}^{3/2}}{3}\frac{V}{\lambda^3}} \tag{4.18}$$

with A and B being polynomial expressions of the variable N. This is an empirical formula, which was derived by fitting data extracted from dark field optical spectroscopy of individual nanorods of various sizes and aspect rations. In a recent work, Au nanorods with very large aspect ratios (around 50), which were synthesized via an electrochemical approach, exhibited a shift in the longitudinal plasmon resonance that was far bigger than that predicted by the Gans' theory [31]. The maximum of the band was at 12 μm, while Gans' theory predicts only 4 μm. This is a clear case in which retardation effects are extremely important.

Finally, it must be noticed that the non-local effects discussed in Sect. 4.3 for small spherical nanoparticles do not influence the longitudinal resonance in ellipsoids, since their long axis is usually longer than the mean free path of the electrons.

4.6 Plasmons in Elongated Nanoparticles of Arbitrary Shape

For nanoparticles of arbitrary shapes, it is not possible to solve analytically the Maxwell equations, therefore numerical approximation methods have to be sought. Many methods have been developed so far, each of them characterized by its peculiarities, advantages, and disadvantages. For a coverage of them, see for example [8, 9].

One popular computational approach is based on the boundary element method (BEM) [32]. This method has been used in many problems of physics and engineering since it can solve differential equations in a space made of regions of different materials [33, 34]. Recently, it has been exploited to calculate the plasmonic response of metallic nanoparticles of arbitrary shapes [34–39]. With respect to other methods, its computational requests are not so high, because it only deals with the interfacial region of the particles and not with the volume (hence there is a reduction of one dimension in the computational problem). In practice, the electromagnetic field inside a region of a given material is completely defined by the fields and the derivatives of the fields at the boundary of the region. In the case of a metal nanoparticle immersed in a medium of another material, one can formulate the electromagnetic field scattered by the particle as boundary charges and currents. Boundary conditions are then imposed such that the parallel components of the electric and magnetic fields are continuous at the interfacial region between the particle and the surrounding medium, and this leads to a system of surface-integral equations. These surface integrals are then discretized, i.e. they are turned into summations over surface elements in which the overall interface is tessellated. An additional advantage of this method is that when the system presents an overall cylindrical symmetry, the calculations are considerably simplified.

Perhaps one of the most popular numerical approaches for calculating the optical response of metal nanoparticles is the discrete dipole approximation (DDA) [4, 9, 40–42]. In this approach the particle is immersed in a cubic box

made of N polarizable cubic "elements". Each element can be occupied by a portion of the nanoparticle, or it can be "external" to the nanoparticle: therefore any arbitrary shape for the nanoparticle can be modeled. Each *i*th element, positioned at distance $\boldsymbol{r}_i$ from the origin of the box, has dipolar polarizability α_i. In each element, the polarization induced by the interaction with the local electric $\boldsymbol{E}_{loc}$ field is:

$$\boldsymbol{P}_i = \alpha_i \boldsymbol{E}_{loc}(\boldsymbol{r}_i) \tag{4.19}$$

The local field in each element (we call it simply $\boldsymbol{E}_{loc,i}$) is the sum of the incident field in the element ($\boldsymbol{E}_{inc,i}$) with the fields generated by all the other dipoles inside the particle ($\boldsymbol{E}_{dipole,i}$):

$$\boldsymbol{E}_{loc}(\boldsymbol{r}_i) = \boldsymbol{E}_{inc,i} + \boldsymbol{E}_{dipole,i} = \boldsymbol{E}_0 exp(i\boldsymbol{k} \cdot \boldsymbol{r}_i) - \sum_{j \neq i} \boldsymbol{A}_{i,j} \cdot \boldsymbol{P}_j \tag{4.20}$$

Each term in the summation above can be considered as the scattered field produced by the element *j* at the position of the element *i*, so it also contains the polarizability α_j of the jth element. Expressions for $\boldsymbol{A}_{i,j}$ can be found in many reviews [4, 9, 40–42]. Therefore, one is faced with a $3N \times 3N$ "interaction" matrix *A*, and needs to solve 3N complex linear equations in order to identify the polarization vector $\boldsymbol{P} = \sum \boldsymbol{P}_i$ from which the optical properties of the particle (including the extinction cross section) can be derived. There are actually many ways of solving the equation above, via various approaches, like for example the iterative approach using the conjugate gradient method [40]. It is clear that to model a nanoparticle accurately, a three dimensional grid with a large number of elements is required, which can be computationally demanding, therefore methods have been developed by which the summation over the dipole fields in the expression (4.20) are performed using code based on Fast Fourier transforms [40].

Based on the DDA approach, the extinction coefficients for particles of a wide variety of shapes have been calculated, including discs, prisms, spheroids, cubes, icosahedra, and so on. Even only focusing on metallic nanorods, it is worth to note that in most cases their resemblance to spheroids is very poor, so that the Gans' approach described above does not give a detailed picture of their optical response. Chemically synthesized gold nanorods, for example, can have pentagonal cross-section, resulting from their multiple-twinned structure [43]. Some of these chemical approaches yield instead rods that are single crystals with octagonal cross section [44]. Also, in some cases the rods have rounded end-caps, while in other cases the end-caps are irregular. With recent advances in chemical synthesis, in optical microscopy of individual nanoparticles, and in computational approaches, it has been possible to study in detail the plasmonic properties of metal nanorods as a function of their geometrical parameters [7, 45, 46]. Especially in the case of nanoparticles synthesized in solution, the samples are basically in the form of diluted colloids, so that particle–particle and particle–substrate coupling effects are not present. Therefore the investigation of their size- and shape-dependent optical

properties is much facilitated. Indeed, the random orientation of nanoparticles dispersed in a medium leads to an absorption spectrum that represents the average contribution of all the plasmon resonances.

Myroshnychenko et al. [8] reported a systematic computational study on the evolution of longitudinal plasmon energy and full-width at half maximum (FWHM) of the band for gold nanoparticles having either ellipsoidal shapes or rod shapes with hemispherical end-caps. These properties were monitored as a function of the length and the aspect ratio of the particles, and were compared to the plasmonic properties of spherical nanoparticles. The calculations were done using the BEM method. The results are summarized in Fig. 4.5. For all the particles considered in the calculations, the plasmon mode is of dipolar character. For the rods and ellipsoids, the calculations are referred to the longitudinal plasmon mode, and the exciting radiation has its electric field oscillating along the long axis of the particles. It can be seen from Fig. 4.5 that, for a fixed aspect ratio (therefore moving along one of the lines connecting the symbols), in both rods and ellipsoids the plasmon resonance shifts to the red, as in spheres. This is basically due to retardation effects, as discussed above. The plasmon resonance in rods and ellipsoids shifts to the red also when the length is fixed, but the aspect ratio is increased (therefore in the graph we are moving from right to left along an horizontal line), but now for a different reason. As we recall from Gans' theory for spherical ellipsoids, an increase in aspect ratio at constant length means a decrease in polarizability along the long axis, which shifts the resonance condition to longer wavelengths.

A further interesting aspect to consider is decrease of FWHM of the longitudinal plasmon peak for rods and ellipsoids at increasing aspect ratios, at fixed length (Fig. 4.5c). This can be explained by considering that the absorption in mainly dictated by the ratio $\varepsilon_{im}/|\varepsilon|$, which drops at increasing wavelength.

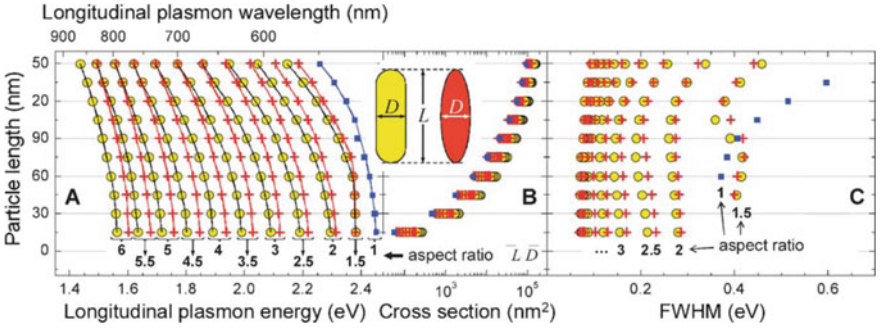

Fig. 4.5 **a** Longitudinal plasmon energy for ellipsoidal Au nanoparticles (*red crosses*) and rod-shaped Au nanoparticles with hemispherical end-caps (*yellow circles*) as a function of the particle length and aspect ratio. The *blue squares* are referred instead to spherical nanoparticles (all particles were considered as being immersed in air); **b** Extinction cross section at the peak maximum; **c** Full width at half maximum for the various series of samples. Taken with permission from Ref. [8]

Therefore a shift to the red in the plasmon resonance is accompanied by a decrease in the absorption. Finally, if the aspect ratio is increased, but the length is increased, the FWHM increases, due to radiation damping effects, which we have discussed before (see also Sect. 4.7 for more details on the plasmon linewidth).

Another systematic study, in this case on the evolution of optical properties in silver, gold and copper nanoparticles of various elongated shapes, was recently carried out by Noguez and co-workers [7]. In their calculations, based on the discrete dipole approximation, they first modeled non-elongated shapes, namely a sphere, a dodecahedron, a decahedron, an octahedron and a cube. Then they elongated these shapes along one direction, and obtained respectively a prolate ellipsoid, an hexagonal prism, a pentagonal prism, a tetrahedral prism and a rectangular prism, all with aspect ratio equal to 2.8 (see Fig. 4.6a). In all the calculations, the volume of the particles was kept constant and equal to that of a sphere of 40 nm radius. The main aim of the study was to highlight the change in the plasmonic properties in a prism when the number of lateral facets goes from practically infinite (the prolate ellipsoid) down to four (the rectangular prism). The extinction efficiencies were calculated by averaging over all the possible orientations of the particles with respect to the incoming radiation, so as to simulate the extinction spectrum of nanoparticles in a colloidal solution.

Figure 4.6b reports the optical extinction spectra, along with the contribution from absorption and scattering, of decahedral shaped particles and of the corresponding pentagonal prisms, for Ag, Au and Cu nanoparticles. In general, at short wavelengths, the contribution from absorption is predominant, while scattering

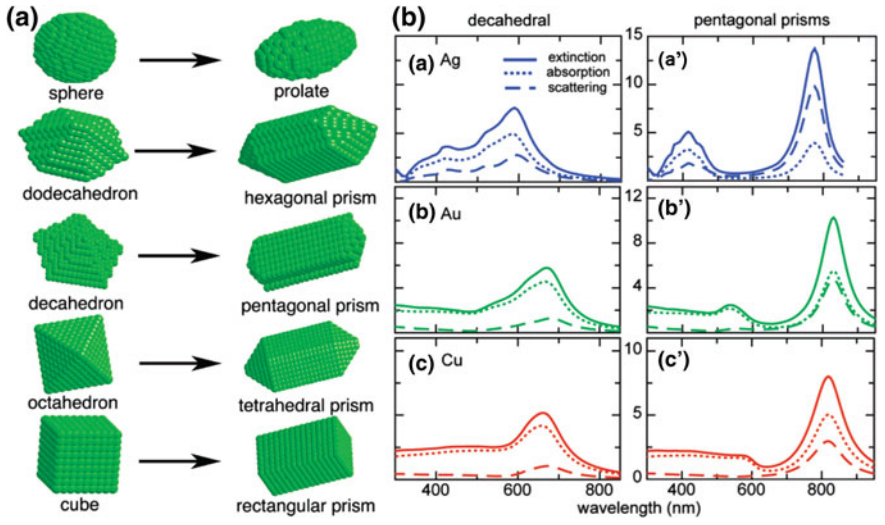

Fig. 4.6 **a** Evolution from sphere, dodecahedron, decahedron, octahedron and cube, to their corresponding elongated shapes. **b** Optical extinction spectra, along with the contribution from absorption and scattering, for decahedral shape particles and the corresponding decahedral prism for Ag, Au and Cu nanoparticles. Taken with permission from Ref. [7]

dominates at longer wavelengths. Also, we notice that the contribution to scattering is higher in Ag than in Au and in Cu. In the spectra of the prisms, one clearly sees the splitting of the plasmon peak into a longitudinal peak at longer wavelength, and a transverse peak at shorter wavelength, with respect to the peak of the "parent" decahedral particle. This transverse plasmon peak is clearly evident in the Ag nanoprisms, less evident in Au, and even less in Cu, because in the two latter materials they start overlapping with absorption due to interband transitions (below 600 nm for copper and below 550 nm for gold). In silver, interband transitions are found below 325 nm, so they do not interfere with the transverse plasmon peaks (the reader is invited to look again at Fig. 4.2, which displays the dependence of the real and imaginary component of the dielectric function on the wavelength). Especially for silver, the transverse plasmon peak is in reality the sum of a multitude of peaks, and this is due to its pentagonal cross section, which strongly deviates from a circular shape: the single transverse mode in the prolate ellipsoid is split into several transverse modes for the pentagonal prism case.

Figure 4.7 reports the extinction spectra for all the shapes studied by the authors. In the case of the sphere, for Ag two peaks can be distinguished clearly, the one at shorter wavelengths being due to the quadrupolar mode, which for Au and Cu is much less intense and practically hidden by inter-band transitions. In the ellipsoids, the dipolar mode splits into a longitudinal one and a transverse one, and again this is much clearer in Ag than in Au and in Cu. In all the other non-elongated shapes different from the sphere (dodecahedron, decahedron, octahedron and tetrahedron), the plasmon band (as anticipated before for the decahedron) is not a single peak, but is the sum of a multitude of peaks. The smaller the number of facets in these shapes, the more distinct and sharper become the individual peaks, each related to a different charge distribution mode, and more spaced they are from each other. The most striking case is that of the silver cube, in which four peaks are clearly visible.

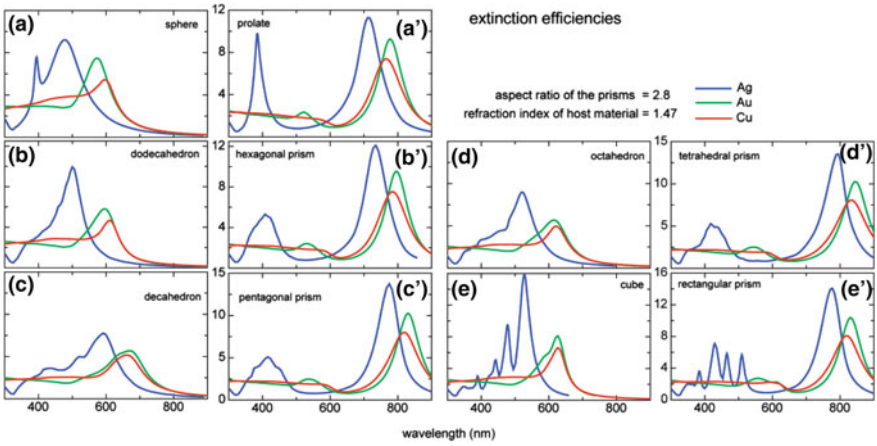

Fig. 4.7 **a** Extinction efficiencies for various nanocrystal shapes in the case of Ag, Au, and Cu. Taken with permission from Ref. [7]

Likewise, in the corresponding silver prisms, for the transverse plasmon band, the smaller the number of lateral facets in the prisms, the more distinct and sharp become the peaks related to the various transverse modes. Again, in the rectangular prism, four distinct and well separated transverse modes are visible.

In recent work by Schmucker et al. [47] Au nanorods of various diameters (from 35–100 nm) and lengths were synthesized electrochemically using anodic aluminum oxide templates. The authors then recorded their optical extinction spectra and carried out a series of calculations based on the discrete dipole approximation. The peculiarity of this work stands in the study of the dependence of the dipole plasmon wavelength on both the length and the diameter of the rods. The results of the calculations, which agreed well with the experimental data, were then used by the authors to derive an equation that correlates the longitudinal plasmon resonance in rods to both their length and diameter, and which is valid even beyond the quasi-static regime [47].

4.7 Dephasing of Surface Plasmons: Spherical Versus Elongated Particles

Surface plasmons in metal nanoparticles dephase (i.e. decay) through both inelastic processes (characterized by a time constant T_1) and elastic processes (characterized by a time constant T^*) [30], and the overall time constant of plasmon decay T_2 is defined as:

$$\frac{1}{T_2} = \frac{1}{2T_1} + \frac{1}{T^*} \tag{4.21}$$

Inelastic processes, which dominate the plasmon decay, can be further classified into radiative and non-radiative decay processes. Radiative processes (i.e. radiation damping) are relevant only in large particles, as discussed above. Non-radiative processes instead are important also in small particles and are due to scattering of individual electrons into electron-hole pairs, i.e. electrons that participate in the collective oscillation can give off part of their energy via a scattering event and form an electron-hole pair. The latter can occur either via intraband excitation (i.e. electron-hole pairs created within the conduction band), or via interband excitation (electrons from the *d* band are promoted in the conduction band). All the various processes are sketched in Fig. 4.8a. In some applications (for example in surface enhanced Raman scattering, see later), it is desirable for the dephasing time to be as long as possible, and furthermore it is important to minimize the non-radiative decay, for example in order to minimize sample heating. The dephasing time is directly correlated to the homogeneous linewidth $\Gamma = 2\hbar/T_2$ of the surface plasmon, which can be measured for individual particles.

Sönnichsen et al. [30] recorded light-scattering spectra from individual gold nanoparticles (both nanorods with various aspect ratios and spherical nanoparticles

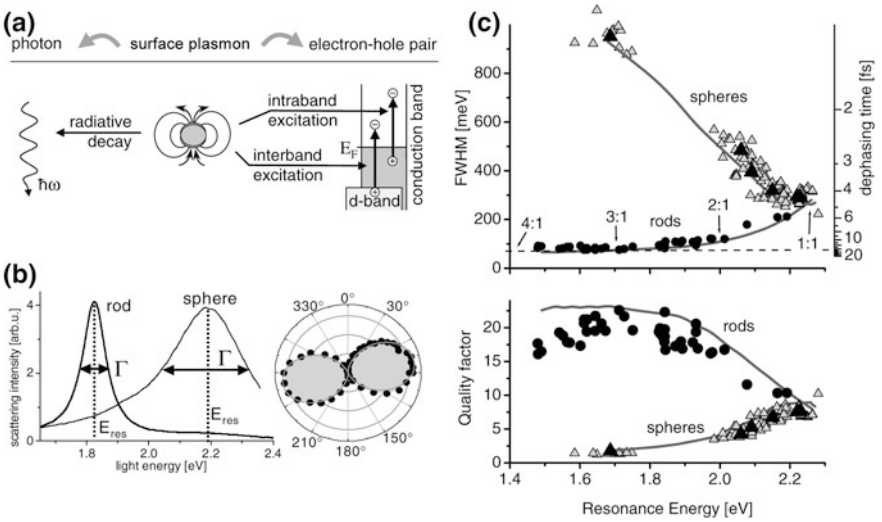

Fig. 4.8 **a** Sketch of the radiative and non-radiative decay processes of surface plasmon modes in metal nanoparticles; **b** Typical scattering spectra of individual spherical gold nanoparticles and nanorods, both excited with linearly polarized light. In the case of nanorods, the resonance was excited by light that was polarized along the long axis of the rod, such as to excite only the longitudinal plasmon mode. On the *left* polar plot of the intensity from the longitudinal plasmon mode in an individual gold nanorod as a function of angle between the long axis of the rod and the polarization direction of the exciting light; **c** *Top graph* full width at half maximum Γ and dephasing time T_2 for the various samples analyzed, as a function of the plasmon resonance energy. *Black circles* are referred to rods, *gray triangles* are referred to spheres, and *black triangles* are referred to averages over several spheres having the same nominal diameter. The *lines* in the graph are the results of exact electrodynamic calculations using the Mie theory. *Bottom graph* same data as in the top graph but plotted as quality factor (resonance energy over plasmon linewidth). Taken with permission from Ref. [30]

with various diameters), they estimated Γ for every particle and from it they derived the dephasing time T_2. Typical scattering spectra of individual spherical nanoparticles and nanorods, both excited with linearly polarized light, are reported in Fig. 4.8b. In the case of nanorods, the resonance was excited by light that was polarized along the long axis of the rod, such as to excite only the longitudinal plasmon mode. The full width at half maximum Γ and the dephasing time T_2 for the various samples analyzed are reported in Fig. 4.8c, top graph, as a function of the plasmon resonance energy. In spherical nanoparticles, the shift towards the red of the resonance energy is due to retardation effects (as discussed earlier), while in nanorods is due to increase in the aspect ratio (the experiment probed the longitudinal plasmon mode in rods). In spheres of the same nominal diameter, there was a distribution of both resonance energies and Γ (gray triangles in the graph of Fig. 4.8c), most likely due to local fluctuations in the environment close to each particle, but averaging both resonance energy and Γ for the samples with the same nominal radius gave values (black triangles in the same graph) that were well in line

with the theory (the solid lines in the graph). In spheres, the dephasing time decreased for the particles with the more red-shifted resonance, hence the larger particles. This can be explained by an increase in the radiation damping, which both shifts the plasmon resonance to lower energies and broadens the peak, as discussed earlier in this section. In rods, however, the dephasing time increased significantly for particles with more red-shifted resonance, hence for larger aspect ratio rods (black circles in the graph). Such increase in dephasing time could not be ascribed to radiative processes, since these processes are negligible in particles with small volumes (contrary to spheres, the rods studied could have large aspect ratios but their overall volume was small). On the other hand, the increase could be explained easily by considering that inter-band excitations require a threshold energy of 1.8 eV. In large aspect ratio rods, longitudinal plasmon modes can have resonance energies comparable to or even smaller than 1.8 eV, therefore for such rods the non-radiative decay channel via inter-band transition is precluded. Also in spheres with plasmon resonance energy below 1.8 this decay channel is precluded, but these spheres have such a large volume that in them radiative damping effects dominate the decay process. Hence in such spheres the overall plasmon decay time is short.

Another important parameter involved in these measurements is the quality factor Q, which is the ratio of the resonance energy over the plasmon linewidth. This is reported in the bottom graph of Fig. 4.8c for the various samples analyzed. It represents the enhancement of the oscillation amplitude of an oscillating system with respect to the driving amplitude, and represents the field enhancement in the case of surface plasmons. This is an important figure of merit in surface enhanced Raman scattering (SERS, see later). Hence one conclusion is that large aspect ratio rods are more suitable than spheres for SERS.

A consequence of the reduction of plasmon dephasing in rods with respect to spheres is that the scattering quantum yield at resonance conditions, defined as the ratio between the scattering efficiency Q_{sca} and the total extinction efficiency Q_{ext} is higher in rods than in spheres [48]. Also, for rods having the same aspect ratio, but different volumes, larger rods have a higher scattering efficiency than smaller rods (the same is true for spheres of different diameters, as discussed above) [48]. Hence large particles are in general more suitable for imaging applications, since they are good light scatterers, while smaller particles, in which a larger fraction of the absorbed light is not re-emitted but instead is converted into heat, are more suitable in applications like for example photothermal therapy [12].

4.8 Ultrafast Electron Dynamics in Metal Nanoparticles: Overview

Ultrafast techniques measure the transient change in the optical properties of a sample. When a femtosecond laser pulse excites a metal, the electron distribution, which is initially in equilibrium and is given by the Fermi distribution, is

perturbed, such that "hot electrons" are created. Electrons then scatter elastically which each other, until a new Fermi distribution is reached, corresponding to a higher temperature of the electron gas. The pulse can be in the infrared region, which perturbs only the electrons in the conduction band, or it can be in the UV–visible region, in which case interband transitions might also occur [49–51].

In order to understand the relaxation dynamics of these hot electrons in metals, the two-temperature model is often invoked, which models how energy is exchanged between electrons and phonons [49–51]. Due to the large population of electrons, electron–electron scattering is fast (it is actually of the order of hundreds of fs), so that the hot electron gas is assumed to thermalize quickly to a temperature T_{el}, which differs from that of the lattice T_{lat}. Also, we can assume that the duration of the laser pulse is much shorter than the electron–phonon relaxation time, the latter being of the order of a few (1-4) ps. Based on these considerations, the dynamics leading to electron thermalization due to exchange of energy with the lattice can be described by a set of two coupled equations [50, 51]:

$$C_{el}(T_e)\frac{\partial T_{el}}{\partial t} = \kappa\Delta^2 T_e - G_{e-ph}(T_{el} - T_{lat}) + LP(z,t) \tag{4.22}$$

$$C_{lat}\frac{\partial T_{lat}}{\partial t} = G_{e-ph}(T_{el} - T_{lat}) \tag{4.23}$$

In the expressions above, $C_{el}(T_e) = GT_e$ is the heat capacity of the electrons, and is proportional to the electron temperature, while C_{lat} is the heat capacity of the lattice, and can be approximated as $3k_B n$, where k_B is the Boltzmann's constant and n is the atomic density of the metal. G is the electron–phonon coupling constant [16]. In the first equation, the first term is related to thermal conductivity losses, the second term describes electron–phonon coupling, and the third term describes the temporal evolution of the heating laser source [50, 51]. The maximum temperature T_e reached by the electron gas is basically dictated by the energy of the laser pulse. El-Sayed et al. [50], starting from different values of G and by modelling a laser heating pulse as a Gaussian with FWHM = 0.3 ps and peaking at 1 ps, solved numerically the two coupled equations above for a film of Cu metal under a specific set of conditions. The evolution of T_e and T_{lat} over time is shown in Fig. 4.9a, b. The difference between (a) and (b) is basically the intensity of the laser pulse. From the figure it can be clearly seen that an increase in the coupling constant leads to a faster decay of T_e and faster increase of T_{lat}, therefore to a shorter relaxation time, while a more intense laser pulse leads to a higher value of T_e and to a longer relaxation time. The latter effect can be easily correlated with the increase in the electronic heat capacity at higher temperature. In a more elaborate approach, which takes into account the surrounding of the metal as a third thermal reservoir at a constant T_{sur} temperature, the second equation is replaced by the following one [52]:

$$C_{lat}\frac{\partial T_{lat}}{\partial t} = G_{e-ph}(T_{el} - T_{lat}) - G_{ph-ph}(T_{lat} - T_{sur}) \tag{4.24}$$

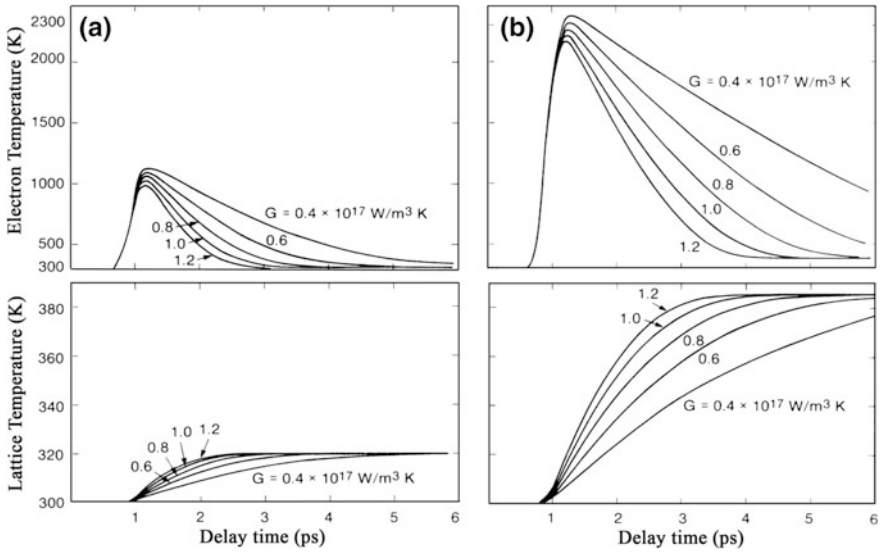

Fig. 4.9 Time evolution of the electron and lattice temperature in a Cu film 200 Angstrom thick, as modeled by solving numerically the coupled Eqs. (4.22) and (4.23), for two different laser pulse energies [15 nJ (**a**) and 65 nJ (**b**), laser pulse modeled as Gaussian with FWHM = 0.3 ps and peaking at 1 ps], and for various values of the electron–phonon coupling constant *G*. *Top panels* refer to electron temperature, *bottom panels* refer to lattice temperature. Taken with permission from Ref. [50]

In the expression above G_{ph-ph} is the coupling constant of the metal with the surrounding medium.

What said so far applies to metals in general. In nanoparticles too, the electron–phonon relaxation time was found to depend on the intensity of the laser pump [53] and is longer at higher pump intensities, for the same reason discussed above (namely the temperature dependence of the electron heat capacity). The questions that we want to address now are first of all if the relaxation dynamics in metal particles depends on particle size, and then how the shape of the nanoparticles influences the electron–phonon interactions. We address the first question here, and the second question in paragraph 4.9. In principle, electron–phonon interactions should decrease with decreasing particle size, which should lead to an increasing lifetime of electron–phonon relaxation. An intuitive guess for this is that the density of states for both electrons and phonons decreases with decreasing particle size, which leads to lower spectral overlap, hence less coupling. However, the bulk band structure in metals like Au is already developed for sizes above 2 nm, and the spacing between the electronic levels is already larger than the thermal energy, so that there is still good spectral overlap between electron and phonon densities of states. At very small sizes, for example less than 1 nm for Au nanoparticles, the relaxation time increases, indicating that in this size regime the

nanoparticles behave like molecular clusters, the spacing between electronic levels increases, and therefore electron–phonon coupling is definitely weaker [54, 55].

On the other hand, the electron free path in metals is in the 30–50 nm range [16], therefore effects related to surface scattering of electrons should contribute to shorten the electron–phonon relaxation time, in this case via coupling with surface phonon modes. This seems reasonable too, since electron-surface scattering was found to be responsible for dephasing of the coherent plasmon oscillations (see above). It turns out however, that coupling of electrons with surface phonons depends on the ratio between the number of valence band electrons and the atomic mass of the metal [56], which influences the electron-surface scattering cross section. This ratio in gold is small (large atomic mass, only one valence electron). Various studies [57, 58] have shown that the electron–phonon relaxation time in gold nanoparticles down to 2–2.5 nm diameter is of the order of 1 ps, which is practically the same as in bulk gold. Therefore the electron-phonon coupling constant, at least for Au, remains practically unchanged down to 2 nm. The ratio is instead larger in other materials, like for example gallium, silver, and in tin (see [31] and references cited therein). As an example, for tin nanoparticles (tin has 4 valence electrons and much lighter mass) decreasing relaxation times with decreasing particle size (from 6 down to 2 nm) were measured [59].

Another point that deserves further attention is that the energy exchange of the metal nanoparticles with the surrounding medium should be quite fast, due to their high surface to volume ratio. The time scale for phonon–phonon coupling is of the order of hundreds of picoseconds, and indeed the relevant parameter is proportional to the square of the nanoparticle radius [11, 60]. Various reports (see for example [11]) have shown that the matrix in which the nanoparticles are embedded has also an influence on the electron-phonon constant, so on the relaxation time for this process, for the same sample of nanoparticles, longer relaxation times are found if the matrix (for example the solvent) has a low thermal conductivity or if there is poor thermal contact between the nanoparticle and the matrix. The latter effect is also dependent on the type of stabilizing molecules that coat the surface of the nanoparticles.

Electron–phonon and phonon–phonon relaxation processes can be followed by monitoring the transient absorption spectra of a solution of nanoparticles at increasing delay times following excitation by a laser pulse (this is done by a second broad band probe pulse with a specific delay time). The plotted signal is the difference between the probe pulse and a reference pulse that is recorded before the pump pulse, which in practice corresponds to the optical absorption spectrum of the unperturbed system (the top spectrum in Fig. 4.10a). The negative transient absorption (ΔA) (a "bleach") observed in the region of the maximum plasmon absortipon means that in the perturbed system, following the laser pulse, there is a decrease and broadening in plasmon absorption. This bleach recovers over time, due to electron–phonon and then to phonon–phonon scattering processes (Fig. 4.10a, inset). The bleach in the plasmon absorption can be explained as due

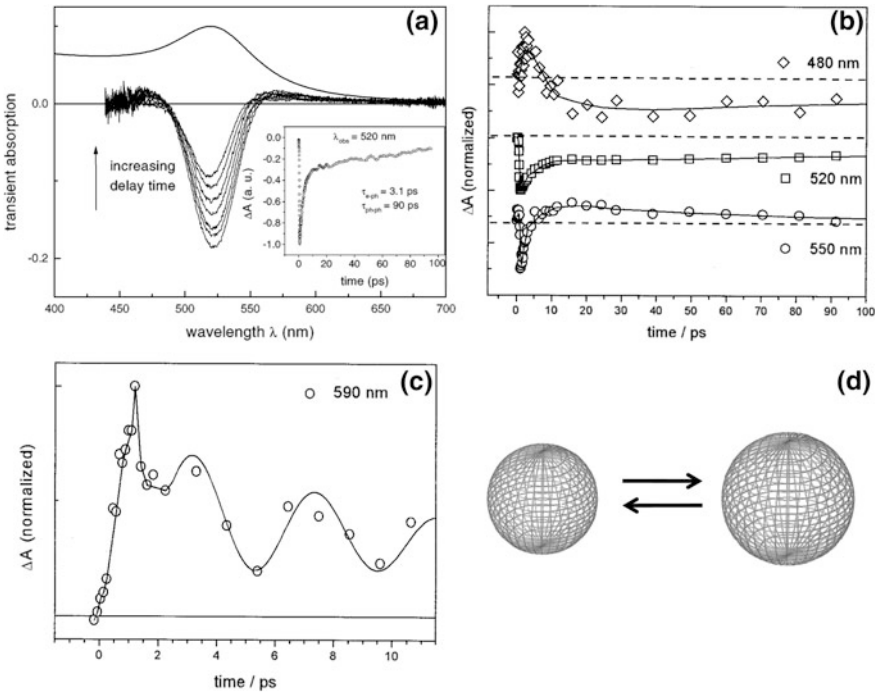

Fig. 4.10 **a** Transient absorption spectra of gold nanoparticles with a diameter of 15 nm at various delay times following a 400 nm femtosecond pulse. The top spectrum corresponds to the reference spectrum, i.e. the optical absorption spectrum of the unperturbed system. The two positive absorption bands that appear in the transient spectra at the opposite sides of the bleach signal are due to the initial broadening of the plasmon band at higher electron temperature. The inset shows the recovery of the bleach signal (at the wavelength corresponding to the maximum of the peak) over time, which can be modeled with two characteristic decay times, a short 3.1 ps time ascribed to electron–phonon coupling, and a much longer time corresponding to phonon–phonon coupling (i.e. thermalization of the particles with the matrix). Electron–electron coupling is beyond the instrument resolution in the present case. Taken with permission from Ref. [11]; **b** Temporal evolution of the transient absorption at various wavelengths (namely 480, 520, and 550 nm). Taken with permission from Ref. [3]; **c** The evolution of the transient absorption signal at 590 nm during the first picoseconds. The oscillation of the signal is ascribed to acoustic phonon breathing mode. Taken with permission from Ref. [3]; **d** Sketch showing the acoustic breathing mode in spherical nanoparticles

to dependence of the dielectric function of the metal on the electron temperature [56]. The higher the electron temperature, the less intense and more broadened is the plasmon absorption, and this can be verified if the modified value of the dielectric function is entered in the Mie equations and the equations are solved. A transient absorption can also be positive in certain regions of the spectrum. This can be ascribed to broadening and shifting of the plasmon band. In Fig. 4.10b, for example, the time trace of the signal at 480 nm, on the blue side of the plasmon

band, shows first a positive absorption, then a bleaching. The initial absorption can be ascribed to broadening of the band. Then, as the energy is transferred from the electron gas to the lattice, the particle heats and expands, leading to a decrease in electron density (i.e. the particle has still same number of electrons, but now has a bigger volume) and as such to lower plasmon absorption. In the 520 nm trace, at the maximum of the plasmon absorption, instead only bleaching is observed, consistent with what said earlier. At 550 nm, the first bleach, like for the 520 nm trace, is due to lower plasmon absorption and broadening due to higher electron temperature. Then, as the lattice heats, the plasmon narrows and shifts to the red, leading to a positive absorption.

One interesting effect concerns the lattice vibrations observed in the electron relaxation dynamics of some metal nanoparticles (see Fig. 4.10c–d). Femtosecond transient absorption spectra have shown modulation of the order of tens to hundred picoseconds. This modulation is explained as due to excitation of a "breathing mode" of the particle, basically a coherent expansion and contraction in the volume of the particle, following a fast heating of the particle (Fig. 4.10d). Since the position of the plasmon depends on particle size, such coherent volume change over time leads to an oscillation in the transient absorption. The frequencies of these acoustic modes are found to be inversely proportional to the nanoparticle radius (see [3, 61] and references therein). Apparently, these frequencies agree well with those calculated from continuum elastic theory [62].

4.9 Ultrafast Dynamics in Elongated Nanoparticles

Various experiments have indicated that the shape of metal nanoparticle does not influence the electron–phonon relaxation time. As an example, Link and El-Sayed [3] recorded the bleach recovery of the plasmon band of two spherical gold nanoparticles having different sizes. These were then compared to the bleach recovery of the longitudinal and transverse plasmon signal of a sample of rod-shaped gold nanoparticles. In the experiments, the optical density of the samples and the intensity of the laser pulse were adjusted so as to reach the same electron temperature in all the samples. In all the experiments, comparable electron–phonon relaxation times were found, thus indicating that neither size nor shape influence electron–phonon coupling significantly (Fig. 4.11a). Other experiments have confirmed these results. In a recent study [31] the surface plasmon behavior of nanorods with very large aspect ratios (around 50) was studied, for which the longitudinal plasmon resonance was found to fall in the mid-infrared (12 μm). Also in that case, electron–phonon coupling constants similar to that of the spheres and shorter rods were measured.

Several groups have found that some aspects of the plasmon dynamics in rods differ from those of spherical nanoparticles [31, 57, 63]. As we have seen before,

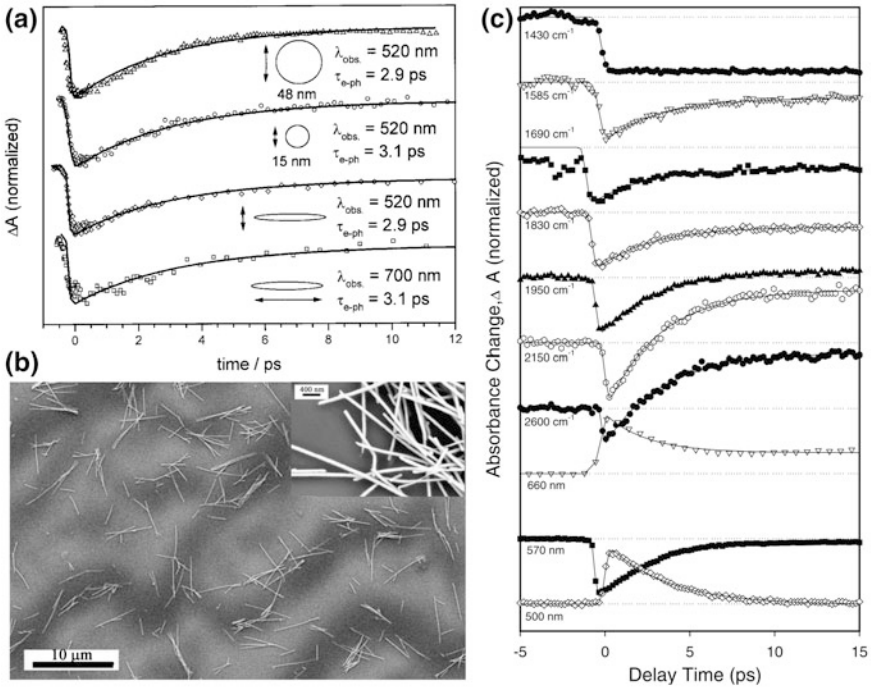

Fig. 4.11 **a** Bleach recovery of the plasmon absorption band for gold nanoparticles with diameters equal to 15 and 48 nm, and for the longitudinal and transverse plasmon mode in a sample of gold nanorods with aspect ratio equal to 3.1. Taken with permission from Ref. [3]; **b** Scanning electron microscope images of Au rods with large aspect ratios (50) and **c** normalized time traces at different frequencies/wavelengths. The sample was excited at 400 nm. The longitudinal plasmon resonance was peaked at 830 cm^{-1}, which means that in all the experiments the sample was probed on the blue side of the plasmon band. As the probe frequency is increased (see for example the traces at 2,150 and 2,660 cm^{-1}), the bleach recovery is followed by absorption. Time traces at 500 and 570 nm probe instead both sides of the transverse plasmon band. **b** and **c** are taken with permission from Ref. [31]

following a laser pulse, the time trace on the blue side of the plasmon band in spherical nanoparticles shows first an absorption (due to plasmon broadening) and then a bleach (due to plasmon narrowing and shifting to the red). In rods of various aspect ratios, instead, first an initial bleach is observed, which later recovers to an absorption [31, 57, 63]. The initial dynamics is consistent with the usual broadening and decrease in intensity of the plasmon band, immediately after the pulse, due to high electron temperature. Then, the bleach recovery to an absorption is consistent with a blue shift of the plasmon band, upon heating of the lattice. This is therefore opposite to what found in spheres. An explanation for this behavior was ascribed to a radial expansion of the rod, due to lattice heating, with a consequent decrease in the aspect ratio of the rod and therefore to a blue shift of the longitudinal plasmon band. An example of such behavior is shown in Fig. 4.11c for long aspect ratio Au nanorods (scanning electron microscope images of the rods

are shown in Fig. 4.11b). Here, the more the time trace is shifted to the blue side of the plasmon band (peaking at 830 cm^{-1}), the more evident is the recovery of the initial bleaching to an absorption.

Also in Ag ellipsoids and Au nanorods, oscillations in the transient absorption signal, following femtosecond excitation, were detected [64–66]. In silver ellipsoids, for example, depending on whether the laser probe was resonant to the longitudinal or to the transverse plasmon band, the oscillation was found to have a period equal to $2L/c_1$ and $2d/c_1$, respectively, with L being the length of the rod and d its diameter, and c_1 is the longitudinal speed of light in bulk gold [64]. On the other hand, from continuum mechanics it can be calculated that in a rod-shaped object made of an elastic isotropic material, in addition to a fundamental breathing mode (i.e. a mode in which both the diameter and the length are simultaneously expanded and compressed), a fundamental extensional mode exists, in which an axial expansion is accompanied with a radial compression and the other way around (Fig. 4.12a). In the first case, the bulk modulus of the material is involved, while in the second case the Young modulus is involved [4, 63].

Hu et al. calculated the natural resonant frequencies for the extensional and breathing modes for a cylindrical rod in the limit of high aspect ratio $(L/d \gg 1)$ and found:

$$\omega_{ext}^{(n)} = \frac{2n+1}{L}\pi\sqrt{\frac{E}{\rho}} \tag{4.25}$$

$$\omega_{br}^{(n)} = \frac{\tau_n}{d}\sqrt{\frac{E(1-\nu)}{\rho(1+\nu)(1-2\nu)}} \tag{4.26}$$

In the expression above, τ_n is an eigenvalue, E is the Young's modulus (defined as the ratio of the stress to the strain of the material, see also Sect. 4.7 of this review article), ρ is the density of the rod, ν is the Poisson's ratio of the rod. The Poisson's ratio is the ratio of the relative contraction strain, or transverse strain normal to the applied load, to the relative extension strain, or axial strain in the direction of the applied load. It varies from material to material, and in bulk gold is 0.42. Figure 4.12b shows the results of finite element analysis on the temporal response of gold rods with aspect ratio equal to 5. In the figure, the Fourier components of the temporal response of the change in volume are reported versus the normalized frequency:

$$\bar{\omega} = \omega\frac{L}{2\pi} \tag{4.27}$$

From the figure it can be seen that the fundamental extensional mode has much lower amplitude than the fundamental breathing mode and it occurs at much lower frequency. These two modes are those that contribute the most to the vibrational dynamics of the rods. From the two equations above, one can derive the ratio of the resonant frequencies of the fundamental extensional and breathing modes:

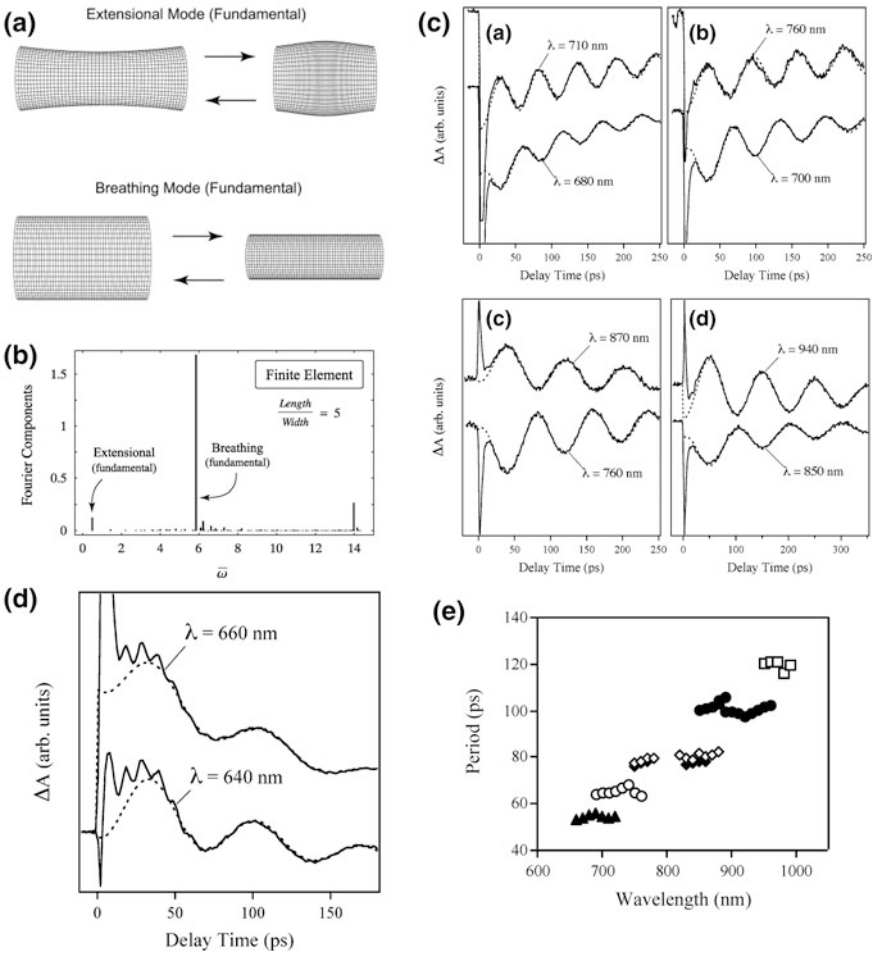

Fig. 4.12 **a** Sketch showing the extensional and breathing modes in a rod; **b** Fourier components for temporal response of change in volume normalized by initial strain, versus normalized frequency for a gold rod of aspect ratio 5, calculated using the finite element approach; **c** Transient absorption spectra of gold nanorods with average lengths of (a) 46 nm and (b) 75 nm, at two different probe laser wavelengths. **d** Transient absorption spectra of gold nanorods with average lengths of (a) 55 nm, showing a fast modulation with a period of around 11 ps, which was assigned to a vibrational mode corresponding to the breathing mode of the rods; **e** Oscillation period versus probe wavelength for rod samples of different average lengths: 46 nm (*filled triangles*), 61 nm (*open circles*), 73 nm (*filled rhombs*), 75 nm (*open rhombs*), 89 nm (*filled circles*), and 108 nm (*open squares*). All images are taken with permission from Ref. [63]

$$\frac{\omega_{br}^{(0)}}{\omega_{ext}^{(0)}} = \frac{\tau_0}{\pi}\left(\frac{L}{d}\right)\sqrt{\frac{(1-\nu)}{(1+\nu)(1-2\nu)}} \tag{4.28}$$

Therefore, in principle the aspect ratio L/d of the rod can be derived by studying the temporal response of the rod. Figure 4.12c reports the transient absorption decays for Au nanorods of two different aspect ratios, as measured by Hu [63] for two different wavelengths of the probe laser, one at each side of the plasmon absorption band. All the traces show a fast (few ps) component related to the electron–phonon relaxation process, followed by a long component (phonon–phonon relaxation) that is modulated by the coherent vibrational modes of the rods. In the various time traces, the oscillation period was in the 40–120 ps range, depending on the aspect ratio of the sample (Fig. 4.12e).

For each sample, on the other hand, the oscillation period in both traces was independent from the probe wavelength (Fig. 4.12e): this is because these particles, among those analyzed in the work, were monodisperse in length, and therefore all wavelengths probed the same nanocrystals. In other words, there was no size selective excitation of nanorods according to their aspect ratio in the sample, because basically all nanoparticles in each sample had the same aspect ratio. These oscillation periods were found to be in good agreement with those calculated using Eq. (4.25) for the fundamental extensional mode of rods of corresponding aspect ratio. The time trace of some samples exhibited in addition a faster modulation (Fig. 4.12d), which the authors attributed to the breathing mode of the rods, and which (according to the authors) should be observed mainly in rods with large diameters.

In principle, from the experimental data, since the expression relating the frequency of the fundamental extension mode to the Young's modulus is known (see above), one should be able to extract the Young's modulus. The value extracted by the authors from the gold nanorods were however much lower than the bulk value [63]. A possible explanation for this discrepancy was that the axis along which the rod stretches in the extensional mode was the pentagonal twinning axis (these rods were multiple twins with an overall pentagonal cross section along their long axis). This has no equivalent in the bulk, so that possibly different mechanical properties are to be found along this direction in nanorods. The reader will find additional details on mechanical properties of elongated nanoparticles in Chap. 7 of this review.

4.10 Near-Field Optical Properties of Metal Nanoparticles: Spheres and Rods

4.10.1 Near-Field Optical Properties: Classical Electromagnetic Theory and Quantum Mechanical Calculations

When surface plasmons in metal nanoparticles are excited by the incident light, the electromagnetic field close to the particle surface is significantly enhanced. This

can be understood in simple terms by considering a plasmon oscillation as a photon confined in the volume of the metal nanoparticle. Hence, since its wavelength in much reduced with respect to the same photon in a bulk medium, its amplitude is considerably increased. The electromagnetic field associated with such confined photon, being dependent on the square of the amplitude of the associated wave, is also quite intense. One can therefore conclude that the confinement of a photon in a nanoparticle leads to a remarkable focusing of the electromagnetic field in the nanoparticle and in the region immediately surrounding it. The nanoparticle therefore behaves as an antenna, actually an "optical antenna" (as opposed to the standard antennas which interact with microwave radiation and which are used in telecommunications). Indeed, the field decays within a distance from the nanoparticle's surface that is comparable to the nanoparticle size [67]. The strength of this field depends on a variety of factors [42, 68]. In a spherical nanoparticle, for example, it increases with the particle size, but past a certain size (for example around 60 nm in gold nanoparticles), the field decreases since the particles starts experiencing radiative damping [67]. The field is also strongly dependent on the shape of the particle. The field enhancement can be defined as $|\boldsymbol{E}|^2/|\boldsymbol{E}_0|^2$, with $\boldsymbol{E}_0$ being the incident field and $\boldsymbol{E}$ the field in the vicinity of the nanoparticle. Particles which possess regions with high curvature, like for example prisms and rods, show a field enhancement in these regions that is much stronger than in the case of spheres [42, 68]. This is also called the "lightening rod effect" [69]. Calculations on rods, spheroids and spheres using the discrete dipole approximation [68] have indicated that in all these particles "hot" sites at the regions of high curvature exhibit field enhancements of the order of 10^3, while spherical particles show enhancements only of the order of 10^2 (see Fig. 4.13).

One major limitation of calculations based on classical electromagnetic theory is that the dielectric function is assumed to change abruptly at the interface between the nanoparticle and the external environment. This assumption however, neglects the tunneling of electrons outside the nanoparticles, i.e. the spill out of their wave function, which indeed leads to a gradual variation of the dielectric function at the interface. A recent work by Zuloaga et al. [70] used first principles time-dependent density functional theory (TDDFT) to study the optical properties of silver nanorods. While the TDDFT calculations yielded longitudinal and transverse plasmon resonances that were in accordance with those found by classical calculations (see above), the local enhancement of the electric field induced by the plasmon as estimated by TDDFT was considerably smaller than that obtained using the classical approach, especially at distances shorter than 0.5 nm from the surface of the nanorod. This effect was attributed by the authors to the spill out of the electron density. Figure 4.14, left panel, a–d, shows the $|\boldsymbol{E}|/|\boldsymbol{E}_0|$ maps for four nanorods of four different aspect ratios ξ (1, 1.5, 2.5 and 3 respectively) and overall length ranging from 3.5 to 5.3 nm, calculated at the corresponding resonant plasmon frequencies [70]. The top four maps refer to classical calculations, while the bottom four maps refer to TDDFT calculations. A much smoother density profile in the TDDFT, with lower peak intensities, can

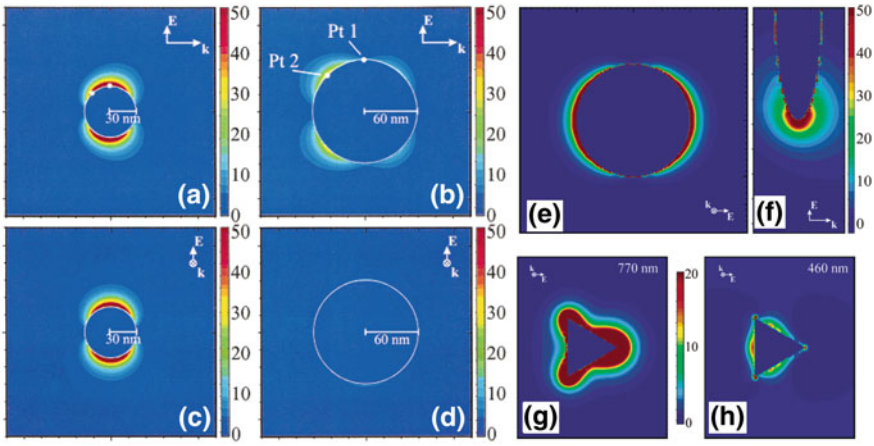

Fig. 4.13 **a–d** Electric field contours around silver nanoparticles with radii equal to 30 and 60 nm, respectively, immersed in vacuum, calculated using the discrete dipole approximation; **a** and **b** represent the cross sections passing through the center of the spheres, along the plane containing both the propagation direction (k) and the polarization direction of the incident field, while **c** and **d** represent the cross sections along the plane along the polarization direction of the incident field (indicated with "E") and perpendicular to the propagation direction. For the 30 nm sphere, the contours **c** are referred to the 369 nm light, which corresponds to the maximum in the dipolar plasmon resonance mode. For the 60 nm spheres, the contours **d** refer to the 358 nm light, which corresponds to the maximum in the quadrupolar plasmon resonance mode; **e**, **f** Electric field contours, at 775 nm (corresponding to the maximum of the longitudinal plasmon mode), around a silver ellipsoid whose volume is equivalent to that of a sphere of 80 nm radius; **e** is the cross section view passing through the center of the ellipsoid, along the plane containing the polarization direction of the incident field and perpendicular to the propagation direction; **f** is the cross section view along the plane containing both the propagation direction and the polarization direction of the incident field; **g**, **h** Electric field contours around a silver trigonal prism. Both images are cross section views passing through the center of the prism, along the plane containing the polarization direction of the incident field and perpendicular to the propagation direction, but for two different wavelengths, namely 770 nm (**g**) and 460 nm (**h**). Taken with permission from Ref. [9]

be already appreciated with respect to the classical map. The plot on the top left panel reports the maximum value of the electromagnetic field enhancement for the rods using both classical electromagnetic theory (red line) and TDDFT (blue line), as a function of aspect ratio ξ of the rod. In both approaches, the enhancement increases with increasing aspect ratio, but the classical calculations yield always a higher enhancement, and the difference with respect to the quantum mechanical calculations becomes more striking at higher aspect ratios.

The central panel of Fig. 4.14, Plot A, shows the equilibrium electronic density $n(d)$ as a function of the distance d from the surface of a rod with aspect ratio 3, both in the longitudinal direction (red line) and in the transverse direction (blue line), and also the electronic density for a sphere (black line), as found by TDDFT (negative values in d are referred to positions inside the nanoparticle). Apart from

the oscillatory behavior of the electron density, in all cases there is a similar spill out of the electronic density for about 1.6 Å (3 Bohr), as this depends only on the Fermi level of the particle [70]. However, it can be seen from Plot B of the central panel, which reports the induced screening charge density $\delta n(d)$ along the same directions as above (at the plasmon frequency), that δn increases for the nanorod along the long axis (red line). This increased electron charge density is responsible for the stronger electric field enhancement at the tip of the nanorod with respect to a sphere. So in this respect quantum mechanical calculations give a result in agreement to that of classical calculations. The main difference is that while classical calculations also predict a higher charge density at the tip of the rods, but this density does not spill out of the rod surface, quantum mechanical calculations show that such charge density can spill out of the rod considerably.

The plot A in the right panel of Fig. 4.14 reports the electric field enhancement as a function of the distance d from the surface of the particle, for a spherical silver nanoparticle, according to classical calculations (red line) and to TDDFT (black line). Plot B, still on the right panel, reports the same data but for the aspect ratio 3 rod. In both cases, one can see that there is agreement between the two types of

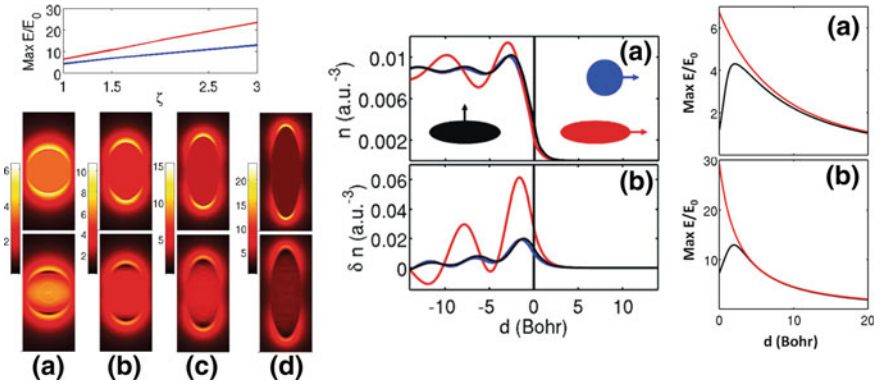

Fig. 4.14 *Left panel top* maximum value of the electromagnetic field enhancement for silver nanorods using both classical electromagnetic theory (*red line*) and TDDFT (*blue line*), as a function of aspect ratio ξ. *Bottom* $|E|/|E_0|$ maps for four nanorods of four different aspect ratios ξ (1, 1.5, 2.5 and 3 respectively) and overall length ranging from 3.5 to 5.3 nm, calculated at the corresponding resonant plasmon frequencies. The top four maps refer to classical calculations, while the bottom four maps refer to TDDFT calculations. *Central panel Plot a* equilibrium electronic density n(d) as a function of the distance d from the surface of a rod with aspect ratio 3, both in the longitudinal direction (*red line*) and in the transverse direction (*blue line*), and also the electronic density for a sphere (*black line*), as found by TDDFT. *Plot b* induced screening charge density δn(d) along the same directions in Plot **a** (at the plasmon frequency). *Right Panel Plot a* electric field enhancement as a function of the distance d from the surface of the particle, for a spherical silver nanoparticle, according to classical calculations (*red line*) and to TDDFT (*black line*). *Plot b* same data as in Plot A but for the aspect ratio 3 rod. All images are taken with permission from Ref. [70]

calculations, i.e. the same field enhancements are obtained, but only for distances larger than around 5 Å (10 Bohr). Below this distance, electric field enhancement is lower according to TDDFT, which predicts that such enhancement should go through a maximum, at about 3 Bohr from the surface, and then decline again for shorter distances. This is in striking contrast with respect to classical calculations, according to which the maximum enhancement is right at the surface of the particle. The discrepancy can be explained by considering that in classical calculations the surface charge can be represented by a delta function peaked at the surface, which results in maximum enhancement right at the surface, while according to quantum mechanics the charge induced by the plasmon resonance is spatially smeared. Such smearing is therefore responsible for both a lower field enhancement and for a shift in the position of the maximum enhancement.

Near field optical properties of individual nanoparticles can now be accessed experimentally. Advances in the fabrication of transmission electron microscopes with monochromatic electron beams (with energy resolution of 0.1 eV), in spectral imaging and in data processing have made possible to map plasmon modes in individual nanoparticles using a technique known as electron energy loss spectroscopy (EELS) [71–73]. In this experiment, high energy electrons from the beam interact with a sample and lose part of their energy by causing excitations of core-level electrons and plasmon oscillations in the sample. These electrons from the beam that have interacted with the sample have therefore less energy than that of the incident electrons. A suitable spectrometer in the microscope records then the EELS spectrum. This technique in general is used to retrieve information on the compositional features of the sample: type of elements, their oxidation state and chemical environment. Recently, several reports have appeared in which plasmon maps of metal nanoparticles of various materials and shapes have been retrieved (via EELS in scanning TEM mode) from the intensities of electrons that have lost an energy corresponding to the specific plasmon mode of the nanoparticles [71–73]. For gold nanorods for example, both longitudinal and transverse plasmon modes of a single nanoparticle have been imaged and the results have been shown to be in good agreement with calculated electron density maps. This near field imaging technique has by far higher resolution than other approaches, such as scanning near field optical microscopy.

One problem with EELS is however, that the acquisition of a spectral image may take several hours, during which contamination and radiation damage may occur in the specimen exposed to the high-intensity electron beam. In addition to this, during such a long experiment the sample may also drift in position, blurring the image and compromising the spatial resolution. To limit these effects, another technique known as Energy Filtered TEM (EFTEM) is used. Since an EELS spectrum consists of electrons that have passed the specimen and the optical system of the microscope, the latter can be used to form images by using the inelastically scattered electrons. Thus, by a specific device called “energy filter”,

an image is formed with electrons that have undergone selected energy losses in the sample. A comparison of EFTEM and STEM EELS plasmon imaging of gold nanoparticles in a monochromated TEM was reported by Schaffer et al. [74] in 2010. Finally, recent studies have even shown the possibility to image coupling of plasmon modes in interacting metal nanoparticles [75, 76].

4.10.2 Surface Enhanced Fluorescence

When a fluorophore molecule or a quantum dot is placed near the surface of a nanoparticle, its fluorescence can be quenched or enhanced. If the fluorophore is directly bound/adsorbed to the particle surface, its fluorescence is usually quenched, while if it is positioned a few nanometers away from the particle surface, there is an enhancement in the fluorescence. This effect is attributed to several reasons, which include increased absorption by the fluorophore, faster radiative decay rate of the fluorophore, and better coupling of the emission to the far field. Hence the metal nanoparticle is practically behaving as a nano-antenna, which collects the incident light, concentrates it spatially, due to the field enhancement effect described above, and conveys it to the fluorophore. This effect is maximized when the plasmon resonance of the particle is tuned such as to maximize the degree of spectral overlap with the dye. Since in metal nanoparticles, especially in nanorods, the frequency of the plasmon resonance can be tuned over a wide spectral range, interesting applications have been proposed in sensing/biosensing based on this mechanism [77, 78]. When an isolated fluorophore is subject to a weak excitation by an electric field $\boldsymbol{E}_0$ (measured at the fluorophore position), its fluorescence S_0 is given by:

$$S_0 = \xi \eta_0 |\boldsymbol{d} \cdot \boldsymbol{E}_0|^2 \tag{4.29}$$

.

In the expression above $\boldsymbol{d}$ is the dipole moment, ξ is the collection efficiency and η_0 is the quantum efficiency of the fluorophore, defined as:

$$\eta_0 = \frac{\Gamma^0_{\text{rad}}}{\Gamma^0_{\text{rad}} + \Gamma^0_{\text{nrad}}} \tag{4.30}$$

Γ^0_{rad} and Γ^0_{nrad} are the radiative and non-radiative decay rates, respectively. When the fluorophore is in the proximity of a metal nanoparticle, it will feel a stronger local field $\boldsymbol{E}$. In addition, it will be characterized by a new radiative decay rate Γ_{rad}, due to coupling of the fluorophore and the plasmon, and an additional non-radiative decay channel will be present, with decay rate Γ_{nrad}, due to absorption by the metal (i.e. metal losses). The fluorescence signal enhancement will then be:

$$\frac{S}{S_0} = \frac{\eta}{\eta_0} \frac{|\boldsymbol{d} \cdot \boldsymbol{E}|^2}{|\boldsymbol{d} \cdot \boldsymbol{E}_0|^2} \tag{4.31}$$

.

The modified quantum efficiency η is given by:

$$\eta = \frac{\eta_0}{\frac{(1-\eta_0)}{F} + \frac{\eta_0}{\eta_a}} \tag{4.32}$$

$F = \Gamma_{\text{rad}}/\Gamma^0_{\text{rad}}$ is the so-called Purcell factor, and describes the enhancement in radiative decay, while $\eta_a = \Gamma_{\text{rad}}/(\Gamma_{\text{rad}} + \Gamma_{\text{nrad}})$ is the "antenna efficiency" [79, 80]. Depending on the relative magnitudes of the various parameters, various cases are found, as described below. If the quantum efficiency η_0 of the fluorophore is 1, then $\eta = \eta_a$ in any case, and there can only be reduction in quantum efficiency when the fluorophore is close to the particle. However, when $\eta_0 < 1$, which is always the case, then η depends both on F and on η_a. When both parameters are large, then η is maximized. Therefore, by looking at the two equations above, one can state that in order to have a strong improvement in the fluorescence, the system has to create a strong electric field locally and it must have a large antenna efficiency and a large Purcell factor.

In principle, one advantage of using elongated metal nanoparticles with respect to spheres is that their near field and far field optical properties can be tuned by tuning the aspect ratio of the rods, which regulates the resonance conditions for the longitudinal plasmon mode. In this way, metal enhancement of the fluorophores emitting in the near infrared region of the spectrum can be achieved [81]. Another potential advantage, as discusses earlier, is that in nanorods the dephasing of the longitudinal plasmon mode is slower than that of spherical nanoparticles, which translates into a higher quality factor (see Sect. 4.7) [30]. Also, elongated nanoparticles and prisms can have sharp corners, near which the field is strongly increased, as discussed above. However, various aspects need to be taken into account in these situations. One of them is the spectral range where the fluorescence enhancement effect is desired. For example, in the short wavelength range spherical particles behave better than nanorods/spheroids [79]. Also, depending on the spectral range, one needs to choose the material of the particle (i.e. aluminum, silver, gold, copper), in order to optimize the Purcell factor. Another important point is that the resonance needs to be in a region in which the dissipation in the metal is minimized [82]. This is a very active area of research at the moment. A recent computational study [80] for example has investigated how gold "nanocones" perform as optical antennas for metal enhanced fluorescence with respect to spheres and rods, highlighting how in these nanocones the longitudinal plasmon resonance can be tuned to shorter wavelengths with respect to rods (by increasing the cone angle), without compromising the Purcell Factor and the antenna efficiency. Furthermore, nanocones with large basal area can be assembled

vertically on a substrate with less effort than for nanorods, which should be useful in a variety of applications (the field enhancement is highest at the region near the apex of the cone, and this region is well exposed in vertically assembled nanocones). For an in-depth coverage of optical antennas, also from an historical perspective, the reader can consult Ref. [83].

4.10.3 Surface Enhanced Raman Scattering

Also the surface enhanced Raman scattering (SERS) effect is related to a molecule in close proximity to a metal nanoparticle or to a roughened metal surface. The effect was discovered in 1977 [84, 85], rationalized in 1978 [86], and since then has been exploited in various applications, until the detection of single molecules was demonstrated. In analogy to metal enhanced fluorescence, the enhancement of the Raman scattering is mainly due to the enhancement of the electromagnetic field near the surface of metal nanoparticles. There are various other effects involved in SERS, most of them playing minor roles (for a coverage of them see for example [87]). In the case of a spherical nanoparticle immersed in a medium of dielectric constant ε_{medium}, assuming that light is incident on the particle, with an electromagnetic field vector $\mathbf{E}_0$ aligned along one of the axes of the particle (say the z-axis), the absolute square of the field outside the sphere $\boldsymbol{E}$ is [88]:

$$|\boldsymbol{E}|^2 = |\boldsymbol{E}_0|^2 \left[|1 - \mathrm{g}|^2 + 3cos^2\Theta \left(2\mathrm{Re}(\mathrm{g}) + |\mathrm{g}|^2 \right) \right] \tag{4.33}$$

$$\mathrm{g} = \frac{\varepsilon - \varepsilon_{medium}}{\varepsilon + 2\varepsilon_{medium}}. \tag{4.34}$$

In the expression above, Θ is the angle between the excitation field vector and the molecule on the surface of the particle. The Raman intensity depends on $|\boldsymbol{E}|^2$. The term g becomes large when resonance conditions are met, and in such case the expression above becomes:

$$|\boldsymbol{E}|^2 = |\boldsymbol{E}_0|^2 |\mathrm{g}|^2 \left[1 + 3cos^2\Theta \right]. \tag{4.35}$$

Then the Raman intensity is highest when the molecule on the surface of the particle is along the z-axis of the particle, so either at 0 or at 180°. In addition to enhancement of the field, therefore to an increase in the probability that the molecule emits a Raman photon, there is a probability that the metal nanoparticle absorbs Raman photons (i.e. surface plasmon of the particle are excited by the Raman photons) and re-emits them. Therefore, the intensity of the Raman signal can be enhanced by two processes, implying the incident and the scattered field, and the overall enhancement can be written as:

$$E_r = \frac{|\boldsymbol{E}|^2|\boldsymbol{E}'|^2}{|\boldsymbol{E}_0|^4} 16|\mathrm{g}|^2|\mathrm{g}'|^2. \tag{4.36}$$

In the expression above the primed variables refer to the re-radiated fields. In the case of a prolate spheroid, assuming that the incident electric field is aligned with the long axis of the spheroid, the enhancement is maximal at the tip regions of the spheroids (where the curvature is highest), and is bigger for more prolate spheroids (for an analytical treatment see for example [87]). However, as discussed above for the case of a sphere, this maximum Raman enhancement would be true only if all the molecules were located at these apex regions. In a real case, however, molecules would be located all over the surface of the particles, therefore one needs to perform an average of the field enhancement over the whole surface of the nanoparticle [87]. It turns out that the averaged enhancement is only 2 for a sphere, and it actually decreases to zero for infinitely prolate ellipsoids. On the other hand, for infinitely oblate ellipsoids, the averaged enhancement is 2.44 [87]. These calculations however, need to be taken with care, since in them the dielectric constant of the metal was considered as that of the Drude model. When considering other terms in the dielectric constant, the maximum averaged enhancement was found for moderately oblate ellipsoids [87]. In analogy with what discussed before on the field enhancement in nanoparticles and on the metal enhanced fluorescence, the magnitude of SERS depends not only on the shape of the particle, but also on its overall size. Factors that tend to reduce field enhancement, hence also SERS, are scattering of electron from the surface, for small particles, and radiation damping for big particles. Hence, depending on the composition of the particles, there is a range of nanoparticle sizes for which SERS is maximized [87].

A recent work by Rodriguez-Fernandez et al. [89] studied the effect of nanoscale surface corrugation on both far and near field optical properties of spherical Au nanoparticles of various sizes, ranging from 100 to 200 nm. Especially for what concerns the near field, the authors were able to probe the optical amplification via ensemble SERS measurements (using 1-naphtalenethiol as a model analyte) and found that the surface corrugation plays an important role in the plasmonic response of the particles: namely, SERS amplification was always higher when working with surface corrugated particles.

4.10.4 Photoluminescence Enhancement from Metal Nanorods

Another important effect related to near field properties of metal nanoparticles is the enhancement in the photoluminescence (PL) from metal nanorods with increasing aspect ratios [90]. PL from bulk metals (for example copper and gold) is

centred near the interband transition edge of the metals and is ascribed to recombination of the electrons in the conduction bands with holes in the d-band. The quantum yield of this PL is relatively low (of the order of 10^{-10}). In Au nanoparticles, excitation at 480 nm for example leads to excitation of surface plasmon modes, involving electrons in the sp band but also to intraband transitions involving d-electrons (see Sect. 4.2), which create holes in the d-band. Recombination of the sp electrons with the d-holes leads to PL. In rod-shaped nanoparticles, due to local field enhancement in the regions of higher curvature, an enhancement in the PL signal is actually observed [90]. An important parameter involved in the estimation of the enhancement in photoluminescence is the so-called "local field enhancement factor", which is generally defined as the ratio of the field acting on an individual emitter to the average field in the medium. It can be shown that for a rotational spheroid of a material with dielectric function $\varepsilon(\omega)$, axes a and b, and volume V, the local field correction factor $L(\omega)$ at an optical wavelength λ is defined by [90]:

$$L(\omega) = \frac{L_{LR}}{\varepsilon(\omega) - 1 + L_{LR}\left(1 + \frac{4\pi^2 iV[1-\varepsilon(\omega)]}{3\lambda^3}\right)} \tag{4.37}$$

The term L_{LR} above is the "lighting rod factor" and is defined by:

$$L_{LR} = 1 - \frac{\xi Q_1'(\xi)}{Q_1(\xi)} \tag{4.38}$$

with:

$$\xi = \frac{1}{\sqrt{1 - \left(\frac{b}{a}\right)^2}};\ Q_1(\xi) = \frac{\xi}{2} ln\left(\frac{\xi + 1}{\xi - 1}\right) - 1;\ Q_1'(\xi) = \frac{dQ_1(\xi)}{d\xi}. \tag{4.39}$$

Based on the expressions above, the single photon luminescence power P_1 for excitation and emission energies $h\omega_{ex}$ and $h\omega_{em}$, for an incident field $\mathbf{E}_0$ can be calculated as:

$$P_1 = 2^4 \beta_1 |\mathbf{E}_0|^2 V \left| L^2(h\omega_{ex}) L^2(h\omega_{em}) \right| \tag{4.40}$$

where β_1 is a proportionality constant. The ratio $P_1/\beta_1|\mathbf{E}_0|^2$ represents actually the enhancement of the single photon PL from the ellipsoid with respect to the PL of bulk gold, and can be calculated. Mohamed et al. [90] calculated the above ratio for a series of gold ellipsoids with constant diameter of 20 nm and increasing lengths. They also synthesized gold nanorods of various aspect ratios and measured their optical emission spectra and PL quantum yields. Their calculations were in agreement with the experimental results, namely the single-photon luminescence power increased with the square of the nanorod lengths, in the range between 20 and 80 nm (Fig. 4.15), and also the PL red-shifted with increasing rod/ellipsoid length.

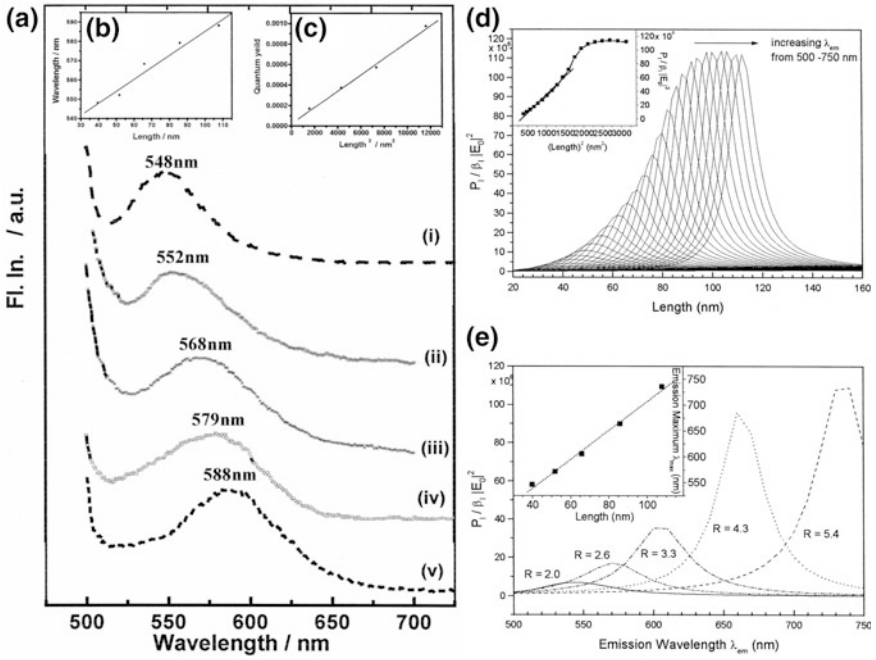

Fig. 4.15 **a** Experimental PL spectra of gold nanorods of average aspect ratios equal to 2.0 (i), 2.6 (ii), 3.3 (iii), 4.3 (iv) and 5.4 (v) and diameters all around 20 nm; **b** The peak in the emission wavelengths scales linearly with the aspect ratios of the rods; **c** The quantum efficiency of the PL emission scales according to the square of the length of the rods; **d** Plot displaying P_1/(β_1 |E_0 |^2) as a function of the gold ellipsoid length for various emission wavelengths. The inset shows how P_1/(β_1 |E_0 |^2) depends on the square of the length of the ellipsoid, in the range of lengths comprised between 20 and 80 nm; **e** Plot of P_1/(β_1 |E_0 |^2) as a function of the emission wavelength for ellipsoids having the same aspect ratios as the rods used in the experiments (see panel **a**). The inset shows how the emission maximum from these ellipsoids scales with the length of the rods, in analogy with the experimental data shown in (**b**). Taken with permission from Ref. [90]

References

1. Klimov V (2004) Semiconductor and metal nanocrystals. Marcel Dekker, New York
2. Noguez C (2005) Optical properties of isolated and supported metal nanoparticles. Opt Mater 27(7):1204–1211
3. Link S, El-Sayed MA (2000) Shape and size dependence of radiative, non-radiative and photothermal properties of gold nanocrystals. Intern Rev Phys Chem 19(3):409–453
4. Perez-Juste J, Pastoriza-Santos I, Liz-Marzan LM, Mulvaney P (2005) Gold nanorods: synthesis, characterization and applications. Coord Chem Rev 249(17–18):1870–1901
5. Schwartzberg AM, Olson TY, Talley CE, Zhang JZ (2006) Synthesis, characterization, and tunable optical properties of hollow gold nanospheres. J Phys Chem B 110(40):19935–19944
6. Zhang JZ, Noguez C (2008) Plasmonic optical properties and applications of metal nanostructures. Plasmonics 3(4):127–150

7. Gonzalez AL, Reyes-Esqueda JA, Noguez C (2008) Optical properties of elongated noble metal nanoparticles. J Phys Chem C 112(19):7356–7362
8. Myroshnychenko V, Rodriguez-Fernandez J, Pastoriza-Santos I, Funston AM, Novo C, Mulvaney P, Liz-Marzan LM, de Abajo FJG (2008) Modelling the optical response of gold nanoparticles. Chem Soc Rev 37(9):1792–1805
9. Kelly KL, Coronado E, Zhao LL, Schatz GC (2003) The optical properties of metal nanoparticles: the influence of size, shape, and dielectric environment. J Phys Chem B 107(3):668–677
10. Meier M (2007) Plasmonics: fundamentals and applications. Springer, Berlin
11. Link S, El-Sayed MA (2003) Optical properties and ultrafast dynamics of metallic nanocrystals. Ann Rev Phys Chem 54:331–366
12. Huang X, Neretina S, El-Sayed MA (2009) Gold nanorods: from synthesis and properties to biological and biomedical applications. Adv Mater 21:4880–4910. doi:10.1002/adma.200802789
13. Liz-Marzan LM (2006) Tailoring surface plasmons through the morphology and assembly of metal nanoparticles. Langmuir 22:32–41. doi:10.1021/la0513353
14. Noguez C (2007) Surface plasmons on metal nanoparticles: the influence of shape and physical environment. J Phys Chem C 111(10):3806–3819
15. Bohren CF, Huffman DR (1998) Absorption and scattering of light by small particles. Wiley, New York
16. Ashroft NW, Mermin ND (1976) Solid State Physics. Brooks Cole, Belmont
17. Kreibig U (1974) Electronic properties of small silver particles: the optical constants and their temperature dependence. J Phys F 4:999–1014
18. Mie G (1908) Beiträge zur Optik trüber Medien, speziell kolloidaler Metallösungen. Ann Physik 25:377–445
19. Baida H, Billaud P, Marhaba S, Christofilos D, Cottancin E, Crut A, Lerme J, Maioli P, Pellarin M, Broyer M, Del Fatti N, Vallee F (2009) Quantitative determination of the size dependence of surface plasmon resonance damping in single $Ag@SiO_2$ nanoparticles. Nano Lett 9(10):3463–3469
20. de Heer WA (1993) The physics of simple metal-clusters—experimental aspects and simple-models. Rev Mod Phys 65:611–676
21. Brack M (1993) The physics of simple metal clusters: self-consistent jellium model and semiclassical approaches. Rev Mod Phys 65:677–732
22. Liebsch A (1997) Electronic excitations at metal surfaces. Plenum Press, New York
23. Meier M, Wokaun A (1983) Enhanced fields on large metal particles: dynamic depolarization. Opt Lett 8(11):581–583
24. Landau LD, Pitaevskii LP, Lifshitz EM (2004) Electrodynamics of continuous media, 2nd edn, vol 8. Elsevier Butterworth-Einemann, London
25. Moroz A (2009) Depolarization field of spheroidal particles. J Opt Soc Am B 26(3):517–527
26. Kuwata H, Tamaru H, Esumi K, Miyano K (2003) Resonant light scattering from metal nanoparticles: practical analysis beyond Rayleigh approximation. Appl Phys Lett 83(22):4625–4627
27. Gans R (1912) Über die form ultramikroskopischer goldteilchen. Ann Physik 342(5):881–900
28. Johnson PB, Christy RW (1972) Optical constants of the noble metals. Phys Rev B 6(12):4370–4379
29. Wilson O, Wilson GJ, Mulvaney P (2002) Laser writing in polarized silver nanorod films. Adv Mater 14(13–14):1000–1004
30. Sonnichsen C, Franzl T, Wilk T, von Plessen G, Feldmann J, Wilson O, Mulvaney P (2002) Drastic reduction of plasmon damping in gold nanorods. Phys Rev Lett 88 (7):077402
31. Sando GM, Berry AD, Campbell PM, Baronavski AP, Owrutsky JC (2007) Surface plasmon dynamics of high-aspect-ratio gold nanorods. Plasmonics 2(1):23–29
32. Brebbia CA, Dominquez J (1992) Boundary elements: an introductory course. Computational Mechanics, Southampton

33. Ramdas Ram-Mohan L (2002) Finite element and boundary element applications in quantum mechanics. Oxford University Press, Oxford
34. Rockstuhl C, Salt MG, Herzig HP (2003) Application of the boundary-element method to the interaction of light with single and coupled metallic nanoparticles. J Opt Soc Am A 20(10):1969–1973
35. de Abajo FJG, Howie A (1998) Relativistic electron energy loss and electron-induced photon emission in lymphogenous dielectrics. Phys Rev Lett 80(23):5180–5183
36. de Abajo FJG, Howie A (2002) Retarded field calculation of electron energy loss in inhomogeneous dielectrics. Phys Rev B 65 (11):115418
37. Aizpurua J, Bryant GW, Richter LJ, de Abajo FJG, Kelley BK, Mallouk T (2005) Optical properties of coupled metallic nanorods for field-enhanced spectroscopy. Phys Rev B 71 (23):235420
38. Pastoriza-Santos I, Liz-Marzan LM (2008) Colloidal silver nanoplates. State of the art and future challenges. J Mater Chem 18 (15):1724–1737
39. Bryant GW, De Abajo FJG, Aizpurua J (2008) Mapping the plasmon resonances of metallic nanoantennas. Nano Lett 8(2):631–636
40. Goodman JJ, Draine BT, Flatau PJ (1991) Application of fast-fourier-transform techniques to the discrete-dipole approximation. Opt Lett 16(15):1198–1200
41. Jensen T, Kelly L, Lazarides A, Schatz GC (1999) Electrodynamics of noble metal nanoparticles and nanoparticle clusters. J Clust Sci 10(2):295–317
42. Hao E, Schatz GC (2004) Electromagnetic fields around silver nanoparticles and dimers. J Chem Phys 120(1):357–366
43. Gai PL, Harmer MA (2002) Surface atomic defect structures and growth of gold nanorods. Nano Lett 2(7):771–774
44. Wang ZL, Mohamed MB, Link S, El-Sayed MA (1999) Crystallographic facets and shapes of gold nanorods of different aspect ratios. Surf Sci 440(1–2):L809–L814
45. Guo HY, Ruan FX, Lu LH, Hu JW, Pan JA, Yang ZL, Ren B (2009) Correlating the shape, surface plasmon resonance, and surface-enhanced raman scattering of gold nanorods. J Phys Chem C 113(24):10459–10464
46. Slaughter LS, Chang WS, Swanglap P, Tcherniak A, Khanal BP, Zubarev ER, Link S (2010) Single-particle spectroscopy of gold nanorods beyond the quasi-static limit: varying the width at constant aspect ratio. J Phys Chem C 114(11):4934–4938
47. Schmucker AL, Harris N, Banholzer MJ, Blaber MG, Osberg KD, Schatz GC, Mirkin CA (2010) Correlating nanorod structure with experimentally measured and theoretically predicted surface plasmon resonance. ACS Nano 4 (9):5453–5463
48. Lee KS, El-Sayed MA (2005) Dependence of the enhanced optical scattering efficiency relative to that of absorption for gold metal nanorods on aspect ratio, size, end-cap shape, and medium refractive index. J Phys Chem B 109(43):20331–20338
49. Anisimov SI, Kapeliovich BL, Perel'man TL (1975) Electron emission from metal surfaces exposed to ultrashort laser pulses. Sov Phys JETP 39:375–377
50. El-Sayed MA, Norris TB, Pessot MA, Mourou GA (1987) Time-resolved observation of electron-phonon relaxation in copper. Phys Rev Lett 58(12):1212–1215
51. Sun CK, Vallee F, Acioli LH, Ippen EP, Fujimoto JG (1994) Femtosecond-tunable measurement of electron thermalization in gold. Phys Rev B 50(20):15337–15348
52. Del Fatti N, Voisin C, Achermann M, Tzortzakis S, Christofilos D, Vallee F (2000) Nonequilibrium electron dynamics in noble metals. Phys Rev B 61(24):16956–16966
53. Link S, Burda C, Wang ZL, El-Sayed MA (1999) Electron dynamics in gold and gold-silver alloy nanoparticles: the influence of a nonequilibrium electron distribution and the size dependence of the electron-phonon relaxation. J Chem Phys 111(3):1255–1264
54. Smith BA, Zhang JZ, Giebel U, Schmid G (1997) Direct probe of size-dependent electronic relaxation in single-sized Au and nearly monodisperse Pt colloidal nano-particles. Chem Phys Lett 270(1–2):139–144
55. Grant CD, Schwartzberg AM, Yang YY, Chen SW, Zhang JZ (2004) Ultrafast study of electronic relaxation dynamics in Au-11 nanoclusters. Chem Phys Lett 383(1–2):31–34

56. Hodak JH, Henglein A, Hartland GV (2000) Electron-phonon coupling dynamics in very small (between 2 and 8 nm diameter) Au nanoparticles. J Chem Phys 112(13):5942–5947
57. Link S, El-Sayed MA (1999) Spectral properties and relaxation dynamics of surface plasmon electronic oscillations in gold and silver nanodots and nanorods. J Phys Chem B 103(40):8410–8426
58. Link S, Furube A, Mohamed MB, Asahi T, Masuhara H, El-Sayed MA (2002) Hot electron relaxation dynamics of gold nanoparticles embedded in $MgSO_4$ powder compared to solution: the effect of the surrounding medium. J Phys Chem B 106(5):945–955
59. Stella A, Nisoli M, DeSilvestri S, Svelto O, Lanzani G, Cheyssac P, Kofman R (1996) Size effects in the ultrafast electronic dynamics of metallic tin nanoparticles. Phys Rev B 53(23):15497–15500
60. Hu M, Hartland GV (2002) Heat dissipation for Au particles in aqueous solution: relaxation time versus size. J Phys Chem B 106(28):7029–7033
61. Hodak JH, Martini I, Hartland GV (1998) Spectroscopy and dynamics of nanometer-sized noble metal particles. J Phys Chem B 102(36):6958–6967
62. Bullen KE (1985) An introduction to seismology, 4th edn. Cambridge University Press, Cambridge
63. Hu M, Wang X, Hartland GV, Mulvaney P, Juste JP, Sader JE (2003) Vibrational response of nanorods to ultrafast laser induced heating: theoretical and experimental analysis. J Am Chem Soc 125(48):14925–14933
64. Perner M, Gresillon S, Marz J, von Plessen G, Feldmann J, Porstendorfer J, Berg KJ, Berg G (2000) Observation of hot-electron pressure in the vibration dynamics of metal nanoparticles. Phys Rev Lett 85(4):792–795
65. von Plessen G, Perner M, Feldmann J (2000) Ultrafast relaxation dynamics of electronic excitations in noble-metal clusters. Appl Phys B 71(3):381–384
66. Hartland GV, Hu M, Wilson O, Mulvaney P, Sader JE (2002) Coherent excitation of vibrational modes in gold nanorods. J Phys Chem B 106(4):743–747
67. Jain PK, Huang WY, El-Sayed MA (2007) On the universal scaling behavior of the distance decay of plasmon coupling in metal nanoparticle pairs: a plasmon ruler equation. Nano Lett 7(7):2080–2088
68. Hao E, Schatz GC, Hupp JT (2004) Synthesis and optical properties of anisotropic metal nanoparticles. J Fluoresc 14(4):331–341
69. Gersten JI (1980) The effect of surface roughness on surface enhanced Raman scattering. J Chem Phys 72:5779
70. Zuloaga J, Prodan E, Nordlander P (2010) Quantum plasmonics: optical properties and tunability of metallic nanorods. ACS Nano 4(9):5269–5276
71. Nelayah J, Kociak M, Stephan O, Garcia de Abajo FJ, Tencé M, Henrard L, Taverna D, Pastoriza-Santos I, Liz-Marzan LM, Colliex C (2007) Mapping surface plasmons on a single metallic nanoparticle. Nat Phys 3:348–353
72. Bosman M, Keast VJ, Watanabe M, Maaroof AI, Cortie MB (2007) Mapping surface plasmons at the nanometre scale with an electron beam. Nanotechnology 18(16):165505
73. N'Gom M, Ringnalda J, Mansfield JF, Agarwal A, Kotov NA, Zaluzec NJ, Norris TB (2008) Single particle plasmon spectroscopy of silver nanowires and gold nanorods. Nano Lett 8(10):3200–3204
74. Schaffer B, Grogger W, Kothleitner G, Hofer F (2010) Comparison of EFTEM and STEM EELS plasmon imaging of gold nanoparticles in a monochromated TEM. Ultramicroscopy 110(8):1087–1093
75. N'Gom M, Li S, Schatz GC, Erni R, Agarwal A, Kotov NA, Norris TB (2009) Electron-beam mapping of plasmon resonances in electromagnetically interacting gold nanorods. Phys Rev B 80:113411
76. Koh AL, Bao K, Khan I, Smith WE, Kothleitner G, Nordlander P, Maier SA, McComb DW (2009) Electron energy-loss spectroscopy (EELS) of surface plasmons in single silver nanoparticles and dimers: influence of beam damage and mapping of dark modes. ACS Nano 3(10):3015–3022

77. Lakowicz JR, Geddes CD, Gryczynski I, Malicka J, Gryczynski Z, Aslan K, Lukomska J, Matveeva E, Zhang JA, Badugu R, Huang J (2004) Advances in surface-enhanced fluorescence. J Fluoresc 14(4):425–441
78. Aslan K, Gryczynski I, Malicka J, Matveeva E, Lakowicz JR, Geddes CD (2005) Metal-enhanced fluorescence: an emerging tool in biotechnology. Curr Opin Biotech 16(1):55–62
79. Mohammadi A, Sandoghdar V, Agio M (2008) Gold nanorods and nanospheroids for enhancing spontaneous emission. New J Phys 10:105015
80. Mohammadi A, Kaminski F, Sandoghdar V, Agio M (2010) Fluorescence enhancement with the optical (bi-) conical antenna. J Phys Chem C 114(16):7372–7377
81. Bardhan R, Grady NK, Cole JR, Joshi A, Halas NJ (2009) Fluorescence enhancement by au nanostructures: nanoshells and nanorods. ACS Nano 3(3):744–752
82. Mohammadi A, Sandoghdar V, Agio M (2009) Gold, copper, silver and aluminum nanoantennas to enhance spontaneous emission. J Comp Theor Nanosci 6(9):2024–2030
83. Bharadwaj P, Deutsch B, Novotny L (2009) Optical antennas. Adv Opt Phot 1:438–483
84. Albrecht MG, Creighton JA (1977) Anomalously intense Raman spectra of pyridine at a silver electrode. J Am Chem Soc 99:5215–5217
85. Jeannaire DL, Van Duyne RP (1977) Surface Raman spectroelectrochemistry: part I. Heterocyclic, aromatic, and aliphatic amines adsorbed on the anodized silver electrode. J Electroanal Chem 84:1–20
86. Moskovits M (1978) Surface roughness and the enhanced intensity of Raman scattering by molecules adsorbed on metals. J Chem Phys 69:4159
87. Schatz GC (1984) Theoretical studies of surface enhanced Raman scattering. Acc Chem Res 17:370–376
88. Schwartzberg AM, Zhang JZ (2008) Novel optical properties and emerging applications of metal nanostructures. J Phys Chem C 112(28):10323–10337
89. Rodriguez-Fernandez J, Funston AM, Perez-Juste J, Alvarez-Puebla RA, Liz-Marzan LM, Mulvaney P (2009) The effect of surface roughness on the plasmonic response of individual sub-micron gold spheres. Phys Chem Chem Phys 11(28):5909–5914
90. Mohamed MB, Volkov V, Link S, El-Sayed MA (2000) The 'lightning' gold nanorods: fluorescence enhancement of over a million compared to the gold metal. Chem Phys Lett 317(6):517–523

Chapter 5
Magnetic Properties of Nanorods

5.1 Introduction

Bulk magnetic materials have found many applications in several technological fields since centuries. But nanoscale magnetic materials arose only in the last two decades. Interest in such finely engineered systems is due to the new unconventional functionalities that they may add to already well-known materials and hence for their capacity to expand their range of application to fields where they would have never been foreseen, like in biomedicine for instance [1, 2].

Magnetic materials are commonly divided based on their magnetic hardness, i.e. on the external energy required for the reversal of their magnetization, or more precisely, the magnetic field required to overcome the energy barrier for the inversion of their magnetic moments. For example, hard magnets such as $SmCo_5$, $Nd_2Fe_{14}B$, CoPt and FePt show high values of coercivity, which is useful for the design of magnetic recording media in magnetic storage devices [3–7]. Hard magnetic nanomaterials have already shown improvements in storage capacities compared to commercial devices, fulfilling the increasing demand by communication and information industry [8]. Additionally they are expected to reduce the size of portable devices as well as their cost and to increase design flexibility without compromising their performance. On the other hand, materials such as metallic iron or cobalt, permalloys and spinel-type ferrites MFe_2O_4 (M = Mn, Fe, Ni, Zn) are called soft magnets due to their low coercive fields. Their high resistivity and high magnetic permeability make them ideal for the design of non-reciprocal electronic components in miniature microwave devices, reading head sensors and recording head cores in hard drives [9].

One of the main breakthroughs in the application of magnetic materials offered by nanostructured systems is found in life sciences and biomedicine. Superparamagnetism is the term used for describing the absence of coercivity and remanent magnetization in particles that still maintain a considerable amount of polarizable spins under the effect of an external magnetic field [10, 11]. Due to their small sizes and their zero net magnetization at zero field, they can be safely exploited in biomedicine, for instance as nanovectors for specific targets that are not accessible via other conventional approaches [12–14]. In the same way, they can also be used

R. Krahne et al., *Physical Properties of Nanorods*,
NanoScience and Technology, DOI: 10.1007/978-3-642-36430-3_5,

in biodetection and bioseparation techniques since once the target molecule has been attached to the nanocrystals, the application of an external magnetic field allows for their recovery [5, 15]. Iron oxide is clearly the most suitable material for such purposes, due to its high chemical stability, biocompatibility and superparamagnetic properties. As a matter of fact, iron oxide nanoparticles are being already used in some diagnostic and therapeutic techniques [16]. On the other hand, magnetic nanocrystals with higher magnetic moment and higher anisotropy would be desirable in order to improve their performance and reduce the required doses. Some metallic nanoparticles fulfill these characteristics but unfortunately they also show a much lower degree of chemical stability and an increased toxicity compared to their oxide analogues.

Targets of current research in materials sciences, such as the achievement of higher coercivity values in reduced size particles for information storage devices, or faster magnetic response for smaller biomedical vectors, could be achieved if one considers not only the finite size effects of spherical nanocrystals but also the additional phenomena derived from the shape anisotropy of particles such as nanorods. Nanorods or other one-dimensional nanosystems could also widen the temperature range of application of a certain magnetic material compared to its bulk form (as will be shown later). The uniaxial shape anisotropy of metallic and oxide nano-objects will probably become a key factor for the development of improved devices.

This chapter is organized as follows: initially, an introduction on nanoscale related magnetic properties is presented. Then, the main examples of elongated, rod-like primary magnetic nanocrystals will be discussed, first for oxide-based materials and later for metals. The study of the magnetization reversal processes in 1D nanostructures is of crucial importance for the development of spintronics technology. The main results obtained in this field will also be reviewed. Finally some conclusions and perspectives will be drawn. Preparation methods for the anisotropic growth of nanocrystals have been extensively reviewed previously and papers and book chapters deal with them [17–22]. We will focus mainly on the description of the structural and magnetic properties of magnetic nanoparticles. Since the assembly of anisotropic nanoparticles is crucial for the exploitation of their properties, special attention will be paid to the work in which some degree of organization of elongated nanoparticles has been achieved.

5.2 General Considerations on Magnetic Nanocrystals

Magnetism originates from the magnetic dipoles associated to the electron spin and orbital moment. Each of these magnetic dipoles can couple with the neighboring ones in the crystal lattice by exchange interaction leading to a collective alignment that causes the macroscopic magnetic effect that we can measure. As shown in Fig. 5.1, three main parameters can describe the magnetic strength and magnetization of the material and are:

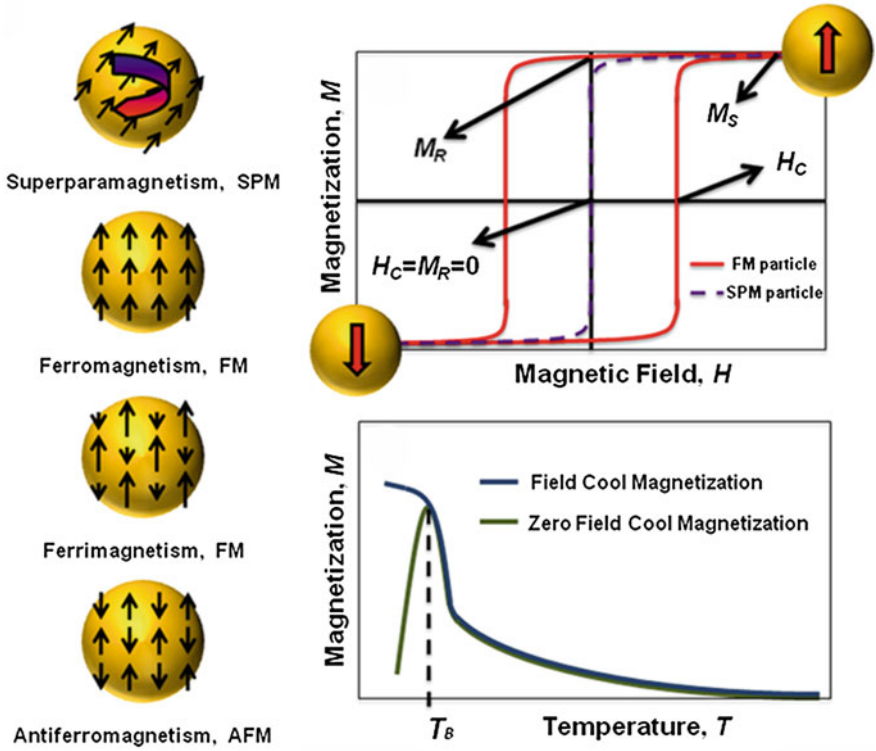

Fig. 5.1 **a** Spin configuration of the 4 types of magnetic exchange observable in magnetic materials without the effect of an external magnetic field; **b** parameters describing the strength and magnetization of superparamagnetic, ferromagnetic and ferrimagnetic materials: coercive field, H_C; saturation magnetization, M_S; and remanent magnetization, M_R; **c** temperature at which a magnetic transition between ordered and randomly oriented phases takes place, T_B

1. The coercive field, H_C, which is the external field required to reduce the magnetization back to zero. H_C is strictly related to the anisotropic energy barrier that must be overcome to invert the direction of the magnetic dipoles of the material. This anisotropic energy barrier can have different sources that will be discussed in detail in Sect. 5.3;
2. The saturation magnetization, M_S, which is the maximum value of magnetization that the material can reach with increasing field;
3. The remanent magnetization, M_R, which indicates the residual magnetization of the material at zero applied field; the squareness of the material is defined as M_R/M_S.

All three parameters can be easily identified in the hysteresis loop produced in field-dependent magnetization measurements. Depending on the magnetic response observed, we can classify magnetic materials as diamagnets, paramagnets, ferromagnets, ferrimagnets or antiferromagnets [23, 24] (see Fig. 5.1). A material that

creates a magnetic field in opposition to an externally applied magnetic field, thus causing a repulsive effect, is called diamagnet. They show weak and negative magnetic susceptibility values, typically from -10^{-6} to -10^{-8}. The perfect diamagnet with a susceptibility value of -1 is what is known as a superconductor. Oppositely to diamagnets, the other types of magnetic materials are attracted by the applied magnetic field: a material in a paramagnetic phase shows randomly oriented magnetic dipoles that can only be aligned in the presence of an external magnetic field and along its direction. Paramagnets show weak but positive susceptibility values, typically ranging from 10^{-3} to 10^{-5}. Without the effect of a magnetic field, the thermal energy is high enough to decouple all the spins. Such behavior is characterized by a complete absence of coercivity and remanence, which means that, when the external magnetic field is switched off, the internal magnetic dipoles randomize again and no energy is required to demagnetize the material. In other words, thermal energy (kT) is higher than the exchange energy between the spins and hence they are not able to maintain co-linearity. However, when the spin exchange energy is sufficiently high as to overcome kT, the spins interact with each other giving rise to different situations, depending on the nature of the exchange and the degree of intrinsic anisotropy of the material. These types of materials are schematized in Fig. 5.1. *Superparamagnetism*, for instance, describes the magnetic behavior of a material in which all the spins are always collinear to each other but its anisotropy energy is too low to keep them aligned along a particularly stable magnetocrystalline direction (easy magnetization axis). As a consequence, a superparamagnetic material exhibits a constant and collective fluctuation of its spins, meaning that they are always aligned parallel one to the other, but they collectively move in a random fashion. Only when an external magnetic field is applied along a certain direction, the spins align along the same direction. A superparamagnetic material shows zero coercivity and remanence. However, superparamagnetism is strictly a time-dependent property: as it will be explained later, the superparamagnetic response depends strongly on the relaxation time of the material and on the measuring time of the technique chosen. Alternatively, when the anisotropy energy of the material is higher than kT, the aligned spins are blocked along a certain direction and cannot fluctuate as in the superparamagnetic case, even in the absence of an external magnetic field. When this happens, depending on the nature of the spin exchange, different behaviors can be observed. If the spins align parallel to each other, an enhanced collective response is observed. This is what is known as *ferromagnetism*. Ferromagnets show large and positive susceptibility values typically ranging from 10^3 to 10^4.

In contrast to the ferromagnetic situation, neighboring magnetic dipoles can align antiparallel in the lattice, which means that they cancel each other. This type of magnetic exchange can lead to two different situations: *antiferromagnetism*, when the magnetic dipoles or spins interacting present the same value and hence the material exhibits a net zero magnetization, and *ferrimagnetism* when the two coupled spins show different values and in that case a net magnetic dipole different than zero still magnetizes the material, even in the absence of external magnetic field. It is important to keep in mind that we only describe magnetic interactions

between dipoles that belong to a single isolated magnetic nanoparticle in a magnetically diluted sample, without taking into account further interactions between nanoparticles that would lead to enhanced collective properties. The reader is redirected to more specialized works on such phenomena [25].

The alignment of the different magnetic dipoles in a superparamagnetic, ferromagnetic or ferrimagnetic material creates a magnetic field in space that is associated to an energy value. This energy can be minimized by creating oppositely faced domains in the material, so that the field, and consequently also the energy, are decreased. The domain walls that are thus created carry a certain value of energy associated as well. The magnetostatic energy due to the alignment of the dipoles increases proportionally to the volume of the particle, while the domain wall energy increases proportionally to the surface area of the domains. When the decreasing dimensions of a magnetic particle approach a critical radius, it may be more energetically favorable for the particle to form a single domain (SD) instead of maintaining its multi-domain character. This defines the *critical radius*, r_c, of the particle. As shown in Fig. 5.2, the competition between magnetostatic and domain wall energies is strongly dependent on the dimensions of the particles and obviously on the intrinsic nature of the material itself, in particular on different anisotropy energy terms [23, 24]. The r_c value below which a particle acts as a single domain particle can be deduced from equating the energies of single and multidomain configurations, which yields:

$$r_c \cong 9(AK_u)^{1/2}/\mu_0 M_s^2 \tag{5.1}$$

In the expression above, A represents the exchange stiffness, K_u is the magnetocrystalline anisotropy, μ_0 is the vacuum permeability. Values of r_c can range from a few nanometers for soft magnets (15 nm for Fe, 35 nm for Co or 30 nm for γ-Fe_2O_3) to some hundreds of nanometers for harder ones (750 nm for $SmCo_5$). The high stiffness of hard magnets is capable of stabilizing large single domain particles. In the SD regime, a particle is considered as a single uniformly magnetized domain. It is important not to confuse the single crystal particle with its single or multidomain magnetic behavior: even a single crystal particle can show multidomain (MD) magnetic features if its dimensions are above r_c.

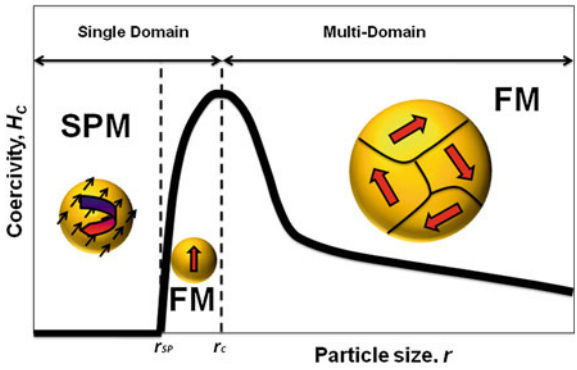

Fig. 5.2 Size dependence of the coercivity of magnetic nanoparticles. The size-dependent transitions between magnetic single and multidomains, as well as those between magnetically ordered and randomly oriented phases, are also indicated

Let us assume that, for a given constant temperature T, a spherical SD particle shows a permanent ferromagnetic alignment of its magnetic dipoles. The size of the particle may then be reduced down to a value of radius at which the thermal energy k_BT (with k_B being the Boltzmann constant) at a given temperature T is enough to overcome the anisotropy barrier (see Fig. 5.2). While the modulus of the magnetization remains unchanged, the fluctuations of the magnetization direction in time would result in a complete randomization and hence in an averaged magnetization value of zero. In other words, the particle would switch to a superparamagnetic state. The radius that defines the superparamagnetic limit, r_{SP}, below which a spherical particle behaves as a superparamagnet, is determined by a magnetic stability with a flipping probability of the magnetic moment equal to 10 % over one second [23, 24] and can be calculated using Eq. 5.2:

$$r_{SP} = (6k_BT/K_u)^{1/3} \tag{5.2}$$

where k_B is the Boltzmann constant. It is easy to understand that a hard magnetic material with a high value of K_u is able to maintain its ferromagnetic alignment down to smaller dimensions (r_{SP} values of 3–4 nm) at room temperature, while softer magnets with lower values of K_u switch to the superparamagnetic regime already at larger dimensions (r_{SP} values of ca. 20 nm) at the same temperature. The same phenomenon can be described from another point of view: for a fixed radius and increasing temperature, and for a ferromagnetic SD spherical particle, a value of temperature T is reached at which again the thermal energy k_BT is enough to overcome the anisotropy barrier. Above that temperature the particle shows random fluctuations of its coupled spins and hence it enters the superparamagnetic regime. This temperature is known as the blocking temperature, T_B, and can be easily identified by the so-called Zero Field Cooling—Field Cooling measurement, ZFC–FC (see Fig. 5.1), where the magnetization of the sample is measured at increasing temperature under a weak external field under two different conditions: (1) by cooling the sample without external field before measuring; (2) by cooling the sample under the effect of a magnetic field. The temperature below which the two curves diverge is known as the irreversibility temperature, T_{irr}, while the maximum of the ZFC curve indicates the T_B of the particles. While for isolated ferromagnetic nanoparticles both temperatures are equal, effects such as inter-particle interactions, spin disorder, spin glass and other phenomena make these values to be different. The blocking temperature of a particle can be expressed as [26]:

$$T_B = K_uV/(k_B\ln(\tau_m/\tau_0)) \tag{5.3}$$

In the expression above V is the volume of the nanoparticle, τ_0 is a time constant characteristic of the material (usually in the 10^{-12}–10^{-9} s range) and τ_m is the characteristic measuring time of the technique. If τ_m is assumed to be 1 min, then Eq. 5.3 becomes $T_B = K_uV/25k_B$. Again it seems clear that, for equal dimensions, hard magnetic materials with high values of K_u are able to maintain their ferromagnetic alignment up to higher temperatures (more energy is required to thermally agitate the spins), while softer magnets with lower values of K_u switch

to the superparamagnetic regime already at low temperatures. However, the values of T_B strongly depend on the measuring time characteristic of the technique (τ_m) chosen for its determination, as shown in Eq. (5.3). Magnetometry techniques usually require quite long measuring times ($\sim 10^2$ s) and hence lower T_B values are measured compared to other faster techniques. For example τ_m as measured from Mössbauer spectroscopy is around 10 orders of magnitude lower. As a consequence, for the same sample, the T_B as measured by Mössbauer spectra is significantly higher than the one measured by magnetometry [27]. It is obvious that the techniques and the conditions used for the T_B determination must be carefully considered before comparing results.

The term *blocking temperature* applies to the transition from a ferromagnetic to a superparamagnetic state when the temperature is increased. It is often used for small nanoparticles and it can range in value from a few degrees Kelvin to temperatures above room temperature, depending on the volume and anisotropy of the particle, as shown in Eq. (5.3). On the other hand, the transition from a ferro- or ferri-magnetic state to a paramagnetic state when increasing temperature in bulk materials is known as the Curie temperature, T_C. T_C values are usually well above room temperature. The transition from an antiferromagnetic to a paramagnetic state in bulk materials when increasing temperature is determined by the so called Néel temperature, T_N. The reader is redirected to Ref. [28] for further details on such magnetic transitions.

5.3 Anisotropy Considerations in Magnetic Nanocrystals

Until now we have discussed the dependence of the transition between a ferro-, ferri- or antiferromagnetic state on one hand, and a superparamagnetic state on the other hand, on the temperature for a constant particle radius, and on the size when temperature is kept constant. Let us now focus on the particle size dependence of the main magnetic parameters that characterize the ordered state of ferro- and ferrimagnetic nanoparticles; these are the coercive field, H_C, and the saturation magnetization, M_S. For this, some considerations about the different anisotropy contributions taking place in the crystal should first be clarified. The magnetic properties of the particles can be described by the anisotropic Heisenberg model:

$$\mathcal{H} = -\frac{1}{2}\mathcal{J}\sum_{ij} s_i \cdot s_j + \mathcal{H}_{anis} \tag{5.4}$$

where $\mathcal{J}$ is the nearest neighbor exchange interaction and $\mathcal{H}_{anis}$ is the Hamiltonian that contains all different sources of magnetic anisotropy. From such Hamiltonian, the whole energy spectrum of the system can be calculated. The total energy of a magnetic material can be considered as the sum of various terms [29]:

$$E_T = E_Z + E_k + E_D + E_\lambda + E_{exch} + E_{surf} + E_{shape} \tag{5.5}$$

The terms are described as follows: E_Z is the Zeeman energy arising from the interaction of the magnetic dipoles of the material with the external magnetic field; E_k is the magnetocrystalline energy; E_D is the magnetostatic dipole–dipole energy; E_λ is the magnetoelastic energy due to the effect of magnetostriction (i.e. a slight change in the dimensions of the crystal when magnetized). The latter induces elastic strains in the lattice, favoring directions of magnetization that minimize these strain energies; E_{exch} is the exchange energy; E_{surf} is the surface anisotropy energy and E_{shape} is the energy arising from the shape of the particle.

The term *magnetic anisotropy* is used to describe the dependence of the internal energy on the direction of the spontaneous magnetization. As a consequence, *easy* and *hard* directions of magnetization appear, which are able to minimize and maximize respectively the total energy of the material. The most energetically stable configuration is the one where the total magnetization vector lies along the easy direction/s. The energy difference between the easy and hard directions results from two microscopic interactions: the spin–orbit interaction and the long-range dipolar coupling of magnetic moments. In general terms, the spin-orbit coupling is responsible for the magnetocrystalline, magnetoelastic and surface anisotropies, while the shape anisotropy is a dipolar contribution [30].

When only bulk samples are taken in consideration, magnetocrystalline, magnetostatic and magnetoelastic energies are usually the main sources of anisotropy in the material. On the other hand, in thin films, fine particles and nanocrystals, surface and shape anisotropies acquire a significant weight, and, even if they cannot overcome the bulk anisotropic contribution in all cases, at least they can strongly compete with it. It is worth to point out that shape anisotropy can be the dominant effect even for bulk materials, when those show large values of M_S and low magnetocrystalline anisotropy [28]. The main effects of the different anisotropy contributions on the direction of the spontaneous magnetization of nanoparticles are shown in Fig. 5.3 and are also discussed below:

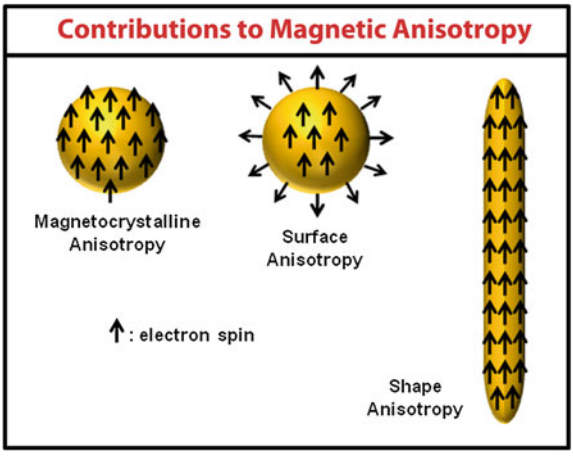

Fig. 5.3 Direction of the spontaneous magnetization of nanoparticles depending on various independent contributions: magnetocrystalline, surface and shape anisotropy

Magnetocrystalline anisotropy: such anisotropy derives from the intrinsic crystalline symmetry of the material (crystal field) and hence reflects the same symmetry [31]. One or more *easy magnetocrystalline axes* can be defined based on the symmetry of such anisotropy; when the magnetization lies along them, the total energy of the material is minimized and the material itself is in the most stable energetic configuration. One of the simplest but also most common forms of magnetocrystalline anisotropy is the uniaxial anisotropy. This type of anisotropy is associated to the hexagonal crystal symmetry and it makes the c axis of its hexagonal crystal lattice become the *easy axis* for its internal magnetization as well. In cubic structures, the three [111] directions of the crystal act as easy axes of magnetization. The magnetocrystalline energy for single domain crystals with uniaxial anisotropy can be calculated from the following expression:

$$E_k^{uni} = K_u V \sin^2\theta \tag{5.6}$$

where K_u is the uniaxial magnetocrystalline anisotropy constant, V is the particle volume and θ is the angle between the easy magnetization axis and the direction of the magnetization. Hence, for such a particle, $K_u V$ would be the magnetocrystalline energy barrier necessary to switch the direction of its magnetization. The higher is the energy barrier, the higher is also the coercivity of a single domain particle. In the single domain regime, and for particles with dimensions above r_{SP}, the coercive field, which strongly depends on E_k, increases with increasing dimensions. When the radius of the particle is in the vicinity of the critical radius r_c, the energy of the whole system reaches high values, but the energy required for the formation of domain walls is still too large. In this range of sizes, particles develop other mechanisms for reducing the total energy without forming multiple domains [32–34]. When these mechanisms are operative, the spins do not align themselves homogeneously along the external magnetic field. Instead, they are now homogeneously varying along one crystal direction, (i.e. *buckling*), or instead rotating in circular symmetry creating a vortex (i.e. *curling*). Buckling is the preferred mechanism for thin nanorods and nanowires, while curling is mostly observed in thin disks. The effect of the activation of such mechanisms in single domain particles is a continuous decrease of the H_C with increasing dimensions. Finally, once the radius of the particle clearly exceeds r_c, the particle decreases its total energy by the formation of several magnetic domains and the inversion of its magnetization takes place by the displacement of such domain walls, further decreasing the coercivity of the particle. The whole picture is described in Fig. 5.2. The magnetocrystalline anisotropy is a completely intrinsic characteristic of the material and does not depend on the presence of an external field, as it is instead the case for the magnetoelastic anisotropy.

Surface anisotropy: compared to bulk samples, nanocrystals show a very high surface to volume ratio and hence all effects arising from the contribution of surface atoms are strongly enhanced. Surface anisotropy can increase by more than one order of magnitude the total anisotropy of the sample with decreasing size from bulk to nanocrystals. As a consequence, it can become the dominant

contribution of the anisotropy, with values above those arising from the magnetocrystalline anisotropy. Atoms located at the surface show an incomplete coordination sphere and this leads to a broken symmetry compared to the core atoms. Such decrease in the crystalline symmetry at the surface induces a different orientation of the surface spins with respect to the magnetization direction, spin pinning and surface-core strains that reduce the surface energy [35]. The surface anisotropy energy can be expressed as follows:

$$E_{surf} = K_{surf} \int \cos^2\theta \ dS \tag{5.7}$$

Here, K_{surf} is the surface anisotropy density constant, θ is the angle between the magnetization and the normal to the surface and dS is the surface element. The sign of the surface energy depends on the nature of the crystal lattice and on the surface orientation. Surface anisotropy has one main effect on the ferro- and ferrimagnetic parameters of nanocrystals compared to the bulk. As previously said, the increased surface area gives rise to a higher amount of pinned spins in the crystal that cannot follow the spontaneous magnetization direction. This is translated into higher values of coercivity, since the anisotropy term has been increased, but also in lower values of saturation magnetization, since not all spins are able to align along the direction of the magnetization under magnetic fields of usual magnitude. The presence of spin-glass shells and the observation of spin-canting phenomena are common surface effects in magnetic nanoparticles [36]. With increasing size of the nanocrystal, and with the consequent decrease in surface to volume ratio, one should expect lower values of H_C and higher values of M_S. However, the final trend of the coercivity with size depends on the fine equilibrium between magnetocrystalline and surface contributions, since they show opposite effects.

The situation can become even more difficult to predict if one takes into account the possible stabilization of magnetic nanocrystals with capping molecules. Surfactant molecules are mainly used in *bottom-up* synthetic approaches where their presence allows a high level of control on the size and the shape of nanocrystals, which are hardly achievable by traditional *top-down* approaches. Depending on the nature of these capping molecules, a relaxation of the surface atoms can be possible [37]: the coordination sphere of the surface atoms is partially recovered, their broken symmetry is reduced and hence the surface spins are more easily aligned with the magnetization direction, thus increasing M_S. Surface effects are hence largely dependent on the synthesis method as well as on the quality of the crystals.

Shape anisotropy. This arises from the demagnetizing field associated with the surface magnetic charge distribution (magnetic dipoles) of a magnetic object [25]. The demagnetizing field generated in non-spherical nanoparticles is a consequence of the long-range dipolar interactions in the particle. The energy associated with the shape anisotropy of a particle can be expressed as the summation of dipolar interactions over the whole cluster [38]:

$$E_{shape}\left(\overrightarrow{m}\right) = -\frac{3\mu_{at}^2}{2}\sum_{i\neq j}\frac{\left(\overrightarrow{m}\cdot\overrightarrow{r_{ij}}\right)^2}{\left\|\overrightarrow{r_{ij}}\right\|^5} \tag{5.8}$$

where $\overrightarrow{m}$ is a unit vector along the cluster magnetization direction, μ_{at} is the atomic magnetic moment and $\overrightarrow{r_{ij}}$ is the vector connecting any two atoms at sites i and j. A uniformly magnetized single domain spherical particle has no shape anisotropy because the demagnetizing factors are isotropic in all directions. However, in the case of a non-spherical particle, it is easier to magnetize the particle along a long axis than along a short one. This is due to the demagnetizing field, which is smaller in the long direction because the induced magnetic poles at the surface are further apart. If we define the magnetization and demagnetization factors relative to the x, y and z directions of the crystal as M_x, M_y, M_z and N_x, N_y, N_z respectively, the shape anisotropy energy of a uniform magnetized ellipsoid can be expressed as [39]:

$$E_{shape} = {}^1\!/_2\mu_0 V\left(N_x M_x^2 + N_y M_y^2 + N_z M_z^2\right) \tag{5.9}$$

where the demagnetization factors satisfy the normalization relation $N_x + N_y + N_z = 1$. Then, the magnetostatic energy for an ellipsoid of revolution around the z-axis is equal to:

$$E_{shape} = {}^1\!/_2\mu_0 V M_S^2(N_z\cos^2\theta + N_x\sin^2\theta) \tag{5.10}$$

where θ is defined as the angle between the direction of magnetization and the long axis z of the particle. From Eq. (5.10), where only shape features have been considered, it is easy to see that an elongated nanocrystal in the z direction minimizes its shape energy by aligning the magnetization direction with the long axis of the particle, while its shape energy is highest for a magnetization direction perpendicular to it.

Shape anisotropy becomes particularly interesting when its competition with the magnetocrystalline anisotropy is considered. Both contributions define easy and hard magnetic axes of magnetization along which the energy of the particle is minimized or maximized, respectively. Two extreme situations can be described: let us consider an elongated single domain magnetic nanocrystal, with uniaxial magnetocrystalline anisotropy, such as a Co nanorod with a hexagonal crystal lattice. The easy magnetization axes of this nanorod, arising from magnetocrystalline and shape contributions, can be either parallel, when the nanorod growth direction corresponds to the easy magnetocrystalline axis (c axis), or perpendicular, when the growth of the crystal is induced in a perpendicular direction with respect to the c axis of the crystal. The combination of these two easy axes of magnetization decides the effective easy magnetization direction in the nanorod and its effective anisotropy energy barrier for the magnetization reversal, as shown in Fig. 5.4. In an isolated single domain elongated particle, in which magnetocrystalline and shape anisotropy are cooperatively coupled, the anisotropy energy is enhanced and accordingly both the T_B and H_C are expected to increase with respect to its spherical analogue.

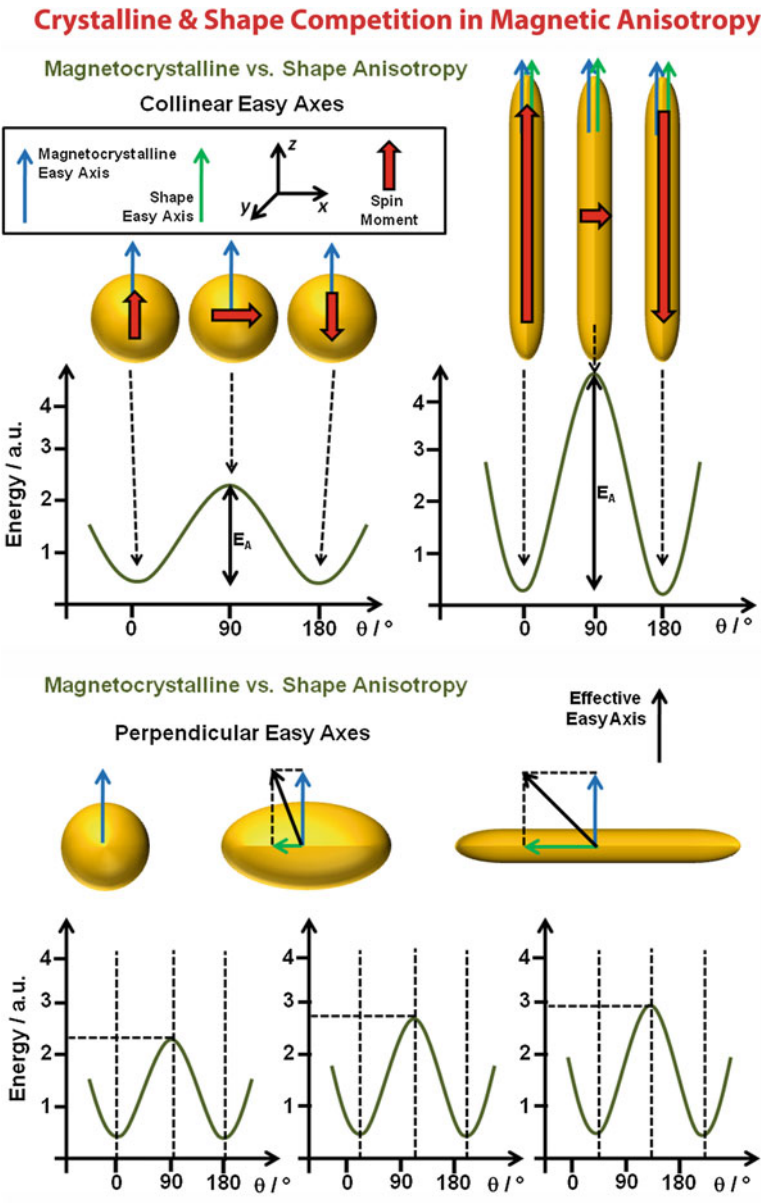

Fig. 5.4 Cooperation/competition between crystalline and shape magnetic anisotropies for the direction of the effective easy magnetic axis of the nanoparticle. The variation of the effective anisotropy energy barrier for the magnetization reversal derived from such competition is also described. θ represents the angle between the magnetocrystalline easy axis and the magnetization direction

Shape anisotropy can therefore be employed to tune or modify several magnetic parameters characterizing the behavior of mainly ferro- and ferrimagnets. Therefore, the control over the magnetic properties by the fine engineering of the morphology of nanocrystals could become a key factor for the use of nanostructured magnetic particles with improved performance in several fields, such as information storage and biomedicine. However, since so many structural, size, shape and surface stabilization factors influence the final magnetic behavior of nanocrystals, clear conclusions or trends cannot be extracted by simple inspection of experimental results.

5.4 Iron Oxide-Based 1D Nanostructures

Iron oxides, being the oldest known magnetic materials in history, are by far the most studied ones, both in bulk systems and in their nanoscale counterparts. Iron oxide can grow in different structures, depending on formation conditions. Hence, clearly different magnetic features can be observed depending on their chemical nature and crystal ordering. Before starting with the review of elongated iron oxide nanocrystals, we therefore briefly describe the basic crystallographic and magnetic features of the most important varieties.

The *wüstite* mineral, FeO, is the most reduced form of iron oxide, with all cations being in the +2 oxidation state. For this reason it is strongly susceptible to disproportion into metallic iron, α-Fe, and *magnetite*, Fe_3O_4. It crystallizes in the cubic crystal system and shows antiferromagnetic order below the bulk T_N of 195 K. Due to its chemical metastability and low values of magnetization and critical temperature, it has not attracted much interest up to now.

On the other hand, the *magnetite* mineral, Fe_3O_4, shows a chemical stability far beyond that of *wüstite*. Fe_3O_4 can be understood as a mixture of $FeO \cdot Fe_2O_3$ crystallized together in the same lattice, not to be confused with a solid solution. It belongs to the inverse spinel group of materials, which show a face-centred cubic lattice. Its structure can be described as a cubic close-packed lattice of O atoms where A^{2+} and B^{3+} cations partially occupy the octahedral and tetrahedral sites, forming AB_2O_4. To be more precise, all Fe^{2+} ions are in Oh sites together with half of the Fe^{3+} ions, in total half of the available Oh sites are occupied; the other half of the Fe^{3+} ions are in the Td sites, meaning that just 1/8 of the available Td sites are filled. Below its T_C of 858 K it shows a ferrimagnetic order, in which spins of Fe^{2+} and Fe^{3+} ions, even if antiferromagnetically coupled, do not cancel in the crystal and a net magnetic polarization is still present in the material. *Magnetite* shows a permanent magnetic moment with nearly full spin polarization at room temperature. For this reason, it has become one of the most studied and used iron oxides. Due to the cubic symmetry of its crystal lattice, it shows a low magnetocrystalline anisotropy, with easy axes along the three [111] directions, while the [100] direction is the magnetically hard one. The M_S for bulk Fe_3O_4 is 92–98 emu/g. *Magnetite* can also show a spontaneous intercorrelated change of

both lattice symmetry and electrical conductivity at 125 K for the bulk. This is what is known as the Verwey transition. Below the Verwey temperature, T_V, crystallographic changes are often accompanied by further anomalies in the electric and magnetic properties. A proper description of such phenomena can be found in the review article of Walz [40]. However, the observation of such transition in nanostructured materials is quite complicated because it seems to be very sensitive to the stoichiometry and crystallinity of the particles. Only a few works pointed out the evidence of the Verwey transition in nanocrystals [41].

Hematite (α-Fe_2O_3) is the most stable iron oxide under ambient conditions. Because of its low cost, high resistance to corrosion and environmentally friendly properties, *hematite* has been used in many applications as catalyst [42], pigment [43], gas-sensor [44] or electrode material [45]. It is characterized by a rombohedrically centered hexagonal structure of corundum-type, with a close-packed oxygen lattice in which two-thirds of the octahedral sites are occupied by Fe^{3+} ions. *Hematite* shows two temperature-dependent magnetic transitions: Below its T_N of 948 K, the low symmetry of the cation sites allows spin-orbit coupling to cause canting of the antiferromagnetically coupled spins toward the plane perpendicular to the hexagonal c axis of the lattice. This condition gives rise to what is known as a "canted antiferromagnet" or "weak ferromagnet" with a low net magnetic moment. However, when lowering the temperature, *hematite* shows a transition from weak ferromagnetic to antiferromagnetic: the Morin temperature, T_M, is the temperature below which the low magnetic moment vanishes due to a change in anisotropy that forces the alignment of the spins along the c direction. For bulk *hematite* T_M is 263 K.

Maghemite, γ-Fe_2O_3, can be regarded as the fully oxidized form of *magnetite*, with an identical cubic spinel structure where the Fe^{2+} ions of the octahedral sites have been completely removed. The loss of magnetic ions results in a slight decrease of the room temperature spontaneous magnetization ($\sim$80 emu/g for the bulk), compared to its mixed valence analogue Fe_3O_4. *Maghemite* shows ferrimagnetic behavior below its T_C of ca. 918 K due to the non-equivalent crystallographic sites of its Fe^{3+} ions; however, this T_C is difficult to determine experimentally since at high enough temperatures *maghemite* undergoes an irreversible crystallographic change to α-Fe_2O_3, with the consequent dramatic loss of magnetization. This phase transition has been observed to occur over a wide range of temperatures and seems to be highly dependent on the grain size and the presence of impurities.

Fe_3O_4 and γ-Fe_2O_3 are hard to distinguish by X-ray diffraction or electron microscopy techniques due to their identical crystal symmetry and almost identical lattice parameters. However, oxidation-state sensitive techniques such as X-ray Absorption Near Edge Structure (XANES) or Mössbauer spectroscopy can easily solve this problem.

It is worth mentioning the existence of the highly metastable ε-Fe_2O_3 phase of iron oxide. This phase has a very narrow temperature range of existence and actually it has only been observed in the nanoscale regime [46]. It can be regarded as an intermediate phase between α-Fe_2O_3 and γ-Fe_2O_3 and it crystallizes in a

non-centrosymmetric orthorhombic structure that opens the possibility to use this oxide as an interesting material for piezo, magneto and pyroelectric applications. From a magnetic point of view, ε-Fe_2O_3 shows a ferrimagnetic behavior below its T_C temperature of 510 K and more interestingly, due to the low symmetry of its crystal lattice it presents high values of magnetocrystalline anisotropy compared to the previous iron oxide allotropes.

5.4.1 Magnetite-Based 1D Nanostructures

A few examples of single crystalline 1D Fe_3O_4 nanostructures have been reported in the literature. Nanorods with average diameters of 40–50 nm and lengths up to 1 μm were synthesized by Lian et al. through hydrolysis of $FeCl_3$ and $FeSO_4$ solutions containing urea. The reaction was carried out under reflux conditions and in the absence of surfactants and it was followed by an aging process [47]. Selected area electron diffraction (SAED) measurements confirmed the single crystalline nature of the rods even though the growth direction could not be discerned. Field-dependent magnetization measurements on randomly oriented samples indicated a value of M_S of 67.55 emu/g, which is significantly lower than the corresponding value for the bulk Fe_3O_4, 92 emu/g. On the contrary, under hydrothermal conditions, and with the assistance of polyethylene glycol as surfactant, Wang et al. obtained uniform nanorods with diameters of 20–25 nm and lengths up to 200–300 nm (Fig. 5.5a) [48]. High-resolution transmission electron microscopy (HRTEM) analysis confirmed the single crystalline character of the rods and further identified the [110] direction as their growth direction (Fig. 5.5b). This direction interestingly matches with one intermediate easy magnetization axis of the cubic structure of *magnetite*. The authors claimed that this could be one reason for the high value of M_S observed, 90.5 emu/g, which is only slightly lower than that in bulk samples. In another work, the same authors used a similar synthetic approach for the synthesis of the first single crystalline Fe_3O_4 nanowires, the main difference being that the reaction was carried out under the effect of an external magnetic field with the hope that this would induce an oriented growth of the material [49]. Depending on the strength of the applied magnetic field, they successfully synthesized polyhedral-shaped nanoparticles, nanowires of 35–100 nm of diameter and 480–2,700 nm of length, as well as nanofibers of 20 nm diameter and 800 nm length approximately (Fig. 5.5c and d). Also in this case, HRTEM allowed to identify the [110] easy magnetocrystalline axis as the growth direction of the wires. In Fig. 5.5e, magnetic properties of powder samples of nanowires and nanofibers are compared with those of cubic or hexagonally-shaped Fe_3O_4 nanocrystals, obtained under the same conditions but in the absence of magnetic field. For 1D systems, M_S values were found to be in the range between 35 and 40 emu/g, less than the half of the value attributed to the bulk and lower than the value observed for cubic or hexagonal nanocrystals (68.7 emu/g). The projection of the magnetization vectors along the field direction is lower for a

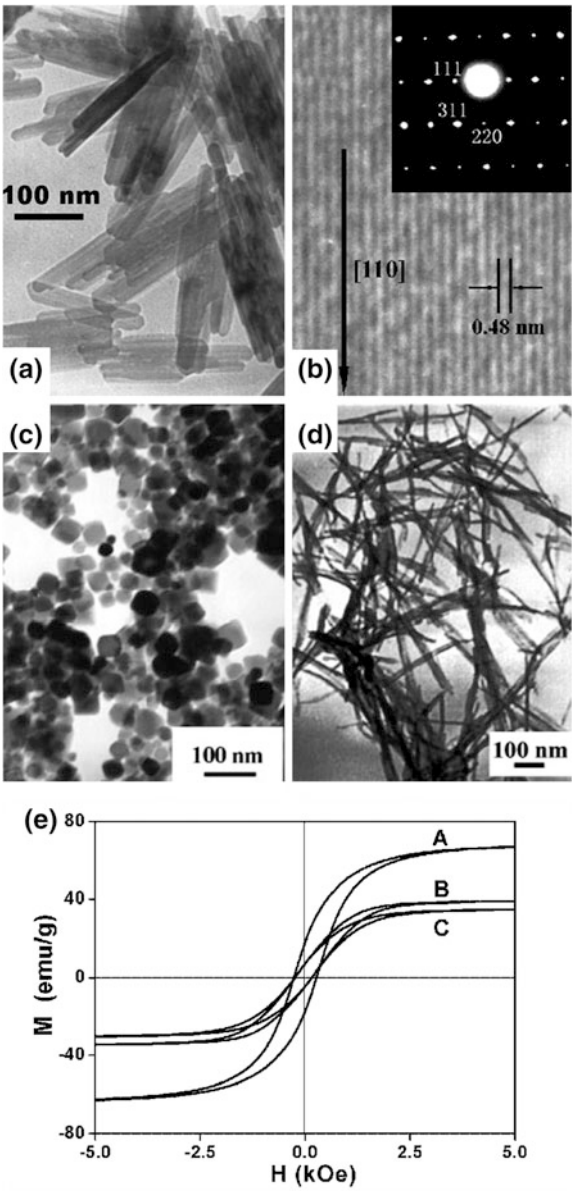

Fig. 5.5 **a** Transmission Electron Microscope (TEM) micrograph of the rod-like nanocrystals from Ref. [48]; **b** high-resolution TEM micrograph of one single nanorod of the sample in **a** confirming its single crystalline character; the inset is the electron diffraction pattern obtained from a single Fe_3O_4 nanorod; TEM micrographs of nanocrystals prepared in Ref. [49] in the absence (**c**), and presence (**d**), of external magnetic field; and **e** magnetic hysteresis curves measured at room temperature for polyhedral–(*A*), nanowire–(*B*) and nanofiber–(*C*) like particles of Ref. [49] taken with permission from Refs. [48] and [49]

randomly oriented sample of nanowires than that for a collection of nanoparticles without shape anisotropy. As a consequence the authors claimed that the total magnetization of the sample could be significantly reduced due to the randomization of the wires. Similar observations were made by Wan et al. [50] for both Fe_3O_4 nanorod and nanowire samples compared to analogous spherical nanoparticles. Additionally, in that case the authors studied the differences in coercivity: higher values of H_C for 1D samples were attributed to the shape anisotropy of the nanocrystals, in agreement with what theory predicts. Similarly, other works also report on the increase of H_C with increasing aspect ratio[51].

Recently, the first preliminary experimental results concerning the performance of rod-shaped magnetic nanocrystals in biomedicine have emerged [52]. Perez and co-workers reported on the synthesis of water-soluble dextran-coated Fe_3O_4 nanorods and their activity as magnetic sensors for bacterial detection. The authors first cross-linked and aminated the dextran coating of the nanorods in order to conjugate them to the antibodies of the test bacterium. They chose *Mycobacterium avium* spp. *paratuberculosis* (MAP) as their model organism because the identification of MAP using current methods is difficult, due to the very slow growth of the bacterium. The detection was made by monitoring the T_2 relaxation times using a 0.47 T relaxometer. A significant improvement was observed in the detection of MAP bacteria in milk samples when nanorod Fe_3O_4 structures were used instead of spherical ones, as compared to their previous publication [53]. Improvements were found both in detection limit and in detection kinetics and they were attributed to the high magnetic water relaxivity associated with nanorods and to the large number of antibodies conjugated per nanorod.

5.4.2 Hematite-Based 1D Nanostructures

Hematite is by far the most studied form of iron oxide due to its high stability and wide range of applications. Several authors reported on the synthesis of *hematite* nanorods [47, 54–57], nanowires or other elongated nanostructures [58–61]. However, just a few of them performed their magnetic analysis. As mentioned before, bulk crystalline α-Fe_2O_3 shows two different magnetic transitions with temperature: below its T_N of 960 K, the material shows a weak ferromagnetism where the spins are antiferromagnetically coupled but slightly canted giving rise to a low magnetic moment in the basal plane of the lattice perpendicular to the hexagonal c axis. Below the T_M of 263 K, the spins are antiferromagnetically aligned along the c axis of the crystal and its magnetic moment is cancelled. It is known that both transition temperatures are significantly affected by the size of the nanocrystal, decreasing with decreasing size [62], in a way that small particles still behave as weak ferromagnets with a non-negligible magnetic moment at low temperatures below the T_M of bulk *hematite*. In the last decade several works have provided experimental evidences of their shape dependence as well. In 1999, Fiorani et al. reported on the low value of the T_M for acicular-shaped α-Fe_2O_3

nanoparticles (length × diameter: 350 × 85 nm) which was observed to be 170 K, a temperature at which the authors observed a sharp increase of the magnetization with increasing temperature due to the appearance of a weakly ferromagnetic phase [63]. They assigned the decrease in T_M compared to the bulk value to the size reduction and shape anisotropy of the particles. A similar value of T_M (ca. 166 K) was also found by Liu et al. for single crystal nanorods of 500–1,100 nm in length and 30–50 nm in diameter [64]. The nanorods showed a magnetic hysteresis loop at room temperature ($H_C = 280$ Oe), which confirmed the high temperature weak ferromagnetic state of the sample.

Woo et al. [65] observed a constant increase of the magnetization from 5 to 300 K for single crystalline *hematite* nanorods (16 × 5 nm), which is representative of a ferromagnetic behavior already at 5 K with an M_R and H_C of 0.28 emu/g and 53 Oe, respectively. No clear T_M value was observed for that sample. It is worth noting that these rods are much thinner than the ones of the previous examples [63, 64]. The Morin transition was found to be strongly dependent on the particle size for spherical nanocrystals and it was usually not observable anymore for particle diameters in the range from 8 to 20 nm or below [62]. For this reason T_M was also expected to follow a similar trend with decreasing diameter of the rod. Some groups made an attempt to study the evolution of the Morin transition with differently sized α-Fe_2O_3 nanorods. Following an hydrothermal synthetic approach with an additional thermal treatment in air, differently sized nanorods with or without a porous morphology were obtained, depending on the presence of particular inorganic salts in the reaction mixture, which did not alter the chemical nature of the *hematite* phase, but only its morphology [66]. Their T_M was correlated with the diameter of the rod-shaped nanoparticles. The magnetic measurements are presented in Fig. 5.6.

These results indicated a classical Morin transition for particles with larger diameters (300–500 nm in one sample and 60–90 nm in the second; the second sample showed a porous morphology with pore diameters in the range between 20 and 50 nm) in which the high temperature weak magnetization dropped drastically upon cooling below the T_M, for both ZFC and FC curves. In both cases T_M was seen to be 255 K, irrespective of the rod diameter and very close to the T_M value for the bulk. On the other hand, samples of nanorods with diameters between 2 and 16 nm showed either lower values of T_M (235 K), or even no apparent Morin transition down to 5 K. In both samples the phenomenon was associated with the decrease in diameter of the rods. The authors claimed that the presence of nanosize internal pores in one sample could be responsible for the disappearance of the antiferromagnetic phase in that case, but no experimental proofs were reported. Other authors have also recently studied the magnetic properties of porous *hematite* nanorods with similar results [67].

Zhao et al. compared the magnetic properties of two single crystal nanorod samples obtained using different synthetic approaches, i.e. iron-water vapour reactions and hydrothermal techniques: needle-shaped rods of sample 1 showed average lengths between 1.5 and 2 μm and diameters of 20 nm at the tips and 100 nm at the base. Sample 2 was formed by ellipsoidal rods with long axis of

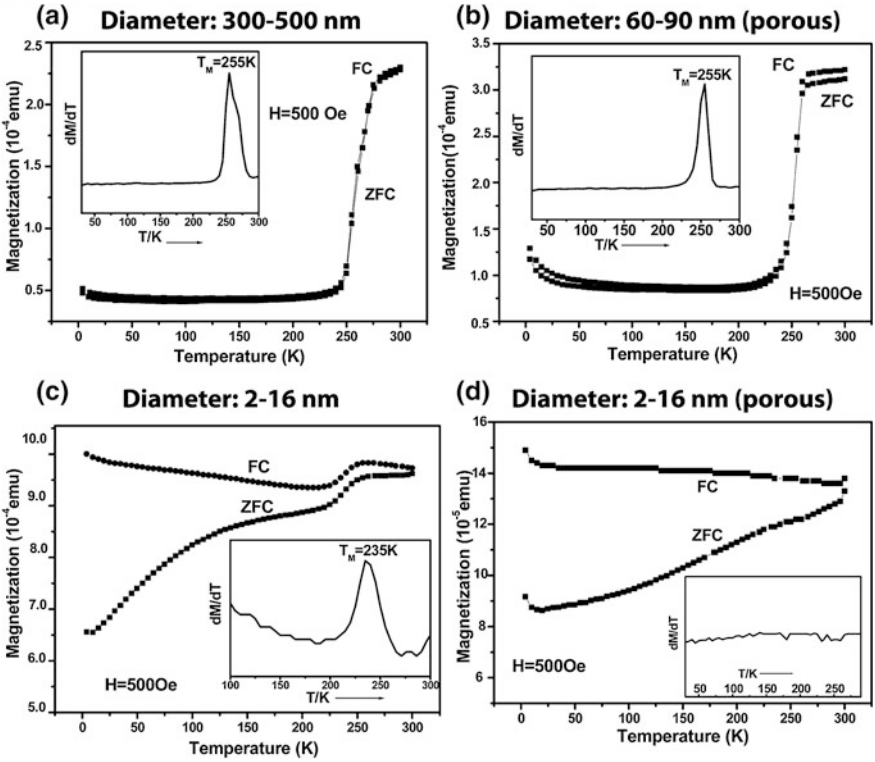

Fig. 5.6 Temperature dependence of ZFC and FC magnetization for an applied field of 500 Oe for samples from Ref. [66]. Insets are their corresponding differential ZFC curves. Taken with permission from Ref. [66]

400–500 nm and short axis of 50–60 nm [68]. Magnetic measurements are shown in Fig. 5.7. At 200 K, the hysteresis loops of samples 1 and 2 showed different values of H_C, those being 198 Oe and 688 Oe, respectively. This observation was in accordance with the multidomain character of sample 1 and the pseudo-single domain character of sample 2, based on the criteria given by Dunlop [69]. Such different magnetic domain features are responsible, as described in Sect. 5.2, for lower coercivity values in the case of multidomain samples, due to the lower energy required for domain wall motion compared to the coherent magnetization rotation of a single domain. An interesting and unexpected phenomenon was observed for sample 1 in the temperature-dependent FC/ZFC measurements recorded at low fields, which was assumed to be strictly related to the shape anisotropy of the nanocrystal. A decrease in the *hematite* magnetization value is expected with decreasing temperature when T_M is reached, due to the weak ferromagnetic to antiferromagnetic transition. The FC/ZFC curves were recorded for both samples at a fixed field value of 100 Oe. The expected profile of the curves was observed for both samples, from which a value of 122 K was determined for

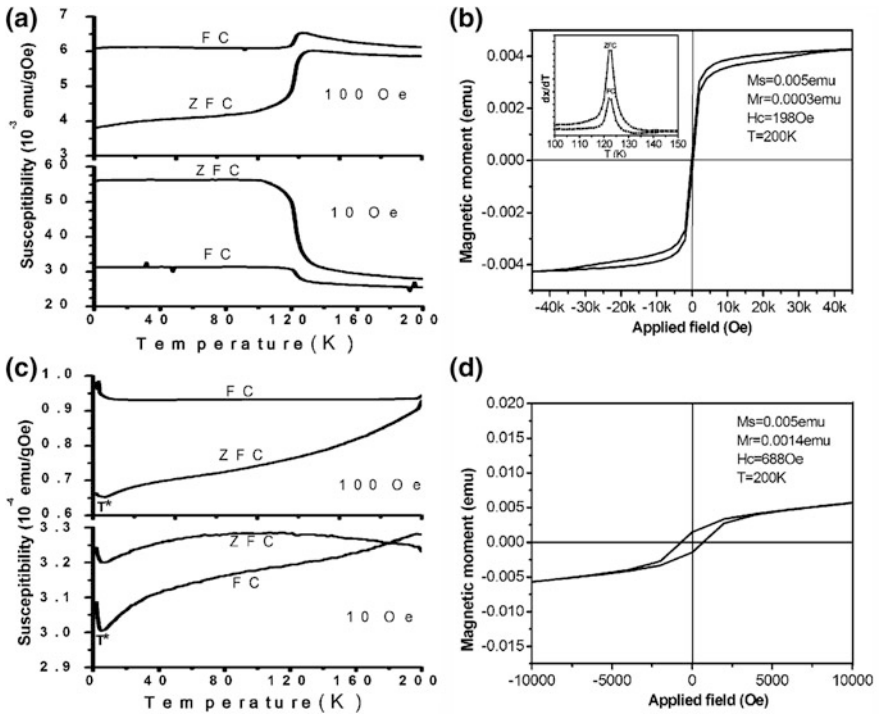

Fig. 5.7 Temperature-dependent magnetic susceptibility measurements and hysteresis loops of *hematite* nanorods from Ref. [68]: **a**, **b** nanorods prepared by iron-water vapour reactions; **c**, **d** nanorods prepared by hydrothermal techniques. The inset in **b** is the $d\chi/dT$ versus T curve for the first sample when an external magnetic field of 100 Oe was applied. Taken with permission from Ref. [68]

T_M of sample 1, while no apparent T_M was seen in sample 2, in accordance with the reduction of size. However, when FC/ZFC experiments were performed under a weak external magnetic field of 10 Oe, sample 1 showed an unexpected sharp increase of magnetization at the same T_M observed in the measurement performed at 100 Oe.

The authors calculated shape anisotropies that were very similar for both samples and very close to the value of magnetocrystalline anisotropy of rhombohedral *hematite*. This strongly suggests a competition of both kinds of anisotropy in the effective magnetization direction in the samples. Below T_M the magnetocrystalline easy axis of magnetization for α-Fe_2O_3 is found along the [111] direction of the crystal; on the other hand, at temperatures above T_M, there are three easy magnetization axes in the basal plane of the structure and each axis is separated from the others by 60°. The shape anisotropy, however, tends to align the magnetization, independently of the temperature, along the growth direction of the rods which, for sample 1 is the [118] direction, while for sample 2 it is the [111] one. Hence, the easy axis of magnetization lies in a direction resulting from the coherence of the

shape and the magnetocrystalline anisotropies, which is clearly different for samples 1 and 2 and also above and below T_M. When weak magnetic fields are applied, the magnetization of the sample is mainly directed by the intrinsic anisotropy of the nanorods and different magnetic behaviors can be expected for samples 1 and 2. In this case, the authors concluded that for sample 1 the magnetic susceptibility along the resultant direction has a larger value for temperatures below T_M than for those above T_M. Alternatively, when higher magnetic fields are applied, e.g. 100 Oe, the pinning of the spins due to shape anisotropy is overcome and hence the expected behavior at T_M is restored. It is interesting to notice that experimental results are usually explained by magnetocrystalline anisotropy considerations, since these dominate in the bulk material. However, in the case of highly anisotropic nanocrystals, where important shape contributions also take place, new phenomena can emerge and conventional arguments need to be reconsidered.

Shape anisotropy, as discussed before, is expected to increase the total anisotropy of the particle, and so higher values of coercivity should arise from higher aspect ratio nanorods. Zeng et al. [70] reported an increase of the value of H_C from low (ca. 1.8) to very high (ca. 21) aspect ratio *hematite* nanorods. The expected trend was observed with H_C values at 5 K running from 67 Oe, for the lowest aspect ratio rods, to 584 Oe for the highest aspect ratio ones, with an intermediate value of 146 for nanorods with an aspect ratio of 18. Other authors reported similar coercivities for nanorod ensembles of different dimensions but similar aspect ratios, confirming the previously described trend [71]. In the case of Zeng et al., the three samples showed a constant increase in magnetization with decreasing temperature and no apparent Morin transition was observed for any of them. This could mean that all samples show a weak ferromagnetic state even at low temperatures, which was supported by the presence of coercivity at 5 K in all cases. The authors believe that the increased surface contribution arising from the high shape anisotropy of the crystals is responsible for the absence of T_M. Contrary to Zeng's observations, Zhang et al. [72] did not observe any difference in magnetic behavior in two samples of nanorods with significantly different aspect ratios. The samples were synthesized according to the same hydrothermal procedure, but at two different temperatures. The observed low temperature hysteresis loop was assigned to a ferromagnetic state that was still present at 5 K, even though no FC/ZFC measurements were reported to check the presence or absence of a Morin transition. Experimentally, by means of temperature-dependent magnetic measurements, the value of T_M can be determined by the sharp peak in the $d\chi/dT$ versus T curve. When such peak is not observed, which means that the susceptibilities of the FC curve do not decrease with decreasing temperature, the sample is said not to show any apparent T_M, and hence coercivity is still expected at low temperatures. However, even when a value of T_M can be determined and consequently the formation of an antiferromagnetic phase is confirmed at $T < T_M$, often an hysteresis can still be observed at low temperatures. Sorescu and co-workers have studied different *hematite* particles with polyhedral, plate-like, disk-shaped and needle-like morphologies, prepared by hydrothermal methods, using Mössbauer spectroscopy [73]. Their results have shown that the weak ferromagnetic and antiferromagnetic phases

can coexist below T_M, but the population of the first strongly depends on the morphology of the particle, being the largest for elongated needle-like nanocrystals, as shown in Fig. 5.8. More recently, Brioude et al. proposed a phenomenological formula to describe the dependence of T_M with the size or diameter (the latter being larger than 15 nm), based both on their own results as well as on previous works [74].

The use of *hematite* nanotubes in antitumoral therapies holds promise, specially with regard to their spherical analogues. Ma et al. [75] have observed a significantly faster internalization of nanorods into different types of carcinoma cells compared to spheres. Similarly, the maximum uptake level was much higher in the case of nanorods. In view of these results, the authors transformed the nanorods into nanotubes to convert them to useful magnetically guided drug vectors. Hydrophobic Paclitaxel (PTX) drug was loaded quantitatively into the nanotubes and the drug-carrier pair was efficiently uptaken by the tumoral cells, where PTX was released due to the lower intracellular pH. Other studies of 1D iron oxide nanostructures have also shown long blood circulation times, enhanced retention at tumor sites and improved targeting efficiency, which suggests that anisotropic iron oxide nanoparticles could potentially lead to further advancement in biomedical applications [76].

5.4.3 Maghemite-Based 1D Nanostructures

As described above, *maghemite* (γ-Fe_2O_3) is an oxidized form of Fe_3O_4. Although ferrimagnetic properties are still present in γ-Fe_2O_3, its magnetization is lower than that of the mixed valence analogue. Special attention should be paid during magnetic characterization: at high enough temperatures, γ-Fe_2O_3 can undergo a

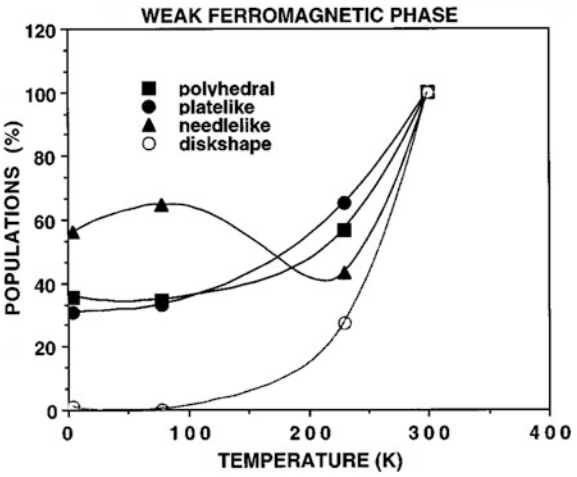

Fig. 5.8 Percentage population of the weak ferromagnetic phase, with respect to the antiferromagnetic one, as a function of temperature, for *hematite* particles of different morphologies [73]. Taken with permission from Ref. [73]

phase transformation to the antiferromagnetic or weak ferromagnetic α-Fe_2O_3. This transformation can occur in a wide range of temperatures depending on grain size and type of impurities. The literature concerning nanorod or elongated nanostructures of the γ phase of iron oxide is limited and it mainly discusses the synthetic procedure for its preparation [56, 77]. Palchoudhury et al. [78] recently studied the mechanistic pathways by which one could induce a shape control during the synthesis of iron oxide. They successfully synthesized pure and crystalline γ-Fe_2O_3 nanowhiskers starting from Fe(III) oleate complexes. Such 1D iron oxide nanostructure did not reach M_S probably due to their large surface-to-volume ratio compared to spheres. In a few reports, the magnetic study of the nanorods was also undertaken to some extent. For example, in 2004 Woo et al. [65] prepared single crystalline *maghemite* nanorods with dimensions 5 × 17 nm. The authors attributed the maximum in the ZFC magnetization versus temperature curve to a value of T_B of 130 K, lower than the T_C value of the bulk, but higher than the value measured for *maghemite* nanospheres with similar diameter [79]. Other authors have undertaken Ferromagnetic Resonance experiments in order to study the increase of magnetic anisotropy due to the shape of γ-Fe_2O_3 nanorods [80].

5.4.4 ε-Fe_2O_3-Based 1D Nanostructures

The highly metastable ε-Fe_2O_3 phase of iron oxide shows a very narrow temperature range of existence and actually it has only been observed in the nanoscale [46]. In 2004, Ohkoshi and co-workers reported for the first time a ε-Fe_2O_3 single phase in the form of nanorods, covered by a thin silica shell (lengths in the range between 100 and 140 nm and diameters of 20–40 nm) [81, 82]. Pure ε-Fe_2O_3 nanorods showed good crystallinity and were observed to grow along the *a* axis of the orthorhombic lattice, as shown in Fig. 5.9a and b. Due to its low symmetry crystal structure, it presents high values of the magnetocrystalline anisotropy compared to previous iron oxides. ε-Fe_2O_3 is a ferrimagnetic material with a T_C of 510 K. However, following the usual trend with reducing size of the crystal, nanorods reported by Ohkoshi showed a T_B of 480 K, i.e. between the high temperature superparamagnetic and the low temperature ferrimagnetic states. This means that such small nanorods were ferrimagnetic at room temperature and, moreover, they showed giant values of coercivity: H_C at room temperature was observed to be 2 T, that is 20,000 Oe, as shown in Fig. 5.9c. The stability of the ε phase in the nanorods is believed to be due not only to the growth of a stabilizing silica shell, but also to the presence of Ba^{2+} ions in the reaction mixture which, by means of the formation of a thin BaO layer, creates an additional space confinement on the surface of the rods [83]. However, the removal of these two components after the synthesis does not seem to alter the magnetic properties of the nanorods. The authors evaluated the different anisotropy contributions taking place in the nanocrystal and they explained the high value of H_C by (1) the single magnetic domain character of the nanorods, due to their small size and high degree

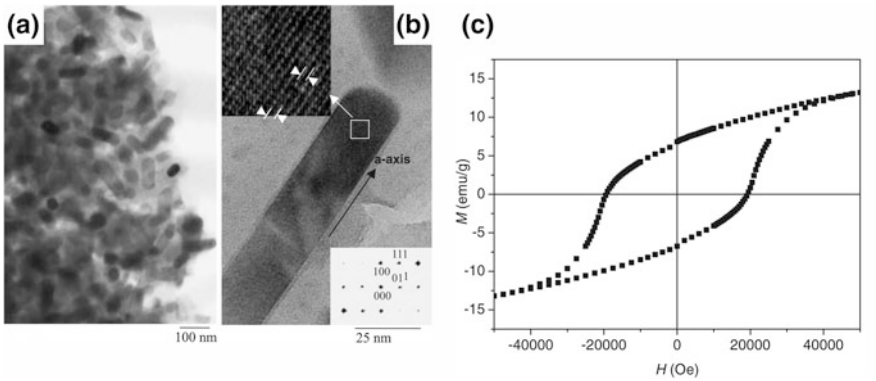

Fig. 5.9 Low (**a**) and high (**b**) resolution TEM micrographs of ε-Fe_2O_3 nanorods from Ref. [81]. The insets are a high resolution TEM image of the particle showing its lattice planes and a selected area of the Fourier transform pattern of this image (crystal planes identified). **c** Magnetization versus field plots at room temperature for ε-Fe_2O_3 nanorods. Taken with permission from Ref. [81]

of crystallinity and (2) their high value of magnetocrystalline anisotropy energy (more than one order of magnitude higher than in α- or γ-Fe_2O_3). However, the calculated shape anisotropy contribution in the rods is suggested to be responsible for 0.53 T of the total H_C of the sample, and hence the shape contribution should not be neglected.

5.4.5 Assembly of Oxide-Based 1D Nanostructures

The regular alignment of 1D magnetic nanoparticles (i.e. rods, wires) is the only configuration that allows for the observation of anisotropic magnetic features that depend on the relative direction of the applied magnetic field with respect to the assembly orientation. Such angular dependence of the magnetic properties of well-aligned magnetic 1D systems is expected to introduce unique characteristics, which could be useful for several devices, and has been matter of study for many decades. The presence of dipolar interactions between nanoparticles in the assembly should also be taken into account: they can significantly modify the magnetic behavior of the single particle, as observed by several groups [84]. Already in 1961 Bate studied the variation of magnetic properties with increasing angles between the applied field and the alignment direction of γ-Fe_2O_3 acicular particles of aspect ratio close to 7, dispersed in a suitable non-ferromagnetic matrix, with different coverage degrees. The results showed clear evidence of different magnetic behavior due to the shape anisotropy of the particles [85].

The synthesis of iron oxides has been usually carried out in solution, either by sol–gel or by hydrothermal techniques, leading to isolated particles that are

randomly oriented in the sample. The effect of the shape anisotropy in such systems could be observed in single particle studies, which are generally difficult to perform. Otherwise, the controlled alignment of the particles is strictly required if one wants to study the angular-dependent magnetic properties of ensembles of particles. However, the experimental difficulty of aligning the as-prepared 1D oxide nanostructures has represented a clear drawback with respect to metal 1D systems for which, as will be discussed later in Sect. 5.5, several experimental procedures have been developed to grow regularly oriented 1D nanorod or nanowire assemblies. Nevertheless, some synthetic approaches have also been reported for the growth of well-aligned oxide 1D nanoparticles. Some of these approaches include: the controlled precipitation of Fe precursors on substrates [86, 87], the thermal oxidation of metal foils under well-controlled conditions [88], pulsed laser deposition techniques [89], metal–organic chemical vapour deposition on substrates (MOCVD) [90] or other vapour-solid routes [91]. As reported previously for randomly oriented 1D nanostructures, α-Fe_2O_3 is also the most widely studied form of iron oxide for what concerns oriented assemblies.

α-Fe_2O_3 nanowires of lengths up to 15 μm with a sharp tip and wider base of 50 nm and 100–300 nm length, respectively, were grown on Fe foils by Kim et al. (Fig. 5.10a–c) [92]. They clearly confirmed their single crystalline character and

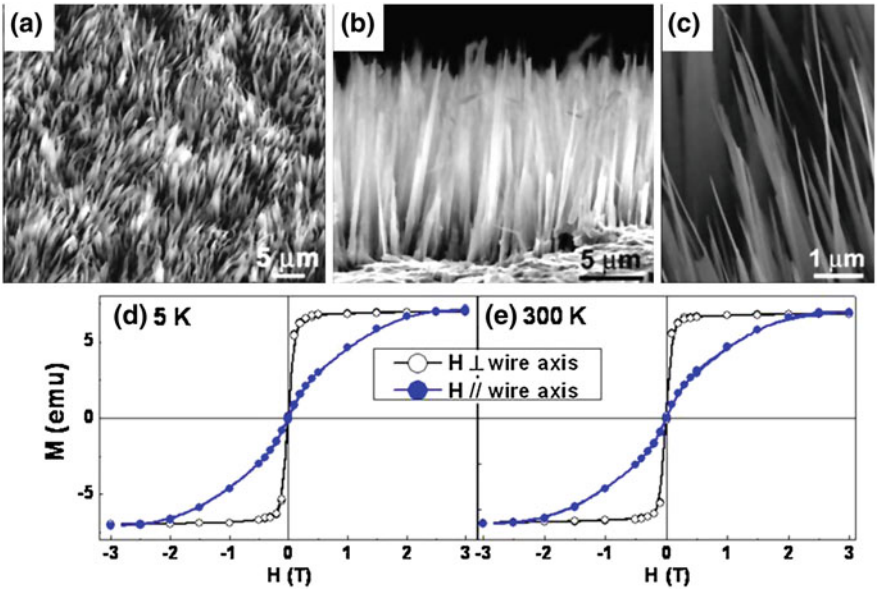

Fig. 5.10 **a** Scanning electron microscope (SEM) micrographs showing the high-density α-Fe_2O_3 nanowire arrays grown on substrates in Ref. [92]; **b** side view reveals the vertical alignment of the nanowires; **c** a magnified view reveals the sharpness of the wire tips; *M-H* curves of α-Fe_2O_3 nanowire arrays, under a magnetic field applied parallel and perpendicular to the nanowire axis. The measurements were carried out at 5 K (**d**) and 300 K (**e**) for these two directions of the magnetic field. Taken with permission from Ref. [92]

their rhombohedral structure where the $[11\bar{2}0]$ was identified as the only growth direction. Temperature and field-dependent magnetic measurements on randomly oriented wires that were detached from the substrate were used to determine a T_M of 125 K (far below the bulk value) and a ferromagnetic state both at room temperature and at 5 K, with a coercive field of 150 Oe at 5 K. The authors also described the results obtained from magnetic measurements performed under an external magnetic field oriented parallel and perpendicular to the nanowire axis (Fig. 5.10d and e). The same T_M value was extracted from data obtained in both configurations. Interestingly, magnetic hysteresis was only observed when the field was applied perpendicular to the growth direction of the nanowires, while zero coercivity was observed when the field was parallel to it. The authors suggested that this was a clear evidence of the dominance of magnetocrystalline anisotropy over shape anisotropy. While the shape anisotropy easy axis is parallel to the $[11\bar{2}0]$ direction, the magnetocrystalline anisotropy easy axis is parallel to the [0001] direction and hence perpendicular to the growth direction. Consequently, when the field is applied in the direction of the magnetocrystalline anisotropy, more square-shaped cycles with non-zero coercivities were observed.

Wu et al. performed similar measurements on α-Fe_2O_3 nanorods vertically aligned on Si substrates with the [104] as the growth direction [90]. In that case, both parallel and perpendicular orientations of the field with the axis of the rods led to similar values of coercivity of 200 Oe. However, the saturation magnetization of the sample was observed to be significantly higher when the field was applied perpendicular to the rod axis, probably indicating the dominance of the magnetocrystalline anisotropy over the shape contribution. Several factors such as the synthetic procedure followed for the sample preparation, and the different size and aspect ratios, compared to the nanowires described before and reported by Kim et al. [92], could be some of the reasons for the different observed behavior. In any case, the resulting easy axis of magnetization depends on the directions of both the magnetocrystalline and the shape easy magnetic axes, as described earlier (Fig. 5.4). Consequently, the different growth directions of the 1D structures in both cases led to effective easy magnetic axes with different orientations. This is probably responsible for the observation of coercivity in the nanorod sample of Ref. [90], independent of the magnetic field direction, while in the nanowire sample of Ref. [92] coercivity was only observed in the perpendicular direction.

Chueh et al. described the synthesis of single crystalline α-Fe_2O_3 nanowires grown on metallic substrates with growth along the [110] direction [91]. A thermal treatment of the as-synthesized α-Fe_2O_3 nanowires was conducted under reducing atmosphere in order to obtain single crystalline Fe_3O_4 nanowires which maintained the original dimensions and shape of the starting wires, but with growth along the $[1\bar{1}0]$ direction. Nanowires of both types were separated from the original substrates and deposited independently on Si substrates before performing magnetic characterization, in order to avoid the magnetic contribution from the metallic substrates. The authors studied the effect of the applied magnetic field on the nanowires lying on the Si substrate. They found that fields up to 5 kOe were not

sufficient to align α-Fe_2O_3 nanowires, due to their extremely weak ferromagnetism in the canted-spin state between the T_N and T_M. On the contrary, magnetic fields of the same magnitude were sufficient to induce a complete alignment of Fe_3O_4 nanowires on the Si substrate. A coercive field of about 220 Oe and high remanent magnetization values were measured when the field was applied parallel to the substrate, i.e. parallel to the wire axis. Instead, when the direction of the external field was applied perpendicular to the substrate, i.e. perpendicular to the wire axes, the coercivity decreased to a value of 140 Oe and also the remanent magnetization suffered a significant decrease with respect to the previous situation. These observations were rationalized by the authors in terms of shape anisotropy.

In the case of $CoFe_2O_4$ 1D structures, the high magnetocrystalline anisotropy is usually predominant over the shape anisotropy [93]. The global anisotropy of $CoFe_2O_4$ elongated nanostructures can be better enhanced by magnetostrictive phenomena than by shape control. This is the case of $CoFe_2O_4$ nanopillars grown along the [110] direction and embedded in a $BaTiO_3$ matrix that induces significant lattice stress on the ferrite material, as reported by Zheng et al. [94].

Other works have reported the assembly of rod-shaped α-Fe_2O_3 nanocrystals in solution to form 3D superstructures. In these cases, however, the orientation-dependent magnetic characterization could not be carried out since the 3D organization of rod-shaped building blocks in the superstructure entailed several different orientations of the same. Zhu et al. [95] described the preparation and characterization of 3D urchin-like α-Fe_2O_3 superstructures. Oriented attachment of isolated nanorods seemed to be the preferred mechanism for the formation of the superstructures. Higher remanent magnetization and coercivity values were measured for such structures compared to the ones observed for the isolated α-Fe_2O_3 nanorods, although the reasons for this were not clarified in the article. The oriented attachment is also the mechanism by which An et al. [96] prepared three different types of 3D α-Fe_2O_3-based superstructures. Depending on the reaction conditions the authors were able to prepare elliptic superstructures made by assembled rod-shaped α-Fe_2O_3 building blocks, spherical superstructures composed of several nanoplatelet crystals, and spindle superstructures with a much integrated nature of the building block components, all shown in Fig. 5.11.

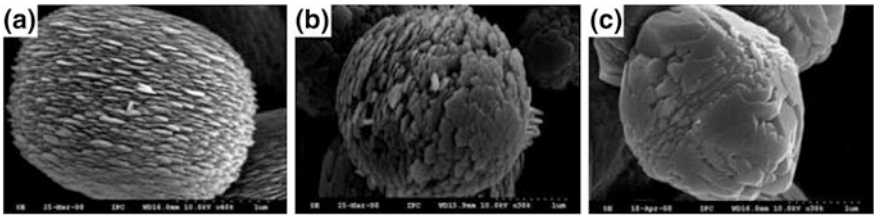

Fig. 5.11 SEM micrographs showing different α-Fe_2O_3 superstructures from Ref. [96]: **a** elliptic superstructures made by assembled nanorods; **b** spherical superstructures composed of several nanoplatelet crystals; and **c** spindle superstructures with a much integrated nature of the building block components. Taken with permission from Ref. [96]

The magnetic characterization of the three final products showed higher values of coercivity for the superstructures with an elliptical shape. The enhanced shape anisotropy of both the superstructure and the initial building blocks seem to be responsible for this. However, saturation magnetization values were lower for the elliptically shaped assemblies, probably due to the smaller size of the individual rod-shaped nanocrystals.

5.5 Metallic 1D Nanostructures

Magnetic metals such as Fe, Co or Ni show higher magnetic moments compared to their oxides. This property can be exploited in both biomedical and magnetic recording media applications. The synthesis of 1D metallic nanostructures has been classically carried out by template or membrane-assisted methods [97], metal evaporation [98], pyrolysis [99], molecular beam epitaxy [100], lithography [22] and surfactant-assisted colloidal methods [101]. All these methods have been proved to successfully lead to well-defined magnetic metal 1D nanostructures. Contrary to oxide-based nanorods or wires, in the case of pure metals synthetic approaches in which 1D structures are grown already regularly oriented on substrates are much more developed. It is important to keep in mind that metals are very sensitive to oxygen and can easily evolve to core–shell or hybrid structures in which the magnetic properties have been modified. Reduced magnetization values or exchange bias phenomena are common fingerprints of oxide-passivated metallic nanostructures [102, 103]. The study of magnetization reversal processes and domain wall dynamics in metallic nanowires is of crucial importance for the development of spintronics. The last part of this section will therefore be devoted to the description of the state-of-the-art concerning this field.

5.5.1 Co 1D Nanostructures

The hexagonal closed-packed structure of Co is the most studied one due to its intrinsic high anisotropy along the *c* axis, which in terms of magnetism obviously defines its magnetocrystalline easy axis. It is also the thermodynamically preferred phase at low temperatures. From what described in the introduction section, the anisotropy of ferromagnetic Co 1D structures grown along the [0001] direction is expected to be significantly large due to cooperating magnetocrystalline and shape contributions. Co nanowires were grown by electrochemical deposition techniques inside the porous structure of polycarbonate membranes by Whitney et al. [104]. This early work led to parallel Co nanowires perpendicularly oriented to the substrate with variable diameters, depending on the size of the pores of the original membrane. The distribution of the nanowires on the substrate was somehow broad, with interwire distances ranging from 5 to 50 nm or more. The wires exhibited

surface roughness and showed a polycrystalline character. Their preferred growth direction coincided with the magnetocrystalline easy axis, [0001], even if other growth directions were also seen, especially for narrower wires. For Co nanowires with a diameter of 60 nm, several conclusions were drawn from the comparison of the magnetic data obtained with magnetic external fields applied parallel and perpendicular to the wire axis. First, larger and square-shaped hysteresis loops were obtained when the field was applied parallel to the wire axis, indicating the resistance of the magnetic moments to be misaligned from the growth direction of the wire. A further proof of preferred orientation of the magnetic moments is given by the significantly higher fields required to reach saturation magnetization when the field was applied perpendicular to the axis. Coercivity values in the range between 150 and 680 Oe were observed depending on the diameter of the wire, increasing with decreasing dimensions but, in any case, always higher than the few tens of Oe measured for bulk Co. The opposite trend between coercivity and diameter was rationalized by the magnetic multidomain character associated to larger nanowires which is responsible for the degradation of their coercivities. The authors highlighted the importance of such oriented ferromagnetic systems for high-density perpendicular recording media, due to the enhanced coercivities observed and to the capacity to retain high values of magnetization in the absence of the magnetic field. The results reported by Whitney et al. were further confirmed by Henry and co-workers some years later [105]. Co nanowires were prepared in this case by analogous synthetic procedures. By means of magnetization and magnetic torque measurements, as well as magnetic force microscopy (MFM), the authors were able to study the cooperative effect of magnetocrystalline and shape anisotropy contributions for nanowires with a single-domain character when diameters were below a critical size of 50 nm. When the field was applied parallel to the revolution axis of the wire, a single magnetic domain was observed, with the magnetic moment aligned parallel to the axis, as shown in Fig. 5.12a–d. Instead, when the field was applied perpendicular to it, the magnetic configuration consisted of a succession of longitudinally magnetized antiparallel domains, as shown in Fig. 5.12e–g. Such a situation arises from the competition between magnetocrystalline and shape anisotropy. On the other hand, for nanowires with diameters larger than 50 nm, complex multidomain patterns were observed in which the magnetization had a large transverse component. However, the origin of the change of crystallographic texture of Co, as the wire became wider, was not clarified.

The electrochemical deposition of metals inside the pores of anodized aluminum oxide templates (AAO) is a simple and inexpensive technique for the growth of aligned polycrystalline metallic nanowires [106]. Kahn et al. [107] grew Co nanowires by exploiting this kind of templates. XRD spectra indicated that the preferred growth direction of the wires was not the one parallel to the *c* axis of the *hcp* Co structure. However, greatly enhanced coercivities were measured when the field was applied parallel to the revolution axis of the wires while very low H_C values were observed in the perpendicular direction. The variation of the coercive field and squareness (M_R/M_S) of the sample with the rotation of the external

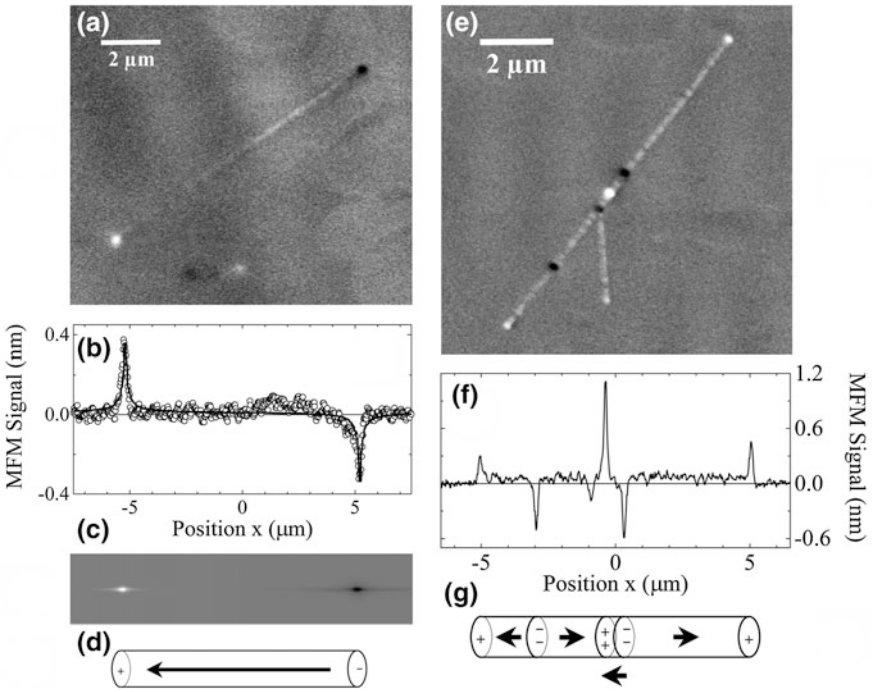

Fig. 5.12 **a** MFM image of a nominal 10 μm long, 35 nm thick Co nanowire after applying an axial feld of 1.3 T (longitudinal remanent state). **b** Experimental (*open circle*) and theoretical (*solid line*) MFM profiles along the wire axis. **c** Simulated MFM contrasts assuming, as for the calculated profile shown in **b**, the magnetic configuration sketched in **d**, *i.e.* a homogeneous longitudinal magnetization in the wire. **e** MFM images, **f** densitometer traces along the wire axis and **g** schematic magnetization distributions for a 10 μm long, 35 nm thick Co nanowire after applying a transverse field of 1.3 T (transverse remanent state). Taken with permission from Ref. [105]

magnetic field showed a clear gradual increase when the field was approaching a parallel direction with respect to the wire axis, confirming the uniaxial anisotropy of the sample. Based on XRD results, the authors concluded that the magneto-crystalline anisotropy was not the predominant contribution in the structures. The large anisotropy appeared to be related to surface and shape effects. The large-scale fabrication of arrays of cobalt nanorods was also achieved by Aslam et al. [108] via a similar AAO template approach, using a modified electrodeposition method. The length of the nanorods could be tuned by simply varying the electrodeposition time. The rod diameter and inter-rod separation in the vertically aligned arrays were 100 and 40 nm, respectively. More homogeneous samples, in terms of nanorod lengths, were obtained when a magnetic field was applied perpendicular to the substrate during the electrodeposition process. XRD and TEM measurements indicated the single crystalline character of the rods and the face-centered cubic symmetry of their lattice. The *fcc* structure is usually obtained at high temperatures, compared to the usual *hcp* one, but it becomes stable also at

room temperature or below when nanoscale objects are considered [109]. With respect to the *hcp* phase, the cubic phase of cobalt shows higher saturation magnetization values but a lower anisotropy. Magnetic measurements were performed for the samples of well-aligned cobalt nanorods of different lengths with the field applied parallel and perpendicular to the growth direction of the rods, see Fig. 5.13, which was parallel to the (220) texture. When the field was applied parallel to the rods, a clear increase in the saturation magnetization was observed for longer rods: actually rods of 14 μm showed a M_S which was an order of magnitude larger than the smaller rods of 750 nm. The saturation of all the samples decreased when the field was applied perpendicular to the growth direction of the rods. This observation was used by the authors to conclude that the effective easy magnetic axis lay along the nanorod axis.

Other template-based methods have exploited the equilibrium self-assembled morphology of asymmetric di-block copolymers in order to create nanopores of high aspect ratios, in which metals can be grown by the previously mentioned electrodeposition techniques [110]. Co nanowires of lengths of about 500 nm, with a high aspect ratio of 36, were prepared (Fig. 5.14a) and magnetically characterized. They showed large coercivities of about 800 Oe at room temperature, compared to the ones of the order of 10 Oe associated with Co films (Fig. 5.14b and c). However, the difference in coercivity between the magnetic field applied along the wire or in the transverse direction was not as high as one could expect considering their high aspect ratio values. The enhanced coercivity was mainly associated to the small diameter of the wires (ca. 14 nm), which is well below the critical single domain diameter of approximately 50 nm. Smaller diameters would in principle allow access to the single domain behavior, increasing in this way the

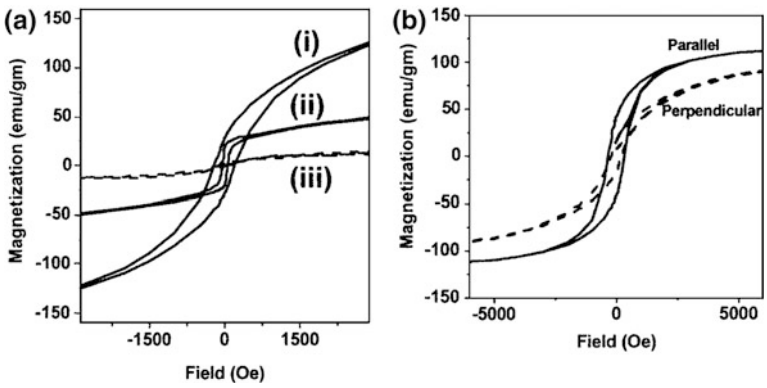

Fig. 5.13 **a** Hysteresis curves measured at 300 K of Co nanorods of different length prepared during an electrodeposition period of (*i*) 30 min (nanorod length ∼14 μm), (*ii*) 8 min (nanorod length ∼3.8 μm), and (*iii*) 3 min (nanorod length ∼0.75 μm). The applied field is oriented along the elongation direction of the nanorods. **b** Hysteresis loop for a 30 min electrodeposited Co nanorods array, the substrate is tilted parallel and perpendicular to the magnetic field. Taken with permission from Ref. [108]

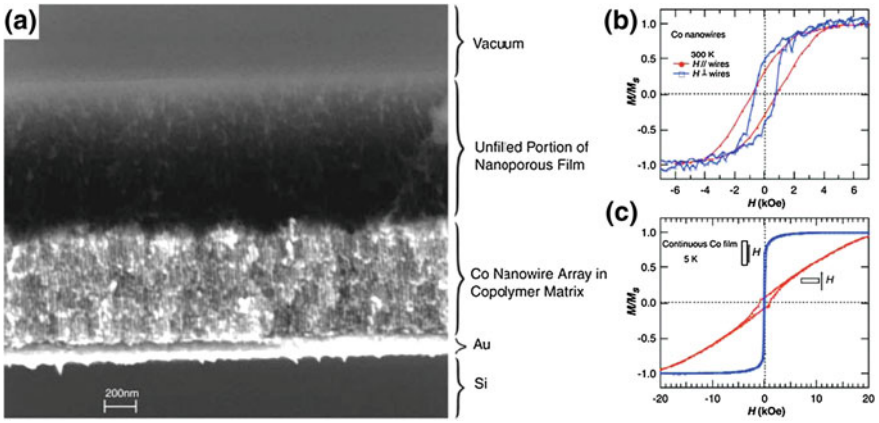

Fig. 5.14 **a** SEM image of a fracture surface of an array of Co nanowires grown within an array of nanopores formed from block copolymers. The growth of the nanowires was terminated before the template was completely filled, and above the nanowires of Co is the unfilled array of nanopores. Magnetic response of Co nanowires: **b** Magnetic hysteresis at 300 K of an array of Co nanowires with diameters of 14 nm, wire lengths of 500 nm, and array period of 24 nm. Curves for the field both parallel to and perpendicular to the wire axis are shown. Each curve was normalized to full saturation. **c** Magnetic hysteresis loops of a continuous Co film (shown for comparison) show considerably smaller coercivity. The electrochemically grown film is 500 nm thick. Taken with permission from Ref. [110]

coercivity of the material. These highly anisotropic vertical arrays of cobalt nanowires with densities in excess of 1.9×10^{11} wires per square centimeter were considered by the authors as good candidates for the future fabrication of ultra-high-density information storage devices.

Colloidal synthetic methods are another type of approach that allow for a precise control over the size of the nanocrystals. Surfactant molecules present in the reaction mixture attach to the nanocrystal surface and limit the further growth of the latter. Moreover, the introduction of a mixture of surfactant molecules in the reaction environment can easily induce a preferential growth of the material leading to well-defined 1D nanostructures. This is usually associated to the different bonding affinities of the surfactants to selective crystallographic facets of the nanocrystals. A precise and clear example to show how the shape anisotropy can overcome the superparamagnetic limit and hence lead to ferromagnetic nano-objects even at room temperature was reported by Dumestre et al. [111]. Pure *hcp* cobalt nanorods and nanowires were prepared by the thermal decomposition of organometallic precursors under a H_2 atmosphere in organic solvents and in the presence of a suitable mixture of long alkyl chain surfactant molecules. All samples were monocrystalline and adopted the *c* axis of the *hcp* structure as the growth axis of the 1D nanoparticle. Nanorods and wires were well protected by capping ligands that stabilized them in solution. Hence, only randomly oriented samples were obtained in this case. The magnetic properties of 3 nm-diameter spherical nanoparticles obtained by analogous procedures were compared to the

properties of 9×40 nm^2 nanorods. The magnetocrystalline anisotropy of *hcp* Co is calculated to be $K_u = 4 \times 10^5$ Jm^{-3} but the total anisotropy of a rod-shaped nanocrystal can be increased by a factor of 2 when estimations on shape anisotropy are considered [23]. The comparison between spherical and rod-like nanocrystals immediately pointed out the increase in anisotropy due to shape effects. Field-dependent magnetization measurements at room temperature showed clear hysteresis loop representative of a ferromagnetic state for the elongated particles, while a superparamagnetic state with absence of coercivity was observed for the spherical ones. Similarly, at 2 K, where both samples showed ferromagnetism, the H_C was observed to increase from a value of 1,100 Oe for the spherical nanoparticles to a maximum value of 8,900 Oe for the rod-shaped ones. An important magnetic feature of these nanoparticles, independently of their shape, is that they maintain a saturation magnetization at low temperature, which is almost identical to that found in bulk cobalt. This behavior was directly linked to the σ-donor character of the amine and acid ligands protecting the nanocrystals. Its effect could somehow decrease the broken symmetry of the surface atoms of the nanocrystals, and consequently their spins would be able to coherently align and rotate with the spins of the internal atoms, further increasing the magnetization of the material.

One year later, the same authors described a procedure to control the length of the rods by using carboxylic acids with different chain lengths [111]. Nanorods of different aspect ratios were synthesized in solution (Fig. 5.15a–c and f). The formation of crystalline 3D superlattices of the previous cobalt nanorods on the TEM copper grid by a crystallization process was also reported (Fig. 5.15d–e). The rods were organized in a hexagonal arrangement with inter-particle distances of approximately 2 nm. The magnetic characterization was performed on all samples and is shown in Fig. 5.15g–i. However, at 2 K, both magnetization and coercivity values were observed to be lower than the ones reported in the previous work, where rods showed no sign of organization. The authors claimed that the source of this magnetization reduction could be found in the expected antiferromagnetic coupling between interacting and laterally aligned nanorods [112, 113]. However they suggested that a remanent ferromagnetic order would be still stabilized through the shape anisotropy of the building blocks in the assembly.

Recently, Viau et al. used the solution-based polyol process for the preparation of highly monodisperse Co nanorods [114]. Well-crystallized *hcp*-Co nanorods of different aspect ratios were obtained, and the *c* axis of the lattice was observed to be parallel to the growth direction of the nanorods (Fig. 5.16a). The mean diameter of the particles could be varied between 8 and 35 nm while the mean length was tuned between 100 and 350 nm, resulting in different samples with definite aspect ratios in the range from 4 to 30. The samples showed a reduction of the saturation magnetization between 30 and 50 % compared to the bulk value, which was assigned mainly to the presence of a thin oxide-passivating layer, as detected by XRD measurements. However, all samples showed ferromagnetism at room temperature. In order to study the magnetic anisotropy features of aligned nanorods, the authors measured the field-dependent magnetization of the samples in two different ways: first, a solution of cobalt nanorods was deposited on a flat

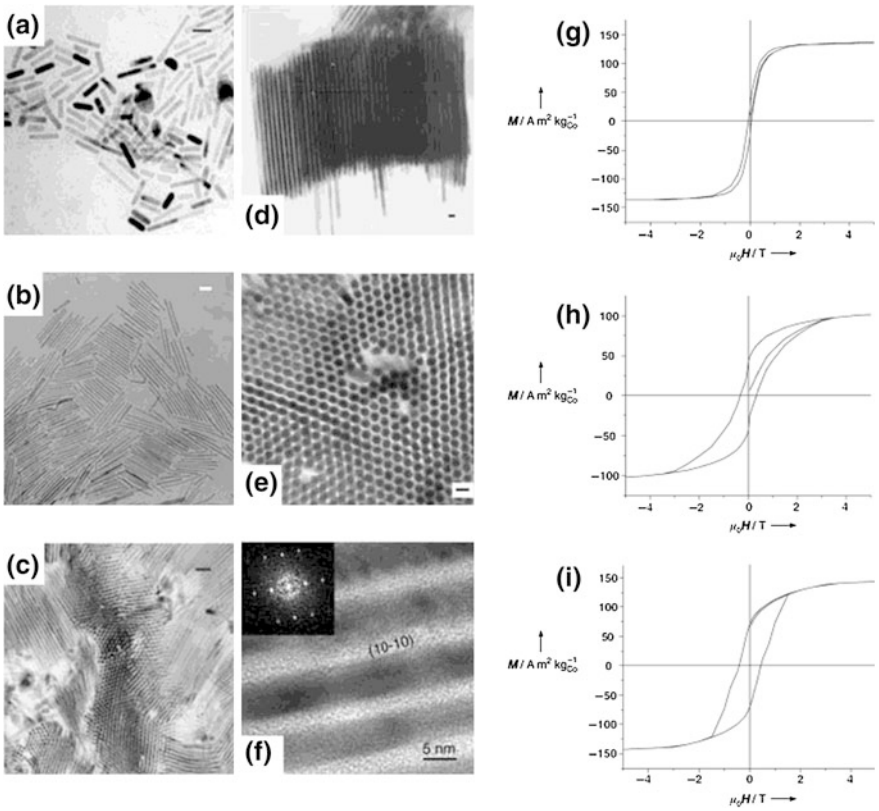

Fig. 5.15 TEM micrographs of Co nanorods from Ref. [111] synthesized by solution methods with dimensions: **a** 9 × 33 nm; **b** 5 × 85 nm and **c** 8 × 128 nm. Scale bar: 30 nm; **d** and **e** TEM micrographs of self-organized nanorods of 8 × 128 nm (scale bar: 10 nm); **f** High resolution TEM micrograph and electron-diffraction pattern of some aligned rods; **g–i** magnetization curves recorded at 2 K of cobalt nanorods in correspondence with TEM images **a–c**. Taken with permission from Ref. [111]

substrate with an external magnetic field applied during the evaporation of the solvent, and second, a toluene suspension of the same cobalt nanorod sample was cooled under a magnetic field and frozen at 140 K. The alignment of the nanorods was achieved in both cases and high values of coercivity were observed, clearly exceeding previously reported data of nanorods obtained by diverse methods, as shown in Fig. 5.16b.

Actually, a value of H_C of 5,500 Oe was measured at room temperature. Under these conditions also the saturation magnetization was maintained to a high degree in the absence of the magnetic field (remanence to saturation ratio $M_R/M_S = 0.81$). At 140 K, the temperature of the frozen solution, an even more square-shaped hysteresis loop was measured with a value of H_C of 9,000 Oe (note, however, that the measuring temperature was lower in this case compared to the previous

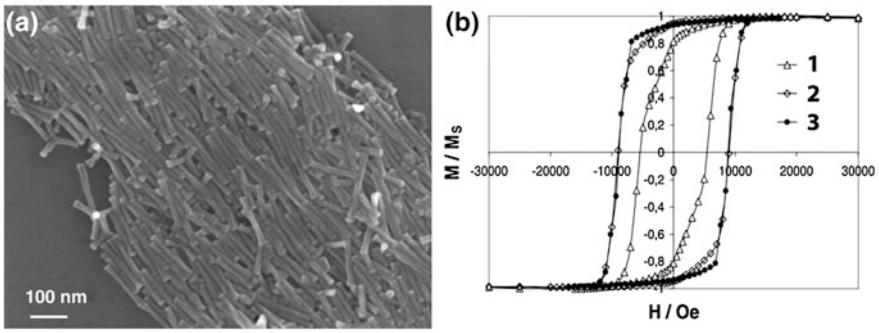

Fig. 5.16 **a** SEM micrograph of cobalt wire assembly, prepared by depositing the wires on a Si substrate while applying a magnetic field; **b** magnetization curves of cobalt nanorods (L = 100 nm; d = 12.5 nm), (*1*) deposited on a flat substrate with an external magnetic field (T = 300 K); (*2*) frozen in toluene under an external magnetic field (T = 150 K); (*3*) simulation of the frozen sample magnetization curve using the Stoner–Wolfarth model for an assembly of non-interacting wires. Taken with permission from Ref. [114]

measurement). A fit of M versus H was carried out for the experimental data recorded at 140 K using a Stoner-Wolfarth model in which both the magneto-crystalline and shape anisotropies were considered together with a standard deviation of the rods orientation of 15° [115]. From the fit, comparable contributions for the two types of anisotropy in the nanorods were extracted: a coercive field of 4,200 Oe was attributed to magnetocrystalline anisotropy while one of 4,700 Oe was associated to the shape anisotropy contribution.

Recently, the same authors suggested the strong effect of the nanorod tip shape on the magnetic hardness of the nanomaterial [116]. They simulated the hysteresis loops for several types of nanorods with the same length but with tips of different shapes, such as simple ellipsoids, cylinders, cylinders with rounded edges, dumbbells (cylinders with spherical ends) and diabolos (cylinders with conical ends). The geometrical models considered for the study are represented in Fig. 5.17a. All calculations were done for Co nanorods. The authors did not consider the magnetocrystalline anisotropy in order to avoid over-parameterization. Ellipsoids seemed to provide the highest coercive fields that can be achieved by using the shape anisotropy, followed by cylinders (Fig. 5.17c). On the other hand, dumbbells and diabolo-like nanorods were magnetically softer, and in them coercive field values were reduced by about a factor of 2 with respect to ellipsoids. The calculations confirmed that H_C increases with the aspect ratio of the nanorod independently of the shape of the tips. Interestingly, they also led to conclusions about the evolution of the coercivity in nanorods as a function of the misalignmet from the applied magnetic field. Indeed, for ellipsoids and cylinders, remarkable changes of H_C were predicted when the magnetic field direction was between 0° and 30° from the revolution axis, as shown in Fig. 5.17b. Further deviations did not modify considerably the value of H_C but mainly changed the shape of the hysteresis loop. Instead, for dumbbells and diabolos, the coercivity should not suffer drastic changes between 0° and 60°.

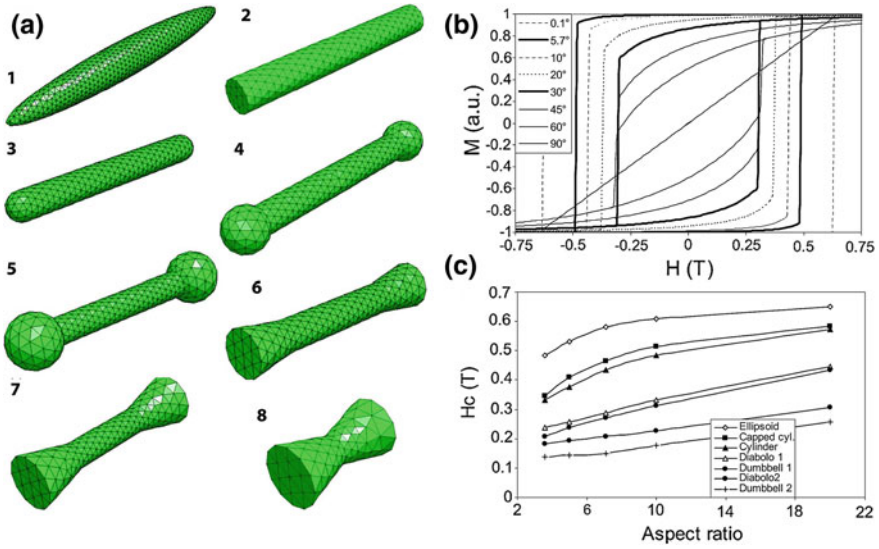

Fig. 5.17 **a** Different types of particles models: *1* Ellipsoids, *2* cylinders, *3* capped cylinders, *4* dumbbells with small spherical ending, *5* dumbbells with larger spherical endings, *6* cylinders with small cone endings, *7* cylinders with larger cone endings, and *8* small diabolos; **b** Evolution of the hysteresis loop as calculated in the Stoner–Wohlfahrt model for an ellipsoid with an aspect ratio of 3.6 for different orientations of the applied field with respect to the easy axis; **c** Evolution of the coercive field as a function of the aspect ratio for the different types of objects. The magnetic field is applied at 5.7° with respect to the object easy axis. Taken with permission from Ref. [116]

As mentioned earlier, single domain magnets are expected to reverse their magnetization coherently, meaning that all individual spins of the particle rotate in unison. However, particular shapes of the particles, such as rods, could induce a slight deviation of the single-domain magnetization reversal mechanism. The results obtained by the authors on differently shaped nanorods were based on the non-coherent magnetization reversal process of mainly dumbbells and diabolos. These particular types of nanorods, due to the shape of their tips, were able to develop vortex-like magnetic states for which the reversal of the magnetization of the whole particle was much less energy demanding. Consequently they showed a drastic drop in coercive field with respect to an ellipsoid, for which calculations indicated that the reversal proceeded in a perfectly coherent way.

5.5.2 Fe 1D Nanostructures

The body-centred cubic structure, *bcc*, of metallic Fe is the most stable one at temperatures up to about 900 °C; this crystal phase is called α-Fe and it shows a T_C of 770 °C, below which the metal becomes ferromagnetic. Due to the high

symmetry of this phase, the enhancement of the magnetic anisotropy of α-Fe nanoparticles by the anisotropic growth of the objects becomes a key advantage in high-density magnetic recording applications. Both physical and chemical methods have been developed for the synthesis of Fe 1D nanostructures and often template-assisted methods have been of great help. As an example, a clean faceted NaCl(110) surface passivated with amorphous SiO_2 has been used as a template for the preparation of Fe nanowires [117]. The deposition of Fe under ultra high vacuum conditions was performed using a collimated electron beam source aligned 65° from the template normal. The so-called *shadow deposition* technique allowed for the selective deposition of Fe on the substrate planes exposed to the beam. As a result, nanowires with an approximate length of 10 μm and diameters of about 30 nm were obtained. The average distance between wires on the substrate was 90 nm. Electron-diffraction patterns confirmed that the nanowires were polycrystalline and no preferential orientation of the Fe grains was observed; consequently the authors did not consider the contribution of magnetocrystalline anisotropy as the predominant factor in the magnetic characterization of the sample. Field-dependent magneto-optical Kerr effect (MOKE) measurements indicated that saturation magnetization is reached already at low fields when the external field was applied longitudinal to the wire growth axis. Moreover, the higher coercivity values of about 2 kOe observed in the same direction led to the conclusion that the easy magnetization axis of the nanowires was parallel to the wire growth axis. Hysteresis loops recorded at different angles between the sample and the external magnetic field seemed to indicate that the reversal process of the magnetization is not dominated by domain wall motion but by a coherent rotation of the spins of the wire.

Alternatively, vertically aligned Fe nanowires were prepared via electrodeposition into the holes of porous anodic aluminum oxide (AAO) templates [118]. Nanowires with diameters of about 35 nm and aspect ratios above 1,000 were observed by SEM measurements (Fig. 5.18a). XRD patterns confirmed that the

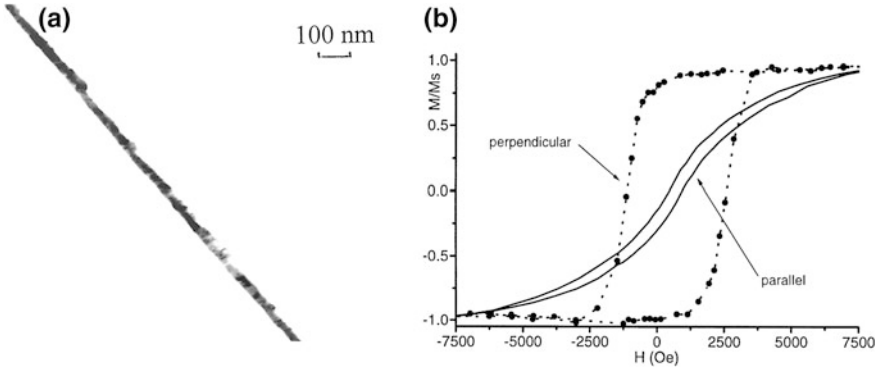

Fig. 5.18 **a** Morphology of a Fe nanowire; **b** hysteresis loops of Fe nanowire array. Perpendicular (parallel) corresponds to the applied field perpendicular (parallel) to the sample plane. Taken with permission from Ref. [118]

α-Fe phase was the only one present in the arrays. Even though no preferential growth direction was ascertained, the authors claimed that the shape anisotropy was responsible for the high magnetic anisotropy observed in the field-dependent magnetization measurements: hysteresis loops recorded with the external field parallel to the nanowire growth axis showed an almost square shape with high values of squareness (remanent to saturation magnetization ratio), as shown in Fig. 5.18b. The coercive field measured under these conditions was 1,832 Oe, which is much higher compared to the low value observed when the field was applied parallel to the substrate, 118 Oe. In the latter case, the sample showed high values of saturation fields and low remanence, indicating that a hard magnetic axis was found in the transverse direction of the wires, while the easy magnetization axis was parallel to the growth direction. The authors claimed that if each of the nanowires was decoupled from the neighboring ones and consequently could act as a recording unit, the high anisotropy observed in the sample together with the high density of wires on the substrate would make this kind of assembly useful for ultra high density perpendicular recording media.

In 2001, Cao et al. [119] described the preparation of arrays of pure metallic Fe nanowires by electrodepositon techniques into the pores of polyaniline nanotubules. Nanowires had lengths of about 60 μm and were coated with polyaniline tubes of external diameter of about 200 nm. Pure α-Fe was confirmed by XRD and EDX spectra. However, the authors did not comment on the direction of growth of the wire, which probably could not be ascertained. Some degree of anisotropy was also observed when the external magnetic field was applied parallel or perpendicular to the wire axis, being H_C equal to 119 and 210 Oe, respectively. Contrary to what was reported by Yang and co-workers in the previously cited work, here the easy axis seems to be perpendicular to the growth direction of the wires.

Single-wall carbon nanotubes can also be exploited as templates for the growth of extremely thin Fe nanowires, as reported by Borowiak-Palen et al. [120] $FeCl_3$ was introduced inside the holes of the nanotubes by simply immersing them in an over-saturated $FeCl_3$ solution. After several washing cycles, the thermal treatment of the filled tubes at 593 K led to the reduction of the Fe^{3+} ions forming long continuous and thin (1 nm) metallic Fe nanowires. The sample exhibited a ferromagnetic behavior with a room temperature coercivity of 180 Oe. The authors suggested that large aspect ratios, high surface areas and significant inter-wire dipolar interactions could all contribute to the room temperature magnetic stabilization of the wires. Magnetic measurements after several months showed identical results compared to the as-prepared samples, confirming the role of the carbon shell as efficient anti-oxidant layers protecting the metallic nanowires contained inside the nanotubes.

Wet chemical routes for the fabrication of 1D iron nanostructures have been explored since years. Oppegard et al. [121] already studied in 1961 the shape anisotropy of axially aligned Fe and FeCo nanoparticles prepared by the reduction in solution of Fe(II) salts under the effect of a magnetic field. However, in this case, the shape anisotropy contribution to coercivity was strongly hindered by agglomeration phenomena. In 2000, Park et al. [122] reported on the synthesis of

α-Fe nanorods via an oriented attachment mechanism of spherical iron nanoparticles induced by the ligand passivation of certain crystal facets. 2 nm-spherical iron nanoparticles were prepared in organic solvents by the thermal decomposition of organometallic precursors in the presence of stabilizing surfactant molecules. The formation of the rods was achieved by the solubilization of previous spherical nanoparticles in pyridine in the presence of an excess of surfactant molecules that were different in nature from the ones that were previously used. The mixture was refluxed until a precipitate appeared. The product was composed of nearly dispersed *bcc* Fe nanorods. The width of the rods was observed to be constant and close to 2 nm, while the length could be varied depending on the concentration of surfactants in the reaction mixture. Nanorods of 11, 22 and 27 nm were formed. Magnetic properties of spherical 2 nm iron nanoparticles and 2 × 11 nm iron nanorods were compared. As observed in Fig. 5.19, nanorod samples showed a much higher T_B compared to their initial spherical particles (110 and 12 K, respectively). The contribution of the larger size and change of shape in the nanorod sample was evaluated in order to rationalize such an increase. Indeed, global magnetic anisotropy constants were estimated for both spherical and rod-shaped nanoparticles and were found to be 9.1×10^6 and 1.6×10^7 ergs/cm^3, respectively. Moreover, in the case of the rod-like particles, the shape contribution to the total anisotropy constant was estimated to be 7.9×10^6 ergs/cm^3 and hence of the same order as for the pure magnetocrystalline one. This explained the significant increase in blocking temperature in the nanorod sample, even if no values were reported for the coercivity.

Porous magnetic nanoparticles are interesting materials for magnetic transportation [123] and sensing applications [124]. However the synthesis has been mainly optimized for oxide-based materials which, as said earlier, possess a much lower value of magnetization compared to metals. Recently, the preparation of acicular Fe nanoparticles with a porous structure was described [125]. Elongated α-Fe_2O_3 nanoparticles were prepared by hydrothermal synthesis. Further annealing of the oxide structures under H_2 led to α-Fe porous nanoparticles that maintained

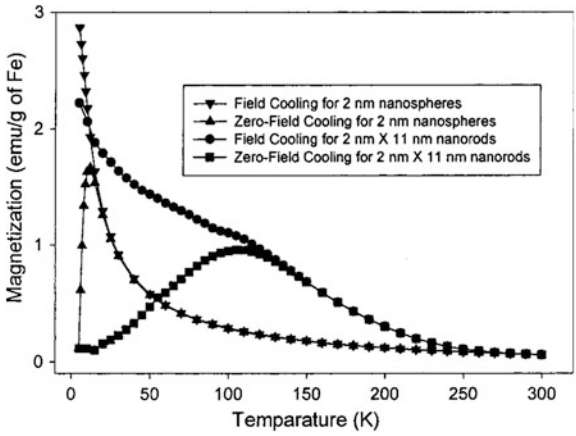

Fig. 5.19 Magnetization normalized by mass versus temperature for the 2 nm spherical iron nanoparticles and the 2 × 11 nm iron nanorods at the applied magnetic field of 100 Oe. Taken with permission from Ref. [122]

the original shape. XPS measurements indicated the presence of iron oxide and phosphate passivation layers, which probably where responsible for the decrease in magnetization with respect to the other nanostructured particles. The large surface areas of the particles and the phosphate molecules attached to them were considered by the authors as reasons why such elongated porous structures had higher coercivity values compared to other nanostructured particles of similar sizes.

In the last two examples, as well as in other wet chemical procedures for the synthesis of rod-like nanoparticles, randomly oriented nanorods have been obtained for which only average magnetic properties could be measured. It is then worth mentioning an innovative approach described by Vayssieres and co-workers, in which the synthesis of vertically aligned α-Fe nanowires was carried out on a substrate from an aqueous solution where no template, surfactant or applied electric or magnetic field was required [87]. The elongated structures were 0.8–1 μm long and had diameters of about 30–40 nm. Each of these 1D structures was observed to be formed by stacking of columns and bundles of nanorods 5–10 nm wide and 15–30 nm long. These small nanorods displayed no preferential relative orientation in the nanowires and probably because of this, no significant difference was found in the coercivity and in the shape of the hysteresis loops recorded with the field parallel and perpendicular to the wires. However, the direction of the easy magnetization axis was suggested to be parallel to the growth direction of the wires, based on the observation that slightly higher magnetization values had been observed with the field applied in this direction, independently of the temperature.

5.5.3 Ni 1D Nanostructures

Metallic nickel crystallizes with a face-centred cubic lattice and exhibits lower values of magnetocrystalline anisotropy than Fe and Co. For this reason works based on the synthesis of metallic Ni are not so abundant as for the other two metals. However, its high permeability and magnetoresistant properties have made it ideal for magnetization reversal and domain wall studies (which are reviewed in Sects. 5.5.5 and 5.5.6, respectively). Some examples of the synthesis of nickel elongated nanostructures have also been reported. Cordente et al. [101] described the synthesis of monocrystalline Ni nanorods in organic solvents by the thermal decomposition of organonickel compounds in the presence of long chain hydrocarbon amines. The amine played a double role in the reaction mixture: (1) it selectively coordinated particular facets of the colloidal Ni particles, confining their further growth in one single direction and (2) its electron σ-donor character avoided the magnetization fading of the magnetic material, which is usually the case when strong π-acceptor ligands are used in the synthesis. TEM analysis determined homogeneous sizes for the nanorods of about 4×15 nm. Nanorods tended to organize on the TEM grids with their long axes parallel to one another, probably because by such arrangement their magnetostatic repulsion is minimized. High resolution TEM confirmed that the growth axis of the nanorods was parallel

to the (111) plane. As expected, the M_S value of the sample at 2 K was very close to the bulk value for Ni due to the presence of amines as capping ligands of the nanocrystals. The ZFC–FC magnetization measurements indicated a T_B of 100 K. Based on this value of T_B [126], the authors estimated a shape anisotropy constant of 7.7×10^5 erg/cm^3, comparable in strength to the magnetocrystalline anisotropy constant for bulk Ni of $7.0(\pm 0.5) \times 10^5$ erg/cm^3. These results showed how the rod-like shape of magnetic nanocrystals can increase the effective anisotropy of the material by a factor of 2. Ni nanorods were also prepared by the reduction of nickel(II) salts in microemulsion systems in the presence of a suitable surfactant [127]. The products isolated at the first stages of the synthesis were composed of 10 nm spherical nanocrystals that further evolved with time until rod-shaped nanocrystals with aspect ratios of 10–20 were formed. Field-dependent magnetization measurements were performed for both the spherical and rod-shaped samples at room temperature. The nanorods showed a coercivity of 332 Oe, which was higher than the coercivity of bulk Ni (100 Oe) and than the one of the initial 10 nm spherical particles (173 Oe).

Also in the case of Ni, AAO templates have been used for the formation of well-aligned 1D nanostructures. Several synthetic and structural parameters can strongly affect magnetization processes. Consequently it is difficult to conclude about the real effect of the aspect ratio of the particles if one considers different examples available in the literature that have not been obtained under equivalent conditions. A representative example that shows the effect of the aspect ratio on the magnetic behavior for 1D nanostructures was reported by Oh et al. [128] The authors used the electrodeposition technique in AAO templates to form Ni nanostructures. All synthetic parameters were kept constant during the synthesis, and just by simply controlling the deposition time in the range from 5 to 15 min, 100 nm spherical nanodots, 400 nm long nanorods and 3.4 μm long nanowires could be synthesized (Fig. 5.20a–c). The diameter of the last two samples was 100 nm, equal to the diameter of the nanospheres. Hysteresis loops were recorded at 5 K for the three samples. The field was applied both parallel and perpendicular to the substrate. When the field was applied perpendicular to the substrate, or in other words parallel to the elongated structures, significant changes were observed in coercivity by varying the aspect ratio of the particles (Fig. 5.20d–f): while Ni nanospheres showed a H_C of 200 Oe, the nanorods and nanowires showed H_C values of 630 and 730 Oe respectively. Also the squareness of the hysteresis loops was increased following the same trend. On the other hand, and confirming the high magnetic anisotropy of the high aspect ratio systems, hysteresis loops recorded with the magnetic field applied parallel to the substrate of the samples showed very similar curves with very low coercivities and remanent magnetizations. It seems then clear that the magnetic properties of the three systems were dominated by their shape anisotropy and, in particular, were associated to the aspect ratio of the nanostructures.

Metallic Ni is known for its negative magnetostriction coefficient, meaning that under the effect of a magnetic field the material undergoes compression. Alternatively one can say that an external stress is able to modulate the anisotropy of the

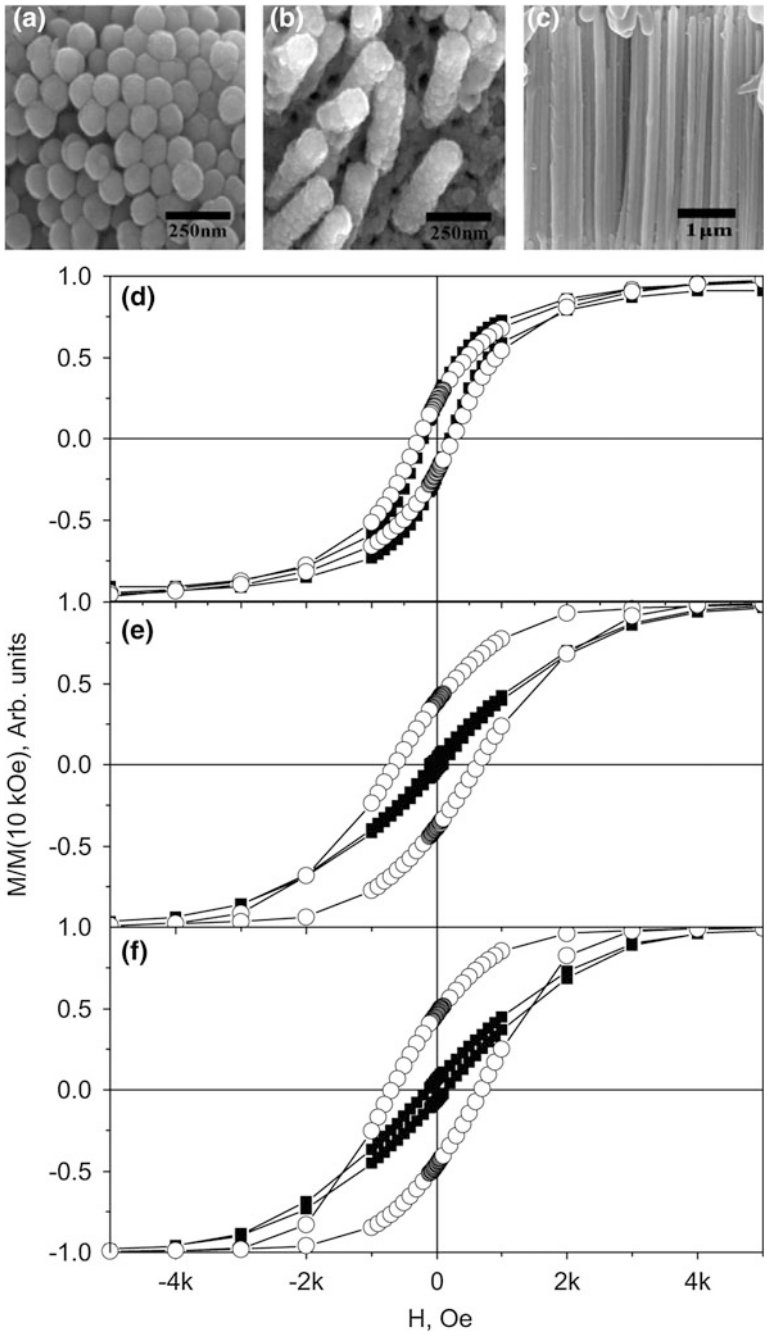

Fig. 5.20 SEM images of nanostructured nickel: **a** nanodots, **b** nanorods and **c** nanowires after removal of the AAO templates. The diameter, length and the distance between the pores of the AAO template are 100 nm, 40 mm, and 210 nm, respectively; **d–f** Hysteresis loops for nickel nanostructures in correspondence with SEM images a-c measured at 5 K with the field applied parallel (*black squares*) and perpendicular (*white circles*) to the membrane plane. Taken with permission from Ref. [128]

material. Since the magnetocrystalline anisotropy of Ni is lower than in Fe or Co metals, the effects of shape and magnetoelastic anisotropies become more apparent in Ni. Kumar et al. [129] reported on the competition between shape and magnetoelastic anisotropies in Ni nanowire arrays fabricated by electrodeposition within the porous of AAO templates. Arrays of nanowires with typical diameters of 30 nm and lengths between 1 and 2 μm were prepared in which the inter-wire distance was observed to be around 100 nm (Fig. 5.21a). XRD patterns indicated the cubic nature of Ni, which appeared to grow along the [111] direction. This means that the growth direction of the wire coincides with one of the three easy magnetization axes of the lattice. Magnetic measurements were carried out for the Ni nanowires embedded in the alumina template and supported on aluminum substrates. The magnetic data recorded at room temperature indicated a clear out-of-plane anisotropy, confirmed by the high value of coercivity (800 Oe) and squareness ($M_R/M_S = 0.82$) obtained when the field was applied perpendicular to the Al substrate, and compared to the narrow hysteresis loops observed when the field was applied parallel to it. These observations are in agreement with the large shape anisotropy of the sample. However, the M_R and H_C values at 50 K, compared to the ones at room temperature, decreased in the out-of-plane measurement and increased in the in-plane one. Such a trend cannot be simply explained by shape anisotropy, which predicts continuous temperature dependence. The authors estimated the temperature dependence compression of the Ni nanowires taking in consideration the different thermal expansion coefficients of the Al substrate, the alumina template and the Ni nanowires themselves. The magnetoelastic anisotropy constants obtained were of the same order of magnitude as the shape anisotropy constants but acting in the perpendicular direction. This fact could well explain the presence of a maximum in the H_C and M_R versus temperature representations shown in Fig. 5.21b and c. The maximum was observed to be at around room temperature. Below this temperature, magnetostrictive anisotropy overcame the shape anisotropy. Hence the array of nanowires gradually increased the component of the effective anisotropy in the direction perpendicular to the growth axis of the wires. Other factors were evaluated in this work, as the width of the Al substrate and the adhesion ability of the wires to the Al substrate and the alumina template. These could explain the trends observed also by other authors [130]. Ni nanorods have also been used to modulate the mechanical properties of ferrogels [131] and to better understand the mechanical environment of the cell nucleus [132]. In both cases the studies are based on the response of the nanorods embedded in a particular matrix under the effect of an external magnetic field.

5.5.4 Alloys of Special Technological Interest

Permanent magnets are defined as those magnetic materials that, once magnetized to saturation, create their own persistent magnetic field even when the external magnetic field is switched off. They are all characterized by very high values of

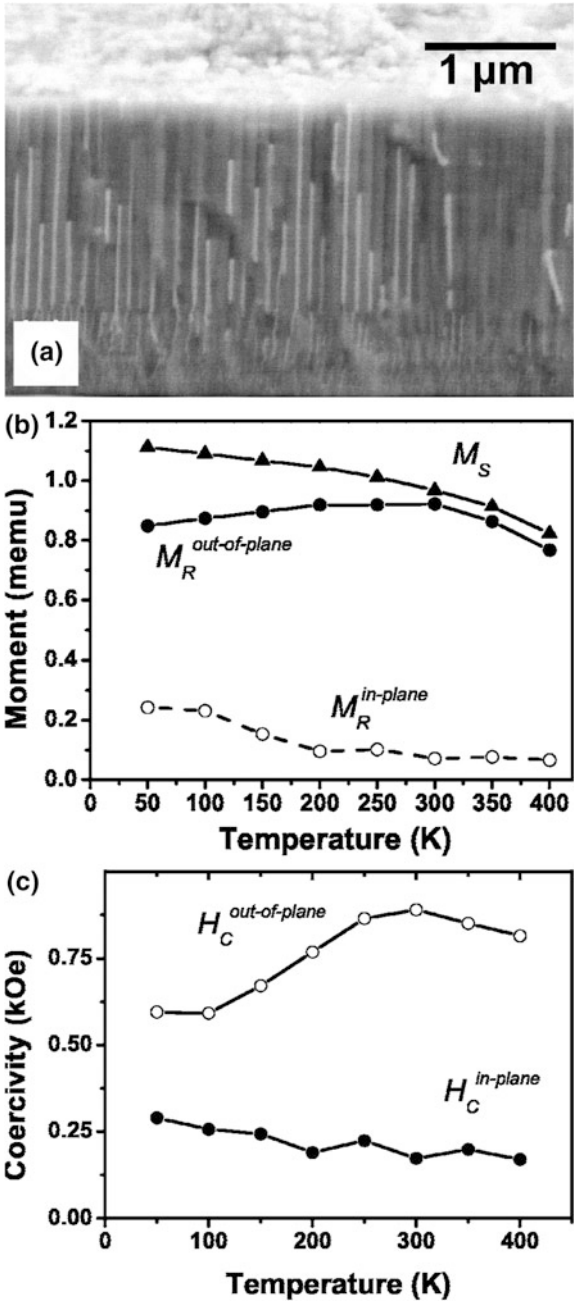

Fig. 5.21 **a** Morphology of a broken alumina template filled with Ni nanowires; **b** temperature dependence of spontaneous magnetization M_S, in-plane and out-of-plane remanence M_R; **c** influence of temperature on the in-plane and out-of-plane coercivity H_C. Taken with permission from Ref. [129]

coercivity as well as remanent magnetization. Hence, the ideal permanent magnet shows a square-shaped hysteresis loop, in which M_S is kept constant in the demagnetizing process until a high value of magnetic field of opposite direction is able to induce magnetization reversal. The parameter that better describes their performance is the BH_{max} product, which represents the maximum achievable energy density of the magnetic field into the air gap surrounding the magnet. These types of materials have special interest in the data storage industry since they are used as magnetic recording media or as head actuators in computer hard disks, where non-volatile data storage systems are required. Apart from this, permanent magnets are used in other applications where strong magnetic fields are necessary: examples are the fabrication of magnetic resonance instruments for research activities or biomedical imaging techniques (MRI). Moreover, permanent magnets can act as transducers for the conversion of electrical signals into sound, and this is why they have become essential components in loudspeakers and headphones, as well as bearings for supporting a load using magnetic levitation, and as a consequence they can be found as components of turbines, pumps, motors and generators. Permanent magnet alloys include $SmCo_5$; $Nd_2Fe_{14}B$; aluminum, nickel and cobalt alloys with iron (Alnico); titanium, cobalt, nickel, and aluminum alloys with iron (Ticonal) and platinum-based alloys such as FePt and CoPt.

Industry has always preferred the classical powder metallurgy process whereby magnets are prepared by pulverizing an ingot precursor and liquid-phase sintering the magnetically aligned powder into dense blocks, which are then thermally treated and finally magnetized. Obviously, such industrial procedures are far from fabricating size and shape controlled nanostructured permanent magnets. However, the possibility to obtain nanoscale permanent magnets, either with a single or multidomain behavior, is highly attractive due to the enhanced magnetic properties expected thereof, as described in the introductory part of this section. Unfortunately, the synthesis of permanent nanomagnets has encountered several difficulties and has been addressed only in the last years, albeit with modest results.

Two main types of rare-earth-based alloys are currently known: $Nd_2Fe_{14}B$ and $SmCo_5$. $Nd_2Fe_{14}B$ is nowadays the strongest permanent magnet available. It shows a tetragonal structure and an exceptionally high value of uniaxial magnetocrystalline anisotropy with a maximum coercivity of 2.5 T and a maximum value of M_S of 1,270 emu/cm^3. Hence, it is highly resistant to demagnetization and has the potential for storing high amounts of magnetic energy, which makes them ideal for permanent magnet applications. Hexagonally close packed $SmCo_5$ magnets are softer and are not able to store an amount of magnetic energy as large as that of $Nd_2Fe_{14}B$. They were the first rare-earth containing magnets to be commercialized and, even if softer than $Nd_2Fe_{14}B$, they show higher Curie temperatures, making them magnetically stable up to at least 700 °C. In practice, the magnetic properties of both types of magnets highly depend on the alloy composition, microstructure, and manufacturing technique employed.

Rare earth metals are specially known for their high reactivity and oxygen sensitivity, which actually increase in nanostructured materials due to their high surface-to-volume ratio. This makes the production of nanoparticles of these

materials a nontrivial task. Moreover, their equilibrium phase diagrams contain several compounds with different crystalline structures and compositions, among which only a few of them show the desired hard magnetic properties. In general, thermal annealing treatments can be effectively used to improve the crystallinity of the material and to obtain its pure desired phase. However, when such treatments are performed on nanosized materials, deterioration rather than improvement of magnetic properties is usually observed, mainly due to oxidation side reactions or sintering processes. A few examples of the synthesis of spherical $SmCo_5$ and $Nd_2Fe_{14}B$ nanoparticles exist in the literature [133, 134], even if they rarely show significant values of coercivity at room temperature due to one of the reasons described above [135–139]. For what concerns the preparation of one-dimensional nanoparticles, such as rods or wires, only a couple of examples can be found in the literature. Chinnasamy et al. [140] reported on the synthesis of $SmCo_5$ nanoblades prepared by the high temperature reduction of the appropriate metal salts in a liquid polyol medium that acts as both the solvent and the reducing agent. The particles were characterized by XRD and high resolution TEM: both the $SmCo_5$ hexagonal structure and the single crystal character of the particles were confirmed. They presented a blade-like structure with an average width of 10 nm and length of 100 nm. The particles were ferromagnetic at room temperature and showed a H_C of 6.1 kOe and a M_S of 40 emu/g. The authors suggested both the shape and the magnetocrystalline anisotropies as responsible for the high values of coercivity observed. In a different publication, $Nd_5Fe_{95-x}B_x$ nanowires were fabricated using electrodeposition techniques in AAO templates [141]. The wires were 40 nm wide in average and showed aspect ratios of approximately 75. However, both SAED and XRD measurements indicated that the structures were amorphous. This could explain the very low values of coercivity measured, together with the fact that the sample was not exhibiting the stoichiometry associated with the $Nd_2Fe_{14}B$ hard magnetic material.

Better results have been obtained in the preparation of magnetic Pt-based one dimensional nanostructures, partially due to their higher chemical stability and resistance to oxidation. FePt and CoPt alloys can form in different stoichiometries and crystalline structures, like the previous rare earth-based magnets. Equiatomic compositions are the optimal ones for enhancing their magnetic properties. Their *fcc* structure presents soft magnetic properties, while their *fct* lattice is the one responsible for their hard behavior. The ordered tetragonal phase is easily synthesized by a thermal annealing of the disordered cubic structure. Among the works published concerning FePt or CoPt 1D nanostructures, often only the synthetic conditions and strategies for their preparation have been described [142–145], while in some others only a very superficial magnetic characterization has been reported [146–150]. The preferred synthetic method for the fabrication of arrays of Pt-based magnetic nanowires is the electrodeposition of the metals in AAO templates [143, 151–158]. However, the synthesis has also been achieved by other methods such as hydrogen reduction of Co and Pt salts inside templates [147], solvothermal methods [142, 148], thermal decomposition of organometallic precursors [145, 149], electron-beam induced deposition techniques [159] and virus-based scaffold methods [144].

A few authors undertook an in-depth study of the magnetic properties of either *fcc* or *fct* FePt or CoPt elongated structures. Yasui et al. [151] developed for instance a fabrication technique by which it was possible to control the crystal orientation of nanometer size *fct* CoPt nanowires. By substituting the W underlayer (which was used as electrode during the electrodeposition process) with a [001] oriented Pt one, the authors were able to induce the growth of the wires with a clear *c*-axis orientation. This orientation is actually the easy magnetocrystalline axis of the tetragonal structure, hence high values of H_C up to 7,400 Oe and squareness up to 0.96 were observed when the applied magnetic field followed the wire direction. For the samples grown over W underlayers, no anisotropic magnetic behavior was observed depending on the direction of the magnetic field, which was assumed to be due to the random *c* axis orientations of the wires in that sample. Similar results for polycrystalline *fct* CoPt nanoparticles have been observed: the absence of anisotropic magnetic properties in such wires has been associated in all cases to a random orientation of the *c*-axis between the wires or between the grains within each wire [154–156].

Mallet et al. studied *fct* CoPt nanowires grown with a preferred [111] direction [153]. No difference was found in the hysteresis loops between the measurements done with the magnetic field applied parallel and perpendicular to the wire axis. In that case, the growth direction of the wires makes an angle of 55.45° with the [001] magnetocrystalline axis and based on this, the measurements confirmed the higher strength of the magnetocrystalline anisotropy with respect to the shape anisotropy of the wires. The authors also studied the anisotropic soft magnetic behavior of the *fcc* CoPt nanowires previous to their annealing. The easy axis of magnetization perpendicular to the wire axis seemed to be clearly dictated by strong dipolar coupling interactions between ferromagnetic wires in the sample, despite the fact that both magnetocrystalline and shape easy axes were collinear in that case.

One year before, the same authors had studied the magnetic anisotropy observed in *fcc* CoPt nanowire arrays fabricated within a polycarbonate membrane [152] instead of an alumina membrane, as was done in the publication discussed above [153]. When polycarbonate membranes were used, lower values of wire packing were observed, and hence also weaker dipolar couplings were expected. Nanowires were also grown along the [111] direction which, in this case, was observed to be the easy magnetization axis. Magnetic measurements with a magnetic field applied parallel to the wires axes yielded a value of H_C of 2,320 Oe and a squareness of 0.98. In the same article, the diameter dependence of the coercivity and squareness for CoPt nanowires was also addressed.

An anisotropic magnetic behavior has been observed also in *fcc* CoPt nanowires by Gao et al. [157]. The wires were polycrystalline and had a preferential [110] texture along the growth direction. Magnetocrystalline and shape contributions to anisotropy are expected to be comparable in magnitude in *fcc* CoPt alloys. The authors studied the hysteresis loops observed in the sample by means of micromagnetic simulations, considering that the [110] direction makes an angle of 35° with the [111] magnetocrystalline easy axis and that, due to the polycrystallinity of the wires, the [111] directions could be randomly distributed with an azimuthal

angle in the cross section perpendicular to the wire axis. The calculated data was in agreement with the experimental results and confirmed the random distribution of the [111] directions. The geometrical dependence of the magnetic behavior in polycrystalline *fcc* CoPt nanowires was studied by Shamaila et al. [158]. A crossover of effective easy axis of magnetization was observed as a function of wire diameter and length.

Besides magnetometric measurements, other alternative techniques have been rarely used to magnetically characterize Pt-based monodimensional nanostructures. In 2005 Che et al. [159] used off-axis electron holography measurements to evaluate the magnetic properties of a single nanorod. Each nanorod was seen to be composed of a chain of crystalline FePt nanoparticles. The measurements indicated that the magnetization of the rod was parallel to their growth direction, and a value of its remanent magnetization of 1.53 T was measured, revealing a hard magnetic nature. Studies on the orbital and spin contribution to the magnetic moment in CoPt nanowires by X-ray Magnetic Circular Dichroism (XMCD) have been undertaken by Li et al. [160].

In contrast to hard magnets, soft magnets are characterized by very low values of coercivity and can reach the magnetically saturated state with relatively low magnetic field values. They are usually characterized by very weak magnetostrictive effects and very high magnetic permeability. The nearly zero values of magnetostriction is of crucial importance in industry since variable stresses derived from their use could strongly affect their magnetic properties. On the other hand, their high magnetic permeabilities make them ideal for magnetic switching applications, for example as magnetic recording head sensors for the magnetic data storage industry.

Most soft magnets are Fe-based materials, such as metallic iron, silicon-iron alloys or iron phosphides. However, nikel-iron alloys are the most representative examples of this type of materials. NiFe alloys are commonly known as Permalloys and the name usually refers to a composition close to $Ni_{80}Fe_{20}$. Several reasons have made of Permalloys one of the most investigated soft materials: they have the highest values of permeability; their electrical resistivity varies within a 5 % range, depending on the strength and direction of an applied magnetic field. Additionally, they are characterized by very low values of magnetocrystalline anisotropy, which makes them ideal for studying physical phenomena derived from their shape anisotropy. Bulk permalloys are usually fabricated in the metallurgical industry by melting and shaping of the precursor ingots. Nanoscale fabrication methods for permalloys and other magnetic nanostructures are also available, and they have been extensively reviewed by Schuller and co-workers [22]. Due to their variable electrical resistance and their high magnetic permeabilities, permalloys have been the subject of study in a large amount of publications dealing with magnetoresistant properties and magnetization reversal studies in one dimensional nanostructures. Some of the most important works published in these fields are reviewed in Sects. 5.5.5 and 5.5.6.

5.5.5 Magnetization Reversal Studies in 1D Metallic Nanostructures

By the end of the last century, thanks to the increasing technological demand focused on the miniaturization of sensors and on higher density magnetic storage devices, the emerging field of spintronics has been intensively addressed and developed [3]. This innovative technology exploits the intrinsic spin of the electron and its associated magnetic moment, in addition to its fundamental electronic charge, in solid-state devices. They use magnetic moment to carry information and this, compared to nowadays technology, could introduce several improvements in terms of low power dissipation, non-volatile data retention, radiation hardness and high integration densities.

From an applied physics point of view, the continuous increase in the density of magnetic recording media must entail a deep knowledge of the behavior of size-confined ferromagnetic structures, thin films and elongated particles. In particular, the understanding of the mechanisms and dynamics of their magnetization reversal processes is crucial to improve the state-of-the-art: the two stable magnetization directions of nanostructured ferromagnetic metals are strictly associated to the two Boolean logic states, 1 and 0, necessary to encode information. They must be stable with time but also reversible. Hence, in the last 20 years, a considerable effort has been made to elucidate the complex physical phenomena occurring during spin reversal and transportation in isolated and size-controlled magnetic particles, with a special attention to nanowire systems.

Based on micromagnetic theories [26, 161, 162], three magnetization reversal modes can be observed for single domain ferromagnetic crystals with a cylindrical or spheroidal shape: the coherent rotation, the curling mode and the buckling mode. The observed mode mainly depends on the radius of the studied wire. The three reversal modes are shown in Fig. 5.22.

In the coherent rotation mechanism, the individual spins of the elongated particle homogeneously rotate following the direction of the external magnetic field until the complete magnetization reversal is accomplished. As assumed by the Stoner-Wohlfarth model [26], such mechanism is only operative in very small particles and the magnitude of the magnetization remains constant along the direction of the magnetic field during the reversal process. Alternatively, for larger particles, two other incoherent reversal modes can take place, which actually are less energy demanding and consequently lead to lower coercive forces. These two incoherent reversal modes rely on the homogeneous variation of the spin vectors along certain crystal directions (buckling) [163] or on their rotation in circular symmetry creating a vortex (curling) [162]. Both of them entail a non constant value of magnetization during the reversal process. The field value at which the reversal takes place is known as the switching field (H_{SW}).

Two main factors have made possible to follow magnetization reversal processes in elongated ferromagnetic systems: on the one hand, the development of new nanofabrication techniques opened the possibility to prepare samples with a

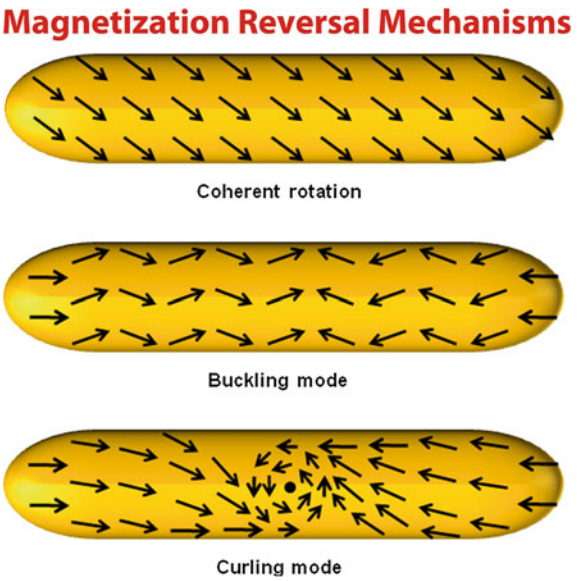

Fig. 5.22 Magnetization reversal modes in elongated nanoparticles. Coherent rotation (*top*) is characterized by an homogeneous rotation of all individual spins following the external magnetic field. Buckling mode (*middle*) is characterized by the homogeneous variation of the spins along certain crystal directions. Curling mode (*bottom*) is characterized by the rotation of the spins in the crystal creating a vortex

high degree of control over their dimensions down to a few nanometers in diameter or thickness. Such structures might display a real 1D behavior compared to previous samples of larger sizes. On the other hand, more sensitive magnetic characterization techniques have been developed with which new insights on the magnetic properties of individual and isolated magnetic particles were obtained. The magnetization of one single magnetic nanowire is of the order of 10^{-11} emu and hence slight changes in its magnetization value during reversal processes cannot be detected by conventional magnetometry techniques. Previous experiments were performed, in general, on large assemblies of theoretically identical particles, even if the real dispersion of the sample in terms of size, morphology, composition, orientation and separation between the different magnetic entities was clearly hiding several factors and limiting the interpretation of the results. Nowadays, electron holography [164], micro-SQUID (Superconducting Quantum Interference Device) [165] and Magnetic Force Microscopy techniques [166, 167] have made possible the study of magnetization switching in single nanowires.

The measurement of the magnetoresistive properties of metals has also been proved to be an appropriate method for the detection of very small magnetization variations. Several authors have used Anisotropic Magnetoresistance (AMR) measurements for the study of magnetic reversal processes. The anisotropic magnetoresistive effect is due to the anisotropy of spin-orbit scattering in transition ferromagnetic metals and leads to changes in the resistivity as the angle between the current and the magnetization is modified. Resistance measurements can be performed both at room and low temperature with high accuracy. Therefore, AMR techniques can be used as a probe of the magnetization orientation with respect to the current, even if the total change in resistivity between the state where the

magnetization is parallel to the current and the state where it is perpendicular is usually very small. The main results reported in the literature concerning the study of the magnetization reversal mechanisms by using previously mentioned techniques are summarized in the next paragraphs.

The first study of an isolated nanowire with a diameter smaller than 100 nm was reported in 1996 by Wernsdorfer et al. [165]. Two Ni nanowires with diameters of 92 ± 4 and 50 ± 5 nm and aspect ratio 100:1 or larger were studied by micro-SQUID techniques at 0.13 and 6 K. Ni nanowires were obtained by the electrochemical filling of the pores of commercial nanoporous polycarbonate membranes of thicknesses between 6 and 10 μm. After the dissolution of the membrane with chloroform, the samples were drop-casted on a chip containing a few hundreds of SQUIDs. SEM observations helped to localize the microbridge dc SQUID where a single nanowire had been trapped, as shown in Fig. 5.23a. TEM measurements confirmed the polycrystalline nature of the wires with a typical crystallite size of 10 nm. The polycrystallinity of the wires allows the assumption

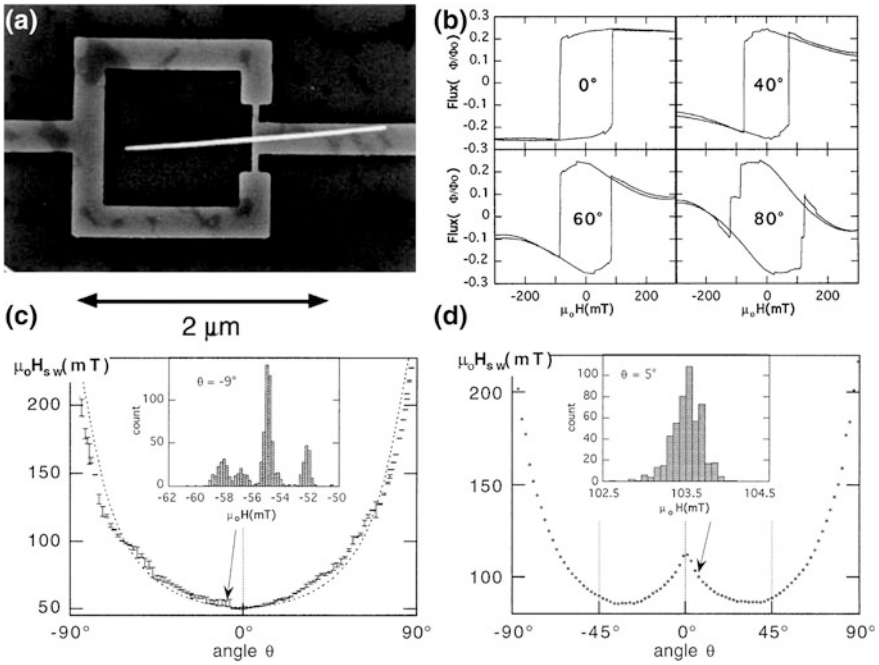

Fig. 5.23 **a** SEM micrograph of a microbridge dc SQUID and a Ni wire of diameter of 65 nm; **b** hysteresis loops of the wire in **a** at several values of the angle between the applied field and the wire axis; **c** angular variation of the switching field of a Ni wire, 92 ± 4 nm in diameter, 5 μm in length. Bars: width of the histograms. Line: prediction of the curling model. Inset: histogram of the switching field at the angle $\theta = -9°$; **d** angular variation of the switching field of a Ni wire, 50 ± 5 nm in diameter, 3.5 μm in length. The width of the switching field distribution is smaller than the dot size. Inset: histogram of the switching field at the angle $\theta = 5°$. Taken with permission from Ref. [165]

that its magnetocrystalline anisotropy is negligible, as hypothesized both in the Stoner-Wohlfarth and in the curling theories. A variable external magnetic field was applied in the plane of the SQUID at several θ angles, where θ is the angle between the magnetic field direction and the wire axis (easy anisotropy direction). The flux induced by the wires was detected by the SQUID. Hysteresis loops of the magnetic flux of the sample under slowly varying applied fields (typically a few mT/s) were recorded for several θ angles and are shown in Fig. 5.23b. They all showed an abrupt change of the signal at a certain value of field. Such sharp transition is associated to the magnetization reversal of the wire, which occurs at the switching field. In the case of the wider nanowires, the experimental data were compared to the predictions of the curling mode of magnetization reversal in an infinite cylinder [161]. Based on this theory, the angular variation of the switching field can be expressed by:

$$H_{SW} = \frac{M_S}{2} \frac{a(1+a)}{\sqrt{a^2 + (1+2a)\cos^2\theta}} \tag{5.11}$$

where $a = -1.08(d_0/d)^2$. The exchange length $d_0 = 2\sqrt{A}/M_S$ (A is the exchange constant) defines the transition from uniform rotation to curling. From the fit shown in Fig. 5.23c, a curling magnetization reversal mode was confirmed and a value of d_0(Ni) of 34 ± 4 nm was extracted, in accordance with previous data reported in literature [168]. The histogram of the H_{SW} values depending on the θ angle (also shown in the inset of Fig. 5.23c) revealed that different spin configurations with different energy barriers of nucleation were contributing to the reversal process.

In contrast to these observations, the angular variation of the H_{SW} for nanowires with diameters smaller than 75 nm showed a local maximum at $\theta = 0$, revealing the presence of coherent rotation reversal mechanisms as predicted by the Stoner-Wohlfarth model (see Fig. 5.23d). This seemed to be due to the small diameters of the wires which were actually close to the d_0 value. The authors explained such behavior by considering a predominant curling mode reversal at small θ angles (with some reminiscence of coherent rotation that gives rise to a moderate maximum at $\theta = 0$) while at larger θ angles a complete coherent rotation was taking place. The narrow histograms of H_{SW} with θ, displayed in Fig. 5.23d, suggested in this case that a single energy barrier is responsible for the reversal. Based on calculations by means of micromagnetic equations, the authors claimed that the magnetization reversal by the curling mode was triggered by the nucleation of a vortex at one end of the nanowire that later propagated along the structure. This concept had been treated analytically before [169]. To confirm this mechanism, switching time measurements at 0.13 K were fitted to an exponential formula of the nonswitching probability $P(t) = e^{-(t/\tau)^\beta}$ where τ defines the mean waiting time and β is a factor considering the distribution of energy barriers. The field and temperature dependence of τ followed an Arrhenius law from which a value of 15,000 K for the energy barrier for magnetization reversal was extracted. This value could be roughly correlated with an activation volume around 20 nm^3, which

was actually more than 200 times smaller than the total volume of the nanowire, confirming the previous nucleation-propagation mechanism. These observations diverge from the ones reported by the same authors for single nanoparticles, which indicated a magnetization reversal by uniform rotation [170]. In a following work, and by means of similar micro-SQUID measurements, the authors studied the dynamics of pinning and depinning of the propagation of the magnetization reversal occurring in some samples as well as the negative effect of chemical oxidation in the reversal process [171]. Both phenomena introduced deviations in the single exponential law for the previously mentioned nonswitching probability.

Compared to micro-SQUID measurements, AMR techniques offer the possibility to study the same systems at room temperature. This represents a significant advantage since the magnetization reversal processes can be studied at temperatures close to working temperatures of potential devices where nanostructures could be integrated. Several examples of the use of this technique have been reported in the last 10 years. The angular dependence of H_{SW} is monitored experimentally by observing the discontinuity of the magnetoresistive hysteresis in this case. The AMR of bulk polycrystalline samples is proportional to $\cos^2\theta$, where θ is the angle between the current (parallel to the wire axis) and the magnetization $M(H)$ (which in turn is a function of the applied field H) [172, 173]. This law originates from the high symmetry of the resistivity tensor in bulk materials. Nevertheless, the finite size effects of the wire lead to diffusive scattering at its surface which is expected to introduce some deviations from this law [173]. Neglecting such deviations, the magnetoresistive curve $R(H)$ is related to the magnetization $M(H)$ by:

$$R(H) = R_0 + (\Delta R)_{max}\left(\frac{M(H)}{M_S}\right)^2 \tag{5.12}$$

In Eq. 5.12, the magnetization is assumed to be uniform and must be measured along the wire axis. In that case, $M(H)$ is proportional to M_S following the equation $M(H) = M_S \cos[\theta(H)]$. The ratio $(\Delta R)_{\max}/R_0$ is known as the AMR ratio.

Wegrowe et al. [174] reported in 1998 the study of the magnetization reversal mechanisms of individual non-interacting Ni nanowires fabricated by electrodeposition techniques in a porous template membrane. The electrical contact for the resistivity measurements was performed in situ by potentiometric techniques, whereby a patterned thin layer gold film electrode was formed on the top of the membrane by sputtering through a mask. The average pore diameter of the membrane was 30 nm and the nanowires obtained showed a polycrystalline character. The magnetoresistance hysteresis loops were recorded at room temperature with a slowly varying applied field of about 0.1 mT/s, for applied fields oriented at $\theta = 10$ and 80° with respect to the wire axis. Irreversible jumps in the loops were observed at the H_{SW} strictly correlated with curling reversal modes, while the rest of the loops was characterized by a reversible trend in accordance with a uniform rotation mechanism. The angular dependence of the H_{SW} for the two θ angles shared many similarities with the graphics reported in Ref. [165] for

nanowires with small diameters, in that case measured by micro-SQUID techniques. The validity of both synthetic and AMR techniques for the study of magnetization reversal processes in single ferromagnetic nanowires was hence confirmed.

The same authors performed later more accurate studies on similar Ni nanowires by AMR measurements, using more elaborated theoretical models of the angular dependence of the H_{SW} [175]. AMR measurements at different angles are reported in Fig. 5.24a, where the irreversible resistance jumps are clearly observed. The $H_{SW}(\theta)$ curve derived from these measurements recorded a significant hump at low angles centered at $\theta = 0°$, as shown in Fig. 5.24b. $H_{SW}(\theta)$ curves for curling reversal modes in infinite cylinders are predicted to have a U-shape, while they present a sharp peak at $\theta = 0°$ if the magnetization reversal occurs by coherent rotation. However, in this case the shape of the curve could not be clearly associated to any of these models. The classical curling theory assumes the absence of magnetocrystalline anisotropy in the cylinder [161]. Nonetheless, a revised version of this model was suggested by Aharoni in which a magnetocrystalline anisotropy parallel to the wire axis was also taken into account in the curling rotational mode [162].

The fit of the experimental data by this new model was able to reproduce the shape of the experimental curve to a high extent, especially for what concerned the low angle values (see Fig. 5.24b). However, the fit overestimated the H_{SW} values by about 0.5 kOe. In other words, an important contribution had been omitted in the model which actually should facilitate the magnetization reversal, as deduced from the lower experimental values. Several contributions were mentioned by the authors as possible reasons to explain the low H_{SW} values measured, such as the effect of surface anisotropy or the presence of a perpendicular magnetocrystalline anisotropy (not considered in the theoretical model). Among the possible explanations the authors claimed that most likely the presence of structural defects in the polycrystalline Ni nanowire could be responsible for the observed phenomenon. The presence of highly defective crystal regions could easily facilitate the nucleation of magnetization reversal domain walls in some small parts of the wire. In this sense, the authors modified the original demagnetizing factors that defined the shape anisotropy of a wire with aspect ratio 100:1, and limited them to those corresponding to a volume with aspect ratio 2:1, in accordance with what they considered to be the activation volume, or the volume in which the magnetization reversal domain wall nucleated. Setting the demagnetizing factors to the values corresponding to a volume 50 times smaller than the one of the entire wire, the fitted values were precisely rescaled to the experimental ones. This confirmed the fact that the curling reversal was not acting simultaneously in the whole length of the wire but instead the mechanism is better described by a nucleation-propagation process, as also ascertained by previous micro-SQUID studies [165]. The authors suggested that the small discrepancies still present at large angles could be due to the pinning of the magnetization by surface defects during propagation or by a deviation from the AMR law (Eq. 5.12), as a consequence of the finite size effects in the wire.

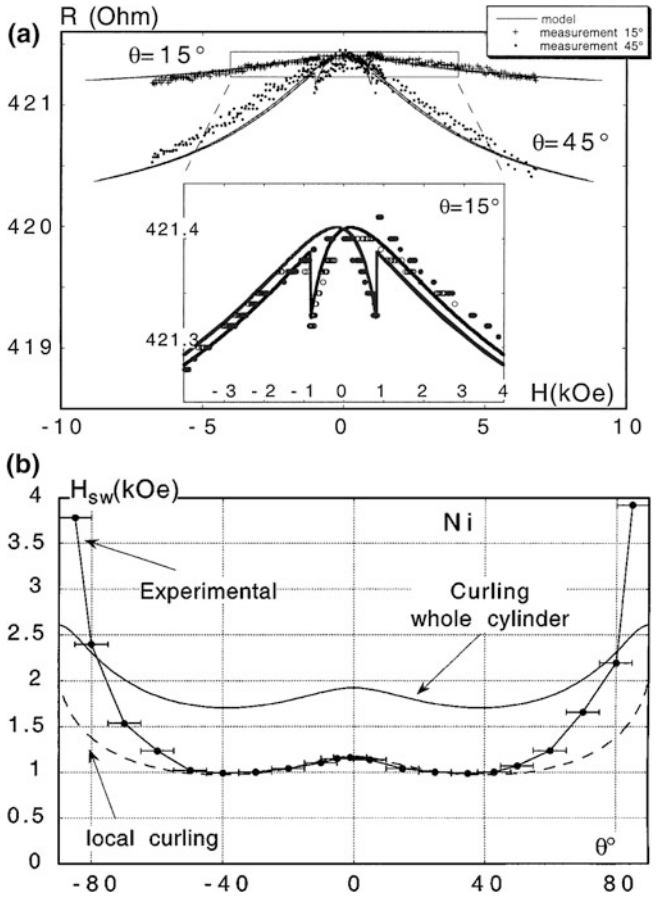

Fig. 5.24 (**a**) Ni magnetoresistive hysteresis at 15° and 45°. Bias current 0.3 mA. The continuous lines are predictions based on the curling model of magnetization reversal and the AMR quadratic dependence of the projection of the magnetization in the direction of the current. Inset: Zoom of the magnetoresistive discontinuity at the switching field H_{SW}, for $\theta = 15°$. The points correspond to increasing (*full circles*) and decreasing (*empty circles*) field measurements; **b** switching field of Ni nanowires vs angle between wire and field. Dotted line: Values of the switching field of the curling reversal mode in the cylinder 100:1, with magnetocrystalline anisotropy K as adjustable parameter. Solid line: Curling with the previous K and adjustable demagnetizing factors D_z and D_x. Taken with permission from Ref. [175]

Other studies were later published by the same group [176] and by Pignard et al. [34] which confirmed these findings. In the last case, the authors observed two irreversible jumps of the resistance as the magnetization was reversed (see Fig. 5.25a). While the first one represented the nucleation of the magnetization reversal as in all previous examples, the second was associated to the trapping of this domain wall at a pinning center during its propagation. The authors claimed that the pinned domain wall could only be released at higher fields leading to the

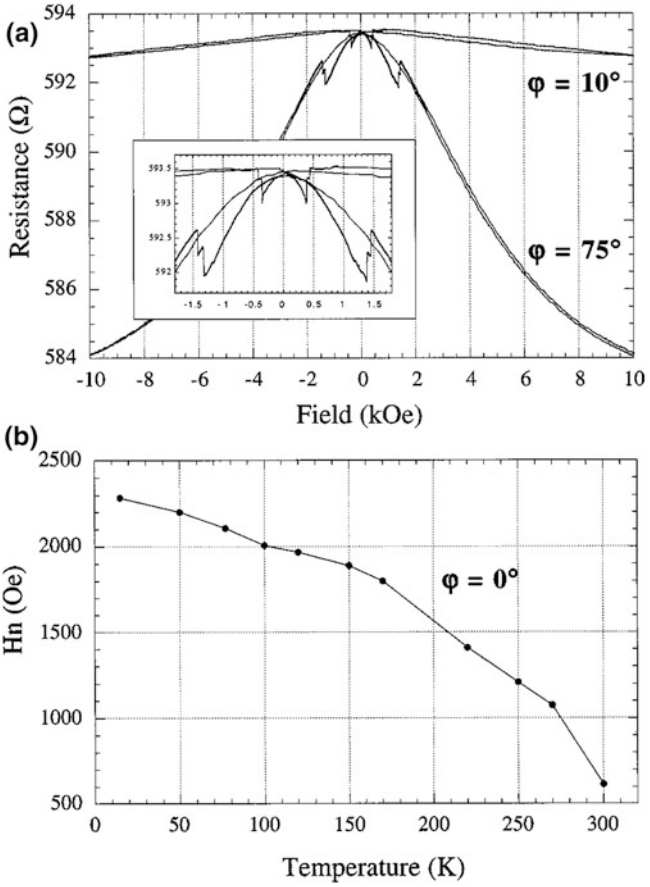

Fig. 5.25 **a** AMR characteristics at 300 K of a single wire for $\varphi = 10°$ and 75° ($d = 75$ nm). Inset: zoom showing the irreversible jumps of the resistance as the magnetization is reversed; **b** nucleation field vs temperature of a single Ni wire ($d = 575$ nm). The applied field is parallel to the wire axis ($\varphi = 0°$). Taken with permission from Ref. [34]

observed second jump, after which the magnetization of the wire was completely reversed. In this work, the temperature dependence of the switching field was also addressed: at $\theta s = 0°$, the H_{SW} increased from 600 to 2,300 Oe when cooling the sample from room temperature down to 10 K as seen in Fig. 5.25b. That means that a decrease in temperature leads to an additional anisotropy contribution that reinforces the wire axis as the easy direction for the magnetization. SQUID magnetometry measurements were performed at different temperatures to extract the anisotropy constants (K) in each case. At room temperature a value of K of 7.2×10^5 erg/cm^3 was obtained, which corresponded to the one associated with the shape anisotropy of an infinite cylinder. It was then clear that magnetocrystalline anisotropy was negligible in the Ni nanowire. Values of K of 11.5×10^5 and 12.3×10^5 erg/cm^3 were obtained at 100 and 35 K respectively. Assuming a

temperature-independent shape anisotropy, the authors stated that the additional uniaxial anisotropy measured had its origin in the well-known magnetoelastic properties of Ni. In the experiments, Ni nanowires were measured as prepared inside the polycarbonate membrane template. Due to the large mismatch of the thermal expansion coefficients between the two materials, Ni nanowires were subjected to variable mechanical stresses depending on temperature, that were studied by the authors by means of XRD spectra. Such stresses were able to increase the whole anisotropy of the system at low temperatures. However, the additional magnetoelastic anisotropy was found not to modify the magnetization reversal mechanism observed in Ni nanowires at room temperature.

AMR techniques have also been used to study magnetization reversal processes in Permalloy nanowires. Oliveira et al. [177] recently reported on the reversal mode of $Ni_{81}Fe_{19}$ nanowires fabricated by means of mechanical lithography using atomic force microscopy. The wires had lengths between 5 and 10 μm, widths between 300 and 400 nm and thicknesses in the range of 3–10 nm. One electrically connected wire is shown in the SEM micrograph of Fig. 5.26a. As evidenced by the dimensions reported, the nanowire did not display a cylindrical shape as in all previously reported examples; instead a long thin narrow tape nanowire had been fabricated this time. Magnetoresistance hysteresis loops were recorded at different angles and usual irreversible jumps were observed in all cases, indicating the values of H_{SW}. The angular dependence of H_{SW}, displayed in Fig. 5.26b and c for two nanowires of different dimensions, could be well-fitted by the equations derived from the curling nucleation mode, which would indicate that the magnetization reversal could evolve through similar mechanisms for thin narrow tape-like or cylinder-like nanowires.

Interestingly, the three demagnetizing factors used in the fit had to be almost equal in value ($D_x = D_y = D_z = 1/3$) in order to reproduce the experimental curve. These demagnetizing factors have no physical meaning for long nanowires of high aspect ratio in which $D_x = D_y \gg D_z$ should be expected. Actually the values of D_i used in the previous fit correspond approximately to a spherical sample and hence they are unrealistic for the sample. These results indicated that a mechanism of magnetization reversal other than curling was acting in such tape-like permalloy nanowires. The shape of the $H_{SW}(\theta)$ curve clearly indicated that coherent rotation was not the predominant mechanism. From the micromagnetic theories, only the buckling reversal mechanism was left, which so far had only been considered in theoretical numerical analysis [163]. The fit of the data using the buckling reversal model was able to reproduce the experimental curves to a high extent by using in this case realistic values of the demagnetizing factors for a tape-like wire. The authors stated that the shape of the wire was responsible for the buckling reversal mechanism in opposition to the well-known Stoner-Wohlfart and curling models for infinite cylinders, and highlighted that in previous studies the data extracted from other long narrow thin tape wires had been interpreted by means of micromagnetic theories developed for ellipsoidal or cylindrical geometries, due to the absence of appropriate models for tape-like geometries.

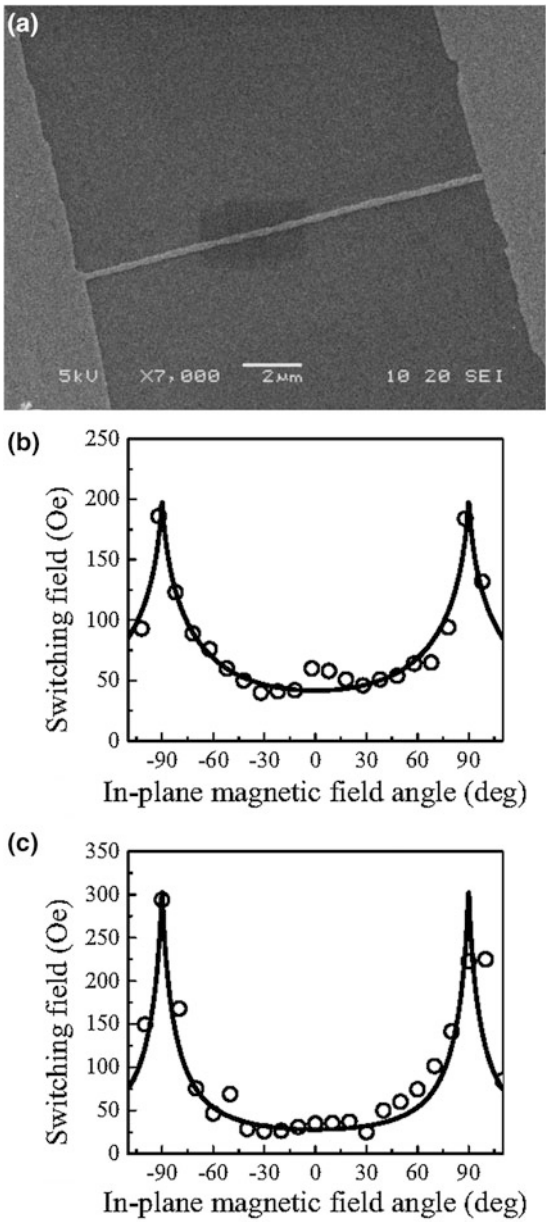

Fig. 5.26 **a** SEM image of a ferromagnetic nanostructure of permalloy consisting of two rectangular pads measuring 70×80 mm^2 connected by a permalloy nanowire having length of 12 μm, width of 290 nm, and thickness of 12 nm; **b** and **c** switching field of permalloy nanowires as a function of the in-plane angle. The *open circles* represent the experimental data measured by AMR and the solid lines are the fits with the theoretical model for the nucleation field using the magnetization buckling mode. The calculations for the two samples were carried out using the following parameters: **b** length = 10 μm, width = 460 nm and thickness = 3.5 nm; **c** length = 6 μm, width = 290 nm and thickness = 12 nm. Taken with permission from Ref. [177]

5.5.6 Domain Wall Dynamics in 1D Metallic Nanostructures

We have discussed so far some representative works dealing with the study of the different magnetization reversal mechanisms acting in size confined 1D magnetic systems. The non-uniform magnetization reversal processes are characterized by the nucleation of a domain wall (DW). The DWs are ten- to hundred-nanometer-size transition regions in which the orientation of local magnetizations M gradually changes between neighboring magnetic domains of different M orientations in an unsaturated magnetization state [178]. When the dimensions of the magnetic particles approach those of the DW regions, as it is the case for sub-micrometer nanowires, it becomes possible to study the motion or dynamics of a single DW along one direction, i.e. the axis of the wire. Some magnetic devices have been proposed, in which DWs encode information and this is further transmitted along the wire length by field- or current-induced DW motion [179, 180]. The working speed of the device is obviously correlated to the DW velocity. To compete with current technologies, high-speed operation, and hence fast wall propagation, is absolutely required. However, nanofabrication technologies and highly sensitive time- and space-resolved measuring techniques have made possible the study of the DW motion only in the last ten years. In this sub-section we will highlight the most significant achievements made in this field.

The Walker's theory [181] was modeled for the study of one dimensional DW motion in thin films. Due to the lack of other models accounting for further dimensional confinements, the propagation of DWs in sub-micrometer metallic nanowires has been studied and interpreted based on this model. In the Walker model, the DW velocity, v, increases linearly with the value of the applied magnetic field H according to the relation:

$$v = \mu H \tag{5.13}$$

where μ is the DW mobility, which can be expressed as:

$$\mu = \gamma \Delta / \alpha \tag{5.14}$$

where γ is the gyromagnetic ratio, Δ is the DW width and α is the phenomenological Gilbert damping parameter (the physical mechanisms behind the latter have not been well-understood yet [182]). Hence, Eq. (5.13) can be expressed as:

$$v = (\gamma \Delta / \alpha) H \tag{5.15}$$

This seems to be true for low magnetic field values, also known as viscous regime. However, the Walker model predicts that a magnetic field threshold value exists, above which the DW propagation velocity suffers a sudden drop and enters the turbulent regime. In this regime, the propagation of DWs evolves from a simple translation to more complex precessional modes. The magnetic field value at which the maximum v is observed is known as the Walker field (H_W). Several authors have observed experimentally this discontinuity and some of them have

studied the morphological, geometrical and physical parameters underlying the DW dynamics in both regimes, and the possible ways to avoid the Walker breakdown phenomenon [183–186].

One of the first in-depth studies concerning DW motion was reported by Ono et al. [187]. They investigated the magnetization reversal dynamics of a single NiFe/Cu/NiFe trilayer wire with thicknesses of 40, 10 and 5 nm, respectively, and width of 500 nm. An initial magnetic field of 500 Oe was applied in order to align M in one direction parallel to the wire axis. The magnetization states of the wire were monitored by giant magnetoresistance (GMR) measurements, where changes in the resistivity of the material were detected as the magnetic field was swept in the opposite direction, while a 100 μA current was applied through the long axis of the wire. The time variation of the resistance during the M reversal revealed how the magnetic DW propagated in the wire. The reversal of the 5 nm thin NiFe layer took place at 80 Oe by the pinning and depinning of the DW, as indicated by the gradual increase of resistivity with increasing magnetic field. Oppositely, the 40 nm thick NiFe layer reverses abruptly at 120 Oe within a time shorter than the 10 ms measuring time used in the experiment. When the measuring time was decreased to 40 ns-intervals, the changes in resistivity with time at 77 K and 121 Oe were measured. The 40 nm thick NiFe layer showed a constant DW propagation velocity of 182 m/s during its magnetization reversal as seen from the linear variation of resistance with time (Fig. 5.27a). The constant velocity suggested that the M reversal takes place by the propagation of a single DW.

The same experiment was performed at different values of the magnetic field and the values of DW velocity v measured as a function of H (between 100 and 150 Oe) were fitted using the Walker equation (Eq. (5.13)). The results are shown in Fig. 5.27b. A value of mobility μ of 2.6 ± 0.2 m/sOe was obtained, which was seen to be constant in the temperature range between 100 and 160 K. This value of μ was much lower than values observed in NiFe thin films of similar thickness [188]. The authors concluded that the DW mobility in the wire was mainly limited by Gilbert damping, since a value of α of 0.63 was calculated using the equation $\mu = \gamma\Delta/\alpha$ and assuming a DW width of 100 nm. Such a large value of α was attributed to the presence of defects at the surface and interface of the wire.

A controversial work was published in 2003 by Atkinson et al., who claimed that lateral constrainment of the DW does not necessarily affect the intrinsic DW propagation velocity with respect to thin films [189]. A 5 nm thick and 200 nm wide permalloy wire was chosen as the object of study. Hence, the wire was 300 nm narrower and 35 nm thinner than the one studied in the previous report [187]. The magnetic switching dynamics at room temperature were monitored in this case by means of continuous-wave laser magneto-optic Kerr effect measurements (MOKE) with nanosecond temporal resolution. The magnetic fields, at which DW propagation velocities were measured, were much weaker compared to the previous work, due to the lower coercivity of the wire, and ranged from 10 to 49 Oe. Very high values of DW velocity were observed in this case: over 500 m/s above 40 Oe and a maximum of 1,500 m/s at 49 Oe. The authors suggested a thermally activated DW motion still within the viscous regime defined in the

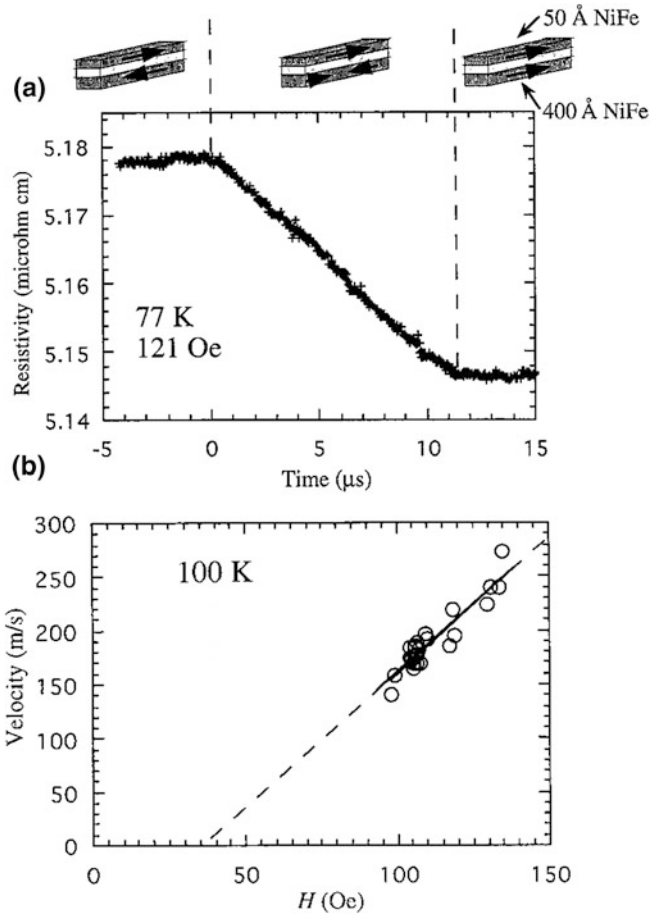

Fig. 5.27 **a** Time variation of the resistance during the M reversal of the 40 nm NiFe layer at 77 K, which was collected at 40-ns intervals. The applied magnetic field simultaneously monitored by digital oscilloscope was 121 Oe. Because the sweeping rate of the applied magnetic field was 20 Oe/s, the variation of the applied magnetic field during M reversal was less than 2×10^{-5} Oe. Thus, the applied magnetic field is regarded as constant during the measurements; **b** dependence of domain wall velocity v on amplitude H of the applied magnetic field at 100 K. Taken with permission from Ref. [187]

Walker model. In this regime, the mobility, defined as the slope of the field dependence of the wall velocity, should be constant in the absence of pinning sites, as stated in Eq. (5.14). However, experimental results showed a field-dependent mobility in this case, which was attributed to the presence of defects in the wire that were pinning the DW propagation, until thermal activation overcame the pinning energy, freeing the DW to move. The authors assumed that, at the highest magnetic field measured, the defects no longer pinned the wall and thus the velocity was defined by the intrinsic mobility of the wire. A value of mobility of

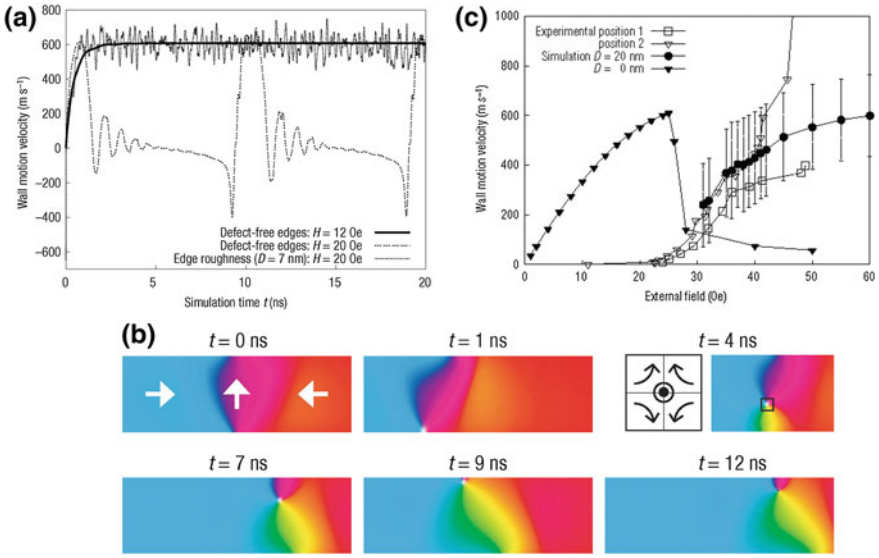

Fig. 5.28 Simulated time-resolved domain wall (DW) motion in a permalloy wire. Wire thickness 5 nm, width 200 nm, damping constant $\alpha = 0.01$. **a** Comparison of wall velocities for perfect (defect-free) edges (field $H = 12$ and 20 Oe applied at time $t = 0$ to a DW in equilibrium) and rough edges ($H = 20$ Oe, grain diameter $D = 7$ nm); **b** pictures at different times of the moving DW at 20 Oe with perfect edges (the picture height is the wire width; the right edge of the pictures at $t > 0$ corresponds to the same physical position; color coding of the magnetization orientation uses the color wheel for the in-plane directions, and goes to white or black when the magnetization becomes out of plane). White arrows depict the DW rest structure. The inset is a representation of the antivortex core structure in the square box; **c** comparison of experimental values (the two data sets of Ref. [189]) and numerical simulations ($\alpha = 0.02$, $D = 0$ and 20 nm). The error bars span twice the standard deviation of the velocity ($D = 20$ nm). For the rough wire, the wall can travel 20 μm without stopping for fields larger than 45 Oe, whereas at 30 Oe it stops within 1 μm (zero temperature calculations). Fast wall motion is seen to extend at least up to 100 Oe. Taken with permission from Ref. [192]

31 m/sOe and of Gilbert damping coefficient of 0.053 were estimated by using Eqs. (5.13) and (5.14) between the origin and the data point measured at the highest field. These values were much closer to the ones previously observed in films [190] and also to the ones predicted by theory [191]. The results were regarded as a proof that the operational speed of potential spintronic devices involving DW motion in magnetic nanostructures would not be affected by structural confinement.

From that moment, several theoretical and experimental studies tried to shed light on the reasons for the divergence in results. Nakatani and co-workers [192] performed a set of micromagnetic simulations on a nanowire of identical dimensions to the one used in the work of Ref. [189]. Initially the authors simulated the time dependence of the DW velocity fixing the nanowire thickness, width and damping constant to 5, 200 nm and 0.01, respectively. The simulations

considering an ideal defect-free wire reversing at applied magnetic fields of 12 or 20 Oe showed the expected results based on the Walker theory. The results of the simulations are displayed in Fig. 5.28a. At low fields, a stationary velocity of 608 m/s was reached in agreement with the viscous regime, while at higher fields the turbulent regime became apparent and the average velocity of propagation decreased to a value of 60 m/s. The nature of the DW motion above the Walker breakdown was explained by the authors as an alternation of transverse magnetization- and antivortex-like walls as shown in Fig. 5.28b.

The transverse magnetization wall is energetically more stable than a vortex and hence propagates at higher velocities. However, this type of wall presented a V-shape and, due to exchange interactions, the precession around the applied field was enhanced at the corner of the V domain. This resulted in the nucleation of an antivortex that absorbed most of the torque supplied by the magnetic field and as a consequence it moved slowly, dramatically decreasing the velocity of the DW motion. This antivortex moved to one edge of the wire where it finally disappeared and the initial transverse magnetization wall and DW velocity were restored. This type of motion explained the inhomogeneous velocity values simulated with time and the low average velocities observed in most experimental cases when measurements are performed in the turbulent regime. Subsequent theoretical [193] and experimental [194] studies have also addressed the DW propagation mechanisms above the Walker field in similar nanowires. Such studies confirmed the periodicity observed in the wall transformation processes during propagation, in contrast to stochastic propagation modes. In the work from Nakatani, the authors also studied the effect of the wire edge roughness on the DW propagation velocity above the Walker field. Results are displayed in Fig. 5.28c. Interestingly, simulations showed that the presence of sufficiently rough edges suppressed the antivortex nucleation at the edges, allowing the DW to move at the highest speed above the Walker field, as the ideal wire was doing in the viscous regime. The authors used a new model for their simulations that took in consideration the grain size (D) of polycrystalline wires as the main source for roughness. They then compared their calculations with experimental results of Atkinson et al. [189]. Calculations considering ideal defect-free wires were only able to reproduce experimental velocity values in the low field region (below 35 Oe). However, when a mean grain diameter of $D = 20$ nm was considered in the simulations, the whole set of experimental velocities at low and high fields in Ref. [189] could be reproduced, as reported in Fig. 5.28c. The authors claimed that all the experimental points were in the roughness-stabilized regime of wall motion. It is assumed by the authors that the roughness must be larger than the exchange length of the wire in that case. The exchange length of soft magnetic materials like permalloys is their characteristic length of micromagnetics and can be expressed as $\left(2A/\mu_0 M_S^2\right)^{1/2}$, where A is the exchange constant and M_S is the saturation magnetization. Since nucleation of antivortexes occurs at the edges of the wires, roughness values larger than the exchange length are optimal to suppress their nucleation. In contrast, in a thicker wire such as the one studied by Ono et al. in

Ref. [187], similar values of roughness do not play the same role and the DW motion is not in the roughness-stabilized regime. By means of theoretical calculations, Nakatani and co-workers suggested the role of the wire edge roughness as a stabilizer of the fast DW motion up to fields much larger than those associated with the Walker breakdown in ideal nanowires. They also stated that roughness should rather be engineered than avoided when fabricating nanostructures for DW propagation. Alternatively, Glathe et al. [195] demonstrated experimentally that the application of a transverse magnetic field can also be used as a way to suppress Walker breakdown events.

It was so far clear that the field-induced DW motion along nanowires could be divided in different propagation regimes depending on the amplitude of the applied magnetic field H, the so-called viscous and turbulent regimes. Therefore, it is obviously necessary to study a wide range of magnetic fields in order to clearly distinguish between one regime and another without uncertainty. However, depending on the intrinsic characteristics of the wire, the fields at which the viscous regime would be observed are lower than the ones required for the domain wall injection into the wire, H_i. In this sense, Beach et al. were able to devise new experimental conditions that allowed for the dynamic measurement of DW propagation in a ferromagnetic permalloy nanowire over a broad field range [185]. A 20 nm thick and 600 nm wide $Ni_{80}Fe_{20}$ wire was studied by longitudinal magneto-optic Kerr effect measurements. In their experiments, a minimum H_i of 24 Oe was required to inject a DW into the wire and induce the magnetization reversal of the latter. However, once the DW had been injected, constant fields down to 1.5 Oe were observed to be sufficient to propagate it. Hence, using specially tailored drive-field waveforms, the authors were able to study the DW dynamics along the wire from 1.5 until 70 Oe. The field dependence of the velocity measured for the permalloy wire is shown in Fig. 5.29.

Three different regimes were clearly discerned, each of them characterized by a different value of the DW mobility, μ. At fields below 4 Oe, the velocity increased linearly with field with mobility close to 25 m/sOe. Above 4 Oe, v began to decrease with increasing H, showing a negative DW mobility in this regime. However the negative μ started increasing gradually with increasing magnetic field and became positive again above 20 Oe. For H values larger than 30 Oe, the field dependence of the DW velocity recovers the linearity, but with a ten-fold reduction in μ compared to the low field regime. These results were in complete agreement with the Walker model for 1D DW systems [181]. At low fields below the Walker transition, the DW motion followed the well-known linear mobility relation of Eq. (5.13) where $\mu = \gamma\Delta/\alpha$. After a regime in which the plane of transverse wall magnetization cants increasingly away from the direction of wall motion, the field-dependent variation of the velocity shows an asymptotically linear relation with a slope defined again by the mobility. However, at large fields the mobility was better expressed as

$$\mu = \gamma\Delta/\left(\alpha + \alpha^{-1}\right) \tag{5.16}$$

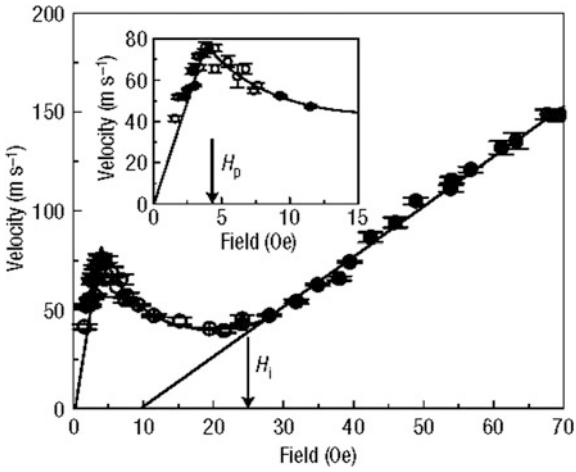

Fig. 5.29 Average domain-wall velocity versus field step amplitude. Arrows mark the domain-wall injection field, *H*i, and velocity peak, *H*p. Straight solid lines are linear fits to the data below *H*p and above *H*i, respectively; the curved line is a visual guide. Filled symbols show velocities obtained for a square-wave drive field and open symbols those obtained using injection pulse waveforms. The inset shows the detail around the velocity peak. Taken with permission from Ref. [185]

This equation was able to explain from a phenomenological point of view the ten-fold drop of mobility above the Walker field. The authors claimed that the slope of v versus H over a limited field range is insufficient to draw conclusions about the intrinsic damping unless one knows the relation of that field range to the Walker breakdown field. In this framework, the authors were able to compare the a priori contradictory results in Refs. [187] and [189]. The measurements of Ref. [187] for a permalloy nanowire of similar width and thickness were only performed at high magnetic fields. They revealed very similar values of v and μ when compared to the ones obtained with the measurements of Beach et al. in the high field regime. The authors suggested that the data presented by Ono et al. in Ref. [187] probably belonged to the linear $v = f(H)$ regime at high fields where μ had to be expressed as in Eq. (5.16). If this was true, the low v and μ values presented would make more sense since the measurements would have been performed within the turbulent regime and not in the viscous one, where the classical Eq. (5.15) can be applied. On the other hand, the wire studied by Atkinson et al. in Ref. [189] was only measured at low H values. The wire, in that case, was characterized by a high mobility value comparable to the one measured by Beach et al. in the low field regime previous to the Walker breakdown phenomenon. Moreover, the value of the Gilbert damping parameter calculated by using Eq. (5.14) was completely reasonable for a permalloy nanowire. Hence, Beach suggested that Atkinson's results had been obtained by measuring the nanowire within its viscous regime. However, that would imply a Walker field in that system much larger than the 4 Oe observed by Beach et al. The roughness

effect on thin nanowires predicted by Nakatani et al. [192] was assumed to be responsible for the shift of the Walker breakdown field to higher values.

As said at the beginning of this sub-section, the Walker's theory [181] was modeled for the study of one dimensional DW motion in thin films. Generally speaking, also nanostructured wires follow the trends marked by the Walker model. However, it should be noted that discrepancies between the Walker model and the experimental results for size constrained magnetic nanowires are often observed. Hence in recent years some theoretical studies have been undertaken in order to evaluate these differences, suggest improved micromagnetic models, and determine the effect of several geometrical or damping parameters on the main parameters describing the DW dynamics of magnetic nanowires, i.e. DW velocity, DW mobility and Walker breakdown field. Most of them are limited to the interpretation of the dynamics in the viscous regime below the Walker field. A. Kunz performed several micromagnetic simulations by using the three dimensional Landau-Lifshitz-Gilbert (LLG) equation of motion of each magnetic moment in the wire [196]. For nanowires of identical dimensions, the effect of the varying Gilbert damping parameter was evaluated from 0.005 to 0.1. Calculations suggested that the maximum DW speed was independent of the α value, while instead the Walker field increased linearly with increasing α values. High values of the damping parameter are thought to suppress the precessional motions and vortex nucleations within the wall, shifting in this way the Walker breakdown phenomenon to higher field values. In a set of subsequent simulations, the α parameter was maintained constant while the width of the wire was gradually increased. It was shown in that case that the value of the Walker field decreased, and the average speed increased as the width of the wire was increased. The new micromagnetic calculations indicated that the classical Walker model overestimates both the DW velocities (by a factor of 3) and the Walker fields. The authors suggested that these discrepancies with the Walker model could be the reason for the need of unphysical DW width and damping parameter values, in order to force experimental data agreement with theory. Recently, Bryan et al. used the same LLG equation in micromagnetic simulations to study the relationship between the wire dimensions and the DW dynamics [197]. In classical 1D models, the magnetization is assumed to be uniform throughout the wire cross-section and, based on this, the value of the Walker field, H_W, and DW mobility, μ, can be expressed as [198]:

$$H_W = \frac{1}{2}\alpha M_S\left(N_z - N_y\right) \tag{5.17}$$

$$\mu = \frac{v}{H_x} = \frac{\gamma\Delta}{\alpha} \tag{5.18}$$

where N_y and N_z are the demagnetizing factors along the wire width and thickness, respectively. The Δ wall width depends on N_y and N_z as well as on the applied field. However, the demagnetizing factors do not depend on the absolute dimensions of the wire, but on the relative ones. Hence in the 1D classical model wires with the same width-to-thickness ratios (w/T) should present identical values of H_W

and μ, regardless of their absolute dimensions. However, calculations performed by the authors suggested that nanowires with identical w/T but different absolute dimensions were not behaving in the same way. The calculated w/T dependence of the DW mobilities for wires of different widths is shown in Fig. 5.30a. The wall mobility clearly increases with increasing w/T, even if agreement with the 1D model was only observed for the narrowest wires, while the wider ones diverged significantly from predictions. Moreover, the dependence of μ on w/T changes as the wire width increases, suggesting that the DW mobility is determined by the absolute, rather than the relative, values of the wire width and thickness. It was also observed in the calculations that as either wire width or thickness is increased, H_W decreases, as shown in Fig. 5.30b and c. New equations were proposed by the authors, which experimentally related the width and thickness of the wire with its DW mobility and Walker field with a better agreement than the equations included in 1D models. In subsequent studies, domain wall dynamics have been investigated both theoretically and experimentally for geometrically-modulated cylindrical nanowires (localized changes of radii, bumps and necks) as a way to control the DW motion through advanced wire engineering or architecture [199, 200].

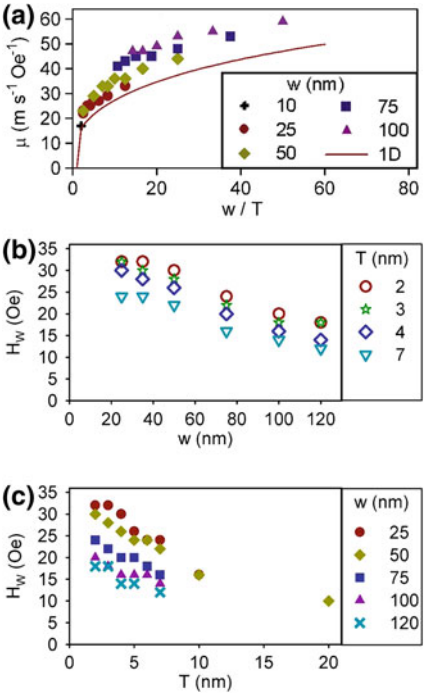

Fig. 5.30 **a** The domain wall mobility, μ, at H_x (below H_W) for permalloy wires of various widths, w, and thicknesses, T, as a function of w/T. The solid line shows wall mobility calculated using a 1D model. The effect of **b** the wire width, w, and **c** the wire thickness, T, on the Walker breakdown field, H_W, for several wire dimensions. Taken with permission from Ref. [197]

All previous examples regarded the magnetic field-induced DW propagation in 1D nanostructured systems. However, in recent years experimental evidences have confirmed the possibility to drive a DW along nanowires by the application of an electrical current. The pioneering theoretical studies predicting the current-induced DW displacement were reported by L. Berger [201, 202]. When a spin-polarized conduction electron crosses a DW, it changes its spin direction trying to follow the local magnetization of the material. In this process, there is a transfer of angular momentum from the electron to the DW, which is responsible for the physical displacement of the latter. This phenomenon is also known as the spin-torque effect. The main advantages arising from such current-induced DW propagation is the simplicity in the design, as it eliminates magnetic field-generating circuits in the device and is seen as a promising alternative for writing in "one bit/one structure devices", such as the spin momentum transfer magnetic random access memory [203]. However, while the field-induced DW motion is quite well-established, current-induced DW dynamics have not been well-understood yet. Several authors have been addressing this phenomenon from both a theoretical [204–208] and experimental [186, 209–214] point of view, in order to unveil and understand the several effects occurring when large electrical currents flow across a DW. For an understanding of the current-induced DW propagation phenomena and its state-of-the-art, the reader is redirected to the previously cited works and the references therein included.

5.6 Applications and Perspectives of 1D Magnetic Nanostructures

The applications of magnetic materials mainly depend on their magnetic strength. Hence, we can classify the materials as hard magnets, soft magnets and superparamagnets depending on the coercivity they show from large to null in this order. However, this property can change significantly when such materials are prepared in the nanoscale, as described previously in this chapter, both in favor or against their traditional use as bulk materials. Considering only hard nanomagnets, their application as permanent magnets has been seeked since years. In theory, higher energy products and larger coercivities could be achieved by finely tuning the size and the shape of the particles at the nanoscale. However, and due to stability and surface matters, low values of coercivity and magnetization are usually observed in particulate systems and consequently the use of elongated magnetic nanoparticles as permanent magnets has not been possible yet: permanent magnets for electric motors and generators, loudspeakers or magnetic resonance imaging (MRI) devices are still prepared by classical methods in which a low degree of control over their size and shape has been achieved. This is not the case of the materials used for magnetic recording media, one of the most popular applications of magnetic materials [215]. Particulate media generally made of

elongated ellipsoidal particles dispersed either longitudinally or perpendicularly in a polymer matrix are mostly used for tape applications [216, 217]. The devices exploited initially the shape anisotropy derived from needle-like or rod-like γ-Fe_2O_3 nanoparticles in order to stabilize one of the two energetically preferred magnetic directions. However, in an attempt to increase the coercivities achieved by iron oxide, highly anisotropic chromium dioxide (CrO_2) acicular particles partially substituted γ-Fe_2O_3 in some cases. Later on, the high versatility and coercivity and relatively low cost of cobalt-modified iron oxides has made of this material the predominant recording media in video tapes, and it is also used in audio tapes and even in disks for high density recording media. Other interesting elongated particles for such purposes have been made of oxide-passivated metals and barium ferrites. Nanowires with large aspect ratio would be extremely advantageous to prevent the onset of the superparamagnetic limit at which the magnetization direction in the magnetic grains can be reversed by the thermal energy k_BT, thereby resulting in loss of recorded data in the magnetic recording medium. Actually, several nanowire arrays are being studied due to their enormous potential in perpendicular magnetic recording media. One of the most impressive advances in this field is the development of race-tracking memory devices for fast storage and reading of information, based on the effect of current-induced domain wall motion [218]. In this sense, the assembly of perpendicularly aligned magnetic nanowires would be of extreme importance even if still several problems have to be faced for the implementation of such technology in the real world. Concerning the use of soft magnets, permalloy nanowires and nanostripes have found applications in transformers and other electrical equipment as well as in magnetic recording heads and magnetic shielding materials due to their low coercivity, high magnetic permeability and variable electrical resistivity depending on an external magnetic field [219]. In the field of spintronics, permalloy nanowires are excellent candidates for the study of field- or current-induced domain wall motion, as a way to encode information and further transmit it along the wire length. However, these last applications are still under investigation and many more fundamental studies must be performed before their integration in practical devices.

Superparamagnetic nanoparticles have emerged as promising systems for their use in biology and biomedical applications, both in vivo and in vitro, due to several possibilities they offer with respect to traditional materials: (1) the size of magnetic nanoparticles is usually smaller than or comparable to the size of cells, virus or proteins and hence their interaction is significantly enhanced; (2) their motion can be easily controlled by an external magnetic field and (3) they can show high magnetization values under the effect of a magnetic field but their net magnetic moment is cancelled when the magnetic field is switched off, which prevents their own aggregation and the potential damage of the tissue that could arise if the particles were left magnetized. In fact, several biomedical techniques are already exploiting the advantages offered by magnetic nanoparticles while some others are still exploring their use with already very promising results [220]. Among all the biomedical techniques that are nowadays benefiting from the properties of superparamagnetic nanoparticles, probably MRI is at the top. Both

T1 and T2 contrast agents based on magnetic nanoparticles have many kinds of products approved by FDA and commercialized [221]. Besides MRI, magnetic nanoparticles are also used as temperature enhancers in therapeutic hyperthermia treatments, as separating agents in magnetic separation techniques, as magnetic bullets in targeted drug delivery and as transfection vectors in magnetofection techniques. Most of these applications, with the exception of MRI, are still under intense study and consequently they are still being developed and tested in laboratories. The fundamental understanding of the performance of magnetic nanoparticles in biomedicine still requires a lot of effort and hence mainly simple and symmetric spherical magnetic nanocrystals have been investigated to date. Even if the increased anisotropy and large surface to volume ratio of elongated magnetic nanoparticles could in principle optimize their performance in biomedical techniques, very few works have addressed this issue so far, some of them described along this chapter. However, and considering the fast speed of development of this field and the huge amount of work being done devoted to the study of the fundamental properties of elongated magnetic nanoparticles, it can be foreseen that magnetic nanorods and nanowires will definitely find their role in biomedicine in the near future.

References

1. Gao J, Gu H, Xu B (2009) Multifunctional magnetic nanoparticles: design, synthesis, and biomedical applications. Acc Chem Res 42(8):1097–1107. doi:10.1021/ar9000026
2. Qiao RR, Yang CH, Gao MY (2009) Superparamagnetic iron oxide nanoparticles: from preparations to in vivo MRI applications (vol 19, p 6274). J Mater Chem 19(48):9286
3. Felser C, Fecher Gerhard H, Balke B (2007) Spintronics: a challenge for materials science and solid-state chemistry. Angew ChemInt Edit 46(5):668–699
4. Li K, Wu Y, Guo Z, Zheng Y, Han G, Qiu J, Luo P, An L, Zhou T (2007) Exchange coupling and its applications in magnetic data storage. J Nanosci Nanotech 7:13–45
5. Lu A-H, Salabas EL, Schüth F (2007) Magnetic nanoparticles: synthesis, protection, functionalization, and application. Angew ChemInt Edit 46(8):1222–1244
6. Millen RL, Kawaguchi T, Granger MC, Porter MD, Tondra M (2005) Giant magneto resistive sensors and super paramagnetic nanoparticles: a chip-scale detection strategy for immunosorbent assays. Anal Chem 77(20):6581–6587. doi:10.1021/ac0509049
7. Sun S, Murray CB, Weller D, Folks L, Moser A (2000) Monodisperse FePt nanoparticles and ferromagnetic FePt nanocrystal superlattices. Science 287(5460):1989–1992. doi:10.1126/science.287.5460.1989
8. Reiss G, Hutten A (2005) Magnetic nanoparticles: applications beyond data storage. Nat Mater 4(10):725–726
9. Wang ZK, Zhang VL, Lim HS, Ng SC, Kuok MH, Jain S, Adeyeye AO (2010) Nanostructured magnonic crystals with size-tunable bandgaps. ACS Nano 4(2):643–648. doi:10.1021/nn901171u
10. Jeong U, Teng X, Wang Y, Yang H, Xia Y (2007) Superparamagnetic colloids: controlled synthesis and niche applications. Adv Mater 19(1):33–60
11. Lin X-M, Samia ACS (2006) Synthesis, assembly and physical properties of magnetic nanoparticles. J Magn Magn Mater 305(1):100–109
12. Dobson J (2006) Magnetic nanoparticles for drug delivery. Drug Dev Res 67(1):55–60

13. Park K, Lee S, Kang E, Kim K, Choi K, Kwon IC (2009) New generation of multifunctional nanoparticles for cancer imaging and therapy. Adv Funct Mater 19(10):1553–1566
14. Wilhelm C, Lavialle F, Péchoux C, Tatischeff I, Gazeau F (2008) Intracellular trafficking of magnetic nanoparticles to design multifunctional biovesicles. Small 4(5):577–582
15. Dave SR, Gao X (2009) Monodisperse magnetic nanoparticles for biodetection, imaging, and drug delivery: a versatile and evolving technology. Wiley Interdiscipl Rev Nanomed Nanobiotechnol 1(6):583–609
16. Figuerola A, Di Corato R, Manna L, Pellegrino T (2010) From iron oxide nanoparticles towards advanced iron-based inorganic materials designed for biomedical applications. Pharm Res 62(2):126–143
17. Hurst SJ, Payne EK, Qin L, Mirkin CA (2006) Multisegmented one-dimensional nanorods prepared by hard-template synthetic methods. Angew ChemInt Edit 45(17):2672–2692
18. Mathur S, Barth S, Werner U, Hernandez-Ramirez F, Romano-Rodriguez A (2008) Chemical vapor growth of one-dimensional magnetite nanostructures. Adv Mater 20(8):1550–1554
19. Wang X, Li Y (2006) Solution-based synthetic strategies for 1-D nanostructures. Inorg Chem 45(19):7522–7534. doi:10.1021/ic051885o
20. Xia Y, Yang P, Sun Y, Wu Y, Mayers B, Gates B, Yin Y, Kim F, Yan H (2003) One-dimensional nanostructures: synthesis, characterization, and applications. Adv Mater 15(5):353–389
21. Caruntu D, Caruntu G, O'Connor CJ (2008) Advanced wet-chemical synthetic approaches to inorganic nanostructures Kerala. Tranworld Research network, Kerala, India
22. Martin JI, Nogues J, Liu K, Vicent JL, Schuller IK (2003) Ordered magnetic nanostructures: fabrication and properties. J Magn Magn Mater 256(1–3):449–501
23. O'Handley RC (2000) Modern magnetic materials: principles and applications. Wiley, New York
24. Spaldin N (2003) Magnetic materials: fundamentals and device applications. Cambridge University Press, Cambridge, UK
25. Bedanta S, Kleemann W (2009) Supermagnetism. J Phys D-Appl Phys 42 (1): Art no 013001. doi:10.1088/0022-3727/42/1/013001
26. Stoner EC, Wohlfarth EP (1948) Phil Trans R Soc A 240:599–642
27. Sohn BH, Cohen RE, Papaefthymiou GC (1998) Magnetic properties of iron oxide nanoclusters within microdomains of block copolymers. J Magn Magn Mater 182(1–2):216–224
28. Cullity BD, Graham CD (2009) Introduction to magnetic materials, 2nd edn. John Wiley & Sons, IEEE Press, NY
29. Dormann JL, Fiorani D, Tronc E (1997) Adv Chem Phys 98:283
30. Miller JS, Drillon M (2001) Magnetism: molecules to materials III. Wiley
31. Blundell S (2001) Magnetism in condensed matter. Oxford University Press, New York
32. Arrott AS, Heinrich B, Aharoni A (1979) IEEE Trans Magn 15:1228
33. Luborsky FE (1961) Development of elongated particle magnets. J Appl Phys 32(3):S171–S183
34. Pignard S, Goglio G, Radulescu A, Piraux L, Dubois S, Declemy A, Duvail JL (2000) Study of the magnetization reversal in individual nickel nanowires. J Appl Phys 87(2):824–829
35. Bødker F, Mørup S, Linderoth S (1994) Surface effects in metallic iron nanoparticles. Phys Rev Lett 72(2):282–285
36. Morales MP, Veintemillas-Verdaguer S, Montero MI, Serna CJ, Roig A, Casas L, Martinez B, Sandiumenge F (1999) Surface and internal spin canting in gamma-Fe_2O_3 nanoparticles. Chem Mater 11(11):3058–3064
37. Dumestre F, Chaudret B, Amiens C, Fromen MC, Casanove MJ, Renaud P, Zurcher P (2002) Shape control of thermodynamically stable cobalt nanorods through organometallic chemistry. Angew ChemInt Edit 41(22):4286–4289
38. Jamet M, Wernsdorfer W, Thirion C, Dupuis V, Mélinon P, Pérez A, Mailly D (2004) Magnetic anisotropy in single clusters. Phys Rev B 69(2):Art no 024401

39. Farle M (1998) Ferromagnetic resonance of ultrathin metallic layers. Rep Progr Phys 61(7):755
40. Walz F (2002) The Verwey transition–a topical review. J Phys: Condens Matter 14(12):R285–R340
41. Roca AG, Marco JF, Morales MD, Serna CJ (2007) Effect of nature and particle size on properties of uniform magnetite and maghemite nanoparticles. J Phys Chem C 111(50):18577–18584
42. Hermanek M, Zboril R, Medrik I, Pechousek J, Gregor C (2007) Catalytic efficiency of iron(III) oxides in decomposition of hydrogen peroxide: competition between the surface area and crystallinity of nanoparticles. J Am Chem Soc 129(35):10929–10936. doi:10.1021/ja072918x
43. Zhang Y, Rao P, Lü M, Zeng D, Wu J (2009) Synthesis and color evolution of silica-coated hematite nanoparticles. J Am Ceram Soc 92(8):1877–1880
44. Gou X, Wang G, Kong X, Wexler D, Horvat J, Yang J, Park J (2008) Flutelike porous hematite nanorods and branched nanostructures: synthesis, characterisation and application for gas-sensing. Chem Eur J 14(19):5996–6002
45. Wu Z, Yu K, Zhang S, Xie Y (2008) Hematite hollow spheres with a mesoporous shell: controlled synthesis and applications in gas sensor and lithium ion batteries. J Phys Chem C 112(30):11307–11313. doi:10.1021/jp803582d
46. Popovici M, Gich M, Niznansky D, Roig A, Savii C, Casas L, Molins E, Zaveta K, Enache C, Sort J, de Brion S, Chouteau G, Nogues J (2004) Optimized synthesis of the elusive epsilon-Fe_2O_3 phase via sol-gel chemistry. Chem Mater 16(25):5542–5548. doi:10.1021/cm048628m
47. Lian SY, Wang E, Kang ZH, Bai YP, Gao L, Jiang M, Hu CW, Xu L (2004) Synthesis of magnetite nanorods and porous hematite nanrods. Solid State Commun 129(8):485–490. doi:10.1016/j.ssc.2003.11.043
48. Wang J, Peng ZM, Huang YJ, Chen QW (2004) Growth of magnetite nanorods along its easy-magnetization axis of 110. J Cryst Growth 263(1–4):616–619. doi:10.1016/j.jcrysgro.2003.11.012
49. Wang J, Chen QW, Zeng C, Hou BY (2004) Magnetic-field-induced growth of single-crystalline Fe_3O_4 nanowires. Adv Mater 16(2):137–140. doi:10.1002/adma.200306136
50. Wan J, Yao Y, Tang G (2007) Controlled-synthesis, characterization, and magnetic properties of Fe_3O_4 nanostructures. Appl Phys A-Mater Sci Process 89(2):529–532. doi:10.1007/s00339-007-4107-5
51. Yang XY, Yu PF, Moats MS, Zhang XF (2011) Wet chemical synthesis of high aspect ratio magnetite rods. Powder Technol 212(3):439–444. doi:10.1016/j.powtec.2011.06.029
52. Nath S, Kaittanis C, Ramachandran V, Dalal NS, Perez JM (2009) Synthesis, magnetic characterization, and sensing applications of novel dextran-coated iron oxide nanorods. Chem Mater 21(8):1761–1767. doi:10.1021/cm8031863
53. Kaittanis C, Naser SA, Perez JM (2006) One-step, nanoparticle-mediated bacterial detection with magnetic relaxation. Nano Lett 7(2):380–383. doi:10.1021/nl062553z
54. Wang X, Chen XY, Gao LS, Zheng HG, Ji MR, Tang CM, Shen T, Zhang ZD (2004) Synthesis of beta-FeOOH and alpha-Fe_2O_3 nanorods and electrochemical properties of beta-FeOOH. J Mater Chem 14(5):905–907. doi:10.1039/b310722a
55. Jia BP, Gao L, Sun J (2007) Synthesis of single crystalline hematite polyhedral nanorods via a facile hydrothermal process. J Am Ceram Soc 90(4):1315–1318. doi:10.1111/j.1551-2916.2007.01523.x
56. Woo K, Lee HJ, Ahn JP, Park YS (2003) Sol-gel mediated synthesis of Fe_2O_3 nanorods. Adv Mater 15(20):1761–1764. doi:10.1002/adma.200305561
57. Cavaliere-Jaricot S, Brioude A, Miele P (2009) Ultrathin polycrystalline hematite and goethite-hematite core-shell nanorods. Langmuir 25(5):2551–2553. doi:10.1021/la803172b
58. Liu XM, Fu SY, Xiao HM, Huang CJ (2005) Preparation and, characterization of shuttle-like alpha-Fe_2O_3 nanoparticles by supermolecular template. J Solid State Chem 178(9):2798–2803. doi:10.1016/j.jssc.2005.06.018

59. Jia CJ, Sun LD, Yan ZG, You LP, Luo F, Han XD, Pang YC, Zhang Z, Yan CH (2005) Iron oxide nanotubes–single-crystalline iron oxide nanotubes. Angew ChemInt Edit 44(28):4328–4333. doi:10.1002/anie.200463038
60. Zhao Yi M, Li Y-H, Ma Ren Z, Roe Martin J, McCartney David G, Zhu Yan Q (2006) Growth and characterization of iron oxide nanorods/nanobelts prepared by a simple iron-water reaction. Small 2(3):422–427
61. Li SZ, Zhang H, Wu JB, Ma XY, Yang DR (2006) Shape-control fabrication and characterization of the airplane-like FeO(OH) and Fe_2O_3 nanostructures. Cryst Growth Des 6(2):351–353. doi:10.1021/cg0495835
62. Zysler RD, Fiorani D, Testa AM, Suber L, Agostinelli E, Godinho M (2003) Size dependence of the spin-flop transition in hematite nanoparticles. Phys Rev B 68 (21):Art no 212408
63. Fiorani D, Testa AM, Suber L, Angiolini M, Montone A, Polichetti M (1999) Size and shape effect on the canted antiferromagnetism in alpha-Fe_2O_3 particles. Nanostruct Mater 12(5–8):939–942
64. Liu L, Kou HZ, Mo WL, Liu HJ, Wang YQ (2006) Surfactant-assisted synthesis of alpha-Fe_2O_3 nanotubes and nanorods with shape-dependent magnetic properties. J Phys Chem B 110(31):15218–15223. doi:10.1021/jp0627473
65. Woo K, Lee HJ (2004) Synthesis and magnetism of hematite and maghemite nanoparticles. J Magn Magn Mater 272:E1155–E1156. doi:10.1016/j.jmmm.2003.12.201
66. Wu CZ, Yin P, Zhu X, OuYang CZ, Xie Y (2006) Synthesis of hematite (alpha-Fe_2O_3) nanorods: Diameter-size and shape effects on their applications in magnetism, lithium ion battery, and gas sensors. J Phys Chem B 110(36):17806–17812. doi:10.1021/jp0633906
67. Cha HG, Kim SJ, Lee KJ, Jung MH, Kang YS (2011) Single-crystalline porous hematite nanorods: photocatalytic and magnetic properties. J Phys Chem C 115(39):19129–19135. doi:10.1021/Jp206958g
68. Zhao YM, Dunnill CW, Zhu YQ, Gregory DH, Kockenberger W, Li YH, Hu WB, Ahmad I, McCartney DG (2007) Low-temperature magnetic properties of hematite nanorods. Chem Mater 19(4):916–921. doi:10.1021/cm062375a
69. Cornell RM (2003) The iron oxides: strucutre, properties, reactions, occurrences and uses. Wiley-VCH Verlag GmbH & Co, KgaA, Weinheim, Germany
70. Zeng SY, Tang KB, Li TW (2007) Controlled synthesis of alpha-Fe_2O_3 nanorods and its size-dependent optical absorption, electrochemical, and magnetic properties. J Colloid Interf Sci 312(2):513–521. doi:10.1016/j.jcis.2007.03.046
71. Cao H, Wang G, Zhang L, Liang Y, Zhang S, Zhang X (2006) Shape and magnetic properties of single-crystalline hematite (alpha-Fe_2O_3) nanocrystals. ChemPhysChem 7(9):1897–1901
72. Zhang XJ, Li QL (2008) Microwave assisted hydrothermal synthesis and magnetic property of hematite nanorods. Mater Lett 62(6–7):988–990. doi:10.1016/j.matlet.2007.07.029
73. Sorescu M, Brand RA, Mihaila-Tarabasanu D, Diamandescu L (1999) The crucial role of particle morphology in the magnetic properties of haematite. J Appl Phys 85(8):5546–5548
74. Eid C, Luneau D, Salles V, Asmar R, Monteil Y, Khoury A, Brioude A (2011) Magnetic properties of hematite nanotubes elaborated by electrospinning process. J Phys Chem C 115(36):17643–17646. doi:10.1021/jp203426j
75. Yue ZG, Wei W, You ZX, Yang QZ, Yue H, Su ZG, Ma GH (2011) Iron oxide nanotubes for magnetically guided delivery and pH-activated release of insoluble anticancer drugs. Adv Funct Mater 21(18):3446–3453. doi:10.1002/adfm.201100510
76. Park JH, von Maltzahn G, Zhang LL, Schwartz MP, Ruoslahti E, Bhatia SN, Sailor MJ (2008) Magnetic iron oxide nanoworms for tumor targeting and imaging. Adv Mater 20(9):1630– +. doi:10.1002/adma.200800004
77. Gonsalves KE, Li H, Santiago P (2001) Synthesis of acicular iron oxide nanoparticles and their dispersion in a polymer matrix. J Mater Sci 36(10):2461–2471

78. Palchoudhury S, An W, Xu YL, Qin Y, Zhang ZT, Chopra N, Holler RA, Turner CH, Bao YP (2012) Synthesis and growth mechanism of iron oxide nanowhiskers. Nano Lett 11(3):1141–1146. doi:10.1021/nl200136j
79. Hyeon T, Lee SS, Park J, Chung Y, Bin Na H (2001) Synthesis of highly crystalline and monodisperse maghemite nanocrystallites without a size-selection process. J Am Chem Soc 123(51):12798–12801. doi:10.1021/ja016812s
80. Milosevic I, Jouni H, David C, Warmont F, Bonnin D, Motte L Facile Microwave process in water for the fabrication of magnetic nanorods. J Phys Chem C 115(39):18999–19004. doi:10.1021/jp205334v
81. Jin B, Ohkoshi S, Hashimoto K (2004) Giant coercive field of nanometer-sized iron oxide. Adv Mater 16(1):48–51. doi:10.1002/adma.200305297
82. Jin J, Hashimoto K, Ohkoshi S (2005) Formation of spherical and rod-shaped epsilon-Fe_2O_3 nanocrystals with a large coercive field. J Mater Chem 15(10):1067–1071. doi:10.1039/b416554c
83. Ohkoshi S, Sakurai S, Jin J, Hashimoto K (2005) The addition effects of alkaline earth ions in the chemical synthesis of epsilon-Fe_2O_3 nanocrystals that exhibit a huge coercive field. J Appl Phys 97 (10):Art no 10K312. doi:10.1063/1.1855615
84. Batlle X, Labarta A (2002) Finite-size effects in fine particles: magnetic and transport properties. J Phys D-Appl Phys 35(6):R15–R42
85. Bate G (1961) Angular variation of the magnetic properties of partially aligned g-Fe_2O_3 particles. J Appl Phys 32(3):239S–240S
86. Vayssieres L, Beermann N, Lindquist S-E, Hagfeldt A (2001) Controlled aqueous chemical growth of oriented three-dimensional crystalline nanorod arrays: application to iron(III) oxides. Chem Mater 13(2):233–235. doi:10.1021/cm001202x
87. Vayssieres L, Rabenberg L, Manthiram A (2002) Aqueous chemical route to ferromagnetic 3-d Arrays of iron nanorods. Nano Lett 2(12):1393–1395. doi:10.1021/nl025840l
88. Wen X, Wang S, Ding Y, Wang ZL, Yang S (2005) Controlled growth of large-area, uniform, vertically aligned arrays of α-Fe_2O_3 nanobelts and nanowires. J Phys Chem B 109(1):215–220. doi:10.1021/jp0461448
89. Morber JR, Ding Y, Haluska MS, Li Y, Liu JP, Wang ZL, Snyder RL (2006) PLD-assisted VLS growth of aligned ferrite nanorods, nanowires, and nanobelts synthesis, and properties. J Phys Chem B 110(43):21672–21679. doi:10.1021/jp064484i
90. Wu J–J, Lee Y-L, Chiang H–H, Wong DK-P (2006) Growth and magnetic properties of oriented α-Fe_2O_3 nanorods. J Phys Chem B 110(37):18108–18111. doi:10.1021/jp0644661
91. Chueh Y-L, Lai M-W, Liang J-Q, Chou L-J, Wang ZL (2006) Systematic study of the growth of aligned arrays of a-Fe_2O_3 and Fe_3O_4 nanowires by a vapor–solid process. Adv Funct Mater 16(17):2243–2251
92. Kim CH, Chun HJ, Kim DS, Kim SY, Park J, Moon JY, Lee G, Yoon J, Jo Y, Jung M-H, Jung SI, Lee CJ (2006) Magnetic anisotropy of vertically aligned alpha-Fe[sub 2]O[sub 3] nanowire array. Appl Phys Lett 89(22):223103
93. Ji G, Tang S, Xu B, Gu B, Du Y (2003) Synthesis of $CoFe_2O_4$ nanowire arrays by sol-gel template method. Chem Phys Lett 379(5–6):484–489
94. Zheng H, Wang J, Lofland SE, Ma Z, Mohaddes-Ardabili L, Zhao T, Salamanca-Riba L, Shinde SR, Ogale SB, Bai F, Viehland D, Jia Y, Schlom DG, Wuttig M, Roytburd A, Ramesh R (2004) Multiferroic $BaTiO_3$-$CoFe_2O_4$ nanostructures. Science 303(5658):661–663. doi:10.1126/science.1094207
95. Zhu LP, Xiao HM, Liu XM, Fu SY (2006) Template-free synthesis and characterization of novel 3D urchin-like alpha-Fe_2O_3 superstructures. J Mater Chem 16(19):1794–1797. doi:10.1039/b604378j
96. An Z, Zhang J, Pan S, Yu F (2009) Facile template-free synthesis and characterization of elliptic α-Fe_2O_3 superstructures. J Phys Chem C 113(19):8092–8096. doi:10.1021/jp9004168
97. Shiraki M, Wakui Y, Tokusima T, Tsuya N (1985) IEEE Trans Magn 1465

98. Kida A, Kajiyama H, Heike S, Hashizume T, Koike K (1999) Self-organized growth of Fe nanowire array on H2O/Si(100)(2 x n). Appl Phys Lett 75(4):540–542
99. Grobert N, Hsu WK, Zhu YQ, Hare JP, Kroto HW, Walton DRM, Terrones M, Terrones H, Redlich P, Ruhle M, Escudero R, Morales F (1999) Enhanced magnetic coercivities in Fe nanowires. Appl Phys Lett 75(21):3363–3365
100. Elmers HJ, Hauschild J, Gradmann U (1998) Magnetism of nanowires of Fe(110) on W(110). J Magn Magn Mater 177:827–828
101. Cordente N, Respaud M, Senocq F, Casanove MJ, Amiens C, Chaudret B (2001) Synthesis and magnetic properties of nickel nanorods. Nano Lett 1(10):565–568. doi:10.1021/nl0100522
102. Nogues J, Sort J, Langlais V, Skumryev V, Surinach S, Munoz JS, Baro MD (2005) Exchange bias in nanostructures. Phys Rep Rev Sect Phys Lett 422(3):65–117
103. Baker C, Hasanain SK, Shah SI (2004) The magnetic behavior of iron oxide passivated iron nanoparticles. J Appl Phys 96(11):6657–6662
104. Whitney TM, Jiang JS, Searson PC, Chien CL (1993) Fabrication and magnetic-properties of arrays of metallic nanowires. Science 261(5126):1316–1319
105. Henry Y, Ounadjela K, Piraux L, Dubois S, George JM, Duvail JL (2001) Magnetic anisotropy and domain patterns in electrodeposited cobalt nanowires. Eur Phys J B 20(1):35–54
106. Qin J, Nogues J, Mikhaylova M, Roig A, Munoz JS, Muhammed M (2005) Differences in the magnetic properties of Co, Fe, and Ni 250–300 nm wide nanowires electrodeposited in amorphous anodized alumina templates. Chem Mater 17(7):1829–1834. doi:10.1021/cm047870q
107. Khan HR, Loebich O, Rauscher G (1996) Crystallographic and magnetic investigations of the cobalt columns electrodeposited in the pores of anodic alumina. Thin Solid Films 275(1–2):207–209
108. Aslam M, Bhobe R, Alem N, Donthu S, Dravid VP (2005) Controlled large-scale synthesis and magnetic properties of single-crystal cobalt nanorods. J Appl Phys 98 (7):Art no 074311. doi:10.1063/1.2073968
109. Kitakami O, Sato H, Shimada Y, Sato F, Tanaka M (1997) Size effect on the crystal phase of cobalt fine particles. Phys Rev B 56(21):13849–13854
110. Thurn-Albrecht T, Schotter J, Kastle CA, Emley N, Shibauchi T, Krusin-Elbaum L, Guarini K, Black CT, Tuominen MT, Russell TP (2000) Ultrahigh-density nanowire arrays grown in self-assembled diblock copolymer templates. Science 290(5499):2126–2129
111. Dumestre F, Chaudret B, Amiens C, Respaud M, Fejes P, Renaud P, Zurcher P (2003) Unprecedented crystalline super-lattices of monodisperse cobalt nanorods. Angew ChemInt Edit 42(42):5213–5216. doi:10.1002/anie.200352090
112. Luttinger JM, Tisza LPR (1946) Phys Rev 70:954
113. Politi P, Pini MG (2002) Dipolar interaction between two-dimensional magnetic particles. Phys Rev B 66 (21):Art No 214414. doi:10.1103/PhysRevB.66.214414
114. Viau G, Garcia C, Maurer T, Chaboussant G, Ott F, Soumare Y, Piquemal JY (2009) Highly crystalline cobalt nanowires with high coercivity prepared by soft chemistry. Phys Status Solidi A- Appl Mat 206(4):663–666. doi:10.1002/pssa.200881260
115. Maurer T, Ott F, Chaboussant G, Soumare Y, Piquemal JY, Viau G (2007) Magnetic nanowires as permanent magnet materials. Appl Phys Lett 91 (17):Art no 172501. doi:10.1063/1.2800786
116. Ott F, Maurer T, Chaboussant G, Soumare Y, Piquemal JY, Viau G (2009) Effects of the shape of elongated magnetic particles on the coercive field. J Appl Phys 105(1):013915–013917
117. Sugawara A, Coyle T, Hembree GG, Scheinfein MR (1997) Self-organized Fe nanowire arrays prepared by shadow deposition on NaCl(110) templates. Appl Phys Lett 70(8):1043–1045
118. Yang SG, Zhu H, Yu DL, Jin ZQ, Tang SL, Du YW (2000) Preparation and magnetic property of Fe nanowire array. J Magn Magn Mater 222(1–2):97–100

119. Cao HQ, Xu Z, Sheng D, Hong JM, Sang H, Du YW (2001) An array of iron nanowires encapsulated in polyaniline nanotubules and its magnetic behavior. J Mater Chem 11(3):958–960
120. Borowiak-Palen E, Mendoza E, Bachmatiuk A, Rummeli MH, Gemming T, Nogues J, Skumryev V, Kalenczuk RJ, Pichler T, Silva SRP (2006) Iron filled single-wall carbon nanotubes–a novel ferromagnetic medium. Chem Phys Lett 421(1–3):129–133. doi:10.1016/j.cplett.2006.01.072
121. Oppegard AL, Darnell FJ, Miller HC (1961) Magnetic properties of single-domain iron and iron-cobalt particles prepared by borohydride reduction. J Appl Phys 32(3):184S–185S
122. Park SJ, Kim S, Lee S, Khim ZG, Char K, Hyeon T (2000) Synthesis and magnetic studies of uniform iron nanorods and nanospheres. J Am Chem Soc 122(35):8581–8582. doi:10.1021/ja001628c
123. Kim J, Lee JE, Lee J, Yu JH, Kim BC, An K, Hwang Y, Shin CH, Park JG, Hyeon T (2006) Magnetic fluorescent delivery vehicle using uniform mesoporous silica spheres embedded with monodisperse magnetic and semiconductor nanocrystals. J Am Chem Soc 128(3):688–689
124. Ichia LSH, Katz E, Wasserman J, Willner I (2002) Magneto-switchable electro generated biochemiluminescence. Chem Commun 2:158–159
125. Lv BL, Xu Y, Wu D, Sun YH (2009) Preparation and magnetic properties of spindle porous iron nanoparticles. Mater Res Bull 44(5):961–965. doi:10.1016/j.materresbull.2008.11.022
126. Dormann JL, Dorazio F, Lucari F, Tronc E, Prene P, Jolivet JP, Fiorani D, Cherkaoui R, Nogues M (1996) Thermal variation of the relaxation time of the magnetic moment of gamma-Fe_2O_3 nanoparticles with interparticle interactions of various strengths. Phys Rev B 53(21):14291–14297
127. Ni XM, Su XB, Yang ZP, Zheng HG (2003) The preparation of nickel nanorods in water-in-oil microemulsion. J Cryst Growth 252(4):612–617. doi:10.1016/s0022-0248(03)00954-0
128. Oh SL, Kim YR, Malkinski L, Vovk A, Whittenburg SL, Kim EM, Jung JS (2007) Magnetic properties of nickel nanostructures grown in AAO membrane. J Magn Magn Mater 310(2):E827–E829. doi:10.1016/j.mmm.2006.10.821
129. Kumar A, Fahler S, Schlorb H, Leistner K, Schultz L (2006) Competition between shape anisotropy and magnetoelastic anisotropy in Ni nanowires electrodeposited within alumina templates. Phys Rev B 73 (6):Art no 064421. doi:10.1103/PhysRevB.73.064421
130. Kato S, Kitazawa H, Kido G (2004) Magnetic properties of Ni nanowires in porous alumina arrays. J Magn Magn Mater 272:1666–1667. doi:10.1016/j.jmmm.2003.12.246
131. Bender P, Gunther A, Tschope A, Birringer R (2011) Synthesis and characterization of uniaxial ferrogels with Ni nanorods as magnetic phase. J Magn Magn Mater 323(15):2055–2063. doi:10.1016/j.jmmm.2011.03.016
132. Celedon A, Hale CM, Wirtz D (2011) Magnetic manipulation of nanorods in the nucleus of living cells. Biophys J 101(8):1880–1886. doi:10.1016/j.bpj.2011.09.008
133. Ono K, Kakefuda Y, Okuda R, Ishii Y, Kamimura S, Kitamura A, Oshima M (2002) Organometallic synthesis and magnetic properties of ferromagnetic Sm-Co nanoclusters. J Appl Phys 91(10):8480–8482. doi:10.1063/1.1456407
134. Gu HW, Xu B, Rao JC, Zheng RK, Zhang XX, Fung KK, Wong CYC (2003) Chemical synthesis of narrowly dispersed $SmCo_5$ nanoparticles. J Appl Phys 93(10):7589–7591. doi:10.1063/1.1537697
135. Chakka VM, Altuncevahir B, Jin ZQ, Li Y, Liu JP (2006) Magnetic nanoparticles produced by surfactant-assisted ball milling. J Appl Phys 99(8):Art no 08e912. doi:10.1063/1.2170593
136. Yue M, Wang YP, Poudyal N, Rong CB, Liu JP (2009) Preparation of Nd-Fe-B nanoparticles by surfactant-assisted ball milling technique. J Appl Phys 105(7):Art no 07a708. doi:10.1063/1.3059228
137. Akdogan NG, Hadjipanayis GC, Sellmyer DJ (2010) Novel Nd(2)Fe(14)B nanoflakes and nanoparticles for the development of high energy nanocomposite magnets. Nanotechnology 21(29):Art no 295705

138. Stoyanov S, Skumryev V, Zhang Y, Huang Y, Hadjipanayis G, Nogues J (2003) High anisotropy Sm-Co nanoparticles: preparation by cluster gun technique and their magnetic properties. J Appl Phys 93(10):7592–7594. doi:10.1063/1.1544503
139. Matsushita T, Iwamoto T, Inokuchi M, Toshima N (2010) Novel ferromagnetic materials of $SmCo_5$ nanoparticles in single-nanometer size: chemical syntheses and characterizations. Nanotechnology 21(9):Art no 095603. doi:10.1088/0957-4484/21/9/095603
140. Chinnasamy CN, Huang JY, Lewis LH, Latha B, Vittoria C, Harris VG (2008) Direct chemical synthesis of high coercivity air-stable SmCo nanoblades. Appl Phys Lett 93(3):Art no 032505. doi:10.1063/1.2963034
141. Gao DQ, Fu JL, Xu Y, Xue DS (2008) Preparation and magnetic properties of Nd_5Fe_{95}-xBx nanowire arrays. Mater Lett 62(17–18):3070–3072. doi:10.1016/j.matlet.2008.01.107
142. Zhang ZT, Blom DA, Gai Z, Thompson JR, Shen J, Dai S (2003) High-yield solvothermal formation of magnetic CoPt alloy nanowires. J Am Chem Soc 125(25):7528–7529. doi:10.1021/ja035185z
143. Chu SZ, Inoue S, Wada K, Kurashima K (2004) Fabrication and structural characteristics of nanocrystalline Fe-Pt thin films and Fe-Pt nanowire arrays embedded in alumina films on ITO/glass. J Phys Chem B 108(18):5582–5587. doi:10.1021/jp0378642
144. Mao CB, Solis DJ, Reiss BD, Kottmann ST, Sweeney RY, Hayhurst A, Georgiou G, Iverson B, Belcher AM (2004) Virus-based toolkit for the directed synthesis of magnetic and semiconducting nanowires. Science 303(5655):213–217
145. Wang Y, Yang H (2005) Synthesis of CoPt nanorods in ionic liquids. J Am Chem Soc 127(15):5316–5317. doi:10.1021/ja043625w
146. Huang YH, Okumura H, Hadjipanayis GC, Weller D (2002) CoPt and FePt nanowires by electrodeposition. J Appl Phys 91(10):6869–6871. doi:10.1063/1.1447524
147. Sui Y, Yue L, Skomski R, Li XZ, Zhou J, Sellmyer DJ (2003) CoPt hard magnetic nanoparticle films synthesized by high temperature chemical reduction. J Appl Phys 93(10):7571–7573. doi:10.1063/1.1544501
148. Hou YL, Kondoh H, Che RC, Takeguchi M, Ohta T (2006) Ferromagnetic FePt nanowires: solvothermal reduction synthesis and characterization. Small 2(2):235–238. doi:10.1002/smll.200500328
149. Chen M, Pica T, Jiang YB, Li P, Yano K, Liu JP, Datye AK, Fan HY (2007) Synthesis and self-assembly of fcc phase FePt nanorods. J Am Chem Soc 129(20):6348–6349. doi:10.1021/ja069057x
150. Khurshid H, Huang YH, Bonder MJ, Hadjipanayis C (2009) Microstructural and magnetic properties of CoPt nanowires. J Magn Magn Mater 321(4):277–280. doi:10.1016/j.jmmm.2008.09.002
151. Yasui N, Imada A, Den T (2003) Electrodeposition of (001) oriented CoPt L1(0) columns into anodic alumina films. Appl Phys Lett 83(16):3347–3349. doi:10.1063/1.1622787
152. Mallet J, Yu-Zhang K, Chien CL, Eagleton TS, Searson PC (2004) Fabrication and magnetic properties of fcc CoxPt1-x nanowires. Appl Phys Lett 84(19):3900–3902. doi:10.1063/1.1739274
153. Mallet J, Yu-Zhang K, Matefi-Tempfli S, Matefi-Tempfli M, Piraux L (2005) Electrodeposited L1(0) CoxPt1-x nanowires. J Phys D-Appl Phys 38(6):909–914. doi:10.1088/0022-3727/38/6/020
154. Rhen FMF, Backen E, Coey JMD (2005) Thick-film permanent magnets by membrane electrodeposition. J Appl Phys 97(11):113908. doi:113908.10.1063/1.1923587
155. Gapin AI, Ye XR, Aubuchon JF, Chen LH, Tang YJ, Jin S (2006) CoPt patterned media in anodized aluminum oxide templates. J Appl Phys 99(8):08g902. doi:10.1063/1.2163289
156. Dahmane Y, Cagnon L, Voiron J, Pairis S, Bacia M, Ortega L, Benbrahim N, Kadri A (2006) Magnetic and structural properties of electrodeposited CoPt and FePt nanowires in nanoporous alumina templates. J Phys D-Appl Phys 39(21):4523–4528. doi:10.1088/0022-3727/39/21/001

157. Gao JH, Sun DL, Zhang XQ, Zhan QF, He W, Sun Y, Cheng ZH (2008) Structure and magnetic properties of the self-assembled Co52Pt48 nanowire arrays. Appl Phys Lett 92(10):Art no 102501. doi:10.1063/1.2894199
158. Shamaila S, Sharif R, Riaz S, Ma M, Khaleeq-ur-Rahman M, Han XF (2008) Magnetic and magnetization properties of electrodeposited fcc CoPt nanowire arrays. J Magn Magn Mater 320(12):1803–1809. doi:10.1016/j.jmmm.2008.02.183
159. Che RC, Takeguchi M, Shimojo M, Zhang W, Furuya K (2005) Fabrication and electron holography characterization of FePt alloy nanorods. Appl Phys Lett 87(22):Art no 223109. doi:10.1063/1.2136071
160. Li WX, Zhang J, Thompson J, Shen TH (2007) Magnetic circular dichroism in Co1-xPtx nanowire bundles at the Co L-2,L-3 edges. Appl Phys Lett 91(13):Art no 133111. doi:10.1063/1.2784186
161. Aharoni A, Shtrikman S (1958) Magnetization curve of the infinite cylinder. Phys Rev 109(5):1522
162. Aharoni A (1997) Angular dependence of nucleation by curling in a prolate spheroid. J Appl Phys 82(3):1281–1287
163. Usov NA, Chang CR, Wei ZH (2002) Buckling instability in thin soft elliptical particles. Phys Rev B 66(18):Art no 184431. doi:10.1103/PhysRevB.66.184431
164. Beeli C, Doudin B, Ansermet JP, Stadelmann P (1996) Study of Co, Ni and Co/Cu nanowires: magnetic flux imaging by off-axis electron holography. J Magn Magn Mater 164(1–2):77–90
165. Wernsdorfer W, Doudin B, Mailly D, Hasselbach K, Benoit A, Meier J, Ansermet JP, Barbara B (1996) Nucleation of magnetization reversal in individual nanosized nickel wires. Phys Rev Lett 77(9):1873–1876
166. Obarr R, Schultz S (1997) Switching field studies of individual single domain Ni columns. J Appl Phys 81(8):5458–5460
167. Belliard L, Miltat J, Thiaville A, Dubois S, Duvail JL, Piraux L (1998) Observing magnetic nanowires by means of magnetic force microscopy. J Magn Magn Mater 190(1–2):1–16
168. Schabes ME (1991) Micromagnetic theory of nonuniform magnetization processes in magnetic recording particles. J Magn Magn Mater 95(3):249–288
169. Broz JS, Braun HB, Brodbeck O, Baltensperger W, Helman JS (1990) Nucleation of magnetization reversal via creation of pairs of bloch walls. Phys Rev Lett 65(6):787–789
170. Wernsdorfer W, Orozco EB, Hasselbach K, Benoit A, Barbara B, Demoncy N, Loiseau A, Pascard H, Mailly D (1997) Experimental evidence of the Neel-Brown model of magnetization reversal. Phys Rev Lett 78(9):1791–1794
171. Wernsdorfer W, Hasselbach K, Benoit A, Barbara B, Doudin B, Meier J, Ansermet JP, Mailly D (1997) Measurements of magnetization switching in individual nickel nanowires. Phys Rev B 55(17):11552–11559
172. McGuire T, Potter R (1975) Anisotropic magnetoresistance in ferromagnetic 3D alloys. IEEE Trans Magn 11(4):1018–1038
173. Rijks T, Coehoorn R, Dejong MJM, Dejonge WJM (1995) Semiclassical calculations of the anisotropic magnetoresistance of nife-based thin-films, wires and multilayers. Phys Rev B 51(1):283–291
174. Wegrowe JE, Gilbert SE, Kelly D, Doudin B, Ansermet JP (1998) Anisotropic magnetoresistance as a probe of magnetization reversal in individual nano-sized nickel wires. IEEE Trans Magn 34(4):903–905
175. Wegrowe JE, Kelly D, Franck A, Gilbert SE, Ansermet JP (1999) Magnetoresistance of ferromagnetic nanowires. Phys Rev Lett 82(18):3681–3684
176. Jaccard Y, Guittienne P, Kelly D, Wegrowe JE, Ansermet JP (2000) Uniform magnetization rotation in single ferromagnetic nanowires. Phys Rev B 62(2):1141–1147
177. Oliveira AB, Rezende SM, Azevedo A (2008) Magnetization reversal in permalloy ferromagnetic nanowires investigated with magnetoresistance measurements. Phys Rev B 78(2):Art no 024423. doi:10.1103/PhysRevB.78.024423

178. Hubert A, Schafer R (1998) Magnetic domains: the analysis of magnetic microstructures. Springer, Berlin
179. Allwood DA, Xiong G, Cooke MD, Faulkner CC, Atkinson D, Vernier N, Cowburn RP (2002) Submicrometer ferromagnetic NOT gate and shift register. Science 296(5575):2003–2006
180. Grollier J, Boulenc P, Cros V, Hamzic A, Vaures A, Fert A, Faini G (2003) Switching a spin valve back and forth by current-induced domain wall motion. Appl Phys Lett 83(3):509–511. doi:10.1063/1.1594841
181. Schryer NL, Walker LR (1974) The motion of 180[degree] domain walls in uniform dc magnetic fields. J Appl Phys 45(12):5406–5421
182. McMichael RD, Twisselmann DJ, Kunz A (2003) Localized ferromagnetic resonance in inhomogeneous thin films. Phys Rev Lett 90 (22):art. n. 227601. doi:227601 10.1103/PhysRevLett.90.227601
183. Zimmermann L, Miltat J (1991) Instability of bubble radial motion associated with chirality changes. J Magn Magn Mater 94(1–2):207–214
184. Honda S, Fukuda N, Kusuda T (1981) Mechanisms of bubble-wall radial motion deduced from chirality switching and collapse experiments using fast-rise bias field pulse. J Appl Phys 52(9):5756–5762
185. Beach GSD, Nistor C, Knutson C, Tsoi M, Erskine JL (2005) Dynamics of field-driven domain-wall propagation in ferromagnetic nanowires. Nat Mater 4(10):741–744. doi:10.1038/nmat1477
186. Hayashi M, Thomas L, Bazaliy YB, Rettner C, Moriya R, Jiang X, Parkin SSP (2006) Influence of current on field-driven domain wall motion in permalloy nanowires from time resolved measurements of anisotropic magnetoresistance. Phys Rev Lett 96 (19):Art no 197207. doi:10.1103/PhysRevLett.96.197207
187. Ono T, Miyajima H, Shigeto K, Mibu K, Hosoito N, Shinjo T (1999) Propagation of a magnetic domain wall in a submicrometer magnetic wire. Science 284(5413):468–470
188. Telesnin R, Ilyicheva E, Kanavina N, Stepanova N, Shishkov A (1969) Domain-wall motion in thin permalloy films in pulsed magnetic field. IEEE Trans Magn 5(3):232–236
189. Atkinson D, Allwood DA, Xiong G, Cooke MD, Faulkner CC, Cowburn RP (2003) Magnetic domain-wall dynamics in a submicrometre ferromagnetic structure. Nat Mater 2(2):85–87
190. Konishi S, Yamada S, Kusuda T (1971) Domain-wall velocity, mobility, and mean-free-path in permalloy films. IEEE Trans Magn 7(3):722–724
191. Redjdal M, Giusti J, Ruane MF, Humphrey FB (2002) Thickness dependent wall mobility in thin permalloy films. J Appl Phys 91(10):7547–7549. doi:10.1063/1.1456403
192. Nakatani Y, Thiaville A, Miltat J (2003) Faster magnetic walls in rough wires. Nat Mater 2(8):521–523. doi:10.1038/nmat931
193. Lee JY, Lee KS, Choi S, Guslienko KY, Kim SK (2007) Dynamic transformations of the internal structure of a moving domain wall in magnetic nanostripes. Phys Rev B 76 (18):Art no 184408. doi:10.1103/PhysRevB.76.184408
194. Hayashi M, Thomas L, Rettner C, Moriya R, Parkin SSP (2007) Direct observation of the coherent precession of magnetic domain walls propagating along permalloy nanowires. Nat Phys 3(1):21–25. doi:10.1038/nphys464
195. Glathe S, Mattheis R, Berkov DV (2008) Direct observation and control of the Walker breakdown process during a field driven domain wall motion. Appl Phys Lett 93 (7):Art no 072508. doi:10.1063/1.2975181
196. Kunz A (2006) Simulating the maximum domain wall speed in a magnetic nanowire. IEEE Trans Magn 42(10):3219–3221. doi:10.1109/tmag.2006.880141
197. Bryan MT, Schrefl T, Allwood DA (2010) Dependence of transverse domain wall dynamics on permalloy nanowire dimensions. IEEE Trans Magn 46(5):1135–1138. doi:10.1109/tmag.2010.2040622
198. Porter DG, Donahue MJ (2004) Velocity of transverse domain wall motion along thin, narrow strips. J Appl Phys 95(11):6729–6731. doi:10.1063/1.1688673

199. Allende S, Arias R Transverse domain wall propagation in modulated cylindrical nanostructures and possible geometric control. Phys Rev B 83(17):11. doi:10.1103/PhysRevB.83.174452
200. Pitzschel K, Bachmann J, Martens S, Montero-Moreno JM, Kimling J, Meier G, Escrig J, Nielsch K, Gorlitz D (2012) Magnetic reversal of cylindrical nickel nanowires with modulated diameters. J Appl Phys 109(3):6. doi:10.1063/1.3544036
201. Berger L (1984) Exchange interaction between ferromagnetic domain wall and electric current in very thin metallic films. J Appl Phys 55(6):1954–1956
202. Berger L (1992) Motion of a magnetic domain-wall traversed by fast-rising current pulses. J Appl Phys 71(6):2721–2726
203. Wolf SA, Treger D, Chtchelkanova A (2006) Spintronics: the future of data storage. MRS Bull 31(5):400–403
204. Tatara G, Kohno H (2004) Theory of current-driven domain wall motion: Spin transfer versus momentum transfer. Phys Rev Lett 92(8):Art no 086601. doi: 10.1103/PhysRevLett.92.086601
205. Zhang S, Li Z (2004) Roles of nonequilibrium conduction electrons on the magnetization dynamics of ferromagnets. Phys Rev Lett 93(12):Art no 127204
206. Thiaville A, Nakatani Y, Miltat J, Suzuki Y (2005) Micromagnetic understanding of current-driven domain wall motion in patterned nanowires. Europhys Lett 69(6):990–996. doi:10.1209/epl/i2004-10452-6
207. Barnes SE, Maekawa S (2005) Current-spin coupling for ferromagnetic domain walls in fine wires. Phys Rev Lett 95 (10):Art no 107204
208. Berger L (2006) Analysis of measured transport properties of domain walls in magnetic nanowires and films. Phys Rev B 73(1):Art no 014407. doi:10.1103/PhysRevB.73.014407
209. Yamaguchi A, Ono T, Nasu S, Miyake K, Mibu K, Shinjo T (2004) Real-space observation of current-driven domain wall motion in submicron magnetic wires. Phys Rev Lett 92(7):Art no 077205
210. Vernier N, Allwood DA, Atkinson D, Cooke MD, Cowbu RP (2004) Domain wall propagation in magnetic nanowires by spin-polarized current injection. Europhys Lett 65(4):526–532
211. Klaui M, Jubert PO, Allenspach R, Bischof A, Bland JAC, Faini G, Rudiger U, Vaz CAF, Vila L, Vouille C (2005) Direct observation of domain-wall configurations transformed by spin currents. Phys Rev Lett 95(2):Art no 026601. doi:10.1103/PhysRevLett.95.026601
212. Beach GSD, Knutson C, Nistor C, Tsoi M, Erskine JL (2006) Nonlinear domain-wall velocity enhancement by spin-polarized electric current. Phys Rev Lett 97 (5):Art no 057203. doi:10.1103/PhysRevLett.97.057203
213. Meier G, Bolte M, Eiselt R, Kruger B, Kim DH, Fischer P (2007) Direct imaging of stochastic domain-wall motion driven by nanosecond current pulses. Phys Rev Lett 98 (18):Art no 187202. doi:10.1103/PhysRevLett.98.187202
214. Hankemeier S, Sachse K, Stark Y, Fromter R, Oepen HP (2008) Ultrahigh current densities in permalloy nanowires on diamond. Appl Phys Lett 92(24):Art no 242503. doi:10.1063/1.2937842
215. Thomson T, Abelman L, Groenland H (2008) Magnetic storage: past, present and future. In: Azzerboni B, Asti G, Pareti L, Ghidini M (eds) Magnetic nanostructures in modern technology. Springer, Dordrecht, pp 237–306
216. Sharrock MP (1989) Particulate magnetic recording media—a review. IEEE Trans Magn 25(6):4374–4389. doi:10.1109/20.45317
217. Cullity BD (1972) Introduction to magnetic materials. Addison-Wesley Publ
218. Parkin SSP, Hayashi M, Thomas L (2008) Magnetic domain-wall racetrack memory. Science 320(5873):190–194. doi:10.1126/science.1145799
219. Freitas PP, Ferreira H, Cardoso S, van Dijken S, Gregg J (2006) Nanostructures for spin electronics. In: Sellmyer D, Skomski R (eds) Advanced magnetic nanostructures. Springer, New York, pp 403–460

220. Nikiforov VN, Filinova EY (2009) Biomedical applications of magnetic nanoparticles. In: Gubin SP (ed) Magnetic nanoparticles .Wiley-VCH Verlag GmbH & Co KGaA, Weinheim, pp 393–455
221. Qiao RR, Yang CH, Gao MY (2009) Superparamagnetic iron oxide nanoparticles: from preparations to in vivo MRI applications. J Mater Chem 19(35):6274–6293. doi:10.1039/b902394a

Chapter 6
Catalytic Properties of Nanorods

6.1 Introduction

In this chapter we will focus on studies concerning nanorods or elongated nanoparticles of metals, metal-oxides, semiconductors and mixed materials as catalysts for a number of chemical reactions. For the various elongated nanocrystals, attempts are made to unravel the relationships between shape-anisotropy (i.e. nanocrystals with varying dimension along their different crystallographic directions) and their catalytic behavior. It is well known that a catalyst is a substance that displays an ability to accelerate the rate of a given chemical reaction, but which remains unchanged at the end of the reaction. If the catalysts species were in the same phase as the reactant species (if for example they are all in the liquid phase), they are termed as "homogeneous catalysis", while in different phases, they are termed "heterogeneous catalysis" (if for example the catalysts are in solid and the reaction species are either in the liquid or in the gas phase). Figure 6.1a sketches the action of a catalyst, in the first place, is to lower the energy barrier associated with a given chemical reaction, referred mainly to the activity. Then, another desirable property of a catalyst is to enhance the rate of a specific reaction pathway over multiple reactions (i.e. B → C instead of B → D or B → E), in order to yield a lower (or even the least) energetically favored product over many other possible products [1, 2], which corresponds to their specificity. In this chapter, we will refer to a catalyst as a solid support, since inorganic nanoparticles are indeed man-sized solids. Both the activity and specificity of a catalyst depends largely on catalyst's surface, on the nature and distribution of surface active sites, onto which reactive species are basically adsorbed, dissociatively adsorbed, reacted and then desorbed, to yield the final or the targeted products. Figure 6.1b, c shows how the adsorption of gaseous molecules on different surfaces could vary, and how the reaction proceeds through on a catalytic surface. This research area however is not fully understood and is widely debated, owing to the complexity of the multiple interactions at different levels on catalytic surfaces.

Nowadays on industrial scales, there is a huge demand for novel catalytic materials, in terms of catalytic efficiency, cost of production, specificity, durability

R. Krahne et al., *Physical Properties of Nanorods*,
NanoScience and Technology, DOI: 10.1007/978-3-642-36430-3_6,

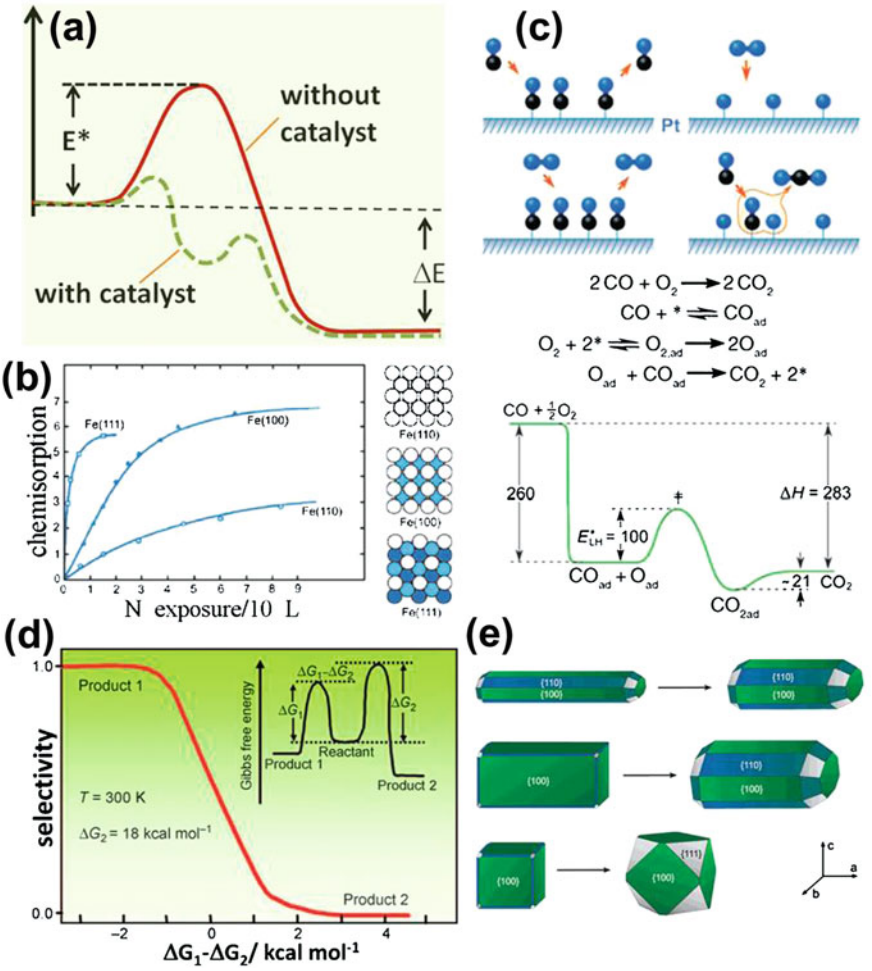

Fig. 6.1 **a** A sketch on the role of a catalytic material in a given chemical reaction. **b** The variation of the relative coverage of N atoms (y) chemisorbed at 693 K on various Fe single-crystal facets, upon exposure to nitrogen gas. **c** Catalytic oxidation of CO on a Platinum (Pt) surface, reaction pathways and energy diagram. **d** Potential-energy graph depicting selectivity in heterogeneous catalyst where the activation barriers for different reactions are the main factor that determines the selectivity. **e** Schematics of some synthesized elongated nanocrystals as new catalytic model system that may furnish effective surface sites for catalytic reactions. Taken with permission from Ref. [3, 60, 61]

and environmental sustainability [3–6]. This demand has accelerated the search towards the exploitation of new nanoscale materials and structures, in which the individual components have specifically been tailored size, shape, exposure of specific reactive surfaces, and suitable combination of materials [7, 8] that are of paramount importance to a catalyst in terms of structure-activity relationship.

Figure 6.1d, e depicts the idea of selectivity of a catalyst, and how such a process could be possible via the elongated nanocrystals as new catalytic surfaces with their extended crystallographic planes (Fig 6.1 e).

6.2 From Single Crystal Surface to Rod-Like Nanocrystals and Catalytic Properties of Inorganic Nanoparticles

Of many catalytic reactions studied on single crystal metal surfaces such as of Pt, Fe and Ru [1, 9], here Fig. 6.2 exemplifies how different crystal facets of a Pt_3Ni alloy crystal exhibit different degree of catalytic activities towards the oxygen reduction reaction ($O_2 + 4H^+ + 4e^- = 2H_2O$) (ORR) [10]. It has been shown experimentally that a certain surface only become highly active in certain catalytic reaction.

On the other hand, micro- and nano-particles (often nearly spherical or irregular) of various materials have been conventionally used as catalysts since many years [11–14], and experimental evidence has been archived so far demonstrative of that the catalytic activity of particles is strongly dependent on their size, and in particular that nanosized particles exhibit increased catalytic activity with respect to larger particles, due to their higher surface to volume ratio [15, 16] and high degree of reactivity. In the last decades extensive surface characterization of nano-

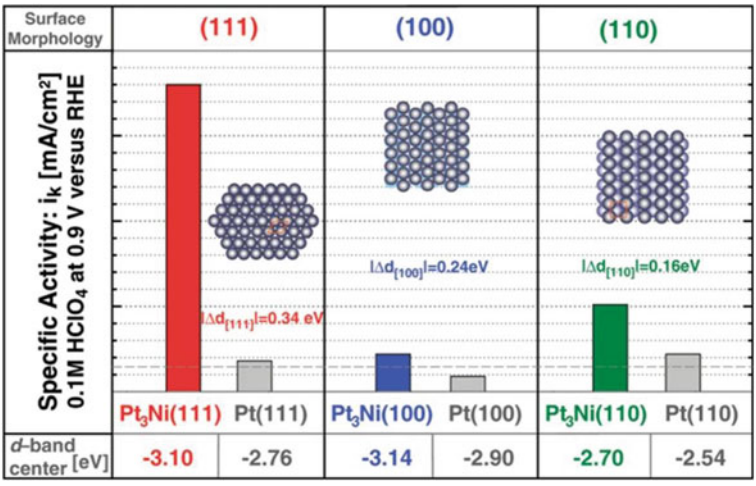

Fig. 6.2 Histograms showing the effect of surface morphology (i.e. crystal facet that is exposed) and electronic surface properties on oxygen reduction reaction kinetics (*ORR*) on Pt_3Ni (hkl) surfaces as compared to the corresponding Pt (hkl) ones [(using rotating ring disk electrodes (*RRDE*) in $HClO_4$ (0.1 M) at 333 K with 1,600 rotations per minute). Specific activity is given as a kinetic current density i_k, measured at 0.9 V versus RHE. Values of d-band center position obtained from ultraviolet photoemission spectra (*UPS*) are listed for each surface morphology and compared between corresponding Pt_3Ni (hkl) and Pt (hkl) surfaces]. Taken with permission from Ref. [10]

catalyst surfaces (via high-resolution electron microscopy, scanning probe microscopy, various surface spectroscopy techniques and surface reconstruction techniques) has helped to understand the reasons behind specific reactivity, selectivity and reaction pathways on different crystal facets of various catalyst materials in a wide range of chemical reactions.

Such understanding has accelerated further advances in the synthesis of inorganic nanoparticles with exquisite control of size and morphology [17–21] that paved the way towards the understanding of how the catalytic performance of those materials is dependent on their shape. Despite the shape dependence of nanocatalysts is not fully understood, some landmark reports have started to draw clear correlations between morphology and catalytic activity in nanoparticles [9, 22–25]. Before we see how the evidence stacked up for the shape dependent catalytic behavior; we will have a closer look at some metal nanorod structure as model system. This will help us to fully appreciate the idea behind the emergence of their strikingly different physical properties when compared to their nearly spherical counterpart nanostructures. The nanorod or elongated nanocrystal means that they grow along a specific axis direction much faster than the rest for instance <100> direction. For example, Fig. 6.3a, b presents a 3d view of gold (Au) nanorod generated by TEM tomographical reconstruction, where one can see more clearer projection and exposition of different planes from gold nanorod. Similarly, c, d the high resolution TEM images of iron (Fe) nanorod structure show a 5-fold twinned crystallography at both the tips of Fe nanorods that have grown along

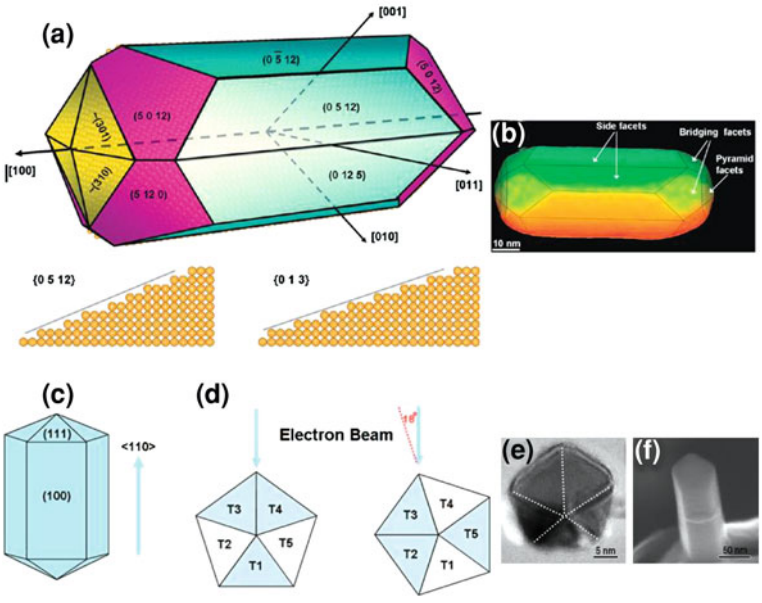

Fig. 6.3 **a**, **b** Schematic and 3D projection (tomographic) of the gold nanorod morphology. **c**–**f** Schematic and TEM images of iron nanorods, reproduced with permission from Ref. [62, 63]

<110> direction. Accordingly, many studies have highlighted (as we see later in this chapter) for example how cube-, rod-, branched and multi-pod shaped nanoparticles can have improved catalytic activity with respect to the corresponding samples with more heterogeneous distribution of shapes, when their specific shape allows for some sets of particularly active facets to be exposed to the external environment.

Here, we therefore will discuss mainly about elongated nanoparticles. However, we will not confine the discussion only to rod-shaped particles, but we will also consider wire-, belt-, and net-like morphologies since they are still elongated. In terms of catalytic properties, the main reasons why an elongated morphology would be preferable over a spherical morphology can be summarized as:

1. At constant volume, the surface to volume ratio increases when the shape evolves from a sphere to an elongated one and as the aspect ratio of the nanoparticle increases further. This translates to a better catalyst if the facets that become more extended in rods are indeed those exhibiting higher catalytic activity (as in Fig. 6.1e). In addition, an increase in surface to volume ratio might lead to an increase in the number of surface active sites. Also, anisotropic crystals could act as efficient charge separation systems, for example in photo catalytic reactions (see later in this section). The elongated nanostructures exhibit enhanced electron transport [26].
2. The mechanical stability of a particle acting as catalyst might increase as a consequence of its elongation along a specific crystallographic direction [27–29], (see Chap. 7 of this book for more insights into mechanical properties of elongated nanoparticles).
3. Nanorods can be assembled with specific geometries with respect to a substrate or with respect to each other (vertical, horizontal and end-to-end) [30–32], which might favor the exposure of a given set of facets to the external environment.
4. Easy identification of the nanorod's morphology among other irregularly shaped support materials used (for example binders, fillers and other diluents, nearly spherical or irregularly shaped) over number of cycles for recovery.

In the following, we will consider a wide range of examples for the catalysts based on metals, core/shell metals, and metal alloy nanoparticles, in order to point out their different roles as summarized above, will be helpful for the understanding of their catalytic properties. We will then also cover some examples representing metal oxide and semiconductor nanorods, as well as nanorods of mixed materials.

6.2.1 Metals, Core/Shell Metals, Segmented Metals and Metal Alloy Nanorods

From the study conducted by Habas et al. [33], a useful insight into the connection between the morphology of nanocrystal and the catalytic properties was presented in case of metallic Pt/Pd core@shell nanoparticles of various shapes, namely

cubes, octahedra and cubo-octahedra (Fig. 6.4a–c). Surprisingly those nanocrystals showed distinctive electrochemical oxidation of formic acid ($HCOOH + 1/2O_2 \rightarrow CO_2 + H_2O$). In essence, the oxidation rate on nanocubes was found to be five times higher than that on octahedral and cubo-octahedral shaped particles. The increased activity in case of nanocubes was related to their specific crystallographic habit, which exposed Pd (100) facets instead of the Pd (111) ones. This clearly demonstrates how one particular set of crystal facets of nanostructures selectively catalyses the reactions than other sets. In addition, by doing an epitaxial overgrowth of gold (Au) on cubic Pd seeds, the formation of Au nanorods containing or embedding Pt cubes was also achieved, see Fig. 6.4d, e. The resulted Au rods grown on Pt cube were found to be pentagonally twinned crystals, growing along the (220) direction. Such nanostructures (nanorods with embedded Pt domains) were strongly proposed for the shape-dependent catalytic studies. The shape dependent catalytic property was further shown in the experiment by Lee et al. [34], in which platinum (Pt) nanoparticles exposing predominantly (111) facets, exclusively favored the formation of cis-2-butene between cis- and trans-2-butene via interconversion reaction. When morphology changes to a rod-shape as in case of gold nanorods by Bai et al. [35], the (100) planes were mainly extended along the nanorod, which exhibited higher activity for the reduction of nitro compounds. This surface sensitivity to a catalytic activity strongly influenced by the shape of the crystal that governs surface atomic arrangement and coordination.

Similarly, Berhault et al. [36] have presented clear indication on the interplay between the morphology of nanocrystals and selective catalytic activity in case of

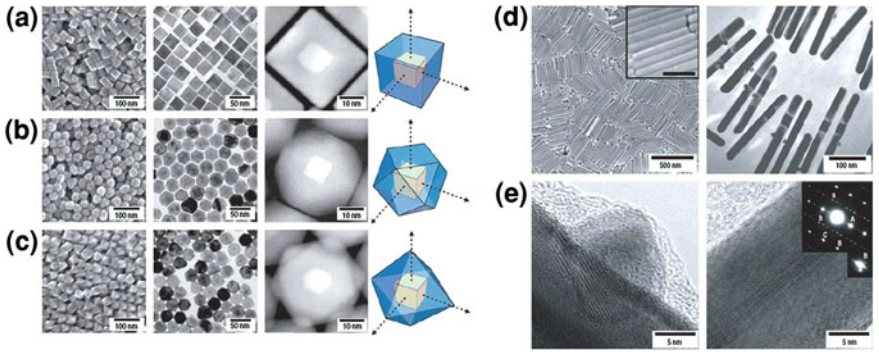

Fig. 6.4 **a** From *left to right*: SEM and TEM images of cubic platinum nanoparticles, high angle annular dark field scanning TEM (HAADF-STEM) image of an individual cubic particle, sketch model showing the axes projection along the (100) direction. **b** Same sequence of images as in (a), but referred to cubo-octahedral particles. Here the sketch model shows the axes projection of the cube along the (100) and the (111) directions. **c** Same sequence of images as in (a), but referred to octahedral particles, the sketch model shows the axes projection of the Pt cube (the seed) along the (111) direction. **d** SEM image (*left*) and TEM image (*right*) of gold nanorods. **e** High resolution TEM image showing the Pt cube on the surface of gold nanorods (*left*) and nanorods viewed from (112) and (100) directions with continuous (111) lattice fringes (*right*). Taken with permission from Ref. [33]

Pd nanorods for the hydrogenation of buta-1, 3-diene to but-2-ene, which was, on the comparison with spherical counterparts, rationalized as due to the exposure of the (100) facets in these rods. On these facets the effective adsorption of reactive species has appeared to be favored than their isotropic Pd catalysts. This characteristic behavior was further manifested in palladium (Pd) rods and in branched nanostructures by Chen et al. [37] (Fig. 6.5a–c). Similar to the Au rods morphology described previously, these Pd nanorods were multiple twins with pentagonal cross section, with selective growth along the <110> direction. When these nanorods were used as catalysts for the Suzuki coupling reaction (carbon-carbon bond formation) [38], they yielded about 90 % yield of the product (biphenyl) in the first time use. Again, the observed activity and selectivity for the reaction were due to specific facets that defined the habit of the nanocrystals. The nanorods were recovered and tested for the second time, which yielded about

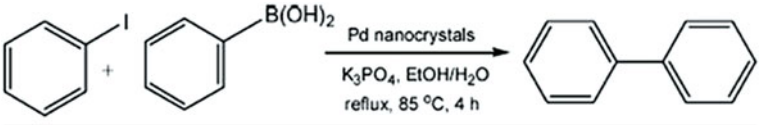

entry	catalyst	yield (%)
1	Pd nanorods	92
2	first recycle	89
3	second recycle	85
1	branched Pd nanocrystals	90
2	first recycle	86
3	second recycle	82

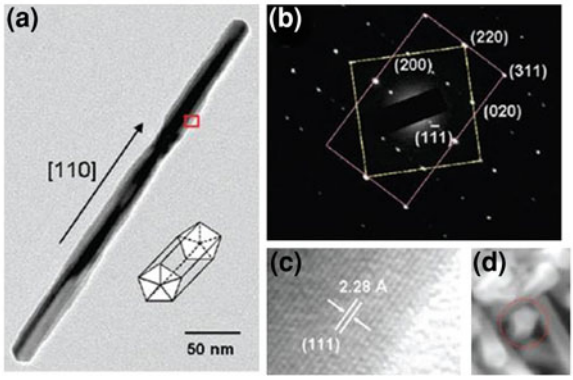

Fig. 6.5 The table on the *top panel* reports the cyclability of the Pd catalysts in the Suzuki coupling reaction. **a** TEM image of Pd nanorods with a sketch showing their fivefold twinned structure. **b** Selected area electron diffraction (*SAED*) pattern demonstrating that the nanorods grow preferentially along the (110) direction, with an overlap of the (001) and (1–1–2) reflexes of the face centered cubic (*FCC*) crystal structure. **c** High resolution TEM view of the panel from (a) showing d spacing of 2.28°A, which corresponds to the (111) lattice planes of Pd. **d** SEM image of Pd nanorods with fivefold twinned structure. Taken with permission from Ref. [37]

85 %, indicating the recyclability of the catalysts see Fig. 6.5. Therefore, the nanorods seemed efficient also for multiple uses, due to their good mechanical properties. It is very interesting to mention that Pd nanowires and rods [39] with 5-fold twinned structure enclosed by five [40] side surfaces along the ⟨110⟩ direction, have shown different reactivity at their tips and sides, for growing Au domains at tips first than the sides, due to difference in the surface adsorption.

A similar trend has also been found in bimetallic PtPb nanorods by Maksimuk et al. [41] (Fig. 6.6a–c). The nanorods were elongated along the <110> direction, and the incorporation of Pb atoms into the Pt lattice was reported to take place in sites with high coordination numbers due to the stronger binding energy of such sites (Fig. 6.5d). The electrochemical oxidation of methanol ($CH_3OH \rightarrow CO_2 + H_2O$) was carried out in order to test PtPb nanorods vs.a commercially available PtRu/C catalyst (from Johnson-Matthey, Pt 30 wt %: Pd 15 wt %). From the anodic peak

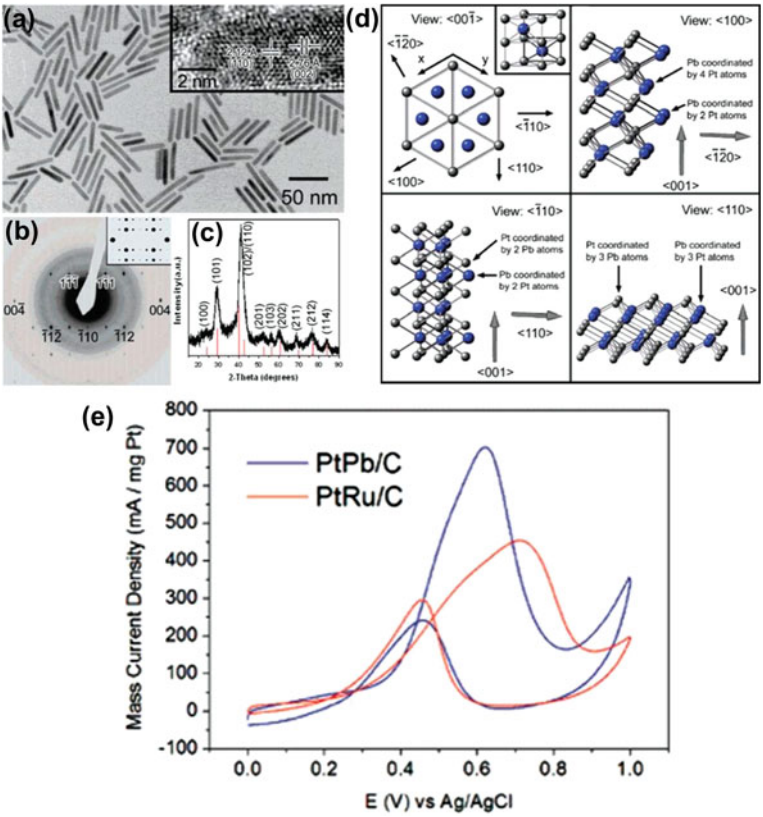

Fig. 6.6 **a** TEM image of PtPb nanorods. **b** Selected are electron diffraction patterns from a single PtPb nanorod. **c** Power x-ray diffraction pattern of an ensemble of PtPb nanorods. **d** Model sketch of four proposed crystal structures of PtPb nanorods. **e** Cyclic voltammogram showing the electro-catalytic oxidation of methanol on PtPb nanorods and on PtRu/C commercial catalyst. Taken with permission from Ref. [41]

current (ipa) in cyclic voltammetry, the activity of the nanorods was found to be higher than the reference catalyst with respect to the normalized unit mass of Pt (Fig. 6.6e), which clearly indicates higher rate of methanol oxidation in the case of nanorods.

Phase segregated bimetallic nanorods in a diameter range 150–200 nm have also been used for catalytic applications. Using electro-deposition in sequences, Liu et al. [42] have prepared multi-segmented Pt-Ru nanorods (Fig. 6.7a–e). The main idea was to combine Pt with an oxophilic metal such as Ru in order to increase the reaction to release CO_2 during the electro-oxidation of methanol. Strikingly, at room temperature, the nanorods were found to electrocatalyze the methanol oxidation reaction in acidic media (Fig. 6.7f). Here, the catalytic activity of the nanorods was found to increase upon increasing the number of Pt-Ru segments, and was explained on the basis of an increased number of Pt-Ru interfaces that considerably diminishes the poisoning of the Pt active sites. Apart from these, the nanorods mechanical stability to render robust active sites and good electron transport during the reaction should not be excluded. For much smaller size range of CuPt metal alloy nanoparticles, as reported by Liu et al. [43], showed shape-dependent catalytic activity. Spherical nanoparticles (2.5 nm) and nanorods of CuPt (20×2 nm) were tested for the CO oxidation reaction ($CO + 1/2\ O_2 \rightarrow CO_2$). The nanostructures were dispersed on a γ-alumina (Al_2O_3) support and were loaded into a CO feedstock. Under identical experimental conditions, the average light-off temperature values (T_{avg}) for both catalysts ($\sim$556 K for nanorods and $\sim$490 K for spherical nanoparticles) were found to be lower than the commercially available Pt (2–3 nm)/Alumina catalyst

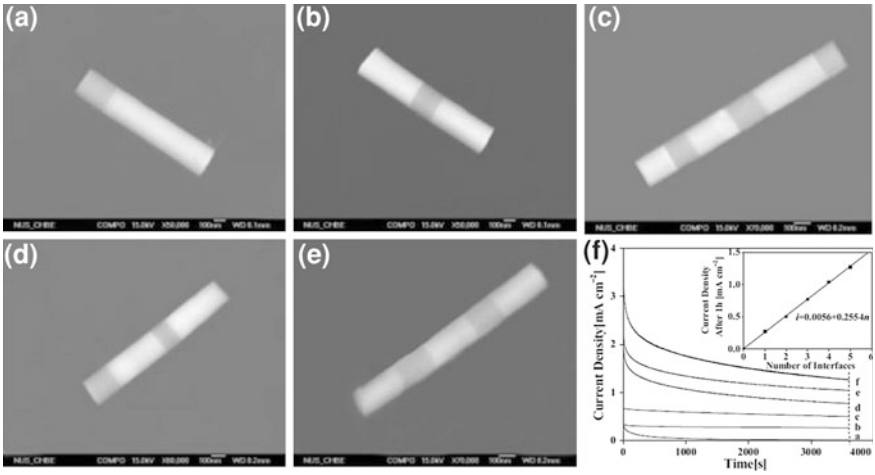

Fig. 6.7 Field emission SEM images of segmented nanorods **a** Pt-Ru, **b** Pt-Ru-Pt, **c** Pt-Ru-Pt-Ru, **d** Pt-Ru-Pt-Ru-Pt, **e** Pt-Ru-Pt-Ru-Pt-Ru. The diameter of the rods was 200 nm in all the samples, and **f** cyclic voltammograms of nanorods, at 0.1 M $HClO_4$ and 0.5 M CH_3OH, polarized at a constant potential versus Ag/AgCl (3 M KCl) at room temperature. Taken with permission from Ref. [42]

(700 K). Therefore, an important consideration is that although the spherical nanoparticles were extremely reactive in such size range (close to ∼2 nm), nanorods with an aspect ratio range ∼5:1–25:1 appeared to be comparatively efficient and more stable than the spherical ones, see Fig. 6.8a–g. In addition to the high surface area of nanostructures used, the surface of the CuPt alloy particles appeared to be less poisoned by CO adsorption, due to the more oxophilic character of the active sites.

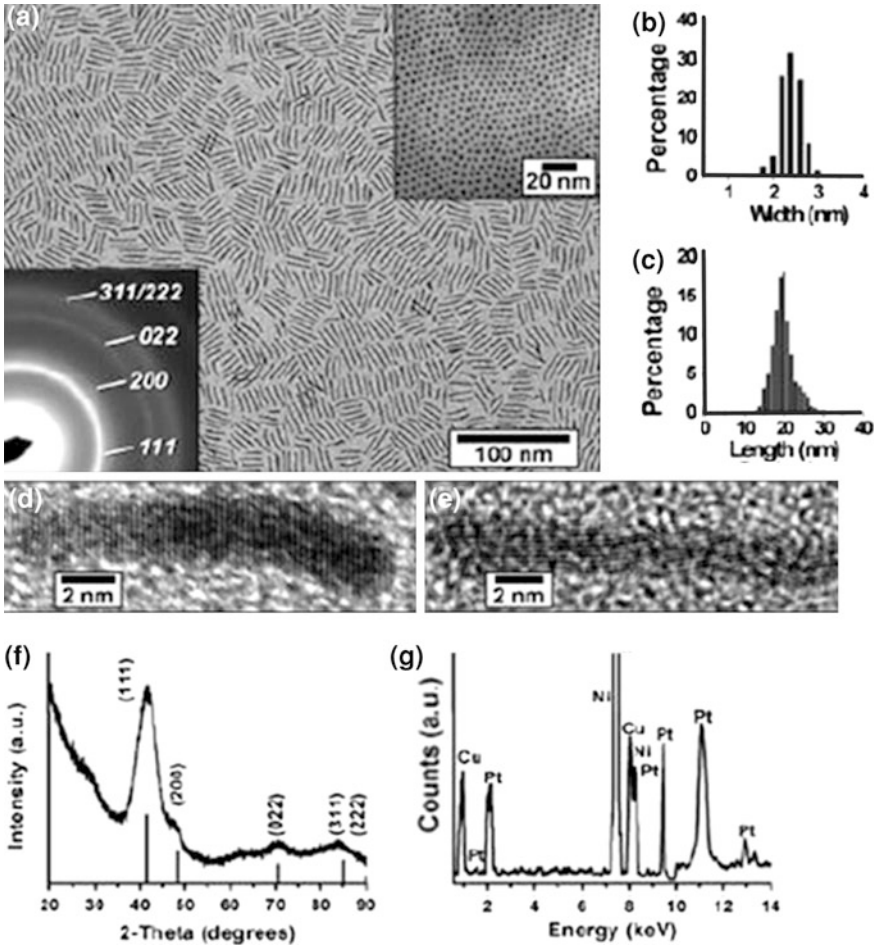

Fig. 6.8 **a** TEM image of CuPt nanorods. *Left inset*: selected area electron diffraction pattern. *Right inset*: TEM image of spherical CuPt nanoparticles. **b–c** Histograms of diameter and length distributions of the nanorods. **d**, **e** HRTEM of nanorods. **f** X-Ray diffraction patterns. **g** Energy dispersive spectroscopy analysis. Taken with permission from Ref. [43]

6.2.2 Metal Oxide, Semiconductor, and Mixed Nanorods

In this section, we will consider some selected examples of metal oxide and metal/metal oxide supported catalytic systems. Among the metal oxide catalysts, the findings on Co_3O_4 nanorods reported by Xie et al. [44] seem to hold a key for the structure-catalytic activity relationship. The nanorods, according to HRTEM analysis were elongated along the <110> direction and were preferentially exposing the (110) facets (Fig. 6.9a–h). These facets accounted for about 41 % of the total surface area of the rods. Remarkably, these rods catalyzed the CO oxidation reaction even at temperatures as low as −77 °C and at room temperature 100 % conversion for 65 h. Therefore they exhibited much higher activity than the more traditionally used metal oxide-supported Au nanoparticles for this type of reaction. From structure reconstruction analysis via HRTEM, it was proposed that the high abundance of Co^{3+} cations on the (110) facets provided effective sites for the oxidation of adsorbed, while the close packed planes such as (001) and (111) mainly contain only Co^{2+} that are relatively less active for CO oxidation. Similar results were also found for the oxidation of propane at high temperature (100 % at 350 °C) and such oxidizing ability of Co_3O_4 nanorods was found to be comparable to that of Pt and Pd catalysts. The higher activity and selectivity were therefore

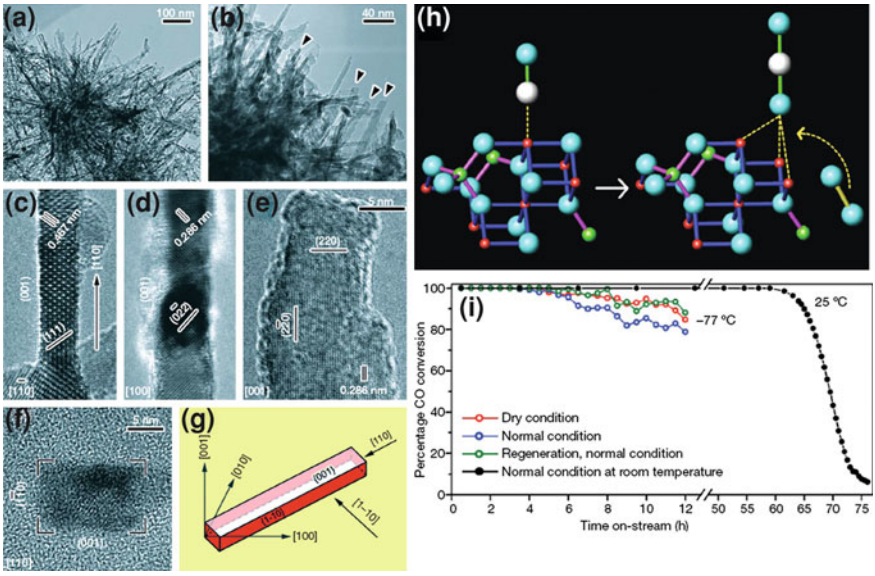

Fig. 6.9 **a**, **b** TEM images of Co_3O_4 nanorods. **c**–**f** HRTEM images of the nanorods, showing (1–10), (100), (001) and (110) lattice fringes. **g** Sketch showing the habit of the nanorods. The *red* shaded facets are the catalytically active ones. **h** Possible reaction pathway for CO oxidation on Co_3O_4 nanorods, with a ball and stick model for CO adsorption and oxidation on the active Co^{3+} site. **i** Effects of moisture content, regeneration and temperature on the oxidation of CO over Co_3O_4 nanorods. Taken with permission from Ref. [44]

directly related to the nanorod morphology, which exposed preferentially the catalytically active sites. Plus, these nanorods were also shown to possess good stability even under high moisture conditions, and they retained the rod shape even upon repeated use (Fig. 6.9i).

Copper oxide (CuO) nanostructures too display strong shape dependent catalytic behavior as reported by Zhou et al. [45]. Anisotropic CuO nanostructures, including belts and platelets, versus spherical nanoparticles (Fig. 6.10a–c) were tested in CO oxidation. The most developed facets in the various nanostructures were the (111) ones for spherical nanoparticles, (001) for nanobelts, and $(01\bar{1})$ for nanoplatelets. From CO oxidation, the conversion rate was found to be in the order of *nanoplatelets* > *nanobelts* > *nanoparticles* (Fig. 6.10d, e). Here, the increased activity of nanoplatelets was attributed to the exposure of the $(01\bar{1})$ facets, which appeared to facilitate desorption of O_2 from the surface, as determined by CO temperature programmed reduction (TPR). In case of nanobelts, the activity was even higher due to the exposure of the (001) facets. As the close packed facets

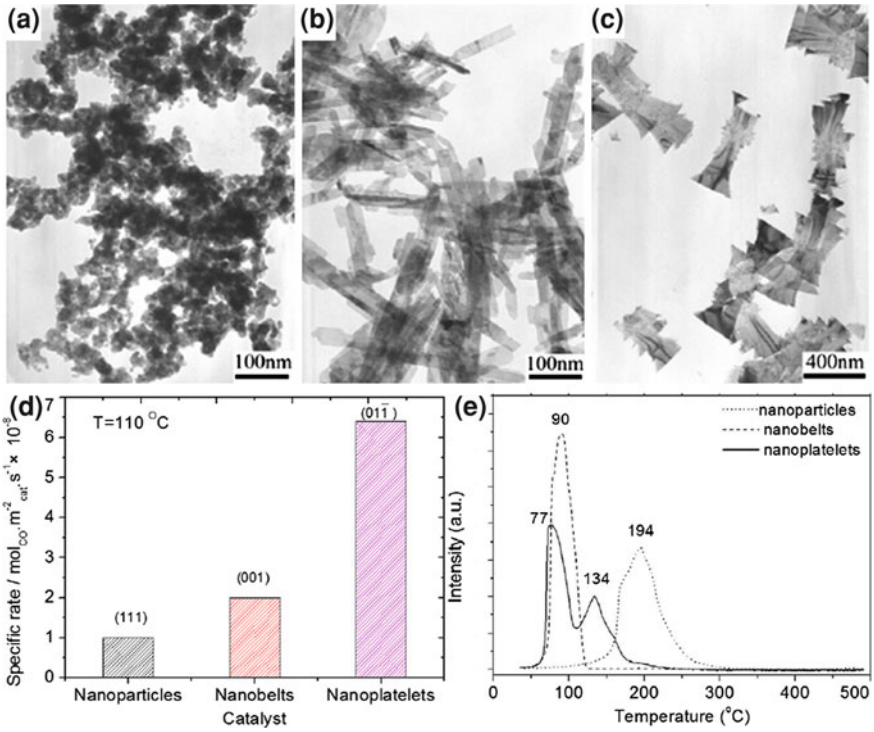

Fig. 6.10 TEM images of **a** CuO nanoparticles, **b** CuO nanobelts, **c** CuO nanoplatelets, **d** specific rate of CO conversion over CuO nanoparticles, nanobelts and nanoplatelets at 110 °C with respect to exposed crystal facets of each nanostructure, (111) for nanoparticles, (001) for nanobeltes and $01\bar{1}$ (01–1) for nanoplatelets, and **e** CO temperature programmed reduction profiles of each nanostructure. Taken with permission from Ref. [45]

(111) of the oxides (which are the most exposed facets in spherical nanoparticles) possess lower surface energy, they are more stable than the $(01\bar{1})$ and (001) open facets. From the successive catalytic cycles, it was also found that the catalysts particles were stable at $\leq$200 °C.

In case of CeO_2, the shape dependent-catalytic activity is significantly pronounced as reported by Si et al. [46]. CeO_2 nanostructures with various crystal habits, namely rods with exposed (110) and (100) facets, cubes with exposed (100) facets and polyhedrons with exposed (111) and (100) facets (Fig. 6.11a–d) were decorated with 1 % gold via hydrothermal synthesis. Upon performing the water gas shift (WGS) reaction ($CO + H_2O \leftrightarrow CO_2 + H_2$) the catalytic activity from light-off curves followed the order: *rods* > *polyhedrons* > *cubes*. Almost 100 % CO conversion efficiency was reported in the case of nanorods (Fig. 6.11e) at 250 °C, while the cubes showed about 20 % at even 350 °C. The higher activity of the nanorods was attributed to their exposed (110) and (100) facets, which appeared to be energetically more favorable for introducing oxygen vacancies that

Sample	$\varepsilon^{[a]}$ [%] (111)	(200)	(220)
CeO_2 rods	1.1	1.3	0.9
CeO_2 cubes	0.3	0.2	0.2
CeO_2 polyhedra	0.9	0.6	0.5
Au-CeO_2 nanorods	0.8	0.8	0.9
Au-CeO_2 nanocubes	0.2	0.3	0.2
Au-CeO_2 nanopolyhedra	0.7	0.6	0.5

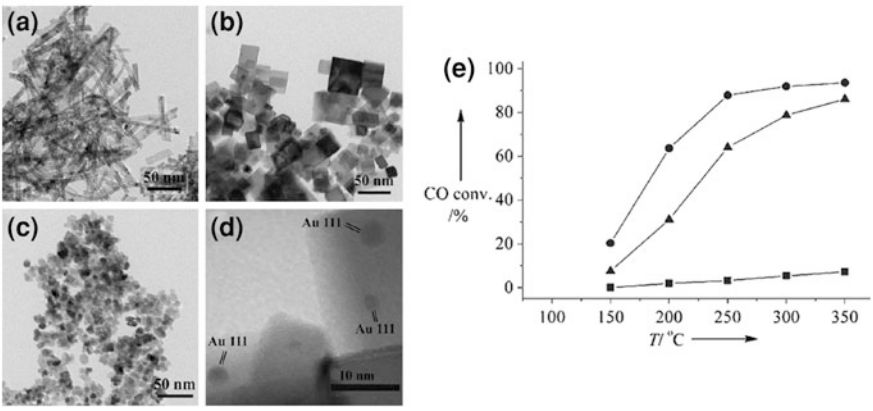

Fig. 6.11 *Top panel*: Lattice micro strain (ε) of different crystal planes of ceria and gold/ceria nanorods, cubes and polyhedra. **a–c** TEM. **d** HRTEM images of gold nanoparticles on ceria nanorods (*a*) cubes (*b*, *d*) and polyhedral (*c*). **e** Water gas shift reaction (*WGS*) light off profiles for 1 % gold on ceria (*circle*) nanorods (*square*) cubes and (*triangle*) polyhedra. Taken with permission from Ref. [46]

stabilize the metallic phase (such as tiny gold cluster) during catalytic reactions (due to the oxygen buffer effect). Besides, when considering the formation energy of anion vacancies for the various CeO_2 facets, the exposed (110) and (100) facets of nanorods were found to be a more favorable support for embedding or dispersing metal domains such as Au, which increases the catalytic activity due to the metal/metal oxide support effect [47, 48]. This also has an implication on the mechanical properties of the nanorods; after growing gold domains, the lattice micro-strain measurements for all three samples revealed that the nanorods were characterized by the large lattice strains, which correlated with the increased catalytic activity of the nanorods, see Fig. 6.11, top panel. Interestingly, Sayle et al. [49] too have pointed out that ceria nanorods with exposed (110) facets exhibit higher elastic deformation than the brittle bulk phase, and a reversible fluorite to rutile transformation took place about 6 % strain for the ceria rods elongated along [110] planes.

Another interesting work on CeO_2 by Han et al. [50] further indicates how the preferentially exposed (110) and (100) facets play a key role in their catalytic activity. First of all, the reduction of CeO_2 nanorods in H_2 started at lower temperature (150 °C) with respect to both spherical nanoparticles and bulk ceria. In the WGS reaction, while the spherical nanoparticles displayed almost no activity, nanorods possessed an increased catalytic activity as a function of the temperature, up to about $\sim$350 °C (Fig. 6.12a, b). The remarkable feature was that the nanorods did not show any structural/morphological changes during WGS, which was also confirmed by in situ XRD analysis. As discussed earlier in the case of ceria nanorods, the amount of oxygen vacancies that formed on the CeO_2 nanorods (i.e. during the reduction process) due to the exposed facets is crucial for their enhanced the catalytic activity. Furthermore, by dispersing Pd nanoparticles onto the nanorods, the activity increased further, as expected due to the metal/metal oxide support effect, where the presence of metal domains help activate the ceria surface (Fig. 6.12c), in addition to the nano size effect [16] from much smaller Pd domains.

Not only the specific shape but also nanostructure's phase can influence the catalytic activity. MnO_2 nanorods of different crystal phases (namely the α, β, γ and δ phases of MnO_2) via hydrothermal method (Fig. 6.13a–d) synthesized by Liang et al. [51] show the dependency of the phase on the catalytic activity. All the nanorods were found to grow mainly along their (002) and (001) crystallographic axes. The surface parameters of the nanorod samples before and after CO oxidation from various characterizations are listed in Fig. 6.13, top panel. Interestingly, the activity of various samples of nanorods towards the CO oxidation was found to rank according to the following order: $\alpha = \delta > \gamma > \beta$ (Fig. 6.13e, f). The higher activity of the δ- and α- MnO_2 nanorods for CO oxidation was found to be strongly influenced by their crystal phase. From a catalytic performance and stability test (CTL), the activity order ($\alpha = \delta > \gamma > \beta$) was found to be the same. Here, the CO adsorption on MnO_2 was also found to be in the order $\delta > \alpha > \gamma > \beta$ MnO_2 by CO temperature programmed desorption (TPD) and this explains the observed activity of the nanorods. On the other hand, Sui et al. [52] reported that

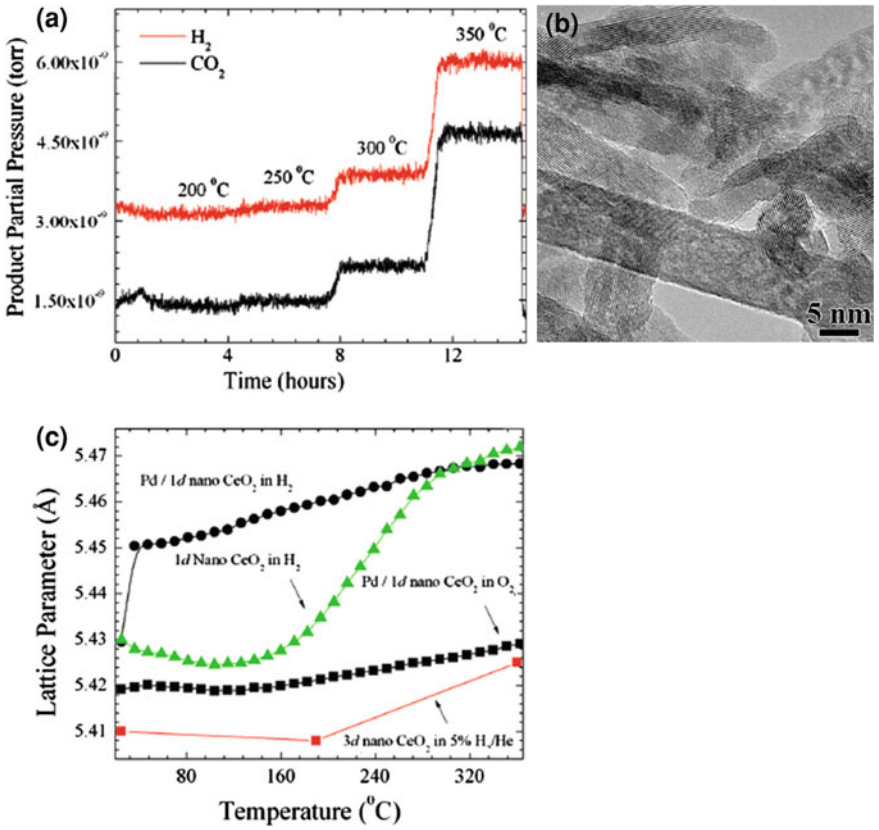

Fig. 6.12 **a** H_2 and CO_2 relative pressure during the water gas shift reaction (*WGS*) on CeO_2 nanorods. **b** TEM image of the samples after the WGS reaction. **c** Variation of the CeO_2 lattice parameters during the temperature ramping for Pd loaded CeO_2 nanorods and bulk CeO_2. Reprinted with permission from Ref. [50]

the β-phase of MnO_2 nanorods elongated along the <001> direction exhibited the highest photocatalytic activity towards the decomposition of rhodamine B than other MnO_2 phases (α, δ, γ), showing the specificity of the nanorods in their catalytic behavior. This has indicated that often nanorods can be highly selective in their catalytic behavior towards a specific reaction. The nanorods were also found to be stable on the repetitive tests for first ten times via XRD and TEM analysis.

The shape effect also plays a role in semiconductor/metal catalytic system. For example, Lin et al. [53] have reported the fabrication of ZnO nanorods/Cu nanoparticles composite and tested them for the oxidation of methanol (Fig. 6.14a–j). Most likely due to the presence of Cu metal, the composites prepared from these nanorods exhibited lower reduction potential than commercial catalysts (such as Cu-ZnO-Al_2O_3, MDC-3). The composite electrodes used, in addition to exhibiting higher rate for methanol oxidation (93 %), had a higher H_2

	before CO oxidation				after CO oxidation			
catalyst	SA[a] ($m^2\ g^{-1}$)	Vp[b] ($mL\ g^{-1}$)	cryst size[c] (nm)	aspect radio[d]	SA[a] ($m^2\ g^{-1}$)	Vp[b] ($mL\ g^{-1}$)	cryst size[c] (nm)	aspect radio[d]
α-MnO_2	36.5	0.16	23.6	8−15	32.5	0.12	31.5	10−25
β-MnO_2	11.9	0.02	55.4	15−20	11.0	0.01	64.7	10−40
γ-MnO_2	61.5	0.25	8.8	5−20	58.9	0.23	14.9	10−20
δ-MnO_2	144.4	0.42	10.7	30	139.0	0.39	12.5	50

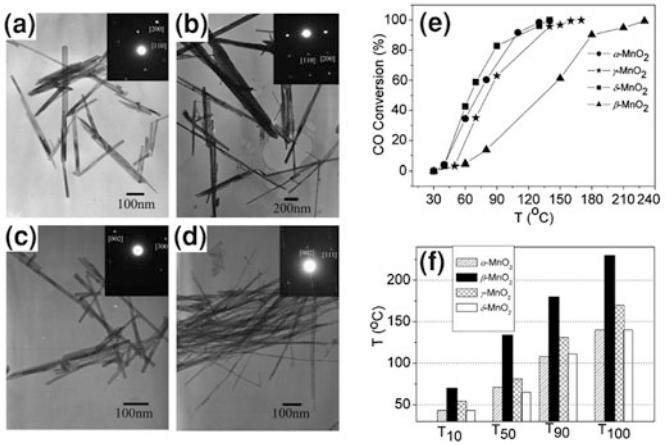

Fig. 6.13 *Top panel*: Surface area, porous volume, crystal size and aspect ratio of the MnO_2 nanorod samples before and after CO oxidation. **a**–**d** TEM images of the MnO_2 nanorods: α-MnO_2, β-MnO_2, γ-MnO_2 and δ-MnO_2 respectively, with insets showing selected area electron diffraction patterns of nanorods. **e** CO oxidation activities of MnO_2 nanorods under 2 volume % CO, 98 volume % air and flow rate of 70 mL min^{-1}. **f** T_{10}, T_{50}, T_{90}, T_{100} are the temperatures of CO conversion 10, 50, 90 and 100 %, respectively. Taken with permission from Ref. [51]

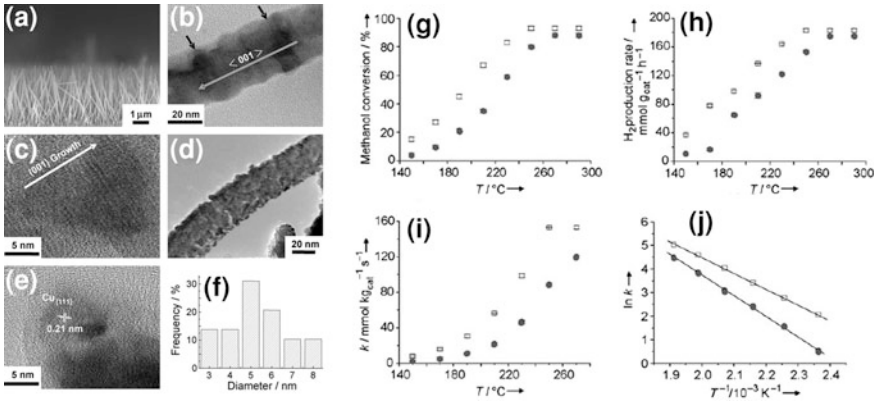

Fig. 6.14 **a** Cross sectional SEM image of vertically aligned ZnO nanorods. **b** TEM image of a single ZnO nanorod showing stacking faults. **c** HRTEM image of ZnO nanorods. **d** TEM image of ZnO NR@ Cu nanoparticles. **e** HRTEM image of Cu nanoparticles on the surface of a single ZnO nanorod. **f** Histogram of Cu nanoparticles from TEM analysis. The catalytic activity of *circle* nanorods vs *square* commercial catalysts. **g** Methanol reforming profiles. **h** Hydrogen production rate as a function of the temperature. **i** Kinetic constant as a function of the temperature. **j** Arrhenius plot for the methanol reforming reaction. Taken with permission from Ref. [53]

production rate (183 mmol $g_{cat}^{-1}h^{-1}$ at 250 °C) than commercial ones. From the Arrhenius plot, the reaction activation energy for the nanorod catalysts was found to be lower (27.5 kJ mol^{-1}) than the commercial catalyst (36.8 kJ mol^{-1}), showing that the methanol oxidation rate could in principle be faster on nanorod shaped catalysts as supported by the evaluation of the kinetic constant (k). Interestingly, from the hi-res TEM analysis, it was found out the Cu NPs were predominantly located along the [002] plane of ZnO with relatively low lattice mismatch, so that the stability of the dispersion of NPs was enhanced. Besides, the high surface area of the nanorods, the metal-nanorods interfacial compatibility and the stability of the electrodes were attributed to such higher activity. Similar observation, has also been noted in ZnO nanorod (preferentially grown along <0001>)@Ag nanorods [54] as a photo catalyst for methyene blue (MB) photo degradation. ZnO narods were eptaxially attached onto Ag nanorod along (111) and (100) surfaces, which exhibited higher photo catalytic activity on the MB degradation.

In case of CdSe, the more elongated rods heavily influence the dispersion tiny metal domains, and Pt-decorated cadmium CdSe nanorods reported by Elmalem et al. [55] showed the distinct photo-catalytic properties (Fig. 6.15a–d). This loading of metal is very important because under irradiation, efficient charge (electron-hole) separation takes place at the metal/semiconductor interface, with the electrons moving to the metal tip region, from where they can induce faradic reactions. Methylene blue (MB) was used as model dye in order to test the visible-light photocatalytic activity of the nanorods. Two kinds of Pt-CdSe nanostructures, namely nanorods and nanonets, were synthesized, and were compared in terms of their catalytic activity. The nanonets were found to be better photocatalysts than the nanorods, due to the smaller Pt domains (1.9 ± 0.5 nm), which were more densely located at their surface (in the samples of nanorods tested the Pt domains had an average size equal to 3.3 ± 1.1 nm).

Similarly, Zinc tungstate ($ZnWO_4$) nanorods containing silver (Ag) nanoparticles were prepared by Yu et al. [56] with a growth along <100>. The photocatalytic properties (Fig. 6.16a–d) of these rods were tested on the degradation of rhodamine-B (RhB) and gaseous formaldehyde under irradiation at $\lambda = 365$ nm, using a UV lamp. The bare $ZnWO_4$ rods exhibited comparatively lower activity than the Ag/$ZnWO_4$ sample. The catalytic activity was attributed to the due to the [100] direct planes which were more active in the observed photo degradation. By increasing the number of Ag domains (~ 3 nm) on the nanorods the activity was shown to increase (Fig. 6.16e). The catalytic activity had a strong dependence on the high surface area, crystallinity and aspect ratio of nanorods.

Metal-doped semiconductor nanorods have also been tested. For example Zhu et al. [57] exploited a thin film of Cr-doped TiO_2 nanorods in Na_2SO_4 electrolyte solution for photo-electrochemical cells. The Cr-doped TiO_2 nanorods showed high photocatalytic activity for the water splitting reaction ($2H_2O \leftrightarrow 2H_2 + O_2$) (Fig. 6.17a–d). Here, another favorable role of the nanorod morphology was that it increased the electron transport of the electrodes since the nanorods could reduce the crystalline contacts between the grain boundaries as they grew directionally.

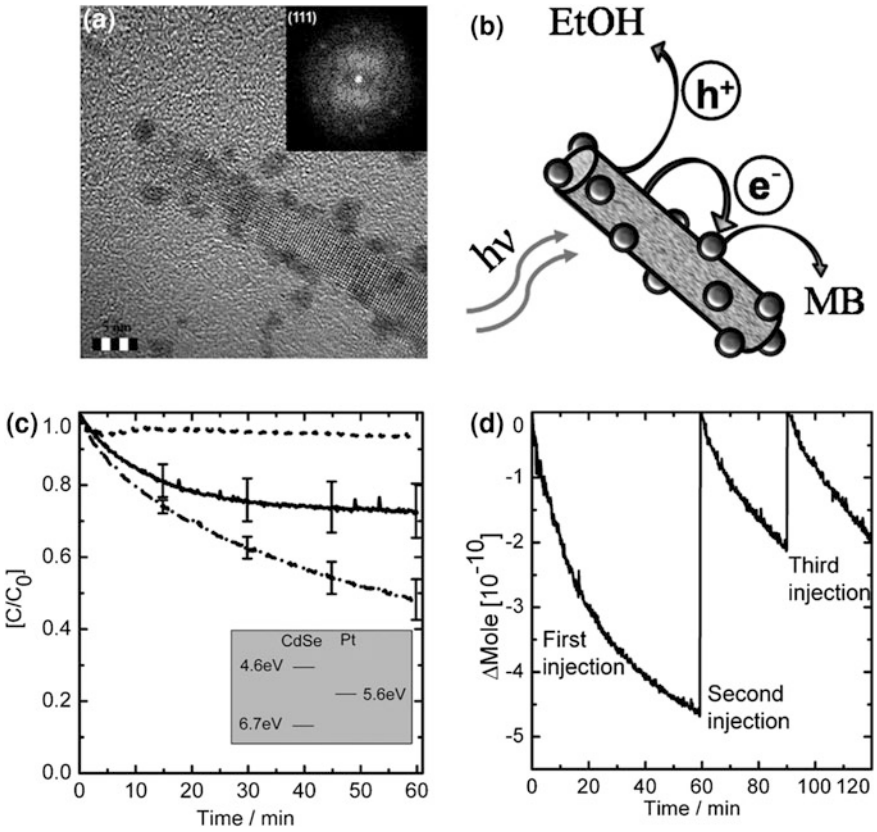

Fig. 6.15 **a** HRTEM image of a single CdSe-Pt hybrid nanostructure grown at pH 10. Inset: fast Fourier transform image showing the (111) reflexes of the Pt nanocrystals. **b** Scheme of a light induced charge separation mechanism in a CdSe-Pt nanorod. **c** Time trace of the normalized concentration of the MB dye in a sol of CdSe-Pt nanonets (*dashed lines*) and nanorods (*solid lines*), measured at pH7. **d** Sequential photocatalysis experiments with CdSe-Pt nanonets showing the catalytic activity during three injections of MB at various times. Taken with permission from Ref. [55]

The morphology of the samples after many cycles of photo catalytic reaction was found to be preserved, which is important for maintaining a well defined electrode/electrolyte interface over cycling.

Even only Sb_2S_3 (band gap 1.64 eV) semiconductor nanorods without any metal domains, as reported by Sun et al. [58], with diameters around 50–100 nm and lengths around 100–1,000 nm possessed photocatalytic activity under visible light (Fig. 6.18a–f). In the presence of nanorods, under visible light irradiation the absorption peak at $\lambda = 464$ nm for methyl orange (MO) was found to decrease over 30 min at a rate faster than when using reference catalysts such as TiO_2-N_2 or CdS. Also, the photocatalytic stability test showed that the nanorods retained their crystal structures, as XRD peak positions and relative intensities were identified as

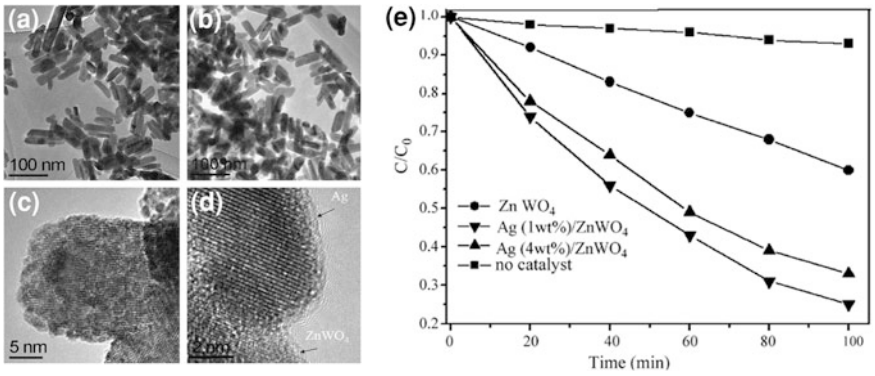

Fig. 6.16 TEM images of: **a** $ZnWO_4$ nanorods, **b** Ag 4 % $ZnWO_4$ nanorods, **c**, **d** HRTEM image of $ZnWO_4$ nanorods, and **e** degradation of rhodamine-B (*RhB*) during irradiation under UV light 365 nm. The profiles show RhB concentration changes. Taken with permission from Ref. [56]

those of the pristine samples. However, loss of activity was observed after the first cycle. The conversion ratio from MO photodegradation using these nanorods was estimated to be up to 97 %. Possibly, the generated of the hydroxyl radicals on the nanorods surface was suggested for such activity.

Chen et al. [59] have reported $SrNb_2O_6$ nanorods with a growth direction <100> as photo catalysts for water splitting reaction, where higher activity was observed for the rods that also possessed high BET surface area. Core/shell nanorods also show surprising catalytic activity as reported by Amirav et al. [40]. The starting materials were CdS nanorods containing a spherical CdSe seed (see also Sects. 6.2, 6.3 of this review). Pt nanoparticles were then grown selectively at the tips of the nanorods (Fig. 6.19a–h). As a comparison, the authors synthesized also "CdS-only" nanorods (i.e. not carrying a CdSe seed buried inside) and grew Pt domains at their tip regions. The CdSe/CdS-Pt nanorods had a higher catalytic activity than the "CdS-only"-Pt nanorods, due to the more efficient charge separation in the former rods; upon photoexcitation, holes were localized quickly in the CdSe region, while electrons were localized in the Pt domains, hence far from the holes. This type of charge separation was not possible for the "CdS-only"-Pt nanorods. The hydrogen evolution rate on the nanorods surface was shown to be a function of the light intensity, indicating that nanorods surface remains active and stable during the reaction. Interestingly, the longer nanorods ($\sim$70 nm) were 4 times more photocatalytically active for hydrogen evolution than the 27 nm long nanorods. Nanorod samples of various other lengths were tested, and this trend was confirmed. Therefore, apart from the enhanced charge separation (in case of CdSe/CdS-Pt nanorods), it is also important to note that the number of active sites suitable for adsorption of the reactive species increased in the longer nanorods, which also helped to increase the activity of the catalysts.

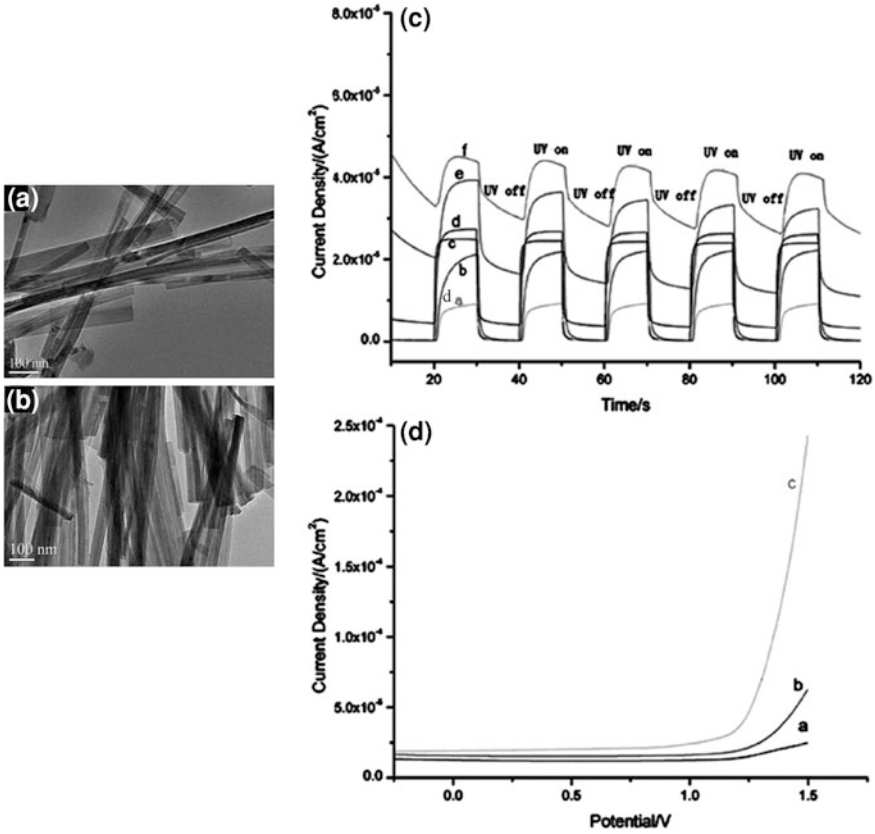

Fig. 6.17 TEM images of **a** undoped TiO_2 nanorods, **b** TiO_2 nanorods doped with 3 mol % Cr, **c** photocurrent response curves for the sample at different applied electrode potentials in 0.5 M Na_2SO_4 under Hg lamp pulsed irradiation ($\sim$8mW/cm^2) [commercial anatase (a), undoped TiO_2 (b), 3 mol Cr % doped TiO_2 (c), commercial TiO_2 1.5 V (d), undoped TiO_2 1.5 V (e), and 3 mol % Cr doped TiO_2 i.5 V (f)], and **d** variation of photo current density vs applied electrode potential for the samples in 0.5 M N_2SO_4, under Hg lamp irradiation ($\sim$8mW/cm^2): [commercial anatase (a), undoped TiO_2 (b), and 3 mol Cr % doped (c)]. Taken with permission from Ref. [57]

6.3 Outlook and Applications

From the recent reports on anisotropic nanocrystals based heterogeneous catalytic systems (mainly rod-shape and branched), we notice clearly that their catalytic properties and other catalytic relevant features strikingly differ from their bulk and isotropic nanostructures in a wide range of catalytic reactions in terms of their activity and specificity. The key factors that account for their enhanced catalytic potential are: their high surface areas, the exposition of the clearly defined crystals planes, and excellent mechanical properties. Remarkably, all these key properties can be tuned by varying the nanocrystal growth, the elongation direction, and the

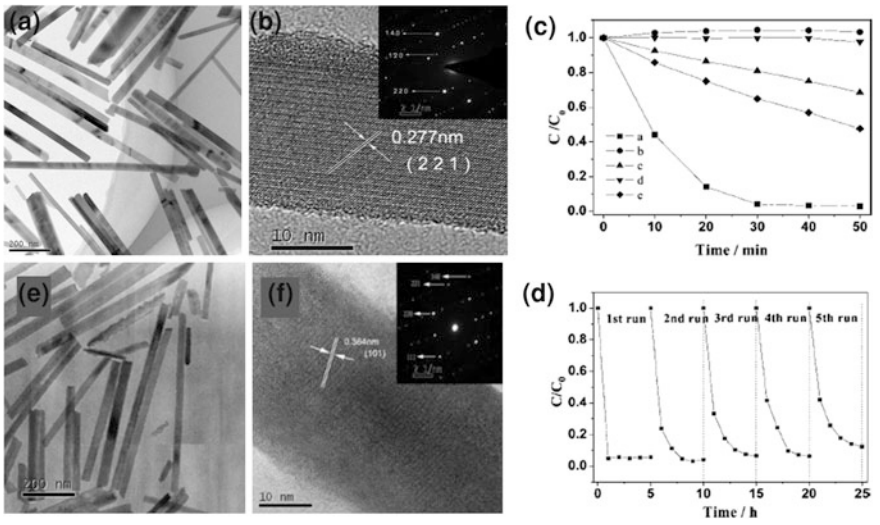

Fig. 6.18 **a** TEM image of Sb_2S_3 nanorods. **b** HRTEM image of a Sb_2S_3 nanorod. **c** Photo catalytic properties of different catalysts: [*square* Sb_2S_3 nanorods under visible light, *circle* Sb_2S_3 nanorods in the *dark*; *triangel* CdS under visible light; *triangle* P25-N under visible light; *black diamond* P25-N under UV light]. **d** Cyclic runs in the photo degradation of MO in the presence of Sb_2S_3 nanorods under visible light irradiation. **e** TEM image. **f** HRTEM image of the Sb_2S_3 nanorods after the catalytic reaction. Taken with permission from Ref. [58]

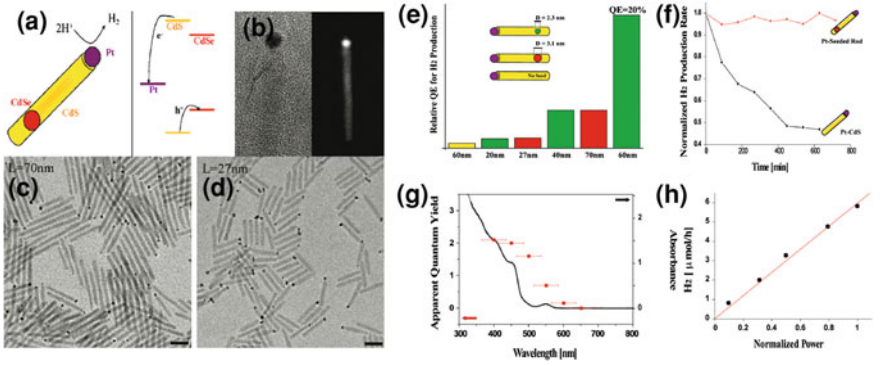

Fig. 6.19 **a** A sketch of the CdSe/CdS-Pt nanorods, with energy band diagram indicating that holes are confined to the CdSe region, while the electrons are transferred to Pt nanoparticles. **b** HRTEM (*left*) and HAADF images (*right*) of a CdSe/CdS-Pt nanorod. **c**, **d** TEM images of Pt-tipped of two samples of CdSe/CdS-Pt nanorods, with lengths equal to 27 and 70 nm, respectively. **e** Relative quantum efficiency of hydrogen production. **f** Hydrogen production rate from CdSe/CdS-Pt nanorods and from "CdS-only"-Pt nanorods. **g** Influence of the incident light wavelength on the quantum yield for hydrogen production. **h** Influence of light intensity (*white light* 0–1.3 W) on the hydrogen production rate. Taken with permission from Ref. [40]

size range and shape. This tunability makes them a technologically viable and efficient material for catalysis. Furthermore, the nanorod-shaped structures have also been shown to be capable of recovery and multiple use. Metal nanorods and metal nanoparticles that incorporated metal-oxide support nanorod hetero-structures seem promising nanocatalysts for a number of highly demanding chemical reactions, such as water-splitting, methanol oxidation, CO oxidation and organic synthesis. Among them, CO oxidation is one of the most studied heterogeneous catalytic reactions, which is regarded as a benchmark for many catalytic studies, in spite of its fundamental importance in three-way catalyst (TWC) for automotive gas exhaust, industrial pollution control and in reformate purification (to remove CO) for proton exchange membrane (PEM) fuel cells. Here, the CO oxidation reaction needs more efficient and yet low cost catalyst particles. In this respect the elongated nanocrystals are often shown to be stable and highly active even at very low temperatures. In parallel, the shape dependent catalytic properties would be much appreciated, if the catalyst particles exhibit a high degree of mechanical stability at the electrodes level, for example as electro-catalysts and photo-electrocatalyst. In such electrodes, the active particles need to be robust upon repetitive oxidation (or reduction) of the eletroactive species at the electrode/electrolyte interface, while promoting efficient e^- transport/transfer without undergoing any physical/chemical degradation. Here the nanorods have demonstrated to meet with such demands.

Here, it is perhaps useful to mention that in lithium ion batteries too, the elongated nanocrystals (rods and wires) show a higher mechanical stability to accommodate the cycling stress that is caused upon lithium ion intercalation/de-intercalation via charge/discharge cycles, such that the overall morphology could be well preserved for a prolonged time of charge/discharge cycles. The specific crystals exposition to the Li ions electrolyte could be beneficial, since the Li ions diffusion to the active particles could be improved. In addition, the rod-shaped or elongated active particles also help to reduce the Li ions diffusion path length in the electrodes, and increases the electrode/electrolyte contact area, which are crucial aspects for developing batteries with high rate capability. In organic synthesis, one feature required of any catalyst is their ability to selectively catalyze the reactions in order to yield the desired product, especially in situations where a number of by-products could be expected. This area of research will significantly be improved and renewed through the specificity of the nanorod catalyst particles. On the other hand, semiconductor and metal nanorods have been introduced as a new class of catalytic materials that exhibit higher activity and selectivity for a variety of reactions. As their absorption can be tuned across ultraviolet, visible and infrared regions, they could be employed as photo-catalysts for a wide range of photo conversion reactions. Here, one appealing aspect of the elongated nanostructures is their tendency to sustain an efficient charge-separation (electron-hole pair generation) that occurs at the semiconductor/metal junction upon illumination. And this could be varied upon tuning the length of the elongation direction of nanocrystals, thus allowing to design photo-anodes with high efficiency.

References

1. Somorjai GA (1996) Modern surface science and surface technologies: an introduction. Chem Rev 96(4):1223–1235. doi:10.1021/cr950234e
2. Christensen CH, Norskov JK (2008) A molecular view of heterogeneous catalysis. J Chem Phys 128(18):182503. doi:10.1063/1.2839299
3. Somorjai GA, Park JY (2008) Molecular factors of catalytic selectivity. Angew Chem Int Ed 47(48):9212–9228. doi:10.1002/anie.200803181
4. Min BK, Friend CM (2007) Heterogeneous gold-based catalysis for green chemistry: low-temperature CO oxidation and propene oxidation. Chem Rev 107(6):2709–2724. doi:10.1021/cr050954d
5. Heitbaum M, Glorius F, Escher I (2006) Asymmetric heterogeneous catalysis. Angew Chem Int Ed 45(29):4732–4762. doi:10.1002/anie.200504212
6. Roucoux A, Schulz J, Patin H (2002) Reduced transition metal colloids: a novel family of reusable catalysts? Chem Rev 102(10):3757–3778. doi:10.1021/cr010350j
7. Norskov JK, Bligaard T, Rossmeisl J, Christensen CH (2009) Towards the computational design of solid catalysts. Nat Chem 1(1):37–46. doi:10.1038/nchem.121
8. Cuenya BR (2010) Synthesis and catalytic properties of metal nanoparticles: size, shape, support, composition, and oxidation state effects. Thin Solid Films 518(12):3127–3150. doi:10.1016/j.tsf.2010.01.018
9. Kiskinova M (1996) Surface structure and reactivity: reactions on face-centered cubic (110) metal surfaces involving adatom-induced reconstructions. Chem Rev 96(4):1431–1447. doi:10.1021/cr950226y
10. Stamenkovic VR, Fowler B, Mun BS, Wang GF, Ross PN, Lucas CA, Markovic NM (2007) Improved oxygen reduction activity on Pt_3Ni (111) via increased surface site availability. Science 315:493–497. doi:10.1126/science.1135941
11. Lewis LN (1993) Chemical catalysis by colloids and clusters. Chem Rev 93(8):2693–2730
12. Schmid G (1992) Large clusters and colloids: metals in the embryonic state. Chem Rev 92(8):1709–1727. doi:10.1021/cr00016a002
13. Astruc D, Lu F, Aranzaes JR (2005) Nanoparticles as recyclable catalysts: the frontier between homogeneous and heterogeneous catalysis. Angew Chem Int Ed 44(48):7852–7872. doi:10.1002/anie.200500766
14. Gates BC (1995) Supported metal clusters: synthesis, structure, and catalysis. Chem Rev 95(3):511–522
15. Wilson OM, Knecht MR, Garcia-Martinez JC, Crooks RM (2006) Effect of Pd nanoparticle size on the catalytic hydrogenation of allyl alcohol. J Am Chem Soc 128(14):4510–4511. doi:10.1021/ja058217m
16. Herzing AA, Kiely CJ, Carley AF, Landon P, Hutchings GJ (2008) Identification of active gold nanoclusters on iron oxide supports for CO oxidation. Science 321(5894):1331–1335. doi:10.1126/science.1159639
17. El-Sayed MA (2004) Small is different: shape-, size-, and composition-dependent properties of some colloidal semiconductor nanocrystals. Acc Chem Res 37(5):326–333
18. Yin Y, Alivisatos AP (2005) Colloidal nanocrystal synthesis and the organic-inorganic interface. Nature 437(7059):664–670
19. Cozzoli PD, Pellegrino T, Manna L (2006) Synthesis, properties and perspectives of hybrid nanocrystal structures. Chem Soc Rev 35(11):1195–1208
20. Tao AR, Habas S, Yang PD (2008) Shape control of colloidal metal nanocrystals. Small 4(3):310–325. doi:10.1002/smll.200701295
21. Chen J, Lim B, Lee EP, Xia Y (2009) Shape-controlled synthesis of platinum nanocrystals for catalytic and electrocatalytic applications. Nano Today 4(1):81–95. doi:10.1016/j.nantod.2008.09.002

22. Komanicky V, Iddir H, Chang KC, Menzel A, Karapetrov G, Hennessy D, Zapol P, You H (2009) Shape-dependent activity of platinum array catalyst. J Am Chem Soc 131(16):5732–5733
23. Narayanan R, El-Sayed MA (2004) Shape-dependent catalytic activity of platinum nanoparticles in colloidal solution. Nano Lett 4(7):1343–1348. doi:10.1021/nl0495256
24. Park KH, Jang K, Kim HJ, Son SU (2007) Near-monodisperse tetrahedral rhodium nanoparticles on charcoal: the shape-dependent catalytic hydrogenation of arenes. Angew Chem Int Ed 46(7):1152–1155
25. Narayanan R, El-Sayed MA (2008) Some aspects of colloidal nanoparticle stability, catalytic activity, and recycling potential. Top Catal 47(1–2):15–21. doi:10.1007/s11244-007-9029-0
26. Wang C, Hu Y, Lieber CM, Sun S (2008) Ultrathin Au nanowires and their transport properties. J Am Chem Soc 130(28):8902–10.1021/ja803408f
27. Petrova H, Perez-Juste J, Zhang Z, Zhang J, Kosel T, Hartland GV (2006) Crystal structure dependence of the elastic constants of gold nanorods. J Mater Chem 16(40):3957–3963. doi:10.1039/b607364f
28. Petrova H, Perez-Juste J, Zhang ZY, Zhang J, Kosel T, Hartland GV (2006) Crystal structure dependence of the elastic constants of gold nanorods. J Mater Chem 16(40):3957–3963. doi:10.1039/b607364f
29. Perez-Juste J, Pastoriza-Santos I, Liz-Marzan LM, Mulvaney P (2005) Gold nanorods: synthesis, characterization and applications. Coord Chem Rev 249(17–18):1870–1901. doi:10.1016/j.ccr.2005.01.030
30. Baranov D, Fiore A, van Huis M, Giannini C, Falqui A, Lafont U, Zandbergen H, Zanella M, Cingolani R, Manna L (2010) Assembly of colloidal semiconductor nanorods in solution by depletion attraction. Nano Lett 10(2):743–749. doi:10.1021/Nl903946n
31. Figuerola A, Franchini IR, Fiore A, Mastria R, Falqui A, Bertoni G, Bals S, Van Tendeloo G, Kudera S, Cingolani R, Manna L (2009) End-to-end assembly of shape-controlled nanocrystals via a nanowelding approach mediated by gold domains. Adv Mater 21(5):550. doi:10.1002/adma.200801928
32. Nobile C, Carbone L, Fiore A, Cingolani R, Manna L, Krahne R (2009) Self-assembly of highly fluorescent semiconductor nanorods into large scale smectic liquid crystal structures by coffee stain evaporation dynamics. J Phys Condens Matter 21(26):264013
33. Habas SE, Lee H, Radmilovic V, Somorjai GA, Yang P (2007) Shaping binary metal nanocrystals through epitaxial seeded growth. Nat Mater 6(9):692–697. doi:10.1038/nmat1957
34. Lee I, Delbecq F, Morales R, Albiter MA, Zaera F (2009) Tuning selectivity in catalysis by controlling particle shape. Nat Mater 8(2):132–138. doi:10.1038/nmat2371
35. Bai X, Gao Y, Liu H-g, Zheng L (2009) Synthesis of amphiphilic ionic liquids terminated gold nanorods and their superior catalytic activity for the reduction of nitro compounds. J Phys Chem C 113(41):17730–17736. doi:10.1021/jp906378d
36. Berhault G, Bisson L, Thomazeau C, Verdon C, Uzio D (2007) Preparation of nanostructured Pd particles using a seeding synthesis approach: application to the selective hydrogenation of buta-1, 3-diene. Appl Catal A Gen 327(1):32–43. doi:10.1016/j.apcata.2007.04.028
37. Chen YH, Hung HH, Huang MH (2009) Seed-mediated synthesis of palladium nanorods and branched nanocrystals and their use as recyclable Suzuki coupling reaction catalysts. J Am Chem Soc 131(25):9114–9121. doi:10.1021/ja903305d
38. Miyaura N, Suzuki A (1995) Palladium-catalyzed cross-coupling reactions of organoboron compounds. Chem Rev 95(7):2457–2483
39. Huang X, Zheng N (2009) One-pot, high-yield synthesis of 5-fold twinned pd nanowires and nanorods. J Am Chem Soc 131(13):4602. doi:10.1021/ja9009343
40. Amirav L, Alivisatos AP (2010) Photocatalytic hydrogen production with tunable nanorod heterostructures. J Phys Chem Lett 1(7):1051–1054. doi:10.1021/jz100075c
41. Maksimuk S, Yang SC, Peng ZM, Yang H (2007) Synthesis and characterization of ordered intermetallic PtPb nanorods. J Am Chem Soc 129(28):8684. doi:10.1021/ja071980r

42. Liu F, Lee JY, Zhou WJ (2005) Multisegment PtRu nanorods: electrocatalysts with adjustable bimetallic pair sites. Adv Funct Mater 15(9):1459–1464. doi:10.1002/adfm.200400523
43. Liu QS, Yan Z, Henderson NL, Bauer JC, Goodman DW, Batteas JD, Schaak RE (2009) Synthesis of CuPt nanorod catalysts with tunable lengths. J Am Chem Soc 131(16):5720. doi:10.1021/Ja810151r
44. Xie XW, Li Y, Liu ZQ, Haruta M, Shen WJ (2009) Low-temperature oxidation of CO catalysed by Co_3O_4 nanorods. Nature 458(7239):746–749. doi:10.1038/nature07877
45. Zhou KB, Wang RP, Xu BQ, Li YD (2006) Synthesis, characterization and catalytic properties of CuO nanocrystals with various shapes. Nanotechnology 17(15):3939–3943. doi:10.1088/0957-4484/17/15/055
46. Si R, Flytzani-Stephanopoulos M (2008) Shape and crystal-plane effects of nanoscale ceria on the activity of Au-CeO_2 catalysts for the water-gas shift reaction. Angew Chem Int Ed 47(15):2884–2887. doi:10.1002/anie.200705828
47. Lee YM, Garcia MA, Huls NAF, Sun SH (2010) Synthetic tuning of the catalytic properties of Au-Fe_3O_4 nanoparticles. Angew Chem Int Ed 49(7):1271–1274. doi:10.1002/anie.200906130
48. Boucher MB, Goergen S, Yi N, Flytzani-Stephanopoulos M (2011) Shape effects in metal oxide supported nanoscale gold catalysts. Phys Chem Chem Phys 13(7):2517–2527. doi:10.1039/c0cp02009e
49. Sayle TXT, Sayle DC (2010) Elastic deformation in ceria nanorods via a fluorite-to-rutile phase transition. ACS Nano 4(2):879–886. doi:10.1021/Nn901612s
50. Han WQ, Wen W, Hanson JC, Teng XW, Marinkovic N, Rodriguez JA (2009) One-dimensional ceria as catalyst for the low-temperature water-gas shift reaction. J Phys Chem C 113(52):21949–21955. doi:10.1021/jp9066444
51. Liang SH, Bulgan FTG, Zong RL, Zhu YF (2008) Effect of phase structure of MnO_2 nanorod catalyst on the activity for CO oxidation. J Phys Chem C 112(14):5307–5315. doi:10.1021/jp0774995
52. Sui N, Duan YZ, Jiao XL, Chen DR (2009) Large-scale preparation and catalytic properties of one-dimensional alpha/beta-MnO_2 nanostructures. J Phys Chem C 113(20):8560–8565. doi:10.1021/jp810452k
53. Lin YG, Hsu YK, Chen SY, Lin YK, Chen LC, Chen KH (2009) Nanostructured zinc oxide nanorods with copper nanoparticles as a microreformation catalyst. Angew Chem Int Ed 48(41):7586–7590. doi:10.1002/anie.200902907
54. Gu C, Cheng C, Huang H, Wong T, Wang N, Zhang T-Y (2009) Growth and photocatalytic activity of dendrite-like ZnO@Ag heterostructure nanocrystals. Cryst Growth Des 9(7):3278–3285. doi:10.1021/cg900043k
55. Elmalem E, Saunders AE, Costi R, Salant A, Banin U (2008) Growth of photocatalytic CdSe-Pt nanorods and nanonets. Adv Mater 20(22):4312–4317. doi:10.1002/adma.200800044
56. Yu CL, Yu JC (2009) Sonochemical fabrication, characterization and photocatalytic properties of Ag/$ZnWO_4$ nanorod catalyst. Mater Sci Eng B-Adv Funct Solid-State Mater 164(1):16–22. doi:10.1016/j.mseb.2009.06.008
57. Zhu H, Tao J, Dong X (2010) Preparation and photoelectrochemical activity of Cr-doped TiO_2 nanorods with nanocavities. J Phys Chem C 114(7):2873–2879. doi:10.1021/Jp9085987
58. Sun M, Li DZ, Li WJ, Chen YB, Chen ZX, He YH, Fu XZ (2008) New photocatalyst, Sb_2S_3, for degradation of methyl orange under visible-light irradiation. J Phys Chem C 112(46):18076–18081. doi:10.1021/Jp806496d
59. Chen D, Ye J (2009) Selective-synthesis of high-performance single-crystalline Sr(2)Nb(2)O(7) nanoribbon and SrNb(2)O(6) nanorod photocatalysts. Chem Mater 21(11):2327–2333. doi:10.1021/cm8034714
60. Ertl G (2008) Reactions at surfaces: from atoms to complexity (Nobel lecture). Angew Chem Int Ed 47(19):3524–3535. doi:10.1002/anie.200800480

61. Xiong Y, Cai H, Wiley BJ, Wang J, Kim MJ, Xia Y (2007) Synthesis and mechanistic study of palladium nanobars and nanorods. J Am Chem Soc 129(12):3665–3675. doi:10.1021/ja0688023
62. Katz-Boon H, Rossouw CJ, Weyland M, Funston AM, Mulvaney P, Etheridge J (2011) Three-dimensional morphology and crystallography of gold nanorods. Nano Lett 11(1):273–278. doi:10.1021/nl103726k
63. Ling T, Yu H, Liu X, Shen Z, Zhu J (2008) Five-fold twinned nanorods of FCC Fe: synthesis and characterization. Cryst Growth Des 8(12):4340–4342. doi:10.1021/cg800108n

Chapter 7
Mechanical Properties of Nanorods and Melting Studies

7.1 Introduction

The synthesis of highly performing materials, the constant miniaturization of micro electro-mechanical devices (MEMS), the fabrication of thin films for the micro- and nano-electronic industry, the development of tribological applications, the deposition of hard coatings on cutting tools, have all raised questions related to the mechanical behavior (and its predictability) at the micro- and nanoscale, both in "bulk" nanostructured materials (i.e. polycrystalline materials composed of grains in the nanosize range), and in individual nanocrystals. The study of mechanical properties in materials of physical geometries in the micron and sub-micron (i.e. nanometer) size range is still in its infancy. "Bulk" nanostructured materials are known to possess increased strength and the early experiments already carried out several decades ago on tensile testing of "single-crystalline" metal whiskers with micrometer transverse sides have evidenced strengths much higher than the bulk value [1]. The increased strength of single nanocrystals could be useful for applications of these materials as active probes in nano-indentation, scanning probe microscopy and field emission [2–4], among others.

In the last decade, pure metals and alloys with at least one dimension in the micro- and nanoscale range have been investigated, thanks to advances in the fabrication of new generations of samples suitable for mechanical testing (for example micropillars prepared by focused ion beam) and in various techniques for studying their stress and deformation properties, under both tensile and compressive deformation, the latter for instance via micro/nano-indentation [5]. All these studies have revealed a marked deviation in the mechanical properties of samples from bulk-like behavior already when their size is of the order of a few micrometers, which is comparable to the length scale of many plasticity mechanisms based on dislocation nucleation and propagation (see next sections).

In the following, after a brief introduction on mechanical properties in general and on the features of "bulk" nanostructured materials (henceforth referred to as "nanocrystalline" materials) we will focus our attention on single micro- and nano-crystals. In the discussion, there will be no particular reason why we will take into consideration elongated micro- and nano-particles (i.e. whiskers and pillars),

R. Krahne et al., *Physical Properties of Nanorods*,
NanoScience and Technology, DOI: 10.1007/978-3-642-36430-3_7,

except for the fact that these shapes are those that have facilitated mechanical testing up to now.

7.2 Mechanical Properties of Materials: A Few Useful Definitions

In this section we will recall a few definitions pertinent to the mechanical properties of materials that will be used in the other sections. For a more scholarly (and comprehensive) coverage of the topic, the reader is referred to various textbooks (for example [6–9]).

All solids are elastic up to some extent. It is possible in other words to identify a set of conditions under which a force is applied to a rigid body, such that the force will cause a slight change in the dimension/shape of the body, due to its twisting, compressing, or pulling, but then the body will return to its initial state once the deforming force is removed. The deforming force (F) per unit area (A) is called stress, or equivalently stated F is the magnitude of the force applied perpendicular to the area A on the solid object. Hence stress produces strain on a physical body. Figure 7.1a for example shows a cylinder undergoing a tensile stress. Here the strain produced due to tensile stress is a dimensionless quantity ($\Delta l/l$). The opposite situation, i.e. the cylinder being compressed uniaxially, is referred to as of "compressive stress".

Under the conditions of perfect elastic behavior of a body, stress and strain are proportional to each other and the proportionality constant is called modulus of elasticity or Young's modulus (E). The Young's modulus of an isotropic elastic material is a parameter that is related to its stiffness, and is defined as:

$$\frac{F}{A} = E\frac{\Delta l}{l} \tag{7.1}$$

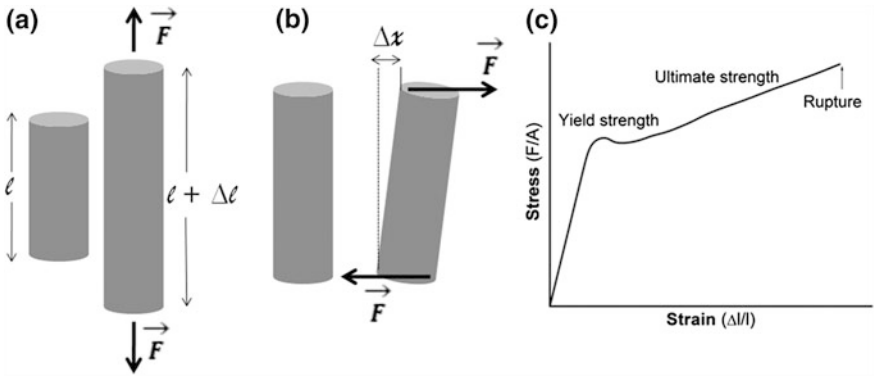

Fig. 7.1 **a** A cylinder shaped solid under tensile stress and **b** under shear stress deforms by an amount Δx; **c** A typical stress–strain curve, in present case is referred to a steel specimen

In case of shear stress (G) the force vector is applied parallel to one face of the material, rather than perpendicular to it (in Fig. 7.1b the force is applied parallel to the basal planes of the cylinder). Here the corresponding modulus is called shear modulus and is written as:

$$\frac{F}{A} = G\frac{\Delta x}{l} \tag{7.2}$$

where $\Delta x/l$ is the dimensionless strain. Shear stress plays for example a crucial role in the buckling of shafts that rotate under a given load.

A stress–strain curve of a material is generated by applying an increasing stress to a sample and by measuring its strain. An example of stress–strain curve is shown in Fig. 7.1c. The stress–strain curve is generally composed of two regions: a region of elastic behavior, in which, as said before, the material returns to its initial states once the stress is removed, and a region of plastic behavior, in which the deformation in the material is irreversible. The value of the stress corresponding to the change from elastic to plastic behavior is defined instead as the "yield stress": it is the stress past which the crystal lattice of the material becomes unstable and does not respond elastically any more. The corresponding point in the stress–strain curve is called the "yield point". The ideal strength of a material is defined as the critical stress at which a perfect, defect-free crystal at 0 K yields under uniform deformation [10]. The "ideal" strength sets an upper limit to the strength that the material can attain under given loading conditions. A real bulk material yields at a stress that is below its ideal strength, due to the presence of lattice defects such as dislocations and grain boundaries.

Work hardening, also known as "strain hardening", is referred to when a metal, at a temperature well below its melting point, is strained past the yield point. What is commonly observed is that an increased stress is needed, past the yield point, to produce a further plastic deformation. Hence the material is hardened, or in other words it becomes more difficult to deform. The behavior can be seen in the plastic region of stress–strain curve of Fig. 7.1c: the curve, past the yield point has a different slope than in the elastic region, but such slope is generally greater than zero (as would be for a perfectly plastic material), and is known as the "work (or strain) hardening coefficient". Work hardening can be explained by considering that a plastic deformation is associated with the movement and multiplication of a large number of dislocations in the crystal. During plastic deformation, the mutual distance between dislocations decreases and they start blocking the movement of each other, i.e. they start forming dislocation *junctions* (a mechanism also known as "dislocation forest hardening"), and additionally they start piling up at grain boundaries. Past this point, a higher stress is required to make the dislocations move further, i.e. to induce a further plastic deformation, up to the ultimate strength, which is the point of maximum stress in the curve. The shape of the

stress–strain curve in the region of plastic behavior region is strongly dependent on the material but also on the conditions under which the test is carried out. For example, the ultimate strength might not correspond to the strength at which the sample ruptures. Often, stress–strain curves are plotted in terms of engineering stress and engineering strain, meaning that the stress and strain are calculated based on the original dimensions of the sample and not based on their values during the measurement. As another useful definition, the ductility of a material can be defined as its ability to undergo a plastic deformation (usually under tensile stress) without fracturing.

It is useful, for the discussion that will follow, to define the concept of dislocation-displacement vector, also known as Burgers vector, associated to a dislocation [9]. To identify this vector in a simple cubic lattice, we draw a closed loop in the crystal once a dislocation has been inserted, making sure that the loops encircles the region where the dislocation line is present and where the displacement from the ideal reference crystal is large (Fig. 7.2a), we then record the number of lattice vectors travelled on each side of the loop. Finally, we trace the same loop in a real crystal, made by the same number of lattice vectors as before. The loop this time will not be closed (Fig. 7.2b). The vector that is required to close the loop is the Burgers vector. In practice, the Burgers vector identifies the direction and the magnitude of the lattice dislocation introduced by the movement of a dislocation. Depending on the type of dislocation, the Burgers vector is parallel (i.e. for a screw dislocation) or perpendicular (i.e. for an edge dislocation) to the dislocation line. For a detailed discussion on Burgers vectors, see for example Ref. [9].

As said before, the motion of dislocations is what produces plastic deformation in a crystal. This plastic deformation is manifested itself by a "slip", i.e. crystal planes glide along each other. Slip in a crystal in general occurs along some specific planes, those that contain the shortest Burgers vectors. For face-centered-cubic (*fcc*) metals, these are the 111 planes (i.e. the close-packed ones) and the directions of slip are any of the $\langle 110 \rangle$ ones. For body-centered-cubic (*bcc*) metals instead, since there are no close-packed planes, any slip along a specific plane type and direction type requires an activation energy. As we will see, this difference

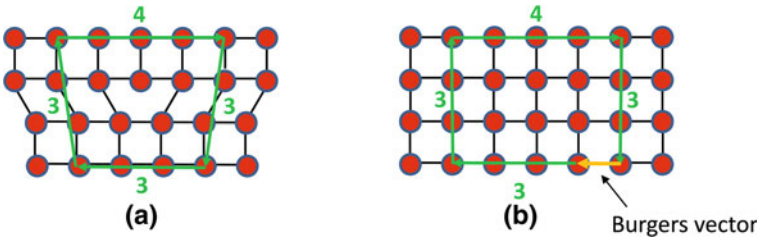

Fig. 7.2 Definition of a Burgers vector. A "Burgers circuit" is drawn in a real crystal (**a**) and in a perfect crystal. (**b**) In both cases the loop spans the same number of lattice vectors. The vector that is required to close the loop in the ideal crystal is the Burgers vector

between *fcc* and *bcc* metals translates into a mechanical behavior that is completely different for the two types of lattices, even at the nanoscale.

7.3 Studies on Elastic Properties of Nanorods and Nanowires

Several methods have been proposed to determine the Young's modulus and more in general to study the elastic properties of nanorods, nanowires and nanotubes, among them AFM bending experiments for metal nanowires [11, 12] time-resolved spectroscopy approaches for nanorods [13, 14] (see also Sect. 7.4), and thermal vibrations using TEM [15, 16], often coupled with theoretical calculations. In an AFM bending experiment, the force mapping function of the instrument is used to perform spatially resolved deformations over the full length of a suspended one-dimensional sample, while in time-resolved spectroscopy studies an ultrafast pump laser is used in order to heat the particles and a tunable pulse is used as a probe. Heating by laser irradiation coherently excites the phonon modes of the particles, which correlate with the expansion coordinates of the particle [17] (see also Sect. 7.4). One has to keep in mind however that both classes of experiments give results that are affected by fairly large uncertainties, due both to intrinsic limitations of the techniques and to the heterogeneity of the samples.

Not always however the measured value of Young's modulus of the nanowires/nanorods is found to be larger than the bulk value. As an example, samples of gold nanorods elongated along their [100] and [110] crystallographic direction exhibited a decrease ($\sim$20–30 %) in the value of Young's modulus with respect to the bulk $E_{[100]}$ and $E_{[110]}$ values [17–19]. Measured values of Young's modulus for the different Au nanorod samples (grown along the [100] direction) plotted against the surface-to-volume ratio are shown in Fig. 7.3. [17]. Similar results were observed by Hu et al. in the case of gold nanorods synthesized by wet chemical approaches [19]. This observation was generally explained as due to the high surface-to-volume ratio of the nanomaterials, since the ratio has a significant influence on their physical properties. Also, as discussed in Sect. 7.4, metal nanorods in some cases are made of multiple twins sharing an edge which corresponds to the elongation direction of the rods. Since such peculiar structure is not found in the corresponding bulk solid, the Young modulus along the elongation direction could differ from that of the bulk.

7.4 Plastic Behavior of Nanocrystalline Materials

Various studies have tried to extract an empirical scaling law effect relating the mechanical properties of a material with a length scale in the micro/nano-meter range. As already mentioned before, nanocrystalline materials exhibit increased

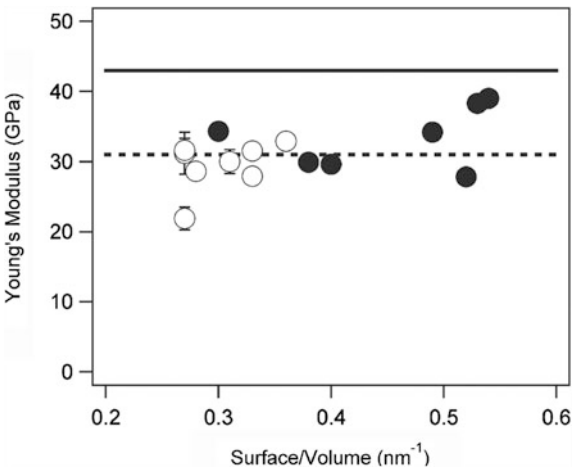

Fig. 7.3 Measured values of Young's modulus (as extracted from optical experiments) for different samples of Au nanorods grown along the [100] direction are plotted against the surface-to-volume ratio of the nanorods (calculated from the average dimensions determined by TEM). The solid horizontal line is the bulk value of $E_{[100]}$ and the dashed line is the average value determined from the experimental data. The open symbols correspond to samples prepared via photochemical reduction samples, whereas the closed symbols correspond to the samples prepared via chemical reduction. Taken with permission from Ref. [17]

yield strength compared to conventional materials, in some cases even approaching the theoretical value [20]. One generally accepted equation that describes this behavior is the so-called "modified Hall-Petch relation" [21] which correlates the yield strength σ_y of the nano/microstructure to its characteristic length scale d (for example the grain size in a microcrystalline material):

$$\sigma_y = \sigma_0 + kd^n \tag{7.3}$$

In the expression above σ_0 is the bulk yield strength and the terms k and n are materials-related constants. For metals n is usually found to be around -0.5, but in a more general expression this exponent can vary considerably (i.e. from -0.5 to -1). One needs to stress that the above expression is an empirical one, hence it does not reflect a universal mechanism. Indeed various physical mechanisms are involved in the plastic deformation of nanomaterials, and the relevance of each mechanism is dependent on a series of parameters (for example the specific material, the aspect ratio of the sample, its initial defect structure and even the type of mechanical test that is performed).

A major cause of plastic deformation in materials is the nucleation, propagation and multiplication of dislocations. Therefore, one commonly accepted reason why in nanocrystalline materials an increase in strength is observed at decreasing grain size is that dislocations cannot propagate freely throughout the material, due to the presence of a large number of two-dimensional obstacles, such as grain and

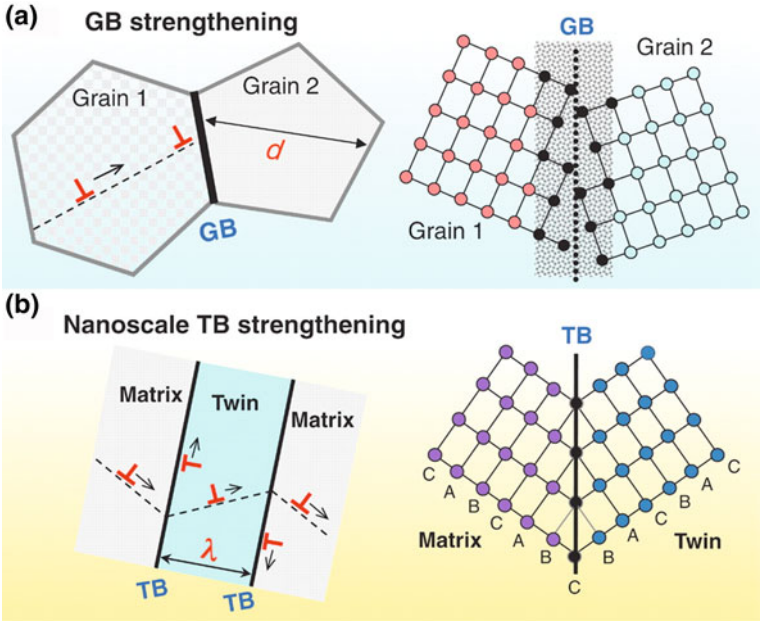

Fig. 7.4 **a** The propagation of a dislocation stops at a grain boundary. A grain boundary is however a incoherent, high-energy interface. **b** When a twin plane is present, the dislocation can slide along the twin plane, which helps improving ductility of the material. Taken with permission from Ref. [22]

interphase boundaries and stacking faults [20]. Stated simply, the smaller the size of the domains, the more obstacles dislocations encounter during their propagation, hence they more likely undergo piling up at such obstacles before they can multiply (Fig. 7.4a). Here, accumulation of stress builds up until dislocations are nucleated at the other side of the boundary, thus releasing stress at the boundary.

The same mechanism that obstructs dislocation motion reduces however the ductility of nanomaterials. Research in this area is very active, since it would be ideal to have nanocomposites for structural applications in which both strength and ductility are improved. Recent studies in the field have shown that carefully engineered coherent internal boundaries in nanoscale materials could achieve this goal [22]. As said before, common strengthening strategies rely on grain boundaries. These however are incoherent, i.e. there are no defined crystallographic relationships between the grains at the boundary, where voids and broken bonds are present. Grain boundaries have therefore high excess energy, and high stresses can deform and rupture the interface between the grains, so that the grains have a limited ability to accommodate dislocations before rupturing. Coherent internal boundaries on the other hand have lower excess energy and among them twin boundaries have high thermal and mechanical stability. Twin boundaries offer an additional pathway for dislocations to propagate: apart from propagation in neighboring domains, i.e. across the twin boundary, dislocations can glide along a

twin boundary. This is possible because of the coherent interface between the two domains along the boundary, which makes it possible for the material to undergo locally substantial shear deformation along the twin boundary, without rupturing (Fig. 7.4b). By such a mechanism, both higher strength and ductility can be achieved. Studies have revealed that higher strength and ductility are achieved at smaller twin thickness λ [22], with λ in the nanometer range.

7.5 Experiments on Plastic Behavior of Single Micro- and Nano-Crystalline Samples

7.5.1 Metallic Whiskers

It is known since many decades that micron and submicron whiskers of pure metals, which are fibrous (i.e. "elongated") single crystals with a high crystallinity, have tensile strengths that are much higher than the bulk value. Cu whiskers for instance have shown significantly high yield strengths, of the order of a few GPa [23]. Tensile tests of dislocation and micro-crack free $\langle 110 \rangle$-oriented single-crystalline elongated molybdenum nanoparticles, with diameters ranging from 25 to 90 nm (at the apex region) were conducted inside a field-ion microscope (FIM) [24]. The experimental values of tensile strength varied between 6.3 and 19.8 GPa and showed an increase with decreasing nanorod diameter. Also SiC nano-whiskers are known to have strengths considerably greater than those observed in corresponding bulk single crystals, approaching theoretical values [25, 26], and the greatest strengths were found for whiskers that fractured at the pinning site where the strain was the greatest, whereas lower values were found for SiC whiskers that fractured at some distance from the pinning site [26]. These observations suggested that defects can limit the strengths of the whiskers.

Thanks to recent advances in synthesis, manipulation and testing of materials, high-quality whiskers with sub-micrometer diameters have been fabricated and their mechanical behavior has been studied under tensile stress, evidencing yield stresses close to the theoretical value. As an example, single-crystalline Cu whiskers, fabricated by physical vapor deposition, of several micrometers in length and diameters below 300 nm were tested using a tensile stage mounted in a scanning electron microscope [27]. The whiskers exhibited an elastic behavior up to very large strain (2 %) and a yield strength as high as 6 GPa, after which either sudden failure or "strain bursts" were observed (i.e. large increases in strain at almost constant stress) [27]. Although no clear trend with size could be identified, due to the somehow stochastic behavior of the samples, samples with the smallest diameters exhibited higher yield stress, close to the theoretical one (Fig. 7.5). Many other examples exist in the literature of similar behavior.

A simple way of explaining the behavior of whiskers is by considering that they are generally defect-free before loading, hence a higher stress is required than in

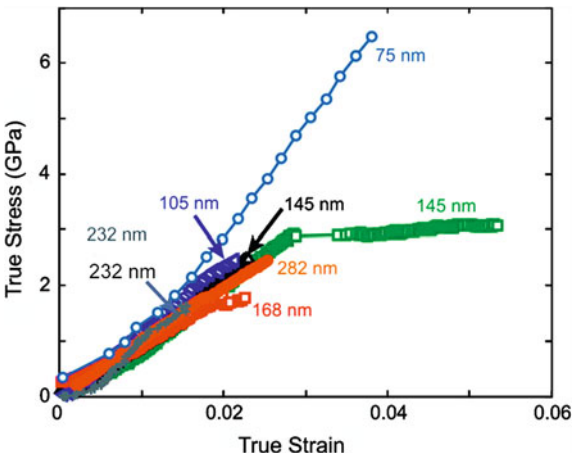

Fig. 7.5 Stress–strain curves from tensile testing of Cu whiskers (single crystals) with several micrometers in length and diameters below 300 nm. Taken with permission from Ref. [27]

the corresponding bulk materials to reach the onset of plastic deformation, because defects need to be generated in them. However, this does not set a basis for rationalizing and quantifying the observed trend in increasing yield strength with decreasing whisker size.

A relation linking yield strength and size can be found via Weibull statistics, which has been used to analyze fracture data in solids, in particular to correlate the probability of fracture as a function of the applied stress [28]. Weibull statistics correlates the number of critical defects in a solid to its volume or its surface area. Simply stated, the smaller the volume V of the sample or of its surface area A, the lower the probability of presence of critical defects, the higher will be its yield strength σ_y:

$$\sigma_y = \sigma_0 \left(\frac{V_0}{V}\right)^{1/m} \text{ or equivalently } \sigma_y = \sigma_0 \left(\frac{A_0}{A}\right)^{1/m} \tag{7.4}$$

In the expression above m is the Weibull parameter, which is an index of the dispersion of the distribution and is material dependent, while σ_0 is the yield strength for a reference volume V_0 or a reference surface A_0. The Weibull statistics however cannot be properly used on nanoscale materials like whiskers, because these are nearly defect-free or have only a small number of critical defects. Indeed, when applied to the analysis of fracture strengths of various nanostructures, it shows a poor correlation coefficient.

A modified version of the Weibull statistics has been proposed by Pugno and Ruoff in 2004 [29] and later termed as "nanoscale Weibull statistics" [30]. The new distribution correlated the yield strength not to the volume or to the surface area of the nanostructure, but to the number of critical defects, and introduced the concept of a "fracture quantum", namely the possibility that even a very small defect could cause the failure of a nearly defect-free structure. This new statistics showed a better correlation with experimental data [30] and was applied to a variety of nanostructures, including for example carbon nanofibers and WS_2 nanotubes [31].

7.5.2 Pillars

In recent years, several reports on deformation of small single crystalline pillars (both micron- and submicron-sized), prepared by focused ion beam, have appeared. Also in these studies an increased strength with decreasing size was observed, and stresses corresponding to a significant fraction of the theoretical strength were obtained in both uniaxial tension and compression tests of nano/micropillars [2, 32–35]. These pillars however were different from the defect-free metal whiskers discussed earlier, as they were characterized by the presence of dislocations already before the loading, therefore they were not defect-free. On the other hand they were single crystalline, therefore the increase in strength in these samples could not be explained by the presence of obstacles (like grain boundaries) to the propagation of dislocations, as for the polycrystalline materials discussed earlier. Therefore, a major conclusion of these works was that the decrease in sample size must somehow start affecting the mechanism connected with generation, multiplication and accumulation of defects.

In this respect it is worth recalling here some of the results of Uchic et al. [32], for example those on pure Ni and Ni_3Al-Ta micropillars. The authors prepared micropillars of various diameters, from 40 μm down to 500 nm, by focused ion beam, and tested them under compressive stress using a conventional nanoindenter equipped with a flat-punch indentation tip. For Ni, the 40 and 20 μm diameter samples behaved more or less like the bulk in terms of stress–strain curves, i.e. similar yield strength as for the bulk, a smooth transition from elastic to plastic behavior, and a steady state work hardening (see Fig. 7.6, top panel). SEM imaging after the loading tests evidenced the presence of slips bands, coherent with a deformation of the pillars along those directions. Pillars of 5 μm or below had a markedly different behavior, namely they were characterized by a much higher yield stress, then past the yield point they exhibited "strain bursts": the strain in the samples rapidly increased to values up to 19 %, so that large flat regions appeared in the stress–strain curve. Equivalently stated, a low work hardening rate was seen. Both the value of yield stress and of the strain burst depended on the sample (several 5 μm pillars were tested, all of them yielding at higher stress than the bulk, but each of them yielding at a different value and exhibiting a varying extent of strain burst). The overall behavior of these samples was therefore different from both larger samples (i.e. bulk-like) and from defect-free whiskers: while their yield strength were not in the high range of defect-free whiskers, they nonetheless were characterized by higher yield strength than the bulk, and also much lower work hardening rate than in the bulk. For Ni_3Al-Ta samples, the transition from bulk-like behavior was seen already for samples of 20 micron size (Fig. 7.6, bottom panel), so that the influence of sample size was observed at comparatively larger sizes than for Ni pillars.

Strain burst in these samples, as well as in the whiskers discussed earlier, are symptomatic of a single catastrophic event that sets the transition from the elastic to the plastic regime. They suggest a mechanism of plastic deformation that does

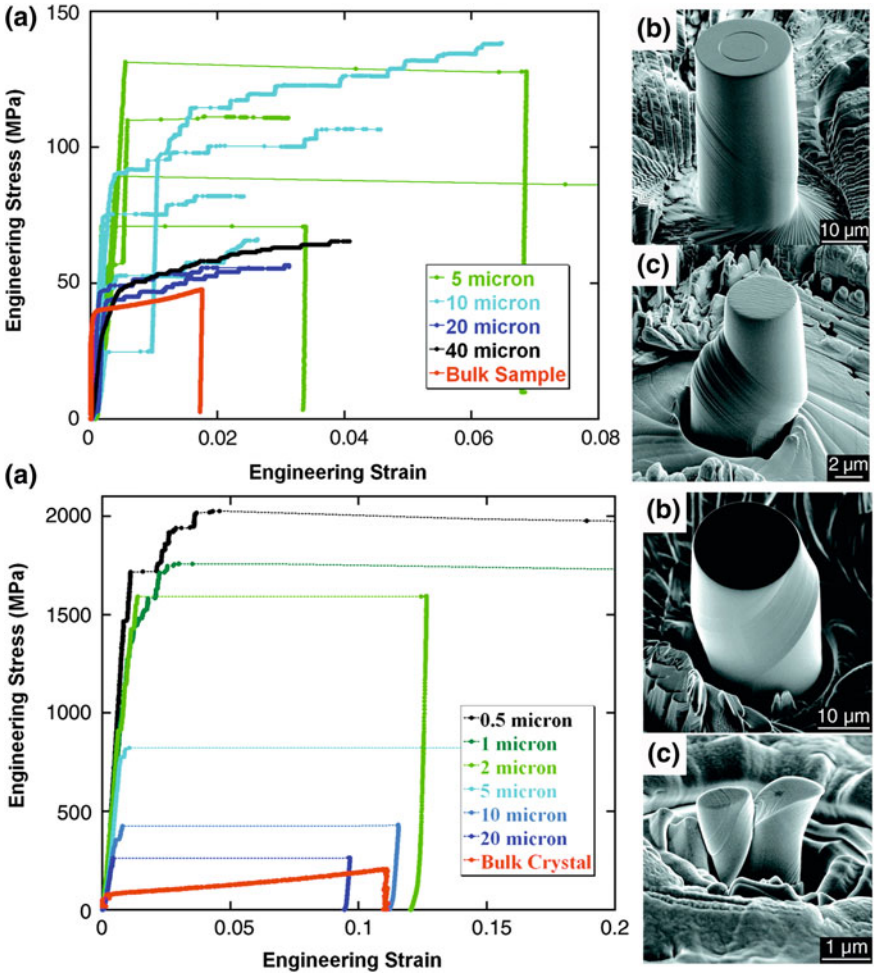

Fig. 7.6 *Top panel* **a** Stress–strain curves at room temperature for Ni micropillars with ⟨134⟩ crystallographic orientation and with various diameters (from 4 to 40 microns) and for a bulk crystal sample. **b** is a scanning electron microscopy image of a single pillar (20 micron diameter) before mechanical testing. The same sample is imaged in **c** after testing. This sample underwent a fast 19 % "strain burst" during testing. Large single-slip plane displacements can be seen in this sample. *Bottom panel* **a** Stress-strain curves at room temperature for Ni_3Al-Ta alloy micropillars with $< 123 >$ crystallographic orientation and with various diameters (from 0.5 to 20 microns) and for a bulk crystal sample. **b** is a scanning electron microscopy image of a singe pillar (20 micron diameter) after mechanical testing. This sample underwent a fast 10 % "strain burst" during testing. **c** This is another pillar, of 1 micron diameter which was completely sheared off during testing as a consequence of a large strain burst. All panels have been adapted with permission from Ref. [32]

not proceed through multiplication and accumulation of dislocations, which would show up in an appreciable work hardening rate, most likely because these dislocation-related processes are inhibited by a size effect.

7.6 Models of Plastic Behavior of Single Micro- and Nano-Crystalline Samples

7.6.1 Strain Gradients

The outcome of experiments like the ones described above has started several studies aiming at elucidating the mechanical behavior in confined systems and numerous computational models have been developed which go beyond the more traditional continuum models [5, 34, 36]. One critical rethinking on plasticity in confined dimensions concerns the common belief about the presence of strain gradients as the major reason of strain hardening in micro- and nano-materials. Indeed, most mechanical testing on these materials in the past had consisted of nano-indentation experiments, in which the plastic deformation was confined in a small region of a given sample. A relationship was found experimentally which correlated the square of the measured hardness of the material to the indentation depth, and is known as the "indentation size effect" [37]. This behavior was explained in the following way: especially when probing shallow depths with indentation, non-uniform stresses and strains are generated in the material, while much smaller stress and strain gradients are present in the material when the indented penetrates at greater depths. Such gradients generate so-called "geometrically necessary" dislocations which contribute to strain hardening of the material. A model was developed then that tried to correlate strain gradients with the indentation strain effect [38]. This model however suffers from the major drawback that it is not applicable to indentations depths shallower than 100 nm (where continuum mechanical models are not appropriate). Also, more recent experiments, such as the compression tests on nanopillars discussed earlier, have involved the uniaxial compression of samples in a way that no strain gradients were generated inside the pillars [33]. These experiments have revealed that pillars with smaller diameters were characterized by larger compressive stresses. Therefore, additional mechanisms should be operative in the plastic deformation of nanomaterials.

7.6.2 Dislocation Starvation

A simple mechanism that explains the increase in strain in single crystal micro- and nano-crystalline samples is the so called "dislocation starvation" [33]. In general, dislocation motion leads at some point to dislocation multiplication. This

process is characterized by a length scale δ, namely a dislocation can travel on average up to a distance δ before it can replicate itself. If however such length scale is comparable or smaller than the size of the crystal, the dislocation reaches the surface of the crystal, where it annihilates, before actually replicating itself. In this crystal, as soon as the "dislocation starvation" condition is met, higher stresses would be required in order to generate dislocations with smaller critical lengths, hence the yield strength of the material is increased. Length scales associated with dislocation multiplication are known for several materials (for example in silver such length scale is around 1 μm) [39], and they set a critical size for the physical dimension of a material below which it can exhibit a plastic behavior that is different from the bulk. The mechanism of dislocation starvation has been proved to be operative for example in in situ analysis of Ni micropillars under compressive strain [40].

We must recall that sub-micrometer crystals with diameters of a few hundreds of nanometers (<500 nm) might be dislocation-free, because their overall volume can be so small that even with a large density of dislocations ($10^{12}/m^2$) no dislocation is found in them. In these cases, the critical stress required to initiate the plastic behavior is the one needed to nucleate a dislocation from the surface. For such samples with "small" diameters the quality of the surface plays a key role. Nano-pillars, which are produced by focused ion beam, have a rather defective surface and in addition their basal plane is still connected to the bulk. Whiskers and nanowires on the other hand have smoother surfaces and they shown indeed higher strengths [41, 42] than pillars of comparable size.

7.6.3 Source Truncation Hardening

More recent studies have challenged the simple model of dislocation starvation [34, 36, 42]. The above model assumes that the initial density of dislocations in a material is independent of its size, and additionally that the number of dislocations in a deformed sample is equal to or even less than that in the initial non-deformed sample. Recent reports, for example on Nickel pillars with diameters in the 1–10 μm range [34], have shown that instead the density of dislocations in the deformed sample could even increase as the dimensions of the sample decrease, and that dislocation density can be higher than the initial density, thus in contradiction with the dislocation starvation mechanism. Therefore, more elaborate models of plasticity in confined dimensions have been proposed. Among them it is worth citing the work of Parthasarathy [42], which is in reality a further elaboration of the dislocation starvation mechanism, but which introduced the so-called "source truncation hardening" mechanism for rationalizing plastic behavior in confined dimensions. The model correlated the limited volume of a sample, the distribution of dislocation source lengths and the truncations of dislocation sources at the surface to the increase in strength in micro-crystals and sub-micrometer crystals.

In order to understand this mechanism, it is important to introduce a few concepts. First of all, we need to define the "critical resolved shear stress" (CRSS), which is the stress required for the first percolation event of a dislocation through the whole sample. In a bulk sample this can be correlated to the stress required to initiate and maintain the processes of dislocation nucleation and multiplication, keeping in mind that these occur in the presence of a dislocation forest. An additional important concept is the image stress. In an infinite, elastic medium, a dislocation generates a stress (tensor) field σ_{ij}^{∞}. In a finite medium, for example a thin film, if one assumes that dislocations generate the same field as in a bulk infinite solid, traction forces then develop at the surface of the film, due to interaction of dislocations with the surface (Fig. 7.7a). In order to cancel such traction forces, an image stress field σ_{ij}^{img} needs to be invoked (Fig. 7.7b). Therefore, the stress field σ_{ij}^{tot} of a finite, traction-free solid can be considered as the superposition of a bulk stress field σ_{ij}^{∞} (i.e. like the one generated if dislocations would propagate to infinity beyond the boundaries of the solid) and of an image stress field σ_{ij}^{img} (Fig. 7.7c):

$$\sigma_{ij}^{tot} = \sigma_{ij}^{\infty} + \sigma_{ij}^{img} \tag{7.5}$$

There are different approaches to calculate such image stress fields [43]. Image stresses, by exerting a force on dislocations, can modify the orientation of dislocations with respect to the surface.

We also need to describe the behavior of a typical source of dislocation, namely the Frank-Read source (see Fig. 7.8a) [8, 9], which is among the weakest sources of dislocation. This is a "double ended" source and starts as a straight dislocation in a crystal slip plane with its two ends pinned [9]. The details of the mechanism are not relevant for the present discussion, while it is sufficient to know that when a shear stress is applied on the slip plane, the dislocation lengthens and curves to an arc, while its ends stay pinned (the two ends will be called the "pins" from now on). Eventually, the dislocation bends further until it separates into a loop encircling the original pins and a new dislocation joining the pinning points. The loop expands further, while a new loop is being formed, and so on (Fig. 7.8a).

The "operation" of such a source in a sample of confined dimensions is shown in Fig. 7.8b, for a single source in a slip plane, and in Fig. 7.8c for an elongated,

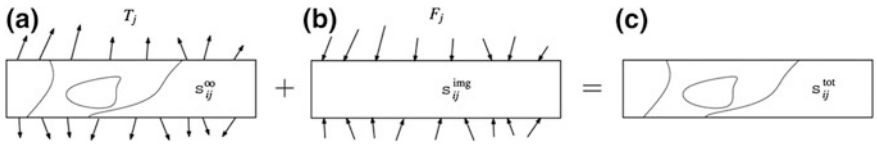

Fig. 7.7 **a** Traction forces developing at the surface of a film when assuming that the dislocations in the film generate the same stress field σ_{ij}^{∞} as in a bulk infinite solid; **b** Such traction forces can be canceled by invoking an image stress field σ_{ij}^{img}; **c** The sum of these two fields yields the stress field σ_{ij}^{tot} inside the film. Taken with permission from Ref. [43]

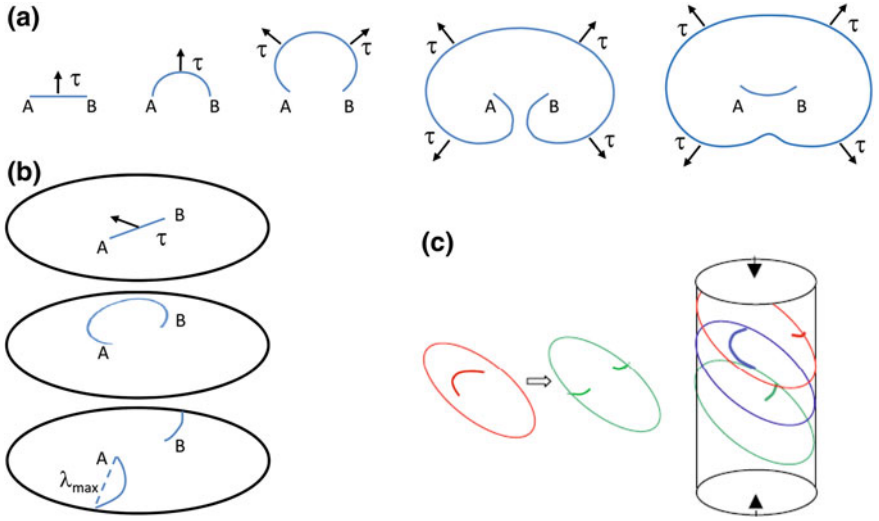

Fig. 7.8 **a** Operation of a Frank-Read source of dislocation. It starts as a straight dislocation in a slip plane. The two ends of the dislocation, named as "A" and "B", stay pinned. As soon as a shear stress is applied on the slip plane, the dislocation lengthens and curves to an arc, while its ends stay pinned. The dislocation bends further and then separates into a loop encircling the pins and into a new dislocation joining the pinning points. While the loop expands further, a new loop is being formed; **b** In a sample of finite dimension, the dislocation separates into two "arms" before it can form a loop, i.e. the source of dislocation is "truncated". The original double-ended source then splits into two single-ended sources. The longest of the two arms, i.e. the one whose pin on average has the longest distance from the free surface (λ_{max} in the figure) is the one that determines the critical resolved shear stress; **c** Single-ended sources in a family of slip planes (i.e. where the "slip" will occur during plastic deformation) in an elongated micro-/nano-particle. Panel c has been adapted with permission from Ref. [42]

cylinder-shaped particle. In a sample of finite dimension, the dislocation will separate into two "arms" before being able to form a loop, because it will meet the surface and will be truncated there. There will be now two single-ended sources, each with one end pinned. The interaction of each source with the surface is difficult to model, but most likely the image stress due to the surface will tend to rotate the dislocation line until it is perpendicular to the surface (as also found for dislocations in free standing films [43]).

The stress required to move each of these arms around its pinning point will depend on the shortest distance of its respective pin from the surface. In particular, the longer arm is the one that will determine the CRSS, because less stress will be required to move this arm. In a sample with a distribution of several single-ended (or equivalently, single-armed) sources, the arm with the longest length will determine the CRSS. The model of Parthasarathy et al. [42] starts with a cylinder of radius R and length L, by considering n pins (i.e. an n number of sources, located randomly in the sample) and evaluates the distribution of these single-armed source lengths. The number of sources is proportional to the dislocation

density in the material (assumed as $10^{12}/m^2$ in nickel microcrystals [44]) and to the volume of the sample: the bigger the volume, the higher the number of sources. The results of both analytical solutions and numerical simulation of their model, for a cylinder of unit radius and with orientation of slip planes equal to 45°, are reported in Fig. 7.9a. They show that the mean source length decreases when decreasing the number of sources, hence with decreasing sample volume. A decrease in source length corresponds to an increase in CRSS. The authors also compared their results with various sets of experimental data, and found a good agreement (Fig. 7.9b). Therefore, this simple model which considered a statistical variation in the source length of dislocations, due to the finite size of the crystal, could rationalize the increase in yield strength at decreasing sample size.

More elaborate models, combining some of the mechanisms described above have been proposed. Recently, Norfleet et al. [34] combined traditional mechanisms of interactions of dislocations during work hardening ("dislocation forest hardening"), with source truncation hardening. Another work, by Malygin [5], presented a theoretical analysis of plasticity in microcrystals and nanocrystals that takes into account also the generation of dislocations from surface sources and escape of dislocations from the surface. While generation of defects from surface leads to strain hardening, their escape from the surface tends to counterbalance it, and equilibration between the two processes is predicted by the model to occur at the early stages of plastic deformation, a mechanism termed as "exhaustion" of strain hardening, which indeed matches with results from experiments. The detailed description of these models is however beyond the scope of this book, and the interested reader is directed to those articles for more insights.

7.6.4 *Surface-Controlled Dislocation Multiplication in Metallic BCC Micro/Nanopillars*

The mechanisms of dislocation starvation and source truncation hardening have been proven plausible for explaining to plastic behavior of micro/nanopillars of various metals, especially the *fcc* ones. However, none of those mechanisms have in reality clarified at a microscopic level how a single dislocation moves inside a micropillar once it is formed, or even why dislocations junctions form. In order to answer all these questions, modeling is needed in addition to experiments. Several numerical simulations of mechanical behavior of materials are now available, which, coupled with experimental results on a wide variety of samples, are starting to shed light on the mechanisms of plasticity in crystals ranging from micron to sub-micron to nanometer scale [46]. Among them, discrete dislocation dynamics and its implementations (for example with finite element approaches) clearly stands out [36, 47–50].

Recent molecular dynamics studies have shown for example that a different mechanism of plasticity can be operative in *fcc* metal micro-pillars [51]. Various

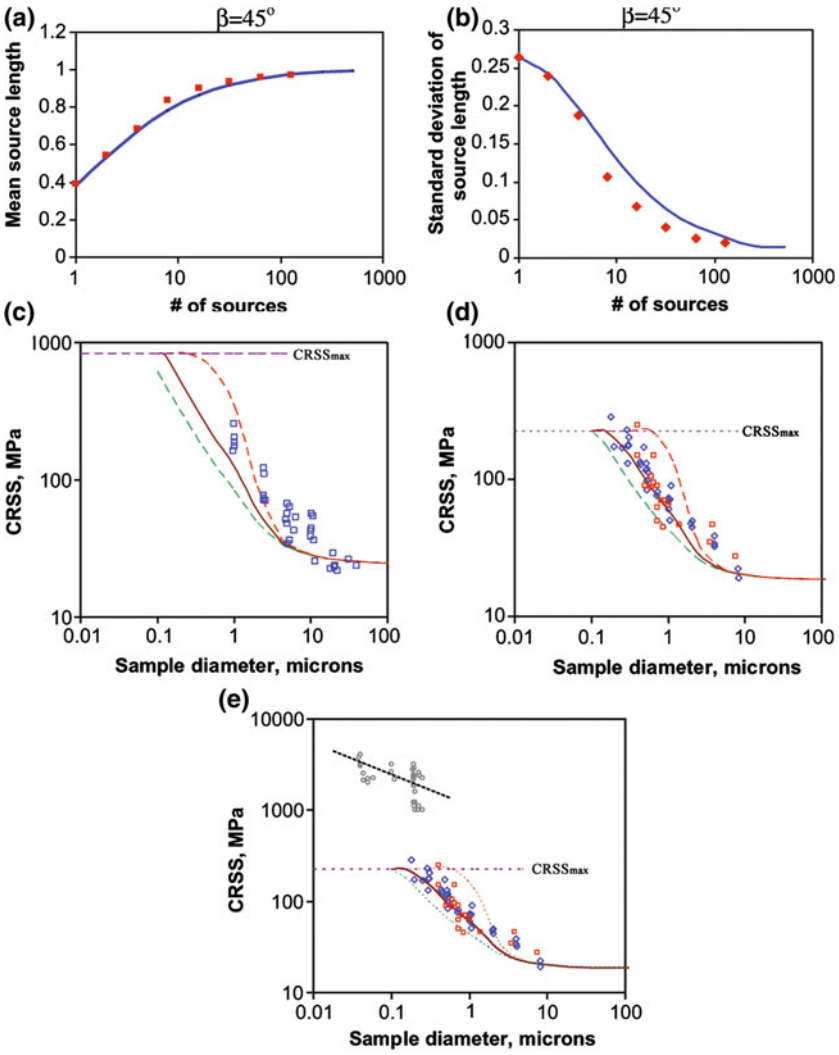

Fig. 7.9 **a** Mean source length and standard deviation, as a function of the number n of sources, using the model of Parthasarathy et al. [42], for a cylinder of unit radius and with orientation of slip planes equal to 45°. All the other parameters used in model are referred to an *fcc* crystal, and the dislocation density is taken as $10^{12}/m^2$ (as measured in nickel). Dots are the results of numerical simulations, lines are the analytical equations; **b** CSSR versus sample diameter for nickel micropillars. Blue squares represent experimental data from Refs. [32, 44]. The continuous line reports the CRSS as calculated by the model using the mean source length as extracted from the distribution, while the dotted lines report the corresponding CRSS calculated using the upper and lower standard deviations from average source length, respectively. The horizontal dotted line is the maximum value of CSSR attainable according to the model; **c** CSSR versus sample diameter for gold micropillars. Blue and red symbols refer to experimental data from Refs. [33, 45] while the various lines refer to the model as described in panel b; **d** This panel reports the same data as in panel **c**, but in addition it displays data from gold nanowires (gray dots interpolated with a black dotted line), taken from Ref. [11]. All panels have been adapted with permission from Ref. [42]

effects have been found to concur to this different behavior, namely image stresses and the different structure of dislocations in *bcc* metals. In brief, simulations have found that a dislocation generated from the surface of a micropillar, before exiting the pillar is able to generate one or more dislocations that move in a direction opposite to it. Since this process can be repeated, a single dislocation can generate several dislocations, hence can cause a considerable amount of plastic deformation, which is remarkably different from the case of *fcc* metal micropillars [51].

The most relevant results of the simulations are shown in Fig. 7.10. A dislocation with Burgers vector $[111]/2$ is initially present in a $(01\bar{1})$ glide plane (Fig. 7.10a). The dislocation quickly reorients with the Burgers vector and becomes a screw dislocation (see Fig. 7.10b, also any non-screw dislocation in a *bcc* crystal would have instead moved fast and left already the crystal). While continuing to move, this dislocation generates a "cusp" (Fig. 7.10c), which later evolves into a loop (Fig. 7.10d). The loop expands further (Fig. 7.10e), until it meets the surface, thus generating two additional dislocations (Fig. 7.10f). Of these two new dislocations, one travels in the same direction as the original dislocation, while the other moves in the opposite direction (i.e. opposite Burgers vector).

These simulations show clearly that a micro/nano-pillar of a *bcc* metal is unlikely to be found in a dislocation starved state, as a well defined mechanism exist in it for dislocation multiplication, and that a *bcc* micropillar should have a higher number of dislocations than a *fcc* micropillar of the same diameter. Results of both molecular dynamics and dislocation dynamics simulations have indicated that there exists a critical stress σ_c, below which this mechanism is however not operative, namely the cusp is able to escape the pillar without generating a loop. Interestingly enough, the larger the pillar, the smaller is σ_c, meaning that in smaller pillars such dislocation multiplication requires a large stress (for example around 5 GPa in a Mo pillar of 36 nm diameter, according to simulations [51]).

Weinberger et al. [51] pointed out that these simulations help to understand the so-called "strain-softening" effect seen in *bcc* Mo micropillars that were initially

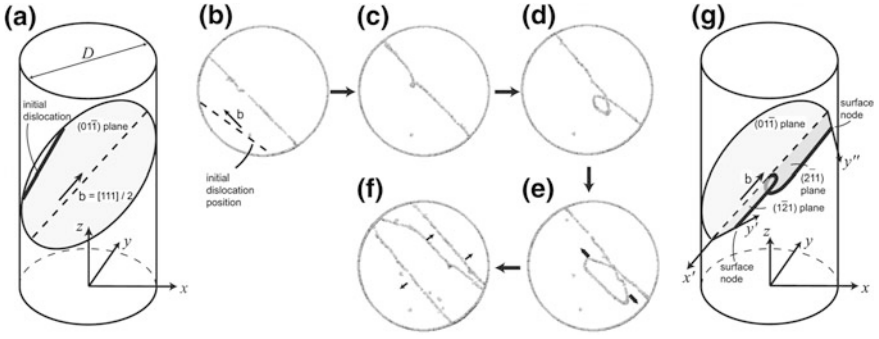

Fig. 7.10 Mechanism of dislocation multiplication in a micropillar of a *bcc* metal. **g** Three-dimensional geometry of the dislocation. Taken with permission from Ref. [51]

defect-free [52] and which behaved elastically up to 10 GPa, and then suddenly collapsed. Indeed, as soon as a critical stress is reached in small micropillars, a large number of dislocations is formed, i.e. a sort of avalanche effect is generated which suddenly leads to a large plastic deformation. Things are more complicate in the case of large micropillars, because in these cases self-multiplication of dislocations creates rapidly a large number of dislocation junctions, which act to stop the further movement of dislocations (i.e. strain hardening occurs).

7.6.5 General Remarks

More in general, by taking into account the various mechanisms, one can identify broadly three size regimes in which plastic deformation follows three different pathways [21]: (1) the nano-regime, below a few hundreds of nm, in which materials exhibit a considerably high strength, because they are mainly dislocation-free. In this regime, the plastic behavior is often stochastic, i.e. is characterized by the "catastrophic" nucleation of a single defect, which can occur at a different stress from sample to sample, and which initiates various events that lead to a sudden deformation of the material, via a "strain burst". So no hardening is usually observed in this size regime and the sample undergoes a brittle failure; (2) In the size range from a few hundred of nm to a few microns, the plastic behavior is governed by effects such dislocation starvation, source truncation, dislocation multiplication (in *bcc* crystals) and other effects as discussed earlier. Broadly speaking, this regime sets in as soon as the average distance between dislocations in of the same order of the size of the sample. Also in this regime plasticity can be governed by stochastic events that can lead to strain bursts, as shown earlier; (3) Above a few microns, the plasticity is basically as in the bulk, hence is dictated by dislocation forest hardening.

7.7 Buckling

Buckling (i.e. lateral bending or bowing) is a failure mode of a column or pillar subject to compressive strain, which is due to mechanical instability. This type of column failure usually happens to columns that are very long and thin. There is another buckling process that is often observed, which is called self buckling. Here a free-standing, vertical column, with density ρ, Young's modulus E, and radius r, will buckle under its own weight if its height exceeds a certain critical height.

The Euler-Bernoulli theory is often used for calculating the maximum axial load that a long, thin, ideal column can carry without buckling [53]. An ideal column is considered as perfectly straight, homogeneous, and free from any initial stress. The maximum load (critical load), causes the column to be in a state of unstable equilibrium, that is, any increase in the load, or the introduction of the

slightest lateral force, will cause the column to fail by buckling. The Bernoulli–Euler equation for a straight column under uniaxial compression is given by:

$$P_{\text{crt}} = \frac{C\pi^2 EI}{L^2} \tag{7.6}$$

where C is a parameter that depends on the end condition of the column, P_{crt} is the critical load, E is Young's modulus of elasticity, L is the length, and I is the moment of inertia. In the case of a rod of diameter d, I is equal to $\pi d^4/64$, while in the case of a tube of inner diameter d_i and outer diameter d_o I is equal to $\pi\left(d_0^4 - d_i^4\right)/64$. The starting point in the formulation of the Euler bending model is to consider the column as an elastic medium, obeying to the linear form of the Hooke's law, and consisting of "fibers" under uniaxial compression and under distributed lateral pressure. A more elaborate version of this theory was developed by Timoshenko, who took into account also the possibility for the beam to be deformed by shear, and which was found to describe more accurately the behavior of low aspect ratio beams [54–56].

Both the Bernoulli–Euler and the Timoshenko models are based on linear elasticity theory. One major over-simplification of this theory however is that the stress at a given point in a material is dependent linearly on the strain at that same point (and only at that point) in the material, while no information is included about the long range interatomic and intermolecular cohesive forces. This lack of length scale information in the "local" elasticity theory makes its application questionable to nanostructures. These cannot be considered any more as a continuum but instead their lattice parameter and/or interatomic distances are not any more negligible with respect to one or more of their dimensions (they should be rather seen as a "granular" medium than as a continuum). An example of behavior that cannot be predicted by the standard "local" Bernoulli–Euler beam model is the decrease in phase velocity of wave propagation in carbon nanotubes at high frequencies, due to a strong contribution of the peculiar nanotube microstructure to the flexural wave dispersion [57].

A major advancement in this field has been first of all the development by Eringen of the theory of non-local continuum mechanics [58, 59], in which the stress at each point of a given body is a function of the strain at all the other points of the body, and as such this theory can take into account the "internal" length scale of the forces for that specific material. The equations of Eringen contain the so-called scale coefficient $e_0 a$, in which a defines the internal characteristic length (for example the lattice parameter or an interatomic distance), while the parameter e_0 is related to the specific material and can be estimated by fitting experimental data. The $e_0 a$ term has the dimensions of a length and can range from a fraction of a nm up to a few nm.

Following the works of Eringen, many reports have appeared on the application of the model of non-continuum mechanics to both the Bernoulli–Euler pillar (see Ref. [60] and references cited therein) and the Timoshenko pillar [57, 61]. Wang et al. for example [61] derived an expression relating the buckling load for a non-local Timoshenko rod/tube P to the buckling load P_E for a local Bernoulli-Euler rod/tube:

$$P = \frac{P_E}{1 + \frac{P_E}{K_s GA} + (e_0 a)^2 \frac{P_E}{EI}} \tag{7.7}$$

in which A is the cross-sectional area of the pillar, K_s is the shear correction factor of the Timoshenko theory, E and I are again Young's modulus of elasticity and the moment of inertia of the pillar, and G is the shear modulus. The expression above shows that the local Euler buckling load is obtained by setting $K_s \to \infty$ and $a = 0$, the non-local Euler buckling load when setting $K_s \to \infty$ and $a \neq 0$, and the local Timoshenko load when $a = 0$. The authors compared the various loads with each other for different aspect ratios of the rods and for different values of the scale coefficient $e_0 a$. They found that the buckling load is reduced when considering the non-local models, especially when the pillars have short aspect ratios (from the expression above one can already deduce that the buckling load P decreases when the scale coefficient $e_0 a$ increases). Therefore, the small scale effect has the same influence on the buckling load as the transverse shear deformation.

Especially in the case of piezoelectric nanodevices, their mechanical characterization and most notably the study of the buckling behavior of a given nanostructure are extremely important. As of today, buckling studies have focused mainly on carbon nanotubes and on ZnO nanorods/nanowires [26, 61–67]. Most notably wurtzite ZnO, due to its noncentrosymmetric nature, has been used as piezoelectric material, for example in piezoelectric thin films for high-frequency bulk acoustic wave and surface acoustic wave transducers and resonators. We will mention here, as a representative experiment, the work of Riaz et al., who studied the buckling behavior of ZnO nanorod arrays and of nanotube arrays obtained by the same nanorods via chemical etching [66]. Each rod on average was 208 nm in diameter and 2219 nm in length, while in the corresponding nanotubes obtained via chemical etching the inner diameter was 125 nm on average. In their experiments, carried out with a nanoindenter, an area containing a large number of rods (or of tubes) was loaded to a given force and then unloaded in a force controlled mode [66]. The mechanical behavior of the two samples is shown in Fig. 7.11. In both samples (Fig. 7.11a, c), the loading portion of the curve can be divided in three zones, namely a prebuckling zone, a buckled zone and a post-buckled zone. In the prebucking zone the force increased linearly with displacement, so both nanorods and nanotubes were stable in this region, up to the buckled zone, in which the rods and the tubes became unstable. The load at which the rods were unstable (2890 μN) was considerably larger than that at which the nanotubes were unstable (697 μN). The postbuckled zone in both samples had many critical points (indicated by 1, 2, 3,… in the curves). At each of this point, there was a buckling event that deformed the samples more and more and also stiffened them more, so that more force was required to generate another buckling event.

It can be clearly seen that the nanotubes array sample was more fragile than the nanorod array sample, first because the buckling load in nanotubes is smaller than in the corresponding "non-hollow" nanorods (i.e. lower moment of inertia), and also because the chemical etching most likely produced structural defects that should be sensitive to buckling. The authors performed also loading–unloading

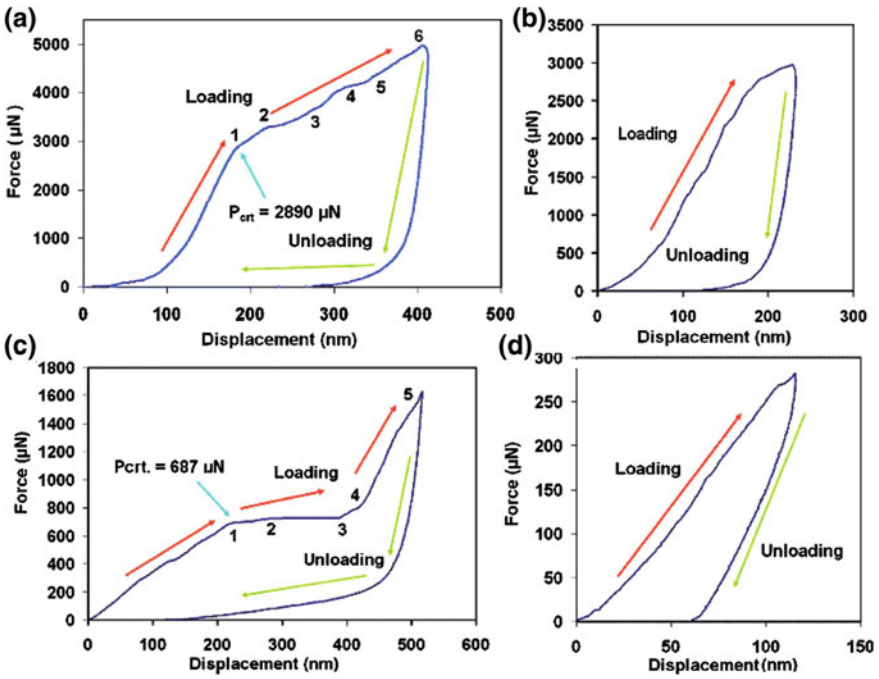

Fig. 7.11 **a–b** Load versus displacement curve of the as grown ZnO nanorods from indentation experiment: **a** buckled ZnO nanorods, and **b** bending flexibility of ZnO nanorods curve. **c–d** Load versus displacement curve of the etched ZnO nanotubes from the nanoindentation experiment, **a** buckled ZnO nanotubes, and **b** bending flexibility of ZnO nanotubes curve. Taken with permission from Ref. [66]

experiments on fresh regions of both samples, but in this case the force applied was only up to the first critical point (Fig. 7.11b, d). These experiments probed in practice the bending flexibility of the sample. No critical point was observed in these experiments, and the nanotube array sample exhibited higher displacement than the nanorods array sample, such that the nanotubes were found to be roughly five times more flexible than the nanorods, which the authors claimed could be useful for piezoelectric devices.

7.8 Melting Studies of Elongated Inorganic Nanoparticles

We close this section with a brief overview of the melting studies in elongated inorganic nanoparticles. At the melting point, a material undergoes a transition from the solid state to the liquid state. The melting point depends both on the specific composition of the material and on its size. Nanoparticles exhibit lower melting point temperatures as compared to their bulk counterpart, because of the large fraction of (more reactive) surface atoms. Such behavior can be explained by

the simple capillary theory of equilibrium of finite phases. The melting temperature in nanoparticles is inversely proportional to the radius of the nanoparticles [68]. Generally, melting of nanoparticles starts at their surfaces. Experimental techniques used to observe the melting of nanoparticles include for example X-ray [69, 70] and electron diffraction [68, 71, 72], calorimetry [73], femtosecond laser spectroscopy [74] and surface Brillouin scattering [75]. Several reports have shown that samples of metal nanorods made of the same material, but differing from each other in terms of average diameters and lengths, have dissimilar melting points. More specifically, shortening of the rod length while keeping the diameter constant results in a lowering of the melting temperature.

Of particular relevance are melting studies involving ultrafast lasers pulses. When gold nanorods in colloidal solution are irradiated with femtosecond pulses having energies in the mJ range, they are transformed into spherical nanoparticles [74]. The femtosecond laser pulse heats the electrons of the gold nanorods, which then couple to the lattice phonons [76, 77]. As the nanorod lattice becomes hot, the nanorod melts and isomerizes into the more thermodynamic stable spherical particle shape. This can be followed optically, by monitoring the change in absorption intensity of the longitudinal surface plasmon band of an aqueous solution of gold nanorods as a function of the number of laser pulses: indeed when complete shape transformation of nanorods to nanospheres takes place, the longitudinal surface plasmon band disappears (see also Sect. 7.4 of this review). An important parameter in these studies is the energy required to melt a nanoparticle. El-Sayed et al. derived this energy in the case of a gold nanorod, based on thermodynamic reasoning, spectroscopic measurements and using bulk values (i.e. the melting temperature T_m and the enthalpy of fusion ΔH_{fus} of gold (63.7 J/g) were used) [78]. The energy E_{NR} required to melt a single gold nanorod was calculated experimentally as:

$$\mathrm{E_{NR}} = \mathrm{c_p} \times \mathrm{m} \times \Delta\mathrm{T} + \mathrm{m} \times \Delta\mathrm{H_{fus}} \tag{7.8}$$

where ΔT is the temperature difference in Kelvin between room temperature (25 °C) and the melting temperature T_m (1064.18 °C) of bulk gold; c_p is the specific heat capacity of metallic gold (0.129 J/g K) and m is the mass of a gold nanorod. This equation could be further used for other metallic nanorod system too. The energy threshold for the complete melting of the nanorod distribution into spherical nanoparticles was determined spectroscopically by Link et al. [78]. It was found that it took about 60 femtojoules (fJ) to melt a gold nanorod with an aspect ratio of 4.1 (44 × 11 nm) [78].

The melting temperature of copper nanorod arrays synthesized via oblique angle sputter deposition was found to be much lower than the bulk melting point (1083 °C) [79]. Different melting stages of Cu nanorods, as observed under SEM, are displayed in Fig. 7.12. The as-deposited nanorods were ∼ 2300 nm in length, ∼100 nm in diameter, and were separated from each other by gaps varying between ∼10 and ∼30 nm. The melting process was investigated via analysis of SEM, TEM, and XRD measurements. A pre-melting stage (or surface melting)

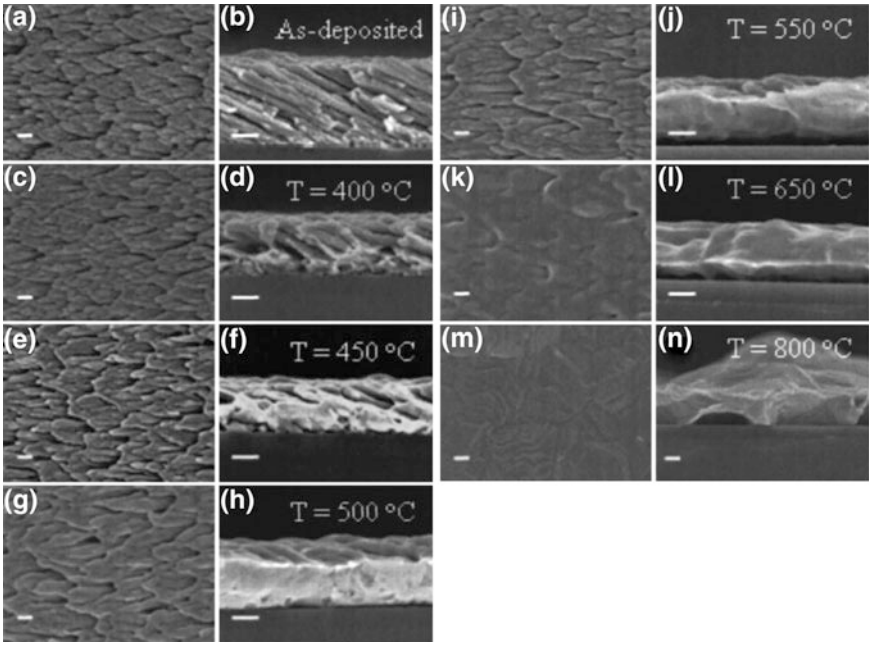

Fig. 7.12 Top views (**a**, **c**, **e**, **g**, **i**, **k**, **m**) and cross-sectional SEM views (**b**, **d**, **f**, **h**, **j**, **l**, **n**) of copper nanorod arrays annealed at various temperatures. A different sample was used for each annealing temperature. Pre-melting starts at ~400 °C and a continuous film is formed at T > 550 °C. The scale bars shown are 300 nm long. Taken with permission from Ref. [79]

was observed to occur at an annealing temperature of ~400 °C under vacuum. As the temperature was raised, the arrays of Cu nanorods started to coalesce and formed a dense continuous film with a (111) texture at ~550 °C. The enhanced surface diffusion and low temperature pre-melting in the present Cu nanorods are believed to be mainly due to their high surface/volume ratio. The authors speculated that the defects in the rods may also play a role in the pre-melting.

7.9 Outlook

The Young's modulus, strength, and toughness of elongated nanostructures are important from the view point of different unmatched proposed applications. However, there is little direct knowledge of these key mechanical properties yet. Still, various studies have investigated many types of different particles and potential applications related to their mechanical properties: the most studied systems are carbon nanotubes, Si-nanowires, CdSe nanorods, CdS nanorods, SnO_2 nanorods, SiC nanorods, etc. To rationalize the applications of elongated nanoparticles, we must discuss carbon nanotubes (CNTs) in the first place which actually finds applications

in vast areas. They are used as novel materials in the field of molecular-scale engineering and quantum technology based on their mechanical properties. The magnitude of higher order of Young's modulus [15, 80] and the capability of sustaining high strains without fracture [81] make CNTs the strongest materials known today. Because of the superior strength, they play a major role as functional components in nanomaterials and nano-electromechanical systems (NEMS). Another application of these CNT's is to excite micro-electromechanical systems (MEMS) by the AC and/or DC electrostatic actuation. Here, by applying nominal potential difference between the CNT (cantilevered) and the electrode, the produced beam bends and approaches the electrode plate and the elastic force tends to return the nanotube back into the undeformed position [82]. Single and multi-walled nanotubes can yield materials with exceptionally high toughness [83, 84]. However, while most of the extraordinary mechanical properties observed in CNTs arise from single nantubes, current applications are mainly limited to composites using bulk amounts of CNTs in their formulation. Motta et al. have fabricated CNT yarns with strengths as high as ~ 9 GPa at small gage lengths of ~ 1 mm [85].

Yang el al. have demonstrated silicon-NW-based resonant NEMS with on-chip integrated electronic actuation and detection at room temperature [86]. By using these Si-NWs for frequency conversion and exploiting their intrinsic strong piezoresistive effect, they have developed a new 2ω piezoresistive detection technique, which provides efficient readout of very high frequency (VHF) devices with progressively shrinking dimensions and high impedances.

SnO_2 nanorods have been used as field emitters in combination with graphene. Actually a fabricated electron source device using a flexible graphene substrate with in situ grown aligned SnO_2 nanorods shows excellent field emission properties with a low threshold field value, and very high current density at a constant applied field [87].

Finally we would like mention some of the commercial applications of elongated nanoparticles in the market. There are few companies which have included elongated nanoparticles (mainly CNTs) in their products. Easton for example has developed a baseball bat using carbon nanotube composite materials to improve strength and toughness (www.eastonsports.com). Nano-Tex used nanofibers in their garment products that repel spills, help stains wash out easily, provide long-lasting protection, extend the life of the fabric and retain the fabric's natural softness (www.nano-tex.com). Another company named Babolat has produced a super light tennis racket with a large head that is made from a CNT composite which in turn becomes ten times stiffer with larger striking surface than conventional graphite racket, but yet lighter (www.babolat.com). In general, many companies claim the use of nanofibers/nanotubes due to their better mechanical properties in their products. Clearly, we expect more companies in this list in the coming years.

References

1. Brenner SS (1959) In: Doremus RH, Roberts BW, Turnbull D (eds) Growth and Perfection of Crystals. Wiley, New York
2. Greer JR, Nix WD (2005) Size dependence of mechanical properties of gold at the sub-micron scale. Appl Phys A-Mater Sci Process 80(8):1625–1629
3. Chattopadhyay S, Chen LC, Chen KH (2006) Nanotips: growth, model, and applications. Crit Rev Solid State Mater Sci 31(1–2):15–53
4. Mazilova TI, Mikhailovskij IM, Ksenofontov VA, Sadanov EV (2009) Field-Ion microscopy of quantum oscillations of linear carbon atomic chains. Nano Lett 9(2):774–778
5. Malygin GA (2010) Size effects under plastic deformation of microcrystals and nanocrystals. Phys Solid State 52(1):49–57
6. Hetzberg RH (1989) Deformation and fracture mechanics of engineering materials. Wiley, London
7. Courtney TH (1999) Mechanical behavior of materials. Wiley, London
8. Hosford WF (2005) Mechanical behavior of materials. Cambridge University Press, Cambridge
9. Hirth JP, Lothe J (1982) Theory of dislocations, 2nd ed. Wiley, London
10. Milstein F (1980) Theoretical elastic behaviour of crystals at large strains. J Mater Sci 15:1071–1084
11. Wu B, Heidelberg A, Boland JJ (2005) Mechanical properties of ultrahigh-strength gold nanowires. Nat Mater 4(7):525–529
12. Wu B, Heidelberg A, Boland JJ, Sader JE, Sun XM, Li YD (2006) Microstructure-hardened silver nanowires. Nano Lett 6(3):468–472
13. Voisin C, Del Fatti N, Christofilos D, Vallee F (2001) Ultrafast electron dynamics and optical nonlinearities in metal nanoparticles. J Phys Chem B 105(12):2264–2280
14. Hartland GV (2006) Coherent excitation of vibrational modes in metallic nanoparticles. Ann Rev Phys Chem 57:403–430
15. Treacy MMJ, Ebbesen TW, Gibson JM (1996) Exceptionally high Young's modulus observed for individual carbon nanotubes. Nature 381(6584):678–680
16. Krishnan A, Dujardin E, Ebbesen TW, Yianilos PN, Treacy MMJ (1998) Young's modulus of single-walled nanotubes. Phys Rev B 58(20):14013–14019
17. Petrova H, Perez-Juste J, Zhang ZY, Zhang J, Kosel T, Hartland GV (2006) Crystal structure dependence of the elastic constants of gold nanorods. J Mater Chem 16(40):3957–3963
18. Hu M, Wang X, Hartland GV, Mulvaney P, Juste JP, Sader JE (2003) Vibrational response of nanorods to ultrafast laser induced heating: Theoretical and experimental analysis. J Am Chem Soc 125(48):14925–14933
19. Hu M, Hillyard P, Hartland GV, Kosel T, Perez-Juste J, Mulvaney P (2004) Determination of the elastic constants of gold nanorods produced by seed mediated growth. Nano Lett 4(12):2493–2497
20. Meyers MA, Mishra A, Benson DJ (2006) Mechanical properties of nanocrystalline materials. Progr Mater Sci 51(4):427–556
21. Kraft O, Gruber PA, Monig R, Weygand D (2010) Plasticity in Confined Dimensions. In: Annual review of materials research, vol 40, pp 293–317
22. Lu K, Lu L, Suresh S (2009) Strengthening materials by engineering coherent internal boundaries at the nanoscale. Science 324(5925):349–352
23. Brenner SS (1956) Tensile strength of whiskers. J Appl Phys 27:1484–1491
24. Shpak AP, Kotrechko SO, Mazilova TI, Mikhailovskij IM (2009) Inherent tensile strength of molybdenum nanocrystals. Sci Technol Adv Mater 10(4):art. n. 045004
25. Petrovic JJ, Milewski JV, Rohr DL, Gac FD (1985) Tensile mechanical-properties of sic whiskers. J Mater Sci 20(4):1167–1177
26. Wong EW, Sheehan PE, Lieber CM (1997) Nanobeam mechanics: elasticity, strength, and toughness of nanorods and nanotubes. Science 277(5334):1971–1975

27. Richter G, Hillerich K, Gianola DS, Moenig R, Kraft O, Volkert CA (2009) Ultrahigh strength single crystalline nanowhiskers grown by physical vapor deposition. Nano Lett 9:3048–3052
28. Weibull W (1951) A statistical distribution function of wide applicability. J Appl Mech 18:293–297
29. Pugno NM, Ruoff RS (2004) Quantized fracture mechanics. Phil Mag 84:2829–2845
30. Pugno NM, Ruoff RS (2006) Nanoscale Weibull statistics. J Appl Phys 99:024301–024304
31. Pugno NM, Ruoff RS (2007) Nanoscale Weibull statistics for nanofibers and nanotubes. J Aerosp Eng 20(2):97–101
32. Uchic MD, Dimiduk DM, Florando JN, Nix WD (2004) Sample dimensions influence strength and crystal plasticity. Science 305:986–989
33. Greer JR, Oliver WC, Nix WD (2005) Size dependence of mechanical properties of gold at the micron scale in the absence of strain gradients. Acta Mater 53(6):1821–1830
34. Norfleet DM, Dimiduk DM, Polasik SJ, Uchic MD, Mills MJ (2008) Dislocation structures and their relationship to strength in deformed nickel microcrystals. Acta Mater 56(13):2988–3001
35. Mikhailovskij IM, Poltinin PY, Fedorova LI (1983) Sov Phys Solid State 23:757
36. Gao Y, Liu ZL, You XC, Zhuang Z (2010) A hybrid multiscale computational framework of crystal plasticity at submicron scales. Comp Mater Sci 49(3):672–681
37. Gerberich WW, Tymiak NI, Grunlan JC, Horstemeyer MF, Baskes MI (2002) Interpretations of indentation size effects. J Appl Mech, Trans ASME 69(4):433–442
38. Nix WD, Gao HJ (1998) Indentation size effects in crystalline materials: a law for strain gradient plasticity. J Mech Phys Solids 46(3):411–425
39. Gilman JJ (1953) Deformation in crystalline materials. Appl Micromech Flow Solids pp 185–190
40. Shan ZW, Mishra RK, Asif SAS, Warren OL, Minor AM (2008) Mechanical annealing and source-limited deformation in submicrometre-diameter Ni crystals. Nat Mater 7(2):115–119
41. Nadgorny EM (1962) The properties of whiskers. Sov Phys 5(3):462–476
42. Parthasarathy TA, Rao SI, Dimiduk DM, Uchic MD, Trinkle DR (2007) Contribution to size effect of yield strength from the stochastics of dislocation source lengths in finite samples. Scripta Mater 56(4):313–316
43. Weinberger CR, Aubry S, Lee SW, Nix WD, Cai W (2009) Modelling dislocations in a free-standing thin film. Model Simul Mater Sci Eng 17:art. n. 075007
44. Dimiduk DM, Uchic MD, Parthasarathy TA (2005) Size-affected single-slip behavior of pure nickel microcrystals. Acta Mater 53(15):4065–4077
45. Volkert CA, Lilleodden ET (2006) Size effects in the deformation of sub-micron Au columns. Phil Mag 86(33–35):5567–5579
46. Koh AS, Lee HP (2006) Shock-induced localized amorphization in metallic nanorods with strain-rate-dependent characteristics. Nano Lett 6(10):2260–2267
47. Zbib HM, de la Rubia TD (2002) A multiscale model of plasticity. Intern J Plast 18(9):1133–1163
48. Espinosa HD, Berbenni S, Panico M, Schwarz KW (2005) An interpretation of size-scale plasticity in geometrically confined systems. Proc Natl Acad Sci 102(47):16933–16938
49. Shiari B, Miller RE, Klug DD (2008) Multiscale modeling of solids at the nanoscale: dynamic approach. Can J Phys 86(2):391–400
50. Liu ZL, Liu XM, Zhuang Z, You XC (2009) A multi-scale computational model of crystal plasticity at submicron-to-nanometer scales. Intern J Plast 25(8):1436–1455
51. Weinberger CR, Cai W (2008) Surface-controlled dislocation multiplication in metal micropillars. Proc Natl Acad Sci 105(38):14304–14307
52. Bei H, Shim S, George EP, Miller MK, Herbert EG, Pharr GM (2007) Compressive strengths of molybdenum alloy micro-pillars prepared using a new technique. Scripta Mater 57(5):397–400
53. Shigley JE, Mischke CR, Budynas RG (2004) Mechanical Engineering Design, 7th edn. McGraw-Hill, New York

54. Timoshenko SP (1921) On the correction for shear of the differential equation for transverse vibrations of prismatic bars. Phil Mag 6(41):744–746
55. Timoshenko SP (1922) On the transverse vibrations of bars of uniform cross section. Phil Mag 6(43):125–131
56. Timoshenko SP, Gere JM (1961) Theory of Elastic Stability, 2nd edn. McGraw-Hill, New Yok
57. Wang LF, Hu HY (2005) Flexural wave propagation in single-walled carbon nanotubes. Phys Rev B 71(19):art. n. 195412
58. Eringen AC (1972) Nonlocal polar elastic continua. Int J Eng Sci 10:1–16
59. Eringen AC, Edelen DGB (1972) On nonlocal elasticity. Int J Eng Sci 10:233–248
60. Peddieson J, Buchanan GR, McNitt RP (2003) Application of nonlocal continuum models to nanotechnology. Int J Eng Sci 41(3–5):305–312
61. Wang CM, Zhang YY, Ramesh SS, Kitipornchai S (2006) Buckling analysis of micro- and nano-rods/tubes based on nonlocal Timoshenko beam theory. J Phys D-Appl Phys 39(17):3904–3909
62. Young SJ, Ji LW, Chang SJ, Fang TH, Hsueh TJ, Meen TH, Chen IC (2007) Nanoscale mechanical characteristics of vertical ZnO nanowires grown on ZnO : Ga/glass templates. Nanotechnology 18(22):art. n. 225603
63. Riaz M, Fulati A, Zhao QX, Nur O, Willander M, Klason P (2008) Buckling and mechanical instability of ZnO nanorods grown on different substrates under uniaxial compression. Nanotechnology 19(41):art. n. 415708
64. Riaz M, Nur O, Willander M, Klason P (2008) Buckling of ZnO nanowires under uniaxial compression. Appl Phys Lett 92(10):art. n. 103118
65. Svensek D, Podgornik R (2008) Confined nanorods: Jamming due to helical buckling. Phys Rev E 77(3):art. n. 031808
66. Riaz M, Fulati A, Amin G, Alvi NH, Nur O, Willander M (2009) Buckling and elastic stability of vertical ZnO nanotubes and nanorods. J Appl Phys 106(3):art. n. 034309
67. Feng G, Nix WD, Yoon Y, Lee CJ (2006) A study of the mechanical properties of nanowires using nanoindentation. J Appl Phys 99(7):art. n. 074304
68. Goldstein AN, Echer CM, Alivisatos AP (1992) Melting In Semiconductor Nanocrystals. Science 256(5062):1425–1427
69. Sheng HW, Lu K, Ma E (1998) Melting of embedded Pb nanoparticles monitored using high-temperature in situ XRD. Nanostruct Mater 10(5):865–873
70. Peters KF, Cohen JB, Chung YW (1998) Melting of Pb nanocrystals. Phys Rev B 57(21):13430–13438
71. Smith DJ, Petfordlong AK, Wallenberg LR, Bovin JO (1986) Dynamic atomic-level rearrangements in small gold particles. Science 233(4766):872–875
72. Buffat P, Borel JP (1976) Size effect on the melting temperature of gold particles. Phys Rev A 13:2287
73. Lai SL, Guo JY, Petrova V, Ramanath G, Allen LH (1996) Size-dependent melting properties of small tin particles: nanocalorimetric measurements. Phys Rev Lett 77(1):99–102
74. Link S, Burda C, Mohamed MB, Nikoobakht B, El-Sayed MA (1999) Laser photothermal melting and fragmentation of gold nanorods: energy and laser pulse-width dependence. J Phys Chem A 103(9):1165–1170
75. Bottani CE, Bassi AL, Tanner BK, Stella A, Tognini P, Cheyssac P, Kofman R (1999) Melting in metallic Sn nanoparticles studied by surface Brillouin scattering and synchrotron-x-ray diffraction. Phys Rev B 59(24):15601–15604
76. Link S, Burda C, Mohamed MB, Nikoobakht B, El-Sayed MA (2000) Femtosecond transient-absorption dynamics of colloidal gold nanorods: Shape independence of the electron-phonon relaxation time. Phys Rev B 61(9):6086–6090
77. Del Fatti N, Flytzanis C, Vallee F (1999) Ultrafast induced electron-surface scattering in a confined metallic system. Appl Phys B 68(3):433–437
78. Link S, El-Sayed MA (2001) Spectroscopic determination of the melting energy of a gold nanorod. J Chem Phys 114(5):2362–2368

79. Karabacak T, DeLuca JS, Wang PI, Ten Eyck GA, Ye D, Wang GC, Lu TM (2006) Low temperature melting of copper nanorod arrays. J Appl Phys 99(6):art. n. 064304
80. Chopra NG, Zettl A (1998) Measurement of the elastic modulus of a multi-wall boron nitride nanotube. Solid State Commun 105(5):297–300. doi:10.1016/s0038-1098(97)10125-9
81. Yakobson BI, Campbell MP, Brabec CJ, Bernholc J (1997) High strain rate fracture and C-chain unraveling in carbon nanotubes. Comp Mater Sci 8(4):341–348. doi:10.1016/s0927-0256(97)00047-5
82. Rasekh M, Khadem SE (2011) Pull-in analysis of an electrostatically actuated nano-cantilever beam with nonlinearity in curvature and inertia. Int J Mech Sci 53(2):108–115. doi:10.1016/j.ijmecsci.2010.11.007
83. Zhang M, Fang SL, Zakhidov AA, Lee SB, Aliev AE, Williams CD, Atkinson KR, Baughman RH (2005) Strong, transparent, multifunctional, carbon nanotube sheets. Science 309(5738):1215–1219. doi:10.1126/science.1115311
84. Dalton AB, Collins S, Munoz E, Razal JM, Ebron VH, Ferraris JP, Coleman JN, Kim BG, Baughman RH (2003) Super-tough carbon-nanotube fibres—These extraordinary composite fibres can be woven into electronic textiles. Nature 423(6941):703. doi:10.1038/423703a
85. Motta M, Moisala A, Kinloch IA, Windle AH (2007) High performance fibres from 'Dog bone' carbon nanotubes. Adv Mater 19(21):3721. doi:10.1002/adma.200700516
86. He R, Feng XL, Roukes ML, Yang P (2008) Self-Transducing silicon nanowire electromechanical systems at room temperature. Nano Lett 8(6):1756–1761. doi:10.1021/nl801071w
87. Rujia Z, Zhang Z, Jiang L, Xu K, Tian Q, Xue S, Hu J, Bando Y, Golberg D (2012) Heterostructures of vertical, aligned and dense SnO_2 nanorods on graphene sheets: in situ TEM measured mechanical, electrical and field emission properties. J Mater Chem 22(36):19196–19201

Chapter 8
Outlook

In this book we covered several aspects connected with the physical properties of nanorods. In the following, we will summarize the major advances in this field, with emphasis on the present and foreseen applications, and we will give an outlook on what, in our opinion, will be the most significant advances and challenges laying ahead in this fascinating area of research.

Semiconductor nanorods have demonstrated extremely promising properties for optical applications both on the single nanoparticle level and for large assemblies. The shape anisotropy of nanorods leads to several interesting features in their optical behavior, such as linearly polarized emission, tunable emission wavelength via the Stark effect, and large absorption cross sections paired with strong quantum confinement. These properties make semiconductor nanorods superior to spherical nanocrystals in many respects and consequently current research makes a strong effort to improve nanorod synthesis and the techniques to implement them into device structures. One critical issue for light emitting applications is the number of defect states, since such states provide channels for non-radiative recombination. In this direction various core-shell types of nanorods have emerged that show superior performance with respect to rod homostructures. In order to achieve brighter emission, one or two shells of higher band gap materials can be grown around the emitting core material. One particularly promising approach for light-emitting devices is the core-shell structure that is fabricated via the seeded growth method, as discussed extensively in Chaps. 2, 3. This geometry, consisting of a spherical low band gap core embedded in a higher band gap rod-shaped shell, has several advantages: (1) the synthesis yields samples with a narrow size distribution, which leads to small FWHM of the emission peak and favors ordered assembly; (2) the emission wavelength and the electron (de)localization can be tailored, within certain limits, via the core size, and (3) non-radiative exciton recombination is greatly reduced compared to homostructures. Such core-shell nanorods can find applications on a single particle level in biological tagging, as single photon emitters (in combination with photonic crystals or cavities), or as light modulators. Self-assembly of nanorods into large scale ordered arrays enables the exploitation of some of the anisotropy-related properties also in macroscopic

R. Krahne et al., *Physical Properties of Nanorods*,
NanoScience and Technology, DOI: 10.1007/978-3-642-36430-3_8,

devices. For example, the polarized emission and the dipole antenna-like light field distribution have been demonstrated for micron to millimeter scale assemblies [1]. Moreover, large ensembles of nanorods show collective properties like amplified stimulated emission and lasing. Also here large research efforts are in progress aiming at increasing the control over the nanorod assemblies and their optical properties. One promising trend focuses on hybrid structures consisting of nanorod layers and organic materials. For example, films consisting of dense nanorod assemblies have already demonstrated their functionality in macro scale devices such as LEDs [2]. Another promising route is the use of collinear nanorod heterostructures, where the band offset at the interface can be tailored for the targeted application. Since such nanorods expose both materials on the surface they will be good candidates for applications as sensors or in photovoltaics.

For what concerns the exploitation of semiconductor nanorods in electrical devices, one critical aspect at present is the contact fabrication on a single nanorod level. This remains very demanding and costly, with little control over the contact resistance, and in most cases with no possibility of up-scaling of the device fabrication. Furthermore, the approaches described in Sect. 3.2 are not compatible with integrated CMOS technology. Therefore, the realization of practical electrical devices with single nanorods as active elements appears unlikely at present. In this sense the studies on single nanorods find their justification more from the basic research point of view, since they provide valuable information on the electronic structure of these novel nano-materials. The current trend goes towards nanorod heterostructures (we discussed the CdSe/CdS core shell rods, and the Au-sphere/nanorod dumbbells), which allow to tailor the band gap, enhance or reduce charge separation within the nanorod, or to combine electrical, magnetic, and optical functionality within a single nanostructure. We expect that basic research will make great advances in the next years in this direction. The situation is different for large scale assemblies of nanorods, where the challenge is to control the uniformity of the nanorod arrays in order to exploit the advantageous properties that result from their anisotropic shape. Large efforts have been made in this respect in the last years that yielded promising results. Centimeter-scale assemblies of laterally and vertically oriented nanorods have been demonstrated. Such large-scale assemblies will make nanorods interesting as active materials for photovoltaics, light emitting diodes, and sensors, in particular, since nanorods have demonstrated excellent optical properties that can be tailored via the shape and material composition.

Plasmonic nanoparticles have been among the most investigated materials in nanoparticle research and have found already application in many fields, like optics, sensing and biosensing, hyperthermia treatment in medicine, photovoltaics, and others. The possibility to tune the shape of nanoparticles, hence to manipulate the optical response both in the near field and in the far field, has opened new scenarios in both fundamental research and technological applications. One very exciting area of research in this field at present is the fabrication of ordered architectures of nanorods/nanowires, as these assemblies have shown coupling between plasmon modes of the individual components that leads to extended and

guided plasmonic modes, similar to photonic waveguides. All these architectures exhibit also tunable values of permittivity depending on the polarization directions, which will be useful for applications in metamaterials. As another example, precisely positioned metallic nanorods have been used as dipole nanoantennas, being capable of receiving optical power from a waveguide, localizing it and thus allowing it to be converted into an electrical signal by means of a plasmonic-to-electronic converter. This has extremely interesting implications for the integration of plasmonics into nanoelectronic circuits. A recent review covering this topic and other recent advances in plasmonics is the one by Gramotnev et al. [3]. Plasmonic nanoparticles, due to their capability of acting as nano-antennas, are finding increasing applications in photovoltaics and in photocatalysis, and certainly the ability to control the shape and the type of assembly of the nanoparticles will play a key role in all those fields.

An enormous effort has been made so far by the scientific community to study one-dimensional magnetic nanoparticles, such as ellipsoids, rods and wires. Even though basic science led this field of research (which is critical for a deep understanding of properties derived from shape-controlled and size-confined materials), the work has been strongly motivated by potential but crucial technological improvements derived from them. The significance of shape anisotropy in magnetic nanoparticles has been confirmed and supported by a huge amount of experimental and theoretical works. Shape anisotropy can significantly enhance the global magnetic anisotropy of small particles: the room temperature stabilization of magnetically ordered states in nanostructured materials has been often attributed to shape effects, in contrast to spherical particles which often show random fluctuations of their magnetic moment at that temperature. Such enhanced anisotropy is mainly translated in increased coercivities without compromising the small sizes of the single particles. Data-storage industry can greatly beneficiate from it by designing new magnetic data storage devices with higher densities, reduced dimensions and faster operational speeds.

Nanofabrication or preparation procedures of different types have been developed in the last decades for both oxide- and metal-based materials, with the exception of permanent nanomagnets, for which still several synthetic difficulties have to be overcome. Consequently, it is now possible to obtain 1D magnetic nanomaterials with controlled sizes down to which magnetic single domain phenomena can be studied. Moreover, high resolution magnetic characterization techniques are nowadays also available, by which classical micromagnetic theories can now be experimentally contrasted. The final exploitation of anisotropic magnetic particles in current industry strictly requires the regular and homogeneous organization of the elongated magnetic building blocks in a device. Several strategies have been shown to be useful for this target, especially for metals, in which research has been much more focused due to their higher technological importance compared to oxides. However, this issue has been only partially addressed and will probably become a key aspect for the future implementation of anisotropic nanoparticles in technology.

Theory has always played an important role in the study of magnetic systems. Despite this, there is still a lack of models accounting for finite size effects present in 1D nanostructures. With the recent experimental capabilities for studying magnetization reversal processes and domain wall dynamics of 1D nanostructured systems, the doors for the development of a new generation of spintronic devices are open. However, classical models seem to be insufficient to predict all physical phenomena occurring in these finely engineered particles. Hence, the formulation of specific micromagnetic theories that can be applied to most of the technologically interesting magnetic materials is, and will probably be, a very active research field.

It is also worth to mention the increasing role of magnetic nanoparticles in biomedicine. Unfortunately, toxicity and chemical stability concerns have significantly limited their study. Therefore, still very few experimental evidences are available to support the use of 1D magnetic nanostructures in this field. From a theoretical point of view, the increased magnetic anisotropies of 1D systems could also be crucial for the development or improvement of innovative diagnostic and therapeutic techniques. The potential of elongated nanoparticles in medicine will probably encourage their study in the coming years.

It is now increasingly evident that the catalytic properties of anisotropic nanocrystals (mainly rod-shape) are different from their bulk and isotropic nanostructures in terms of their activity and specificity for various reactions. In particular, in the rod-like or elongated morphology their high surface areas and the exposure of clearly defined crystals facets are the main factors that can enhance their catalytic properties. However, the shape-dependent catalytic function of anisotropic nanocrystals needs to be investigated further in terms of their surface and electronic properties. This will help not only to draw clear relationships between the shape and catalytic properties but also to develop the application methods of such catalysts that are appropriate for different reaction conditions. Metal nanorods and metal NPs incorporated metal-oxide (support) nanorods hetero-structures seem promising nanocatalysts for a number of useful chemical reactions, such as water-splitting, methanol oxidation, CO oxidation, and obviously in organic synthesis. As their optical absorption sweeps across ultraviolet, visible and infra-red regions, they could be employed as photo-catalysts for a wide range of photo conversion reactions. Thus, such catalytic systems based on nanorods or elongated nanocrystals can offer energy-efficiency and precise scalability of materials conversion into targeted products, and their exploitation in cells and electrochemical super capacitors is expected to increase in the years to come.

For what concerns the mechanical properties of elongated nanoparticles, we can certainly say that research in this area is still in its infancy. Only recently, thanks to advances in synthesis and micro/nanofabrication, as well as in the development of more sophisticated setups for mechanical testing, reliable data has become available, but the results are not always straightforward to interpret. Various studies have for example shown that mechanical behavior in confined dimensions is dependent on a wide range of parameters, including the conditions of the experiment itself, and various open questions (for example as to whether Young's

modulus is a good stiffness indicator for nanostructures) will require increasing attention in the future. Also, modeling of mechanical properties at the nanoscale is still a formidable challenge and only in the last few years, thanks to innovations in modeling and increased computing power, it has been possible to carry out large scale simulations in three dimensions. Issues in this area are particularly critical as devices are being increasingly miniaturized and their mechanical response needs to be addressed. Further exciting directions in this field are for example the study of phase transitions in confined systems, as well as shock-induced amorphization, as it has been observed that metallic one-dimensional structures are transformed into amorphous structures when subject to high strain rates [4]. All these transformations need to be carefully studied, especially considering that nanoscale materials and devices in the future are expected to be used in applications involving extreme conditions.

References

1. Carbone L, Nobile C, De Giorgi M, Sala FD, Morello G, Pompa P, Hytch M, Snoeck E, Fiore A, Franchini IR, Nadasan M, Silvestre AF, Chiodo L, Kudera S, Cingolani R, Krahne R, Manna L (2007) Synthesis and micrometer-scale assembly of colloidal CdSe/CdS nanorods prepared by a seeded growth approach. Nano Lett 7(10):2942–2950
2. Rizzo A, Nobile C, Mazzeo M, De Giorgi M, Fiore A, Carbone L, Cingolani R, Manna L, Gigli G (2009) Polarized light emitting diode by long-range nanorod self-assembling on a water surface. ACS Nano 3(6):1506–1512
3. Gramotnev DK, Bozhevolnyi SI (2010) Plasmonics beyond the diffraction limit. Nat Phot 4(2):83–91
4. Koh AS, Lee HP (2006) Shock-induced localized amorphization in metallic nanorods with strain-rate-dependent characteristics. Nano Lett 6(10):2260–2267

Index

R. Krahne et al., *Physical Properties of Nanorods*,
NanoScience and Technology, DOI: 10.1007/978-3-642-36430-3,